CELL DEATH AND TARGETED CANCER THERAPIES

EDITED BY: Ozgur Kutuk, Triona Ni Chonghaile, Tugba Bagci-Onder and Uwe Knippschild

PUBLISHED IN: Frontiers in Cell and Developmental Biology

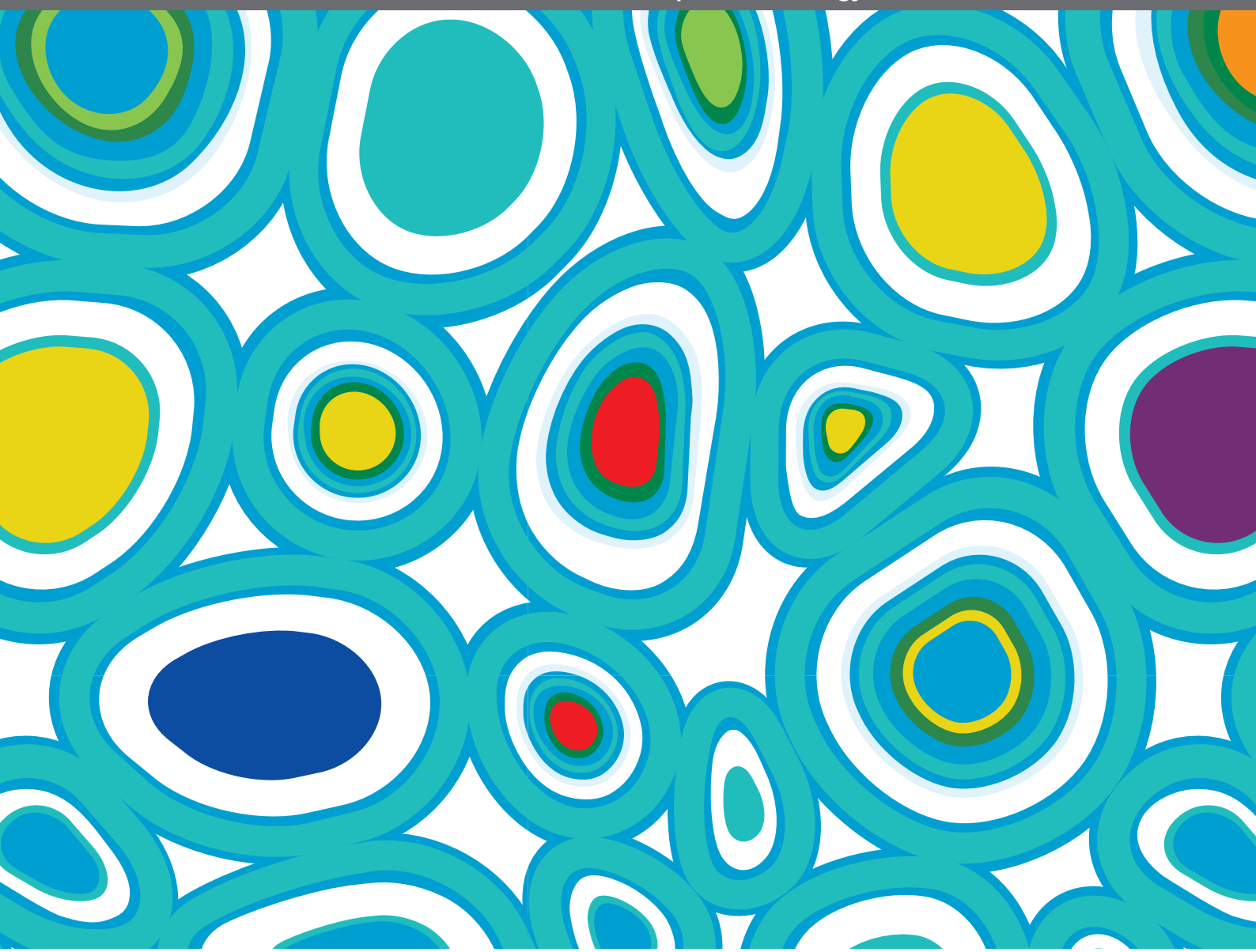

frontiers Research Topics

ISSN 1664-8714
ISBN 978-2-88976-684-0
DOI 10.3389/978-2-88976-684-0

About Frontiers

Frontiers is more than just an open-access publisher of scholarly articles: it is a pioneering approach to the world of academia, radically improving the way scholarly research is managed. The grand vision of Frontiers is a world where all people have an equal opportunity to seek, share and generate knowledge. Frontiers provides immediate and permanent online open access to all its publications, but this alone is not enough to realize our grand goals.

Frontiers Journal Series

The Frontiers Journal Series is a multi-tier and interdisciplinary set of open-access, online journals, promising a paradigm shift from the current review, selection and dissemination processes in academic publishing. All Frontiers journals are driven by researchers for researchers; therefore, they constitute a service to the scholarly community. At the same time, the Frontiers Journal Series operates on a revolutionary invention, the tiered publishing system, initially addressing specific communities of scholars, and gradually climbing up to broader public understanding, thus serving the interests of the lay society, too.

Dedication to Quality

Each Frontiers article is a landmark of the highest quality, thanks to genuinely collaborative interactions between authors and review editors, who include some of the world's best academicians. Research must be certified by peers before entering a stream of knowledge that may eventually reach the public - and shape society; therefore, Frontiers only applies the most rigorous and unbiased reviews.
Frontiers revolutionizes research publishing by freely delivering the most outstanding research, evaluated with no bias from both the academic and social point of view. By applying the most advanced information technologies, Frontiers is catapulting scholarly publishing into a new generation.

What are Frontiers Research Topics?

Frontiers Research Topics are very popular trademarks of the Frontiers Journals Series: they are collections of at least ten articles, all centered on a particular subject. With their unique mix of varied contributions from Original Research to Review Articles, Frontiers Research Topics unify the most influential researchers, the latest key findings and historical advances in a hot research area! Find out more on how to host your own Frontiers Research Topic or contribute to one as an author by contacting the Frontiers Editorial Office: frontiersin.org/about/contact

CELL DEATH AND TARGETED CANCER THERAPIES

Topic Editors:
Ozgur Kutuk, Başkent University, Turkey
Triona Ni Chonghaile, Royal College of Surgeons in Ireland, Ireland
Tugba Bagci-Onder, Koç University, Turkey
Uwe Knippschild, University of Ulm, Germany

Citation: Kutuk, O., Chonghaile, T. N., Bagci-Onder, T., Knippschild, U., eds. (2022). Cell Death and Targeted Cancer Therapies. Lausanne: Frontiers Media SA. doi: 10.3389/978-2-88976-684-0

Table of Contents

frontiers | Frontiers in Cell and Developmental Biology

EDITORIAL
published: 06 July 2022
doi: 10.3389/fcell.2022.967720

Editorial: Cell Death and Targeted Cancer Therapies

Tugba Bagci-Onder[1], Ozgur Kutuk[2], Triona Ni Chonghaile[3] and Uwe Knippschild[4]*

[1]Koç University School of Medicine, Istanbul, Turkey, [2]Department of Immunology, School of Medicine, Başkent University, Ankara, Turkey, [3]Department of Physiology and Medical Physics, Royal College of Surgeons in Ireland, Dublin, Ireland, [4]Department of General and Visceral Surgery, Surgery Center, Ulm University Medical Center, Ulm, Germany

Keywords: cell death, cancer, therapy resistance, apoptosis, ferroptosis, pyroptosis

Editorial on the Research Topic

Cell Death and Targeted Cancer Therapies

Cell death is critical for organismal development, maintenance of tissue homeostasis and the prevention of diseases, such as cancer. The most well-established mechanism of cell death is apoptosis, and cancer cells are known to adopt mechanisms to evade it. However, the roles of non-apoptotic cell death mechanisms, such as pyroptosis, necroptosis, and ferroptosis, in regulating cancer progression and therapy response are emerging. Development of therapy resistance involves the de-regulation of these cell death programs as well as tumor cell-microenvironment interactions. Our understanding of the precise mechanisms of cell death signaling networks in response to cancer therapies continue to evolve.

Resistance to therapy poses a prominent problem for the successful treatment of cancer, and there is a vast amount of information emerging in the field of therapy resistance. One of the important players in regulating resistance to therapies is the tumor microenvironment. For example, the bone marrow microenvironment can provide survival signals to leukemic stem cells, enabling survival of cells leading eventually to relapse of the disease. O'Reilly et al. developed an *in vitro* model system to study quiescent acute myelogenous leukemia (AML) cells in the bone marrow microenvironment. Using a hydrogel co-culture system, they induced quiescence in AML cells, which was enhanced in hypoxic conditions. Next, they screened a total of 1,600 drugs to identify therapeutics that could activate quiescent AML cells. Sequential treatments with hedgehog inhibitors, adipocyte peptides and tyrosine kinase inhibitors could move a proportion of cells into a cycling state. It was not clear from the studies if this also enhanced apoptosis within cells. Potentially, this could be a useful strategy to target residual quiescent cells in the bone marrow to prevent disease relapse.

Tumor treatment responses are also likely limited by layers of immune suppression in the tumor microenvironment. Yun et al. showed that the immune modulator cytotoxic T-lymphocyte-associated protein 4 (CTLA-4) had an interesting cytoplasmic role. Through anchoring phosphatase PP2A in the cytosol it led to activation of ataxia-telangiectasia mutated (ATM), thereby enhancing the DNA damage response induced by the antibiotic zeocin. This raises a hypothesis on whether CTLA-4 inhibitors could potentially have dual function in protecting T-cells from DNA damage and enhancing immune function–this however was not explored in this study and would require further validation. Next, Hagelund and Trauzold investigated the effect of the microenvironmental pH may have on the death receptor agonist TRAIL in pancreatic cancer. They found that adaptation to changes in extracellular pH could alter the response to TRAIL, with acidic pH increasing TRAIL sensitivity in one of the pancreatic cell lines. However, it is not clear how the extracellular pH could be manipulated in a therapeutic manner in the clinic. Cevatemre et al. investigated the link between metabolism and epithelial to mesenchymal transition (EMT) in the lung cancer cell line A549. Inhibition of pyruvate dehydrogenase through small molecule inhibitors or genetic approaches confers resistance to cytotoxic agents and showed phenotypic

OPEN ACCESS

Edited and reviewed by:
You-Wen He,
Duke University, United States

****Correspondence:***
Tugba Bagci-Onder
tuonder@ku.edu.tr

Specialty section:
This article was submitted to Cell Death and Survival, a section of the journal Frontiers in Cell and Developmental Biology

Received: *13 June 2022*
Accepted: *14 June 2022*
Published: *06 July 2022*

Citation:
Bagci-Onder T, Kutuk O, Chonghaile TN and Knippschild U (2022) Editorial: Cell Death and Targeted Cancer Therapies. Front. Cell Dev. Biol. 10:967720. doi: 10.3389/fcell.2022.967720

evidence of EMT. Together, these studies show that the microenvironment can be modelled and provide survival signals to the tumor, blocking cell death.

Brain tumors, especially glioblastoma, show a high resistance to standard therapies. Therefore, Burster et al. critically discuss the potential of new therapeutic concepts in their review. To activate apoptotic processes in glioblastoma cells, dual inactivation of BCL-2/BCL-xL, and MCL-1 seems to be necessary. However, drawbacks in an appropriate therapy development to induce apoptotic processes require still the establishment of new combinatorial inhibition approaches. Furthermore, new therapeutic approaches using small molecule inhibitors, oncolytic viruses, immunomodulators, or immunotherapy including peptide and mRNA-based vaccines have shown promising antitumor effects. However, only a few patients responded to immunotherapy. To improve immunotherapy concepts, it is therefore important, on the one hand, to elucidate the underlying pathophysiological mechanisms of glioblastoma and, on the other hand, to sensitize glioblastoma to immunotherapies by personalized therapy using a combination of drugs.

Since initial therapy for medulloblastoma, the most common brain tumor in children, is associated with severe side effects, research for new agents is also ongoing for this tumor entity. In this context, Dwucet et al. demonstrated that the imirilone derivate OBC201/TIC10 inhibits the growth of medulloblastoma cell lines independently of their *c-myc* status and shows synergistic effects in combination with the glycolysis inhibitor 2-deoxyglucose. Since both substances can pass the blood-brain barrier, the combined treatment of medulloblastoma patients seems to be promising approach.

Since low-dose radiation significantly increases the sensitivity of tumor cells, while protecting normal tissues at the same total dose compared with conventional fractionated radiotherapy due to the hyper-radiosensitivity/induced radioresistance (HRS/IRR) phenomenon, Wang et al. analyzed the underlying mechanism in lung cancer cells. Their results show that ATM can modulate autophagy, which is involved in regulating the hypersensitivity of lung cancer cells to low-dose radiation, via phospho c-Jun N-terminal kinase (p-JNK), and autophagy and Beclin 1 Regulator 1 (AMBRA1).

Hematological malignancies define a collective term for the heterogenous neoplastic diseases of the hematopoietic and lymphoid tissues. These disorders clinically manifest as leukemia, lymphoma or myeloma, accounting for more than 1.3 million new cases worldwide. While several treatment options including targeted therapies, monoclonal antibodies, and CAR-T cells significantly improved survival of patients with hematological malignancies, development of resistance to therapies is a prominent drawback, leading to relapse and treatment failure. Liang et al. utilized state-of-the-art data mining and network pharmacology strategies to identify common targets of a novel histone deacetylase inhibitor (chidamide) and ASA (acetylsalicylic acid, Aspirin) in AML-myelodysplastic syndrome cells. They demonstrated that combination of chidamide and ASA led to mitochondrial apoptosis in AML-myelodysplastic cells by inhibiting PI3K/AKT pathway. In addition, treatment of cells with chidamide plus ASA resulted in accumulation of cells in G0/G1 because of cell cycle arrest through downregulation of CDK4 and CDK2 and upregulation of p21 expression. Zhu et al. demonstrated that circular RNA circADD2 with a potential miR-149-5p binding site was downregulated in acute lymphoblastic leukemia (ALL) cell lines and bone marrow samples of children with ALL. Accordingly, they showed that circADD2 overexpression could trigger apoptosis in ALL through sponging miR-149-5p and reducing AKT2 expression. Of note, direct targeting of AKT2 by circADD2 remains to be validated. In another elegant study, Manzano-Munoz et al. used dynamic BH3 profiling (DBP) to identify MEK inhibitor trametinib in NALM-6 B-cell precursor acute lymphoblastic leukemia (BCP-ALL) cell line with a mutation in NRAS. Furthermore, DBP testing identified trametinib plus sunitinib (multi-target tyrosine kinase inhibitor) in SEM BCP-ALL cell line overexpressing FLT3. Importantly, coimmunoprecipitation experiments showed that trametinib led to increased MCL-1 expression to sequester BH3-only protein BIM and sunitinib promoted neutralization of BIM by BCL-2 and MCL-1 when used at lower concentrations. Targeting MCL-1 and BCL-2 by using BH3 mimetics S63845 (MCL-1 inhibitor) and venetoclax (BCL-2 inhibitor) restored sensitivity to trametinib and sunitinib in BCP-ALL cell lines, accordingly. Together, these studies explored distinct cell signaling pathways to pinpoint prosurvival signals in hematological malignancies, which may pave the way for novel combinatorial treatment options.

Non-apoptotic cell death mechanisms such as necroptosis or pyroptosis, which evoke inflammatory response, can actively participate in cancer progression. Zhang et al. performed in-depth statistical analysis of The Cancer Genome Atlas (TCGA) database and provided a pyroptosis-related gene (PRG) signature with predictive power for the clinical outcomes in endometrial cancer (EC), a highly common and aggressive gynecological tumor. Specifically, the prognostic PRG panel included ELANE, GPX4, GSDMS, and TIRAP, whose expressions were differentially regulated between EC and normal endometrial tissue. Cao et al. Similarly, demonstrated a prognostic PRG signature for uveal melanoma (UVM). In this study, authors stratified the patients into high-risk and low-risk groups and identified PRGs associated with each group. ANO6, CEBPB, and TMEM173 were upregulated, and VIM and TXNIP were downregulated in the high-risk group. Authors further examined the role of one of these PRGs, ANO6, via functional assays in UVM cell culture and showed that ANO6 silencing led to attenuation of cell migration. Pyroptosis is mainly an inflammatory cell death mechanism and involves the perforation of cell membrane and release of cellular contents. Its de-regulation is not exclusive to cancer, but also observed in several other diseases, such as the Osteoarthritis (OA). Yang et al. Compiled a large body of evidence to demonstrate the relation of pyroptotic, apoptotic, necroptotic and ferroptotic cell death mechanisms to OA. Accordingly, understanding these links will provide the design of successful treatment strategies. Finally, ferroptosis is an alternative cell death mechanism characterized by iron accumulation and lipid peroxidation. Yan et al. provided a ferroptosis-related gene signature composed of 6 genes (CISD1, CRYAB, FTH1, ACACA, ZEB1, and SQLE) with prognostic value in bladder cancer (BC), using TCGA and Gene Expression Omnibus databases. Authors constructed a pedictive risk model that

involved ferroptosis-related genes and found relevance to the EMT status, immune response and mutation status of key BC-related genes. Tang et al. comprehensively reviewed the mechanisms of ferroptosis, its relation to cancer and provided future perspectives for cancer therapy. Accordingly, induction of ferroptosis using single agents or combination therapies with immunotherapy, radiotherapy, chemotherapy, or photodynamic therapy may be successful anti-cancer approaches. However further research is necessary for clinical translation. Combined, these studies show the complexities of tumor resistance to standard and targeted treatments. Novel combinatorial approaches were identified that may pave the way to improved treatment outcomes.

AUTHOR CONTRIBUTIONS

All authors listed have made a substantial, direct, and intellectual contribution to the work by writing and editing the manuscript. Furthermore, all authors approved it for publication.

ACKNOWLEDGMENTS

The authors thank the contributors to this Research Topic as well as the Editorial support of the Journal.

Conflict of Interest: The authors declare that the research was conducted in the absence of any commercial or financial relationships that could be construed as a potential conflict of interest.

frontiers in Cell and Developmental Biology

ORIGINAL RESEARCH
published: 12 May 2021
doi: 10.3389/fcell.2021.650819

The Role and Mechanism of ATM-Mediated Autophagy in the Transition From Hyper-Radiosensitivity to Induced Radioresistance in Lung Cancer Under Low-Dose Radiation

*Qiong Wang†, Yangyang Chen†, Haiyan Chang, Ting Hu, Jue Wang, Yuxiu Xie and Jing Cheng**

Cancer Center, Union Hospital, Tongji Medical College, Huazhong University of Science and Technology, Wuhan, China

OPEN ACCESS

Edited by:
Uwe Knippschild, Ulm University, Germany

Reviewed by:
Michael Weinfeld, University of Alberta, Canada
Hong Zhu, Zhejiang University, China

***Correspondence:**
Jing Cheng
chenjin1118@hotmail.com

†These authors share first authorship

Specialty section:
This article was submitted to Cell Death and Survival, a section of the journal Frontiers in Cell and Developmental Biology

Received: *08 January 2021*
Accepted: *07 April 2021*
Published: *12 May 2021*

Citation:
Wang Q, Chen Y, Chang H, Hu T, Wang J, Xie Y and Cheng J (2021) The Role and Mechanism of ATM-Mediated Autophagy in the Transition From Hyper-Radiosensitivity to Induced Radioresistance in Lung Cancer Under Low-Dose Radiation. Front. Cell Dev. Biol. 9:650819. doi: 10.3389/fcell.2021.650819

Objective: This study aimed to investigate the effect of ataxia telangiectasia mutated (ATM)–mediated autophagy on the radiosensitivity of lung cancer cells under low-dose radiation and to further investigate the role of ATM and its specific mechanism in the transition from hyper-radiosensitivity (HRS) to induced radioresistance (IRR).

Methods: The changes in the HRS/IRR phenomenon in A549 and H460 cells were verified by colony formation assay. Changes to ATM phosphorylation and cell autophagy in A549 and H460 cells under different low doses of radiation were examined by western blot, polymerase chain reaction (PCR), and electron microscopy. ATM expression was knocked down by short interfering RNA (siRNA) transfection, and ATM-regulated molecules related to autophagy pathways were screened by transcriptome sequencing analysis. The detection results were verified by PCR and western blot. The differential metabolites were screened by transcriptome sequencing and verified by colony formation assay and western blot. The nude mouse xenograft model was used to verify the results of the cell experiments.

Results: (1) A549 cells with high expression of ATM showed positive HRS/IRR, whereas H460 cells with low expression of ATM showed negative HRS/IRR. After the expression of ATM decreased, the HRS phenomenon in A549 cells increased, and the radiosensitivity of H460 cells also increased. This phenomenon was associated with the increase in the autophagy-related molecules phosphorylated c-Jun N-terminal kinase (p-JNK) and autophagy/Beclin 1 regulator 1 (AMBRA1). (2) DL-Norvaline, a product of carbon metabolism in cells, inhibited autophagy in A549 cells under low-dose radiation. DL-Norvaline increased the expression levels of ATM, JNK, and AMBRA1 in A549 cells. (3) Mouse experiments confirmed the regulatory role of ATM in autophagy and metabolism and its function in HRS/IRR.

Conclusion: ATM may influence autophagy through p-JNK and AMBRA1 to participate in the regulation of the HRS/IRR phenomenon. Autophagy interacts with the cellular carbon metabolite DL-Norvaline to participate in regulating the low-dose radiosensitivity of cells.

Keywords: low-dose radiation, HRS/IRR, autophagy, ATM, lung cancer

INTRODUCTION

Radiotherapy is an important treatment method for lung cancer. Radiotherapy resistance and damage to surrounding normal tissue during radiotherapy limit its application in clinical practice. Some tumor cells exhibit hyper-radiosensitivity (HRS) to low-dose radiation: Within a radiation dose range < 1 Gy, cell destruction is enhanced per unit dose at an extremely low dose (<0.3–0.5 Gy), while cells show induced radioresistance (IRR) to higher doses (Marples and Collis, 2008). Due to the presence of the HRS/IRR phenomenon, at the same total dose, compared with conventionally fractionated radiotherapy, low-dose fractionated radiotherapy can significantly increase the radiosensitivity of tumor cells, increase the tumor control rate, and protect normal tissues (Valentini et al., 2010; Gupta et al., 2011; Dilworth et al., 2013; Schoenherr et al., 2013; Zhang et al., 2015). Few studies have focused on the mechanism of HRS in tumor cells, but whether this HRS phenomenon can be applied in conventional radiotherapy is an important topic.

Ataxia telangiectasia mutated (ATM) protein is an important factor affecting the radiosensitivity of tumor cells (Cremona and Behrens, 2013). When radiation causes DNA double-strand breaks (DNA DSBs), the Mre11–Rad50–Nbs1 complex first recognizes DSBs, then activates the kinase activity of ATM proteins and enables the phosphorylation of downstream substrates involved in DNA damage repair and cell cycle arrest, thereby playing a role in the recognition and repair of DSBs (Lavin et al., 2015). Xue et al. (2009, 2015). Observed the HRS/IRR phenomenon in human skin fibroblasts after carbon ion irradiation, and the HRS/IRR phenomenon showed different responses to treatment with specific ATM activators or inhibitors before radiation. Słonina et al. (2018) showed that in the fibroblasts of patients with HRS-positive tumors, the HRS phenomenon was closely related to the number of focal points of phosphorylated (p)-ATM. Enns et al. (2015) detected p-ATM expression in GM38, A549, and MCF7 cells after low-dose radiation. The results showed that the level of p-ATM was significantly increased in the presence of IRR. The above experimental results all suggest that ATM plays an important role in the transition from HRS to IRR under low-dose radiation.

Autophagy plays an important role in tumor radiotherapy. After autophagy is initiated, a series of phagy activities can be carried out through lysosomes to remove radiation-induced injury In lung cancer H1299 cells, radiotherapy-induced DNA damage regulates cellular autophagy through the ATM–MAPK14 pathway, thereby regulating the radiosensitivity of H1299 cells (Gewirtz, 2014; Liang et al., 2015). Our previous study showed that autophagy participated in the regulation of the transition from HRS to IRR in A549 lung cancer cells. HRS was enhanced in A549 cells by the autophagy inhibitor 3-methyladenine (3-MA) (Zhao et al., 2013). Therefore, we speculated that the transition from HRS to IRR, which involves autophagy, is regulated by the ATM gene, and the involved signaling pathways were explored in this study.

MATERIALS AND METHODS

Cells and Radiotherapy

A549 and H460 human lung adenocarcinoma cell lines were purchased from the Cell Bank of Type Culture Collection of Chinese Academy of Sciences, Shanghai, China. They were cultured in RPMI 1640 medium at 37°C and 5% CO_2. The concentration of fetal calf serum (FBS) was 10%; RPMI-1640 and FBS were purchased from Gibco (United States). After thawing, the cells did not contain mycoplasma. The number of aggregates (up to five cells) was kept as low as possible. Irradiation was performed using a Varian Unique-SN2236 linear accelerator (Siemens, Germany) at a dose rate of 1.32 cGy/s. Cellular radiosensitivity was detected using the colony formation method.

Colony Formation

Approximately 300 cells were inoculated into six-well plates and irradiated at the dose of 0, 0.2, 0.3, 0.5, 0.8, 1.0, or 2.0 Gy. The culture medium was replaced every 3–4 days. After incubation for 10–14 days, colonies were fixed with paraformaldehyde and stained with standard crystal violet solution. Colonies containing more than 50 cells were counted, and the plating efficiency was calculated as follows: (number of colonies/number of cells seeded) × 100%. Using the R language, the survivor fraction (SF) was fitted using the modified induced repair model (MIRM) with the following formula:

$$SF = \exp(-\alpha D - \beta D\ 2)$$
$$\alpha = \alpha_{res}\ \{1 + [\alpha_{sen}/(\alpha_{res} - 1)]\}\ \exp(-D/Dc)$$

The colony formation results were used for MIRM model construction in the R language. The survival curves were fitted, and the parameters were calculated: D = radiation dose value, α_{sen} = enhanced radiation effect at low-dose irradiation, α_{res} = radiation effect at high-dose irradiation, and Dc = dose inflection point at which HRS transforms to IRR. The standard for the existence of HRS/IRR is $\alpha_{sen} > \alpha_{res}$, whose confidence limit has no overlap, along with $Dc > 0$.

Western Blot

Total protein was extracted using a combination of RIPA buffer, phenylmethylsulfonyl fluoride, and phosphatase inhibitors. The

protein lysates were separated by sodium dodecyl sulfate–polyacrylamide gel electrophoresis and then transferred to poly(vinylidene fluoride) membranes. The membranes were blocked in 5% skim milk at room temperature for 1 h and then incubated with the designated primary antibodies at 4°C overnight. The excess primary antibody was washed off with Tris-buffered saline with Tween 20, and the corresponding secondary antibody was incubated at room temperature for 1 h. A United Kingdom UV imaging system was used for exposure imaging. ImageJ was used to analyze the experimental results. Western Blot antibodies:ATM antibody, Cell signaling (#2873); Phospho-ATM (Ser1981) antibody, Cell signaling (#13050); LC3B antibody, Abcam (AB192890); SAPK/JNK Antibody, Cell signaling (#9252); Phospho-SAPK/JNK (Thr183/Tyr185) (81E11) antibody (#4668); AMBRA1 antibody, AB clonal (A12578); GAPDH antibody, AB clonal (AC002).

Polymerase Chain Reaction (PCR)

After the cells were subjected to different treatments, cellular RNA was extracted on ice to prevent RNA degradation. The cells were evenly spread in the six well plates, and cell densities were adjusted as needed. The entire process was handled on ice. The medium was removed and the cells washed twice with PBS. Trizol (1 ml) was added and the cells were kept on ice for 5 min before being transferred to a 1.5-ml eppendorf tube. After chloroform (200 μl) was added to the tube, the mixture was vortexed until fully emulsified, and then centrifuged at 4°C for 15 min. About 200–400 μl of the aqueous phase was transferred to a new 1.5-ml tube. An equal volume of isopropanol was added and mixed well. The mixture was then centrifuged at 12,000 × *g* at 4°C for 10 min. The supernatant was discarded. The precipitate was dried for a few minutes and then dissolved in DEPC water. The concentration of RNA was measured. The optimal concentration was 300–500 ng/ml. 10-μl reverse transcription reactions were prepared. 500 ng RNA and 2-μl 5× prime script RT Master Mix buffer were added to each 10-μl reaction. The above system was prepared on ice, and then put in a polymerase chain reaction (PCR) machine for reverse transcription using the following reaction conditions: 37°C for 15 min; 85°C for 5 s; 4°C for 4 min. cDNA was stored at −80°C. The relative expression levels of target mRNA were calculated and statistically analyzed.

Short Interfering RNA (siRNA) Transfection

Cells were digested, counted, and then cultured in six-well plate; the cell density on the next day was approximately 40–50%. Two RNase-free 1.5-ml Eppendorf tubes (A and B) were used, and 250 μl Opti-MEM + 5 μl RNAiMAX was added into tube A, while 250 μl Opti-MEM + 5 μl short interfering RNA (siRNA) was added into tube B. Opti-MEM was purchased from Gibco. The solutions were uniformly mixed by gently pipetting, then allowed to stand for 5 min. Solutions in tube A and tube B were uniformly mixed by gently pipetting and allowed to stand for 20 min. The mixed solutions of the two tubes were added into six-well plates and gently mixed. After 6 h, the medium was replaced with normal complete medium. The transfection efficiency was determined by PCR and western blot.

siATM1: CUGCCGUCAACUAGAACAUTT
AUGUUCUAGUUGACGGCAGTT
siATM2: GCAGUAUGCUGUUUGACUUTT
AAGUCAAACAGCAUACUGCTT
siATM3: GCUUGAGGCUGAUCCUUAUTT
AUAAGGAUCAGCCUCAAGCTT
siRNA JNK: 5″-AGAAGGUAGGACAUUCUUU-3″
siRNA AMBRA1: 5″-GGCCTATGGTACTAACAAA-3″

Electron Microscopy

Electron microscopy is still one of the most accurate methods for quantitating autophagic vacuole accumulation. A549 and H460 cells were cultured in 6-well plates. The cells were subjected to varying doses of low radiation, and then collected in 2–4 h after radiotherapy by trypsinization and centrifugation at 1000 rpm for 5 min. The supernatant was discarded, and electron microscope fixatives were slowly added along the tube walls. Cells were then refrigerated at 4°C until used. The electron microscope specimens were sent to Wuhan Google Biotechnology Co. for subsequent treatment. The results of the electron microscopy were statistically analyzed.

Transcriptome Sequencing

Short interfering RNA transfection knocked down the gene expression of ATM in A549 cells. After 48–72 h of transfection, the cells were collected, and 1 ml TRIzol was added to each well of a six-well plate. The cell suspension was transferred into a 1.5-ml Eppendorf tube and placed in a −80°C freezer for later use. The samples were sent to BGI Group, China for subsequent treatment. Kyoto Encyclopedia of Genes and Genomes (KEGG) pathway analysis was used to screen the genes related to autophagy. After obtaining the analytical results, the sequencing results were validated by PCR.

Metabolomic Analysis

Short interfering RNA transfection knocked down the gene expression of ATM, JNK, and autophagy/Beclin 1 regulator 1 (AMBRA1) in A549 cells. The cells were scraped off using a sterile scraper, and then the cells were aspirated into the cryopreservation tube and centrifuged at 1000 rpm for 5 min. The supernatant was discarded, and the cryopreservation tube was quickly frozen in liquid nitrogen. The specimen was sent to Anachro Technologies Inc. for gas chromatography–mass spectrometry metabolomic sequencing. In the VIP scores graph, the larger the VIP value means the greater contribution. Generally, the variables with the VIP value greater than 1 have significant differences. In the *t*-test diagram, each colored dot represents a metabolite. The points marked in the graph are the metabolite with VIP value greater than 1 obtained by PLS-DA analysis.

Nude Mouse Xenograft Model

One hundred microliters of cell suspension (1×10^8 cells mixed with 50 μl Matrigel) was subcutaneously inoculated into 5-week-old female nude mice. When the tumor volume reached

approximately 120 mm^3, nude mice were randomly divided into six groups: control group, ATM inhibitor group, 2 Gy radiotherapy group, 0.2 Gy radiotherapy group, 2 Gy + ATM inhibitor group, and 0.2 Gy + ATM inhibitor group. BALB/C nude mice were used in the experiment, with five mice in each group. The concentration of ATM inhibitor (Ku-55933, Selleck, NO s1092) was 10 mg/kg. The method of administration was intraperitoneal injection. The drug was given 1 day before radiotherapy and every other day. In the process of radiotherapy, the interval of 0.2 Gy irradiation was 3 min. Tumor volume and mouse body weight were measured every 2–3 days. Animal experiments followed the *Guidelines for the Care and Use of Experimental Animals* (Ministry of Science and Technology of China, 2006) and were approved by the Animal Care and Use Committee of Tongji Medical College of Huazhong University of Science and Technology, China.

Statistical Analysis

The experimental data were statistically analyzed using GraphPad Prism 5.0. One-way analysis of variance and Student's *t*-test were performed. $P < 0.05$ indicated that a difference was statistically significant.

RESULTS

The Sensitivity of Human Lung Cancer A549 and H460 Cells to Low-Dose Radiation and the Differences in ATM Expression

The radiosensitivity of A549 and H460 cells exposed to low-dose irradiation was examined using clone survival analysis. Radioresistance was observed in A549 cells at 0.3–0.5 Gy, which is consistent with the HRS/IRR phenomenon. In addition, the radiosensitivity of H460 cells was dose-dependent, in line with the linear–quadratic (LQ) model (**Figures 1A,B**).

The ATM expression at the transcriptional and translational levels in human lung adenocarcinoma A549 and H460 cells were detected by PCR and western blot. In the HRS-positive A549 cells, the ATM mRNA and protein expression were higher than those of the H460-negative H460 cell line (**Figures 1C,D**).

Correlation Between ATM and the HRS/IRR Phenomenon in A549 and H460 Cells

Human lung cancer A549 and H460 cells were irradiated with the dose of 0, 0.2, 0.3, 0.5, 0.8, 1.0, or 2.0 Gy. Western blot was used to detect changes in ATM phosphorylation level in the two groups of cells. After A549 cells received different low-dose radiotherapies, the p-ATM was upregulated and showed dose-dependent effects (in the case of low-dose irradiation). There was significant phosphorylation after 0.3 and 0.5 Gy irradiation, which was in line with a transition from HRS to IRR in A549 cells. The relative expression levels of p-ATM in H460 cells after 0.2, 0.3, and 0.5 Gy irradiation did not have statistically significant differences (**Figures 2A,B**).

To further confirm whether ATM participates in the regulation of the HRS/IRR phenomenon under low-dose radiation, we used siRNA transfection to downregulate the expression of ATM protein in A549 and H460 cells. We also used the colony formation method to analyze the changes in radiosensitivity at low doses in A549 and H460 cells. Compared to the negative control, siRNA2 and siRNA3 significantly reduced ATM expression in A549 and H460 cells (**Figures 2C,D**). Decreased expression of ATM makes the clone number of A549 and H460 cells decrease significantly (**Figure 2E**). The survival curve of A549 cells fitted by MIRM showed the HRS/IRR phenomenon (**Figure 2F**). After knockdown of ATM, the HRS phenomenon of A549 cells was enhanced (**Figure 2G**); the survival curve of H460 cells was consistent with the traditional LQ model (**Figure 2H**), and radiosensitivity was also increased at low doses in H460 cells after ATM downregulation (**Figure 2I**).

ATM Regulates the Autophagy Levels in A549 Cells Under Different Low Doses of Radiation

Ataxia telangiectasia mutated protein expression in A549 cells was downregulated by siRNA transfection. The control group and ATM knockdown group were given low-dose irradiation of 0, 0.2, 0.3, 0.5, 0.8, 1.0, or 2.0 Gy. The effects of ATM knockdown on the phosphorylation level of ATM and the cellular autophagy level under different amounts radiation were analyzed by western blot. In the range of low-dose irradiation ($\leq$0.5 Gy), the expression levels of p-ATM and LC3-II in the control group increased dose-dependently, and the increases were more significant at 0.3 and 0.5 Gy, while they decreased at 0.8 Gy. This manifestation was consistent with the transition from HRS to IRR in A549 cells. Knockdown of ATM inhibited ATM phosphorylation and the increase in cellular autophagy under low-dose radiation (**Figures 3A–C**).

To further confirm the above experimental results, we prepared cells 4–6 h after radiotherapy for electron microscopy. The results are shown in **Figures 3D,E**. ATM knockdown inhibited the increase in the number of autophagic vacuoles in A549 cells under low-dose radiation.

Changes in ATM-Regulated Autophagy Pathway–Related Molecules Under Low-Dose Irradiation

The A549 cells in the control group and ATM knockdown group were subjected to transcriptome sequencing, and the molecules involved in the regulation of autophagy downstream of ATM were analyzed through KEGG pathway analysis. The differences in the expression of JNK and AMBRA1 were the most significant. In addition, the sequencing results were verified by PCR (**Figures 4A–D**).

Various low doses of radiation were given to the control group and the ATM knockdown group, and the differences in phosphorylated c-Jun N-terminal kinase (p-JNK), JNK, and AMBRA1 expression were analyzed by western blot. In the range of low-dose irradiation ($\leq$0.5 Gy), p-JNK and AMBRA1 increased in a dose-dependent manner in the control group;

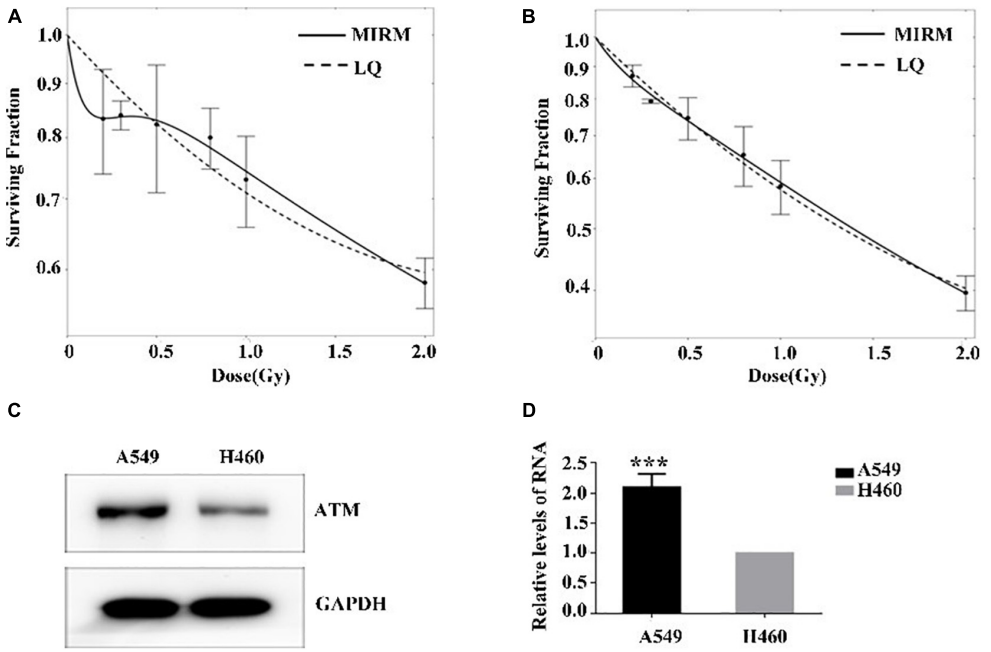

FIGURE 1 | Low-dose radiosensitivity and ATM protein expression in A549 cells and H460 cells. **(A)** A549 cells showed radioresistance to 0.3–0.5 Gy. **(B)** The radiosensitivity of H460 cells was dose-dependent. **(C,D)** The mRNA and protein levels of ATM in A549 cells were both higher than those of H460 cells. *** $p < 0.001$.

the expression increased more significantly at 0.3 and 0.5 Gy, decreased at 0.8 Gy, and increased again at 1 Gy. Both p-JNK and AMBRA1 were downregulated under low-dose radiation after ATM knockdown (**Figures 4E–G**).

Effects of AMBRA1 and JNK on the Low-Dose Radiosensitivity and Autophagy Level of A549 Cells

JNK1 and AMBRA1 were knocked down in A549 cells by siRNA transfection, and the knockdown effect was verified by western blot and PCR (**Figures 5A–D**). Different (low) doses of radiation were given to the control group, JNK1-knockdown group, and AMBRA1-knockdown group. Colony formation analysis showed that knockdown of JNK1 and AMBRA1 affected the radiosensitivity of A549 cells at low doses. Specifically, it enhanced the low-dose radiosensitivity of A549 cells (**Figures 5E,F**).

After siRNA transfection knocked down JNK and AMBRA1 in A549 cells, western blotting was used to detect the expression of the autophagy-related molecule LC3B. Knockdown of JNK and AMBRA1 inhibited the increase in this autophagy protein at different low-dose radiation ranges (**Figures 5G,H**).

Metabolic Processes Associated With Low-Dose HRS

Cell metabolism plays an important role in tumor occurrence, development, and treatment (White et al., 2015). Cellular autophagy itself belongs to a process of catabolism, which is closely related to the metabolic processes of glucose metabolism, lipid metabolism, and amino acid metabolism in tumor cells, and these processes complement each other (Kimmelman and White, 2017). We screened the differential metabolite DL-Norvaline that is regulated jointly by ATM, JNK, and AMBRA1 through metabolomic sequencing (**Figures 6A–F**) and verified the effect of DL-Norvaline on A549 cell radiosensitivity at low doses through colony formation. The results showed that DL-Norvaline reduced the sensitivity of A549 cells under low-dose radiation (**Figure 6G**). We also examined the effect of DL-Norvaline (Selleck, art. No. s6334, the concentration was 10 ug/ml) on the expression levels of ATM, JNK, and AMBRA1 in A549 cells using western blot. The results showed that DL-Norvaline increased the expression levels of ATM, JNK, and AMBRA1 in A549 cells (**Figures 6H,I**). Next, we examined the expression of AMBRA1 and JNK in the negative control group, DL-Norvaline treatment group, and siATM + DL-Norvaline treatment group. The results showed that siRNA knockdown of ATM inhibited the increase in AMBRA1 and JNK expression by DL-Norvaline. Finally, we tested the effect of DL-Norvaline on autophagy level of A549 by Western blot. The results showed that DL-Norvaline increased the autophagy level of A549 cells (**Figures 6J,K**), which further confirmed the interaction within ATM, DL-Norvaline and autophagy.

The Effect of ATM on Tumor Growth Under Low-Dose Radiation Is Verified by *in vivo* Experiments

To explore the effect of ATM on tumor growth under low-dose radiation, female nude mice were used as study objects. Nude

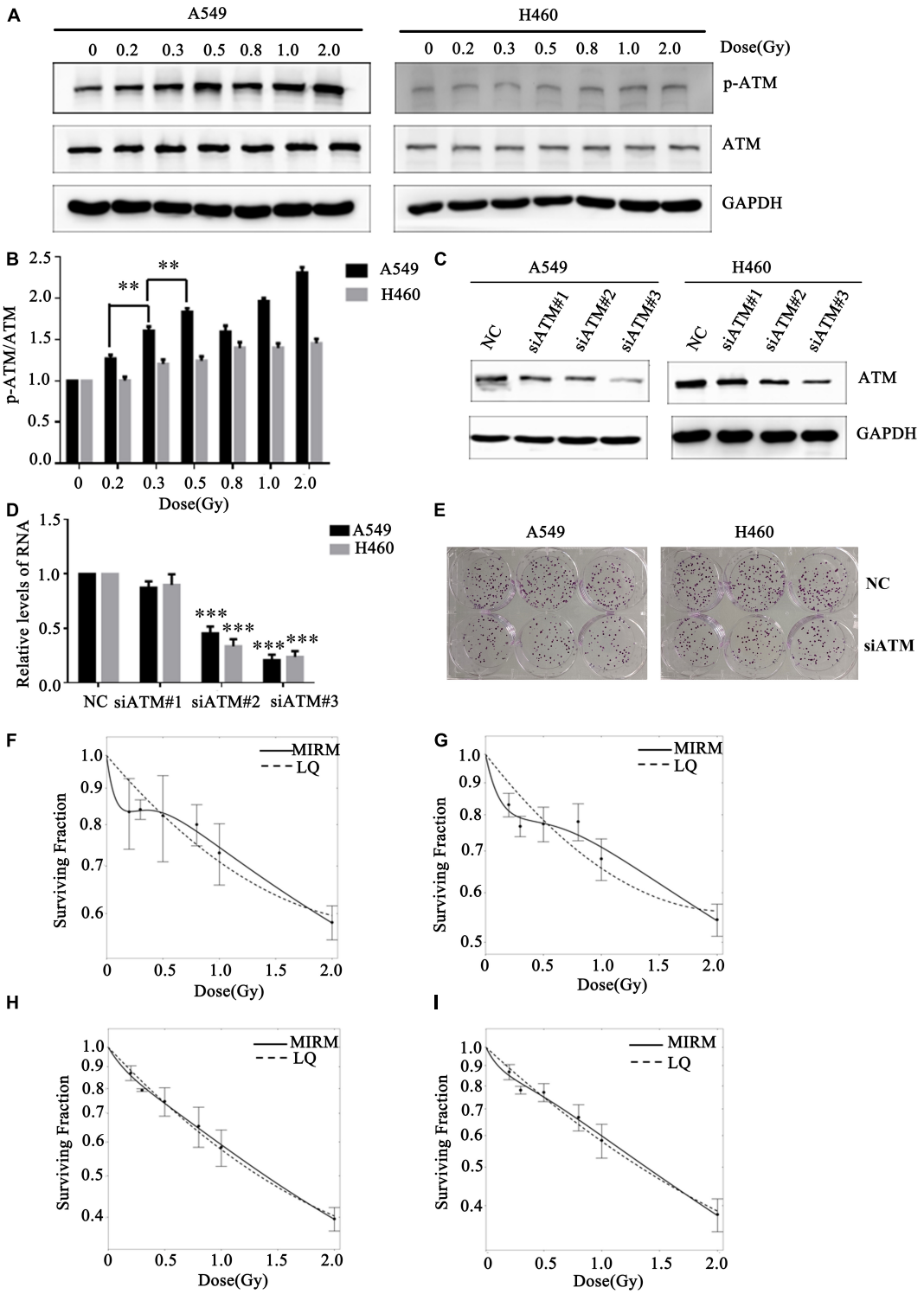

FIGURE 2 | Effect of ATM on the low-dose radiosensitivity of A549 and H460 cells. **(A,B)** Level of p-ATM in A549 and H460 cells under low-dose radiation. **(C,D)** siRNA transfection knocked down ATM gene expression in A549 and H460 cells. **(E)** Decreasing the expression of ATM inhibited the proliferation of A549 and H460. **(F)** The survival curve of A549 cells fitted by MIRM showed the HRS/IRR phenomenon. **(G)** The HRS phenomenon of A549 cells was enhanced after ATM knockdown. **(H)** The survival curves of H460 cells were in line with the traditional LQ model. **(I)** Radiosensitivity was enhanced in H460 cells after ATM knockdown. *** $p < 0.001$, ** $p < 0.01$.

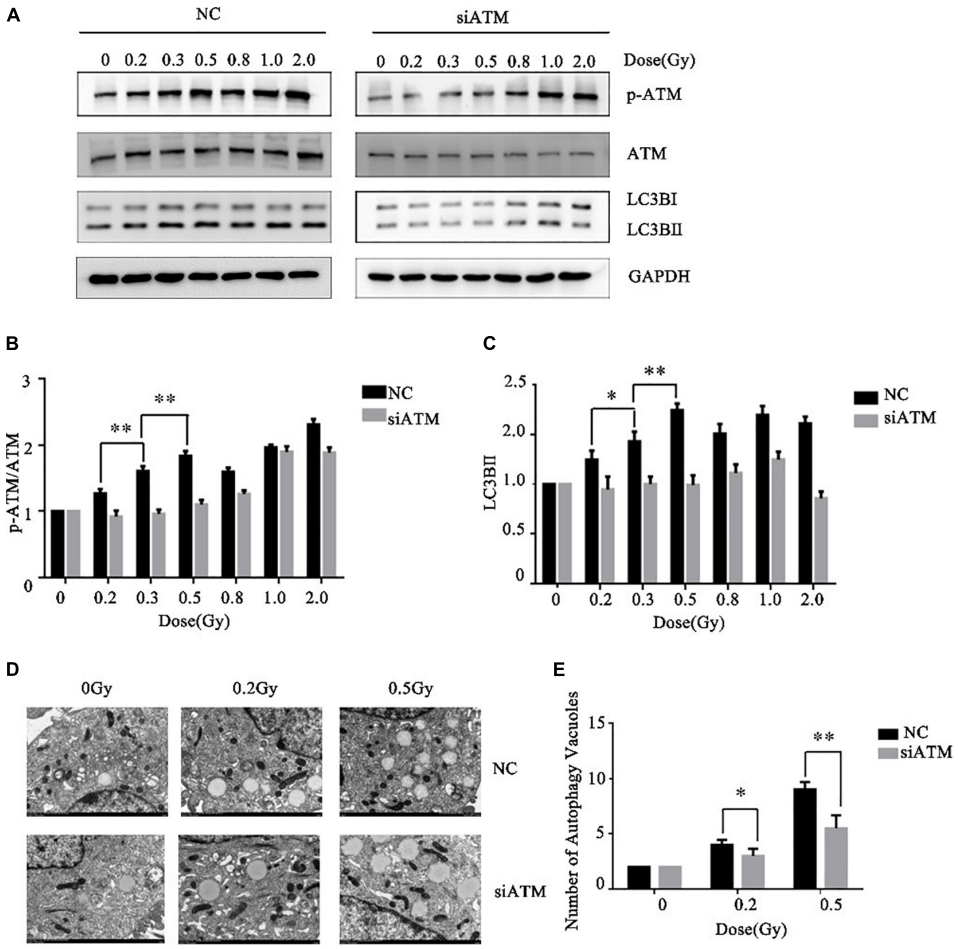

FIGURE 3 | Ataxia telangiectasia mutated (ATM) regulates the level of autophagy in A549 cells after radiotherapy. **(A–C)** Changes in p-ATM and autophagy levels in the control group and ATM-knockdown group under low-dose radiation were detected by western blot. **(D,E)** Changes in the number of cellular autophagic vacuoles in the control group and ATM-knockdown group were detected by electron microscopy. ** $p < 0.01$, * $p < 0.05$.

mice were randomly divided into six groups: control group, ATM inhibitor group, 2 Gy radiotherapy group, 0.2 Gy radiotherapy group, 2 Gy + ATM inhibitor group, and 0.2 Gy + ATM inhibitor group. Compared with the negative control, the ATM inhibitor alone inhibited the growth of A549 tumors; 2 Gy/session × 5 sessions of radiotherapy alone or 0.2 Gy × 10/session × 5 sessions of radiotherapy alone slowed down the proliferation of A549 cell tumors. Compared to 2 Gy/session × 5 sessions of radiotherapy, 0.2 Gy × 10/session × 5 sessions had a more pronounced inhibitory effect on tumor growth. When radiotherapy and ATM inhibitors were used jointly, 0.2 Gy × 10/session × 5 sessions had a more pronounced inhibitory effect on tumor growth (**Figures 7A,B**). There is no obvious difference within 6 treatment conditions on the body weight of nude mice (**Figure 7C**).

DISCUSSION

The low-dose ultra-microfractionated radiotherapy technique divides the conventional dose into several parts and delivers them at a certain intervals (Miciak and Bunz, 2017; Terashima et al., 2017). Due to the presence of low-dose HRS, hyper-fractionated low-dose radiotherapy has unique clinical advantages. However, the current research on the mechanism of low-dose HRS is still not very clear (Olobatuyi et al., 2017, 2018).

This study used HRS/IRR-positive A549 cells and HRS/IRR-negative H460 cells as study objects. The expression level of ATM in HRS-positive A549 cells was significantly higher than that in HRS/IRR-negative H460 cells. After different low-dose radiation treatments of A549 cells, p-ATM was significantly upregulated in a dose-dependent manner, most significantly after 0.3 and 0.5 Gy, whereas the relative expression levels of p-ATM in H460 cells were not significantly different between the 0.2, 0.3, and 0.5 Gy groups. After siRNA knockdown of ATM, the sensitivities of A549 cells and H460 cells under low-dose radiation were both increased, and the HRS of A549 cells was enhanced. The above experimental results all confirm that ATM was involved in the regulation of low-dose radiation hypersensitivity in lung cancer cells.

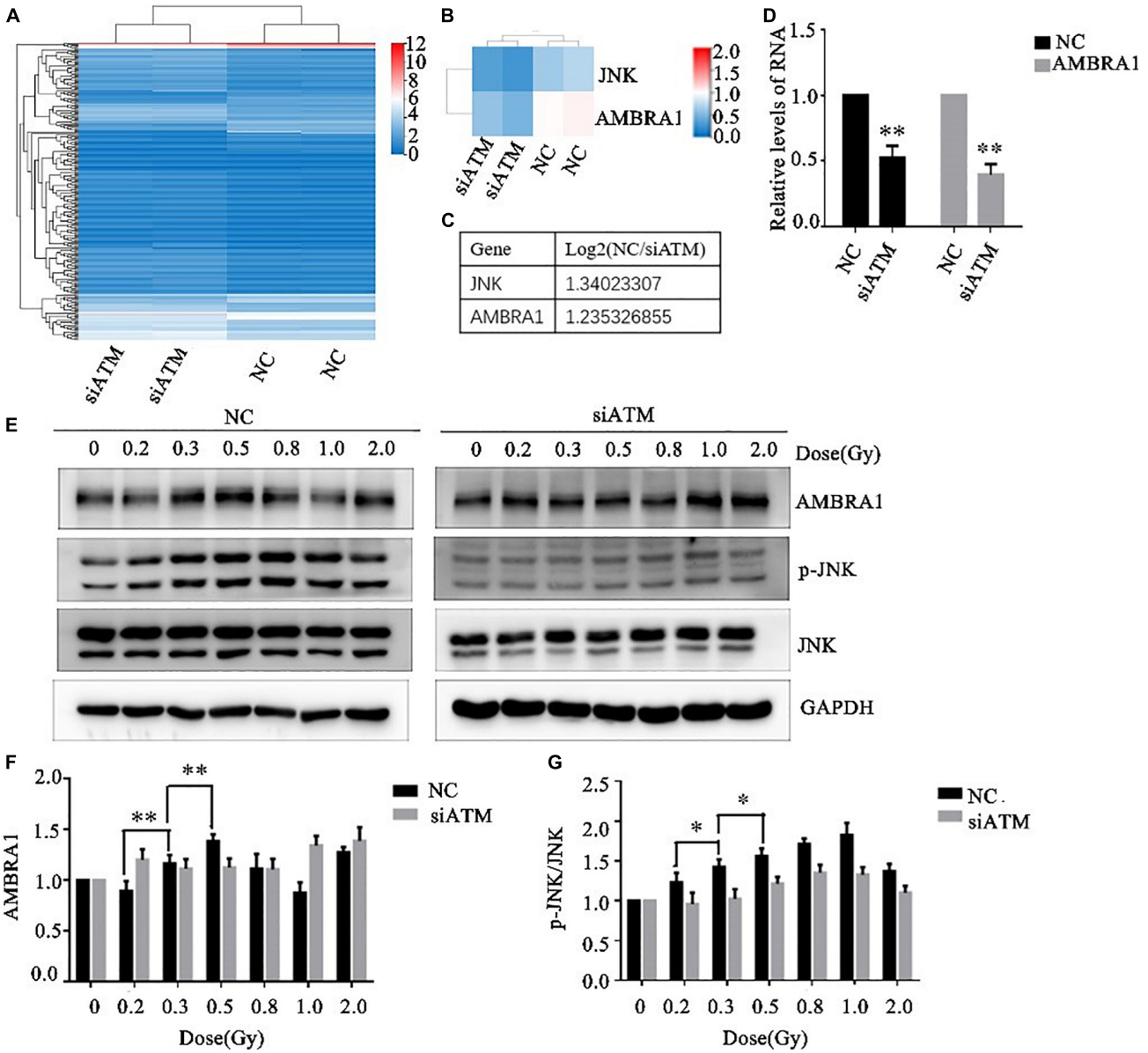

FIGURE 4 | Ataxia telangiectasia mutated (ATM) regulates changes in autophagy pathway-related molecules. **(A–C)** Transcriptome sequencing analysis of the differences in autophagy pathway–related molecules between the control group and the ATM downregulated group. The differences in JNK and AMBRA1 between the two groups were the most significant. **(D)** The sequencing results were verified by PCR. **(E–G)** Changes in the levels of p-JNK and AMBRA1 in the control group and the ATM-knockdown group under low-dose radiation. ** $p < 0.01$, * $p < 0.05$.

Our previous experiments showed that treatment with the autophagy inhibitor 3-MA enhanced radiosensitivity under low doses in A549 cells, suggesting that autophagy is an important factor inducing HRS/IRR phenomenon (Zhao et al., 2013). Did ATM-regulated autophagy participate in the regulation of the sensitivity of the A549 lung cancer cells at low doses and participate in the transition from HRS to IRR? Our results showed that in the low-dose range (≤0.5 Gy), the expression levels of p-ATM and LC3-II in the control group increased in a dose-dependent manner, most significantly after 0.3 and 0.5 Gy. After siRNA knockdown of ATM, the phosphorylation of ATM and the increase in autophagy levels under low-dose radiation were inhibited. Our electron microscopy results also showed that after inhibiting the expression of ATM, the number of autophagic vacuoles in A549 cells decreased, and the volume of autophagic vacuoles relatively increased under different low doses of radiation. These results further confirm our hypothesis that ATM-regulated autophagy is involved in the transition from HRS to IRR under low-dose radiation.

To further investigate the mechanism through which ATM regulates autophagy under low-dose radiation and

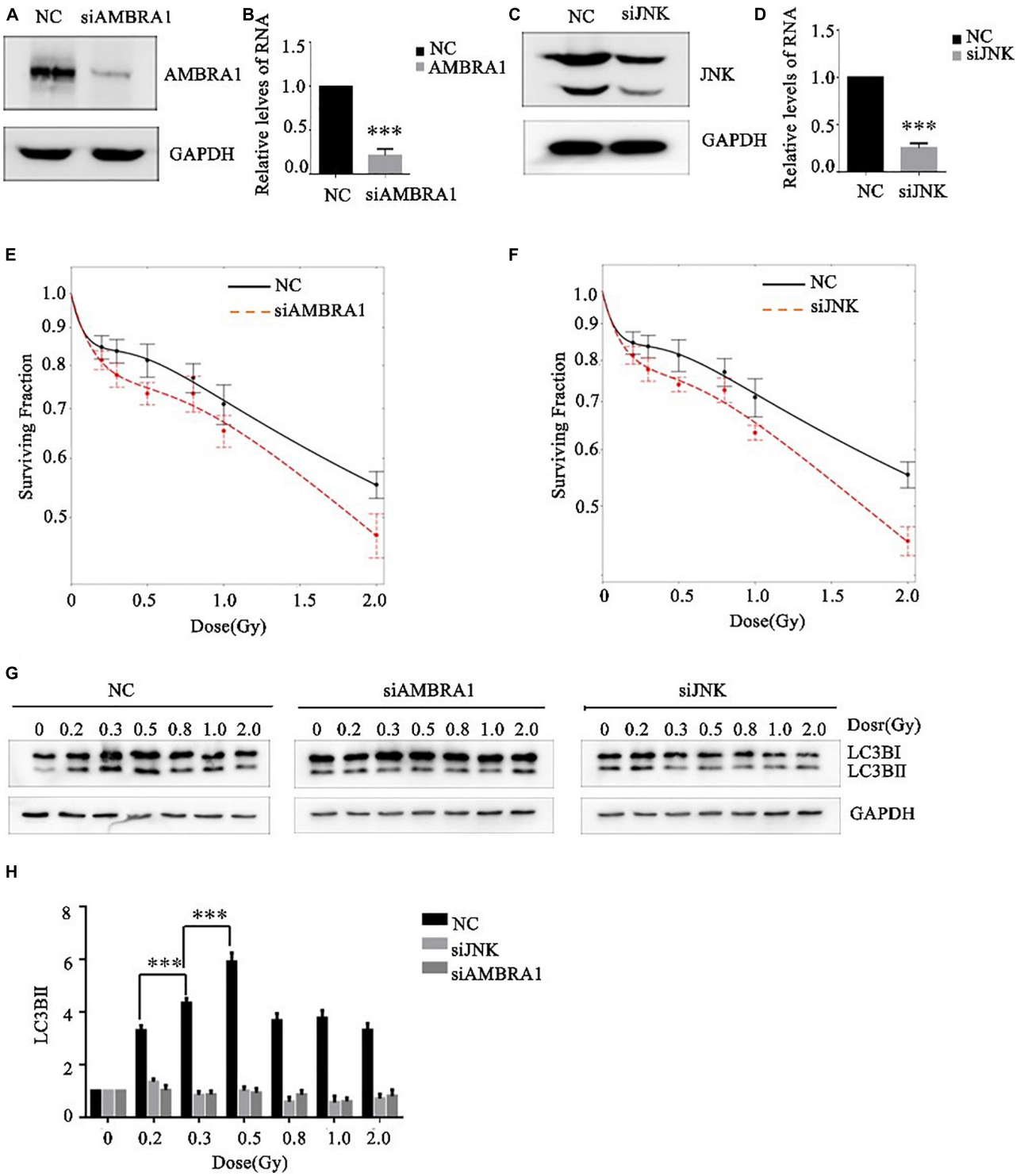

FIGURE 5 | Effects of AMBRA1 and JNK on the radiosensitivity and autophagy of A549 cells. **(A,B)** siRNA transfection inhibited AMBRA1 gene expression in A549 cells. **(C,D)** siRNA transfection inhibited JNK gene expression in A549 cells. **(E,F)** When AMBRA1 and JNK were knocked down in A549 cells, the sensitivity of cells to low-dose radiation increased, and the HRS phenomenon was enhanced. **(G,H)** When AMBRA1 and JNK were knocked down in A549 cells, cellular autophagy under low-dose radiation was inhibited. *** $p < 0.001$.

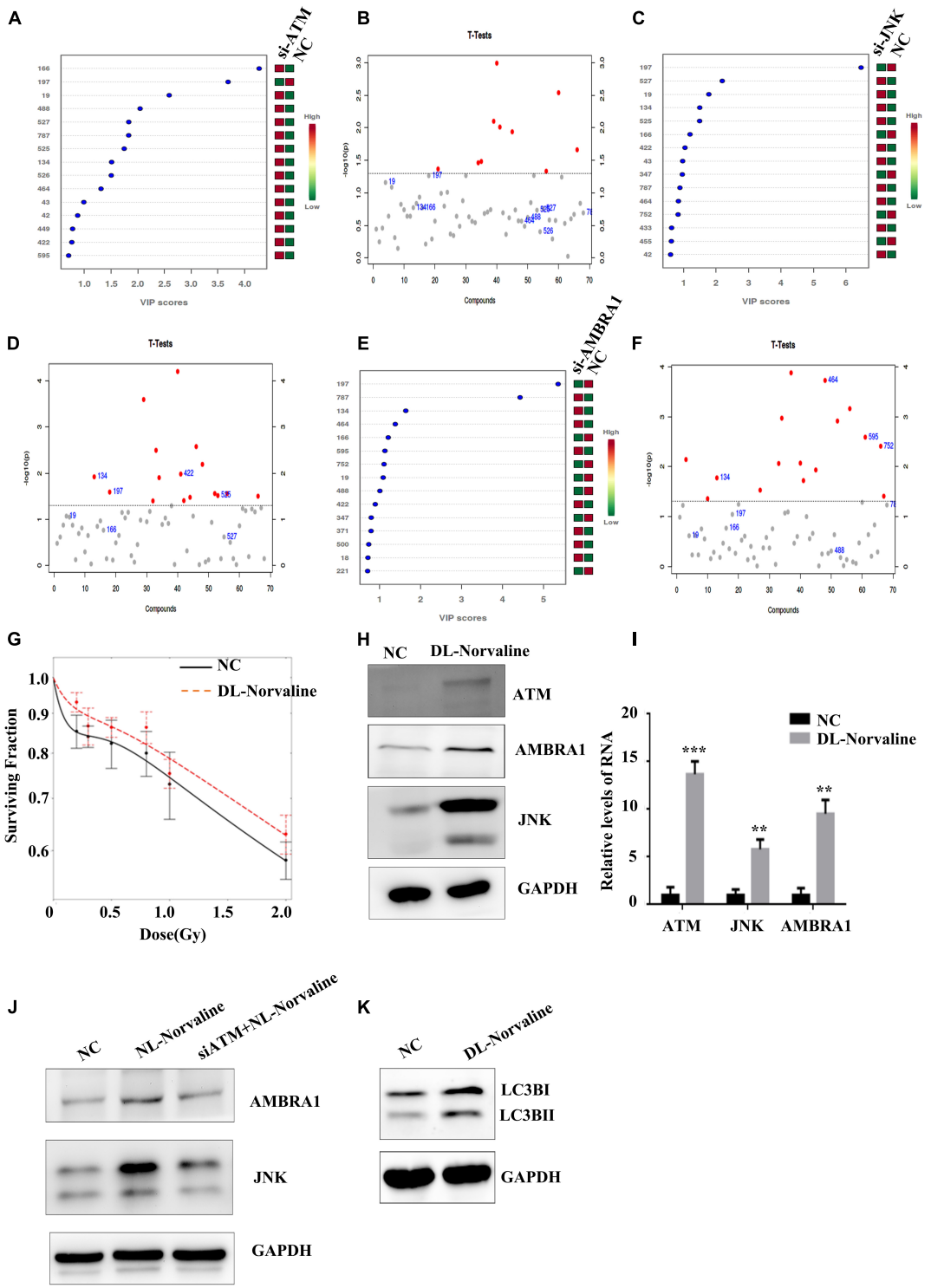

FIGURE 6 | Metabolic processes associated with the low-dose HRS phenomenon. **(A,B)** Differences in metabolites between the ATM-knockdown group and the control group. **(C,D)** Differences in metabolites between the JNK-knockdown group and the control group. **(E,F)** Differences in metabolites between the AMBRA1-knockdown group and the control group. **(G)** Effect of DL-Norvaline on the low-dose radiosensitivity of A549 cells. **(H,I)** Effect of DL-Norvaline on the expression levels of ATM, JNK, and AMBRA1 in A549 cells. **(J)** Effect of siRNA knockdown of ATM on the DL-Norvaline effect. **(K)** Effect of DL-Norvaline on autophagy ***$p < 0.001$, **$p < 0.01$.

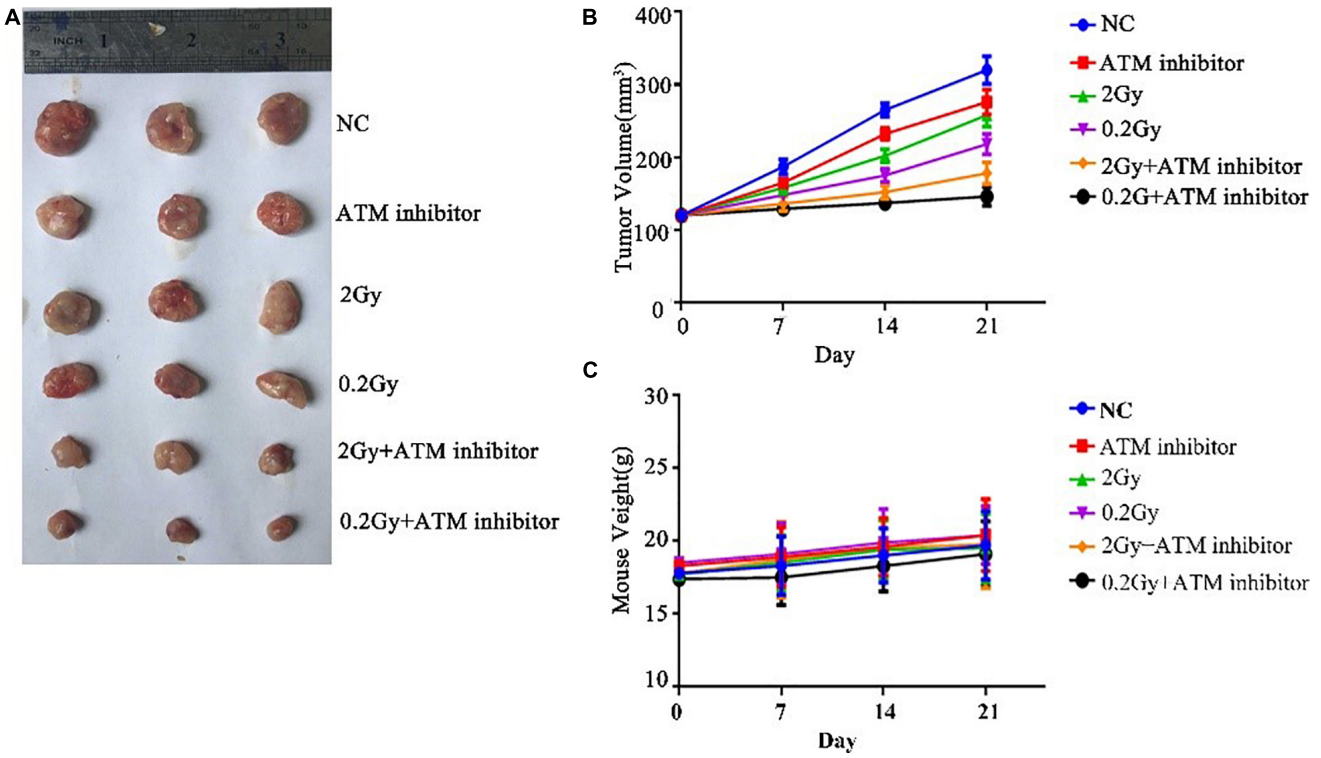

FIGURE 7 | The effect of ATM on tumor growth under low-dose irradiation. **(A,B)** Effects of different treatment conditions on tumor xenograft volume in nude mice. **(C)** Effects of different treatment conditions on the body weight of nude mice.

thereby regulates the transition of HRS to IRR, we screened for differentially expressed genes associated with autophagy pathways downstream of ATMs by transcriptome sequencing analysis. This screen returned JNK and AMBRA1. JNK, the c-Jun N-terminal kinase, is a member of the mitogen-activated protein kinase family and belongs to protein kinases. After JNK is activated, it regulates cell proliferation, survival, differentiation, and metabolism through downstream substrates (Wu et al., 2019). JNK is involved in the autophagy induced by various types of stimuli, including nutritional deficiency, reduction of cytokines and growth factors, and neurotoxic drugs (Vegliante et al., 2016; Zhang et al., 2018; Bai et al., 2019). JNK activation can induce Bcl-2 phosphorylation, destroy the Bcl-2/Beclin 1 complex, and promote the release of Beclin 1 to induce autophagy (Yang et al., 2015). AMBRA1, also known as autophagy/Beclin-1 modulator 1, plays an important role in the regulation of autophagy and acts as a positive regulator of Beclin-1, thereby promoting the formation of autophagosomes (Capizzi et al., 2017). Our results showed that under low-dose radiation (≤0.5 Gy), the levels of p-JNK and AMBRA1 in A549 cells increased in a dose-dependent manner; the increases were most significant at 0.5 Gy; and ATM knockdown inhibited the increases in p-JNK and AMBRA1 after different low doses of radiation. The above experimental results confirm that ATM can regulate JNK phosphorylation and AMBRA1 expression under low-dose radiation.

To further verify whether ATM regulated the autophagy level of cells under low-dose radiation through JNK1 and AMBRA1 and thereby regulate the radiosensitivity of A549 cells, we knocked down JNK1 and AMBRA1 in A549 cells through siRNA transfection and analyzed the effects of JNK1 and AMBRA1 on the radiosensitivity of A549 cells under low doses by a colony formation assay. The results showed that JNK1 and AMBRA1 knockdown increased the radiosensitivity of A549 cells at low doses. At the same time, we examined the autophagy levels of cells under different low doses of radiation. JNK1 and AMBRA1 knockdown inhibited the increase in autophagy levels in A549 cells caused by low-dose irradiation. The above experimental results further confirmed that ATM might regulate the radiosensitivity of A549 cells under low-dose irradiation through p-JNK and AMBRA1.

Autophagy is inseparable from many cellular metabolic processes. We screened the differential metabolite DL-Norvaline by metabolomic analysis. DL-Norvaline is an important metabolic product involved in the process of carbon metabolism in cells. The colony formation assay showed that DL-Norvaline inhibited the autophagy level of A549 cells under low-dose radiation. DL-Norvaline increased the expression levels of ATM, JNK, and AMBRA1 in A549 cells. siRNA knockdown of ATM inhibited the increased expression of AMBRA1 and JNK by

DL-Norvaline. Therefore, we hypothesized that under low-dose radiation, ATM interacts with DL-Norvaline through autophagy regulated by JNK and AMBRA1 to jointly regulate the low-dose radiosensitivity of A549 cells. Finally, we validated the results of cell experiments in mouse experiments.

CONCLUSION

In conclusion, our study found that ATM may affect autophagy through p-JNK and AMBRA1 and thus participate in the regulation of HRS/IRR phenomenon. Autophagy participates in the regulation of low-dose radiosensitivity in cells by interacting with DL-Norvaline, a carbon metabolism product. Next, we will validate and investigate the regulatory mechanism of this HRS in conventional-dose and high-dose radiotherapy to help improve the radiosensitivity of lung adenocarcinoma.

DATA AVAILABILITY STATEMENT

The original contributions presented in the study are publicly available. This data can be found here: https://www.ncbi.nlm.nih.gov/bioproject/PRJNA725505, PRJNA725505.

ETHICS STATEMENT

The animal study was reviewed and approved by Huazhong University of Science and Technology Institutional Animal Care and Use Committee.

AUTHOR CONTRIBUTIONS

QW: conceptualization, investigation, data curation, formal analysis, methodology, validation, visualization, and writing–original draft. YC: conceptualization, investigation, data curation, methodology, and visualization. HC: investigation and resources. TH: investigation. JW and YX: methodology and resources. JC: conceptualization, data curation, formal analysis, funding acquisition, supervision, validation, visualization, and writing–review and editing. All authors contributed to the article and approved the submitted version.

FUNDING

This study has received funding by the National Natural Science Funds (81672977) from the National Natural Science Foundation of China.

REFERENCES

Bai, Y., Liu, X., Qi, X., Liu, X., Peng, F., Li, H., et al. (2019). PDIA6 modulates apoptosis and autophagy of non-small cell lung cancer cells via the MAP4K1/JNK signaling pathway. *EBioMedicine* 42, 311–325. doi: 10.1016/j.ebiom.2019.03.045

Capizzi, M., Strappazzon, F., Cianfanelli, V., Papaleo, E., and Cecconi, F. (2017). MIR7-3HG, a MYC-dependent modulator of cell proliferation, inhibits autophagy by a regulatory loop involving AMBRA1. *Autophagy* 13, 554–566. doi: 10.1080/15548627.2016.1269989

Cremona, C. A., and Behrens, A. (2013). ATM signalling and cancer. *Oncogene* 33, 3351–3360.

Dilworth, J. T., Krueger, S. A., Dabjan, M., Grills, I. S., Torma, J., Wilson, G. D., et al. (2013). , Pulsed low-dose irradiation of orthotopic glioblastoma multiforme (GBM) in a pre-clinical model: effects on vascularization and tumor control. *Radiother. Oncol.* 108, 149–154. doi: 10.1016/j.radonc.2013.05.022

Enns, L., Rasouli-Nia, A., Hendzel, M., Marples, B., and Weinfeld, M. (2015). Association of ATM activation and DNA repair with induced radioresistance after low-dose irradiation. *Radiat. Prot. Dosimetry* 166, 131–136. doi: 10.1093/rpd/ncv203

Gewirtz, D. A. (2014). The Four Faces of Autophagy: implications for Cancer Therapy. *Cancer Res.* 74, 647–651. doi: 10.1158/0008-5472.can-13-2966

Gupta, S., Koru-Sengul, T., Arnold, S. M., Devi, G. R., Mohiuddin, M., and Ahmed, M. M. (2011). Low-Dose Fractionated Radiation Potentiates the Effects of Cisplatin Independent of the Hyper-Radiation Sensitivity in Human Lung Cancer Cells. *Mol. Cancer Ther.* 10, 292–302. doi: 10.1158/1535-7163.mct-10-0630

Kimmelman, A. C., and White, E. (2017). Autophagy and Tumor Metabolism. *Cell Metab.* 25, 1037–1043. doi: 10.1016/j.cmet.2017.04.004

Lavin, M., Kozlov, S., Gatei, M., Kijas, A., and Dependent Phosphorylation, A. T. M. - (2015). of All Three Members of the MRN Complex: from Sensor to Adaptor. *Biomolecules* 5, 2877–2902. doi: 10.3390/biom5042877

Liang, N., Zhong, R., Hou, X., Zhao, G., Ma, S., Cheng, G., et al. (2015). Ataxia-telangiectasia mutated (ATM) participates in the regulation of ionizing radiation-induced cell death via MAPK14 in lung cancer H1299 cells. *Cell Prolif.* 48, 561–572. doi: 10.1111/cpr.12203

Marples, B., and Collis, S. J. (2008). Low-dose hyper-radiosensitivity: past, present, and future. *Int. J. Radiat. Oncol. Biol. Phys.* 70, 1310–1318. doi: 10.1016/j.ijrobp.2007.11.071

Miciak, J., and Bunz, F. (2017). Understanding the pluses of pulses. *Cell Cycle* 16, 1325–1325. doi: 10.1080/15384101.2017.1337979

Olobatuyi, O., de Vries, G., and Hillen, T. (2017). A reaction-diffusion model for radiation-induced bystander effects. *J. Math. Biol.* 75, 341–372. doi: 10.1007/s00285-016-1090-5

Olobatuyi, O., de Vries, G., and Hillen, T. (2018). Effects of G2-checkpoint dynamics on low-dose hyper-radiosensitivity. *J. Math. Biol.* 77, 1969–1997. doi: 10.1007/s00285-018-1236-8

Schoenherr, D., Krueger, S. A., Martin, L., Marignol, L., Wilson, G. D., and Marples, B. (2013). Determining if low dose hyper-radiosensitivity (HRS) can be exploited to provide a therapeutic advantage: a cell line study in four glioblastoma multiforme (GBM) cell lines. *Int. J. Radiat. Biol.* 89, 1009–1016. doi: 10.3109/09553002.2013.825061

Słonina, D., Kowalczyk, A., Janecka-Widła, A., Kabat, D., Szatkowski, W., and Biesaga, B. (2018). Low-Dose Hypersensitive Response for Residual pATM and γH2AX Foci in Normal Fibroblasts of Cancer Patients. *Int. J. Radiat. Oncol. Biol. Phys.* 100, 756–766. doi: 10.1016/j.ijrobp.2017.10.054

Terashima, S., Hosokawa, Y., Tsuruga, E., Mariya, Y., and Nakamura, T. (2017). Impact of time interval and dose rate on cell survival following low-dose fractionated exposures. *J. Radiat. Res.* 58, 782–790. doi: 10.1093/jrr/rrx025

Valentini, V., Massaccesi, M., Balducci, M., Mantini, G., Micciche, F., Mattiucci, G. C., et al. (2010). Low-dose hyperradiosensitivity: is there a place for future investigation in clinical settings? *Int. J. Radiat. Oncol. Biol. Phys.* 76, 535–539. doi: 10.1016/j.ijrobp.2009.02.075

Vegliante, R., Desideri, E., Di Leo, L., and Ciriolo, M. R. (2016). Dehydroepiandrosterone triggers autophagic cell death in human hepatoma cell line HepG2 via JNK-mediated p62/SQSTM1 expression. *Carcinogenesis* 37, 233–244. doi: 10.1093/carcin/bgw003

White, E., Mehnert, J. M., and Chan, C. S. (2015). Autophagy, Metabolism, and Cancer. *Clin. Cancer Res.* 21, 5037–5046. doi: 10.1158/1078-0432.ccr-15-0490

Wu, Q., Wu, W., Fu, B., Shi, L., Wang, X., and Kuca, K. (2019). JNK signaling in cancer cell survival. *Med. Res. Rev.* 39, 2082–2104. doi: 10.1002/med.21574

Xue, L., Furusawa, Y., and Yu, D. (2015). ATR signaling cooperates with ATM in the mechanism of low dose hypersensitivity induced by carbon ion beam. *DNA Repair* 34, 1–8. doi: 10.1016/j.dnarep.2015.07.001

Xue, L., Yu, D., Furusawa, Y., Cao, J., Okayasu, R., and Fan, S. (2009). ATM-Dependent Hyper-Radiosensitivity in Mammalian Cells Irradiated by Heavy Ions. *Int. J. Radiat. Oncol. Biol. Phys.* 75, 235–243. doi: 10.1016/j.ijrobp.2009.04.088

Yang, J., Yao, S., and Bcl-, J. N. K. - (2015). 2/Bcl-xL-Bax/Bak Pathway Mediates the Crosstalk between Matrine-Induced Autophagy and Apoptosis via Interplay with Beclin 1. *Int. J. Mol. Sci.* 16, 25744–25758. doi: 10.3390/ijms161025744

Zhang, P., Wang, B., Chen, X., Cvetkovic, D., Chen, L., Lang, J., et al. (2015). Local Tumor Control and Normal Tissue Toxicity of Pulsed Low-Dose Rate Radiotherapy for Recurrent Lung Cancer. *Dose Response* 13:1559325815588507.

Zhang, Z., Ren, Z., Chen, S., Guo, X., Liu, F., Guo, L., et al. (2018). ROS generation and JNK activation contribute to 4-methoxy-TEMPO-induced cytotoxicity, autophagy, and DNA damage in HepG2 cells. *Arch. Toxicol.* 92, 717–728. doi: 10.1007/s00204-017-2084-9

Zhao, Y.-X., Cheng, C., Zhu, F., Wu, H.-G., Ren, J.-H., Chen, W.-H., et al. (2013). Suppression of low-dose hyper-radiosensitivity in human lung cancer cell line A549 by radiation-induced autophagy. *J. Huazhong Univ. Sci. Technol. Med. Sci.* 33, 770–774. doi: 10.1007/s11596-013-1195-7

Conflict of Interest: The authors declare that the research was conducted in the absence of any commercial or financial relationships that could be construed as a potential conflict of interest.

frontiers in Cell and Developmental Biology

ORIGINAL RESEARCH
published: 13 May 2021
doi: 10.3389/fcell.2021.639910

Mechanism of circADD2 as ceRNA in Childhood Acute Lymphoblastic Leukemia

Yuting Zhu[1,2†], Xiaopeng Ma[1,2†], Heng Zhang[1,2†], Yijun Wu[1,2], Meiyun Kang[1,2], Yongjun Fang[1,2] and Yao Xue[1,2*]*

[1] Department of Hematology and Oncology, Children's Hospital of Nanjing Medical University, Nanjing, China, [2] Key Laboratory of Hematology, Nanjing Medical University, Nanjing, China

OPEN ACCESS

Edited by:
Tugba Bagci-Onder,
Koç University, Turkey

Reviewed by:
Zengli Guo,
University of North Carolina at Chapel Hill, United States
Mario Cioce,
Campus Bio-Medico University, Italy

***Correspondence:**
Yongjun Fang
fyj322@189.cn
Yao Xue
yaoyao82986@126.com

† These authors have contributed equally to this work

Specialty section:
This article was submitted to Cell Death and Survival, a section of the journal Frontiers in Cell and Developmental Biology

Received: 10 December 2020
Accepted: 21 April 2021
Published: 13 May 2021

Citation:
Zhu Y, Ma X, Zhang H, Wu Y, Kang M, Fang Y and Xue Y (2021) Mechanism of circADD2 as ceRNA in Childhood Acute Lymphoblastic Leukemia. Front. Cell Dev. Biol. 9:639910. doi: 10.3389/fcell.2021.639910

Background: Acute lymphocytic leukemia (ALL) is the most common malignant tumor in children. Increasing evidence suggests that circular RNAs (circRNAs) play critical regulatory roles in tumor biology. However, the expression patterns and roles of circRNAs in childhood acute lymphoblastic leukemia (ALL) remain largely unknown.

Methods: circADD2 was selected by microarray assay and confirmed by qRT-PCR; *in vitro* effects of circADD2 were determined by CCK-8 and flow cytometry; while mice subcutaneous tumor model was designed for *in vivo* analysis. RNA immunoprecipitation and dual-luciferase assay were applied for mechanistic study. Protein levels were examined by Western blot assay.

Results: circADD2 was down-regulated in ALL tissues and cell lines. Overexpression of circADD2 inhibited cell proliferation and promoted apoptosis both *in vitro* and *in vivo*. Briefly, circADD2 could directly sponge miR-149-5p, and the level of AKT2, a target gene of miR-149-5p, was downregulated by circADD2.

Conclusion: circADD2, as a tumor suppressor in ALL, can sponge miR-149-5p, and may serve as a potential biomarker for the diagnosis or treatment of ALL.

Keywords: circADD2, ceRNA, miR-149-5p, childhood ALL, AKT2

INTRODUCTION

Acute lymphoblastic leukemia (ALL), a clonal dysplastic disease originating from the bone marrow where B-line or T-line lymphocytes are generated, is commonly found in children (Iacobucci and Mullighan, 2017; Teachey and Pui, 2019). The prognosis of childhood ALL has been significantly improved. However, relapses even deaths still appear due to treatment failure (Inaba et al., 2013; Hunger and Mullighan, 2015). Therefore, the pathogenesis of ALL needs further exploration before the establishment of new treatment options.

Circular RNAs (circRNAs) are a class of endogenous non-coding RNAs, characterized by a covalent closed-loop structure without neither a 5′ cap nor a 3′ Poly A tail (Meng et al., 2017; Yu et al., 2019). Unlike linear RNAs, circRNAs demonstrate remarkable stability, high abundance, evolutionary conservation, and tissue-specific expression (Aufiero et al., 2019). New

RNA sequencing (RNA-seq) technology has discovered more functional circRNAs (Szabo and Salzman, 2016). In multiple cancers, circRNAs regulate important cellular processes, including proliferation, invasion and metastasis (Wang et al., 2018; Zeng et al., 2018). However, the mechanisms of circRNAs in ALL remain unclear.

MicroRNA-149-5p (miR-149-5p) is dysregulated in multiple tumors (Ye et al., 2019; Zhang et al., 2019). Studies have shown that miR-149-5p acts an oncogene in leukemia through facilitating the proliferation and apoptosis (Tian and Yan, 2016). Bearing miRNA binding sites, some circRNAs can serve as "miRNA sponges" (Chen X. et al., 2019; Shang et al., 2019). However, the interplay between circRNAs and related miRNAs in childhood ALL has not been elucidated.

In the present study, we first identified that circADD2 is derived from the ADD2 gene, downregulated in bone marrow and cell lines of childhood ALL, and involved in the progression of ALL by sponging miR-149-5p. Our findings provide a potential clinical marker for childhood ALL.

MATERIALS AND METHODS

Clinical Samples

The study was approved by the Ethics Committee of Nanjing Medical University and all patients received written consent from their parents. Thirty bone marrow samples were obtained from newly diagnosed pediatric ALL patients receiving therapy at Children's Hospital of Nanjing Medical University (Nanjing, China) during 2018 and 2019. The control samples were obtained from children without malignant diseases.

Cell Lines

Jurkat, 6T-CEM (T-ALL lines), Nalm-6 (B-ALL lines), and 293T cells were purchased from the Shanghai Institute of Cell Biology, Chinese Academy of Sciences (Shanghai, China). The Jurkat,6T-CEM, and Nalm-6 cells were cultured in RPMI 1640 (Gibco, Carlsbad, CA, United States), 293T cells were cultured with DMEM (Gibco, Carlsbad, CA, United States) containing 10% fetal bovine serum and 1% penicillin and streptomycin. All these cell lines were maintained at 37℃ with 5% CO_2 in a humidified incubator.

Cell Transfection

For analyze circRNA overexpression, pcDNA-based circADD2 overexpression vector and pcDNA vector were synthesized by Genepharma (Shanghai, China). Stable transfection in ALL cells was performed according to manufacturer agreement. MiR-149-5p mimics (or miR-149-5p inhibitor) and NC mimics (or NC inhibitor) were obtained from RiboBio (Guangzhou, China) and transfected with Lipofectamine 2000 (Invitrogen, United States).

CircRNA Selection

For circRNAs selection, a circRNA chip (Capitalbiotech, Beijing, China) was used to predict the differentially expressed circRNAs. MiRanda was used to predict the potential binding relationship between miR-149-5p and circRNAs. circRNAs with potential miR-149-5p binding sites and significantly different expressions were selected for further verification. A larger sample size was used to verify the top three differentially expressed circRNAs (hsa_circ_0102690, hsa_circ_0120872, and hsa_circ_0027732) in the bone marrow of 30 ALL cases and 30 controls.

RNA Isolation and Quantitative Real-Time PCR (qRT-PCR)

Total RNA was extracted from bone marrow and cells by TRIzol (Invitrogen, Carlsbad, CA, United States) based on the manufacturer's protocol. We use HiScript Q RT SuperMix (Vazyme, Jiangsu, China) to reverse transcribe total RNA into cDNA for qPCR. Quantitative RT-PCR methods was performed with SYBR Green PCR Master Mix (Vazyme, Jiangsu, China). RNA relative expression was calculated by $2^{-\Delta\Delta CT}$ method. GAPDH was used as internal control for quantification of circADD2 and AKT2, while U6 for miR-149-5p.

CCK-8 Viability Assay

Cells transfected with overexpressed circADD2 were seeded into 96-well plates (5×10^3 cells/well). After 0, 24, 48, or 72 h of incubation, 10 μL of CCK-8 (Dojindo, Kumamoto, Japan) was added into each well and allowed for incubation of 2 h. The solution was measured spectrophotometrically at 450 nm.

Antibodies and Flow Cytometry Analysis

In cell apoptosis assay, the Annexin V-FITC/PI apoptosis detection kit (BD, United States) was used. First, the cells were seeded into six-well plates (5×10^5 cells/well). After 48 h, the cells exposed to different treatments were collected and washed in cold phosphate buffered saline (PBS). Then, the cells were double-stained by 5 μL of propidium iodine (PI) and 5 μL of Annexin V-fluorescein isothiocyanate (FITC), at room temperature away from light for 15 min. The stained cells were detected by flow cytometer (Beckman Coulter, Brea, CA, United States).

The proportion of Ki-67 in cells was analyzed by flow cytometry to evaluate the protein levels of Ki-67. Then, the cells were seeded into six-well plates (5×10^5cells/well). After 48 h, the cells exposed to different treatments were collected and washed for several times using PBS and 0.3 μL of phycoerythrin(PE)-conjugated mouse anti-Ki-67 antibody (Invitrogen, United States) was incubated with cells at room temperature for 20 min. Then the cells were detected by flow cytometer (Beckman Coulter, Brea, CA, United States), and the data were processed by CytExpert 2.0. We also detected Ki-67 value in untransfected ALL cells with stained antibody as isotype controls.

Tumor Xenograft Assay

The study involved in mice model was permitted by the Animal Management Committee of Nanjing Medical University. A total of 5×10^7 Jurkat cells steadily transfected with circADD2 or control vector were subcutaneously injected into 10 BALB/c nude mice (4–5 weeks old, male). Volume (V), length (L), and width (W) were measured every week and the tumors' volume was calculated with the formula $V = (W^2 \times L)/2$. After 6 weeks, the

mice were killed, the tumors were removed, and the weight of the tumor was measured.

Nuclear and Cytoplasmic Extraction Assay

Nuclear and cytoplasmic fraction was separated, followed by RNA extraction. To isolate nuclear and cytoplasmic fractions, kit of Thermo Fisher (Invitrogen, AM1921, Lithuania) was applied according to the manufacturer's agreement. The relative gene expression was calculated with $2^{-\Delta CT}$ method.

RNA Immunoprecipitation (RIP)

According to the manufacturer's protocol, RIP was conducted by Magna RIP kit (Millipore, Billerica, MA, United States). Considering the low expression of endogenous miR-149-5p in 293T, we used miR-149-5p mimics to make our experiment results more prominent. 293T cells were then transfected with miR-149-5p mimics and NC mimics. RIP experiment was carried out using AGO2 antibody (anti-AGO2) (Millipore, Billerica, MA, United States). IgG was the negative control for AGO2, while miR-NC was the negative control for miR-149-5p mimics. After 48 h, the lysated cells were incubated with the RIP buffer containing magnetic beads conjugated to anti-AGO2 or control immunoglobulin G (anti-IgG) (Millipore, Billerica, MA, United States) overnight at 4°C overnight. After washing with buffer for several times, the qRT-PCR was performed to analyze the purified RNA.

Dual-Luciferase Reporter Assay

For the dual-luciferase reporter assay, the wild-type and the mutated 3′UTRs of circADD2 containing the binding cites of miR-149-5p were subcloned into the pmiR-RB-Report™ vectors (RiboBio, Guangzhou, China) to, respectively, get pmiR-RB-REPOR-circADD2-WT and pmiR-RB-REPORT-circADD2-MUT. The circADD2-WT primers were forward 5′-GCGCTCGAGTTTCCACCTGGATGTTTGAGGT-3′ and reverse 5′-AATGCGGCCGCTCATGGAAGATGTCGGGAAGA-3′, and the circADD2-MUT primers were forward 5′-ACC CCCACCTCTGTGACGAGTGAACAGAACCTCGGTTCCTCA GGGCTGGGCCAGCCTCC-3′ and reverse 5′-GAGG AACCGAGGTTCTGTTCACTCGTCACAGAGGTGGGGGTA GCTCCACTCTCAAGGGTGC-3′. MiR-149-5p mimics and NC mimics were cotransfected into 293T cells, with the luciferase reporter vectors, respectively. Luciferase activity was measured 48 h later according to manufacture's procedures (Promega, Madison, WI, United States).

Western Blot Analysis

The total protein of cells was exacted with RIPA buffer, separated with SDS-PAGE and transferred onto PVDF membranes (Bio-Rad, CA, United States). The membranes were blocked with 5% skimmed milk powder and incubated with primary antibodies against AKT2, p-AKT2, p-AKT, AKT (CST, 1:1,000) and GAPDH (CST, 1:2,000) at 4°C overnight, then incubated with secondary antibodies (CST, 1:5,000) at room temperature for 1 h. Membranes were detected by chemiluminescence system(Bio-Rad).

Immunohistochemistry (IHC)

As for IHC staining, after procedures of dewaxing, rehydration and antigen retrieval, the sections were incubated with primary anti-AKT2 antibody (CST, 1:1,000) overnight at 4°C, then with secondary antibody for 2 h at 37°C. The slices were added with HRP-labeled streptavidin solution, then stained by 3,30-diaminobenzidine (DAB), counterstained with hematoxylin, and photographed under a microscope (Leica, Wetzlar, Germany).

Bioinformatics Analyses

We used several databases to pinpoint the target genes of miR-149-5p. miRTarBase[1], miRWalk[2], and StarBase[3]. The miR-149-5p-mRNAs regulatory networks were visualized using the Cystoscope software V3.8.0.

Statistical Analysis

All data were presented as the means ± standard error of mean (SEM). Unpaired *t*-tests was used to compare group differences. Statistical analyses were conducted using GraphPad Prism 8 software (GraphPad Prism, Inc., La Jolla, CA, United States). $P < 0.05$ was considered significant.

RESULTS

Selection of CircADD2 in Childhood ALL

We used a chip to detect the differentially expressed circRNAs in the bone marrow of children with ALL and the non-tumor control group (**Figure 1A**). We have uploaded the raw data and analyzed data to a public database, which could be checked in https://www.ncbi.nlm.nih.gov/geo/query/acc.cgi?acc=GSE166579. Based on the cutoff value of corrected *P*-value < 0.05, we selected 11163 circRNAs with differential expression, including 3976 up-regulated and 7187 down-regulated. To determine the circRNAs regulating miR-149-5p, we calculated the sequence matching and free energy between circRNAs and miRNAs based on the miRanda algorithm. Then we selected circRNAs with potential miR-149-5p binding sites and significantly differential expressions between ALL and non-ALL tissues ($p < 0.05$). We continued to expand the sample size to verify the top three differentially expressed circRNAs (hsa_circ_0102690, hsa_circ_0120872, and hsa_circ_0027732) in the bone marrow of 30 ALL cases and 30 controls. The results showed that the expression level of hsa_circ_0120872 in children with ALL was significantly lower in the control group, which was consistent with the results of preliminary screening (**Figure 1B**). Besides, has_circ_0120872 was found lowly expressed in ALL cells (Jurkar, 6T-CEM and Nalm-6) than in normal cell line 293T (**Figure 1C**). Hsa_circ_0120872 was derived from exon 2-4 of ADD2 gene located in the region chr2:70931452-70940316. The

[1]http://mirtarbase.cuhk.edu.cn/php/index.php

[2]http://mirwalk.umm.uni-heidelberg.de/

[3]http://starbase.sysu.edu.cn/

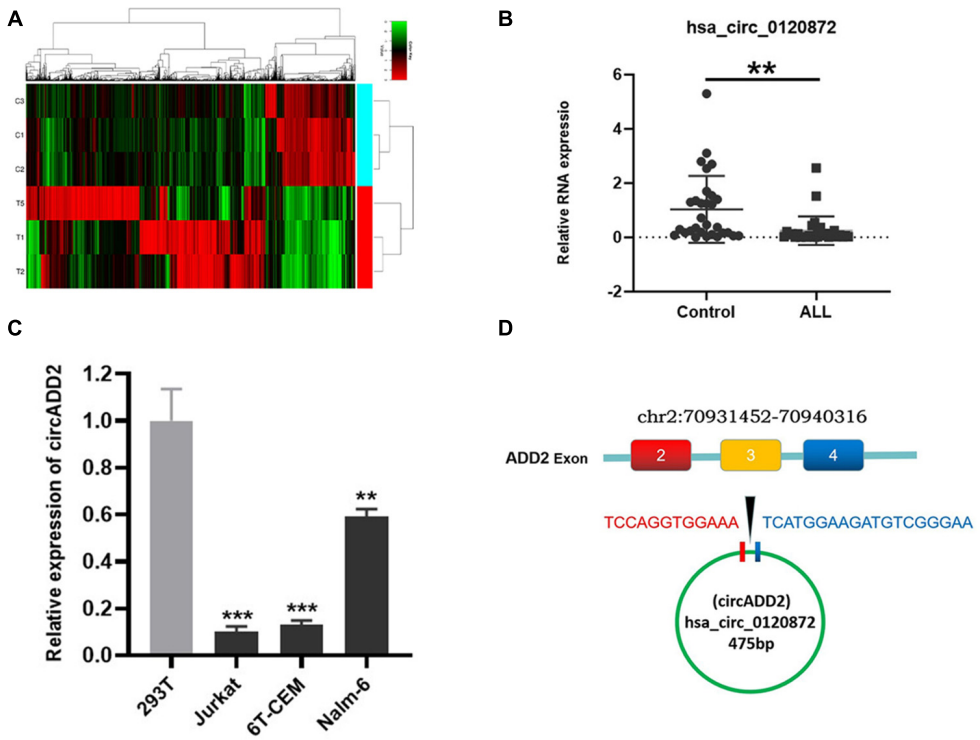

FIGURE 1 | Detection of circRNA expression in childhood ALL. **(A)** A heatmap showing the differentially expressed circRNAs in ALL and control groups. The results showed a distinguishable circRNA expression profile among samples. Red: upregulation; green: downregulation; black: no change. **(B)** qRT-PCR confirmed the low expression of circADD2 in children with ALL compared with control group ($n = 30$). **(C)** The circADD2 expression in ALL cell lines was prominently lower than the normal cell line 293T. **(D)** Genomic loci of ADD2 and circADD2. Data were showed as mean ± SD and analyzed by unpaired *t*-test, $^{**}P < 0.01$, $^{***}P < 0.001$.

ADD2 gene sequence was 8,864 bp in length and the spliced mature circRNA was 475 bp (**Figure 1D**). We therefore named hsa_circ_0120872 as circADD2.

CircADD2 Inhibits the Proliferation of ALL Cells *in vitro*

To explore the biological function of circADD2 in ALL, we overexpressed circADD2 in ALL cell lines (**Figure 2A**). CCK-8 assay demonstrated that circADD2 overexpression significantly decreased the proliferation of Jurkat, 6T-CEM and Nalm-6 cells after a transfection of 48 h and 72 h, as shown by their growth curves (**Figure 2B**). As shown in **Figures 2C,D**, compared with NC groups, the proportion of apoptotic ALL cells in circADD2 overexpressed groups were significantly elevated, revealing that circADD2 overexpression promoted cell apoptosis. Meanwhile, we detected the level of Ki-67, a typical marker of proliferation. Lower level of Ki-67 was observed in ALL cells with overexpressed circADD2 (**Figures 2E,F**), which was also consistent with the results of CCK-8 assay.

CircADD2 Suppresses Tumor Growth *in vivo*

Additionally, to investigate whether circADD2 overexpression retards ALL growth *in vivo*, a subcutaneous tumor mice model was constructed. Jurkat cells stably transfected with circADD2 or control vector were injected subcutaneously into the nude mice. Three weeks after injection, the tumor volumes were measured weekly. The results showed that circADD2 overexpression significantly inhibited tumor growth *in vivo* (**Figures 3A,B**). As shown in **Figure 3C**, tumor growth curves were made in different groups. The tumor volume was significantly reduced in circADD2 overexpressed group 5–6 weeks after cell injection. Then, we removed the tumor tissue and weighed it. Compared with the control group, the weight of tumor was significantly lighter in circADD2-treated group (**Figure 3D**). Taken together, circADD2 suppressed ALL progression, both *in vitro* and *in vivo*.

CircADD2 May Regulate Cell Proliferation and Apoptosis Through Sponging miR-149-5p

To investigate the enrichment of circADD2 in the cells, we extracted and separated cytoplasmic RNA and nuclear RNA and evaluated circADD2 expression using qRT-PCR. Results revealed that circADD2 was preferentially expressed in the cytoplasm of Jurkat and 6T-CEM cells (**Figure 4A**). Given that circADD2 was enriched in the cytoplasm, we then carried out RNA immunoprecipitation assay (RIP) with argonaute2 (AGO2) antibodies. Studies have shown that circRNA-AGO2-miRNA may form a ternary complex. To increase the percentage

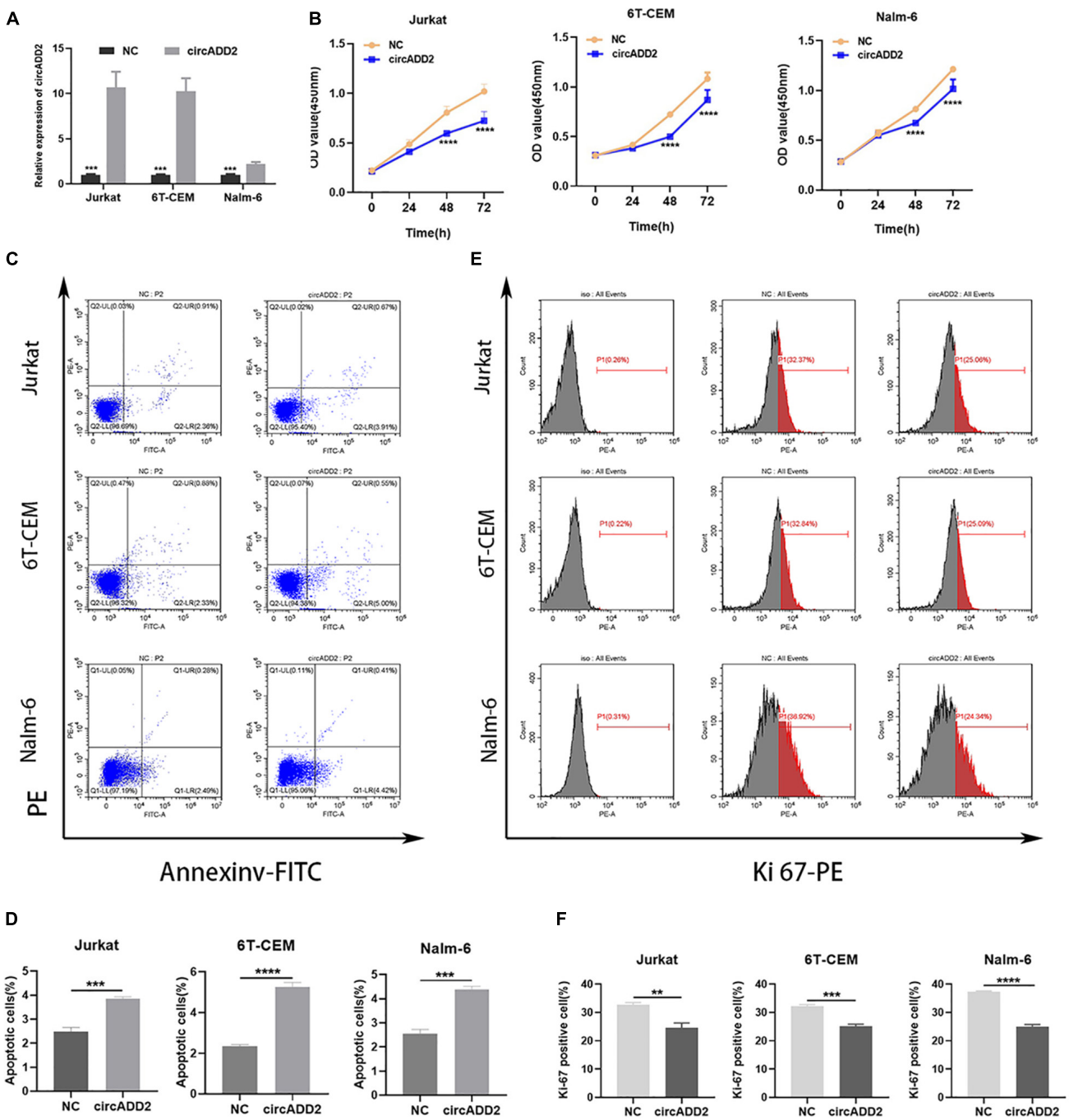

FIGURE 2 | CircADD2 overexpression suppressed ALL progression. **(A)** Expression of circADD2 was detected in Jurkat, 6T-CEM and Nalm-6 cells transfected with circADD2 overexpression vector and control vector by qRT-PCR. Results indicated successful overexpression of circADD2. **(B)** CCK-8 assay showed that after circADD2 overexpressing vector was transfected in Jurkat, 6T-CEM and Nalm-6 cells for 48 and 72 h, proliferation of the ALL cells was significantly inhibited. **(C,D)** Apoptotic rate of Jurkat, 6T-CEM and Nalm-6 cell lines was analyzed by flow cytometry. After overexpression of circADD2, ALL cell apoptotic rate was remarkably increased. **(E,F)** The ratio of Ki-67 in Jurkat, 6T-CEM and Nalm-6 cells was detected by flow cytometry. The level of Ki-67 positive cells was significantly reduced after overexpression of circADD2. Data were showed as mean ± SD and analyzed by unpaired *t*-test, $^{**}P < 0.01$, $^{***}P < 0.001$, $^{****}p < 0.0001$.

of the miR-149-5p-AGO2 complex, miR-149-5p mimics were transfected into 293T cells, the expression of miR-149-5p increased 12.05-fold (**Supplementary Figure 2**), and then we detected significant enrichment of circADD2 in the RNA complex immunoprecipitated by AGO2 antibody, indicating the potential combination of miR-149-5p with circADD2

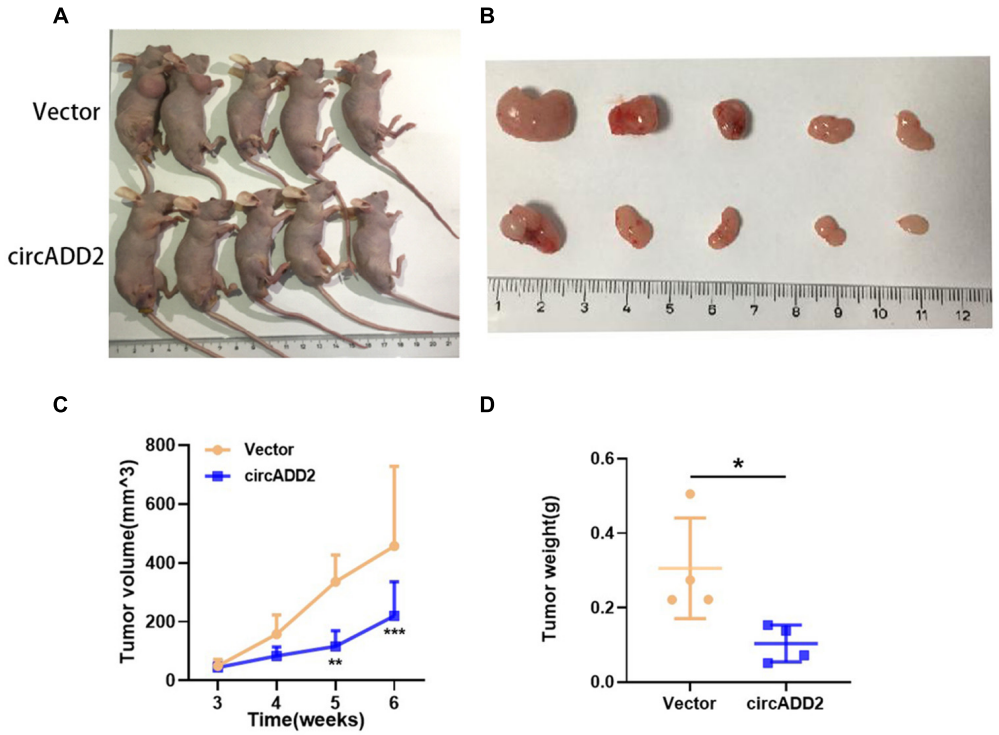

FIGURE 3 | Over-expressed circADD2 Jurkat cells were injected into nude mice to detect the effect of circADD2 ($n = 5$) *in vivo*. **(A)** Jurkat cells stably transfected with circADD2 or control vector were injected into nude mice with established subcutaneous xenograft tumors. **(B)** Representative pictures of xenograft tumor formation in nude mice (top: control group; bottom: treated group). **(C,D)** Compared with the vector group, circADD2-treated nude mice exhibited significantly smaller tumor volume and significantly lighter tumor weight after cell injection for 5–6 weeks. Data were showed as mean ± SD and analyzed by unpaired *t*-test, $^{*}P < 0.05$, $^{**}P < 0.01$, $^{***}P < 0.001$.

(**Figure 4B**). Furthermore, we found that overexpression of circADD2 reduced miR-149-5p level in ALL cells (**Figure 4C**). We also detected the expression levels of miR-149-5p and circADD2 in RNA extracted from the tissue of mouse tumor that was induced by subcutaneously injected Jurkat cells. Results suggested that miR-149-5p level was significantly decreased after circADD2 overexpression *in vivo*, while circADD2 level was elevated (**Figure 4D**). Then, the luciferase reporter assay was used to demonstrate the interaction between circADD2 and miR-149-5p in 293T cells, and the results showed that miR-149-5p significantly reduced the luciferase activity of circADD2 WT reporter, but not that of the reporters with mutated miR-149-5p binding site (**Figures 4E,F**). These results suggest that circADD2 sponges miR-149-5p.

To confirm whether circADD2 acts by sponging miR-149-5p, circADD2 overexpressing plasmid and miR-149-5p were co-transfected into Jurkat and 6T-CEM cells in rescue assays. The cells transfected with NC plus miR-NC were used as controls. The proliferative rate showed no significant change after circADD2 overexpressing plasmid and miR-149-5p were co-transfected into Jurkat and 6T-CEM cells (**Figure 5A**). We observed that compared with the NC + miR-NC groups, the apoptosis did not change in circADD2 + miR-149-5p groups (**Figures 5B,C**). Also, there was no remarkable difference in the levels of Ki-67-positive cells between treated and control groups (**Figures 5D,E**). Taken together, circADD2 sponged miR-149-5p, with competition in their regulation.

CircADD2 Modulates the Expression of AKT2

We exported the downstream genes of miR-149-5p through databases (i.e., miRTarBase, miRWalk, and StarBase), finding that 119 mRNAs were overlapped (**Figure 6A**). We used Cytoscape to visualize the 119 target genes of miR-149-5p (**Figure 6B**). Using Kyoto Encyclopedia of Genes and Genomes (KEGG) pathway analysis, the enrichment pathways of these 119 target genes are shown in **Figure 6C**. We found that AKT2 was highly enriched in these signaling pathways. Interestingly, AKT2 was a gene predicted in all miRTarBase, miRWalk, and StarBase databases. Then, we selected AKT2 as one target gene of miR-149-5p. Western blot and qRT-PCR results showed that overexpression of miR-149-5p increased the level of AKT2, and inhibition of miR-149-5p reduced the level of AKT2 (**Figures 6D,E**). Considering the function of ceRNA, we hypothesized that cirADD2 may regulate the expression of AKT2 through sponging miR-149-5p. As expected, we found that circADD2 overexpression markedly decreased the protein and mRNA levels of AKT2 in Jurkat, 6T-CEM and Nalm-6 cells, as well as the protein level of p-AKT2 (**Figures 6F,G**). Moreover, we removed the

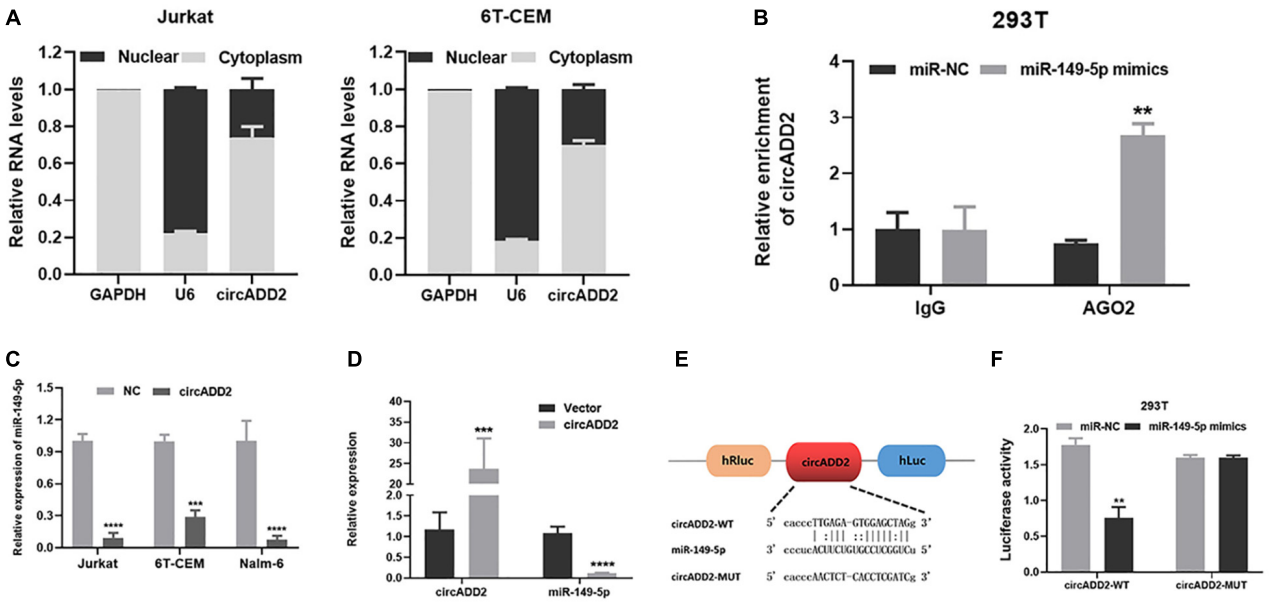

FIGURE 4 | CircADD2 sponged miR-149-5p. **(A)** Cellular localization of circADD2 in Jurkat and 6T-CEM. Results revealed that circADD2 was mainly expressed in the cytoplasm ALL cells. **(B)** CircADD2 levels in purified RNA collected from products of anti-AGO2 or anti-IgG was detected by RT-qPCR. After miR-149-5p mimics was transfected into 293T cells, significant enrichment of circADD2 in the RNA complex immunoprecipitated by AGO2 antibody was observed. **(C)** qRT-PCR confirmed the decreased level of miR-149-5p in ALL cells after overexpression of circADD2. **(D)** CircADD2 and miR-149-5p levels were detected by qRT-PCR in tumor cells from xenograft generated by Jurkat cells stably transfected with circADD2 or control vector. MiR-149-5p level was significantly decreased after circADD2 overexpression *in vivo*, while circADD2 level was elevated. **(E,F)** Dual luciferase reporter assay was used to prove the binding between circADD2 and miR-149-5p. The fluorescence activity of circADD2–WT was reduced and the fluorescence activity in circADD2–MUT was basically unchanged when transfected with miR–149-5p mimics. Data were showed as mean ± SD and analyzed by unpaired *t*-test, $^{**}P < 0.01$, $^{***}P < 0.001$, $^{****}P < 0.0001$.

animal tumors and extracted RNA. The results showed that circADD2 overexpression reduced the expression of AKT2 *in vivo* (**Figure 6H**). IHC (Immunohistochemistry) analysis showed that the expression of AKT2 was reduced in the tumors formed by ALL cells over-expressing circADD2 (**Figure 6I**). These results suggested that circADD2 could regulate the expression of AKT2 in ALL.

DISCUSSION

CircRNAs, as a class of abundant and stable endogenous ncRNAs, are gaining considerable attention for their potentials of regulating cancer development (Jeck and Sharpless, 2014; Geng et al., 2018). Our study reported the down-regulation of circADD2 in childhood ALL bone marrow and ALL cell lines. Our *in vitro* and *in vivo* experiments verified that circADD2 could competitively bind to miR-149-5p to adversely affected ALL cell lines *in vitro* and *in vivo*, reducing AKT2 expression, and thereby inhibit the progression of ALL.

Studies have shown that circRNAs are differentially expressed between tumor and normal tissues, suggesting their important roles in tumorigenesis (Song et al., 2016; Lu et al., 2018). In the present study, we first identified the differentially expressed circRNAs in childhood ALL through microarray analysis. Next, we screened out circADD2, a significantly down-regulated circRNA with a potential miR-149-5p binding site. In the present study, we confirmed the low expression of circADD2 in bone marrow samples of 30 children with ALL, as well as three ALL cell lines. Subsequently, the functional analysis showed that the overexpression of circADD2 in Jurkat, 6T-CEM and Nalm-6 cells could inhibit the proliferation and apoptosis of ALL cells. These results suggested that circADD2 overexpression could suppress the proliferation and promote apoptosis of ALL cells.

Accumulating evidence indicates that circRNAs may function through competitively binding to miRNAs (ceRNAs), and the ceRNA hypothesis indicates that circRNAs may sponge miRNA to counter the latter's effects on its target genes (Zhong et al., 2018; Chen S. et al., 2019). For example, circCCDC9 sponges miR-6792-3p to suppress the progression of gastric cancer through up regulating CAV1 expression (Luo et al., 2020). In another example, circCTNNA1 promotes colorectal cancer progression via circCTNNA1/miR-149-5p/FOXM1 axis (Chen et al., 2020). Also, circSLC8A1 plays a suppressive role in bladder cancer progression via sponging miR-130b/miR-494 and upregulating downstream PTEN (Lu et al., 2019). It should be noted that miR-149-5p has been identified as an oncogene in childhood leukemia. For instance, Tian demonstrated that miR-149-5p was highly expressed in AML, and could promote AML progression by decreasing cell apoptosis (Tian and Yan, 2016). Another example showed miR-149-5p was highly expressed in T-ALL, and that miR-149-5p functioned as an oncogene via regulating proliferation, cell cycle, and apoptosis

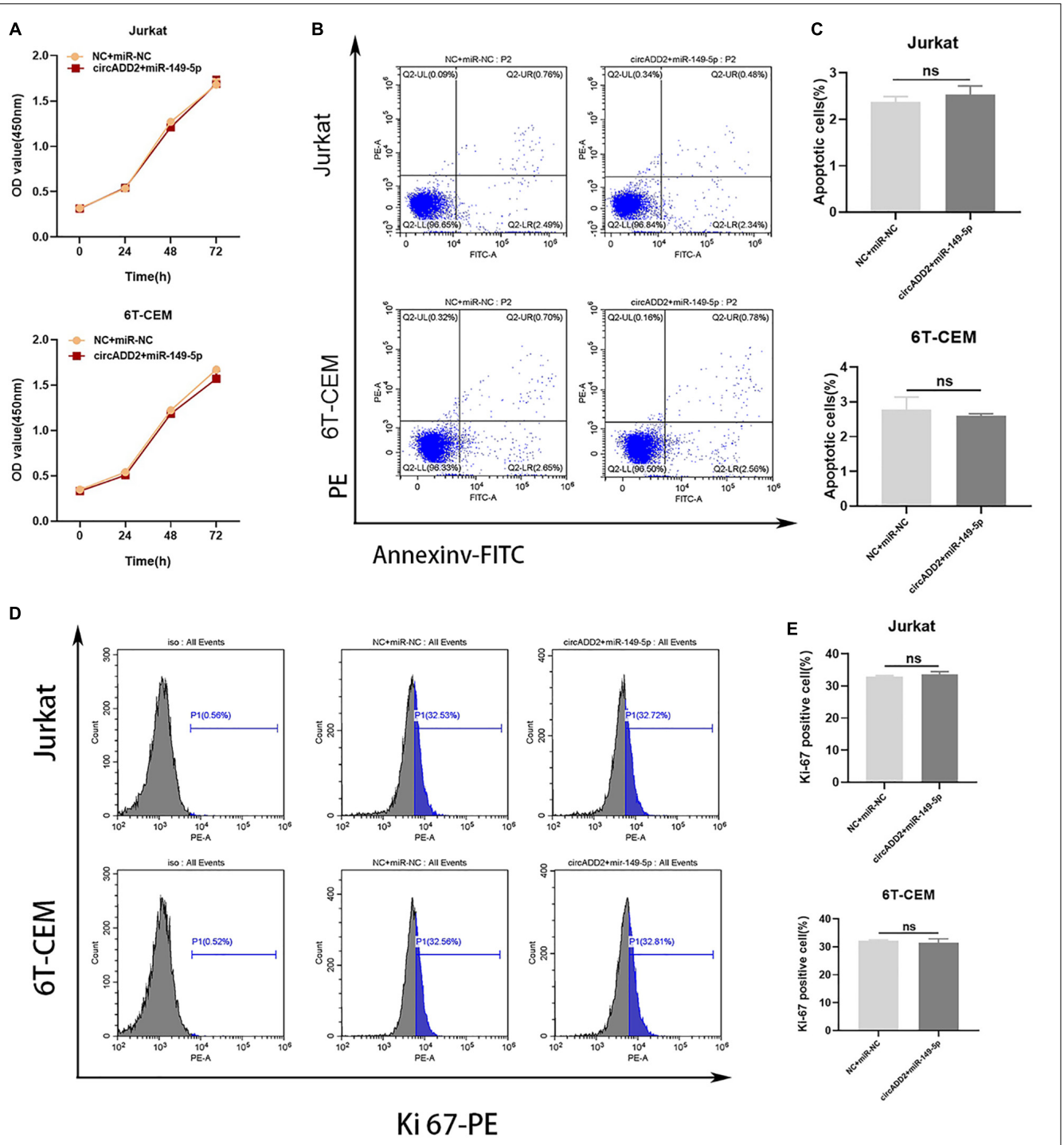

FIGURE 5 | MiR-149-5p overexpression eliminated the effect of circADD2 overexpression. **(A)** CCK-8 assay showed no significant change in proliferation rate after circADD2 overexpressing plasmid and miR-149-5p were co-transfected into Jurkat and 6T-CEM cells. **(B,C)** Apoptotic rate of cells transfected with NC + miR-NC or circADD2 + miR-149-5p was analyzed by flow cytometry. Compared with the NC + miR-NC groups, there was no change in apoptosis in the circADD2 + miR-149-5p groups. **(D,E)** There was no remarkable difference of the levels of Ki-67-positive cells between circADD2 + miR-149-5p group and NC + miR-NC group. Data were showed as mean ± SD and analyzed by unpaired *t*-test, ns: no significance.

(Fan et al., 2016). Based on these observations, we aimed to identify how circADD2 works in childhood ALL through sponging miR-149-5p.

AGO2 is an indicator protein in the sponging of circRNA, and studies have confirmed that circRNA-AGO2-miRNA may form a ternary complex (Chen Y. et al., 2019). In the present study, the

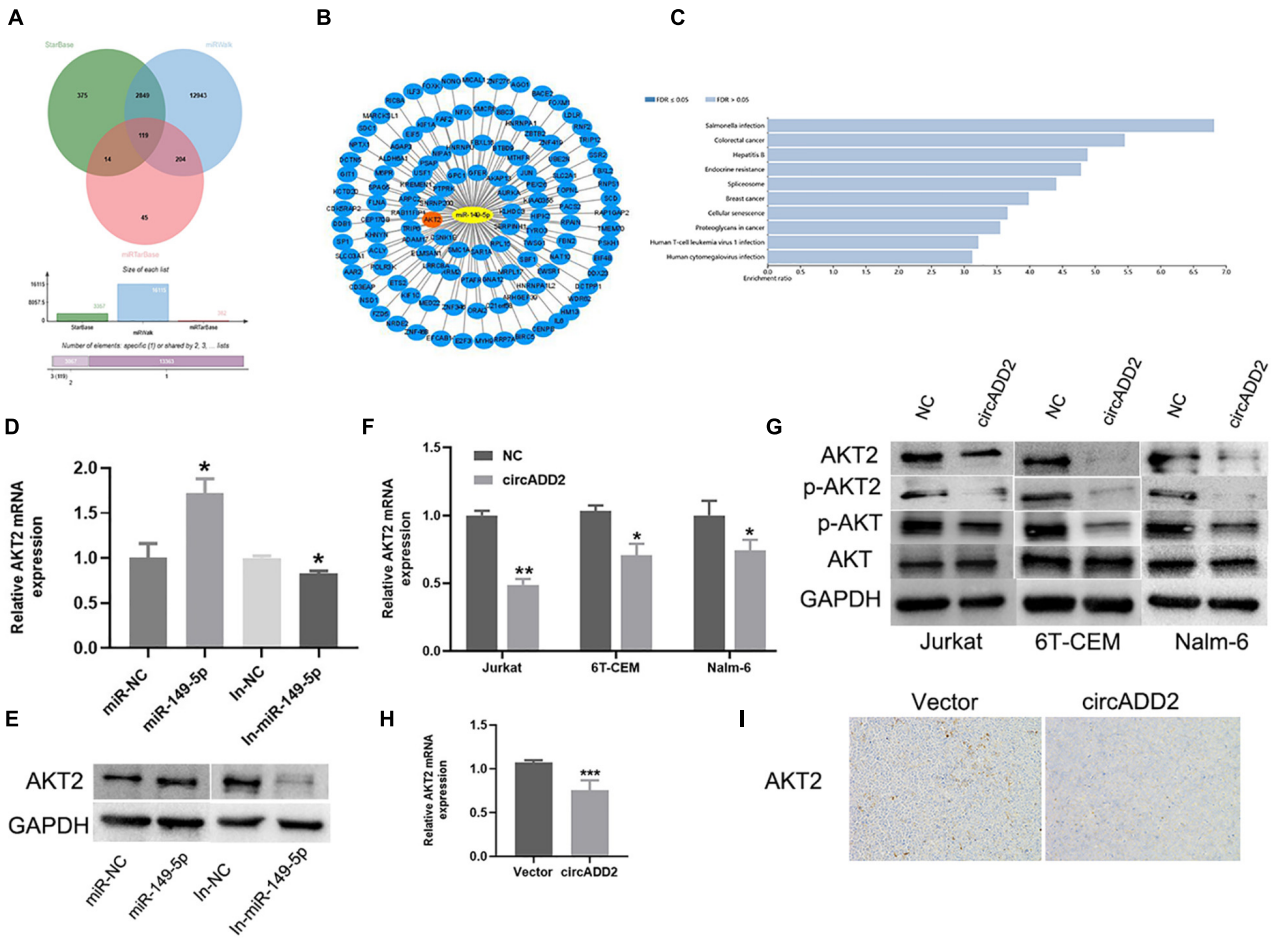

FIGURE 6 | Overexpression of circADD2 reduced the expression of AKT2. **(A)** The Venn plots showed downstream genes binding to miR-149-5p. **(B)** Cytoscape graphs of miR-149-5p and target genes. **(C)** KEGG enriched the signal pathways of miR-149-5p target genes. **(D,E)** Jurkat cells transfected with miR-149-5p mimics or miR-149-5p inhibitor. The level of AKT2 was detected by qRT-PCR and western blot. The results showed that miR-149-5p increased AKT2 expression, while inhibition of miR-149-5p decreased AKT2 expression. **(F,G)** Relative expression of AKT2 was detected by qRT-PCR and Western blot in ALL cells transfected with circADD2. We found that after overexpression of circADD2, the level of AKT2 and its phosphorylation decreased. **(H)** AKT2 levels were detected by qRT-PCR in tumor cells from xenograft generated by Jurkat cells stably transfected with circADD2 or control vector. AKT2 level was significantly decreased after circADD2 overexpression *in vivo*. **(I)** IHC staining was used to detect the expression of AKT2 in the xenografts, and the level of AKT2 in the circADD2 groups was significantly reduced. Data were showed as mean ± SD and analyzed by unpaired *t*-test, $^{*}P < 0.05$, $^{**}P < 0.01$, $^{***}P < 0.001$.

RIP assay of 293T cells confirmed that circADD2 could bind to AGO2 and act as miRNAs sponge. Using dual-luciferase reporter assay, the present study revealed that circADD2 could sponge miR-149-5p in ALL cells, laying a foundation for further research on the biological characteristics of circADD2. This evidence proved the potential of circADD2 as a novel biomarker and a therapeutic target in childhood ALL.

Furthermore, we used some bioinformatics tools to filter out the target genes of miR-149-5p. Accordingly, KEGG analysis revealed that AKT2 was significantly enriched in several cancer-related signaling pathways, suggesting that AKT2 may act as a cancer gene in childhood ALL. Studies have also demonstrated that AKT2 plays important roles in the carcinogenesis of leukemia (Gong et al., 2014; Ying et al., 2018). Most studies have shown that miRNAs could repress the expression of target genes by binding to the 3′untranslated region (3′UTR) (Hausser et al., 2013; Wang et al., 2015). However, our study discovered that miR-149-5p overexpression up-regulated AKT2 in ALL cells. We inferred that after miR-149-5p is overexpressed, AKT2 was upregulated in a compensatory manner. Besides, although many studies have suggested that miRNA can down-regulate its target genes, miRNA can play positive roles in regulating the expression of target genes. miRNAs positively regulate gene transcription through targeted promoters, a process called RNA activation (RNAa) (Huang et al., 2012; Zheng et al., 2014; Portnoy et al., 2016). A subset of miRNAs from enhancer sites can activate transcription and function as an activator (Xiao et al., 2017). This may explain our findings. In the present study, we found that circADD2 could reduce the expression of AKT2, a condition probably involving ceRNA mechanism of circADD2 and miR-149-5p. Considering the promotive role of AKT2 in leukemia, we hypothesized that circADD2 may

sponge miR-149-5p to regulate AKT2 expression in childhood ALL. Further studies should be conducted to confirm AKT2 as the direct effector of circADD2/miR-149-5p/AKT2 axis in the pathogenesis of ALL.

Here we identified that circADD2 could restrain ALL progression. Further studies with a larger sample size, including bone marrow samples collected in both diagnosis and treatment process of childhood ALL, should be organized to comprehensively evaluate the value of circADD2 as a biomarker in childhood ALL.

CONCLUSION

The expression of circADD2 is down-regulated in childhood ALL. This circRNA can sponge miR-149-5p to inhibit the proliferation of leukemia cells *in vitro* and *in vivo*. circADD2 can regulate the expression of AKT2 probably through its ceRNA effect on miR-149-5p. circADD2 may serve as a potential biomarker and a therapeutic target in childhood ALL.

DATA AVAILABILITY STATEMENT

The datasets presented in this study can be found in online repositories. The names of the repository/repositories and accession number(s) can be found below: NCBI Gene Expression Omnibus, accession no: GSE166579.

ETHICS STATEMENT

The studies involving human participants were reviewed and approved by the Ethics Committee of Nanjing Medical University. Written informed consent to participate in this study was provided by the participants' legal guardian/next of kin. The animal study was reviewed and approved by Animal Management Committee of Nanjing Medical University. Written informed consent was obtained from the minor(s)' legal guardian/next of kin for the publication of any potentially identifiable images or data included in this article.

AUTHOR CONTRIBUTIONS

YF, YX, and YZ contributed to the design of the study. YZ, XM, and HZ wrote the first edition of the manuscript and performed the experiments. YW and MK made the figures. YF and YX revised the version of the manuscript finally. All authors have reviewed and approved this manuscript and consented to publish this manuscript.

FUNDING

This research was supported by the National Natural Science Foundation of China (81602913, 81670155, and 81903383), China Postdoctoral Science Foundation funded project (2019M650118), the Nanjing Medical Science and Technology Development Foundation (QRX17164), the Natural Science Foundation of Jiangsu Province (BK20150085), and Special Fund for Health Science and Technology Development in Nanjing (JQX19008).

SUPPLEMENTARY MATERIAL

The Supplementary Material for this article can be found online at: https://www.frontiersin.org/articles/10.3389/fcell.2021.639910/full#supplementary-material

REFERENCES

Aufiero, S., Reckman, Y. J., Pinto, Y. M., and Creemers, E. E. (2019). Circular RNAs open a new chapter in cardiovascular biology. *Nat. Rev. Cardiol.* 16, 503–514. doi: 10.1038/s41569-019-0185-2

Chen, P., Yao, Y., Yang, N., Gong, L., Kong, Y., and Wu, A. (2020). Circular RNA circCTNNA1 promotes colorectal cancer progression by sponging miR-149-5p and regulating FOXM1 expression. *Cell Death Dis.* 11:557. doi: 10.1038/s41419-020-02757-7

Chen, S., Yang, C., Sun, C., Sun, Y., Yang, Z., Cheng, S., et al. (2019). miR-21-5p suppressed the sensitivity of hepatocellular carcinoma cells to cisplatin by targeting FASLG. *DNA Cell Biol.* 38, 865–873. doi: 10.1089/dna.2018.4529

Chen, X., Yang, T., Wang, W., Xi, W., Zhang, T., Li, Q., et al. (2019). Circular RNAs in immune responses and immune diseases. *Theranostics* 9, 588–607. doi: 10.7150/thno.29678

Chen, Y., Yang, F., Fang, E., Xiao, W., Mei, H., Li, H., et al. (2019). Circular RNA circAGO2 drives cancer progression through facilitating HuR-repressed functions of AGO2-miRNA complexes. *Cell Death Differ.* 26, 1346–1364. doi: 10.1038/s41418-018-0220-6

Fan, S. J., Li, H. B., Cui, G., Kong, X. L., Sun, L. L., Zhao, Y. Q., et al. (2016). miRNA-149* promotes cell proliferation and suppresses apoptosis by mediating JunB in T-cell acute lymphoblastic leukemia. *Leuk. Res.* 41, 62–70. doi: 10.1016/j.leukres.2015.11.016

Geng, Y., Jiang, J., and Wu, C. (2018). Function and clinical significance of circRNAs in solid tumors. *J. Hematol. Oncol.* 11:98. doi: 10.1186/s13045-018-0643-z

Gong, J. N., Yu, J., Lin, H. S., Zhang, X. H., Yin, X. L., Xiao, Z., et al. (2014). The role, mechanism and potentially therapeutic application of microRNA-29 family in acute myeloid leukemia. *Cell Death Differ.* 21, 100–112. doi: 10.1038/cdd.2013.133

Hausser, J., Syed, A. P., Bilen, B., and Zavolan, M. (2013). Analysis of CDS-located miRNA target sites suggests that they can effectively inhibit translation. *Genome Res.* 23, 604–615. doi: 10.1101/gr.139758.112

Huang, V., Place, R. F., Portnoy, V., Wang, J., Qi, Z., Jia, Z., et al. (2012). Upregulation of Cyclin B1 by miRNA and its implications in cancer. *Nucleic Acids Res.* 40, 1695–1707. doi: 10.1093/nar/gkr934

Hunger, S. P., and Mullighan, C. G. (2015). Acute Lymphoblastic Leukemia in Children. *N. Engl. J. Med.* 373, 1541–1552. doi: 10.1056/NEJMra1400972

Iacobucci, I., and Mullighan, C. G. (2017). Genetic basis of acute lymphoblastic Leukemia. *J. Clin. Oncol.* 35, 975–983. doi: 10.1200/JCO.2016.70.7836

Inaba, H., Greaves, M., and Mullighan, C. G. (2013). Acute lymphoblastic leukaemia. *Lancet* 381, 1943–1955. doi: 10.1016/S0140-6736(12)62187-4

Jeck, W. R., and Sharpless, N. E. (2014). Detecting and characterizing circular RNAs. *Nat. Biotechnol.* 32, 453–461. doi: 10.1038/nbt.2890

Lu, C., Shi, X., Wang, A. Y., Tao, Y., Wang, Z., Huang, C., et al. (2018). RNA-Seq profiling of circular RNAs in human laryngeal squamous cell carcinomas. *Mol. Cancer.* 17:86. doi: 10.1186/s12943-018-0833-x

Lu, Q., Liu, T., Feng, H., Yang, R., Zhao, X., Chen, W., et al. (2019). Circular RNA circSLC8A1 acts as a sponge of miR-130b/miR-494 in suppressing bladder cancer progression via regulating PTEN. *Mol. Cancer* 18:111. doi: 10.1186/s12943-019-1040-0

Luo, Z., Rong, Z., Zhang, J., Zhu, Z., Yu, Z., Li, T., et al. (2020). Circular RNA circCCDC9 acts as a miR-6792-3p sponge to suppress the progression of gastric cancer through regulating CAV1 expression. *Mol. Cancer* 19:86. doi: 10.1186/s12943-020-01203-8

Meng, S., Zhou, H., Feng, Z., Xu, Z., Tang, Y., Li, P., et al. (2017). CircRNA: functions and properties of a novel potential biomarker for cancer. *Mol. Cancer* 16:94. doi: 10.1186/s12943-017-0663-2

Portnoy, V., Lin, S. H., Li, K. H., Burlingame, A., Hu, Z. H., Li, H., et al. (2016). saRNA-guided Ago2 targets the RITA complex to promoters to stimulate transcription. *Cell Res.* 26, 320–335. doi: 10.1038/cr.2016.22

Shang, Q., Yang, Z., Jia, R., and Ge, S. (2019). The novel roles of circRNAs in human cancer. *Mol. Cancer* 18:6. doi: 10.1186/s12943-018-0934-6

Song, X., Zhang, N., Han, P., Moon, B. S., Lai, R. K., Wang, K., et al. (2016). Circular RNA profile in gliomas revealed by identification tool UROBORUS. *Nucleic Acids Res.* 44:e87. doi: 10.1093/nar/gkw075

Szabo, L., and Salzman, J. (2016). Detecting circular RNAs: bioinformatic and experimental challenges. *Nat. Rev. Genet.* 17, 679–692. doi: 10.1038/nrg.2016.114

Teachey, D. T., and Pui, C. H. (2019). Comparative features and outcomes between paediatric T-cell and B-cell acute lymphoblastic leukaemia. *Lancet Oncol.* 20, e142–e154. doi: 10.1016/S1470-2045(19)30031-2

Tian, P., and Yan, L. (2016). Inhibition of MicroRNA-149-5p induces apoptosis of acute myeloid leukemia cell line THP-1 by targeting Fas Ligand (FASLG). *Med. Sci. Monit.* 22, 5116–5123. doi: 10.12659/msm.899114

Wang, J. X., Gao, J., Ding, S. L., Wang, K., Jiao, J. Q., Wang, Y., et al. (2015). Oxidative modification of miR-184 enables it to target Bcl-xL and Bcl-w. *Mol. Cell* 59, 50–61. doi: 10.1016/j.molcel.2015.05.003

Wang, R., Zhang, S., Chen, X., Li, N., Li, J., Jia, R., et al. (2018). EIF4A3-induced circular RNA MMP9 (circMMP9) acts as a sponge of miR-124 and promotes glioblastoma multiforme cell tumorigenesis. *Mol. Cancer* 17:166. doi: 10.1186/s12943-018-0911-0

Xiao, M., Li, J., Li, W., Wang, Y., Wu, F., Xi, Y., et al. (2017). MicroRNAs activate gene transcription epigenetically as an enhancer trigger. *RNA Biol.* 14, 1326–1334. doi: 10.1080/15476286.2015.1112487

Ye, Z. M., Yang, S., Xia, Y. P., Hu, R. T., Chen, S., Li, B. W., et al. (2019). LncRNA MIAT sponges miR-149-5p to inhibit efferocytosis in advanced atherosclerosis through CD47 upregulation. *Cell Death Dis.* 10:138. doi: 10.1038/s41419-019-1409-4

Ying, X., Zhang, W., Fang, M., Zhang, W., Wang, C., and Han, L. (2018). miR-345-5p regulates proliferation, cell cycle, and apoptosis of acute myeloid leukemia cells by targeting AKT2. *J. Cell Biochem.* doi: 10.1002/jcb.27461 [Epub ahead of print].

Yu, T., Wang, Y., Fan, Y., Fang, N., Wang, T., Xu, T., et al. (2019). CircRNAs in cancer metabolism: a review. *J. Hematol. Oncol.* 12:90. doi: 10.1186/s13045-019-0776-8

Zeng, K., He, B., Yang, B. B., Xu, T., Chen, X., Xu, M., et al. (2018). The pro-metastasis effect of circANKS1B in breast cancer. *Mol. Cancer* 17:160. doi: 10.1186/s12943-018-0914-x

Zhang, X., Wang, S., Wang, H., Cao, J., Huang, X., Chen, Z., et al. (2019). Circular RNA circNRIP1 acts as a microRNA-149-5p sponge to promote gastric cancer progression via the AKT1/mTOR pathway. *Mol. Cancer* 18:20. doi: 10.1186/s12943-018-0935-5

Zheng, L., Wang, L., Gan, J., and Zhang, H. (2014). RNA activation: promise as a new weapon against cancer. *Cancer Lett.* 355, 18–24. doi: 10.1016/j.canlet.2014.09.004

Zhong, Y., Du, Y., Yang, X., Mo, Y., Fan, C., Xiong, F., et al. (2018). Circular RNAs function as ceRNAs to regulate and control human cancer progression. *Mol. Cancer* 17:79. doi: 10.1186/s12943-018-0827-8

Conflict of Interest: The authors declare that the research was conducted in the absence of any commercial or financial relationships that could be construed as a potential conflict of interest.

frontiers in Cell and Developmental Biology

REVIEW
published: 16 August 2021
doi: 10.3389/fcell.2021.695325

Critical View of Novel Treatment Strategies for Glioblastoma: Failure and Success of Resistance Mechanisms by Glioblastoma Cells

Timo Burster[1], Rebecca Traut[2], Zhanerke Yermekkyzy[1], Katja Mayer[2], Mike-Andrew Westhoff[3], Joachim Bischof[2] and Uwe Knippschild[2]*

[1] Department of Biology, School of Sciences and Humanities, Nazarbayev University, Nur-Sultan, Kazakhstan, [2] Department of General and Visceral Surgery, Surgery Center, Ulm University Hospital, Ulm, Germany, [3] Department of Pediatrics and Adolescent Medicine, University Medical Center Ulm, Ulm, Germany

OPEN ACCESS

Edited by:
Dwayne G. Stupack, University of California, San Diego, United States

Reviewed by:
Thomas Griffith, University of Minnesota Twin Cities, United States
Gabriela Brumatti, Walter and Eliza Hall Institute of Medical Research, Australia

***Correspondence:**
Timo Burster
timo.burster@nu.edu.kz

Specialty section:
This article was submitted to Cell Death and Survival, a section of the journal Frontiers in Cell and Developmental Biology

Received: *14 April 2021*
Accepted: *29 July 2021*
Published: *16 August 2021*

Citation:
Burster T, Traut R, Yermekkyzy Z, Mayer K, Westhoff M-A, Bischof J and Knippschild U (2021) Critical View of Novel Treatment Strategies for Glioblastoma: Failure and Success of Resistance Mechanisms by Glioblastoma Cells. Front. Cell Dev. Biol. 9:695325. doi: 10.3389/fcell.2021.695325

According to the invasive nature of glioblastoma, which is the most common form of malignant brain tumor, the standard care by surgery, chemo- and radiotherapy is particularly challenging. The presence of glioblastoma stem cells (GSCs) and the surrounding tumor microenvironment protects glioblastoma from recognition by the immune system. Conventional therapy concepts have failed to completely remove glioblastoma cells, which is one major drawback in clinical management of the disease. The use of small molecule inhibitors, immunomodulators, immunotherapy, including peptide and mRNA vaccines, and virotherapy came into focus for the treatment of glioblastoma. Although novel strategies underline the benefit for anti-tumor effectiveness, serious challenges need to be overcome to successfully manage tumorigenesis, indicating the significance of developing new strategies. Therefore, we provide insights into the application of different medications in combination to boost the host immune system to interfere with immune evasion of glioblastoma cells which are promising prerequisites for therapeutic approaches to treat glioblastoma patients.

Keywords: glioblastoma, immunotherapy, immune evasion, tumor microenvironment, peptide and mRNA vaccines

INTRODUCTION

Glioblastoma is the most invasive and therapy-insensitive type of glial tumor. The subpopulation of glioblastoma cells is disposed to proliferate quickly and in an uncontrolled manner, where alternative subsets infiltrate into nearby healthy tissue making an entire resection impossible. The high heterogeneity of glioblastoma contributes to tumor progression and recurrence which causes resistance from therapeutic drugs (Vieira de Castro et al., 2020; Zhang and Liu, 2020). On the molecular level, glioblastoma cells, for instance, often fail the proper regulation of pro- and anti-apoptotic proteins leading to apoptotic resistance (Vengoji et al., 2018). Additionally, glioblastoma stem cells (GSCs), using altered signaling pathways, do not only play a critical role in resistance to conventional therapies and tumor recurrence, but also in tumor initiation and progression (Dean et al., 2005; Vengoji et al., 2018; Bhaduri et al., 2020; Vieira de Castro et al., 2020). Hypoxia is a prominent microenvironmental factor that results from a rapid growth of glioblastoma and the

need for oxygen, provoking angiogenesis as well as anaerobic glycolysis. This, in turn, generates a local accumulation of lactate with a decreased pH environment and encourages glioblastoma cells for migration (Xie et al., 2014).

The aim of the review is to provide a critical overview of the common as well as novel treatment strategies of glioblastoma based on the resistant mechanisms developed by glioblastoma cells and to ascertain combination therapies to improve the failure of monotherapies.

Standard Care Therapies for Glioblastoma

Standard of care therapies for glioblastoma include resection, radio- and chemotherapy with the administration of temozolomide (TMZ) or nitrosoureas components. Chemoresistance during medication is a major drawback and includes several mechanisms (**Figure 1**), such as drug metabolic inactivation, increased DNA-repair mechanisms, inhibition of prodrug conversion, and lowering the intracellular drug concentration by enhanced drug efflux via enhanced expression of transporters (Wee et al., 2016; Sharifzad et al., 2019; Pessina et al., 2020). TMZ is frequently described as a DNA alkylating prodrug that induces double-strand breaks of the DNA which eventually lead to apoptosis (Karachi et al., 2018; Sharifzad et al., 2019). Recently, a debate has emerged casting doubt on the precise molecular function of this component (Strobel et al., 2019; Kaina, 2019; Stepanenko and Chekhonin, 2019; Westhoff et al., 2020; Herbener et al., 2020). According to the traditionally proposed model, TMZ alkylates bases that are present in the DNA, leading to a mismatch during replication and induces futile rounds of DNA repair, finally ending in DNA strand breaks and apoptosis (Kaina, 2019). The O^6-methylguanine-DNA-methyltransferase (MGMT) can resolve some of the TMZ-induced alterations and thus mediate survival, but is frequently found not to be expressed in approximately half of all glioblastoma cells, i.e., about 45% of patients considered to benefit from TMZ (Karachi et al., 2018; Miyauchi and Tsirka, 2018; Arora and Somasundaram, 2019). The standard practice, however, is still to prescribe TMZ treatment notwithstanding a patient's methylation level (Kamson and Grossman, 2021), although studies show no statistically significant difference in survival between the groups controlling for TMZ in the absence of MGMT methylation (Hegi et al., 2005). Indeed, even the predictive value of MGMT promotor methylation with regards to tumor response to TMZ is not uncontroversial (Stepanenko and Chekhonin, 2019; Yu et al., 2020). Overall, TMZ treatment extends patient survival from 12.1 to 14.6 months (Strobel et al., 2019), i.e., modulating its therapeutic potency is unlikely to be curative, but might further extend the therapeutic window.

MGMT inhibitors are therefore considered to be of interest to improve the clinical response to TMZ treatment (Karachi et al., 2018; Arora and Somasundaram, 2019). However, systemic inhibition of MGMT might lead to increased apoptosis or even the accumulation of mutations in healthy tissue, so that localized application of inhibiting pseudo-substrates or tumor-specific delivery of blocking peptides have been considered as strategies to increase the efficiency of TMZ treatment while not concurrently sensitizing healthy tissue to the alkylating agent (Yu et al., 2020; Wängler et al., 2020, respectively). Some of these strategies are currently being evaluated clinically and are showing rather promising results (Yu et al., 2020). Alternatively, metronomic application of TMZ might suffice to sensitize relatively resistant glioblastoma cells to this drug, as MGMT is a suicide enzyme that is destroyed upon de-alkylating a base (Karachi et al., 2018; Miyauchi and Tsirka, 2018; Arora and Somasundaram, 2019; Le Rhun et al., 2019; Strobel et al., 2019).

The treatment of recurrent glioblastoma encompasses nitrosourea compounds, namely lomustine (Brandes et al., 2016; Le Rhun et al., 2019). Nitrosoureas are alkylating reagents which are able to cross the blood-brain barrier due to their high lipophilicity, causing cell damage and apoptosis. However, lomustine implies severe adverse reactions (prolonged thrombocytopenia and dose-limiting pulmonary toxicity was determined) (Brandes et al., 2016). The small increase of overall survival (OS) while the progression-free survival (PFS) for newly diagnosed as well as recurring glioblastoma denotes the need for

Abbreviations: ACE2, angiotensin-converting enzyme 2; ADCs, antibody-drug conjugates; AIF, apoptosis-inducing factor; AIM-2, absent in melanoma 2; APCs, antigen-presenting cells; ARG1, arginase; B7-H1, B7-homolog 1; Bak, Bcl-2 antagonistic killer; Bax, Bcl-2 associated X protein; Bcl-2, B cell lymphoma-2 protein; Bcl-Xl, Bcl-extra-long; BBB, blood-brain barrier; BH3, Bcl-2 homology domain 3; CAR, chimeric antigen receptor; CCR2, C-C chemokine receptor type 2; CD, cluster of differentiation; CNS, central nervous system; CRS, cytokine release syndrome; CSCs, cancer stem-like cells; CTLs, cytotoxic T lymphocytes; CTLA-4, cytotoxic T-lymphocyte-associated protein 4; CXCR4, C-X-C chemokine receptor type 4; DCs, dendritic cells; DNA, deoxyribonucleic acid; DNRII, dominant-negative TGF-beta receptor II; EGFR, epidermal growth factor receptor; EGFRvIII, epidermal growth factor receptor variant III; ECM, extracellular matrix; FcRn, neonatal Fc receptor; FDA, US Food and Drug Administration; G-CSF, granulocyte-colony stimulating factor; GAMs, glioma-associated microglia/macrophages; GDNF, glial-derived neurotrophic factor; GLUT, glucose transporter; GM-CSF, granulocyte-macrophage colony-stimulating factor; GSCs, glioblastoma stem cells; HER2/neu, human epidermal growth factor receptor 2; HGF/SF, hepatocyte growth factor/scatter factor; HIF-1, hypoxia-inducible factor 1; HSP, heat shock protein; HSV, herpes simplex virus; IAPs, inhibitors of apoptosis; IDO, indolamine 2,3-dioxygenase 1; IFN-γ, interferon-gamma; IKK, IκB kinase; IL, interleukin; IL-13Rα2, interleukin-13 receptor alpha 2; ILT/LIR, Ig-like transcript/leukocyte Ig-like receptors; KIR, killer-cell Ig-like receptors; mAb, monoclonal antibody; mTOR, mammalian target of rapamycin; mTORC2, mTOR complex 2; M-CSF, macrophage colony-stimulating factor; Mcl-1, myeloid cell leukemia factor 1; MCP-1, monocyte chemotactic protein 1; MDSCs, myeloid-derived suppressor cells; MDR-1, multidrug resistance protein 1; MGMT, methyl guanine methyl transferase; MHC I, major histocompatibility complex class I; MHC II, major histocompatibility complex class II; MMP, matrix metalloproteinase; MTIC, 3-methyl-(triazen-1-yl) imidazole-4-carboxamide; NFκB, nuclear factor kappa-light-chain-enhancer of activated B cells; NOS2, nitric oxide synthase 2; NSCLC, non-small cell lung cancer; OS, overall survival; P-gp, permeability glycoprotein; PD-1, programmed cell death protein 1; PD-L1, programmed death-ligand 1; PDK1, pyruvate dehydrogenase lipoamide kinase isozyme 1; PFS, progression-free survival; PI3K, phosphoinositide 3-kinase; PIP2, phosphatidylinositol 4,5-bisphosphate; PIP3, phosphatidylinositol (3,4,5)-trisphosphate; PTEN, phosphatase and tensin homolog; RNA, ribonucleic acid; ROS, reactive oxygen species; RTK, receptor tyrosine kinase; SARS-CoV-2, severe acute respiratory syndrome coronavirus 2; STAT3, signal transducer and activator of transcription 3; TAA, tumor-associated antigens; TAMs, tumor-associated macrophages; TGF-β, transforming growth factor-β; Th, T helper; TILs, tumor-infiltrating lymphocytes; TIM-3, T cell immunoglobulin and mucin domain-containing protein 3; TME, tumor microenvironment; TMPRSS2, transmembrane protease serine subtype 2; TMZ, temozolomide; TNF, tumor necrosis factor; TNFR1, tumor necrosis factor receptor 1; Treg, T regulatory cell; TRP-2, tyrosine-related protein 2; UCB, umbilical cord blood; VEGF, vascular endothelial growth factor.

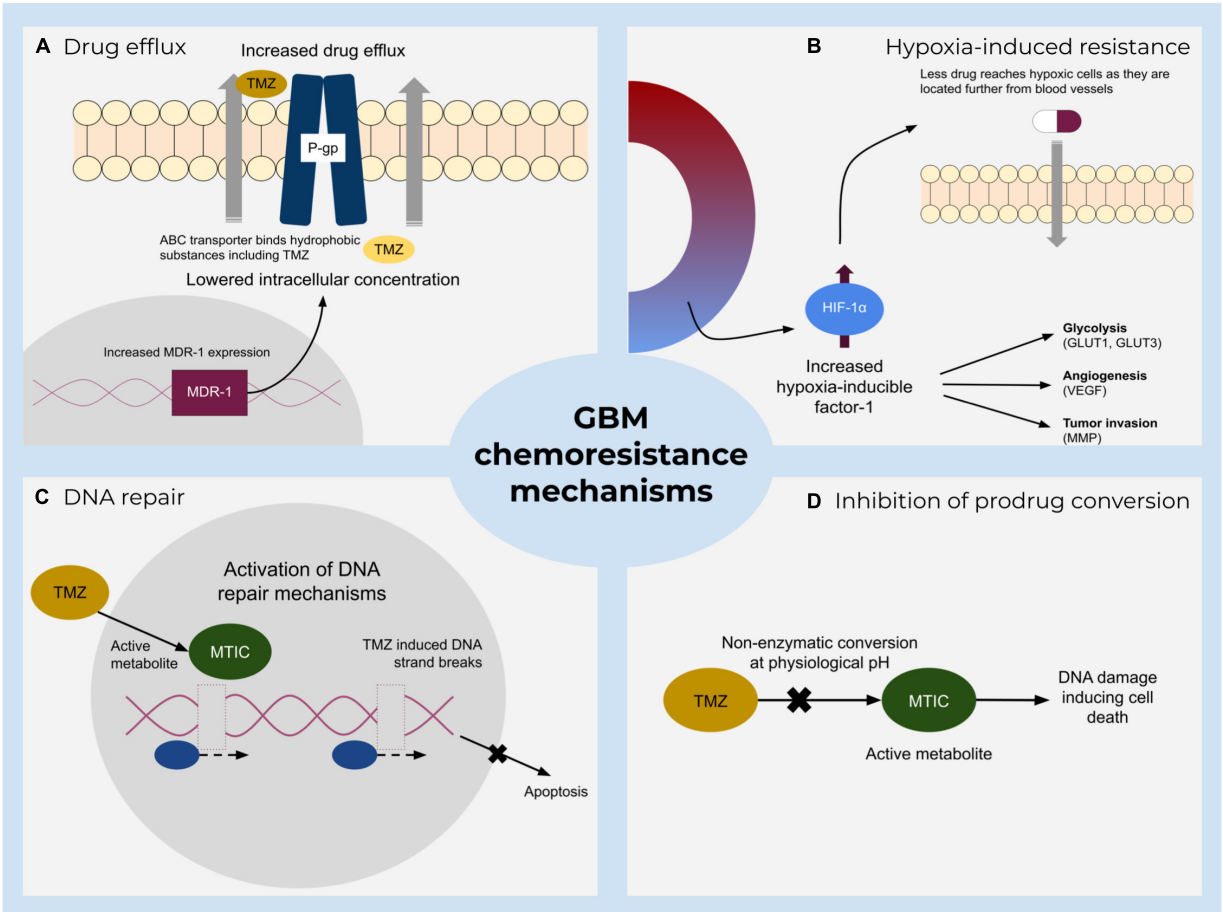

FIGURE 1 | A summary of major resistance mechanisms to standard treatment of glioblastoma. Main impeding factors include **(A)** increased active TMZ efflux by ATP-binding cassette transporters that lower the drug concentration and hence its effect. **(B)** Hypoxia-mediated chemoresistance caused by various hypoxia-inducible factor-1 (HIF-1) activities. **(C)** Direct and indirect DNA damage repair mechanisms and **(D)** inhibition of prodrug conversion which prevents DNA damage.

better management of the disease by reducing severe side effects and preventing resistance.

Glioblastoma Cells Are Resistant to Apoptosis

Apoptosis plays an important role in the elimination of damaged cells in multicellular organisms to sustain normal biological processes (**Figure 2**). A dysregulation of apoptosis can lead to cancer and other pathophysiological disorders. In the case of preventing apoptosis or establishing resistance, anti-apoptotic proteins (e.g., B cell lymphoma-2 protein family members Bcl-2 or Bcl-xL) bind to pro-apoptotic family members (e.g., Bcl-2 homologous antagonist/killer (Bak) or Bax) resulting in the neutralization of their activity (Tsujimoto, 1998; Ola et al., 2011).

Another attractive target for sensitization to therapy is the Bcl-2 family, including Bcl-2, Bcl-xL and Bcl-w, which inhibit the release of mitochondrial apoptogenic factors by sequestering Bak and Bax (Strik et al., 1999; Wick et al., 2004; Stegh et al., 2007). Apart from overexpression of anti-apoptotic proteins, the downregulation of pro-apoptotic proteins (Bak, Bax, Box, and NOXA) has been described for glioblastoma (Strik et al., 1999; Tyagi et al., 2002; Steinbach and Weller, 2004). Low protein levels in glioblastoma patients have been detected for Apaf-1 and procaspase-9 (Blahovcova et al., 2015). Consequently, the initiation of apoptosis is circumvented and therapeutic response is poor (Tagscherer et al., 2008). The Bcl-2 family proteins act as a critical regulator of life-death decisions within the apoptotic pathway and especially the inactivation or downregulation of anti-apoptotic Bcl-2 family members, represent an interesting target for anticancer therapies. The expression and activity of the Bcl-2 protein can be decreased by using antisense oligonucleotides, small molecules, or peptides (Ola et al., 2011). Antisense oligonucleotides, for instance Genasense (not approved by FDA), lead to the degradation of *bcl-2* mRNA or incites a steric hindrance of translation, which reduces Bcl-2 expression (Julien et al., 2000; Frankel, 2003). Small molecule inhibitors, such as ABT-737, ABT-263 (navitoclax), or more recently the FDA approved alternative ABT-199 (venetoclax), BH3 mimetics, were designed to block the BH3 domain binding

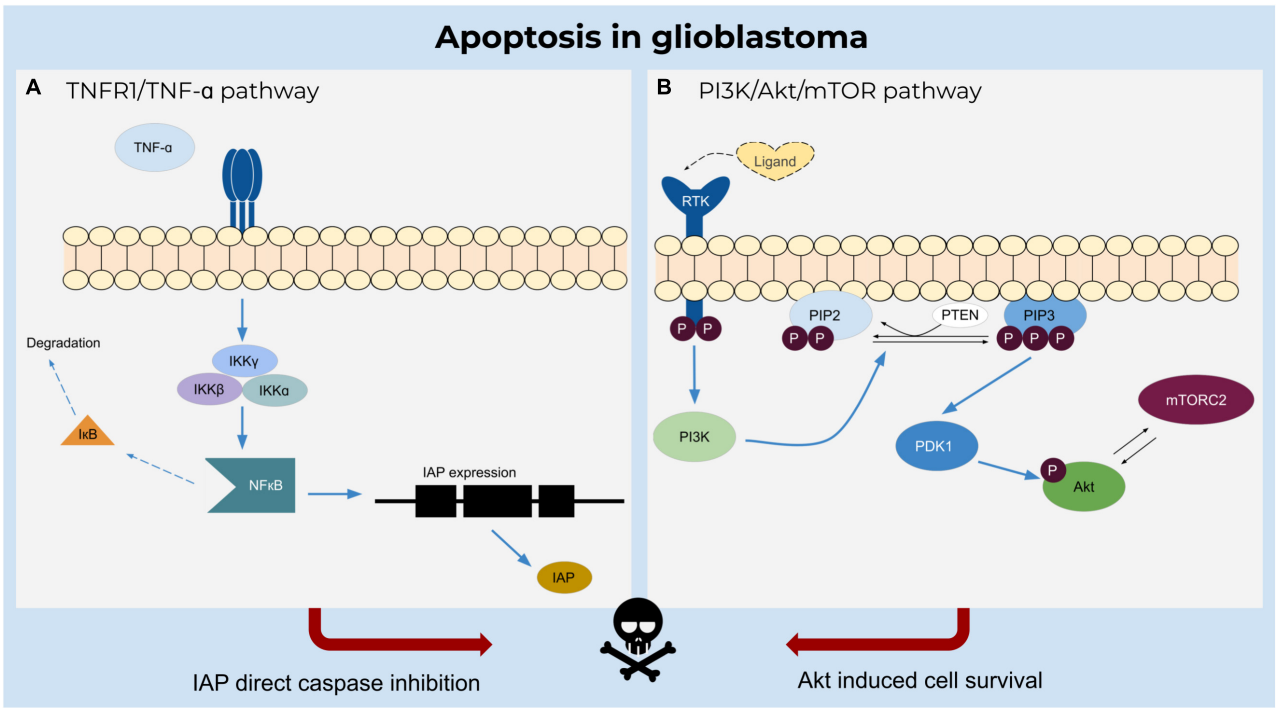

FIGURE 2 | Apoptosis in glioblastoma. **(A)** TNF-α induces inhibition of caspases by activating NFκB upon binding to TNFR1 receptor and triggering the IKK complex to degrade the inactivating factor IκB. NFκB regulates the expression of IAPs which inhibit apoptosis. **(B)** Ligand binding to the receptor tyrosine kinase induces catalytic activity of PI3K and further phosphorylates PIP2 to PIP3. The phosphorylation of the Akt molecule is mediated by PDK1 and activated by PIP3, resulting in a cascade of cell survival.

site on the surface of Bcl-2 and/or Bcl-xL, preventing inhibition of pro-apoptotic Bak or Bax (An et al., 2004; Kouri et al., 2012; Singh et al., 2019). Interestingly, in the context of glioblastoma, navitoclax has been the more promising substance, suggesting that modulation of Bcl-xL is needed for therapeutic efficacy (Hlavac et al., 2019; Nguyen et al., 2019), unfortunately navitoclax is also associated with serious, but manageable side effects, such as thrombocytopenia and neutropenia, severely limiting its therapeutic value (Wilson et al., 2010; Kuter, 2015). Additionally, the anti-apoptotic Bcl-2 family member myeloid cell leukemia factor-1 (Mcl-1), which interferes in early cascade events by suppressing cytochrome c release from mitochondria, is highly expressed in human glioblastoma (Michels et al., 2005; Karpel-Massler et al., 2017). High levels of Mcl-1 mediate BH3-mimetic resistance, suggesting that a dual inactivation of Bcl-2/Bcl-xL and Mcl-1 is necessary for apoptosis of glioblastoma cells (Kouri et al., 2012; Karpel-Massler et al., 2017; Shang et al., 2020). AT-101, a small molecule targeting Mcl-1, is presently being examined in a clinical trial (Xiang et al., 2018). Although inhibition of Mcl-1 has received certain attention as a potential drug target, only slowly implemented in clinical applications and poses challenges in glioblastoma treatment due to high molecular weight and the blood brain barrier. With the aim to overcome such drawbacks the use of combinatory approaches is further explored (Tron et al., 2018; Shang et al., 2020).

In order to circumvent apoptosis resistance of glioblastoma, inhibitor of apoptosis (IAP) proteins can also be targeted by small molecule inhibitors resulting in enhanced sensitivity to radiation and TRAIL (Vellanki et al., 2009; Lincoln et al., 2018).

Regarding the death receptor-mediated pathways, gene expression of several members of the TNF receptor family as well as FAS and FADD but also caspase-8 and caspase-7 was found to be reduced in human glioblastoma tissue. Subsequently, DISC formation and initiation of apoptosis by both the death receptor and mitochondrial pathway are affected favoring resistance to apoptosis and different therapies (Blahovcova et al., 2015; Wang et al., 2017). As an approach to sensitize glioblastoma cells to TRAIL-induced cell death, lanatoside C has been shown to upregulate expression of TRAIL-R2 as well as to activate a necrosis-like and caspase-independent cell death pathway. Low doses of lanatoside C demonstrated significant anti-glioblastoma activity in cell culture and glioblastoma xenografts when combined with low doses of TRAIL (Badr et al., 2011). However, even if the expression of TRAIL-R1 and TRAIL-R2 is increased in glioblastoma cells, resistance to TRAIL-induced apoptosis can be caused by low levels of caspase-8 and FADD (Knight et al., 2001).

THE TUMOR MICROENVIRONMENT PROVOKES RESISTANCE

Advances in immunotherapies are promising approaches for an efficient management of glioblastoma. However, resistance

mechanisms to immunotherapy and poor understanding of the glioblastoma microenvironment are still a major drawback for the development of novel therapies (Razavi et al., 2016; Adhikaree et al., 2020).

The Immune System in the Brain

The idea of an immune privileged location of the brain is challenged by the facts that the CNS possesses a lymphatic vessel network, which can attract leukocytes to migrate from the cerebrospinal fluid to the cervical lymphatics and back. These leukocytes can traverse to the CNS even with an intact blood-brain barrier (Li et al., 2001; Razavi et al., 2016), which offers new perspectives for immunotherapy. Besides that, inflammation increases the permeability of the blood-brain barrier enabling the intrusion of circulating monocytes and lymphocytes into the brain (Sharifzad et al., 2019; Adhikaree et al., 2020). In particular, the blood-brain barrier is disrupted in glioblastoma, increasing the numbers of immune cells in the CNS (Amin et al., 2012) by compromised tight junctions and degradation of proteoglycans of the extracellular matrix by proteases (Schneider et al., 2004). Furthermore, glioblastoma is known as a highly vascularized tumor with vessels having a larger diameter. Pericytes, which normally surround endothelial cells, are sparse along these vessels, thereby expanding the leakiness of the blood-brain barrier (Miyauchi and Tsirka, 2018).

Professional antigen-presenting cells (APCs), like dendritic cells (DCs), can display exogenous tumor antigens on major histocompatibility complex class I (MHC I) or II molecules, priming $CD8^+$ T cells (cytotoxic T lymphocytes, CTLs) or $CD4^+$ T cells (T helper cells, Th), respectively. IFN-γ signaling is responsible for the upregulation of MHC I and MHC II molecules on target cells, allowing an increased ability to present antigenic peptides on MHC for T cell inspection and amplify an anti-tumor specific immune response by migrating into the brain parenchyma (Engelhardt and Ransohoff, 2012; Candeias and Gaipl, 2016). Contrastingly, reduced levels of MHC I molecules are found on glioblastoma cells, depending on the patient sample or cell lines investigated, which represents an immune evasion mechanism of glioblastoma cells (summarized in Burster et al., 2021).

The Tumor Microenvironment and Immune Evasion

The tumor microenvironment is surrounded by cytokines, chemokines, and growth factors to recruit immune cells to enable tumor growth and progression, seriously affecting the therapeutic cure (**Figure 3**). Examples for cells in this niche are B cells and T cells, such as T regulatory cells (Tregs), so-called tumor-infiltrating lymphocytes (TILs), tumor-associated macrophages (TAMs), myeloid-derived suppressor cells (MDSCs), and blood-brain barrier cells, which communicate by secreted mediators to facilitate cell growth, invasion, therapeutic resistance, and immune evasion (Ou et al., 2020).

Glioblastoma is characterized by the growth of new capillaries from existing blood vessels, containing hyperpermeable vessels with an enlarged diameter. The vasculature in solid tumors ensures tumor growth and sufficient oxygen and nutrient supply (Weathers and de Groot, 2015; Ahir et al., 2020). The high vascularization is caused by the expression of angiogenetic factors, including VEGF, interleukin 6 (IL-6), IL-8, and transforming growth factor-β (TGF-β). Clinical studies demonstrated that the abundance of glioma-associated microglia/macrophages (GAMs) is higher in high-grade gliomas compared to low-grade gliomas (De et al., 2016). GAMs are polarized into an immunosuppressive state by TGF-β, periostin, versican, macrophage colony-stimulating factor (M-CSF), and granulocyte-macrophage colony-stimulating factor (GM-CSF). Immunosuppressive mediators, such as IL-10 and B7-homolog 1 (B7-H1), are highly expressed in glioblastoma. Chemoattractants [*inter alia*, hepatocyte growth factor (HGF), TGF-β, and granulocyte-colony stimulating factor (G-CSF)] attract different cell populations to the tumor microenvironment and lead from a decreased pro-inflammatory to an amplified anti-inflammatory state (Hanahan and Weinberg, 2011; De et al., 2016). Macrophages and microglia are able to switch between two distinctive phenotypes, the M1 pro-inflammatory and the M2 cytoprotective and immunosuppressive subpopulation, contributing to tumor cell proliferation, migration, and invasion. M2 are subdivided to M2a, M2b, and M2c due to the functional activation state. Of these, the M2c subset is dominant in gliomas (Gabrusiewicz et al., 2016). M2 macrophages produce immunosuppressive cytokines (TGF-β and IL-10), activating M2c (Gieryng et al., 2017), and are well-known to regulate T cell function (Wu et al., 2010). GAMs are recruited to the tumor site and being polarized into the M2 phenotype by different mediators, for instance, M-CSF and GM-CSF (Pyonteck et al., 2013). In addition, TGF-β isoform 1 and 2, prostaglandin E2, and the extracellular matrix protein periostin are involved in M2 polarization (Strepkos et al., 2020). Accordingly, TGF-β2 stimulates the synthesis of the proteoglycan versican by glioblastoma cells, which promotes GAM-induced inflammatory cytokine production to enhance glioma invasion (Arslan et al., 2007; Strepkos et al., 2020). GSCs also secrete factors to polarize GAMs to M2 and impede phagocytosis of M1 (Wu et al., 2010). Accordingly, targeting the interaction of cytotoxic and apoptotic effects of M2 receptor activation, several preclinical and phase I studies are currently on the way to promote GAM M1-like polarization or alter the microglia polarization, including emactuzumab, plerixafor, and maraviroc (Di Bari et al., 2015; Mercurio et al., 2016; Laudati et al., 2017). Nevertheless, the sophisticated crosstalk of tumor microenvironment and tumor heterogeneity of glioblastoma significantly contribute to therapy resistance (Strepkos et al., 2020).

The heterogenous population of immune cells from the myeloid lineage, MDSCs, are important for tumor survival within the tumor microenvironment. The amount of these cells is higher in the glioblastoma tumor microenvironment and suppress cytotoxic NK cell, $CD4^+$- and $CD8^+$ T cell function (Marvel and Gabrilovich, 2015; Gieryng et al., 2017). Two subsets of MDSCs exist: Polymorphonuclear- and mononuclear-MDSCs. Both use different mechanisms to suppress $CD8^+$ T cells. Polymorphonuclear-MDSCs, predominantly found in glioblastoma, produce high levels of reactive oxygen species,

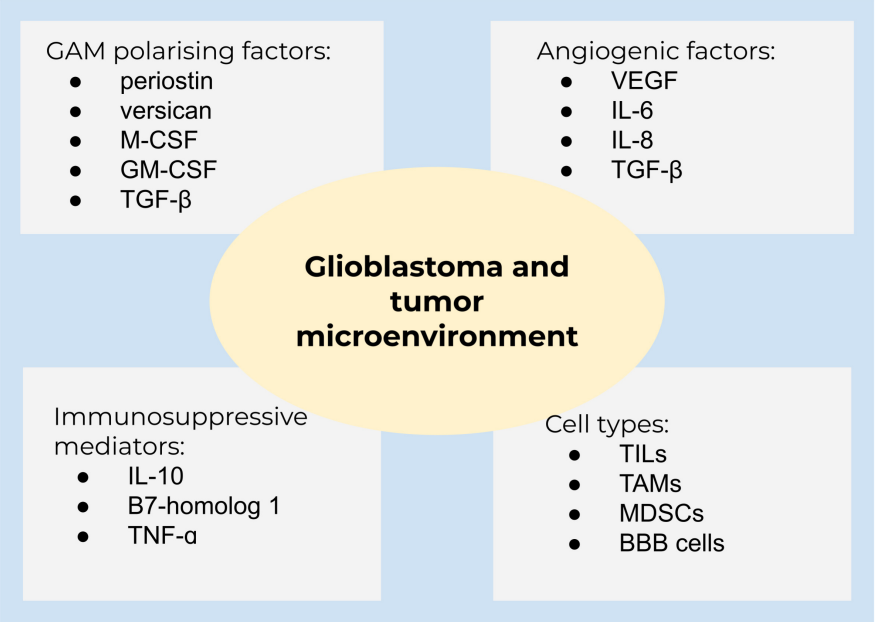

FIGURE 3 | Glioblastoma and the tumor microenvironment. A summary of main components of the tumor microenvironment in glioblastoma.

cross-talk with Tregs, and secret immunosuppressive cytokines. Mononuclear-MDSCs express, for instance, nitric oxide synthase 2 and arginase (ARG1), which inhibit T cell proliferation and further promote T cell apoptosis (Marvel and Gabrilovich, 2015; Gieryng et al., 2017).

NK cells are important for killing cancer cells (Gieryng et al., 2017). However, NK cells are found to be impaired in the glioblastoma tumor microenvironment since these cells express a limited amount of MHC I molecules, binding to inhibitory NK cell receptors, and quench NK cell activation (Wiendl et al., 2002; Gieryng et al., 2017; Burster et al., 2021). The inhibitory receptors are isoforms of the killer-cell Ig-like receptors (KIR) and Ig-like transcript/leukocyte Ig-like receptors (ILT/LIR). Moreover, TGF-β1 downregulated the expression of activating NK cell receptors, e.g., NKG2D and NKp30, thus inhibiting NK cell function (Castriconi et al., 2003). Additionally, TGF-β represses the mammalian target of the rapamycin (mTOR) pathway, which in turn reduces the proliferation and metabolic activity of NK cells (Viel et al., 2016).

Recruitment of non-neoplastic cells to the tumor microenvironment is implemented by glioblastoma. GAMs and glioblastoma cells express hepatocyte growth factor/scatter factor (HGF/SF), which binds to c-Met tyrosine kinase and promotes proliferation and invasion of glioblastoma cells (Kunkel et al., 2001). Monocyte chemotactic protein 1 (MCP-1 also named CCL2) and 3 are responsible for cell migration, for example, the binding of MCP-1 to CCR2 direct immune cells to infiltrate the tissue (Strepkos et al., 2020). This is in contrast to microglia which are attracted by a glial-derived neurotrophic factor (GDNF) expressed by neurons and glial cells (Ku et al., 2013).

Immune evasion by glioblastoma cells is achieved via immune checkpoint molecules. The programmed death-ligand 1 (PD-L1), an immune checkpoint molecule, is expressed on APCs, NK cells, parenchymal cells, and glioblastoma cells (Huang et al., 2017). After binding of PD-L1 to the PD-1 receptor, which is expressed on activated T cells, PD-L1-PD-1 receptor complex provokes T cell anergy or apoptosis (Razavi et al., 2016; Huang et al., 2017). Additional immune checkpoint molecules include cytotoxic T-lymphocyte-associated protein 4 (CTLA-4), T cell Ig, and mucin domain 3 (TIM-3) (Razavi et al., 2016). Furthermore, the immunomodulatory mechanism in glioblastoma is achieved through indolamine 2,3-dioxygenase 1, which is a cytosolic enzyme, inhibits T effector function and supports Treg expansion and activation, hence contributing to suppressing an immune response (Adhikaree et al., 2020).

IMMUNOTHERAPY AND LIMITATION IN GLIOBLASTOMA

Immunotherapy is based on the concept that the immune system is capable of recognizing and destroying tumor cells. However, the success of immunotherapy remains challenging since tumor cells developed various pathways to avoid being detected by the immune system, leading to low therapeutic efficiency. Glioblastoma adapted a high resistance and only a few patients respond to certain immunotherapies (Jackson et al., 2019).

Antibody Drug Conjugates (ADCs)

EGFR gene amplification and mutations in the EGFR variant III (EGFRvIII) gene (Malkki, 2016; van den Bent et al., 2017) can be utilized for glioblastoma therapy by using antibody drug

conjugates (ADCs). ADCs are monoclonal antibodies linked to different cytotoxic drug components (van den Bent et al., 2017). ADCs are designed to bind to tumor-specific antigens, which are internalized through receptor-mediated endocytosis. During this process, the cytotoxic components are released from the antibody due to the low pH environment of the endocytic compartment. While the receptor is recycled back to the cell surface, the delivered cytotoxic components induce apoptosis in tumor cells. One cavity of application is the fact that ADCs might be extracellularly released because of the proteolytic labile linker or ADCs are recycled back to the cell surface without delivering the cytotoxic component, leading to a reduced drug concentration in the cell (Polson et al., 2009; Peters and Brown, 2015; Scotti et al., 2015). The recycling mechanism of ADCs is caused by the high affinity of ADCs to neonatal Fc receptors (FcRns) within early endosomes that reach the cell surface recurrently, where ADCs are released from the FcRn under physiological pH. Notably, the FcRn is predominantly expressed in the endosomes of endothelial cells (Peters and Brown, 2015).

The ADCs are often DNA alkylating agents, inhibitors of tubulin polymerization, or enediyne antibiotics which lead to DNA double-strand breaks (Scotti et al., 2015). Limitations of ADC application is indicated by the restriction of available specific tumor-associated antigens (TAA), downregulation of TAAs, and the transport of ADCs to the brain (Phillips et al., 2016; Miyauchi and Tsirka, 2018). On the other hand, previous studies acknowledged the possible uptake of ADCs in patients by disrupted blood-brain barrier (Phillips et al., 2016). Of note, distinct glioblastoma patients have a relatively low mutational burden compared to non-small cell lung cancer, minimizing the amount of potential TAAs (Miyauchi and Tsirka, 2018). Lack of blood-brain barrier penetration, tumor heterogeneity, and resistance to the cytotoxic agent impede therapy success (Gieryng et al., 2017). Although a successful uptake of ADCs through the blood-brain barrier of low-grade gliomas with little disrupted blood-brain barrier compared to high-grade gliomas could undermine complete penetration due to the size of ADCs. High-grade gliomas exhibit augmented microvascular permeability, allowing penetration of larger molecules (Roberts et al., 2000; Schneider et al., 2004). Certainly, a specific antigen for targeting glioblastoma is needed; however, tumor heterogeneity or reduced levels of antigens are one of several reasons for therapy resistance (Gan et al., 2017). An additional limitation of this approach is an acquired resistance to the cytotoxic agent of ADC, namely active efflux of the internalized drug is possible through transporters of the adenosine triphosphate-binding cassette family (Scotti et al., 2015).

Immune Checkpoint and Chemokine Inhibitors

Monoclonal antibodies, known as nivolumab, pembrolizumab, ipilimumab, and atezolizumab, are widely used in cancer treatment by interrupting checkpoint signaling pathways and leading to an immune-mediated elimination of tumor cells (Juszczak et al., 2012; Darvin et al., 2018). While the patients benefit from prolonged OS, distinct immune-related adverse reactions exist, including pneumonitis or lymphocytic hypophysitis (an inflammation of the pituitary gland). The use of monoclonal antibodies are limited and not suitable for patients which suffer from autoimmunity because immune checkpoints in general act as barriers against autoimmune disorders (Juszczak et al., 2012). Approved immune checkpoint inhibitors are presently tested for primary and recurrent brain malignancies. The administration of nivolumab (anti-PD-1 monoclonal antibody) caused mild side effects, whereas nivolumab in combination with ipilimumab initiated severe (grade 3 and 4) adverse effects in 80% of the treated patients. Notably, 50% discontinued the medication due to intolerability. The 6-months OS rate for nivolumab was 75, 80% for the combination therapy. Currently, nivolumab in combination with bevacizumab is being tested in a phase III clinical trial (NCT02017717) (Sampson et al., 2015). Despite encouraging results in OS, only a limited number of patients benefit from monoclonal antibodies, as many tumors downregulate T cell activity or prevent T cells from infiltrating the tissue, indicating an urgent need for better predictive biomarkers (Darvin et al., 2018).

Chemokines are highly expressed in the tumor microenvironment and support tumor progression; therefore, blocking of chemokine receptors is a promising approach (Laudati et al., 2017). In a preclinical study, maraviroc, a CCR5 receptor blocker, polarized microglia toward the cytotoxic M1 phenotype by reducing the gene expression of ARG1 and IL-10, which are two M2 macrophage markers. Additionally, M1 markers are upregulated by inhibition of the mTOR pathway. The treatment with maraviroc, a small molecule CCR5 antagonist (Carter and Keating, 2007), led to a reduction of microglia migration (Laudati et al., 2017). Plerixafor, another small molecule CXCR4 antagonist, binds to the three acidic residues of the CXCR4 ligand-binding pocket (Fricker, 2008) and impairs the proliferation of glioma cells by inhibiting the invasion of CXCR4/CXCR7-expressing GSCs *in vitro* (Mercurio et al., 2016; Hira et al., 2017). Plerixafor, on the other hand, is not highly specific for CXCR4 as Plerixafor might bind to the receptor of CXCL12, CXCR4, and CXCR7. As a result, cardiotoxicity is one of the adverse reactions. Interestingly, a novel CXCR4 antagonist, Peptide R [Arg-Ala-(Cys-Arg-Phe-Phe-Cys), with the square brackets indicating cyclization *via* a disulfide bridge], reduced toxicity in mice (Portella et al., 2013; Mercurio et al., 2016).

Targeting STAT3, which is involved in maintaining an immunosuppressive environment in glioblastoma and is consistently activated in a variety of tumors, is an alternative therapeutic strategy for glioblastoma (See et al., 2012). The STAT3 inhibitor WP1066, also a small molecule, polarizes GAMs to a M1 cytotoxic phenotype and can block glioma growth *in vivo* (Hussain et al., 2007). A major challenge occurs with differences in the immune system between humans and animals; therefore, further clinical studies are needed to determine the benefits for patients (Horuk, 2009). Furthermore, long-term application of chemokine receptor inhibitors, e.g., CXCR4, is needed since considerable disadvantageous adverse reactions could occur in healthy tissue (Wang et al., 2016). Functional inhibition of CXCR4 can also cause stem cell mobilization,

causing leukocytosis, thrombocytopenia, or spleen rupture when administered in a long-term manner (Wang et al., 2016; Kwon et al., 2019).

Chimeric Antigen Receptor (CAR) T Cell Therapy

The function of $CD8^+$ T cells is largely inhibited by the tumor and the surrounding tumor microenvironment. A promising approach is the use of $CD8^+$ T cells to eliminate tumor cells by a so-called chimeric antigen receptor (CAR) T cell therapy. T cells are taken from a patient and transduced with a lentiviral vector to express a modified T cell receptor specifically recognizing TAAs. CAR-T cells are a complex of an Ig molecule and the T cell receptor. After *ex vivo* cell culture and stimulation, CAR-T cells are transferred back to the patient in order to eliminate tumor cells (Salinas et al., 2020). The advantage of CAR-T cells is that they are not dependent on MHC, as MHC expression is often downregulated in glioblastoma to hinder T cell activation (Fousek and Ahmed, 2015; Miyauchi and Tsirka, 2018). In a phase I study, recurrent glioblastoma and refractory glioblastoma were treated with CAR-T cells that have a high affinity to TAA interleukin-13 receptor α 2 (IL-13Rα2), which is overexpressed in recurrent glioblastoma. CAR-T cells were introduced into the tumor resection cavity, followed by infusions into the ventricular system of the brain. After administration the disease remission was sustained for 7.5 months with augmented levels of cytokines in one patient. It was suggested that recurrence occurs by decreased expression of IL-13R α2 (Brown et al., 2016; Dunn-Pirio and Vlahovic, 2017). One of the most severe complications in CAR-T cell treatment is cytokine release syndrome since inflammatory cytokines and chemokines are released, leading to nausea, headaches, tachycardia, hypotension, rashes, shortness of breath, and even multiorgan failure. Reversing the cytokine release syndrome with corticosteroids and anti-cytokine therapy is possible (Dunn-Pirio and Vlahovic, 2017). An alternative approach is the use of engineered CAR-NK cells to attack glioblastoma cells. However, CAR-NK cells demonstrated a minimal and unreliable response after application of NK cell lines. Primary NK cells from umbilical cord blood (UCB) could overcome this cavity and stimulation with IL-2 and IL-15 or UCB-derived NK cells expressing the TGF-β- dominant-negative receptor II, consuming TGF-β of the tumor microenvironment of glioblastoma is of interest (Burster et al., 2021).

Vaccination to Induce Immune Responses Against Glioblastoma

A different study followed the idea of tumor vaccination to induce immune responses against specific antigens, peptides, DNA or mRNA-based (with or without vector) components. Vaccination could be used to target highly immunogenic TAAs or tumor-specific antigens to trigger a specific immune response. In this regard, glioblastoma care is challenging since tumor mutational load (burden) is rather low compared to other cancer types and glioblastoma patients have high variations of mutations. The tumor mutational burden correlates with the abundance of neoantigens, which can be potential biomarkers for immunotherapy (Hodges et al., 2017; Wang L. et al., 2020).

Rindopepimut—a peptide vaccine—targets EGFRvIII, which was administrated in combination with TMZ, displayed an improvement in early clinical trials, but did not reach the criteria for therapeutic efficacy in phase III (NCT01480479) (Malkki, 2016). The reappearance of the wildtype EGFR in recurrent glioblastoma precludes further treatment with Rindopepimut targeting EGFRvIII (Schuster et al., 2015). This mechanism is one immune evasion strategy by glioblastoma, which could be overcome by the use of vaccines directing homogenously expressed markers to tackle tumor cells, such as transformed IDH, targeting a broader range of TAAs (Phuphanich et al., 2013). For instance, a vaccine (IMA 950) directed 11 different human peptides (brevican; chondroitin sulfate proteoglycan 4; fatty acid binding protein 7; hepatitis B virus core antigen; insulin-like growth factor 2 messenger RNA-binding protein 3; neuronal cell adhesion molecule; protein tyrosine phosphatase, receptor-type, Z polypeptide 1; tenascin C; baculoviral inhibitor of apoptosis protein repeat-containing 5; Met proto-oncogene; neuroligin 4 X-linked). Of these, the first nine were previously identified on MHC I (human leukocyte antigen A*02, HLA-A*02), the other two are MHC II peptides derived from primary glioblastoma (Halford et al., 2014; Rampling et al., 2016). IMA 950 combined with poly-ICLC, a vaccine adjuvant enhancing innate and adaptive immune responses, revealed both $CD4^+$ T cell and $CD8^+$ T cell activation; with a median OS of 19 months (NCT01920191) (Migliorini et al., 2019). Peptide vaccines are specific for the respective tumor cells; however, peptide vaccines may only work for a small group of patients and might lead to immune evasion (Schneble et al., 2016). Targeting homogenously expressed targets or multi-peptide vaccines could interfere with immune evasion of tumor cells. Moreover, vaccination for glioblastoma management fail to sufficiently stimulate the immune system to achieve a clinical benefit, further approaches, e.g., combinational therapy, should be considered (Schneble et al., 2016; Lim et al., 2018).

In general, DC-based vaccines are generated by exposing DCs isolated from patients to the respective antigens and thereby educate DCs to maintain an adaptive immune response (Phuphanich et al., 2013). More precisely, DC-based vaccine ICT-07 targets six glioblastoma markers. Three of the six glioblastoma markers are human epidermal growth factor receptor 2 (HER2/neu), tyrosine-related protein 2, and absent in melanoma 2 which are also overexpressed in cancer stem-like cells (Phuphanich et al., 2013; Wen et al., 2019). Therefore, ICT-07 is thought to improve PFS and reduce the number of GSCs. Newly diagnosed glioblastoma patients had an increased OS and significantly extended PFS by 2.2 months in phase II. The vaccine was well tolerated with only a mild negative impact (due to insufficient financial resources, the phase III study is currently suspended, NCT02546102) (Phuphanich et al., 2013; Wen et al., 2019). Furthermore, a DC-based vaccine (DCVax®-L), where DCs are pulsed with tumor cell lysate and injected into the patient, is used for medication of newly diagnosed glioblastoma (NCT00045968). Phase I/II clinical trials determined the safety of the vaccine (Liau et al., 2018). 33% of patients with glioblastoma

had a median OS of 48 months, 27% even achieved a median OS of 72 months in the long-term survival analysis, encouraging the use of DCVax®-L for glioblastoma therapy in the future (Dunn-Pirio and Vlahovic, 2017). Nevertheless, developing vaccines for individual neoantigens of patients is expensive and time-consuming because preparation of vaccines from the tumor samples take between 3–5 months (Peng et al., 2019). An additional limitation is the generation of sufficient DCs, as DCs comprise only < 1% of peripheral blood mononuclear cells. To overcome this obstacle, DCs were generated from monocytes *ex vivo*. However, it is questionable whether these monocyte-derived DCs compared to primary DCs from peripheral blood are efficient in an anti-tumor immune response (Huber et al., 2018). Furthermore, phagocytosis of tumor cells by APCs was enhanced by blocking the anti-phagocytosis molecule CD47 in combination with TMZ, inducing an effective anti-tumor immune response (von Roemeling et al., 2020). However, the use of whole tumor lysate to pulse DCs could cause autoimmune encephalitis since tumor lysate contains healthy brain tissue and induces an immune response toward the normal brain (Polyzoidis and Ashkan, 2014).

Moreover, a highly promising approach for cancer immunotherapy, denotes mRNA vaccine, which express tumor-specific antigens or TAA in APCs, has become into focus to treat glioblastoma. mRNA does not pose the risk of an infectious or an integrating agent, the potential of mRNA vaccines is the effectiveness, safety in administration, and low cost of manufacturing (Pardi et al., 2018; Weng et al., 2020). A phase I study utilizing DCs, loaded with TAA mRNA targeting cytomegalovirus pp65 protein that is expressed in > 90% of glioblastoma cases, demonstrated an OS of 35 months. As a consequence, co-delivery of mRNA vaccines together with immunotherapeutics can increase the host anti-tumor immune response (Batich et al., 2020; Miao et al., 2021). Notwithstanding the expected advantages, several factors limit the use of mRNA in therapy, including immunosuppressive effects of the tumor, half-life period of mRNA, and delivery complications *in vivo* (Vik-Mo et al., 2013; Weng et al., 2020). To overcome such issues, the chemical nucleotide modifications, capping analogs, and alternative delivery are currently being investigated and hold a great promise with current successful use of lipid nanoparticles to deliver mRNA vaccines (Weng et al., 2020; Rui and Green, 2021) or the use of viral vectors (Weng et al., 2020) and is therefore anticipated to increase the attention in glioblastoma immunotherapy.

Heat Shock Protein (HSP) Vaccines

The exposure of environmental stress to cells leads to the production of HSPs. While HSPs act as chaperones, stabilizing protein conformation, and preventing protein aggregation, HSPs might also force misfolded proteins for degradation. Interestingly, a correlation between cancer and high levels of HSPs was determined, possibly by the excess of misfolded proteins found within the tumor (Ampie et al., 2015). On the one hand, gliomas overexpress HSP70 and HSP90 to prevent stress-induced apoptosis; on the other hand, HSPs have the ability to bind TAAs to elicit an immune response, making HSPs an interesting protein for immunotherapy (Ampie et al., 2015). The binding of HSPs to antigens can encounter the cell surface receptor CD91 of APCs in order to stimulate endocytosis and cross-present antigens to $CD8^+$ T cells (Ampie et al., 2015). Although the application of an autologous HSP96-based vaccine (gp96-associated cellular peptides non-covalently bound to HSP96, HSPPC-96) in patients with recurrent glioblastoma are promising, this strategy is limited since the peptide pool is generated from the patient's tumor and the amount of vaccine depends on the tumor size (Crane et al., 2013). Anti-inflammatory cytokines, such as IL-10 and TGF-β, segregated by the tumor microenvironment may also interfere with gp-96 vaccines and limits current clinical trials (Ampie et al., 2015; Li et al., 2020). Additionally, surgical resection is not always possible, the biopsy needs to be taken from glioblastoma patients to generate the vaccine, indicating the possibility of tumor progression (Bloch et al., 2014).

ONCOLYTIC VIRUSES IN IMMUNOTHERAPY

Myeloid cells are often activated by an oncolytic viral infection, which promotes an inflamed microenvironment by infiltration of T cells into the tumor. Therefore, oncolytic virotherapy is thought to be useful for overcoming the immunosuppressive environment in glioblastoma (Mogensen, 2009; Lim et al., 2018). Current oncolytic viral treatment applies replication-competent viruses rather than replication-incompetent viruses, explicitly adeno- and retroviruses, herpes simplex viruses, or measles- and polioviruses. Replication-competent viruses have the advantage of overcoming low transduction efficiency and vector loss. These viruses are genetically engineered to selectively infect and lyse cancer cells but the surrounding brain parenchyma is spared (Dunn-Pirio and Vlahovic, 2017; Foreman et al., 2017; Lim et al., 2018).

Oncolytic poliovirus originates from the oral poliovirus Sabin type I, which was genetically modified to replace its internal ribosome entry site with a human rhinovirus type 2 to eliminate neurovirulence. Oncolytic poliovirus infects cells expressing the poliovirus receptor (CD155), an oncofetal cell adhesion molecule, which is also expressed in glioblastoma, and subsequently in an immunogenic clearance of cancer cells (Desjardins et al., 2016; Mehta et al., 2017). Contrastingly, side effects of the viral treatment include cerebral edema as a result of a local inflammatory response and also known as pseudoprogression. Pseudoprogression is common in solid cancers after immunotherapy. In the case of brain malignancies, differentiation is difficult between pseudoprogression and tumor progression based on the neuroimages (Payer, 2011).

The replication-incompetent adenovirus is a tumoricidal gene vector. Aglatimagene besadenovec (AdV-tk) provokes the expression of the HSV-TK gene, which allows the conversion of prodrug ganciclovir or valacyclovir into a toxic nucleotide analog. This nucleotide analog kills replicating tumor cells by damaging the DNA and is also known as gene-mediated cytotoxic immunotherapy (Lim et al., 2018; Miyauchi and Tsirka, 2018).

Two phase II clinical trials (BrTK02 and HGG-01) administered the virus intratumorally (BrTK02) or by intra-arterial cerebral infusion (HGG-01). Common detrimental effects were mostly fatigue, fever, and headaches (NCT00589875 for BrTK02 and NCT00870181 for HGG-01) (Chiocca et al., 2011; Ji et al., 2016; Wheeler et al., 2016). Nevertheless, non-replicating adenoviruses indicate limited distribution and low transduction efficiency of the vector (Ji et al., 2016). Furthermore, only a small amount of the injected adenovirus reaches the tumor due to elimination of the virus through the liver or by inactivation via binding to blood cells, complement, or to neutralizing antibodies, limiting further the successful application (Gao et al., 2014). The immune response represents an important factor for the efficiency of the drug. On the one hand, immune response limits the efficacy of oncolytic viruses, on the other hand, an anti-tumor immune response is crucial to fight against tumor cells.

COMBINATION THERAPIES ARE MORE EFFECTIVE IN TREATMENT OF GLIOBLASTOMA

Despite the expected potential of immunotherapy to treat glioblastoma, many monotherapy trials failed to reach sufficient efficiency. Besides the use of standard care of radiation/chemotherapy, combination therapies provide further enhancement in disease management (Dunn-Pirio and Vlahovic, 2017).

Adaptive resistance of tumor cells is an important factor contributing to the failure of monotherapy. Based on the nature of self-tolerance of the immune system, cancer cells can upregulate various immune checkpoint pathways to disturb the immune response (Medikonda et al., 2021). Notwithstanding that the use of monoclonal antibodies against these pathways might prevent inhibition of the immune response, phase II/III clinical studies targeting a single immune checkpoint pathway failed to be beneficial for glioblastoma patients (Majc et al., 2021; Medikonda et al., 2021). It is possible that immune checkpoint monotherapy forces PD-1-blockade resistance and upregulation of alternative immune checkpoint molecules, for instance, TIM-3 in a lung adenocarcinoma model (Koyama et al., 2016) may occur. While concurrent administration of anti-PD-1 and anti-TIM-3 antibodies improved preclinical glioblastoma, therapies with both antibodies and stereotactic radiosurgery resulted in 100% OS (Kim et al., 2017) and anti-PD-1 led to an enhanced vaccination-induced immune response (Antonios et al., 2016). Optimal timing of administration is important and concomitant treatment marks an optimal disease management (Lesterhuis et al., 2013). Other benefits of combining immune checkpoint inhibitors with standard care therapies or control of immune checkpoints, increase $CD8^+$ T cell activity and decrease the infiltration of Treg cells (Huang et al., 2017). Bevacizumab in combination with common care (radio- and chemotherapy) remain below the expectation for immunotherapy since preclinical studies defined that high doses of TMZ lower the anti-PD-1 related immune response. Furthermore, the impact of chemotherapy to immunity is critical, for instance, it was not feasible to induce an antitumor response in mice treated with systemic chemotherapy when enabling a tumor re-challenge (Mathios et al., 2016; Lim et al., 2018).

Similarly, a combinatorial approach of different immunotherapies, including vaccines, immune checkpoint inhibitors, and effector lymphocytes, was verified for efficacy in glioblastoma treatment (Weenink et al., 2020). A recent study of CAR-T cell therapy combined with immune checkpoint blockade exhibited an enhanced tumor suppression effect compared to a single CAR-T construct in murine and canine models (Yin et al., 2018). Currently, clinical trials assessing the safety of CAR-T cells in combination with monoclonal antibodies (pembrolizumab, ipilimumab, and nivolumab; NCT03726515 and NCT04003649) are on the way. A different clinical trial, comprising neoantigen vaccination, indicated a systemic immune response and expression of multiple inhibitory checkpoints by infiltrating vaccine specific T cells, which was limited to individuals not receiving dexamethasone, suggesting a potential for combination of neoantigen vaccines with immune checkpoint inhibitors (Keskin et al., 2019). Nevertheless, severe side effects caused by the combination of nivolumab and ipilimumab (anti-CTLA-4) requires careful consideration of the possibility of disadvantageous reactions by combining different immunotherapies (Sampson et al., 2015).

FURTHER COMPLICATIONS IN GLIOBLASTOMA

The 2019 severe acute respiratory syndrome coronavirus 2 (SARS-CoV-2) outbreak has brought its own significant obstacles to the care of patients suffering from glioblastoma. The pandemic disturbed the healthcare system leading to high hospital resource loads, risk of lack of treatment, and exposure to viral infection. Systemic immunosuppressive effects of standard anticancer medication, such as surgery and combined radio- and chemotherapy is a particular concern for glioblastoma patients. These patients are at a higher risk of infection and consequent complications (Amoo et al., 2020; Bernhardt et al., 2020; Noticewala et al., 2020).

SARS-CoV-2 belongs to a family of coronaviruses that are known as respiratory system pathogens, using their spike protein to bind cell surface receptors. In the case of SARS-CoV-2, this is mainly angiotensin-converting enzyme 2 (ACE2), which is a metallocarboxypeptidase present on surfaces of respiratory tract epithelial cells (Letko et al., 2020). Viral entrance is mediated by the serine protease transmembrane protease serine subtype 2 (TMPRSS2) that hydrolyze and prime the spike protein or alternatively via cathepsin B and cathepsin L in early endosomes (Wu et al., 2020). High abundance of ACE2 and TMPRSS2 in respiratory epithelial tissues explain the pathogenesis; however, expression of ACE2 is not limited to respiratory tract tissues, but is also found on brain cells (**Figure 4**). Moreover, an increasing number of obtained data on SARS-CoV-2 pathology indicate the presence of various neurological symptoms, such as fatigue, headaches, as well as smell- and taste impairments among more than a third of all the infected individuals (Mao et al., 2020). Cases

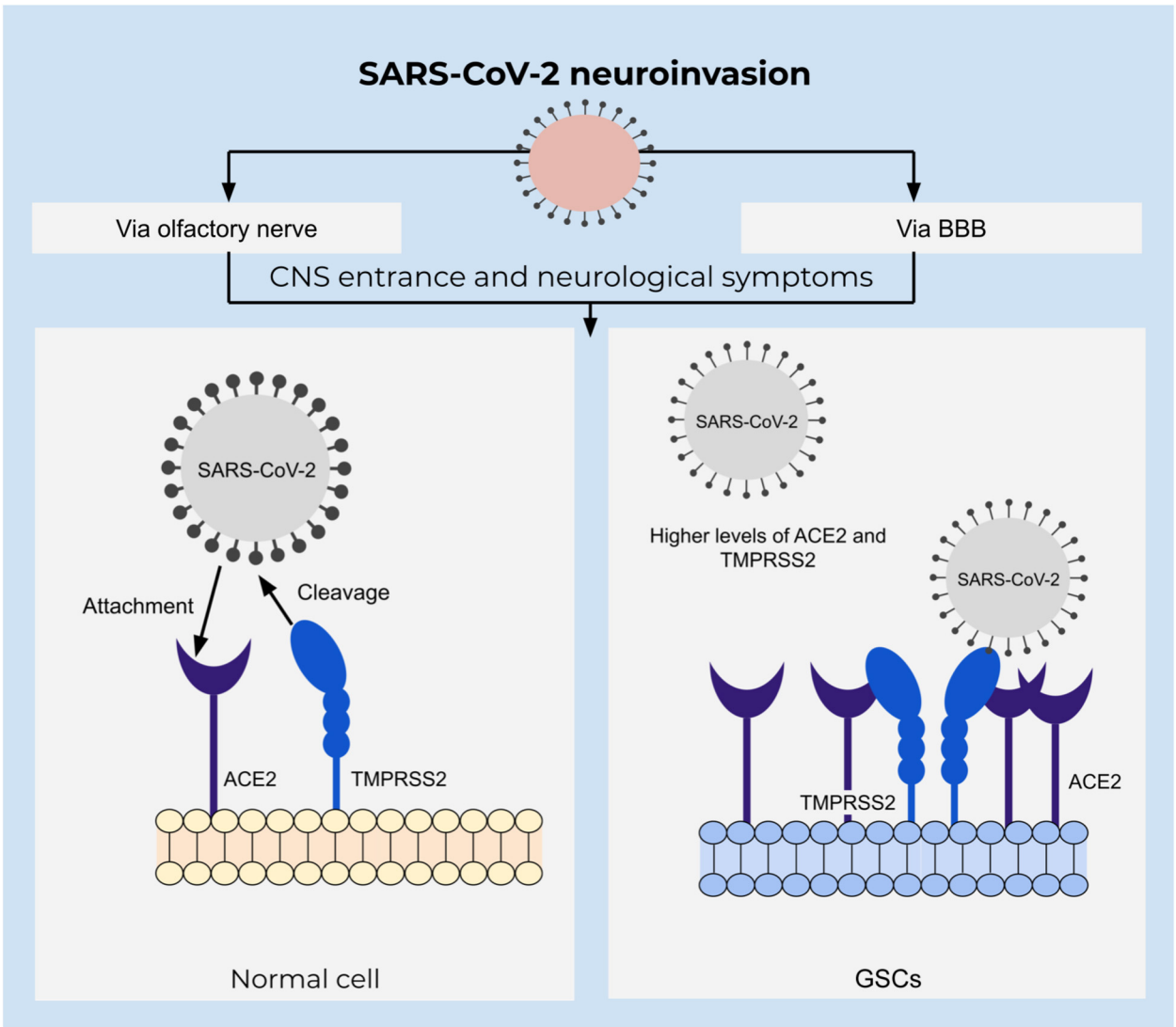

FIGURE 4 | Integrative view of neuroinvasion and glioblastoma susceptibility to SARS-CoV-2. SARS-CoV-2 entrance depends on the attachment of the spike protein to the ACE2 receptor that is mediated by TMPRSS2 in a proteolytic manner. ACE2 is upregulated in GSCs and might increase susceptibility to SARS-CoV-2 infection.

of acute cerebrovascular disease with impaired consciousness suggests neural invasion of the virus (Conde Cardona et al., 2020; Mao et al., 2020). Several studies have identified the presence of the viral RNA in the central nervous system (Puelles et al., 2020; Meinhardt et al., 2021) as well as brain damage evidenced by neuroimaging studies (Coolen et al., 2020).

Accompanied by an increased vascular permeability caused by active chemokine secretion upon the viral infection, CNS becomes particularly susceptible to viral invasion (McGavern and Kang, 2011; Letko et al., 2020). An alternative route of CNS invasion was identified via the olfactory bulb and peripheral neurons, which was outlined to be the dominant pathway of entrance by the virus in transgenic mice (Wu et al., 2020; Song et al., 2021). Neurotropism and neural invasion of SARS-CoV-2 are defined by single cell transcriptome sequencing analysis of glioblastoma tissue (Wu et al., 2020). Moreover, an analysis of both U-87 and U-373 glioblastoma cell lines defined a susceptibility to infection and resistance to apoptosis. Additionally, these cells express ACE2, TMPRSS2, cathepsin B as well as cathepsin L which is important for entrance of SARS-CoV-2 to the target cell (Bielarz et al., 2021). An abundance of ACE2 receptors in glioblastoma tissue suggests glioblastoma patients to be at a particularly high risk of acquiring infection (Wu et al., 2020).

Preliminary findings from experimental studies on cancer patients prompt an involvement of tumor markers as additional sites for SARS-CoV-2 entry. One of the promising candidates is CD147 (also termed basigin) that was found to be overexpressed in glioblastoma tissue and positively correlated with the viral invasion. CD147 is involved in the assessment of T cells

engineered to express CAR specific for CD147 (CD147-CART) treatment in an anticancer therapy under the phase I trial in patients with recurrent glioblastoma (NCT04045847) (Landras et al., 2019; Wang K. et al., 2020; Xia and Dubrovska, 2020). Despite the findings that CD147 is used for the entrance of SARS-CoV-2 to the target cell, these data are currently challenged (Shilts et al., 2021). While innovative insights have to be considered during the pandemic, tumor heterogeneity and immunosuppressive state are important in the development of more potent therapeutic applications for glioblastoma patients.

CONCLUSION

In recent years, the debate of using immunotherapy in glioblastoma care has continuously been raised. The application of ADCs, peptides or mRNA vaccines, CAR-T cells and CAR-NK T cells, checkpoint and chemokine inhibitors, or oncolytic viruses are hopeful treatment constituents. Notwithstanding these encouraging strategies, only a few patients respond to immunotherapy, indicating the improvement of therapies or co-delivery of multiple immunotherapeutics to be successful in the management of glioblastoma. The complications can be attributed to immonoresistance mechanisms and the complex heterogenous nature of the tumor. Understanding the pathophysiological features of glioblastoma provides an emergence of different immunotherapy strategies, including the focus on a combination of medications and personalized approaches to sensitize glioblastoma to immunotherapies and improve the treatment outcome.

AUTHOR CONTRIBUTIONS

TB, RT, ZY, KM, M-AW, JB, and UK: writing, reviewing, and editing. All authors contributed to the article and approved the submitted version.

FUNDING

TB was funded by the Nazarbayev University Faculty-Development Competitive Research Grants Program, reference: 280720FD1907.

ACKNOWLEDGMENTS

We appreciate the support of Annette Blatz for including the references.

REFERENCES

Adhikaree, J., Moreno-Vicente, J., Kaur, A. P., Jackson, A. M., and Patel, P. M. (2020). Resistance Mechanisms and Barriers to Successful Immunotherapy for Treating Glioblastoma. *Cells* 9:2. doi: 10.3390/cells9020263

Ahir, B. K., Engelhard, H. H., and Lakka, S. S. (2020). Tumor Development and Angiogenesis in Adult Brain Tumor: Glioblastoma. *Mol. Neurobiol.* 57, 2461–2478. doi: 10.1007/s12035-020-01892-8

Amin, M. M., Shawky, A., Zaher, A., Abdelbara, M., Wasel, Y., and Gomaa, M. (2012). Immune cell infiltrate in different grades of astrocytomas: possible role in the pathogenesis. *Egyptian J. Pathol.* 32:5.

Amoo, M., Horan, J., Gilmartin, B., Nolan, D., Corr, P., MacNally, S., et al. (2020). The provision of neuro-oncology and glioma neurosurgery during the SARS-CoV-2 pandemic: a single national tertiary centre experience. *Ir. J. Med. Sci.* 2020:7. doi: 10.1007/s11845-020-02429-7

Ampie, L., Choy, W., Lamano, J. B., Fakurnejad, S., Bloch, O., and Parsa, A. T. (2015). Heat shock protein vaccines against glioblastoma: from bench to bedside. *J. Neurooncol.* 123, 441–448. doi: 10.1007/s11060-015-1837-7

An, J., Chen, Y., and Huang, Z. (2004). Critical upstream signals of cytochrome C release induced by a novel Bcl-2 inhibitor. *J. Biol. Chem.* 279, 19133–19140. doi: 10.1074/jbc.M400295200

Antonios, J. P., Soto, H., Everson, R. G., Orpilla, J., Moughon, D., Shin, N., et al. (2016). PD-1 blockade enhances the vaccination-induced immune response in glioma. *JCI Insight* 1:10. doi: 10.1172/jci.insight.87059

Arora, A., and Somasundaram, K. (2019). Glioblastoma vs temozolomide: can the red queen race be won? *Cancer Biol. Ther.* 20, 1083–1090. doi: 10.1080/15384047.2019.1599662

Arslan, F., Bosserhoff, A. K., Nickl-Jockschat, T., Doerfelt, A., Bogdahn, U., and Hau, P. (2007). The role of versican isoforms V0/V1 in glioma migration mediated by transforming growth factor-beta2. *Br. J. Cancer* 96, 1560–1568. doi: 10.1038/sj.bjc.6603766

Badr, C. E., Wurdinger, T., Nilsson, J., Niers, J. M., Whalen, M., Degterev, A., et al. (2011). Lanatoside C sensitizes glioblastoma cells to tumor necrosis factor-related apoptosis-inducing ligand and induces an alternative cell death pathway. *Neuro Oncol.* 13, 1213–1224. doi: 10.1093/neuonc/nor067

Batich, K. A., Mitchell, D. A., Healy, P., Herndon, J. E. II, and Sampson, J. H. (2020). Once, Twice, Three Times a Finding: Reproducibility of Dendritic Cell Vaccine Trials Targeting Cytomegalovirus in Glioblastoma. *Clin. Cancer Res.* 26, 5297–5303. doi: 10.1158/1078-0432.CCR-20-1082

Bernhardt, D., Wick, W., Weiss, S. E., Sahgal, A., Lo, S. S., Suh, J. H., et al. (2020). Neuro-oncology Management During the COVID-19 Pandemic With a Focus on WHO Grade III and IV Gliomas. *Neuro Oncol.* 2020:113. doi: 10.1093/neuonc/noaa113

Bhaduri, A., Di Lullo, E., Jung, D., Muller, S., Crouch, E. E., Espinosa, C. S., et al. (2020). Outer Radial Glia-like Cancer Stem Cells Contribute to Heterogeneity of Glioblastoma. *Cell Stem Cell* 4:e46. doi: 10.1016/j.stem.2019.11.015

Bielarz, V., Willemart, K., Avalosse, N., De Swert, K., Lotfi, R., Lejeune, N., et al. (2021). Susceptibility of neuroblastoma and glioblastoma cell lines to SARS-CoV-2 infection. *Brain Res.* 1758:147344. doi: 10.1016/j.brainres.2021.147344

Blahovcova, E., Richterova, R., Kolarovszki, B., Dobrota, D., Racay, P., and Hatok, J. (2015). Apoptosis-related gene expression in tumor tissue samples obtained from patients diagnosed with glioblastoma multiforme. *Int. J. Mol. Med.* 36, 1677–1684. doi: 10.3892/ijmm.2015.2369

Bloch, O., Crane, C. A., Fuks, Y., Kaur, R., Aghi, M. K., Berger, M. S., et al. (2014). Heat-shock protein peptide complex-96 vaccination for recurrent glioblastoma: a phase II, single-arm trial. *Neuro Oncol.* 16, 274–279. doi: 10.1093/neuonc/not203

Brandes, A. A., Bartolotti, M., Tosoni, A., and Franceschi, E. (2016). Nitrosoureas in the Management of Malignant Gliomas. *Curr. Neurol. Neurosci. Rep.* 16:13. doi: 10.1007/s11910-015-0611-8

Brown, C. E., Alizadeh, D., Starr, R., Weng, L., Wagner, J. R., Naranjo, A., et al. (2016). Regression of Glioblastoma after Chimeric Antigen Receptor T-Cell Therapy. *N. Engl. J. Med.* 375, 2561–2569. doi: 10.1056/NEJMoa1610497

Burster, T., Gartner, F., Bulach, C., Zhanapiya, A., Gihring, A., and Knippschild, U. (2021). Regulation of MHC I Molecules in Glioblastoma Cells and the Sensitizing of NK Cells. *Pharmaceuticals* 14:3. doi: 10.3390/ph14030236

Candeias, S. M., and Gaipl, U. S. (2016). The Immune System in Cancer Prevention, Development and Therapy. *Anticancer. Agents Med. Chem.* 16, 101–107. doi: 10.2174/1871520615666150824153523

Carter, N. J., and Keating, G. M. (2007). Maraviroc. *Drugs* 67, 2277–2288. doi: 10.2165/00003495-200767150-00010

Castriconi, R., Cantoni, C., Della Chiesa, M., Vitale, M., Marcenaro, E., Conte, R., et al. (2003). Transforming growth factor beta 1 inhibits expression of NKp30 and NKG2D receptors: consequences for the NK-mediated killing of dendritic cells. *Proc Natl Acad Sci U S A* 100, 4120–4125. doi: 10.1073/pnas.0730640100

Chiocca, E. A., Aguilar, L. K., Bell, S. D., Kaur, B., Hardcastle, J., Cavaliere, R., et al. (2011). Phase IB study of gene-mediated cytotoxic immunotherapy adjuvant to up-front surgery and intensive timing radiation for malignant glioma. *J. Clin. Oncol.* 29, 3611–3619. doi: 10.1200/JCO.2011.35.5222

Conde Cardona, G., Quintana Pajaro, L. D., Quintero Marzola, I. D., Ramos Villegas, Y., and Moscote Salazar, L. R. (2020). Neurotropism of SARS-CoV 2: Mechanisms and manifestations. *J. Neurol. Sci.* 412:116824. doi: 10.1016/j.jns.2020.116824

Coolen, T., Lolli, V., Sadeghi, N., Rovai, A., Trotta, N., Taccone, F. S., et al. (2020). Early postmortem brain MRI findings in COVID-19 non-survivors. *Neurology* 95, e2016–e2027. doi: 10.1212/WNL.0000000000010116

Crane, C. A., Han, S. J., Ahn, B., Oehlke, J., Kivett, V., Fedoroff, A., et al. (2013). Individual patient-specific immunity against high-grade glioma after vaccination with autologous tumor derived peptides bound to the 96 KD chaperone protein. *Clin. Cancer Res.* 19, 205–214. doi: 10.1158/1078-0432.CCR-11-3358

Darvin, P., Toor, S. M., Sasidharan Nair, V., and Elkord, E. (2018). Immune checkpoint inhibitors: recent progress and potential biomarkers. *Exp. Mol. Med.* 50, 1–11. doi: 10.1038/s12276-018-0191-1

De, I., Steffen, M. D., Clark, P. A., Patros, C. J., Sokn, E., Bishop, S. M., et al. (2016). CSF1 Overexpression Promotes High-Grade Glioma Formation without Impacting the Polarization Status of Glioma-Associated Microglia and Macrophages. *Cancer Res.* 76, 2552–2560. doi: 10.1158/0008-5472.CAN-15-2386

Dean, M., Fojo, T., and Bates, S. (2005). Tumour stem cells and drug resistance. *Nat. Rev. Cancer* 5, 275–284. doi: 10.1038/nrc1590

Desjardins, A., Sampson, J. H., Peters, K. B., Vlahovic, G., Randazzo, D., Threatt, S., et al. (2016). Patient survival on the dose escalation phase of the Oncolytic Polio/Rhinovirus Recombinant (PVSRIPO) against WHO grade IV malignant glioma (MG) clinical trial compared to historical controls. *J. Clin. Oncol.* 34, 2061–2061. doi: 10.1200/JCO.2016.34.15_suppl.2061

Di Bari, M., Tombolillo, V., Conte, C., Castigli, E., Sciaccaluga, M., Iorio, E., et al. (2015). Cytotoxic and genotoxic effects mediated by M2 muscarinic receptor activation in human glioblastoma cells. *Neurochem. Int.* 90, 261–270. doi: 10.1016/j.neuint.2015.09.008

Dunn-Pirio, A. M., and Vlahovic, G. (2017). Immunotherapy approaches in the treatment of malignant brain tumors. *Cancer* 123, 734–750. doi: 10.1002/cncr.30371

Engelhardt, B., and Ransohoff, R. M. (2012). Capture, crawl, cross: the T cell code to breach the blood-brain barriers. *Trends Immunol.* 33, 579–589. doi: 10.1016/j.it.2012.07.004

Foreman, P. M., Friedman, G. K., Cassady, K. A., and Markert, J. M. (2017). Oncolytic Virotherapy for the Treatment of Malignant Glioma. *Neurotherapeutics* 14, 333–344. doi: 10.1007/s13311-017-0516-0

Fousek, K., and Ahmed, N. (2015). The Evolution of T-cell Therapies for Solid Malignancies. *Clin Cancer Res.* 21, 3384–3392. doi: 10.1158/1078-0432.CCR-14-2675

Frankel, S. R. (2003). Oblimersen sodium (G3139 Bcl-2 antisense oligonucleotide) therapy in Waldenstrom's macroglobulinemia: a targeted approach to enhance apoptosis. *Semin. Oncol.* 30, 300–304. doi: 10.1053/sonc.2003.50041

Fricker, S. P. (2008). A novel CXCR4 antagonist for hematopoietic stem cell mobilization. *Expert Opin. Investig. Drugs* 17, 1749–1760. doi: 10.1517/13543784.17.11.1749

Gabrusiewicz, K., Rodriguez, B., Wei, J., Hashimoto, Y., Healy, L. M., Maiti, S. N., et al. (2016). Glioblastoma-infiltrated innate immune cells resemble M0 macrophage phenotype. *JCI Insight* 1:2. doi: 10.1172/jci.insight.85841

Gan, H. K., van den Bent, M., Lassman, A. B., Reardon, D. A., and Scott, A. M. (2017). Antibody-drug conjugates in glioblastoma therapy: the right drugs to the right cells. *Nat Rev Clin Oncol* 14, 695–707. doi: 10.1038/nrclinonc.2017.95

Gao, Q., Chen, C., Ji, T., Wu, P., Han, Z., Fang, H., et al. (2014). A systematic comparison of the anti-tumoural activity and toxicity of the three Adv-TKs. *PLoS One* 9:e94050. doi: 10.1371/journal.pone.0094050

Gieryng, A., Pszczolkowska, D., Walentynowicz, K. A., Rajan, W. D., and Kaminska, B. (2017). Immune microenvironment of gliomas. *Lab. Invest.* 97, 498–518. doi: 10.1038/labinvest.2017.19

Halford, S., Rampling, R., James, A., Peoples, S., Mulholland, P., Al-Salihi, O., et al. (2014). 1057PD - Final Results from a Cancer Research Uk First in Man Phase I Trial of Ima950 (A Novel Multi Peptide Vaccine) Plus Gm-Csf in Patients with Newly Diagnosed Glioblastoma. *Ann. Oncol.* 25:iv364. doi: 10.1093/annonc/mdu342.10

Hanahan, D., and Weinberg, R. A. (2011). Hallmarks of cancer: the next generation. *Cell* 144, 646–674. doi: 10.1016/j.cell.2011.02.013

Hegi, M. E., Diserens, A. C., Gorlia, T., Hamou, M. F., de Tribolet, N., Weller, M., et al. (2005). MGMT gene silencing and benefit from temozolomide in glioblastoma. *N. Engl. J. Med.* 352, 997–1003. doi: 10.1056/NEJMoa043331

Herbener, V. J., Burster, T., Goreth, A., Pruss, M., von Bandemer, H., Baisch, T., et al. (2020). Considering the Experimental use of Temozolomide in Glioblastoma Research. *Biomedicines* 8:151. doi: 10.3390/biomedicines8060151

Hira, V. V., Verbovsek, U., Breznik, B., Srdic, M., Novinec, M., Kakar, H., et al. (2017). Cathepsin K cleavage of SDF-1alpha inhibits its chemotactic activity towards glioblastoma stem-like cells. *Biochim. Biophys. Acta Mol. Cell Res.* 1864, 594–603. doi: 10.1016/j.bbamcr.2016.12.021

Hlavac, M., Dwucet, A., Kast, R. E., Engelke, J., Westhoff, M. A., Siegelin, M. D., et al. (2019). Combined inhibition of RAC1 and Bcl-2/Bcl-xL synergistically induces glioblastoma cell death through down-regulation of the Usp9X/Mcl-1 axis. *Cell Oncol.* 42, 287–301. doi: 10.1007/s13402-019-00425-3

Hodges, T. R., Ott, M., Xiu, J., Gatalica, Z., Swensen, J., Zhou, S., et al. (2017). Mutational burden, immune checkpoint expression, and mismatch repair in glioma: implications for immune checkpoint immunotherapy. *Neuro Oncol.* 19, 1047–1057. doi: 10.1093/neuonc/nox026

Horuk, R. (2009). Chemokine receptor antagonists: overcoming developmental hurdles. *Nat. Rev. Drug. Discov.* 8, 23–33. doi: 10.1038/nrd2734

Huang, J., Liu, F., Liu, Z., Tang, H., Wu, H., Gong, Q., et al. (2017). Immune Checkpoint in Glioblastoma: promising and challenging. *Front. Pharmacol.* 8:242. doi: 10.3389/fphar.2017.00242

Huber, A., Dammeijer, F., Aerts, J., and Vroman, H. (2018). Current State of Dendritic Cell-Based Immunotherapy: Opportunities for in vitro Antigen Loading of Different DC Subsets? *Front. Immunol.* 9:2804. doi: 10.3389/fimmu.2018.02804

Hussain, S. F., Kong, L. Y., Jordan, J., Conrad, C., Madden, T., Fokt, I., et al. (2007). A novel small molecule inhibitor of signal transducers and activators of transcription 3 reverses immune tolerance in malignant glioma patients. *Cancer Res.* 67, 9630–9636. doi: 10.1158/0008-5472.CAN-07-1243

Jackson, C. M., Choi, J., and Lim, M. (2019). Mechanisms of immunotherapy resistance: lessons from glioblastoma. *Nat. Immunol.* 20, 1100–1109. doi: 10.1038/s41590-019-0433-y

Ji, N., Weng, D., Liu, C., Gu, Z., Chen, S., Guo, Y., et al. (2016). Adenovirus-mediated delivery of herpes simplex virus thymidine kinase administration improves outcome of recurrent high-grade glioma. *Oncotarget* 7, 4369–4378. doi: 10.18632/oncotarget.6737

Julien, T., Frankel, B., Longo, S., Kyle, M., Gibson, S., Shillitoe, E., et al. (2000). Antisense-mediated inhibition of the bcl-2 gene induces apoptosis in human malignant glioma. *Surg. Neurol.* 53, 360–368. doi: 10.1016/s0090-3019(00)00178-6

Juszczak, A., Gupta, A., Karavitaki, N., Middleton, M. R., and Grossman, A. B. (2012). Ipilimumab: a novel immunomodulating therapy causing autoimmune hypophysitis: a case report and review. *Eur. J. Endocrinol.* 167, 1–5. doi: 10.1530/EJE-12-0167

Kaina, B. (2019). Temozolomide in glioblastoma therapy: role of apoptosis, senescence and autophagy. comment on Strobel et al., temozolomide and other alkylating agents in glioblastoma therapy. Biomedicines 2019, 7, 69. *Biomedicines* 7:90. doi: 10.3390/biomedicines7040090

Kamson, D. O., and Grossman, S. A. (2021). The Role of Temozolomide in Patients With Newly Diagnosed Wild-Type IDH, Unmethylated MGMTp Glioblastoma During the COVID-19 Pandemic. *JAMA Oncol.* 7, 675–676. doi: 10.1001/jamaoncol.2020.6732

Karachi, A., Dastmalchi, F., Mitchell, D. A., and Rahman, M. (2018). Temozolomide for immunomodulation in the treatment of glioblastoma. *Neuro Oncol.* 20, 1566–1572. doi: 10.1093/neuonc/noy072

Karpel-Massler, G., Ishida, C. T., Bianchetti, E., Zhang, Y., Shu, C., Tsujiuchi, T., et al. (2017). Induction of synthetic lethality in IDH1-mutated gliomas through inhibition of Bcl-xL. *Nat. Commun.* 8:1067. doi: 10.1038/s41467-017-00984-9

Keskin, D. B., Anandappa, A. J., Sun, J., Tirosh, I., Mathewson, N. D., Li, S., et al. (2019). Neoantigen vaccine generates intratumoral T cell responses in phase Ib glioblastoma trial. *Nature* 565, 234–239. doi: 10.1038/s41586-018-0792-9

Kim, J. E., Patel, M. A., Mangraviti, A., Kim, E. S., Theodros, D., Velarde, E., et al. (2017). Combination Therapy with Anti-PD-1, Anti-TIM-3, and Focal Radiation Results in Regression of Murine Gliomas. *Clin. Cancer Res.* 23, 124–136. doi: 10.1158/1078-0432.CCR-15-1535

Knight, M. J., Riffkin, C. D., Muscat, A. M., Ashley, D. M., and Hawkins, C. J. (2001). Analysis of FasL and TRAIL induced apoptosis pathways in glioma cells. *Oncogene* 20, 5789–5798. doi: 10.1038/sj.onc.1204810

Kouri, F. M., Jensen, S. A., and Stegh, A. H. (2012). The role of Bcl-2 family proteins in therapy responses of malignant astrocytic gliomas: Bcl2L12 and beyond. *Sci. World J.* 2012:838916. doi: 10.1100/2012/838916

Koyama, S., Akbay, E. A., Li, Y. Y., Herter-Sprie, G. S., Buczkowski, K. A., Richards, W. G., et al. (2016). Adaptive resistance to therapeutic PD-1 blockade is associated with upregulation of alternative immune checkpoints. *Nat. Commun.* 7:10501. doi: 10.1038/ncomms10501

Ku, M. C., Wolf, S. A., Respondek, D., Matyash, V., Pohlmann, A., Waiczies, S., et al. (2013). GDNF mediates glioblastoma-induced microglia attraction but not astrogliosis. *Acta Neuropathol.* 125, 609–620. doi: 10.1007/s00401-013-1079-8

Kunkel, P., Muller, S., Schirmacher, P., Stavrou, D., Fillbrandt, R., Westphal, M., et al. (2001). Expression and localization of scatter factor/hepatocyte growth factor in human astrocytomas. *Neuro Oncol.* 3, 82–88. doi: 10.1093/neuonc/3.2.82

Kuter, D. J. (2015). Managing thrombocytopenia associated with cancer chemotherapy. *Oncology* 29, 282–294.

Kwon, S. G., Park, I., Kwon, Y. W., Lee, T. W., Park, G. T., and Kim, J. H. (2019). Role of stem cell mobilization in the treatment of ischemic diseases. *Arch Pharm Res* 42, 224–231. doi: 10.1007/s12272-019-01123-2

Landras, A., Reger, de Moura, C., Jouenne, F., Lebbe, C., Menashi, S., et al. (2019). CD147 Is a Promising Target of Tumor Progression and a Prognostic Biomarker. *Cancers* 11:11. doi: 10.3390/cancers11111803

Laudati, E., Curro, D., Navarra, P., and Lisi, L. (2017). Blockade of CCR5 receptor prevents M2 microglia phenotype in a microglia-glioma paradigm. *Neurochem Int* 108, 100–108. doi: 10.1016/j.neuint.2017.03.002

Le Rhun, E., Preusser, M., Roth, P., Reardon, D. A., van den Bent, M., Wen, P., et al. (2019). Molecular targeted therapy of glioblastoma. *Cancer Treat Rev.* 80:101896. doi: 10.1016/j.ctrv.2019.101896

Lesterhuis, W. J., Salmons, J., Nowak, A. K., Rozali, E. N., Khong, A., Dick, I. M., et al. (2013). Synergistic effect of CTLA-4 blockade and cancer chemotherapy in the induction of anti-tumor immunity. *PLoS One* 8:e61895. doi: 10.1371/journal.pone.0061895

Letko, M., Marzi, A., and Munster, V. (2020). Functional assessment of cell entry and receptor usage for SARS-CoV-2 and other lineage B betacoronaviruses. *Nat. Microbiol.* 5, 562–569. doi: 10.1038/s41564-020-0688-y

Li, C., Du, Y., Zhang, Y., and Ji, N. (2020). Immunotherapy with heat shock protein 96 to treat gliomas. *Chin. Neurosurg. J.* 6:31. doi: 10.1186/s41016-020-00211-3

Li, J. Y., Boado, R. J., and Pardridge, W. M. (2001). Blood-brain barrier genomics. *J. Cereb. Blood Flow Metab.* 21, 61–68. doi: 10.1097/00004647-200101000-00008

Liau, L. M., Ashkan, K., Tran, D. D., Campian, J. L., Trusheim, J. E., Cobbs, C. S., et al. (2018). First results on survival from a large Phase 3 clinical trial of an autologous dendritic cell vaccine in newly diagnosed glioblastoma. *J. Transl. Med.* 16, 142. doi: 10.1186/s12967-018-1507-6

Lim, M., Xia, Y., Bettegowda, C., and Weller, M. (2018). Current state of immunotherapy for glioblastoma. *Nat. Rev. Clin. Oncol.* 15, 422–442. doi: 10.1038/s41571-018-0003-5

Lincoln, F. A., Imig, D., Boccellato, C., Juric, V., Noonan, J., Kontermann, R. E., et al. (2018). Sensitization of glioblastoma cells to TRAIL-induced apoptosis by IAP- and Bcl-2 antagonism. *Cell Death Dis.* 9:1112. doi: 10.1038/s41419-018-1160-2

Majc, B., Novak, M., Kopitar-Jerala, N., Jewett, A., and Breznik, B. (2021). Immunotherapy of Glioblastoma: Current Strategies and Challenges in Tumor Model Development. *Cells* 10:2. doi: 10.3390/cells10020265

Malkki, H. (2016). Trial Watch: Glioblastoma vaccine therapy disappointment in Phase III trial. *Nat. Rev. Neurol.* 12:190. doi: 10.1038/nrneurol.2016.38

Mao, L., Jin, H., Wang, M., Hu, Y., Chen, S., He, Q., et al. (2020). Neurologic manifestations of hospitalized patients with coronavirus disease 2019 in Wuhan, China. *JAMA Neurol.* 77, 683–690. doi: 10.1001/jamaneurol.2020.1127

Marvel, D., and Gabrilovich, D. I. (2015). Myeloid-derived suppressor cells in the tumor microenvironment: expect the unexpected. *J. Clin. Invest.* 125, 3356–3364. doi: 10.1172/JCI80005

Mathios, D., Kim, J. E., Mangraviti, A., Phallen, J., Park, C. K., Jackson, C. M., et al. (2016). Anti-PD-1 antitumor immunity is enhanced by local and abrogated by systemic chemotherapy in GBM. *Sci. Transl. Med.* 8:370ra180. doi: 10.1126/scitranslmed.aag2942

McGavern, D. B., and Kang, S. S. (2011). Illuminating viral infections in the nervous system. *Nat. Rev. Immunol.* 11, 318–329. doi: 10.1038/nri2971

Medikonda, R., Dunn, G., Rahman, M., Fecci, P., and Lim, M. (2021). A review of glioblastoma immunotherapy. *J. Neurooncol.* 151, 41–53. doi: 10.1007/s11060-020-03448-1

Mehta, A. M., Sonabend, A. M., and Bruce, J. N. (2017). Convection-Enhanced Delivery. *Neurotherapeutics* 14, 358–371. doi: 10.1007/s13311-017-0520-4

Meinhardt, J., Radke, J., Dittmayer, C., Franz, J., Thomas, C., Mothes, R., et al. (2021). Olfactory transmucosal SARS-CoV-2 invasion as a port of central nervous system entry in individuals with COVID-19. *Nat. Neurosci.* 24, 168–175. doi: 10.1038/s41593-020-00758-5

Mercurio, L., Ajmone-Cat, M. A., Cecchetti, S., Ricci, A., Bozzuto, G., Molinari, A., et al. (2016). Targeting CXCR4 by a selective peptide antagonist modulates tumor microenvironment and microglia reactivity in a human glioblastoma model. *J. Exp. Clin. Cancer Res.* 35:55. doi: 10.1186/s13046-016-0326-y

Miao, L., Zhang, Y., and Huang, L. (2021). mRNA vaccine for cancer immunotherapy. *Mol. Cancer* 20:41. doi: 10.1186/s12943-021-01335-5

Michels, J., Johnson, P. W., and Packham, G. (2005). Mcl-1. *Int. J. Biochem. Cell Biol.* 37, 267–271. doi: 10.1016/j.biocel.2004.04.007

Migliorini, D., Dutoit, V., Allard, M., Grandjean Hallez, N., Marinari, E., Widmer, V., et al. (2019). Phase I/II trial testing safety and immunogenicity of the multipeptide IMA950/poly-ICLC vaccine in newly diagnosed adult malignant astrocytoma patients. *Neuro Oncol.* 21, 923–933. doi: 10.1093/neuonc/noz040

Miyauchi, J. T., and Tsirka, S. E. (2018). Advances in immunotherapeutic research for glioma therapy. *J. Neurol.* 265, 741–756. doi: 10.1007/s00415-017-8695-5

Mogensen, T. H. (2009). Pathogen recognition and inflammatory signaling in innate immune defenses. *Clin. Microbiol. Rev.* 22, 240–273. doi: 10.1128/CMR.00046-08

Nguyen, T. T. T., Ishida, C. T., Shang, E., Shu, C., Torrini, C., Zhang, Y., et al. (2019). Activation of LXRbeta inhibits tumor respiration and is synthetically lethal with Bcl-xL inhibition. *EMBO Mol. Med.* 11:e10769. doi: 10.15252/emmm.201910769

Noticewala, S. S., Ludmir, E. B., Bishop, A. J., Chung, C., Ghia, A. J., Grosshans, D., et al. (2020). Radiation for Glioblastoma in the Era of Coronavirus Disease 2019 (COVID-19): Patient Selection and Hypofractionation to Maximize Benefit and Minimize Risk. *Adv. Radiat. Oncol.* 5, 743–745. doi: 10.1016/j.adro.2020.04.040

Ola, M. S., Nawaz, M., and Ahsan, H. (2011). Role of Bcl-2 family proteins and caspases in the regulation of apoptosis. *Mol Cell Biochem* 351, 41–58. doi: 10.1007/s11010-010-0709-x

Ou, A., Yung, W. K. A., and Majd, N. (2020). Molecular Mechanisms of Treatment Resistance in Glioblastoma. *Int. J. Mol. Sci.* 22:1. doi: 10.3390/ijms22010351

Pardi, N., Hogan, M. J., Porter, F. W., and Weissman, D. (2018). mRNA vaccines - a new era in vaccinology. *Nat. Rev. Drug. Discov.* 17, 261–279. doi: 10.1038/nrd.2017.243

Payer, F. (2011). Pseudoprogression oder Pseudorespons: Herausforderung an die Bildgebung des Glioblastoma multiforme. *Wiener Medizinische Wochenschrift* 161, 13–19. doi: 10.1007/s10354-010-0860-8

Peng, M., Mo, Y., Wang, Y., Wu, P., Zhang, Y., Xiong, F., et al. (2019). Neoantigen vaccine: an emerging tumor immunotherapy. *Mol. Cancer* 18:128. doi: 10.1186/s12943-019-1055-6

Pessina, F., Navarria, P., Bellu, L., Clerici, E., Politi, L. S., Tropeano, M. P., et al. (2020). Treatment of patients with glioma during the COVID-19 pandemic: what we learned and what we take home for the future. *Neurosurg. Focus* 49:E10. doi: 10.3171/2020.9.FOCUS20704

Peters, C., and Brown, S. (2015). Antibody-drug conjugates as novel anti-cancer chemotherapeutics. *Biosci. Rep.* 35:4. doi: 10.1042/BSR20150089

Phillips, A. C., Boghaert, E. R., Vaidya, K. S., Mitten, M. J., Norvell, S., Falls, H. D., et al. (2016). ABT-414, an Antibody-Drug Conjugate Targeting a Tumor-Selective EGFR Epitope. *Mol. Cancer Ther.* 15, 661–669. doi: 10.1158/1535-7163.MCT-15-0901

Phuphanich, S., Wheeler, C. J., Rudnick, J. D., Mazer, M., Wang, H., Nuno, M. A., et al. (2013). Phase I trial of a multi-epitope-pulsed dendritic cell vaccine for patients with newly diagnosed glioblastoma. *Cancer Immunol. Immunother.* 62, 125–135. doi: 10.1007/s00262-012-1319-0

Polson, A. G., Calemine-Fenaux, J., Chan, P., Chang, W., Christensen, E., Clark, S., et al. (2009). Antibody-drug conjugates for the treatment of non-Hodgkin's lymphoma: target and linker-drug selection. *Cancer Res* 69, 2358–2364. doi: 10.1158/0008-5472.CAN-08-2250

Polyzoidis, S., and Ashkan, K. (2014). DCVax(R)-L–developed by Northwest Biotherapeutics. *Hum. Vaccin. Immunother.* 10, 3139–3145. doi: 10.4161/hv.29276

Portella, L., Vitale, R., De Luca, S., D'Alterio, C., Ierano, C., Napolitano, M., et al. (2013). Preclinical development of a novel class of CXCR4 antagonist impairing solid tumors growth and metastases. *PLoS One* 8:e74548. doi: 10.1371/journal.pone.0074548

Puelles, V. G., Lutgehetmann, M., Lindenmeyer, M. T., Sperhake, J. P., Wong, M. N., Allweiss, L., et al. (2020). Multiorgan and renal tropism of SARS-CoV-2. *N. Engl. J. Med.* 383, 590–592. doi: 10.1056/NEJMc2011400

Pyonteck, S. M., Akkari, L., Schuhmacher, A. J., Bowman, R. L., Sevenich, L., Quail, D. F., et al. (2013). CSF-1R inhibition alters macrophage polarization and blocks glioma progression. *Nat Med* 19, 1264–1272. doi: 10.1038/nm.3337

Rampling, R., Peoples, S., Mulholland, P. J., James, A., Al-Salihi, O., Twelves, C. J., et al. (2016). A Cancer Research UK First Time in Human Phase I Trial of IMA950 (Novel Multipeptide Therapeutic Vaccine) in Patients with Newly Diagnosed Glioblastoma. *Clin. Cancer Res.* 22, 4776–4785. doi: 10.1158/1078-0432.CCR-16-0506

Razavi, S. M., Lee, K. E., Jin, B. E., Aujla, P. S., Gholamin, S., and Li, G. (2016). Immune Evasion Strategies of Glioblastoma. *Front. Surg.* 3:11. doi: 10.3389/fsurg.2016.00011

Roberts, H. C., Roberts, T. P., Brasch, R. C., and Dillon, W. P. (2000). Quantitative measurement of microvascular permeability in human brain tumors achieved using dynamic contrast-enhanced MR imaging: correlation with histologic grade. *AJNR Am. J. Neuroradiol.* 21, 891–899.

Rui, Y., and Green, J. J. (2021). Overcoming delivery barriers in immunotherapy for glioblastoma. *Drug. Deliv. Transl. Res.* 2021:2. doi: 10.1007/s13346-021-01008-2

Salinas, R. D., Durgin, J. S., and O'Rourke, D. M. (2020). Potential of Glioblastoma-Targeted Chimeric Antigen Receptor (CAR) T-Cell Therapy. *CNS Drugs* 34, 127–145. doi: 10.1007/s40263-019-00687-3

Sampson, J. H., Vlahovic, G., Sahebjam, S., Omuro, A. M. P., Baehring, J. M., Hafler, D. A., et al. (2015). Preliminary safety and activity of nivolumab and its combination with ipilimumab in recurrent glioblastoma (GBM): CHECKMATE-143. *J. Clin. Oncol.* 33, 3010–3010. doi: 10.1200/jco.2015.33.15_suppl.3010

Schneble, E., Clifton, G. T., Hale, D. F., and Peoples, G. E. (2016). Peptide-Based Cancer Vaccine Strategies and Clinical Results. *Methods Mol. Biol.* 1403, 797–817. doi: 10.1007/978-1-4939-3387-7_46

Schneider, S. W., Ludwig, T., Tatenhorst, L., Braune, S., Oberleithner, H., Senner, V., et al. (2004). Glioblastoma cells release factors that disrupt blood-brain barrier features. *Acta Neuropathol.* 107, 272–276. doi: 10.1007/s00401-003-0810-2

Schuster, J., Lai, R. K., Recht, L. D., Reardon, D. A., Paleologos, N. A., Groves, M. D., et al. (2015). A phase II, multicenter trial of rindopepimut (CDX-110) in newly diagnosed glioblastoma: the ACT III study. *Neuro Oncol.* 17, 854–861. doi: 10.1093/neuonc/nou348

Scotti, C., Iamele, L., and Vecchia, L. (2015). Antibody–drug conjugates: targeted weapons against cancer. *Antibody Technol. J.* 1:52914. doi: 10.2147/ANTI.S52914

See, A. P., Han, J. E., Phallen, J., Binder, Z., Gallia, G., Pan, F., et al. (2012). The role of STAT3 activation in modulating the immune microenvironment of GBM. *J. Neurooncol.* 110, 359–368. doi: 10.1007/s11060-012-0981-6

Shang, E., Nguyen, T. T. T., Shu, C., Westhoff, M. A., Karpel-Massler, G., and Siegelin, M. D. (2020). Epigenetic Targeting of Mcl-1 Is Synthetically Lethal with Bcl-xL/Bcl-2 Inhibition in Model Systems of Glioblastoma. *Cancers* 12:8. doi: 10.3390/cancers12082137

Sharifzad, F., Ghavami, S., Verdi, J., Mardpour, S., Mollapour Sisakht, M., Azizi, Z., et al. (2019). Glioblastoma cancer stem cell biology: potential theranostic targets. *Drug Resist. Updat.* 42, 35–45. doi: 10.1016/j.drup.2018.03.003

Shilts, J., Crozier, T. W. M., Greenwood, E. J. D., Lehner, P. J., and Wright, G. J. (2021). No evidence for basigin/CD147 as a direct SARS-CoV-2 spike binding receptor. *Sci. Rep.* 11:413. doi: 10.1038/s41598-020-80464-1

Singh, R., Letai, A., and Sarosiek, K. (2019). Regulation of apoptosis in health and disease: the balancing act of BCL-2 family proteins. *Nat. Rev. Mol. Cell Biol.* 20, 175–193. doi: 10.1038/s41580-018-0089-8

Song, E., Zhang, C., Israelow, B., Lu-Culligan, A., Prado, A. V., Skriabine, S., et al. (2021). Neuroinvasion of SARS-CoV-2 in human and mouse brain. *J Exp Med* 218, 3. doi: 10.1084/jem.20202135

Stegh, A. H., Kim, H., Bachoo, R. M., Forloney, K. L., Zhang, J., Schulze, H., et al. (2007). Bcl2L12 inhibits post-mitochondrial apoptosis signaling in glioblastoma. *Genes Dev.* 21, 98–111. doi: 10.1101/gad.1480007

Steinbach, J. P., and Weller, M. (2004). Apoptosis in Gliomas: molecular Mechanisms and Therapeutic Implications. *J. Neurooncol.* 70, 247–256. doi: 10.1007/s11060-004-2753-4

Stepanenko, A. A., and Chekhonin, V. P. (2019). On the critical issues in temozolomide research in glioblastoma: clinically relevant concentrations and MGMT-independent resistance. *Biomedicines* 7:92. doi: 10.3390/biomedicines7040092

Strepkos, D., Markouli, M., Klonou, A., Piperi, C., and Papavassiliou, A. (2020). Insights in the immunobiology of glioblastoma. *J. Mole. Med.* 98:4. doi: 10.1007/s00109-019-01835-4

Strik, H., Deininger, M., Streffer, J., Grote, E., Wickboldt, J., Dichgans, J., et al. (1999). BCL-2 family protein expression in initial and recurrent glioblastomas: modulation by radiochemotherapy. *J. Neurol. Neurosurg. Psychiatr.* 67, 763–768. doi: 10.1136/jnnp.67.6.763

Strobel, H., Baisch, T., Fitzel, R., Schilberg, K., Siegelin, M. D., Karpel-Massler, G., et al. (2019). Temozolomide and Other Alkylating Agents in Glioblastoma Therapy. *Biomedicines* 7:3. doi: 10.3390/biomedicines7030069

Tagscherer, K. E., Fassl, A., Campos, B., Farhadi, M., Kraemer, A., Bock, B. C., et al. (2008). Apoptosis-based treatment of glioblastomas with ABT-737, a novel small molecule inhibitor of Bcl-2 family proteins. *Oncogene* 27, 6646–6656. doi: 10.1038/onc.2008.259

Tron, A. E., Belmonte, M. A., Adam, A., Aquila, B. M., Boise, L. H., Chiarparin, E., et al. (2018). Discovery of Mcl-1-specific inhibitor AZD5991 and preclinical activity in multiple myeloma and acute myeloid leukemia. *Nat. Commun.* 9:5341. doi: 10.1038/s41467-018-07551-w

Tsujimoto, Y. (1998). Role of Bcl-2 family proteins in apoptosis: apoptosomes or mitochondria? *Genes Cells* 3, 697–707. doi: 10.1046/j.1365-2443.1998.00223.x

Tyagi, D., Sharma, B. S., Gupta, S. K., Kaul, D., Vasishta, R. K., and Khosla, V. K. (2002). Expression of Bcl2 proto-oncogene in primary tumors of the central nervous system. *Neurol. India* 50, 290–294.

van den Bent, M., Gan, H. K., Lassman, A. B., Kumthekar, P., Merrell, R., Butowski, N., et al. (2017). Efficacy of depatuxizumab mafodotin (ABT-414) monotherapy in patients with EGFR-amplified, recurrent glioblastoma: results from a multi-center, international study. *Cancer Chemother. Pharmacol.* 80, 1209–1217. doi: 10.1007/s00280-017-3451-1

Vellanki, S. H., Grabrucker, A., Liebau, S., Proepper, C., Eramo, A., Braun, V., et al. (2009). Small-molecule XIAP inhibitors enhance gamma-irradiation-induced apoptosis in glioblastoma. *Neoplasia* 11, 743–752. doi: 10.1593/neo.09436

Vengoji, R., Macha, M. A., Batra, S. K., and Shonka, N. A. (2018). Natural products: a hope for glioblastoma patients. *Oncotarget* 9, 22194–22219. doi: 10.18632/oncotarget.25175

Vieira de Castro, J., Goncalves, C. S., Hormigo, A., and Costa, B. M. (2020). Exploiting the Complexities of Glioblastoma Stem Cells: Insights for Cancer Initiation and Therapeutic Targeting. *Int. J. Mol. Sci.* 21:15. doi: 10.3390/ijms21155278

Viel, S., Marcais, A., Guimaraes, F. S., Loftus, R., Rabilloud, J., Grau, M., et al. (2016). TGF-beta inhibits the activation and functions of NK cells by repressing the mTOR pathway. *Sci. Signal* 9:ra19. doi: 10.1126/scisignal.aad1884

Vik-Mo, E. O., Nyakas, M., Mikkelsen, B. V., Moe, M. C., Due-Tonnesen, P., Suso, E. M., et al. (2013). Therapeutic vaccination against autologous cancer stem cells

with mRNA-transfected dendritic cells in patients with glioblastoma. *Cancer Immunol. Immunother.* 62, 1499–1509. doi: 10.1007/s00262-013-1453-3

von Roemeling, C. A., Wang, Y., Qie, Y., Yuan, H., Zhao, H., Liu, X., et al. (2020). Therapeutic modulation of phagocytosis in glioblastoma can activate both innate and adaptive antitumour immunity. *Nat Commun* 11, 1508. doi: 10.1038/s41467-020-15129-8

Wang, H. B., Li, T., Ma, D. Z., Ji, Y. X., and Zhi, H. (2017). Overexpression of FADD and Caspase-8 inhibits proliferation and promotes apoptosis of human glioblastoma cells. *Biomed. Pharmacother.* 93, 1–7. doi: 10.1016/j.biopha.2017.05.105

Wang, K., Chen, W., Zhou, Y.-S., Lian, J.-Q., Zhang, Z., Du, P., et al. (2020). SARS-CoV-2 invades host cells via a novel route: CD147-spike protein. *bioRxiv* 2020:988345. doi: 10.1101/2020.03.14.988345

Wang, L., Ge, J., Lan, Y., Shi, Y., Luo, Y., Tan, Y., et al. (2020). Tumor mutational burden is associated with poor outcomes in diffuse glioma. *BMC Cancer* 20:213. doi: 10.1186/s12885-020-6658-1

Wang, Y., Xie, Y., and Oupicky, D. (2016). Potential of CXCR4/CXCL12 Chemokine Axis in Cancer Drug Delivery. *Curr. Pharmacol. Rep.* 2, 1–10. doi: 10.1007/s40495-015-0044-8

Wängler, B., Schirrmacher, R., and Wängler, C. (2020). Aiming at the tumor-specific accumulation of MGMT-inhibitors: first description of a synthetic strategy towards inhibitor-peptide conjugates. *Tetrahed. Lett.* 61:151840. doi: 10.1016/j.tetlet.2020.151840

Weathers, S. P., and de Groot, J. (2015). VEGF Manipulation in Glioblastoma. *Oncology* 29, 720–727.

Wee, B., Pietras, A., Ozawa, T., Bazzoli, E., Podlaha, O., Antczak, C., et al. (2016). ABCG2 regulates self-renewal and stem cell marker expression but not tumorigenicity or radiation resistance of glioma cells. *Sci. Rep.* 6:25956. doi: 10.1038/srep25956

Weenink, B., French, P. J., Sillevis Smitt, P. A. E., Debets, R., and Geurts, M. (2020). Immunotherapy in Glioblastoma: current shortcomings and future perspectives. *Cancers* 12:3. doi: 10.3390/cancers12030751

Wen, P. Y., Reardon, D. A., Armstrong, T. S., Phuphanich, S., Aiken, R. D., Landolfi, J. C., et al. (2019). A Randomized Double-Blind Placebo-Controlled Phase II Trial of Dendritic Cell Vaccine ICT-107 in Newly Diagnosed Patients with Glioblastoma. *Clin Cancer Res* 25, 5799–5807. doi: 10.1158/1078-0432.CCR-19-0261

Weng, Y., Li, C., Yang, T., Hu, B., Zhang, M., Guo, S., et al. (2020). The challenge and prospect of mRNA therapeutics landscape. *Biotechnol. Adv.* 40:107534. doi: 10.1016/j.biotechadv.2020.107534

Westhoff, M. A., Baisch, T., Herbener, V. J., Karpel-Massler, G., Debatin, K. M., and Strobel, H. (2020). Comment in response to "temozolomide in glioblastoma therapy: role of apoptosis, senescence and autophagy etc. by B. Kaina". *Biomedicines* 8:93. doi: 10.3390/biomedicines8040093

Wheeler, L. A., Manzanera, A. G., Bell, S. D., Cavaliere, R., McGregor, J. M., Grecula, J. C., et al. (2016). Phase II multicenter study of gene-mediated cytotoxic immunotherapy as adjuvant to surgical resection for newly diagnosed malignant glioma. *Neuro Oncol.* 18, 1137–1145. doi: 10.1093/neuonc/now002

Wick, W., Wild-Bode, C., Frank, B., and Weller, M. (2004). BCL-2-induced glioma cell invasiveness depends on furin-like proteases. *J. Neurochem.* 91, 1275–1283. doi: 10.1111/j.1471-4159.2004.02806.x

Wiendl, H., Mitsdoerffer, M., Hofmeister, V., Wischhusen, J., Bornemann, A., Meyermann, R., et al. (2002). A functional role of HLA-G expression in human gliomas: an alternative strategy of immune escape. *J. Immunol.* 168, 4772–4780. doi: 10.4049/jimmunol.168.9.4772

Wilson, W. H., O'Connor, O. A., Czuczman, M. S., LaCasce, A. S., Gerecitano, J. F., Leonard, J. P., et al. (2010). Navitoclax, a targeted high-affinity inhibitor of BCL-2, in lymphoid malignancies: a phase 1 dose-escalation study of safety, pharmacokinetics, pharmacodynamics, and antitumour activity. *The Lancet Oncol.* 11, 1149–1159. doi: 10.1016/s1470-2045(10)70261-8

Wu, A., Wei, J., Kong, L. Y., Wang, Y., Priebe, W., Qiao, W., et al. (2010). Glioma cancer stem cells induce immunosuppressive macrophages/microglia. *Neuro Oncol.* 12, 1113–1125. doi: 10.1093/neuonc/noq082

Wu, B., Wang, W., Wang, H., Zou, Q., Hu, B., Ye, L., et al. (2020). Single-Cell Sequencing of Glioblastoma Reveals Central Nervous System Susceptibility to SARS-CoV-2. *Front. Oncol.* 10:566599. doi: 10.3389/fonc.2020.566599

Xia, P., and Dubrovska, A. (2020). Tumor markers as an entry for SARS-CoV-2 infection? *FEBS J.* 287, 3677–3680. doi: 10.1111/febs.15499

Xiang, W., Yang, C. Y., and Bai, L. (2018). MCL-1 inhibition in cancer treatment. *Onco Targets Ther.* 11, 7301–7314. doi: 10.2147/OTT.S146228

Xie, Q., Mittal, S., and Berens, M. E. (2014). Targeting adaptive glioblastoma: an overview of proliferation and invasion. *Neuro Oncol.* 16, 1575–1584. doi: 10.1093/neuonc/nou147

Yin, Y., Boesteanu, A. C., Binder, Z. A., Xu, C., Reid, R. A., Rodriguez, J. L., et al. (2018). Checkpoint Blockade Reverses Anergy in IL-13Ralpha2 Humanized scFv-Based CAR T Cells to Treat Murine and Canine Gliomas. *Mol. Ther. Oncolytics* 11, 20–38. doi: 10.1016/j.omto.2018.08.002

Yu, W., Zhang, L., Wei, Q., and Shao, A. (2020). O(6)-methylguanine-DNA methyltransferase (MGMT): challenges and new opportunities in glioma chemotherapy. *Front. Oncol.* 9:1547. doi: 10.3389/fonc.2019.01547

Zhang, Q., and Liu, F. (2020). Advances and potential pitfalls of oncolytic viruses expressing immunomodulatory transgene therapy for malignant gliomas. *Cell Death Dis.* 11:485. doi: 10.1038/s41419-020-2696-5

Conflict of Interest: The authors declare that the research was conducted in the absence of any commercial or financial relationships that could be construed as a potential conflict of interest.

Publisher's Note: All claims expressed in this article are solely those of the authors and do not necessarily represent those of their affiliated organizations, or those of the publisher, the editors and the reviewers. Any product that may be evaluated in this article, or claim that may be made by its manufacturer, is not guaranteed or endorsed by the publisher.

frontiers in Cell and Developmental Biology

ORIGINAL RESEARCH
published: 20 August 2021
doi: 10.3389/fcell.2021.712230

A Novel Ferroptosis-Related Prognostic Signature Reveals Macrophage Infiltration and EMT Status in Bladder Cancer

Yilin Yan[1†], Jinming Cai[1†], Zhengnan Huang[1], Xiangqian Cao[1], Pengfei Tang[2], Zeyi Wang[2], Fang Zhang[1], Shujie Xia[1,3*] and Bing Shen[1*]*

[1] Department of Urology, Shanghai General Hospital, Shanghai Jiao Tong University School of Medicine, Shanghai, China, [2] Department of Urology, Shanghai General Hospital Affiliated to Nanjing Medical University, Shanghai, China, [3] Institute of Urology, Shanghai Jiao Tong University, Shanghai, China

Bladder cancer (BC) belongs to one of the most common and highly heterogeneous malignancies. Ferroptosis is a newly discovered regulated cell death (RCD), characterized by accumulation of toxic lipid peroxides, and plays a crucial role in tumor progression. Here, we conducted a comprehensive analysis on the transcriptomics data of ferroptosis-related genes in BC based on The Cancer Genome Atlas (TCGA) and three Gene Expression Omnibus (GEO) datasets. In our study, a 6-gene signature was identified based on the potential prognostic ferroptotic regulatory genes. Furthermore, our signature revealed a good independent prognostic ability in BC. Patients with low-risk score exhibited higher FGFR3 mutation rates while high risk score had a positive association with higher RB1 mutation rates. Meanwhile, higher proportions of macrophages were observed in high BC risk group simultaneously with four methods. Unexpectedly, the risk score showed a significant positive correlation with epithelial-mesenchymal transition (EMT) status. Functional assays indicated that CRYAB and SQLE knockdown was associated with attenuated invasion capacity. Our study revealed a ferroptosis-related risk model for predicting prognostic and BC progression. Our results indicate that targeting ferroptosis may be a therapeutic strategy for BC.

Keywords: bladder cancer, ferroptosis, prognostic signature, macrophage, EMT status

OPEN ACCESS

Edited by:
Triona Ni Chonghaile, Royal College of Surgeons in Ireland, Ireland

Reviewed by:
Thomas Griffith, University of Minnesota, Twin Cities, United States
Federico Bocci, University of California, Irvine, United States

***Correspondence:**
Fang Zhang
medego@shsmu.edu.cn
Shujie Xia
xsjurologist@163.com
Bing Shen
urodrshenbing@shsmu.edu.cn

† These authors have contributed equally to this work

Specialty section:
This article was submitted to Cell Death and Survival, a section of the journal Frontiers in Cell and Developmental Biology

Received: *20 May 2021*
Accepted: *03 August 2021*
Published: *20 August 2021*

Citation:
Yan Y, Cai J, Huang Z, Cao X, Tang P, Wang Z, Zhang F, Xia S and Shen B (2021) A Novel Ferroptosis-Related Prognostic Signature Reveals Macrophage Infiltration and EMT Status in Bladder Cancer. Front. Cell Dev. Biol. 9:712230. doi: 10.3389/fcell.2021.712230

INTRODUCTION

Bladder cancer (BC) belongs to one of most common malignancies in genitourinary system which can been further classified into two subtypes: muscle-invasive bladder cancer (MIBC) and non-muscle-invasive bladder cancer (NMIBC) (Siegel et al., 2020). Conventional treatment options for BC include surgery, radiation, and cisplatin-based chemotherapy. Yet, despite considerable advances in diagnosis and treatment, BC still exhibits high rates of recurrence and metastasis due

to the high-level heterogeneity and genomic instability of BC (Alfred Witjes et al., 2017; Dy et al., 2017). BC responds differently to treatment resulting from different driver events. For example, BC patients with a mesenchymal related signature appears resistant to platinum-based chemotherapy and sensitive to immunotherapy (Wang et al., 2018a). Therefore, there is an urgent need for the development of novel therapeutic strategies so as to improve outcome.

Conventional therapy aims to suppress tumor cells through activating a certain kind of regulated cell death (RCD) (Stockwell et al., 2017). Ferroptosis is a unique cell death pathway driven by iron-dependent lipid peroxidation. Increasing evidence has determined the pivotal role of ferroptotic regulatory genes, such as TP53 (Xie et al., 2017), CISD1 (Yuan et al., 2016), GPX4 (Ingold et al., 2018), FINO2 (Gaschler et al., 2018), in tumor progression of numerous cancer types. In addition, chemotherapeutic drugs can improve efficacy on various tumor cells when combined with ferroptosis inducer (Guo et al., 2018; Belavgeni et al., 2019). Notably, previous studies indicated the significant role of ferroptosis in diagnosis and treatment management of BC (Drayton et al., 2014; Guo et al., 2020). Therefore, ferroptosis can serve as a potential target for intervention in BC patients. However, there are still few scientific studies on the correlation between BC and ferroptosis. Despite significant progress in BC, few have considered the use of ferroptosis-related gene characteristics to construct a prognostic signature in BC. The precise underlying molecular mechanism and critical molecules of ferroptosis in BC progression remain to be illuminated.

Epithelial–mesenchymal transition (EMT), a plastic process in which epithelial cells gain mesenchymal characteristics, plays an important role in embryonic development (Sha et al., 2020; Yang et al., 2020a). Growing evidences showed that this physiological process was closely related to enhanced capacity for BC invasion (Schulz et al., 2019). Activation of EMT was reported to promote cell growth and metastasis in the BC (Wang et al., 2020). And we also proved this assumption in our previous research (Yan et al., 2020b). Moreover, evidence has shown that EMT-related gene and immune cell infiltration could impact outcomes in BC patients treated with immunotherapy. Infiltrated immune cells play important roles in iron homeostasis and ferroptosis (Wang et al., 2018b). Many immune cells, such as Th1 cells and macrophages, are reported to be involved in the maintenance of iron metabolism (Ganz and Nemeth, 2015). In addition, immunoregulation was found to efficiently inhibit tumor progression by synergistic ferroptosis. Reports claimed that increased ferroptotic level enhances the anti-tumor therapeutic effect of immunotherapy. Meanwhile, immunotherapy can activate T cells infiltration to promote the lipid-ROS formation and ferroptosis in tumor cells (Wang et al., 2019).

Herein, we evaluated publicly available BC datasets and identified differentially expressed ferroptosis-related genes strongly correlated to the prognosis of BC. Then we constructed a predictive risk model and validated its prognostic accuracy. Alterations of mutation profile and immune cell infiltration were also explored. Furthermore, functional enrichment analysis and the underlying mechanisms were ultimately confirmed via *in vitro* experiments. Our findings may help lead to a deeper understanding of BC progression and further provide novel therapeutic targets for BC.

MATERIALS AND METHODS

Data Acquisition and Processing

All datasets used in this study were available to the public. Data of gene expression and clinical information were obtained from the Cancer Genome Atlas (TCGA) data portal,[1] the GTEx database,[2] GSE13507 dataset, GSE31684 dataset, GSE48075 datasets. Data from the GTEx database were selected to expand the subset of data from TCGA data portal. Then, Robust Multiarray Average was used to normalize the raw expression data (Irizarry et al., 2003). Sixty ferroptosis-related genes were obtained from the previous literature (Stockwell et al., 2017; Bersuker et al., 2019; Doll et al., 2019; Hassannia et al., 2019). HPA[3] is a platform that contains representative immunohistochemistry images expression data for common kinds of cancers (Thul et al., 2017). In this study, images of protein expression of SQLE and CRYAB between normal and BC samples were directly visualized by HPA.

Construction and Validation of the Prognostic Model

Differentially expressed genes (DEGs) between normal and tumor tissues were identified with the "limma" R package with a false discovery rate (FDR) <0.05 as cutoff threshold (Ritchie et al., 2015). BC patients in TCGA database were randomized into two groups at a ratio of 3:1 using the R package "caret." Univariate Cox regression analysis of overall survival (OS) was used to identify prognostic ferroptosis-related genes by "survival" R package filtered by $p < 0.05$. Then, "Venn" R package was implemented to get the intersect genes between ferroptosis-related DEGs and prognostic genes. For the selection of predictor variables, Least Absolute Shrinkage and Selection Operator (LASSO) regression analysis was applied to construct a prognostic model using "glmnet" on R (Simon et al., 2011). At last, a ferroptosis-related prognostic model was identified by extracting the coefficients, and the risk score for each case was determined by multiplying the level of each selected gene with its corresponding coefficient. The BC tissues were then divided into low- and high-risk group according to the median risk score. Univariate and multivariate Cox regression analyses were utilized to explore whether the risk score calculated from our model could play as an independent prognostic factor for BC patients after considering other clinical factors including gender, age, stage, T and N stage. The results were acquired by application of the "forestplot" package. To assess the predictive power of the signature, survival analysis and area under the curve (AUC) was calculated with "timeROC" R package. Somatic mutation data, which stored in the form of Mutation Annotation Format (MAF),

[1] https://portal.gdc.cancer.gov/

[2] https://xena.ucsc.edu/

[3] http://www.proteinatlas.org

were visualized and analyzed using "maftools." For subgroup analysis, patients were divided into different groups based on features as follows: gender (Male or Female), age (≤70 years old or >70 years old), stage status (Stage I, II or III, IV) and N status (N0 or >N0).

Pathway Enrichment Analysis

To understand the underlying mechanisms affecting the risk signature, BC samples were divided into two cohorts depending on risk score of each patient, and then gene set enrichment analysis (GSEA) enrichment analysis was performed via "javaGSEA" to show the result (Subramanian et al., 2005). Nominal $p < 0.05$ and FDR < 0.05 were considered significant. Enrichment of hallmark pathways within modules on a single sample to calculate a signaling pathway variation score was implemented through gene set variation analysis via "gsva" R package (Hanzelmann et al., 2013).

Evaluation of Immune Cell Infiltration

Transcriptome profiles from TCGA-BLCA cohort were used to estimate tumor immune infiltrate populations by TIMER, quanTIseq, TIP, and ssGSEA algorithm. TIMER[4] is a method that it only makes estimations of six immune cell types, taking the tissue specificity into consideration (Li et al., 2020). QuanTIseq performs an absolute quantification of cell types in the samples (Finotello et al., 2019). Tumor ImmunoPhenotype (TIP) pipeline was applied for immune activity estimation (Xu et al., 2018). Single sample Gene Set Enrichment analysis (ssGSEA) was applied to evaluate the enrichment scores.

Construction and Evaluation of the Nomogram

The clinical features and risk signature were extracted to construct a prognostic nomogram to assess the OS probability as a single numerical value. The "rms" R package was used to draw the nomogram (Feng et al., 2017). In addition, Calibration plots were generated to explore the performance characteristics of the nomograms. The clinical usefulness of the risk model was evaluated using decision curve analysis (DCA).

Transient Transfections

For siRNA knockdown experiments, human BC cell lines were either transfected with CRYAB siRNA, SQLE siRNA, or non-silencing control siRNA, using Lipofectamine® 3000 Reagent according to the manufacturer's protocol. The sequences were as follows: siNC (non-coding control): 5′-UUCUCCGAACGUGUCACGU-3′; siSQLE: 5′-GGUGUUGUGUUACAGUUAU-3′; siCRYAB: 5′-CAGAGG AACUCAAAGUUAA-3′.

RNA Extraction and RT-qPCR

Total RNA isolation and purification were performed using TRIzol RNA and then reverse-transcribed by Prime-Script Reverse Kit (TaKaRa) per manufacturer's instructions. The expression levels of genes were quantified with SYBR Green. The primers used were the following: SQLE forward 5′-TGACAATTCTCATCTGAGGTCCA-3′, reverse 5′-CAGGGATACCCTTTAGCAGTTTT-3′; CRYAB forward 5′-CCTGAGTCCCTTCTACCTTCG-3′, reverse 5′-CACATCTCCCAACACCTTAACTT-3′.

Western Blotting

Western Blotting was performed using the routine methods as described before (Yan et al., 2020b). Briefly, cells were lysed by RIPA buffer, then 20 μg proteins were separated by SDS-PAGE and transferred onto PVDF membrane. After blocking with 5% non-fat milk in PBST, the membrane was incubated with primary antibodies overnight at 4°C. β-actin was used as a loading control. The membranes were then incubated with secondary anti-body respectively. The Western blots were visualized using the ECL substrate kit. The antibodies against CRYAB, SQLE were purchased from Proteintech (Rosemont, IL, United States). β-actin were purchased from Sigma-Aldrich (Saint Louis, MO, United States).

Transwell Invasion Assay

8.0-μm-pore polycarbonate membrane were used to assess cell invasion ability of BC cells as previously described (Yan et al., 2020b). Briefly, after the Matrigel was coagulated, 1×10^5 cells were plated on the Matrigel. After incubation, cells were fixed in 4% formaldehyde and stained with crystal violet. Cells were visualized using light microscopy.

RESULTS

Identification of Bladder Cancer-Specific Ferroptosis Related Genes and Construction of the Prognostic Model

Figure 1 shows the study flow chart. A total of 403 BC patients from the TCGA-BLCA, 165 patients from the GSE13507, 93 patients from the GSE31684 and 73 patients from the GSE 48075 were finally included. After data collection, 60 ferroptosis-related genes were identified. DEGs between normal and tumor tissues within these genes were identified and were subsequently analyzed by Cox regression and LASSO regression to construct a prognostic ferroptosis-related risk signature. This signature was further evaluated using Cox regression analysis, ROC curve analysis, clinical stratification analysis, mutation correlation analysis, immune cell infiltration comparison, and external dataset validation. Finally, an optimized model and nomogram were established. The three GEO datasets were subjected to validation of all results. To determine the prognostic value of the above ferroptosis-related genes in BC, univariate Cox regression analysis identified 16 genes as significantly correlated with BC survival (**Figure 2A**), and 9 of them were differentially expressed between tumor tissues and adjacent carcinoma tissues (**Figure 2B**). Expression correlations between these genes is shown in **Figure 2C**. LASSO and multivariable Cox regression analysis were performed to identify a risk

[4]https://cistrome.shinyapps.io/timer/

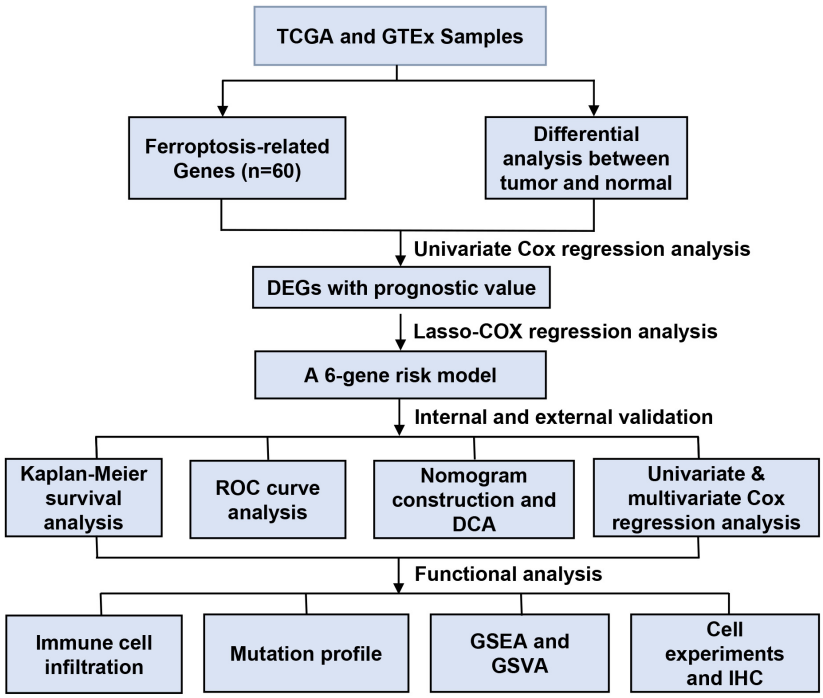

FIGURE 1 | Data processing flow chart.

model based on the expression level of the above nine genes (**Supplementary Figure 1**). A 6-gene signature was identified and risk score was calculated by following formula: (0.251 × CISD1) + (0.135 × CRYAB) + (0.225 × FTH1) + (0.656 × ACACA) + (0.242 × ZEB1) + (0.202 × SQLE).

Next, risk score of each BC tissue was calculated and patients were assigned into a low- or a high-risk group according to the median cut-off value (**Figure 2D**). Survival status of the BC patients was visualized in **Figure 2E**. The proportion of mortality in high-risk group was 48%, much higher than 27% in the low-risk group. PCA analysis showed clear separation of patients in different risk groups (**Figure 2F**). Kaplan-Meier survival curve revealed significant difference in OS between the groups. As demonstrated, more deaths happened in the high-risk groups than those in low-risk groups, suggesting that the risk model could accurately distinguish BC patients with poor prognosis. We then evaluated the predictive power and accuracy of the risk signature with ROC curve analysis. A time-dependent ROC curve was performed and the AUC was 0.709 at 3-years and 0.725 at 5-years (**Figures 2G,H**).

Validation of the 6-Gene Risk Model

To evaluate whether the risk model exhibits similar predictive performance and accuracy in other BC patient cohorts, robustness of the 6-gene signature was then tested in TCGA internal cohort and another three independent GEO BC cohorts. Survival analysis results confirmed that patients of high-risk correlated with poor OS (**Figures 3A–D**). As shown in **Figures 3E–H**, the AUC was 0.677, 0.684, 0.625, 0.690 for 5-year survival prediction and 0.648, 0.689, 0.603, 0.636 for 3-year survival prediction in TCGA, GSE48075, GSE31684, and GSE13507. Heat maps were shown to present the expression levels of the six genes and clinical features ordered by risk score in the above four datasets. Clinical and pathological features, such as TNM stage and grade were enriched BC cases with high-risk score (**Figures 3I–L**). Therefore, we believe that the ferroptosis-based risk model indicates good prediction stability and performance.

Prognosis Analysis of the 6-Gene Risk Signature With Clinicopathological Features

Relationship between OS, clinicopathological parameters and risk score were further analyzed to assess whether the risk score was an independent predictor of outcome. Univariate and multivariate Cox analysis were used based on OS of BC patients, using the co-variables including risk score, age, gender, stage, T and N stage to validate the independence of the risk model among other clinic-pathologic characteristics. Results from univariate and corresponding multivariable Cox regression analysis demonstrated that our risk model could serve as an independent prognostic factor ($p < 0.05$; **Figures 4A, B**). Then we further evaluated the effects of clinical characteristics, such as different stage and lymph node metastatic status on outcome among BC patients, and found that high risk score was highly correlated with poor outcome (**Figures 4C–J**). These results demonstrated that the ferroptosis-related prognostic model

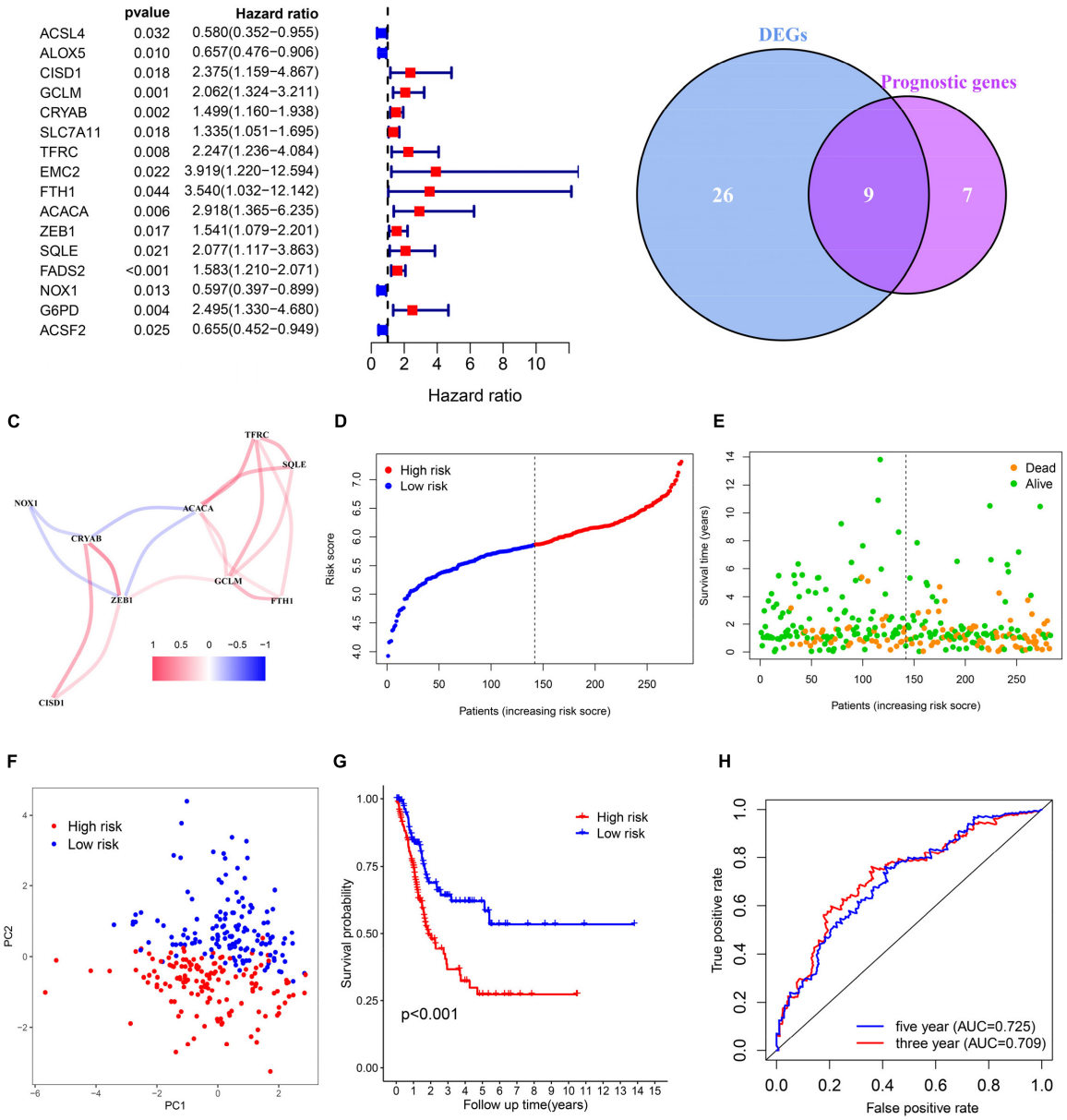

FIGURE 2 | Identification of bladder cancer-specific ferroptosis-related genes and construction of the prognostic model. **(A)** Forest plots based on univariate survival analysis in patients with BC. **(B)** Venn diagram for overlapping genes among differentially expressed genes (DEG) correlated with patient outcome. **(C)** The correlation network of candidate genes. **(D–F)** Risk score distribution, overall survival (OS) status and PCA plot of high and low risk BC cases in the TCGA data. **(G)** Kaplan-Meier survival curves of patients in BC groups of different risk score in the TCGA cohort. **(H)** Time-dependent ROC curves of overall survival at 3- (red) and 5-years (blue).

could predict the prognosis of patients with BC regardless of clinical conditions.

Construction and Evaluation of a Predictive Nomogram

Furthermore, we utilized a quantitative method by integrating the risk score and clinical features to construct a nomogram (**Figure 5A**). Female patients had a higher risk of a poor prognosis while the higher age, tumor stage and risk score indicated a lower survival rate in patients. Combined with our risk model and clinical feature, net benefits were presented in our DCA curve, and we found that compared to a single factor, the combined showed the optimal net benefit (**Figure 5B**). Meanwhile, the calibration plot for the probability of 3-, 5-, and 10-year survival showed an optimal consistency between

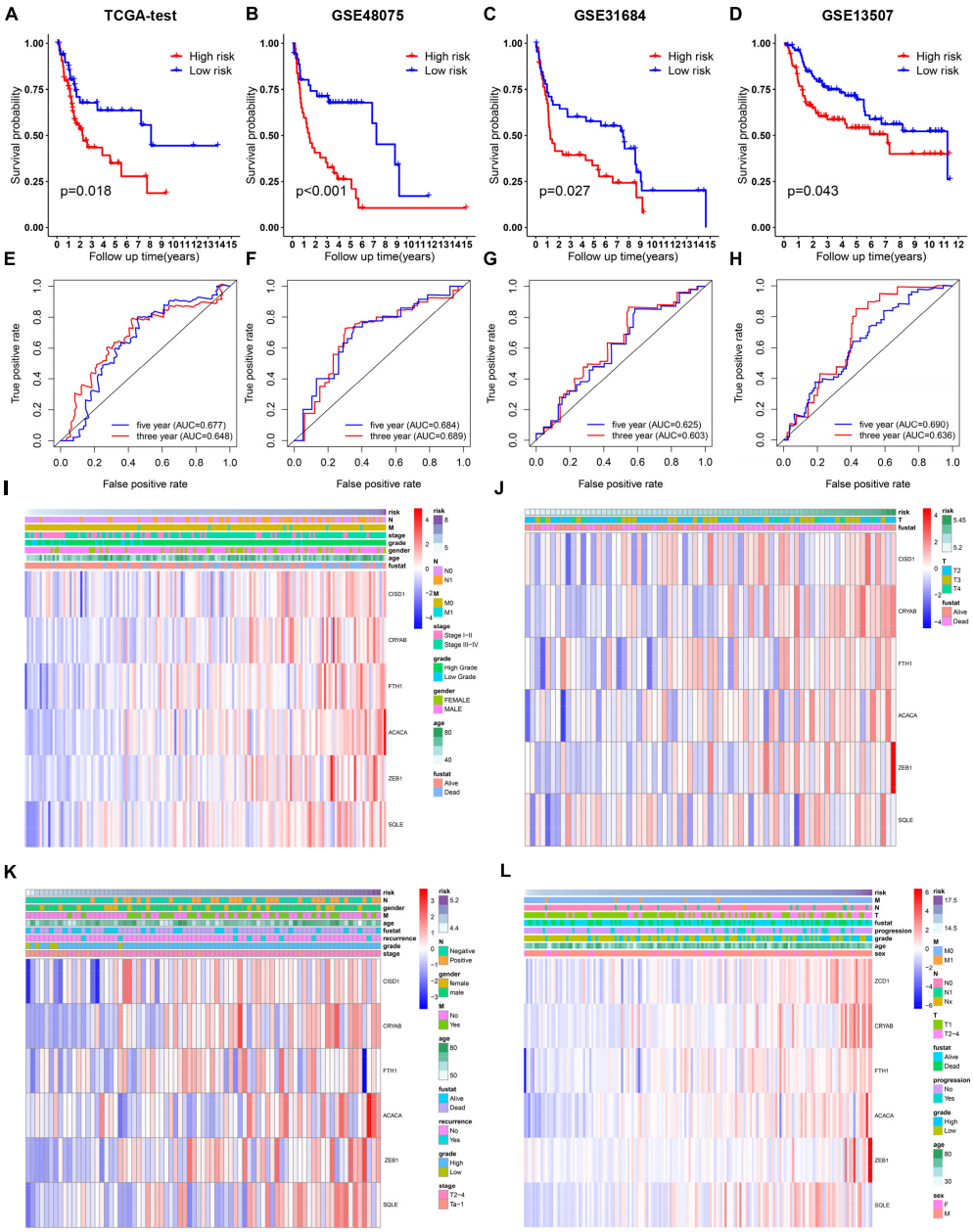

FIGURE 3 | Validation of the 6-gene signature model in the internal TCGA and another indicated three independent public datasets. **(A–D)** Kaplan-Meier survival curves for bladder cancer patients based on risk score in TCGA, GSE48075, and GSE31684, and GSE13507 datasets. **(E–H)** ROC curve analysis for predicting 3- and 5-year overall survival in the above four BC cohorts. **(I–L)** Heatmaps showing the expression level of 6 selected ferroptosis-related genes ranked by risk score in the above four BC cohorts.

observation and predictive curves (**Figures 5C–E**). These results indicate that the nomogram has proper clinical applicability.

Correlation of Mutation and Immune Cell Infiltration Landscape With the Risk Model

To determine whether the risk model was correlated with tumor mutation of BC, relationship between the model and gene mutations was analyzed. The profile of somatic mutation is visualized in **Supplementary Figure 2**. The mutation profile distribution based on patients' risk score were shown in **Figures 6A,B**. Notably, the low-risk tumor groups have significantly lower rates of FGFR3 mutation while the overall mutation rates of RB1 appeared to be higher in the high-risk subgroup. FGFR mutation was reported to be significantly enriched in the luminal papillary subtype, characterized by lower stage, while high RB1 mutation frequencies are significantly

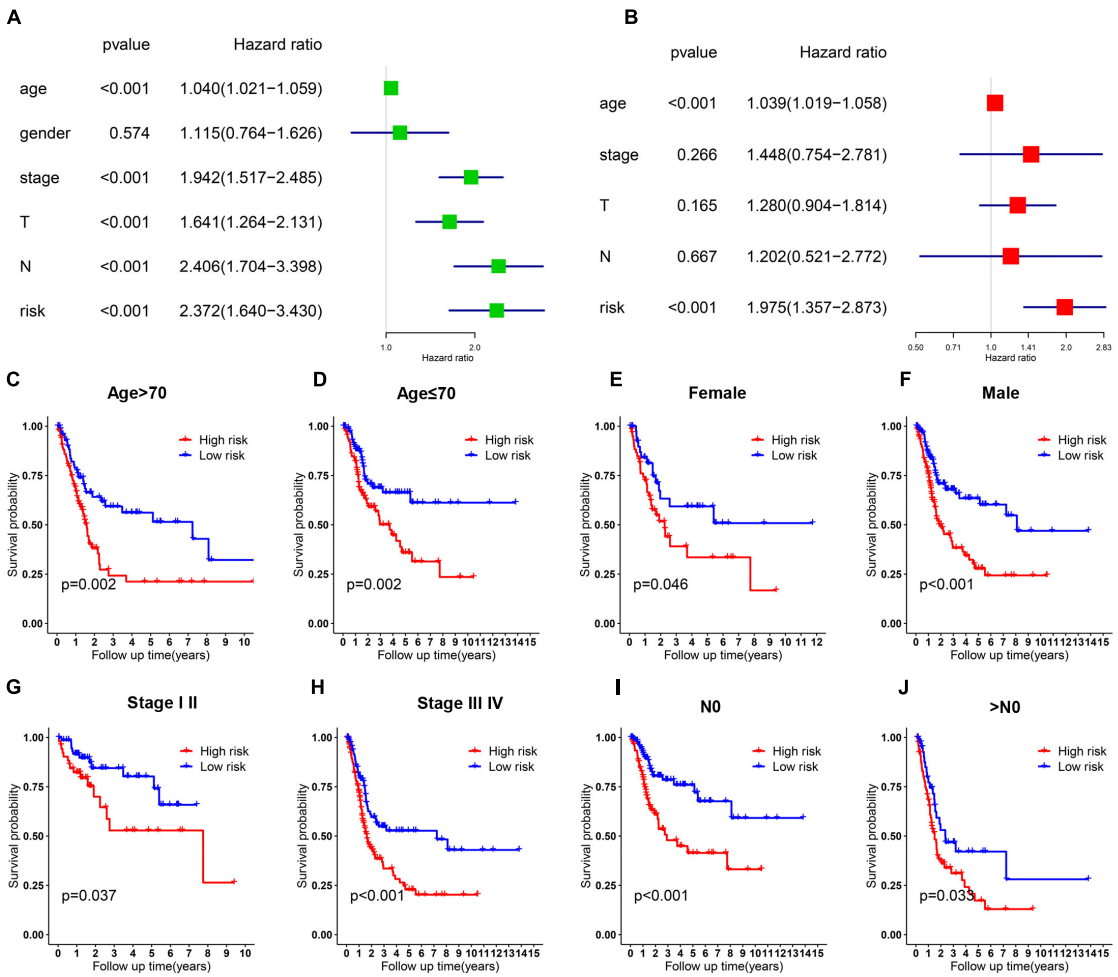

FIGURE 4 | Cox regression and stratified analysis of the 6 gene risk model. **(A,B)** Results of univariate and multivariate regression analysis of the relation between clinical features and risk model. **(C–J)** Kaplan–Meier survival curves for bladder cancer patients with age **(C,D)**, gender **(E,F)**, stage **(G,H)**, and N metastasis **(I,J)**.

high in basal-squamous and neuronal subtypes, indicating lower survival rate. Then we evaluated the TIICs proportions with the aid of TIMER, quanTIseq, TIP and ssGSEA, four well-accepted methods for comprehensive analysis of TIICs. Two distinct patterns of immune infiltrate were observed in high and low-risk cohorts. Surprisingly, tissues with high risk generally had higher density of macrophage (**Figures 6C–F**). Increased proportions of tumor-infiltrating macrophages have been reported to be involved in tumor progression and metastasis of BC. These evidences demonstrated that high RB1 mutation and tumor-infiltrating macrophages may account for the poor prognosis in high-risk group.

Identification of the 6-Gene Risk Model Correlated Biological Pathways

Gene set enrichment analysis (GSEA) analysis of BC patients with a different risk score was performed to investigate the possible biological function of the risk model in the carcinogenesis of BC. The results showed that, in four BC groups, high-risk score was positively correlated to important tumor related pathways, especially "HALLMARK_EMT" and "HALLMARK_HYPOXIA" (**Figures 7A–D**). Meanwhile, the GSVA scores of such two pathways were significantly higher in high-risk score cohort, respectively (**Figure 7E**). Survival analysis showed a positive correlation between EMT score and the OS in patients with BC (**Figure 7F**), while the difference was not significant for HYPOXIA score (**Figure 7G**). In addition, expression of EMT-related markers was elevated in high-risk group (**Figure 7H**). These results indicated that the risk model played a critical role in predicting EMT-related function in BC.

Functions of the Identified Biomarkers in BC Invasion

EMT progress was previously reported to contribute to cancer cell invasion, resulting in rapid tumor development. Within the six genes, higher level of CRYAB, SQLE, and ZEB1 significantly correlated with advanced stage (**Figures 8A–C**). Considering the important role of ZEB1 in tumor metastasis, we thus

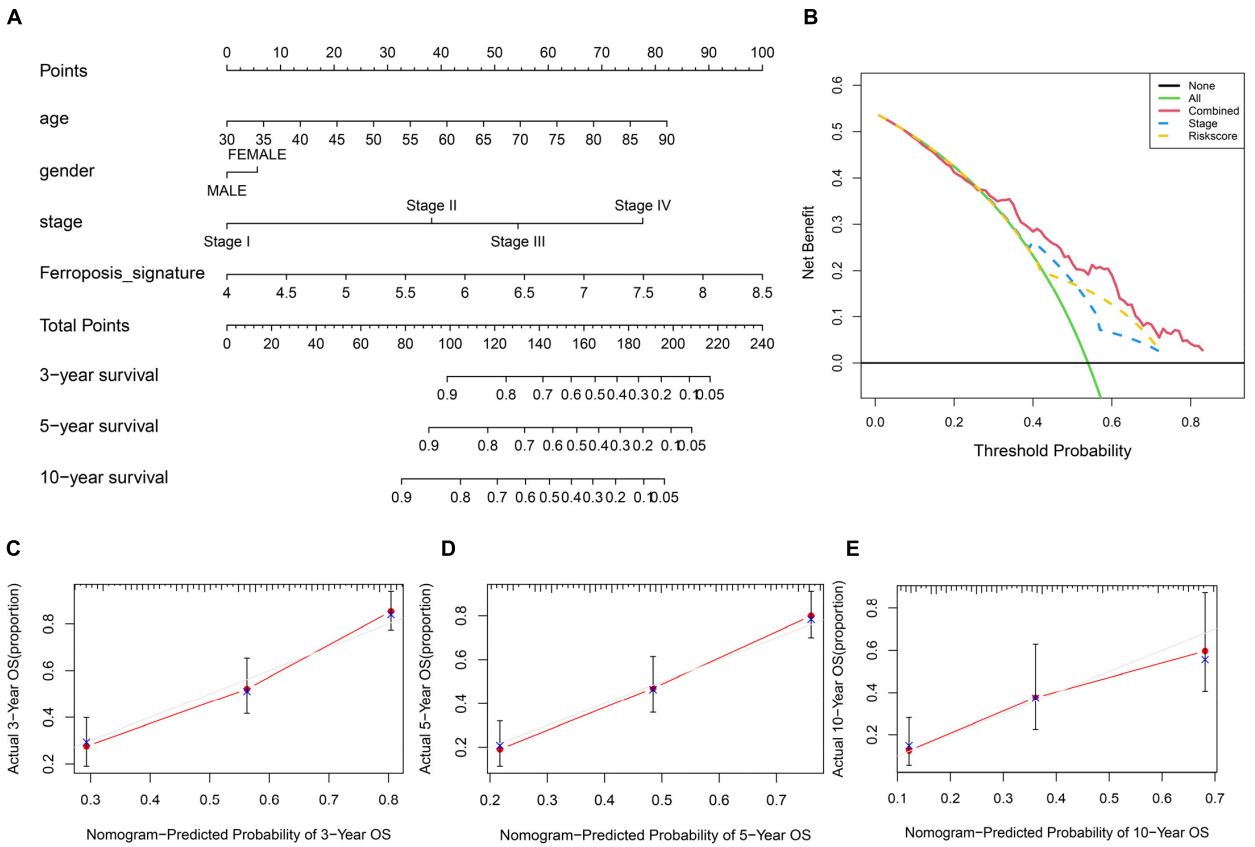

FIGURE 5 | Construction and validation of a nomogram. **(A)** Prognostic nomogram predicting overall survival probability of BC patients. **(B)** DCA curves analysis for the nomogram. **(C–E)** Calibration curves of the nomogram for predicting overall survival probability.

focused on another two genes. Then we performed functional studies after transfection using specific small interfering RNAs (siRNAs) (**Figures 8D, E**). The results showed that knockdown of CRYAB and SQLE in BC cell lines inhibited cell migration and invasion ability (**Figures 8F, G**). Moreover, overexpression of these two genes promoted the invasive ability of bladder tumor cell (**Figures 8D–G**). Immunohistochemical analysis indicated the positive staining intensity for CRYAB and SQLE in BC tissues as significantly stronger than in the normal urothelium tissues. Moreover, BC tissues with high malignancy exhibited strong staining intensity than tissues with low malignancy by HPA (**Figure 8H**). These results confirmed that CRYAB and SQLE were correlated well with the grade of tumorigenesis.

DISCUSSION

Bladder cancer (BC) has been reported among the most common malignancies, presenting a major health burden for society. How to optimize therapeutic protocols for mortality reduction of patients with advanced BC remains a challenge. Therefore, there is an urgent need to identify key biomarkers that affect the outcome of BC. With future expansion of the database and multi-omics data, improved data mining algorithms can have an essential impact on tumor biology (Angus et al., 2019; Nacev et al., 2019; Liu et al., 2020; Tabassum et al., 2020). Transcriptome profiling provided us with novel insights into assessing prognostic of the individual patient when combining the corresponding clinical information. Multiple risk signatures have been identified in various tumors for the past few years (Yu et al., 2019; Yan et al., 2020a). However, most studies have failed to be applied to clinical practice owning to lack of systematic evaluation and a broad roll-out. Therefore, these questions illustrate the urgent need to identify the prognostic factors of BC to predict to identify high-risk populations.

Increasing evidence has shown that induction of cell death is among the most effective anticancer strategy and ferroptosis belongs to a RCD in which iron metabolism plays a vital role (Badgley et al., 2020; Yang et al., 2020b). However, molecular changes and mechanism of ferroptosis in BC has yet to be elucidated. In the current research, we have identified a ferroptosis-related risk model for BC. We used BC samples from TCGA as training group, GSE13507, GSE48075, and GSE31684 as validation groups. Our risk model is composed of6 differentially expressed ferroptosis-related genes (CISD1, CRYAB, FTH1, ACACA, ZEB1, SQLE) that correlate with patient outcome. We found that risk scores of our model were highly associated with stage and metastatic status. We further demonstrated that the

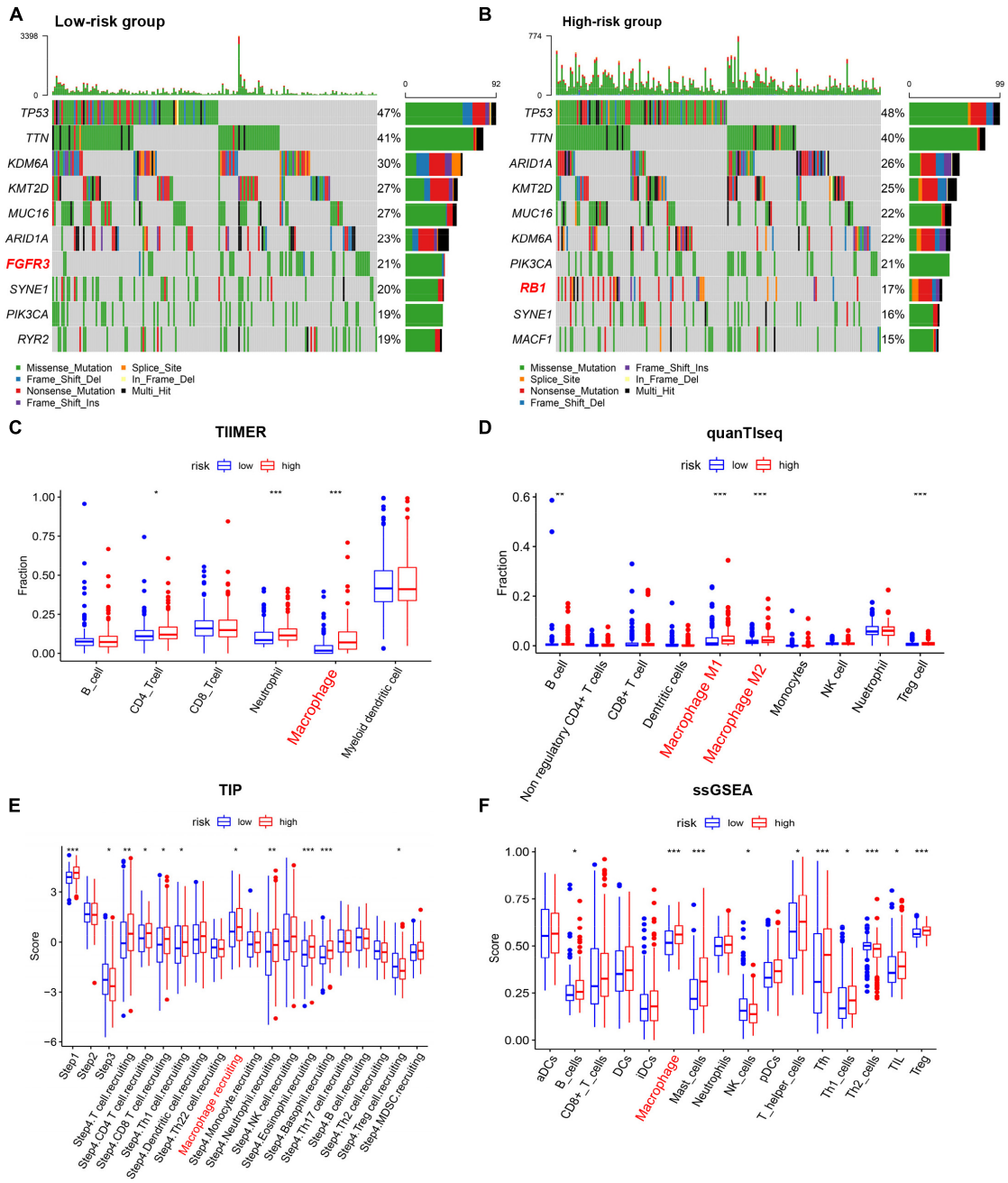

FIGURE 6 | Characterization of immune cell infiltration and mutation landscape in BC tissues among different risk groups. **(A,B)** Somatic mutation profiles of BC tissues among different risk groups. **(C–F)** Boxplots of Immune cell infiltration with high and low risk scores estimated using TIMER, quanTIseq, TIP, and ssGSEA. $^{*}p < 0.05$, $^{**}p < 0.01$, $^{***}p < 0.001$.

risk model serves as an accurate predictor of BC survival and an independent predictor for BC prognosis by validating it in another three independent BC datasets. Besides, the nomogram performed well with a good calibration, indicating that the model is an accurate prognostic tool. Our results suggested that the model can well distinguish BC patients and predict prognosis, thereby helping to develop optimal treatment options based on risk score.

We identified several ferroptosis-related genes that predict the outcome of BC patients. Most of the genes have been reported in previous studies to be closely related to ferroptosis and cancer development of malignancies. CDGSH iron sulfur domain 1 (CISD1) is an iron-containing protein and could negatively modulates ferroptosis. Increasing stabilization of CISD1 inhibits erastin-induced mitochondrial iron uptake and oxidative damage (Yuan et al., 2016). Crystallin alpha B (CRYAB, also known as

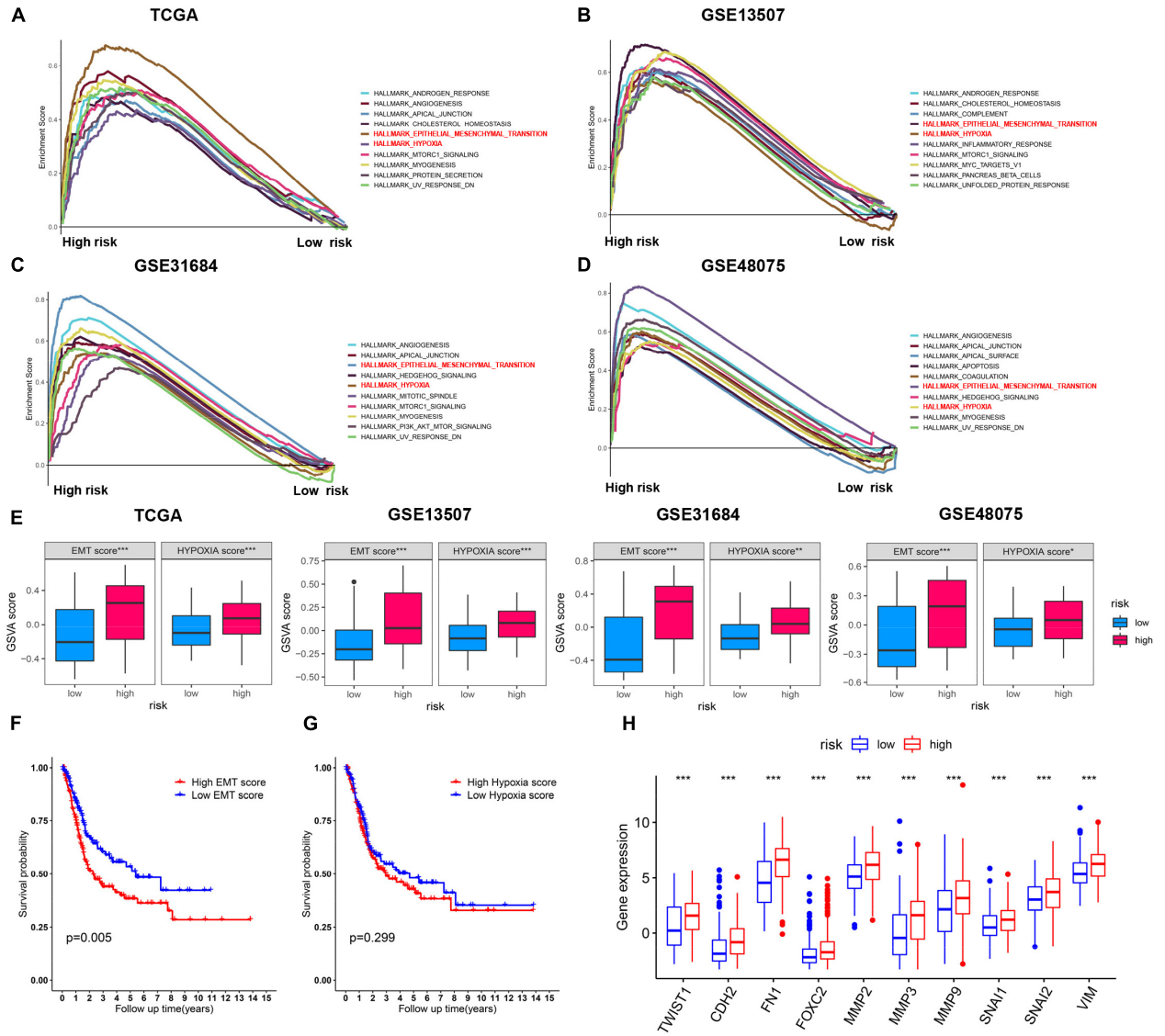

FIGURE 7 | Validation of the expression patterns of risk model. **(A–D)** Top 10 enriched hallmark gene sets with high and low risk score in TCGA, GSE13507, GSE48075, and GSE31684 datasets. **(E)** GSVA score of EMT and hypoxia gene set in the above four BC cohorts. **(F,G)** Kaplan–Meier survival curves for BC patients classified by EMT and hypoxia score. **(H)** The correlation analysis between the expression levels for EMT-related genes and the risk subgroups. ***$p < 0.001$.

HSP beta-5) belongs to the small heat shock protein (HSP20) family and is reported to regulate iron uptake and GPX4 abundance (Stockwell et al., 2017). Ferritin heavy chain 1 (FTH1) is one of the subunits of Ferritin and plays an essential role in cellular iron balance in ferroptosis. Knockdown of FTH1 could lead to iron overabsorption and promote ferroptosis in the intestines of mice (Sun et al., 2016). acetyl-CoA carboxylase alpha (ACACA) is implicated in catalyzing the committed steps in fatty acids' biosynthesis A and was reported to suppress FIN56-, but not erastin- or RSL3- induced ferroptosis (Shimada et al., 2016). Zinc finger E-box-binding homeobox 1 (ZEB1) function as a transcription factor that influences cell developmental and homeostasis cell fates. Knockout of ZEB1 suppressed GPX4-depletion-induced ferroptosis (Viswanathan et al., 2017). Squalene monooxygenase (SQLE) is a key rate-limiting enzyme in the biosynthesis of cholesterol. Overexpression of SQLE sensitizes ALCL cells to ferroptosis (Garcia-Bermudez et al., 2019).

Studies have indicated that gene mutations play an important role in the development of carcinoma including BC (Lawson et al., 2020). Mutations of the several genes, such as p53, FGFR3 and RB1, have been reported to be involved in BC with a high incidence (Robertson et al., 2018). Therefore, we further attempt to study whether there were gene mutation alterations between different groups in BC patients. Interestingly, in our study, higher FGFR3 mutation rate was observed in low-risk BC patients. FGFR mutation was significantly enriched in the luminal papillary subtype, characterized by lower stage, lower risk for progression and papillary morphology. These

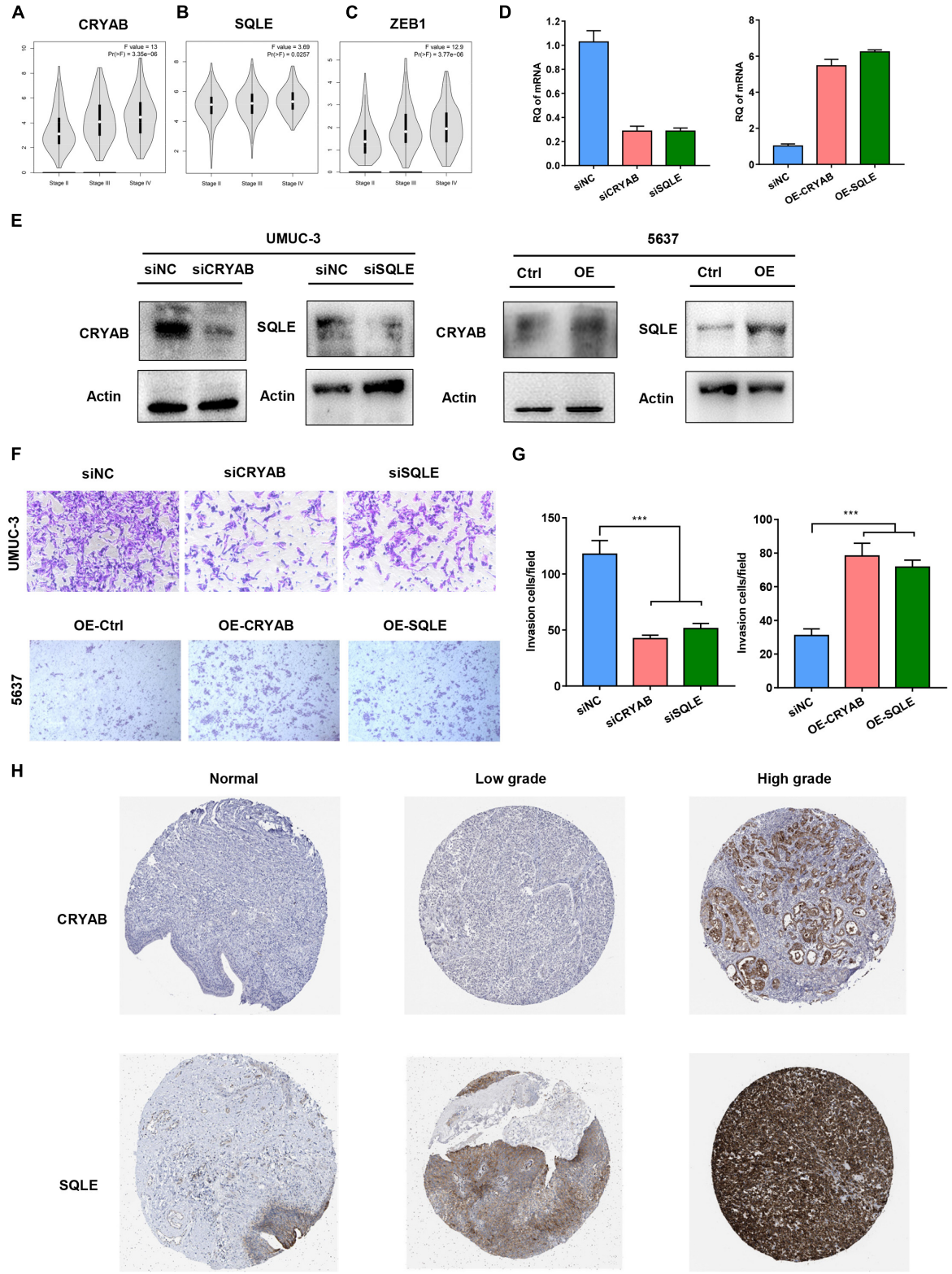

FIGURE 8 | Functions of the Identified Biomarkers in BC Invasion. **(A–C)** The correlation between expression of CRYAB, SQLE, ZEB1, and the clinical stage in different BC stages. **(D,E)** Knockdown and overexpression efficiency was confirmed by real-time RT-PCR and Western blot. **(F,G)** Transwell invasion assay analyzed the effect of CRYAB and SQLE knockdown and overexpression on cell invasion *in vitro*. Scale bar, 100 μm. **(H)** Immunohistochemical (IHC) staining of the expression of CRYAB and SQLE in normal urothelium and BC tissues with different degree of malignancy. ***$p < 0.001$.

results suggested specific inhibitors designed against FGFR3 as a treatment option for these patients. Conversely, patients of high-risk score accounted for higher RB1 mutation. High RB1 mutation frequencies are significantly high in basal-squamous and neuronal subtypes, indicating worse OS and resistance to platinum-based chemotherapy. Immune cells were reported to be involved in the process of iron metabolism and ferroptosis level could promote the anti-tumor efficacy of immunotherapy (Nairz and Weiss, 2020; Tang et al., 2020). Interestingly, the infiltrating immune cells exhibit significant disparities among different groups in our study. Additionally, with four well-accepted methods, our signature identified higher proportion of macrophages in the high-risk group compared with the low-risk group. Previous researches have shown that increased proportions of tumor-infiltrating macrophages contributed to a propensity of metastases and poor prognosis for BC (Chen et al., 2018; Kobatake et al., 2020). Therefore, high infiltration of tumor-associated macrophages in patients with high risk may be an explanation for their poor outcome.

To investigate the underlying mechanisms, GSEA and GSVA were subsequently subjected to the pathway enrichment of each group. Interestingly, the enrichment analysis revealed that high risks were significantly enriched in EMT and hypoxia hallmark pathways. Of these two, only EMT was significantly associated with poor prognosis. EMT is an essential biological process, which plays a vital role in modulating tissue homeostasis and development (Bakir et al., 2020). Besides, EMT has been implicated in tumor progression and metastasis. In our study, high levels of EMT gene expression were observed in high-risk BC patients. Among genes of the risk model, we identified three genes (CRYAB, SQLE, and ZEB1) that were found to be was significantly and positively associated with clinical stage. Numerous studies have reported that ZEB1 contributes to cancer progression, while the role of CRYAB and SQLE in BC is rarely reported. We found that knockdown of CRYAB or SQLE significantly attenuated the invasive abilities of BC cells. Nevertheless, the potential mechanism of the two biomarkers might contribute to the carcinogenesis of BC remain unknown, and further investigation of potential mechanisms is needed.

Nonetheless, some limitations are inevitable. This risk model is highly dependent upon public databases. Further investigations need to be undertaken in future clinical researches. Moreover, protein level could differ from RNA expression, making it unavoidable to validate its clinical utility in more sets.

In summary, this research is the first to identify a novel signature of ferroptosis-related genes for predicting outcomes of BC patients. Results suggest that variation in gene mutation, immune response and EMT status might be several possible reasons for this model's prognostic ability. These findings may help unveil new targets for the prevention, diagnosis, and treatment of BC.

DATA AVAILABILITY STATEMENT

The datasets presented in this study can be found in online repositories. The names of the repository/repositories and accession number(s) can be found in the article/ **Supplementary Material**.

AUTHOR CONTRIBUTIONS

BS and SX: conception and design. YY and FZ: acquisition of the data. YY and JC: analysis of the data. YY, ZH, and XC: writing, review, and revision of the manuscript. PT and ZW: administrative, technical, or material support. BS: study supervision. All authors read and approved the final manuscript.

FUNDING

This work was supported by the National Natural Science Foundation (92059112 and 82072821), the Shanghai Songjiang Municipal Science and Technology Commission Natural Science Foundation (20SJKJGG250), and the Shanghai Specialized Research Fund for Integrated Chinese and Western Medicine in General Hospitals (ZHYY-ZXYJHZX-1-201705).

ACKNOWLEDGMENTS

We are truly grateful to the TCGA, GEO, and GTEx for the contribution of the data.

SUPPLEMENTARY MATERIAL

The Supplementary Material for this article can be found online at: https://www.frontiersin.org/articles/10.3389/fcell.2021.712230/full#supplementary-material

REFERENCES

Alfred Witjes, J., Lebret, T., Comperat, E. M., Cowan, N. C., De Santis, M., Bruins, H. M., et al. (2017). Updated 2016 EAU guidelines on muscle-invasive and metastatic bladder cancer. *Eur. Urol.* 71, 462–475. doi: 10.1016/j.eururo.2016.06.020

Angus, L., Smid, M., Wilting, S. M., van Riet, J., Van Hoeck, A., Nguyen, L., et al. (2019). The genomic landscape of metastatic breast cancer highlights changes in mutation and signature frequencies. *Nat. Genet.* 51, 1450–1458. doi: 10.1038/s41588-019-0507-7

Badgley, M. A., Kremer, D. M., Maurer, H. C., DelGiorno, K. E., Lee, H. J., Purohit, V., et al. (2020). Cysteine depletion induces pancreatic tumor ferroptosis in mice. *Science* 368, 85–89. doi: 10.1126/science.aaw9872

Bakir, B., Chiarella, A. M., Pitarresi, J. R., and Rustgi, A. K. (2020). EMT. MET, Plasticity, and Tumor Metastasis. *Trends Cell Biol.* 30, 764–776. doi: 10.1016/j.tcb.2020.07.003

Belavgeni, A., Bornstein, S. R., von Mässenhausen, A., Tonnus, W., Stumpf, J., Meyer, C., et al. (2019). Exquisite sensitivity of adrenocortical carcinomas to induction of ferroptosis. *Proc. Natl. Acad. Sci. USA* 116, 22269–22274. doi: 10.1073/pnas.1912700116

Bersuker, K., Hendricks, J. M., Li, Z., Magtanong, L., Ford, B., Tang, P. H., et al. (2019). The CoQ oxidoreductase FSP1 acts parallel to GPX4 to inhibit ferroptosis. *Nature* 575, 688–692. doi: 10.1038/s41586-019-1705-2

Chen, C., He, W., Huang, J., Wang, B., Li, H., Cai, Q., et al. (2018). LNMAT1 promotes lymphatic metastasis of bladder cancer via CCL2 dependent macrophage recruitment. *Nat. Commun.* 9:3826. doi: 10.1038/s41467-018-06152-x

Doll, S., Freitas, F. P., Shah, R., Aldrovandi, M., da Silva, M. C., Ingold, I., et al. (2019). FSP1 is a glutathione-independent ferroptosis suppressor. *Nature* 575, 693–698. doi: 10.1038/s41586-019-1707-0

Drayton, R. M., Dudziec, E., Peter, S., Bertz, S., Hartmann, A., Bryant, H. E., et al. (2014). Reduced expression of miRNA-27a modulates cisplatin resistance in bladder cancer by targeting the cystine/glutamate exchanger SLC7A11. *Clin. Cancer Res.* 20, 1990–2000. doi: 10.1158/1078-0432.ccr-13-2805

Dy, G. W., Gore, J. L., Forouzanfar, M. H., Naghavi, M., and Fitzmaurice, C. (2017). Global burden of urologic cancers, 1990-2013. *Eur. Urol.* 71, 437–446. doi: 10.1016/j.eururo.2016.10.008

Feng, L. H., Dong, H., Lau, W. Y., Yu, H., Zhu, Y. Y., Zhao, Y., et al. (2017). Novel microvascular invasion-based prognostic nomograms to predict survival outcomes in patients after R0 resection for hepatocellular carcinoma. *J. Cancer Res. Clin. Oncol.* 143, 293–303. doi: 10.1007/s00432-016-2286-1

Finotello, F., Mayer, C., Plattner, C., Laschober, G., Rieder, D., Hackl, H., et al. (2019). Molecular and pharmacological modulators of the tumor immune contexture revealed by deconvolution of RNA-seq data. *Genome Med.* 11:34. doi: 10.1186/s13073-019-0638-6

Ganz, T., and Nemeth, E. (2015). Iron homeostasis in host defence and inflammation. *Nat. Rev. Immunol.* 15, 500–510. doi: 10.1038/nri3863

Garcia-Bermudez, J., Baudrier, L., Bayraktar, E. C., Shen, Y., La, K., Guarecuco, R., et al. (2019). Squalene accumulation in cholesterol auxotrophic lymphomas prevents oxidative cell death. *Nature* 567, 118–122. doi: 10.1038/s41586-019-0945-5

Gaschler, M. M., Andia, A. A., Liu, H., Csuka, J. M., Hurlocker, B., Vaiana, C. A., et al. (2018). FINO(2) initiates ferroptosis through GPX4 inactivation and iron oxidation. *Nat. Chem. Biol.* 14, 507–515. doi: 10.1038/s41589-018-0031-6

Guo, J., Xu, B., Han, Q., Zhou, H., Xia, Y., Gong, C., et al. (2018). Ferroptosis: a novel anti-tumor action for cisplatin. *Cancer Res. Treat.* 50, 445–460. doi: 10.4143/crt.2016.572

Guo, P., Wang, L., Shang, W., Chen, J., Chen, Z., Xiong, F., et al. (2020). Intravesical in situ immunostimulatory gel for triple therapy of bladder cancer. *ACS Appl. Mater. Interfaces* 12, 54367–54377. doi: 10.1021/acsami.0c15176

Hassannia, B., Vandenabeele, P., and Vanden Berghe, T. (2019). Targeting ferroptosis to iron out cancer. *Cancer Cell* 35, 830–849. doi: 10.1016/j.ccell.2019.04.002

Hanzelmann, S., Castelo, R., and Guinney, J. (2013). GSVA: gene set variation analysis for microarray and RNA-seq data. *BMC Bioinform.* 14:7. doi: 10.1186/1471-2105-14-7

Ingold, I., Berndt, C., Schmitt, S., Doll, S., Poschmann, G., Buday, K., et al. (2018). Selenium utilization by gpx4 is required to prevent hydroperoxide-induced ferroptosis. *Cell* 172, 409–422. doi: 10.1016/j.cell.2017.11.048

Irizarry, R. A., Hobbs, B., Collin, F., Beazer-Barclay, Y. D., Antonellis, K. J., Scherf, U., et al. (2003). Exploration, normalization, and summaries of high density oligonucleotide array probe level data. *Biostatistics* 4, 249–264. doi: 10.1093/biostatistics/4.2.249

Kobatake, K., Ikeda, K. I., Nakata, Y., Yamasaki, N., Ueda, T., Kanai, A., et al. (2020). Kdm6a deficiency activates inflammatory pathways, promotes m2 macrophage polarization, and causes bladder cancer in cooperation with p53 dysfunction. *Clin. Cancer Res.* 26, 2065–2079. doi: 10.1158/1078-0432.ccr-19-2230

Lawson, A. R. J., Abascal, F., Coorens, T. H. H., Hooks, Y., O'Neill, L., Latimer, C., et al. (2020). Extensive heterogeneity in somatic mutation and selection in the human bladder. *Science* 370, 75–82. doi: 10.1126/science.aba8347

Li, T., Fu, J., Zeng, Z., Cohen, D., Li, J., Chen, Q., et al. (2020). TIMER2.0 for analysis of tumor-infiltrating immune cells. *Nucleic Acids Res.* 48, W509–W514. doi: 10.1093/nar/gkaa407

Liu, J., Wang, Y., Chu, Y., Xu, R., Zhang, D., and Wang, X. (2020). Identification of a TLR-induced four-lncRNA signature as a novel prognostic biomarker in esophageal carcinoma. *Front. Cell Dev. Biol.* 8:649. doi: 10.3389/fcell.2020.00649

Nacev, B. A., Feng, L., Bagert, J. D., Lemiesz, A. E., Gao, J., Soshnev, A. A., et al. (2019). The expanding landscape of 'oncohistone' mutations in human cancers. *Nature* 567, 473–478. doi: 10.1038/s41586-019-1038-1

Nairz, M., and Weiss, G. (2020). Iron in infection and immunity. *Mol. Aspects Med.* 75:100864. doi: 10.1016/j.mam.2020.100864

Ritchie, M. E., Phipson, B., Wu, D., Hu, Y., Law, C. W., Shi, W., et al. (2015). limma powers differential expression analyses for RNA-sequencing and microarray studies. *Nucleic Acids Res.* 43:e47. doi: 10.1093/nar/gkv007

Robertson, A. G., Kim, J., Al-Ahmadie, H., Bellmunt, J., Guo, G., Cherniack, A. D., et al. (2018). Comprehensive molecular characterization of muscle-invasive bladder cancer. *Cell* 174:1033. doi: 10.1016/j.cell.2018.07.036

Schulz, A., Gorodetska, I., Behrendt, R., Fuessel, S., Erdmann, K., Foerster, S., et al. (2019). Linking NRP2 with EMT and chemoradioresistance in bladder cancer. *Front. Oncol.* 9:1461. doi: 10.3389/fonc.2019.01461

Sha, Y., Wang, S., Zhou, P., and Nie, Q. (2020). Inference and multiscale model of epithelial-to-mesenchymal transition via single-cell transcriptomic data. *Nucleic Acids Res.* 48, 9505–9520. doi: 10.1093/nar/gkaa725

Shimada, K., Skouta, R., Kaplan, A., Yang, W. S., Hayano, M., Dixon, S. J., et al. (2016). Global survey of cell death mechanisms reveals metabolic regulation of ferroptosis. *Nat. Chem. Biol.* 12, 497–503. doi: 10.1038/nchembio.2079

Siegel, R. L., Miller, K. D., and Jemal, A. (2020). Cancer statistics, 2020. *CA Cancer J. Clin.* 70, 7–30. doi: 10.3322/caac.21590

Simon, N., Friedman, J., Hastie, T., and Tibshirani, R. (2011). Regularization paths for cox's proportional hazards model via coordinate descent. *J. Stat. Softw.* 39, 1–13. doi: 10.18637/jss.v039.i05

Stockwell, B. R., Friedmann Angeli, J. P., Bayir, H., Bush, A. I., Conrad, M., Dixon, S. J., et al. (2017). Ferroptosis: a regulated cell death nexus linking metabolism. redox biology, and disease. *Cell* 171, 273–285. doi: 10.1016/j.cell.2017.09.021

Subramanian, A., Tamayo, P., Mootha, V. K., Mukherjee, S., Ebert, B. L., Gillette, M. A., et al. (2005). Gene set enrichment analysis: a knowledge-based approach for interpreting genome-wide expression profiles. *Proc. Natl. Acad. Sci. USA* 102, 15545–15550. doi: 10.1073/pnas.0506580102

Sun, X., Ou, Z., Chen, R., Niu, X., Chen, D., Kang, R., et al. (2016). Activation of the p62-Keap1-NRF2 pathway protects against ferroptosis in hepatocellular carcinoma cells. *Hepatology* 63, 173–184. doi: 10.1002/hep.28251

Tabassum, N., Cereser, B., and Stebbing, J. (2020). A cell-cycle signature classifier for pan-cancer analysis. *Oncogene* 39, 6041–6042. doi: 10.1038/s41388-020-01426-5

Tang, R., Xu, J., Zhang, B., Liu, J., Liang, C., Hua, J., et al. (2020). Ferroptosis, necroptosis, and pyroptosis in anticancer immunity. *J. Hematol. Oncol.* 13:110. doi: 10.1186/s13045-020-00946-7

Thul, P. J., Åkesson, L., Wiking, M., Mahdessian, D., Geladaki, A., Ait Blal, H., et al. (2017). A subcellular map of the human proteome. *Science* 356:aal3321. doi: 10.1126/science.aal3321

Viswanathan, V. S., Ryan, M. J., Dhruv, H. D., Gill, S., Eichhoff, O. M., Seashore-Ludlow, B., et al. (2017). Dependency of a therapy-resistant state of cancer cells on a lipid peroxidase pathway. *Nature* 547, 453–457. doi: 10.1038/nature23007

Wang, L., Saci, A., Szabo, P. M., Chasalow, S. D., Castillo-Martin, M., Domingo-Domenech, J., et al. (2018a). EMT- and stroma-related gene expression and resistance to PD-1 blockade in urothelial cancer. *Nat. Commun.* 9:3503. doi: 10.1038/s41467-018-05992-x

Wang, W., Green, M., Choi, J. E., Gijón, M., Kennedy, P. D., Johnson, J. K., et al. (2019). CD8(+) T cells regulate tumour ferroptosis during cancer immunotherapy. *Nature* 569, 270–274. doi: 10.1038/s41586-019-1170-y

Wang, Y., Yu, L., Ding, J., and Chen, Y. (2018b). Iron metabolism in cancer. *Int. J. Mol. Sci.* 20:95. doi: 10.3390/ijms20010095

Wang, Z., Shang, J., Li, Z., Li, H., Zhang, C., He, K., et al. (2020). PIK3CA Is regulated by CUx1, promotes cell growth and metastasis in bladder cancer via activating epithelial-mesenchymal transition. *Front. Oncol.* 10:536072. doi: 10.3389/fonc.2020.536072

Xie, Y., Zhu, S., Song, X., Sun, X., Fan, Y., Liu, J., et al. (2017). The tumor suppressor p53 limits ferroptosis by blocking DPP4 activity. *Cell Rep.* 20, 1692–1704. doi: 10.1016/j.celrep.2017.07.055

Xu, L., Deng, C., Pang, B., Zhang, X., Liu, W., Liao, G., et al. (2018). TIP: a web server for resolving tumor immunophenotype profiling. *Cancer Res.* 78, 6575–6580. doi: 10.1158/0008-5472.can-18-0689

Yan, Y., Huang, Z., Cai, J., Tang, P., Zhang, F., Tan, M., et al. (2020a). Identification of a novel immune microenvironment signature predicting survival and

therapeutic options for bladder cancer. *Aging* 12:2327. doi: 10.18632/aging.202327

Yan, Y. L., Huang, Z. N., Zhu, Z., Cui, Y. Y., Li, M. Q., Huang, R. M., et al. (2020b). Downregulation of TET1 promotes bladder cancer cell proliferation and invasion by reducing DNA Hydroxymethylation of AJAP1. *Front. Oncol.* 10:667. doi: 10.3389/fonc.2020.00667

Yang, J., Antin, P., Berx, G., Blanpain, C., Brabletz, T., Bronner, M., et al. (2020a). Guidelines and definitions for research on epithelial-mesenchymal transition. *Nat. Rev. Mol. Cell. Biol.* 21, 341–352. doi: 10.1038/s41580-020-0237-9

Yang, Y., Luo, M., Zhang, K., Zhang, J., Gao, T., Connell, D. O., et al. (2020b). Nedd4 ubiquitylates VDAC2/3 to suppress erastin-induced ferroptosis in melanoma. *Nat. Commun.* 11:433. doi: 10.1038/s41467-020-14324-x

Yu, F., Quan, F., Xu, J., Zhang, Y., Xie, Y., Zhang, J., et al. (2019). Breast cancer prognosis signature: linking risk stratification to disease subtypes. *Brief Bioinform.* 20, 2130–2140. doi: 10.1093/bib/bby073

Yuan, H., Li, X., Zhang, X., Kang, R., and Tang, D. (2016). CISD1 inhibits ferroptosis by protection against mitochondrial lipid peroxidation. *Biochem. Biophys. Res. Commun.* 478, 838–844. doi: 10.1016/j.bbrc.2016.08.034

Conflict of Interest: The authors declare that the research was conducted in the absence of any commercial or financial relationships that could be construed as a potential conflict of interest.

Publisher's Note: All claims expressed in this article are solely those of the authors and do not necessarily represent those of their affiliated organizations, or those of the publisher, the editors and the reviewers. Any product that may be evaluated in this article, or claim that may be made by its manufacturer, is not guaranteed or endorsed by the publisher.

frontiers in Cell and Developmental Biology

ORIGINAL RESEARCH
published: 09 September 2021
doi: 10.3389/fcell.2021.685954

Network Pharmacology and Experimental Validation Reveal the Effects of Chidamide Combined With Aspirin on Acute Myeloid Leukemia-Myelodysplastic Syndrome Cells Through PI3K/AKT Pathway

*Simin Liang[1], Xiaojia Zhou[2], Duo Cai[1], Fernando Rodrigues-Lima[3], Jianxiang Chi[4] and Li Wang[1]**

[1] Department of Hematology, The First Affiliated Hospital of Chongqing Medical University, Chongqing, China, [2] Department of Hematology, The Third Affiliated Hospital of Chongqing Medical University, Chongqing, China, [3] Université de Paris, Unité de Biologie Fonctionnelle et Adaptative, CNRS UMR 8251, Paris, France, [4] Center for the Study of Hematological Malignancies, Karaiskakio Foundation, Nicosia, Cyprus

OPEN ACCESS

Edited by:
Ozgur Kutuk,
Başkent University, Turkey

Reviewed by:
Hou Yuzhu,
The College, University of Chicago, United States
Haitao Wang,
Nankai University, China

***Correspondence:**
Li Wang
liwangls@yahoo.com

Specialty section:
This article was submitted to Cell Death and Survival, a section of the journal Frontiers in Cell and Developmental Biology

Received: 26 March 2021
Accepted: 23 August 2021
Published: 09 September 2021

Citation:
Liang S, Zhou X, Cai D, Rodrigues-Lima F, Chi J and Wang L (2021) Network Pharmacology and Experimental Validation Reveal the Effects of Chidamide Combined With Aspirin on Acute Myeloid Leukemia-Myelodysplastic Syndrome Cells Through PI3K/AKT Pathway. Front. Cell Dev. Biol. 9:685954. doi: 10.3389/fcell.2021.685954

Chidamide (CDM), a novel histone deacetylase inhibitor, is currently used for patients with peripheral T-cell lymphoma. Aspirin (ASA), an anti-inflammatory drug, has been shown to exert anticancer activity. Herein, we investigated the effect of CDM combined with ASA on myelodysplastic syndromes-derived acute myeloid leukemia (AML-MDS) cells and explored the underlying mechanism. The putative targets of CDM and ASA were predicted by network pharmacology approach. GO functional and KEGG pathway enrichment analyses were performed by DAVID. Furthermore, experimental validation was conducted by Cell Counting Kit-8 assay, Flow cytometry and Western blotting. Network pharmacology analysis revealed 36 AML-MDS-related overlapping genes that were targets of CDM and ASA, while 10 hub genes were identified by the plug-in cytoHubba in Cytoscape. Pathway enrichment analysis indicated CDM and ASA significantly affected PI3K/AKT signaling pathway. Functional experiments demonstrated that the combination of CDM and ASA had a remarkable synergistic anti-proliferative effect by blocking the cell cycle in G0/G1 phase and inducing apoptosis. Mechanistically, the combination treatment significantly down-regulated the phosphorylation levels of PI3K and AKT. In addition, insulin-like growth factor 1 (IGF-1), an activator of PI3K/AKT pathway, reversed the effects of the combination treatment. Our findings suggested that CDM combined with ASA exerted a synergetic inhibitory effect on cell growth by inactivating PI3K/AKT pathway, which might pave the way for effective treatments of AML-MDS.

Keywords: chidamide, aspirin, network pharmacology, myelodysplastic syndromes, PI3K/Akt pathway

INTRODUCTION

Myelodysplastic syndromes (MDS) are a heterogeneous group of myeloid disorders characterized by ineffective hematopoiesis, peripheral blood cytopenia and high risk of transformation to acute myeloid leukemia (AML) with poor prognosis (Cogle et al., 2011; Scalzulli et al., 2020). MDS-derived AML (AML-MDS) shows slower hematologic recovery and poorer outcomes following intensive remission-induction chemotherapy than *de novo* AML (Boddu et al., 2017; Ramadan et al., 2020). Additionally, allogeneic stem cell transplantation (alloSCT) remains the only curative option for patients with AML-MDS. But unfortunately, it is only suitable for a minority (Schroeder et al., 2019). Therefore, a novel effective treatment strategy with minimal cytotoxicity still needs to be developed for AML-MDS.

Chidamide (CDM), a novel histone deacetylase inhibitor, selectively inhibits HDAC1, 2, 3, and 10, and has been approved for treatment of patients with recurrent or refractory peripheral T cell lymphoma (PTCL) in China (Shi et al., 2015; Lu et al., 2016). Strikingly, a number of studies have suggested that CDM exerts cytotoxic effects on lymphoma (Zhou et al., 2018), multiple myeloma (MM) (Sun et al., 2019), MDS (Liu et al., 2016), and leukemia (Li et al., 2015), as well as non-hematological malignancies, including lung cancer (Wu et al., 2019), colon cancer (Liu et al., 2010) and hepatocellular carcinoma (Wang et al., 2012). Moreover, CDM has been shown to synergize effects with other anti-tumor agents. For example, several studies have showed that CDM combined with hypomethylating agents, including decitabine, resulted in synergistic effects on the proliferation and apoptosis of myeloid leukemia cells (Xu et al., 2019; Li et al., 2020). Co-treatment with CDM and Bortezomib reduced proliferation, invasion and migration of gastric cancer cells (Zhang et al., 2020). Co-treatment with CDM and Rituximab inhibited tumor growth by upregulating CD20 in diffuse large B-cell lymphoma (DLBCL) (Guan et al., 2020).

Aspirin (acetylsalicylic acid, ASA) has been widely used as an anti-inflammatory, analgesic drug, as well as in cardiovascular disease and platelet aggregation. ASA can reduce the morbidity and mortality of several malignancies, including gastric cancer (García Rodríguez et al., 2020), lung cancer (Erickson et al., 2018) and prostate cancer (Hurwitz et al., 2019). Recent studies revealed that ASA combined with other drugs, such as sorafenib and atorvastatin, exhibited strong anti-cancer effects *in vitro* and *in vivo* (Pennarun et al., 2013; He et al., 2017). In addition, since ASA could affect histone methylation, we aimed to investigate the potential effects and mechanisms of CDM combined with ASA on AML-MDS.

Recently, network pharmacology has been used to predict the therapeutic targets and efficacy of drugs by constructing drug-drug, drug-target and other networks, using a variety of database resources. Through preliminary experiment, we found that CDM and ASA had synergistic inhibitory effect on cell growth in leukemia cells. In this study, we aimed to investigate the anti-tumor activity of CDM combined with ASA in AML-MDS, explore underlying mechanisms by predicting related targets through the network pharmacology approach, so as to provide theoretical and experimental basis for the treatment of AML-MDS. The flowchart of this study design was presented in **Figure 1**.

MATERIALS AND METHODS

Target Prediction Based on Network Pharmacology

SwissTargetPrediction[1] and PharmMapper[2] were used to establish the targets of CDM and ASA. Genomic targets of MDS, AML and AML-MDS were obtained from GeneCards[3] and overlapping genes were collected. Subsequently, CDM- and ASA-associated targets were mapped to these overlapping disease-targets, followed by therapeutic targets of CDM and ASA against AML-MDS were obtained. The STRING database[4] was used to obtain interactions among potential targets of CDM, ASA and the aforementioned diseases. Protein interactions with a combined score > 0.4 were selected. Cytoscape 3.2.1 was used to construct and analyze the protein-protein interaction (PPI) network. DAVID database[5] was used to perform Gene Ontology (GO) and Kyoto Encyclopedia of Genes and Genomes (KEGG) pathway enrichment analyses.

Reagents and Antibodies

CDM (CS055, purity $> 95\%$) was supplied by Chipscreen Biosciences (Shenzhen, China), while ASA was obtained from Maclin (A800349, Shanghai, China). IGF-1 was purchased from MedChemExpress (MCE, Shanghai, China). The following primary antibodies were used: rabbit anti-Bcl-2 (YT0470), cleaved Caspase-3 (YC0006) from ImmunoWay (Texas, United States). PI3K (bsm-33219M), p-PI3K (AB1235888), and Caspase-3 (bs-0081R) from Bioss (Beijing, China). AKT (4691T), p-AKT (4060T), $p21^{CIP1}$ (2947T) from Cell Signaling Technology (Danvers, United States). CDK2 (H08211543) and CDK4 (H10082274) from Wanleibio (Shenyang, China). Mouse anti-β-actin (KM9001) from Sungene (Tianjin, China). Horseradish peroxidase (HRP)-conjugated goat anti-rabbit IgG (A0239) and anti-mouse IgG (A0258) were purchased from Beyotime Biotechnology (Shanghai, China).

Cell Lines and Cell Culture

The human AML-MDS cell line, SKM-1, was a gift from Professor Jianfeng Zhou working in Tongji Medical College of Huazhong University of Science and Technology (Wuhan, China), while the T cell acute lymphoblastic leukemia (T-ALL) cell line Molt-4 was provided by the Children's Hospital of Chongqing Medical University (Chongqing, China). The cells were maintained in RPMI-1640 (Gibco, Thermo Fisher Scientific, MA, United States) supplemented with 10% fetal bovine serum (PAN seratech, Germany) and 100 U/ml penicillin and 100 μg/ml streptomycin ($1 \times$ P/S).

[1]http://swisstargetprediction.ch/

[2]http://www.lilab-ecust.cn/pharmmapper/index.html

[3]https://www.genecards.org/

[4]http://string-db.org/

[5]http://David.ncifcrf.gov/

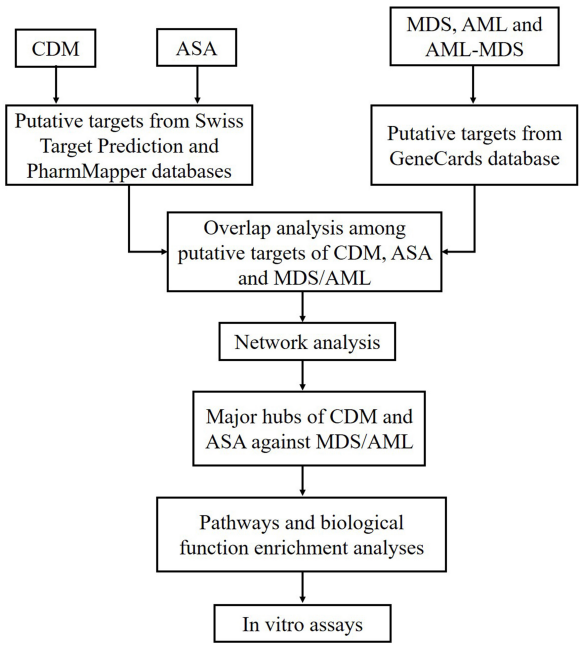

FIGURE 1 | Flowchart of the study design based on network pharmacology approaches for deciphering the mechanisms of CDM and ASA acting on AML-MDS. CDM, Chidamide; ASA, Aspirin; MDS, myelodysplastic syndrome; AML, acute myeloid leukemia; AML-MDS, myelodysplastic syndromes-derived acute myeloid leukemia.

Cell Viability Assay

Cells in the logarithmic growth phase were seeded at a density of 1,500 cells/well and cultured overnight. Drugs were administered at 0.1 μL per well. After a 72-h incubation, cell viability was measured using Cell Titer-Glo luminescent cell viability assay kit (Promega, Madison, United States) and luminescence was quantified using Envision Plate-Reader.

Cell viability was also measured by Cell Counting kit-8 (CCK-8) assay (MCE, Shanghai, China). Briefly, cells were seeded at 3,000 cells/100 μL and treated with different concentrations of CDM and ASA for 24, 48, and 72 h. CCK-8 reagent was added and incubated for 3 h. The absorbance at 450 nm was measured using a Multiskan Go Microplate Spectrophotometer (Thermo Fisher Scientific, United States). Cell proliferation inhibition rate was calculated based on the formula: absorbance of (control group − experimental group)/absorbance of (control group – blank group) × 100%.

Cell Cycle and Cell Apoptosis

CDM, at a concentration of 0.5 μM, or ASA, at a concentration of 1 mM, was added to 1 million cells for 48 h. For cell cycle analysis, cells were fixed with ice-cold 75% ethanol overnight at 4°C and then incubated with 50 mg/ml of propidium iodide (PI) for 30 min at room temperature. For apoptosis, cells were incubated with 5 μl of Annexin V-FITC and 10 μl of PI, at 4°C for 15 min in the dark. Cell cycle and apoptosis were analyzed using a flow cytometer (CytoFLEX, Beckman Coulter, United States).

RNA Isolation and Reverse Transcription-Quantitative PCR (RT-qPCR)

Total RNA was extracted from cells using TRIzol reagent (Beyotime, China) according to the manufacturer's instructions. cDNA was synthesized using PrimeScript Reverse Transcription reagent kit (Takara, Japan). Quantitative PCR (qPCR) was performed using a CFX96 Touch^{TM} Real-Time PCR Detection System (Bio-Rad, Hercules, CA, United States). The following RT-qPCR parameters were used: 95°C for 30 s; 95°C for 5 s, and 60°C for 30 s repeated over 40 cycles. All primers were synthesized by Tsingke (Beijing, China) and the sequences were as follows: P21 forward: 5′-CTGCCTTAGTCTCAGTTTGTGT-3′; P21 reverse: 5′-AACCTCTCATTCAACCGCCTA-3′; Bcl-2 forward: 5′-CTGCACCTGACGCCCTTC-3′; Bcl-2 reverse: 5′-ACACATGACCCCACCGAAC-3′; caspase-3 forward: 5′-TGC TGAAACAGTATGCCGACA-3′; caspase-3 reverse: 5′-CAAAT TCTGTTGCCACCTTTCG-3′; β-actin forward: 5′-CCCAAA GTTCACAATGTGGC-3′; β-actin reverse: 5′-GACTTCCTGT AACAACGCATC-3′. Transcript levels were normalized to β-actin expression and the target gene expression was calculated using the formula $2^{-\Delta\Delta Ct}$.

Western Blot Analysis

Total protein from the cells was harvested using RIPA lysis buffer supplemented with 1 μM PMSF (Beyotime, Shanghai, China) and 30 μg protein was separated on a 10% SDS-polyacrylamide gradient gel. The proteins were transferred onto PVDF membranes and blocked with 5% non-fat milk in Tris Buffered Saline with Tween-20 (TBST) for 2 h at room temperature. The blots were then incubated with primary antibodies overnight at 4°C. Membranes were then washed 3 times with TBST and incubated with secondary antibodies for 1 h at room temperature. Protein bands were visualized with an ECL kit (Advansta, United States) and the band intensity was analyzed using Vilber Fusion software (Fusion, FX5 Spectra, France). β-actin was used as a loading control.

Statistical Analysis

All data was presented as means ± standard deviation (SD) and statistical analyses were performed using GraphPad Prism 5.01 (GraphPad Software Inc., San Diego, CA, United States). The results were analyzed using one-way and two-way ANOVA followed by the Bonferroni *post hoc* test. A value of $p < 0.05$ was considered as statistically significant. All experiments were performed in triplicates.

RESULTS

Putative Targets of CDM and ASA for the Treatment of AML-MDS

A total of 522 possible targets of CDM and ASA were predicted by Swiss Target Prediction and PharmMapper (**Supplementary Table 1**), and 607 overlapping targets of MDS, AML and

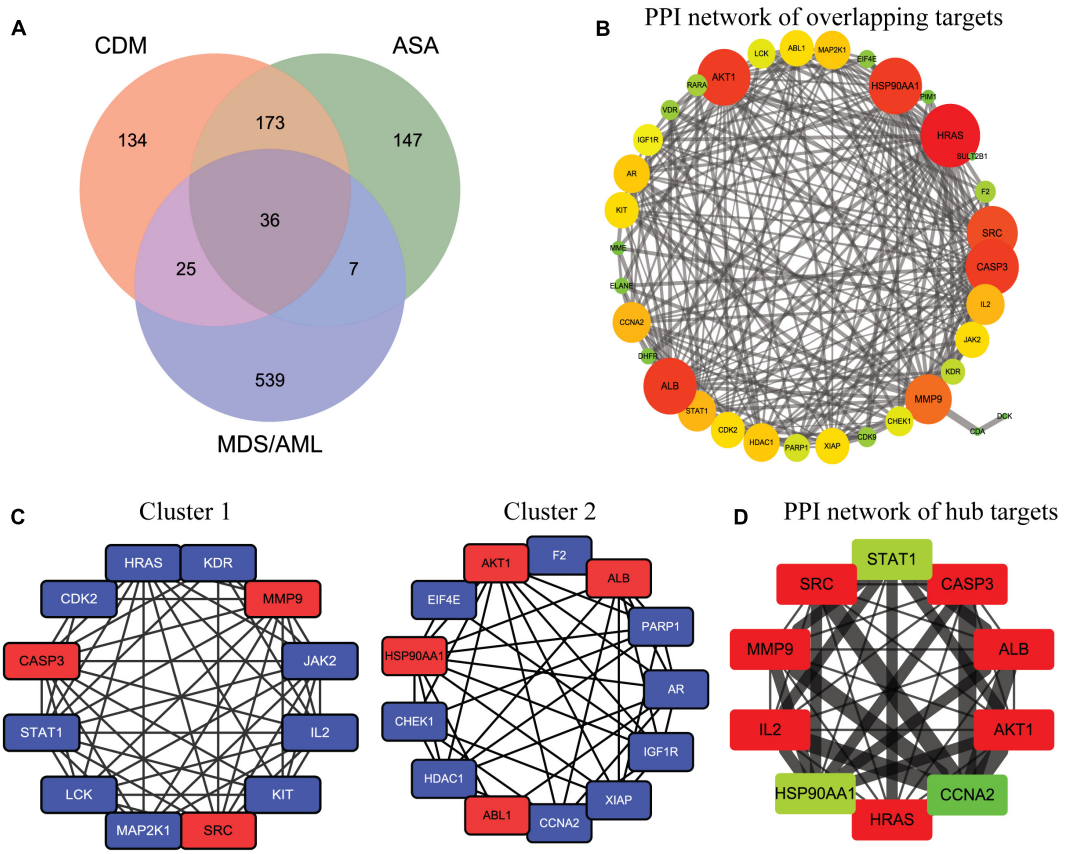

FIGURE 2 | The network pharmacology of CDM and ASA against AML-MDS and cluster analysis. **(A)** The Venn diagram of the potential targets of CDM and ASA against AML-MDS. **(B)** A PPI network of the overlapping targets of CDM and ASA against AML-MDS by Cytoscape software. **(C)** Clusters of interacted proteins by use of MCODE algorithm. **(D)** Hub targets of the PPI network by use of cytoHubba. The size of node and edge was mapped to the degree and edge betweenness, respectively. The color of the node represents the size of the degree value. The redder the color, the larger the node and the more important it is in the network. Conversely, the greener the color, the smaller the node and the less important it is in the network.

AML-MDS were obtained from the GeneCards database (**Supplementary Table 2**). Ultimately, 36 targets of CDM and ASA against AML-MDS were collected (**Figure 2A** and **Supplementary Table 3**). A PPI network of these predicted targets was analyzed using STRING database and constructed by Cytoscape, and the network contained 35 nodes and 245 edges (**Figure 2B**). Clustering subnetworks were produced using the MCODE algorithm (**Figure 2C**). Specifically, 10 nodes were identified as hub genes by the cytoHubba plugin in Cytoscape and grouped together, including AKT1, ALB, CASP3, SRC, MMP9, IL2, HRAS, CCNA2, STAT1, HSP90AA1 (**Figure 2D** and **Supplementary Table 4**).

Biological Function and Pathway Enrichment Analyses of Hub Targets

GO and KEGG pathway enrichment analyses of these hub genes were performed using the DAVID database. GO analysis showed that these targets were associated with negative regulation of apoptotic processes and cell proliferation (**Figure 3A**). Enrichment in cellular component and molecular function was presented in **Figures 3B,C**, respectively. Additionally, KEGG analysis revealed that these 10 hub targets were involved in 42 pathways, which were mainly enriched in cancer-related pathways, especially PI3K/AKT and VEGF signaling pathways (**Supplementary Table 5** and **Figure 3D**).

The Synergistic Antiproliferative Effects of CDM Combined With ASA on AML-MDS

Then sensitivity of SKM-1 cells to the drugs was determined according to the converting plasma concentrations. The results showed that SKM-1 cells were sensitive to CDM and ASA (**Figure 4A**). For further validation, SKM-1 and Molt-4 cells were treated with different concentrations of the two drugs alone. The results of CCK-8 assay showed that both CDM and ASA inhibited cells viability in a dose- and time-dependent manner (**Figures 4B,C**). At 48 h, the half-maximal inhibitory concentration (IC_{50}) of CDM on SKM-1 and Molt-4 cells was (19.54 ± 3.34) μM and (1.69 ± 0.08) μM, respectively, and IC_{50} value of ASA was (1.69 ± 0.06) mM and (1.84 ± 0.08) mM, respectively. Moreover, to evaluate the synergistic effect of co-treatment on cell viability, these cells were treated with a low-dose

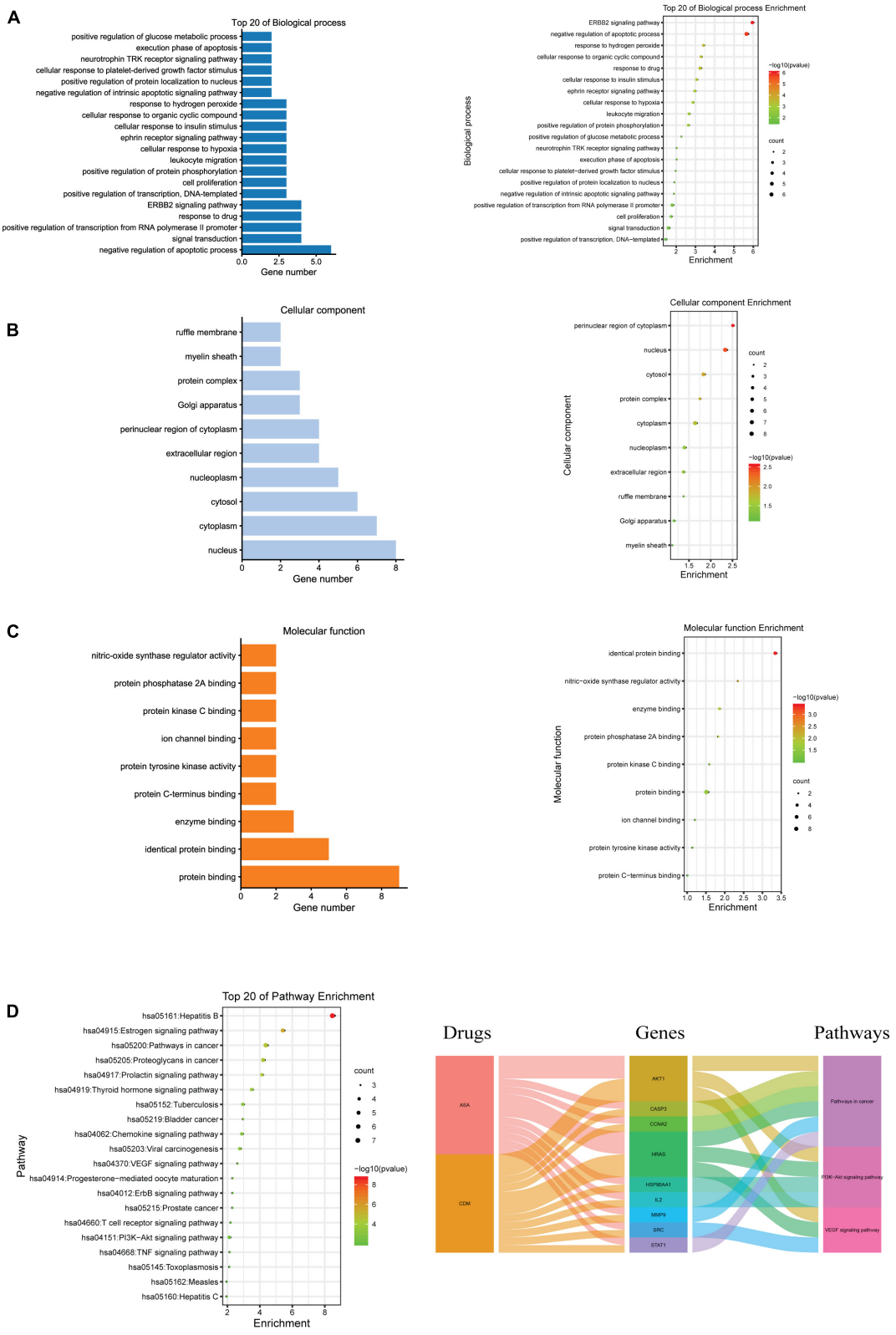

FIGURE 3 | GO and KEGG pathway enrichment analyses for the hub genes of CDM and ASA against AML-MDS. **(A)** Biological process (BP); **(B)** cellular component (CC); **(C)** molecular function (MF); **(D)** the top 20 of KEGG enrichment analysis (left panel), alluvial plot of interaction among drugs, major hub genes and three main pathways (right panel).

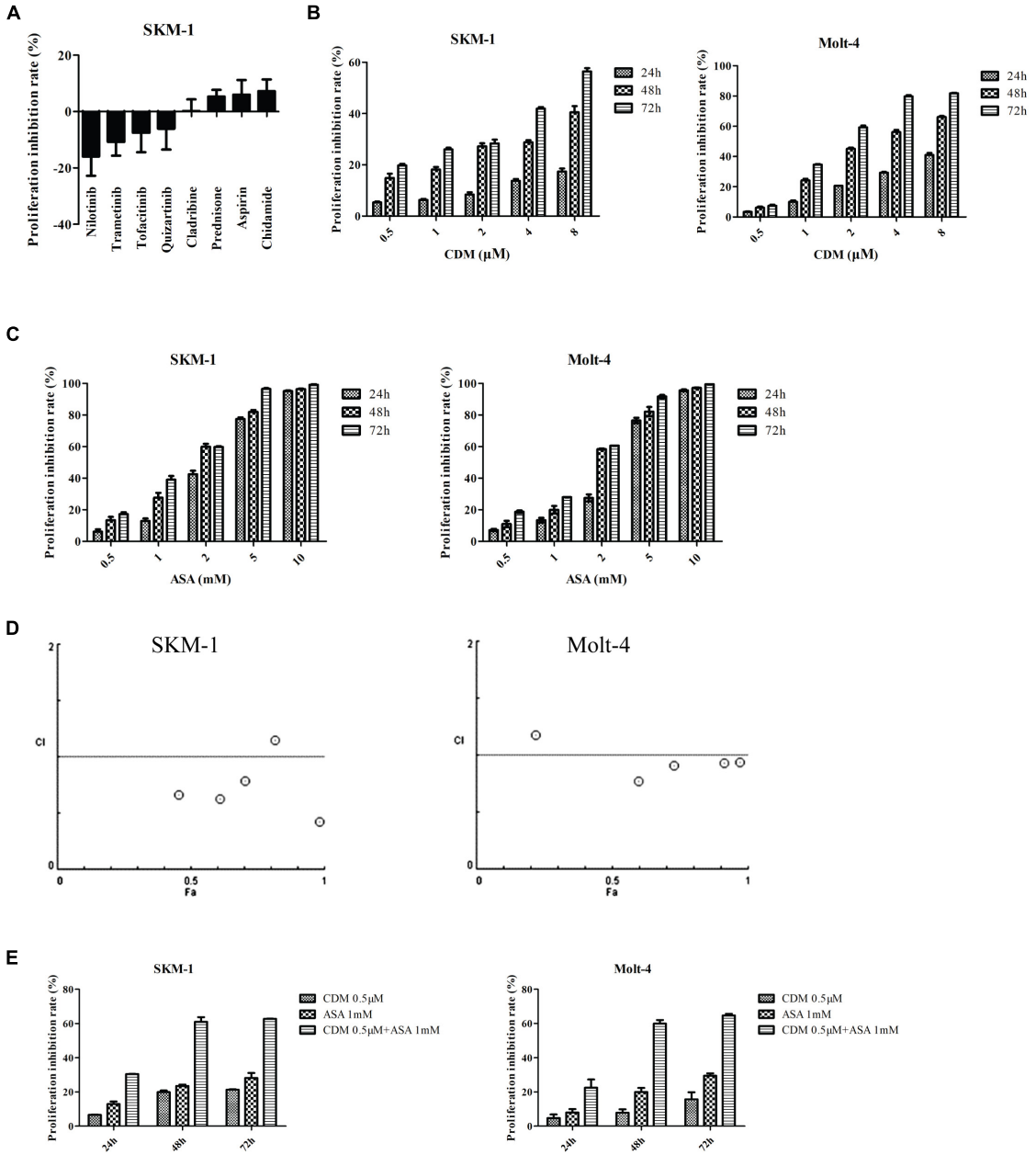

FIGURE 4 | CDM in combination with ASA inhibited the proliferation of AML-MDS cells. **(A)** Cell viability detected by Cell Titer-Glo luminescent cell viability assay in SKM-1 cells treated with 8 drugs. **(B,C)** SKM-1 and Molt-4 cells were exposed to CDM (0.5, 1, 2, 4, and 8 μM) or ASA (0.5, 1, 2, 5, and 10 mM) alone. **(D)** Combination index values were calculated with CompuSyn software. CI < 1 indicates synergy; CI = 1 is additive; and CI > 1 means antagonism. CI, combination index; Fa, effect levels. **(E)** SKM-1 and Molt-4 cells were treated with 0.5 μM CDM combined with 1 mM ASA for 24, 48, and 72 h. The cell viability was determined by CCK-8 assay. Data are mean ± SD of three independent experiments.

CDM (0.5 μM) combined with different concentrations of ASA for 48 h. When combined with ASA, low-dose CDM decreased the IC_{50} of ASA to (0.63 ± 0.06) mM and (0.94 ± 0.05) mM in SKM-1 and Molt-4 cells, respectively. The combination index (CI) demonstrated that CDM combined with ASA had a distinct synergistic effect calculated by CompuSyn software (**Figure 4D**). As shown in **Figure 4E**, CDM combined with ASA significantly enhanced the inhibitory effect. Therefore, a combination of 0.5 μM CDM and 1 mM ASA, a value close to the IC_{50}, was selected for subsequent experiments.

Combination of CDM and ASA Caused Cell Cycle Arrest at the G0/G1 Phase

To investigate the efficacy of the combination treatment on cell cycle, cell cycle distribution of each group was detected

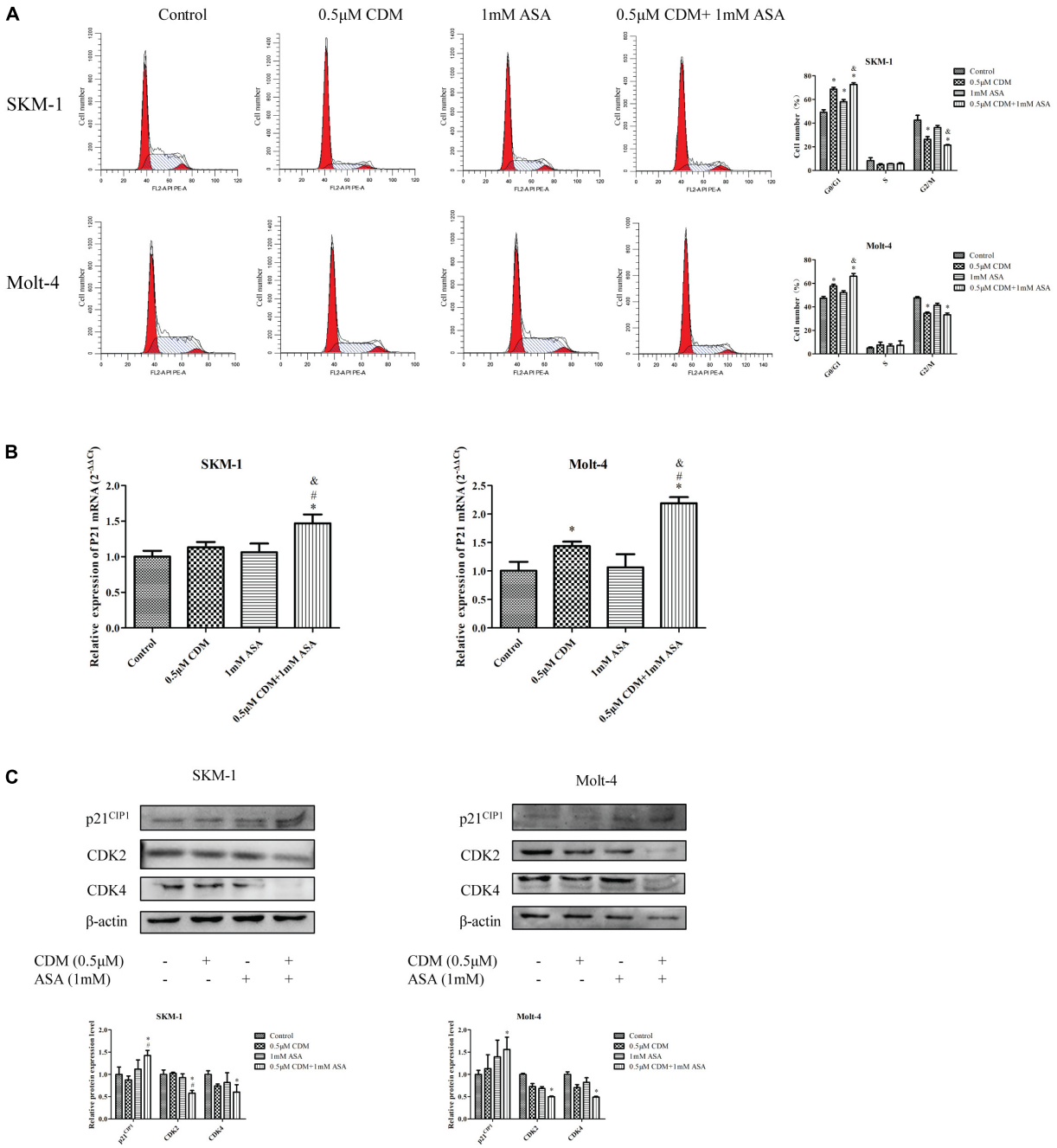

FIGURE 5 | CDM in combination with ASA arrested the cell cycle at G0/G1 phase in AML-MDS cells. **(A)** Cell cycle distribution was detected by flow cytometry after treatment with 0.5 μM CDM and 1 mM ASA for 48 h. The red color areas on the left and right of the images represent the proportion of cells in the G0/G1 and G2/M phases, respectively. **(B)** Relative expression of P21 mRNA compared with the control group. **(C)** Expressions of cell cycle related protein (CDK2, CDK4, p21) were detected by western blot. β-actin was used as a loading control. Data are mean ± SD of three independent experiments. "*" indicates a significant difference relative to the control group ($^{*}p < 0.05$), "#" indicates a significant difference relative to CDM-treated group ($^{\#}p < 0.05$), "&" indicates a significant difference relative to ASA-treated group ($^{\&}p < 0.05$).

by flow cytometry with PI staining assay. As shown in **Figure 5A**, the combination of CDM and ASA resulted in a significant increase in the proportion of G0/G1 phase cells compared with the two drugs alone. A high mRNA expression of p21 in the combined treatment group (**Figure 5B**) was observed, but there was no statistical difference between the two mono-treatment groups. Also, Western blotting indicated that after combined treatment, the protein expression of CDK2 and CDK4 was down-regulated while p21 was up-regulated (**Figure 5C**).

Combination of CDM and ASA Synergistically Induced Apoptosis

Next, flow cytometry was used to detect the apoptotic effects of the combination treatment on SKM-1 and Molt-4 cells, and apoptosis rate was calculated as the sum of percentage of Annexin^{+} cells. As shown in **Figure 6A**, the co-treatment remarkably induced apoptosis compared with CDM and ASA mono-treatment. Furthermore, Western blotting showed that the expression of apoptosis-related protein cleaved caspase-3 was up-regulated and the expression of Bcl-2 was down-regulated, while no change in caspase-3 was observed. The observation was consistent with the results of RT-qPCR (**Figures 6B,C**).

Combination of CDM and ASA Suppressed PI3K/AKT Signaling Pathway

Based on the results of GO and KEGG analyses, we focused on PI3K/AKT signaling pathway and hypothesized that the combination of CDM and ASA could synergistically inhibit the activation of PI3K/AKT pathway. The results of Western blotting demonstrated that the expression levels of p-PI3K and

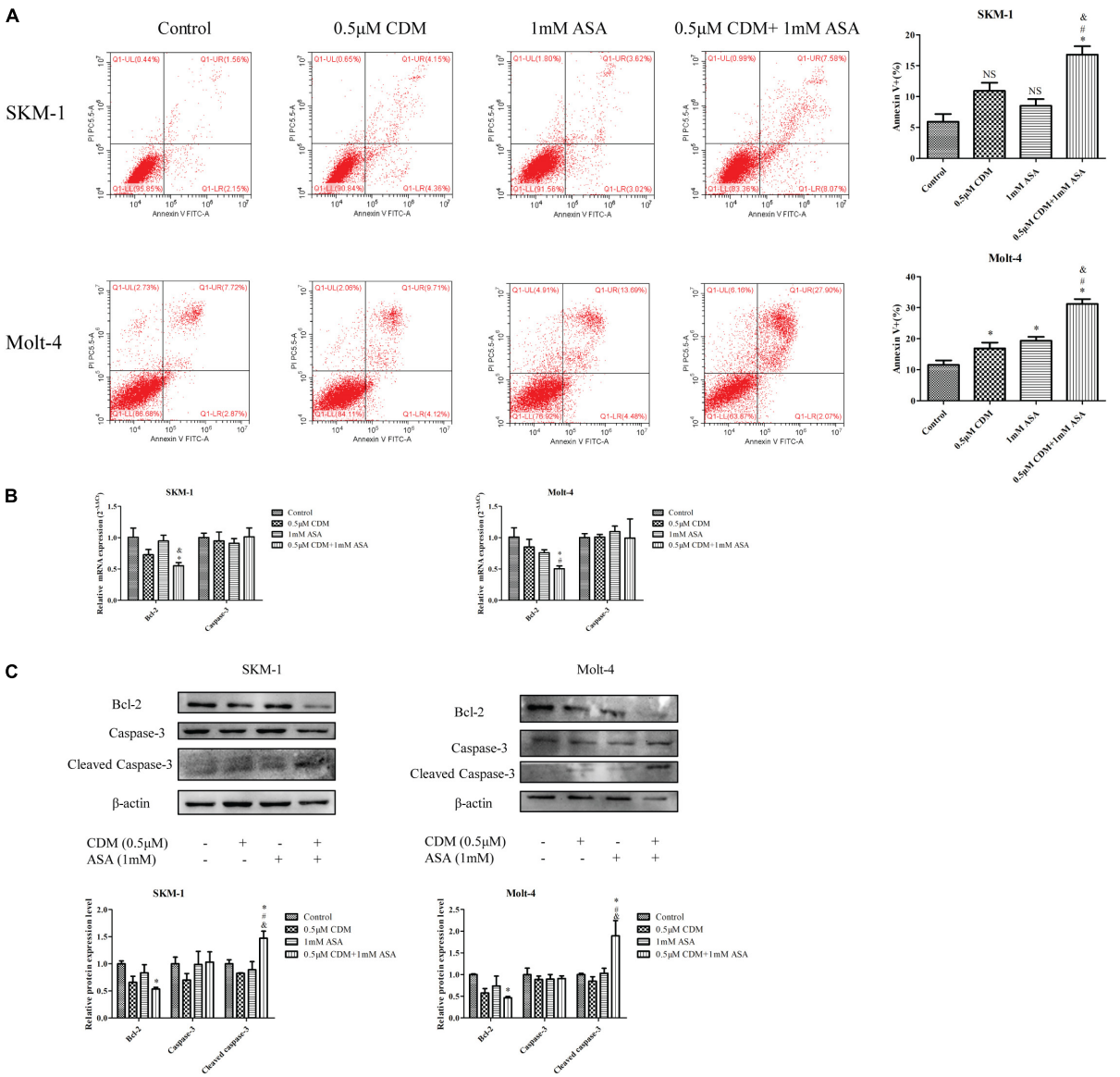

FIGURE 6 | CDM in combination with ASA induced cell apoptosis in AML-MDS cells. **(A)** Cell apoptotic rate was detected by flow cytometry after treatment of the combination of 0.5 μM CDM and 1 mM ASA for 48 h. **(B)** Relative mRNA expression of Bcl-2 and caspase-3 compared with the control group. **(C)** Expressions of the apoptosis-related protein (Bcl-2, caspase-3, cleaved caspase-3) were detected by western blot. β-actin was used as a loading control. Data are mean ± SD of three independent experiments. "*" indicates a significant difference relative to the control group ($^{*}p < 0.05$), "#" indicates a significant difference relative to CDM-treated group ($^{\#}p < 0.05$), "&" indicates a significant difference relative to ASA-treated group ($^{\&}p < 0.05$), "NS" indicates no significant difference relative to ASA-treated group or CDM-treated group.

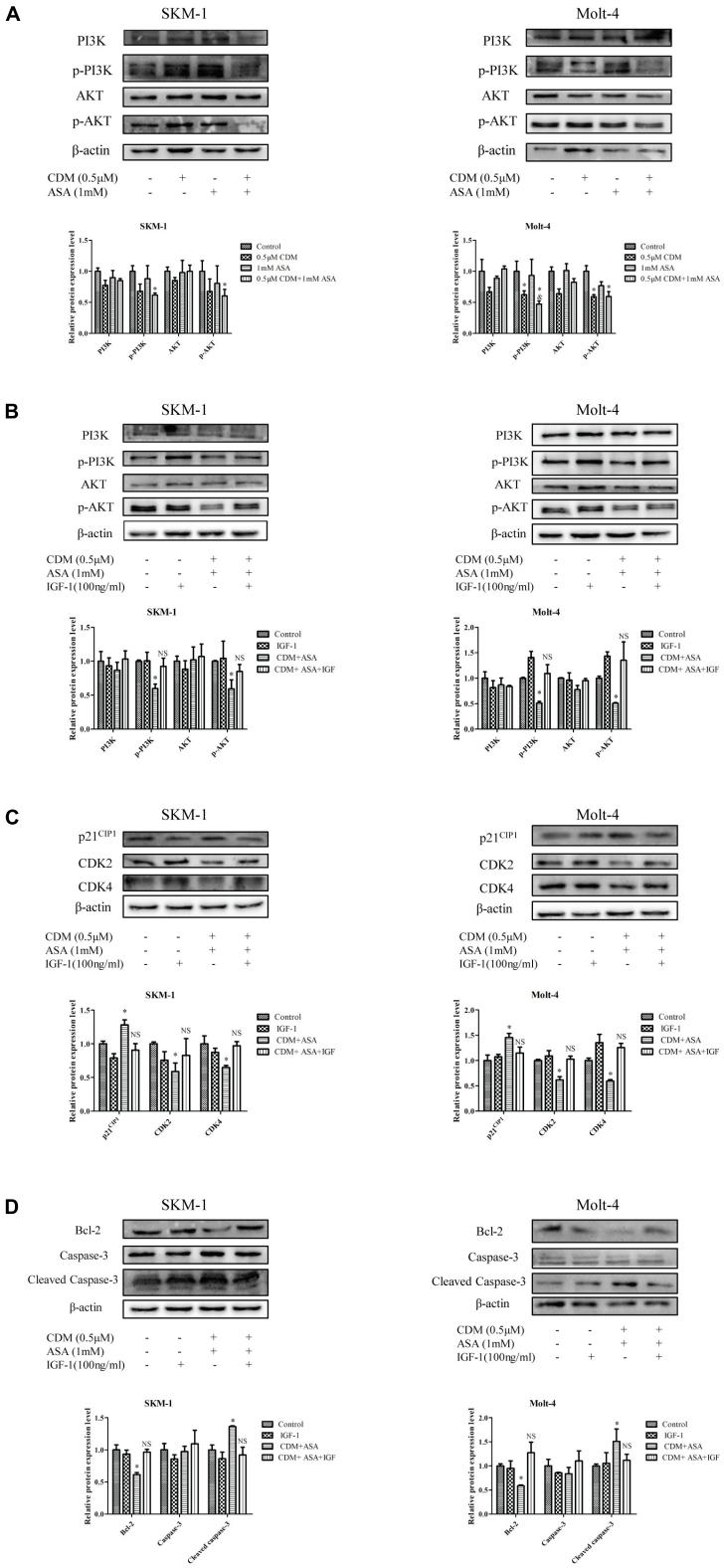

FIGURE 7 | CDM combined with ASA inhibited the activation of PI3K/AKT pathway in AML-MDS cells. **(A)** Western blot analysis of PI3K, p-PI3K AKT, p-AKT. **(B)** Western blotting of PI3K, p-PI3K, AKT and p-AKT. **(C)** Western blotting of CDK2, CDK4 and p21. **(D)** Western blotting of Bcl-2, caspase-3 and cleaved caspase-3. IGF-1 reversed the effect of CDM combined with ASA on AML-MDS cells. β-actin served as a loading control. Data are mean ± SD of three independent experiments. "*" indicates a significant difference relative to the control group (*$p < 0.05$), "&" indicates a significant difference relative to ASA-treated group (&$p < 0.05$), "NS" indicates no significant difference relative to the control group.

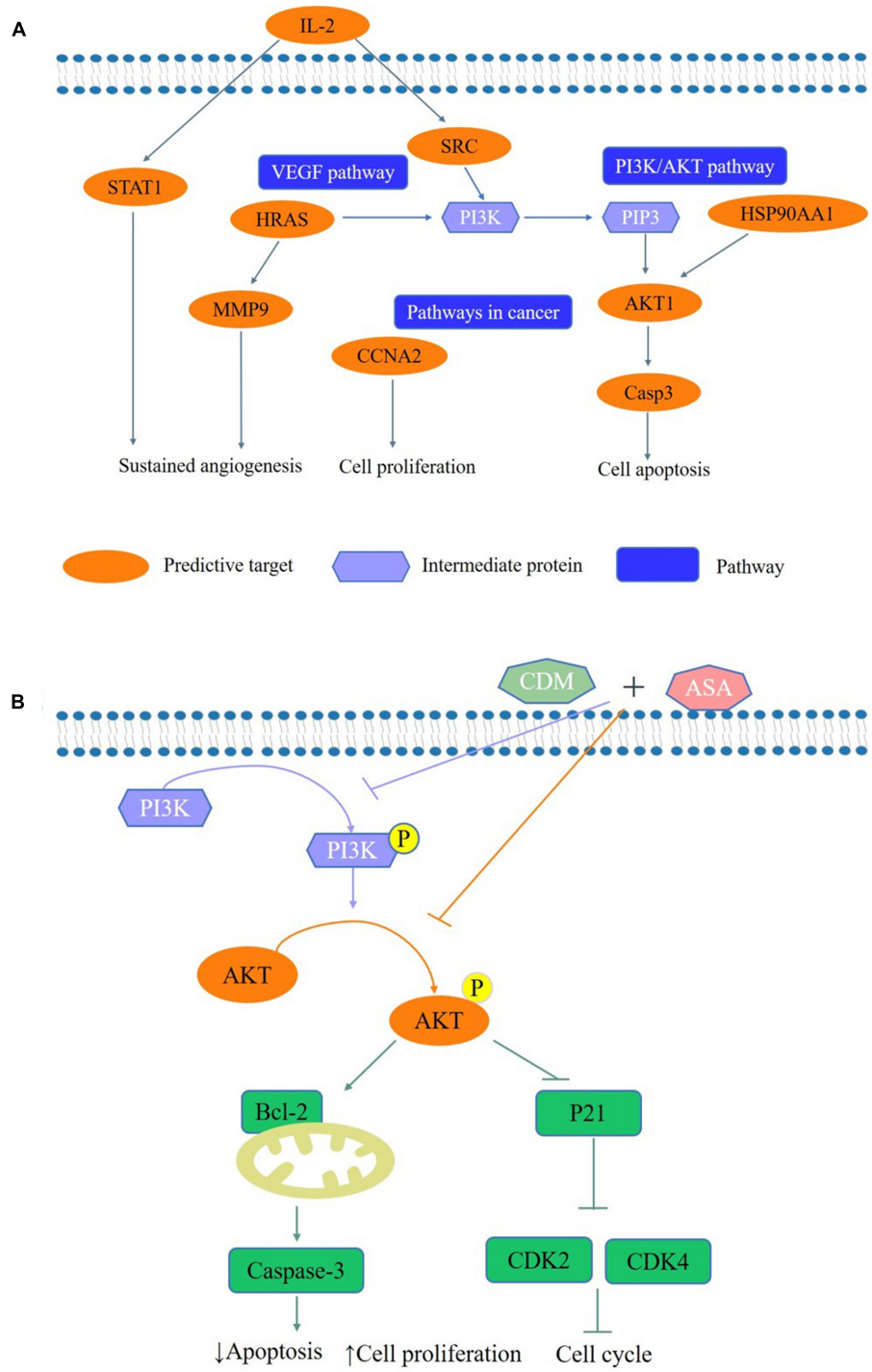

FIGURE 8 | A schematic representation of the proposed pathway responsible for CDM combined with ASA in AML-MDS cells. **(A)** The predictive pathways of CDM and ASA in AML-MDS through network pharmacology. **(B)** CDM combined with ASA could inhibited the activation of PI3K/AKT signaling pathways, and then affected the expression of cell cycle and apoptosis-related proteins to induce cell cycle arrest and apoptosis in AML-MDS cells through experimental validation.

p-AKT in the combination treatment group were distinctly lower than those in each drug alone and control group, while the level of total PI3K and AKT remained constant (**Figure 7A**). Intriguingly, IGF-1, an agonist of PI3K/AKT signaling pathway, reversed the effects of the combination treatment on cell cycle and apoptosis-related proteins (**Figures 7B–D**), indicating that PI3K/AKT pathway was involved in the process induced by the combination treatment of CDM and ASA.

DISCUSSION

Drug combination has been proposed as a promising therapeutic strategy with fewer side effects and lower toxicity, which could be used to improve the efficacy of single-agent treatment. There was evidence that ASA synergized with HDAC inhibitors (FK228) to inhibit growth of COX-1 positive ovarian cancer cells (Son et al., 2010). Zhang H. et al. (2018) also reported that in the presence of CDM, ASA significantly suppressed tumor growth of natural killer/T-cell lymphoma (NKTCL). In line with previous reports, our study showed that the efficiency of co-treatment was superior to CDM or ASA mono-treatment alone in inhibiting growth of AML-MDS cells, suggesting that a small dose of drug combination may be an effective therapy. However, the underlying molecular mechanisms remain unclear.

To identify the mechanisms in which CDM and ASA affected cell viability, we examined the cell cycle distribution and apoptotic rate. Dysregulation of cell cycle progression is a hallmark of cancer that enables limitless cell division. It has been reported that CDM and ASA inhibit tumor cell proliferation by inducing cell cycle arrest in G0/G1 and G2/M phases (Liu et al., 2016; Fan et al., 2017; He et al., 2018; Zhang X. et al., 2018). Our data showed that the efficiency of inducing cell cycle arrest was significantly improved when CDM was combined with ASA. The interactions of cyclin, cyclin-dependent kinases (CDKs) and CDK inhibitors play indispensable roles in controlling cell cycle. CDK2 is necessary for transition from G1 phase to S phase, while CDK4 controls G1 phase, both of which are positive regulators of the cell cycle (Lim and Kaldis, 2013). On the contrary, p21, a putative tumor-suppressor protein, is negative regulator that inhibits the CDKs/cyclin complexes in the G1 phase (Rodriguez-Cupello et al., 2020). Our study manifested that the combination of CDM and ASA synergistically down-regulated CDK2 and CDK4, and up-regulated p21, leading to G0/G1 arrest.

Dysregulation of apoptosis causes excessive cell proliferation or excessive apoptosis, resulting in disease. As a signaling pathway that regulates cell apoptosis and survival, the Bcl-2/Cleaved caspase-3 apoptotic pathway has been implicated in many cancers including leukemia (Tian et al., 2019; Zhang et al., 2019). Bcl-2 is a member of anti-apoptotic Bcl-2 family proteins, which plays an important role in maintaining the integrity of the outer mitochondrial membrane (OMM), while the pro-apoptotic protein Bax inserts into the OMM and facilitates the release of inter-membrane space (IMS) protein, leading to the activation of caspases (Renault and Chipuk, 2014; Delbridge et al., 2016). Cleaved caspase-3 is an activated form of caspase-3, a major effector protease in apoptosis that triggers the apoptotic cascade (Braunstein et al., 2020). We found that CDM combined with ASA significantly accelerated cell apoptosis by downregulation of Bcl-2 and activation of caspase-3, indicating that the combination treatment might be a potential strategy for the treatment of leukemia.

Based on the network pharmacology approach, we collected 36 putative targets of CDM and ASA against AML-MDS, and revealed that AKT1 was one of the hub genes. Through KEGG enrichment analysis, PI3K/AKT signaling pathway was highlighted as a potential target. The expression of PI3K/AKT signaling pathway is often dysregulated in various cancers and activated PI3K/AKT pathway is implicated in a variety of processes, including inducing tumor cell proliferation, inhibiting apoptosis and promoting invasion and metastasis (Yang et al., 2019). Previous studies have confirmed that blocking PI3K/AKT pathway induces cell death by regulating cell proliferation, apoptosis and cell cycle in leukemia (Bertacchini et al., 2015; Banerjee et al., 2016; Cheng et al., 2019). CDM was able to increase the acetylation levels of histone H3 and inhibit PI3K/AKT signaling pathway, resulting in arresting colon cancer cells at G1 phase and accelerating cell apoptosis (Liu et al., 2010). ASA was shown to inhibit cell proliferation by blocking cell cycle by suppressing the activation of the phosphorylation of AKT (Zhang X. et al., 2018). Consistently, our data showed that the expression levels of p-PI3K and p-AKT were remarkably downregulated by the combination of CDM and ASA, leading to the inactivation of the PI3K/AKT pathway. To confirm this, cells were treated with IGF-1, a PI3K/AKT agonist. The results showed that IGF-1 reversed the inhibitory effect of the combination treatment on PI3K/AKT pathway. The above results suggested that the combination of CDM and ASA inhibited cell proliferation, induced cell cycle arrest and promoted apoptosis in AML-MDS cells partially through suppressing the PI3K/AKT pathway (**Figure 8**).

CONCLUSION

Our study demonstrated that CDM and ASA exerted synergistic effect on G0/G1 arrest and apoptosis by inhibiting the PI3K/AKT pathway *in vitro*. This provides a promising chemotherapeutic strategy for AML-MDS in combination with low dose agents. Future studies should focus on the *in vivo* efficacy of the combination treatment and the determination of the optimal combination regimens.

DATA AVAILABILITY STATEMENT

The original contributions presented in the study are included in the article/**Supplementary Material**, further inquiries can be directed to the corresponding author/s.

AUTHOR CONTRIBUTIONS

SL and XZ conceived and designed the experiments. SL, XZ, and DC performed the experiments. LW contributed as regards the reagents, materials, and analysis tools. SL, XZ, DC, FR-L, JC, and LW participated to the analysis and interpretation of the results. SL wrote the manuscript. All authors reviewed and approved the final manuscript.

FUNDING

This study was supported by Natural Science Foundation Project of Chongqing (cstc2018jcyjAX0688), the Chongqing Science and Health joint project (2018ZDXM001), the Chongqing Education

Commission Foundation (KJ1702017), and the Science and Technology Planning Project of Yuzhong District of Chongqing City (20190121).

ACKNOWLEDGMENTS

We thank the Chongqing Key Laboratory of Translational Medicine in Major Metabolic Diseases (The First Affiliated Hospital of Chongqing Medical University, Chongqing, China) for providing laboratory facilities.

SUPPLEMENTARY MATERIAL

The Supplementary Material for this article can be found online at: https://www.frontiersin.org/articles/10.3389/fcell.2021.685954/full#supplementary-material

REFERENCES

Banerjee, K., Das, S., Sarkar, A., Chatterjee, M., Biswas, J., and Choudhuri, S. K. (2016). A copper chelate induces apoptosis and overcomes multidrug resistance in T-cell acute lymphoblastic leukemia through redox imbalance and inhibition of EGFR/PI3K/Akt expression. *Biomed. Pharmacother.* 84, 71–92. doi: 10.1016/j.biopha.2016.08.056

Bertacchini, J., Heidari, N., Mediani, L., Capitani, S., Shahjahani, M., Ahmadzadeh, A., et al. (2015). Targeting PI3K/AKT/mTOR network for treatment of leukemia. *Cell. Mol. Life Sci.* 72, 2337–2347. doi: 10.1007/s00018-015-1867-5

Boddu, P., Kantarjian, H., Garcia-Manero, G., Ravandi, F., Verstovsek, S., Jabbour, E., et al. (2017). Treated secondary acute myeloid leukemia: a distinct high-risk subset of AML with adverse prognosis. *Blood Adv.* 1, 1312–1323. doi: 10.1182/bloodadvances.2017008227

Braunstein, I., Engelman, R., Yitzhaki, O., Ziv, T., Galardon, E., and Benhar, M. (2020). Opposing effects of polysulfides and thioredoxin on apoptosis through caspase persulfidation. *J. Biol. Chem.* 295, 3590–3600. doi: 10.1074/jbc.RA119.012357

Cheng, J. Y., Li, Y., Liu, S. Q., Jiang, Y. J., Ma, J., Wan, L., et al. (2019). CXCL8 derived from mesenchymal stromal cells supports survival and proliferation of acute myeloid leukemia cells through the PI3K/AKT pathway. *FASEB J.* 33, 4755–4764. doi: 10.1096/fj.201801931R

Cogle, C. R., Craig, B. M., Rollison, D. E., and List, A. F. (2011). Incidence of the myelodysplastic syndromes using a novel claims-based algorithm: high number of uncaptured cases by cancer registries. *Blood* 117, 7121–7125. doi: 10.1182/blood-2011-02-337964

Delbridge, A. R., Grabow, S., Strasser, A., and Vaux, D. L. (2016). Thirty years of BCL-2: translating cell death discoveries into novel cancer therapies. *Nat. Rev. Cancer* 16, 99–109. doi: 10.1038/nrc.2015.17

Erickson, P., Gardner, L. D., Loffredo, C. A., St George, D. M., Bowman, E. D., Deepak, J., et al. (2018). Racial and Ethnic Differences in the Relationship between Aspirin Use and Non-Small Cell Lung Cancer Risk and Survival. *Cancer Epidemiol. Biomarkers Prev.* 27, 1518–1526. doi: 10.1158/1055-9965.epi-18-0366

Fan, W. S., Li, J. H., Chen, J. F., Zhu, L., Wang, Y. M., Sun, B. L., et al. (2017). Aspirin inhibits the proliferation of synovium-derived mesenchymal stem cells by arresting the cell cycle in the G0/G1 phase. *Am. J. Transl. Res.* 9, 5056–5062.

García Rodríguez, L. A., Soriano-Gabarró, M., Vora, P., and Cea Soriano, L. (2020). Low-dose aspirin and risk of gastric and oesophageal cancer: A population-based study in the United Kingdom using The Health Improvement Network. *Int. J. Cancer* 147, 2394–2404. doi: 10.1002/ijc.33022

Guan, X. W., Wang, H. Q., Ban, W. W., Chang, Z., Chen, H. Z., Jia, L., et al. (2020). Novel HDAC inhibitor Chidamide synergizes with Rituximab to inhibit diffuse large B-cell lymphoma tumour growth by upregulating CD20. *Cell Death Dis.* 11:20. doi: 10.1038/s41419-019-2210-0

He, J. S., Chen, Q. X., Gu, H. Y., Chen, J., Zhang, E. F., Guo, X., et al. (2018). Therapeutic effects of the novel subtype-selective histone deacetylase inhibitor chidamide on myeloma-associated bone disease. *Haematologica* 103, 1369–1379. doi: 10.3324/haematol.2017.181172

He, Y., Huang, H. R., Farischon, C., Li, D. L., Du, Z. Y., Zhang, K., et al. (2017). Combined effects of atorvastatin and aspirin on growth and apoptosis in human prostate cancer cells. *Oncol. Rep.* 37, 953–960. doi: 10.3892/or.2017.5353

Hurwitz, L. M., Joshu, C. E., Barber, J. R., Prizment, A. E., Vitolins, M. Z., Jones, M. R., et al. (2019). Aspirin and Non-Aspirin NSAID Use and Prostate Cancer Incidence, Mortality, and Case Fatality in the Atherosclerosis Risk in Communities Study. *Cancer Epidemiol. Biomarkers Prev.* 28, 563–569. doi: 10.1158/1055-9965.epi-18-0965

Li, Q., Huang, J. C., Liao, D. Y., and Wu, Y. (2020). Chidamide plus decitabine synergistically induces apoptosis of acute myeloid leukemia cells by upregulating PERP. *Am. J. Transl. Res.* 12, 3461–3475.

Li, Y., Chen, K., Zhou, Y., Xiao, Y. R., Deng, M. M., Jiang, Z. W., et al. (2015). A New Strategy to Target Acute Myeloid Leukemia Stem and Progenitor Cells Using Chidamide, a Histone Deacetylase Inhibitor. *Curr. Cancer Drug Targets* 15, 493–503. doi: 10.2174/1568009615061508051532 30

Lim, S., and Kaldis, P. (2013). Cdks, cyclins and CKIs: roles beyond cell cycle regulation. *Development* 140, 3079–3093. doi: 10.1242/dev.091744

Liu, L., Chen, B. A., Qin, S. K., Li, S. Y., He, X. M., Qiu, S. M., et al. (2010). A novel histone deacetylase inhibitor Chidamide induces apoptosis of human colon cancer cells. *Biochem. Biophys. Res. Commun.* 392, 190–195. doi: 10.1016/j.bbrc.2010.01.011

Liu, Z. Y., Ding, K., Li, L. J., Liu, H., Wang, Y. H., Liu, C. Y., et al. (2016). A novel histone deacetylase inhibitor Chidamide induces G0/G1 arrest and apoptosis in myelodysplastic syndromes. *Biomed. Pharmacother.* 83, 1032–1037. doi: 10.1016/j.biopha.2016.08.023

Lu, X. P., Ning, Z. Q., Li, Z. B., Cao, H. X., and Wang, X. H. (2016). Development of chidamide for peripheral T-cell lymphoma, the first orphan drug approved in China. *Intractable Rare Dis. Res.* 5, 185–191. doi: 10.5582/irdr.2016.01024

Pennarun, B., Kleibeuker, J. H., Boersma-van, Ek, W., Kruyt, F. A., Hollema, H., et al. (2013). Targeting FLIP and Mcl-1 using a combination of aspirin and sorafenib sensitizes colon cancer cells to TRAIL. *J. Pathol.* 229, 410–421. doi: 10.1002/path.4138

Ramadan, S., Suciu, S., Stevens-Kroef, M., Willemze, R., Amadori, S., de Witte, T., et al. (2020). Survival Improvement over Time of 960 s-AML Patients Included in 13 EORTC-GIMEMA-HOVON Trials. *Cancers* 12:3334. doi: 10.3390/cancers12113334

Renault, T. T., and Chipuk, J. E. (2014). Death upon a kiss: mitochondrial outer membrane composition and organelle communication govern sensitivity to BAK/BAX-dependent apoptosis. *Chem. Biol.* 21, 114–123. doi: 10.1016/j.chembiol.2013.10.009

Rodriguez-Cupello, C., Dam, M., Serini, L., Wang, S., Lindgren, D., Englund, E., et al. (2020). The STRIPAK Complex Regulates Response to Chemotherapy Through p21 and p27. *Front. Cell Dev. Biol.* 8:146. doi: 10.3389/fcell.2020.00146

Scalzulli, E., Pepe, S., Colafigli, G., and Breccia, M. (2020). Therapeutic strategies in low and high-risk MDS: What does the future have to offer? *Blood Rev.* 45:100689. doi: 10.1016/j.blre.2020.100689

Schroeder, T., Wegener, N., Lauseker, M., Rautenberg, C., Nachtkamp, K., Schuler, E., et al. (2019). Comparison between Upfront Transplantation and different Pretransplant Cytoreductive Treatment Approaches in Patients with High-Risk Myelodysplastic Syndrome and Secondary Acute Myelogenous Leukemia. *Biol. Blood Marrow Transplant.* 25, 1550–1559. doi: 10.1016/j.bbmt.2019.03.011

Shi, Y., Dong, M., Hong, X., Zhang, W., Feng, J., Zhu, J., et al. (2015). Results from a multicenter, open-label, pivotal phase II study of chidamide in relapsed or refractory peripheral T-cell lymphoma. *Ann. Oncol.* 26, 1766–1771. doi: 10.1093/annonc/mdv237

Son, D. S., Wilson, A. J., Parl, A. K., and Khabele, D. (2010). The effects of the histone deacetylase inhibitor romidepsin (FK228) are enhanced by aspirin (ASA) in COX-1 positive ovarian cancer cells through augmentation of p21. *Cancer Biol. Ther.* 9, 928–935. doi: 10.4161/cbt.9.11.11873

Sun, Y. F., Li, J., Xu, Z., Xu, J. D., Shi, M. J., and Liu, P. (2019). Chidamide, a novel histone deacetylase inhibitor, inhibits multiple myeloma cells

proliferation through succinate dehydrogenase subunit A. *Am. J. Cancer Res.* 9, 574–584.

Tian, Y., Jia, S. X., Shi, J., Gong, G. Y., Yu, J. W., Niu, Y., et al. (2019). Polyphyllin I induces apoptosis and autophagy via modulating JNK and mTOR pathways in human acute myeloid leukemia cells. *Chem. Biol. Interact.* 311:108793. doi: 10.1016/j.cbi.2019.108793

Wang, H. J., Guo, Y., Fu, M., Liang, X., Zhang, X. Y., Wang, R. Z., et al. (2012). Antitumor activity of Chidamide in hepatocellular carcinoma cell lines. *Mol. Med. Rep.* 5, 1503–1508. doi: 10.3892/mmr.2012.858

Wu, Y. F., Ou, C. C., Chien, P. J., Chang, H. Y., Ko, J. L., and Wang, B. Y. (2019). Chidamide-induced ROS accumulation and miR-129-3p-dependent cell cycle arrest in non-small lung cancer cells. *Phytomedicine* 56, 94–102. doi: 10.1016/j.phymed.2018.09.218

Xu, F. F., Guo, H. G., Shi, M. Y., Liu, S. W., Wei, M., Sun, K., et al. (2019). A combination of low-dose decitabine and chidamide resulted in synergistic effects on the proliferation and apoptosis of human myeloid leukemia cell lines. *Am. J. Transl. Res.* 11, 7644–7655.

Yang, Q., Jiang, W., and Hou, P. (2019). Emerging role of PI3K/AKT in tumor-related epigenetic regulation. *Semin. Cancer Biol.* 59, 112–124. doi: 10.1016/j.semcancer.2019.04.001

Zhang, H., Lu, J., Jiao, Y., Chen, Q., Li, M., Wang, Z., et al. (2018). Aspirin Inhibits Natural Killer/T-Cell Lymphoma by Modulation of VEGF Expression and Mitochondrial Function. *Front. Oncol.* 8:679. doi: 10.3389/fonc.2018.00679

Zhang, X., Feng, H., Li, Z., Guo, J., and Li, M. (2018). Aspirin is Involved in the Cell Cycle Arrest, Apoptosis, Cell Migration, and Invasion of Oral Squamous Cell Carcinoma. *Int. J. Mol. Sci.* 19:2029. doi: 10.3390/ijms19072029

Zhang, W. J., Niu, J. W., Ma, Y. C., Yang, X. W., Cao, H. X., Guo, H. G., et al. (2020). The Synergistic Antitumor Activity of Chidamide in Combination with Bortezomib on Gastric Cancer. *Onco Targets Ther.* 13, 3823–3837. doi: 10.2147/ott.s240721

Zhang, Y., Yang, X., Ge, X. H., and Zhang, F. Y. (2019). Puerarin attenuates neurological deficits via Bcl-2/Bax/cleaved caspase-3 and Sirt3/SOD2 apoptotic pathways in subarachnoid hemorrhage mice. *Biomed. Pharmacother.* 109, 726–733. doi: 10.1016/j.biopha.2018.10.161

Zhou, J. N., Zhang, C. J., Sui, X. X., Cao, S. X., Tang, F., Sun, S. H., et al. (2018). Histone deacetylase inhibitor chidamide induces growth inhibition and apoptosis in NK/T lymphoma cells through ATM-Chk2-p53-p21 signalling pathway. *Invest. New Drugs* 36, 571–580. doi: 10.1007/s10637-017-0552-y

Conflict of Interest: The authors declare that the research was conducted in the absence of any commercial or financial relationships that could be construed as a potential conflict of interest.

Publisher's Note: All claims expressed in this article are solely those of the authors and do not necessarily represent those of their affiliated organizations, or those of the publisher, the editors and the reviewers. Any product that may be evaluated in this article, or claim that may be made by its manufacturer, is not guaranteed or endorsed by the publisher.

frontiers in Cell and Developmental Biology

ORIGINAL RESEARCH
published: 09 September 2021
doi: 10.3389/fcell.2021.695225

MCL-1 Inhibition Overcomes Anti-apoptotic Adaptation to Targeted Therapies in B-Cell Precursor Acute Lymphoblastic Leukemia

*Albert Manzano-Muñoz[1], Clara Alcon[1], Pablo Menéndez[2,3], Manuel Ramírez[4], Felix Seyfried[5], Klaus-Michael Debatin[5], Lüder H. Meyer[5], Josep Samitier[1,6,7] and Joan Montero[1]**

[1] Institute for Bioengineering of Catalonia (IBEC), Barcelona Institute of Science and Technology (BIST), Barcelona, Spain, [2] Stem Cell Biology, Developmental Leukemia and Immunotherapy, Josep Carreras Leukemia Research Institute-Campus Clinic, Department of Biomedicine, School of Medicine, University of Barcelona, Barcelona, Spain, [3] Centro de Investigación Biomédica en Red de Cáncer (CIBERONC), Instituto de Salud Carlos III (ISCIII), Institució Catalana de Recerca i Estudis Avançats (ICREA), Barcelona, Spain, [4] Department of Pediatric Hematology and Oncology, Niño Jesús University Children's Hospital, Madrid, Spain, [5] Department of Pediatrics and Adolescent Medicine, Ulm University Medical Center, Ulm, Germany, [6] Department of Electronics and Biomedical Engineering, Faculty of Physics, University of Barcelona, Barcelona, Spain, [7] Networking Biomedical Research Center in Bioengineering, Biomaterials and Nanomedicine (CIBER-BBN), Madrid, Spain

OPEN ACCESS

Edited by:
Tugba Bagci-Onder, Koç University, Turkey

Reviewed by:
Elodie Lafont, INSERM U1242 Laboratoire COSS, France
Triona Ni Chonghaile, Royal College of Surgeons in Ireland, Ireland

***Correspondence:**
Joan Montero
jmontero@ibecbarcelona.eu

Specialty section:
This article was submitted to Cell Death and Survival, a section of the journal Frontiers in Cell and Developmental Biology

Received: *14 April 2021*
Accepted: *20 August 2021*
Published: *09 September 2021*

Citation:
Manzano-Muñoz A, Alcon C, Menéndez P, Ramírez M, Seyfried F, Debatin K-M, Meyer LH, Samitier J and Montero J (2021) MCL-1 Inhibition Overcomes Anti-apoptotic Adaptation to Targeted Therapies in B-Cell Precursor Acute Lymphoblastic Leukemia. Front. Cell Dev. Biol. 9:695225. doi: 10.3389/fcell.2021.695225

Multiple targeted therapies are currently explored for pediatric and young adult B-cell precursor acute lymphoblastic leukemia (BCP-ALL) treatment. However, this new armamentarium of therapies faces an old problem: choosing the right treatment for each patient. The lack of predictive biomarkers is particularly worrying for pediatric patients since it impairs the implementation of new treatments in the clinic. In this study, we used the functional assay dynamic BH3 profiling (DBP) to evaluate two new treatments for BCP-ALL that could improve clinical outcome, especially for relapsed patients. We found that the MEK inhibitor trametinib and the multi-target tyrosine kinase inhibitor sunitinib exquisitely increased apoptotic priming in an NRAS-mutant and in a *KMT2A*-rearranged cell line presenting a high expression of FLT3, respectively. Following these observations, we sought to study potential adaptations to these treatments. Indeed, we identified with DBP anti-apoptotic changes in the BCL-2 family after treatment, particularly involving MCL-1 – a pro-survival strategy previously observed in adult cancers. To overcome this adaptation, we employed the BH3 mimetic S63845, a specific MCL-1 inhibitor, and evaluated its sequential addition to both kinase inhibitors to overcome resistance. We observed that the metronomic combination of both drugs with S63845 was synergistic and showed an increased efficacy compared to single agents. Similar observations were made in BCP-ALL *KMT2A*-rearranged PDX cells in response to sunitinib, showing an analogous DBP profile to the SEM cell line. These findings demonstrate that rational sequences of targeted agents with BH3 mimetics, now extensively explored in clinical trials, may improve treatment effectiveness by overcoming anti-apoptotic adaptations in BCP-ALL.

Keywords: pediatric leukemia, targeted therapies, resistance, apoptosis, BH3 mimetics

INTRODUCTION

Acute lymphoblastic leukemia (ALL) is characterized by uncontrolled growth of lymphoid cells and it accounts for 25% of all pediatric cancers (Howlader et al., 2015). Three out of four cases of pediatric ALL are caused by B-cell precursors, also named BCP-ALL (Schwab and Harrison, 2018). BCP-ALL diagnosed patients are typically treated with a chemotherapeutic combination of vincristine, asparaginase, a corticosteroid (prednisone or dexamethasone) and an anthracycline (doxorubicin or daunorubicin), and most patients achieve a complete remission (PDQ Pediatric Treatment Editorial Board, 2002). Despite this outstanding treatment effectiveness, around 15–20% of patients relapse (Locatelli et al., 2012) causing an overall survival rate of 90% (O'Brien et al., 2018). And because of its high incidence this type of tumor is still the deadliest pediatric cancer. Relapsed and refractory patients (R/R) that fail to achieve a complete remission, present highly resistant tumors forcing clinicians to use more aggressive and highly toxic treatments (Oskarsson et al., 2018). Even those patients that are cured face long-term secondary effects including mental problems, functional impairment, cardiotoxicity and increased morbidity (Mody et al., 2008). There is a clear need for new treatments to enhance tumor elimination while reducing lasting toxicity.

Important efforts have been made to identify and characterize oncogenic molecular targets to block them and impair tumor growth and progression. Since the first successes treating pediatric ALL patients using folic acid antagonists achieved by Sydney Farber in the late 1940s (Miller, 2006), a myriad of compounds targeting multiple proteins have been explored in clinical trials. The first and most successful targeted therapy approved for hematological malignancies was imatinib for adult chronic myelogenous leukemia (Deininger, 2008). Interestingly, imatinib targets the BCR-ABL fusion protein that is also present in the Philadelphia chromosome-positive (Ph +) B-cell acute lymphoblastic leukemia (B-ALL) subtype. Clinical trials evaluating imatinib and dasatinib for pediatric and young adult Ph + B-ALL showed improvement in treatment response (Biondi et al., 2012; Gore et al., 2018). Besides BCR-ABL fusion protein, JAK/STAT pathway proteins, FLT3 receptor, MAPK pathway proteins, precursor-B-cell receptor (pre-BCR) or the ubiquitin-proteasome system have been proposed as potential targets for different B-ALL subtypes, increasing the armamentarium of potential targeted therapies for this disease (Kuhlen et al., 2019).

Identifying new effective treatments for pediatric cancer is challenging. If these therapies are not correctly assigned, there is a risk to provoke undesired secondary effects. Precision medicine aims to correctly assign effective treatments to every patient based on molecular characterization of the tumor (Jameson and Longo, 2015). Its successful implementation will lead to more effective therapeutic regimes and reduce side effects (Mathur and Sutton, 2017). Genetic analyses are the most common strategy used to identify cancer patients that would benefit from targeted therapies (Malone et al., 2020). However, the pediatric population presents a low number of mutations compared to adult population, making difficult to identify predictive biomarkers (Savary et al., 2020). In contrast, functional assays overcome these drawbacks by directly exposing patient-isolated tumor cells to different treatment options and measuring their effectiveness (Howard et al., 2017). Yet, this approach presents a major limitation: primary cells rapidly decay, lose their viability and experience phenotypic changes, preventing their use in prolonged assays (Meijer et al., 2017). In this regard, the functional assay dynamic BH3 profiling (DBP) (Montero et al., 2015) can identify effective anti-cancer treatments in less than 24 h directly on patient samples.

Most anti-cancer agents engage cell death by apoptosis, a process regulated by the BCL-2 family of proteins. Inside this family, BAX and BAK are considered effector members and once activated, oligomerize to form pores and induce the Mitochondrial Outer Membrane Permeabilization (MOMP) which represents the point of no return for the apoptotic process (Wei et al., 2001) and the cell commitment to die (Letai, 2011). MOMP induces the release of cytochrome c (and other proteins) from the mitochondria into the cytosol, and its binding to APAF-1 and caspase-9 form the apoptosome, which activates downstream effector caspases and executes apoptosis. Effector proteins are activated by proteins presenting a unique BCL-2 homology (BH) domain, known as BH3-only activator proteins (BIM, BID, and PUMA). The anti-apoptotic BCL-2 family proteins (BCL-2, BCL-xL, MCL-1, BCL-w, and BFL-1) can inhibit both effectors and activator members, hence protecting cells from apoptosis. A fourth subgroup of BCL-2 family proteins, the sensitizers – that include BAD, HRK and NOXA among others – exert a pro-apoptotic effect by specifically inhibiting the anti-apoptotic proteins (Letai et al., 2002).

Dynamic BH3 profiling uses synthetic peptides that mimic the BH3 domain of the pro-apoptotic BH3-only, with a similar effect as the full-length protein. It uses these peptides to measure how close cells are to commit apoptosis, or how "primed" are for death, after a short incubation with the treatment. DBP has been extensively used to identify effective anti-cancer treatments in cell lines, patient-derived xenografts (PDX) and directly on patient-isolated cells from different types of cancer (Montero et al., 2015, 2017, 2019; Wu et al., 2015; Townsend et al., 2016; Deng et al., 2017; Alcon et al., 2020) with an excellent predictive capacity. Interestingly, using sensitizer-analog BH3 peptides, DBP can identify the anti-apoptotic protein used by cancer cells to survive therapy (Frenzel et al., 2009; Montero and Letai, 2018). In fact, most cytogenetic abnormalities found in BCP-ALL regulate anti-apoptotic BCL-2 proteins. For example, the BCR-ABL fusion protein upregulates BCL-2 and ETV6/RUNX1 promotes BCL-xL overexpression (Brown et al., 2017). Hereof, BH3 mimetics, anti-apoptotic inhibitors widely explored in clinical trials, can be used to overcome this therapy-acquired resistance. In fact, it has been demonstrated in ALL that combining standard-of-care treatment with BH3 mimetics can greatly increase efficacy (Ni Chonghaile et al., 2014; Iacovelli et al., 2015; Khaw et al., 2016; Seyfried et al., 2019). But the key question remains unsolved: how and when to better utilize them in the clinic.

Here, we use DBP to identify new effective therapeutic strategies for pediatric and adolescent BCP-ALL. We tested two promising targeted therapies, trametinib (MEK inhibitor)

and sunitinib (multi-target tyrosine kinase inhibitor), currently explored in pre-clinical studies. We found that both caused an MCL-1 dependence to protect BCP-ALL cells from apoptotic cell death and that its inhibition with a BH3 mimetic significantly enhanced leukemia cell death. Finally, we were able to observe similar anti-apoptotic adaptations in a pediatric BCP-ALL PDX, demonstrating its potential use in the clinic.

MATERIALS AND METHODS

Cell Lines and Treatments

NALM-6 and SEM cell lines were kindly provided by Prof. PM laboratory at the Josep Carreras Leukaemia Research Institute. Both cell lines were cultured in RPMI 1640 medium (31870, Thermo Fisher, Gibco, Paisley, Scotland) with 10% of heat-inactivated fetal bovine serum (10270, Thermo Fisher, Gibco), 1% of L-glutamine (25030, Thermo Fisher, Gibco) and 1% of penicillin/streptomycin (15140, Thermo Fisher, Gibco). Cells were maintained inside a humidified incubator at 37°C and 5% of CO_2. Imatinib, dasatinib, sunitinib, trametinib, ibrutinib and ruxolitinib were purchased at SelleckChem (Munich, Germany) and ABT-199, A-1331852 and S63845 were purchased at MedChemExpress (Monmouth Junction, NJ, United States). These reagents were diluted in dimethyl sulfoxide (DMSO) (D8418, Sigma-Aldrich, Saint Louis, MO, United States) and added to the culture media at the indicated concentration and incubation time for every experiment.

Cell Death Assay

After treatment, cells were resuspended in staining buffer (100 mM HEPES free acid, 40 mM KCl, 1.4 M NaCl, 7.5 mM $MgCl_2$ and 25 mM $CaCl_2$ at pH 7.4) with Alexa Fluor 647® conjugated Annexin V (640912, BioLegend) and DAPI (62248, Thermo Fisher). Cells were analyzed with a Gallios flow cytometer (Beckman Coulter, Nyon, Switzerland) and results were analyzed with FlowJo software to quantify viable cells (Annexin V and DAPI negative events). Results were represented as the mean of %Cell death (100-%viable cells) of at least three independent experiments.

Dynamic BH3 Profiling

Dynamic BH3 profiling (DBP) was performed as previously described (Ryan et al., 2016; Montero et al., 2019; Alcon et al., 2020). After treatment, cells were stained using the viability marker Zombie Violet (423113, BioLegend, Koblenz, Germany) for 10 min at room temperature, washed with PBS and resuspended in 330 μL of MEB buffer (150 nM mannitol, 10 mM HEPES-KOH pH 7.5, 150 mM KCl, 1 mM EGTA, 1 mM EDTA, 0.1% BSA and 5 mM succinate). In parallel, peptide solutions were prepared using MEB buffer with 0.002% of digitonin (D141, Sigma-Aldrich) and 12 different peptide solutions with final concentrations of 25 μM of alamethicin (BML-A150-0005, Enzo Life Sciences, Lörrach, Germany), 10 μM, 3 μM, 1 μM, 0.3 μM, 0.1 μM, 0.03 μM, and 0.01 μM of BIM BH3 peptide, 0.1 μM of BAD BH3 peptide, 100 μM of HRK BH3 peptide, 10 μM of MS1 BH3 peptide and a DMSO only control. A 25 μL of cells was added to 25 μL of each peptide solution in a 96-well plate (3795, Corning, Madrid, Spain) and incubated at room temperature for 1 h. After this incubation, cells were fixed with 25 μL of an 8% paraformaldehyde solution for 15 min and neutralized with 50 μL of N2 buffer (1.7 M tris base, 1.25 M glycine at pH 9.1). Finally, 25 μL of intracellular staining buffer (1% Tween20, 5% BSA in PBS) with 1:1,000 dilution of the cytochrome C antibody (Alexa Fluor® 647 anti-Cytochrome c—6H2.B4, 612310, BioLegend) was added and plates were incubated overnight at 4°C. Results were analyzed using a Sony flow cytometer (SONY SA3800, Surrey, United Kingdom) and processed with FlowJo to quantify cytochrome c release (%priming). Δ%priming stands for the difference of %priming between non-treated cells and treated cells for every specific peptide. All results are represented as the mean of at least three independent experiments.

Protein Extraction

After treatment, cells were collected and washed with PBS. Then, cells were resuspended in RIPA buffer [150 mM NaCl, 5 mM EDTA, 50 mM Tris–HCl pH = 8, 1% Triton X-100, 0.1% SDS, EDTA-free Protease Inhibitor Cocktail (4693159001, Roche, MannKind, Germany)] and lysed for 30 min on ice following centrifugation at 4°C for 10 min at 16,000*g*. Protein in the supernatant was quantified using Pierce™ BCA Protein Assay Kit (23227, Thermo Fisher) and stored at −20°C.

Immunoprecipitations

Lysates were obtained following the protein extraction protocol but using immunoprecipitation (IP) lysis buffer (150 mM NaCl, 10 mM Hepes, 2 mM EDTA, 1% Triton X-100, 1.5 mM $MgCl_2$, 10% glycerol and EDTA-free Protease Inhibitor Cocktail (4693159001, Roche, MannKind, Germany). Again, the protein extracted was quantified with Pierce™ BCA Protein Assay Kit and stored at −20°C. Equivalent amount of protein was incubated at 4°C overnight with magnetic beads (161-4021, Bio-Rad, Madrid, Spain) previously conjugated to 5 μg of rabbit anti-MCL-1 antibody (CST94296, Cell Signaling, Leiden, Netherlands) or 5 μg of rabbit-IgG antibody (CST2729, Cell Signaling). A 30 μL of protein for each condition was stored at −20°C as the input fraction. After incubation, tubes were magnetized to obtain the binding fraction. The supernatant was extracted and stored at −20°C as the unbound fraction. The binding fraction was cleaned with PBS-T (PBS with 0.1% Tween 20) and resuspended in 40 μL of 4× Laemmli sample buffer (161-0747, Bio-Rad), then heated at 70°C to allow separation between the target protein and the magnetic beads-antibody complex. The sample was magnetized again and the supernatant containing the pulled-down proteins was stored at −20°C as IP fractions.

Immunoblotting

An equal amount of protein was prepared in 4× Laemmli buffer (161-0747, Bio-Rad) and heated at 96°C for 10 min. The sample was loaded in an SDS-PAGE gel (456-1025, Bio-Rad) and proteins were separated for 2 h. Then, proteins were transferred to a PVDF membrane (10600023, Amersham Hybond, Pittsburgh, PA, United States) at 55V for 2 h at 4°C. The membrane was blocked with 5% dry milk in TBS-T (50 mM Tris–HCl pH = 7.5, 150 mM NaCl and 1% Tween20) for 1 h and washed with

TBS-T. After blocking, the membrane was probed overnight at 4°C in TBS-T with 3%BSA and 1:1,000 dilution of the primary antibody against the protein of interest: rabbit anti-BCL-2 (CST4223, Cell Signaling), rabbit anti-BCL-xL (CST2764, Cell Signaling), rabbit anti-MCL-1 (CST5453, Cell Signaling), rabbit anti-BIM (CST2933, Cell Signaling), rabbit anti-BAX (CST2772, Cell signaling), rabbit anti-BAK (CST12105, Cell signaling), phospho-p44/42 MAPK (Erk1/2) (Thr202/Thr204) (CST4370, Cell signaling), phospho-BIM (Ser69) (CST4585, Cell signaling) and rabbit anti-Actin (CST4970, Cell Signaling) followed by 1 h at room temperature with 1:3,000 of anti-rabbit IgG HRP-linked secondary antibody (CST7074, Cell Signaling). When necessary, membranes were stripped using mild stripping buffer (0.1 M glycine pH 2.5 and 2% SDS) for two cycles of 20 min at 50°C and extensively washed with TBS (50 mM Tris–HCl pH = 7.5 and 150 mM NaCl). Membranes were developed using Clarity ECL Western substrate (1705060, Bio-Rad) in a LAS4000 imager (GE Healthcare Bio-Sciences AB, Uppsala, Sweden). Bands were quantified using ImageJ software to measure the integrated optical density.

Precursor BCP-ALL PDX Model Generation

The primary leukemia specimen was obtained from peripheral blood of an infant patient with newly diagnosed pro-B ALL after informed written consent with the legal guardians and in accordance with the institution's ethical review board. Xenograft cells were established by intravenous injection of ALL cells into female NOD/SCID mice (NOD.CB17-Prkdcscid, Charles River) as described earlier (Meyer et al., 2011; Seyfried et al., 2019). Animal experiments were approved by the appropriate authority (Tierversuch Nr. 1260, Regierungspräsidium Tübingen).

DBP With PDX Cells

After treatment, cells were stained using the viability marker Zombie Violet (423113, BioLegend, Koblenz, Germany) for 10 min on ice, followed by staining for 30 min on ice with 1:200 dilution of Alexa Fluor® 488 anti-human CD45 antibody (368536, BioLegend) and PE anti-human CD19 antibody (392506, BioLegend) in TBS with 10%FBS. Then, cells were washed with PBS and resuspended in 330 μL of MEB buffer. After this, DBP was done as explained in point 2.3.

Statistical Analysis

For the ROC curve analysis, data sets were separated as responders (cell death >10%) and non-responders (cell death <10%) and their corresponding values of Δ%priming were used to perform the analysis. Synergies were calculated using the Bliss Independent model (Foucquier and Guedj, 2015) were the Combination Index (CI) is calculated as $CI = (CD_A + CD_B - CD_A{*}CD_B)/CD_{combination}$ (CD stands for the percentage of cell death after treatment A, B or the combination of them). Combinations with CI < 1 were considered synergistic. GraphPad Prism 9 was used to perform statistical analyses and generate graphs.

RESULTS

DBP Predicts Cytotoxicity in BCP-ALL Cell Lines

Targeted therapies are currently explored in clinical trials to treat pediatric and young adult BCP-ALL. For example, imatinib and dasatinib for patients presenting the BCR-ABL fusion protein (Ph + cases); trametinib for RAS-mutant patients (Jerchel et al., 2018); sunitinib for cases with overexpression or activating mutations of FLT3 (Brown et al., 2005); ruxolitinib for tumors with constitutive activation of the JAK/STAT signaling pathway (Ding et al., 2018), and ibrutinib when pre-BCR is active (Kim et al., 2017). We sought to explore the effects of these targeted therapies, particularly on the apoptotic pathway, in BCP-ALL.

To explore the pro-apoptotic effect of these therapies, we performed DBP in two pediatric and young adult cell lines, SEM (presenting *KMT2A*-rearrangement and high expression of FLT3) and NALM-6 (NRAS-mutant), respectively (**Figure 1A**). After a short incubation with treatments, we observed that sunitinib induced a high increment in apoptotic priming when exposed to the BIM peptide in the SEM cell line, while trametinib increased it mildly in both cell lines. In contrast, imatinib, dasatinib, ruxolitinib and ibrutinib did not produce any induction of apoptosis (**Figure 1B**). To validate DBP's predictions, we treated these cells for longer timepoints with the same therapies and assessed cell death induction. When comparing Δ%priming and cytotoxicity, similarly to DBP's predictions, we observed that sunitinib in the SEM cell line and trametinib in both cell lines were more efficient than the rest of the therapies inducing cell death (**Figure 1C**). The receiver operating characteristic curve analysis was then used to assess the predictive capacity of DBP on identifying cytotoxic treatments. Our results showed an area under the curve of 1, confirming that DBP is an excellent predictor for this experimental subset (**Supplementary Figure 1A**). Furthermore, Δ%priming strongly correlated with cell death after 3 days of treatment, suggesting that a higher increase in apoptotic priming is an early predictor for cytotoxicity in these cells (**Supplementary Figure 1B**). Altogether, these results demonstrate that DBP could be used as a predictive biomarker to find effective therapies for BCP-ALL.

Trametinib Induces MCL-1 Dependence in NALM-6 Cell Line

As previously mentioned, trametinib was the only targeted therapy tested that showed some efficacy in NALM-6 cells. However, only 20% of the cells were dead after 72 h of treatment, showing a modest efficacy. Multiple studies previously reported cancer cells' adaptation to therapy and the key role of the anti-apoptotic BCL-2 family proteins in their resistance to cell death (Reed et al., 1996; Mansoori et al., 2017; Maji et al., 2018; Wei et al., 2020). We next sought to study the role of these proteins after trametinib treatment on NALM-6. We repeated the DBP analyses, but instead of using the BIM BH3 peptide, we used peptides mimicking the sensitizer members of the BCL-2 family to specifically identify the anti-apoptotic proteins' contribution. In this case, we used a low concentration of the

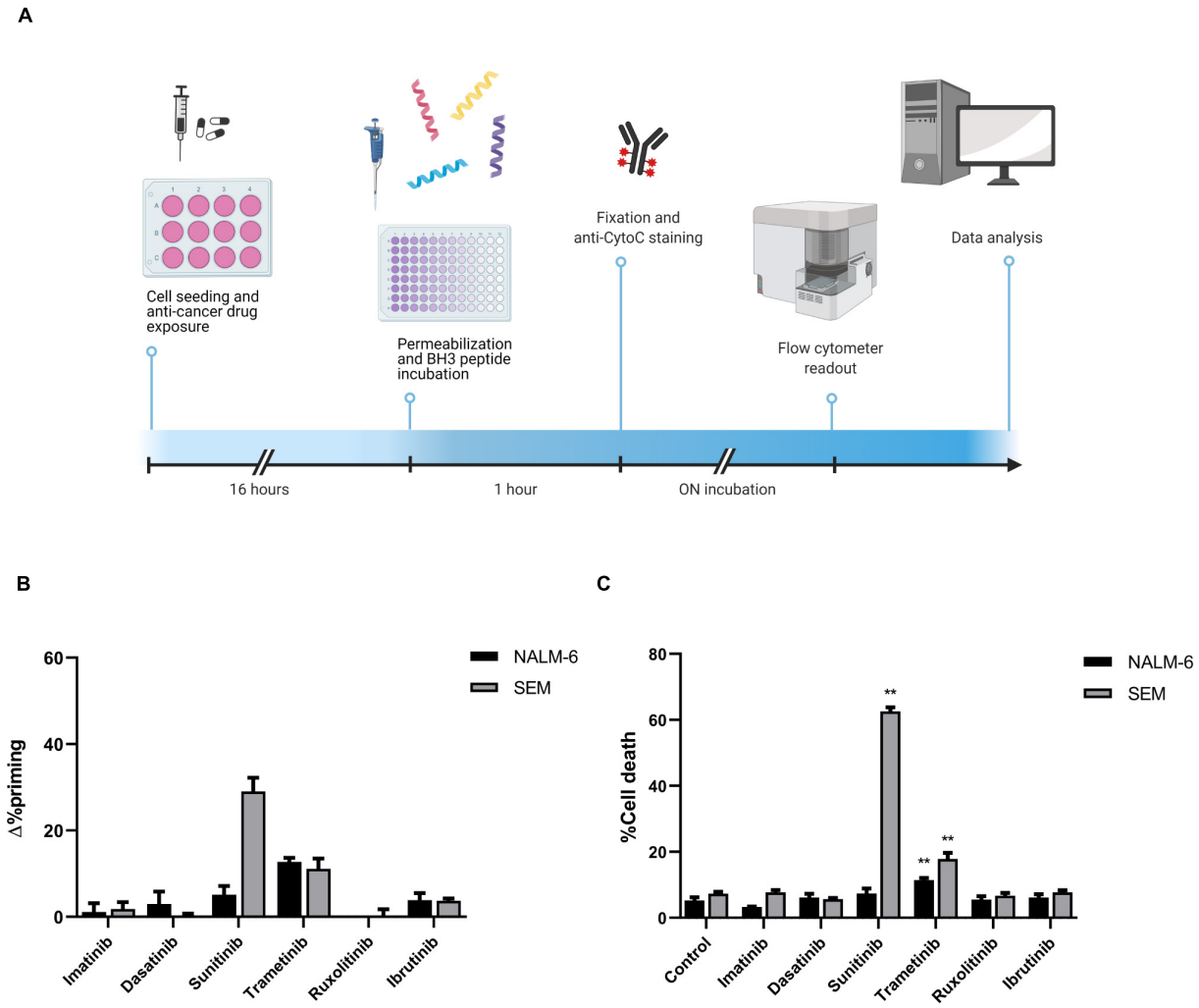

FIGURE 1 | Cytotoxicity induced by targeted drugs in BCP-ALL cell lines. **(A)** Graphical scheme of the DBP technique where cancer cells are plated and treated for 16 h. After drug exposure, cells are plated in 96-well plates and exposed to the different BH3 peptides. After 1 h, cells were fixed and stained with an anti-Cytochrome C antibody overnight. Finally, analyses were performed using a flow cytometer for drug-response curves. Designed with BioRender.com. **(B)** DBP with BIM BH3 peptide after 16 h of incubation with 1,000 nM imatinib, 100 nM dasatinib, 1,000 nM sunitinib, 100 nM trametinib, 100 nM ruxolitinib, and 1,000 nM ibrutinib in NALM-6 and SEM cell lines. Δ%priming stands for the difference in %priming between treatment and control conditions. **(C)** Cytotoxicity expressed as percentage of dead cells after 72 h of treatment with the same therapies assessed by Annexin V/DAPI staining. All results are expressed as the mean ± standard error of the mean (SEM) of at least three biologically independent replicates. Statistical significance was calculated using Student's *t*-test comparing to control condition and considering $*p < 0.05$ and $**p < 0.01$.

BAD BH3 peptide, due to the exquisite sensitivity of both BCP-ALL cell lines to this peptide. In brief, an increase in apoptotic priming after incubation with BAD BH3 peptide would mean that BCL-2 and perhaps BCL-xL are involved in cell resistance to trametinib. Similarly, a gain in apoptotic priming with HRK BH3 would indicate an enhanced BCL-xL contribution, while an MS1 BH3 signal increase would point to MCL-1. When we analyzed NALM-6 treated with trametinib, we observed a positive signal from all sensitizer peptides (**Figure 2A**), suggesting that multiple anti-apoptotic proteins may be involved in cell survival after therapy. We next studied how to overcome this acquired resistance by preincubating the cells with trametinib and then adding specific BH3 mimetics – small molecules that specifically block anti-apoptotic proteins. When we sequentially combined trametinib with the BCL-2 inhibitor ABT-199 (venetoclax), the BCL-xL inhibitor A-1331852 or the MCL-1 inhibitor S63845, we observed enhanced cytotoxicity in all the combinations tested compared to single agent treatment. However, the dual inhibition of MEK and MCL-1 was significantly more effective and clearly synergistic (CI = 0.28), achieving almost a complete elimination of these cells (**Figure 2B**).

We next examined the molecular mechanism behind the strong trametinib and S63845 synergy. The BCL-2 family of proteins is a complex interactome, thus explaining the observed effectiveness could be challenging. It is well reported that trametinib treatment leads to an increase of the activator

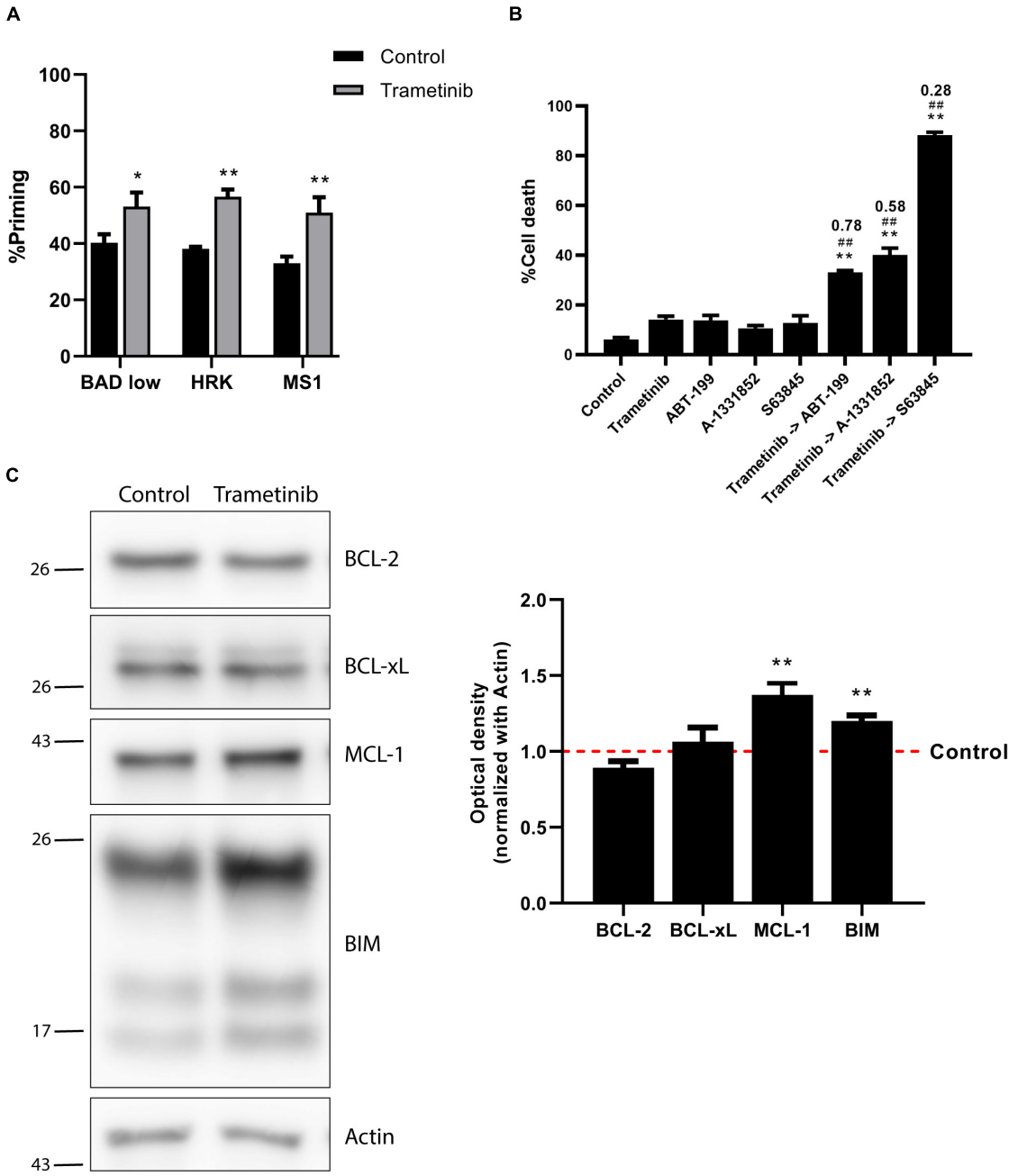

FIGURE 2 | Trametinib synergizes with S63845 in NALM-6 cells, increasing BIM and MCL-1 protein expression. **(A)** DBP results using sensitizer peptides to study anti-apoptotic dependence of BCL-2 and BCL-xL with BAD 0.1 μM, BCL-xL with HRK 100 μM and MCL-1 with MS1 10 μM after 16 h of incubation with trametinib 100 nM in NALM-6 cell line. **(B)** Cytotoxicity was assessed by Annexin V/DAPI staining after 96 h incubation with trametinib 100 nM, ABT-199 100 nM, A-1331852 100 nM and S63845 1,000 nM in NALM-6 cell line. BH3 mimetics in combination with trametinib were added 16 h after treatment. **(C)** Western blot analysis for anti-apoptotic and BIM proteins in NALM-6 cells after 16 h of treatment with trametinib 100 nM. Quantification of optical density for each protein was normalized to actin, and fold-change was calculated comparing to protein expression in the control condition. All results are expressed as the mean ± standard error of the mean (SEM) of at least three biologically independent replicates. Statistical significance was calculated using Student's *t*-test compared to control condition and considering $*p < 0.05$ and $**p < 0.01$. Significance was also calculated comparing combination conditions with both single agents and considering $\#p < 0.05$ and $\#\#p < 0.01$. Combination Index (CI) is indicated on top of every combination where CI < 1 indicates synergy.

BIM, which was also detected in the NALM-6 cell line (**Figure 2C**). MEK inhibition using trametinib caused a reduction of ERK1/2 phosphorylation, that also reduced BIM phosphorylation (**Supplementary Figure 2A**), and avoided its proteasomal degradation (O'Reilly et al., 2009). This increase in BIM causes priming for apoptosis, yet the anti-apoptotic

members of the BCL-2 family could sequester this protein and block the initiation of apoptosis. When we analyzed the anti-apoptotic proteins expression, we found that this MEK inhibitor selectively promoted MCL-1 increase, while BCL-2 and BCL-xL levels remained unchanged (**Figure 2C**). In the case of the effector proteins, BAX was not detected in this cell line and BAK slightly increased after trametinib treatment (**Supplementary Figure 2B**). To confirm that MCL-1 is the main protein binding to BIM, we decided to immunoprecipitate it and study their interaction. MCL-1 was detected in the normal rabbit-IgG unbound fraction but not in the anti-MCL-1 antibody condition (**Figure 3A**), confirming that we were able to effectively pull it down. As previously observed, trametinib treatment caused an increased binding of MCL-1 with BIM, and S63845 caused a marked increase in MCL-1 (**Figure 3B**) due to protein stabilization, as described elsewhere (Kotschy et al., 2016; Li et al., 2019; Montero et al., 2019). As expected, the interaction between MCL-1 and BIM in the IP fraction increased when treated with trametinib compared to control, and was almost completely displaced when S63845 was sequentially added (**Figure 3C**). These findings confirm MCL-1 as the main pro-survival protein and correlate with the observed synergy (**Figure 2B**).

MCL-1 preferentially blocks the increase of BIM protein after trametinib exposure, and when sequentially inhibited with the BH3 mimetic S63845, over 80% of the cells succumbed to this synergistic combination (**Figure 2B**). Interestingly, when we combined trametinib with ABT-199 or A-1331852 only a modest cytotoxic effect was observed (**Figure 2B**). Based on these findings, we conclude that MCL-1 is the main anti-apoptotic protein against trametinib-induced apoptosis in NALM-6, and that BCL-2 and BCL-xL play a minor role.

Combination of Low-Dose Sunitinib and BH3 Mimetics Synergize to Maintain Treatment Efficacy

Secondary effects resulting from anti-cancer therapy are particularly threating for the pediatric population

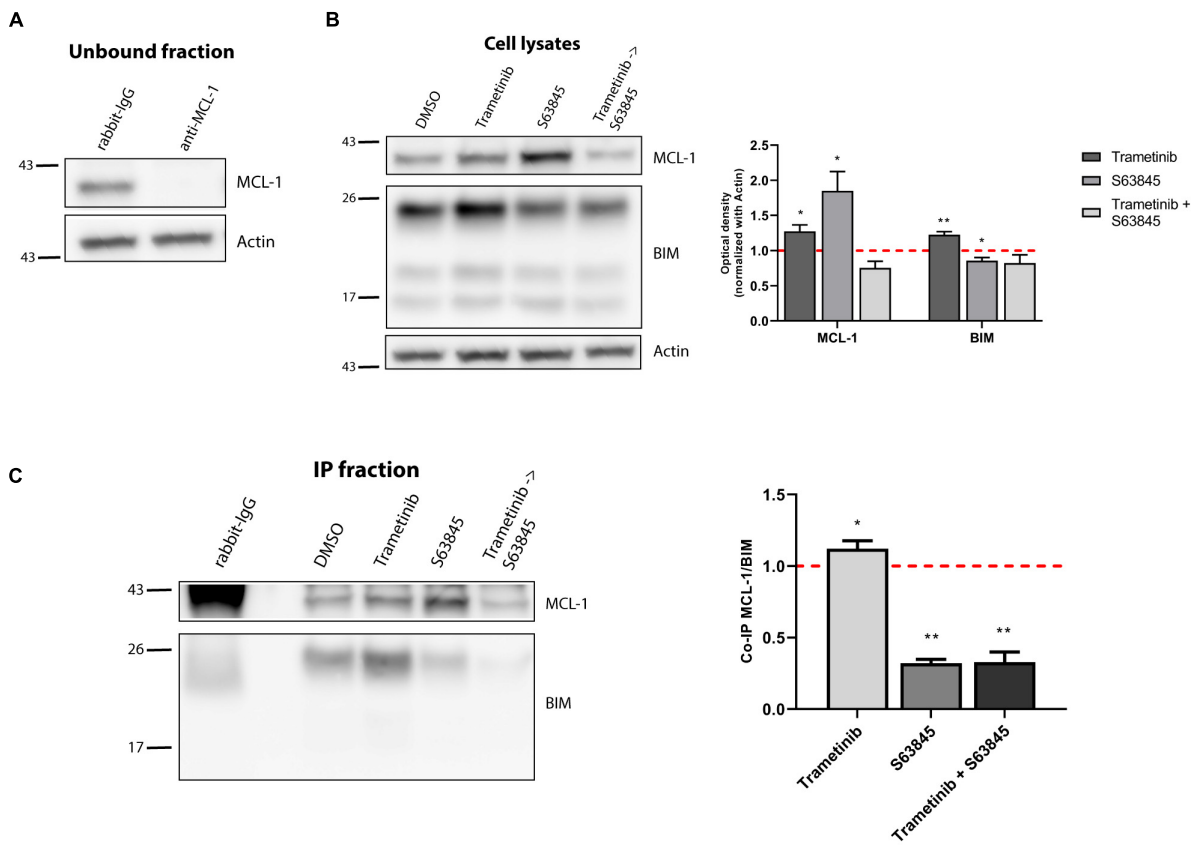

FIGURE 3 | Synergy of trametinib and S63845 in NALM-6 is explained by an increased interaction between MCL-1 and BIM. **(A)** Western blot analysis of the unbound fraction after MCL-1 immunoprecipitation. **(B)** Immunodetection of MCL-1 and BIM initial expression in cell lysates after 16 h of incubation with trametinib 100 nM, and 2 h of incubation with S63845 1,000 nM in the specified conditions. Quantification of optical density for each protein was normalized to actin and fold-change was calculated comparing to protein expression in the control condition. **(C)** Western blot of the immunoprecipitated fraction was used to study the interaction between MCL-1 and BIM after treatment with trametinib 100 nM and 2 h with S63845 1,000 nM. To quantify this binding, BIM optical density was normalized to MCL-1 optical density and fold-change was calculated comparing to protein expression in the control condition. All results are expressed as the mean ± SEM of at least three biologically independent replicates. Statistical significance was calculated using Student's *t*-test compared to control condition and considering $*p < 0.05$ and $**p < 0.01$.

(Sarosiek et al., 2017). As a result, there is a trend to substitute high-dose single agent treatment for low-dose combinations targeting different vulnerabilities to maximize efficacy and reduce toxicity (Satti, 2009). In this regard, we sought to find a combination with BH3 mimetics that could synergize with sunitinib, currently explored in pre-clinical investigations for adult and pediatric BCP-ALL (Brown et al., 2005; Griffith et al., 2016). In the SEM cell line, sunitinib, administered as a

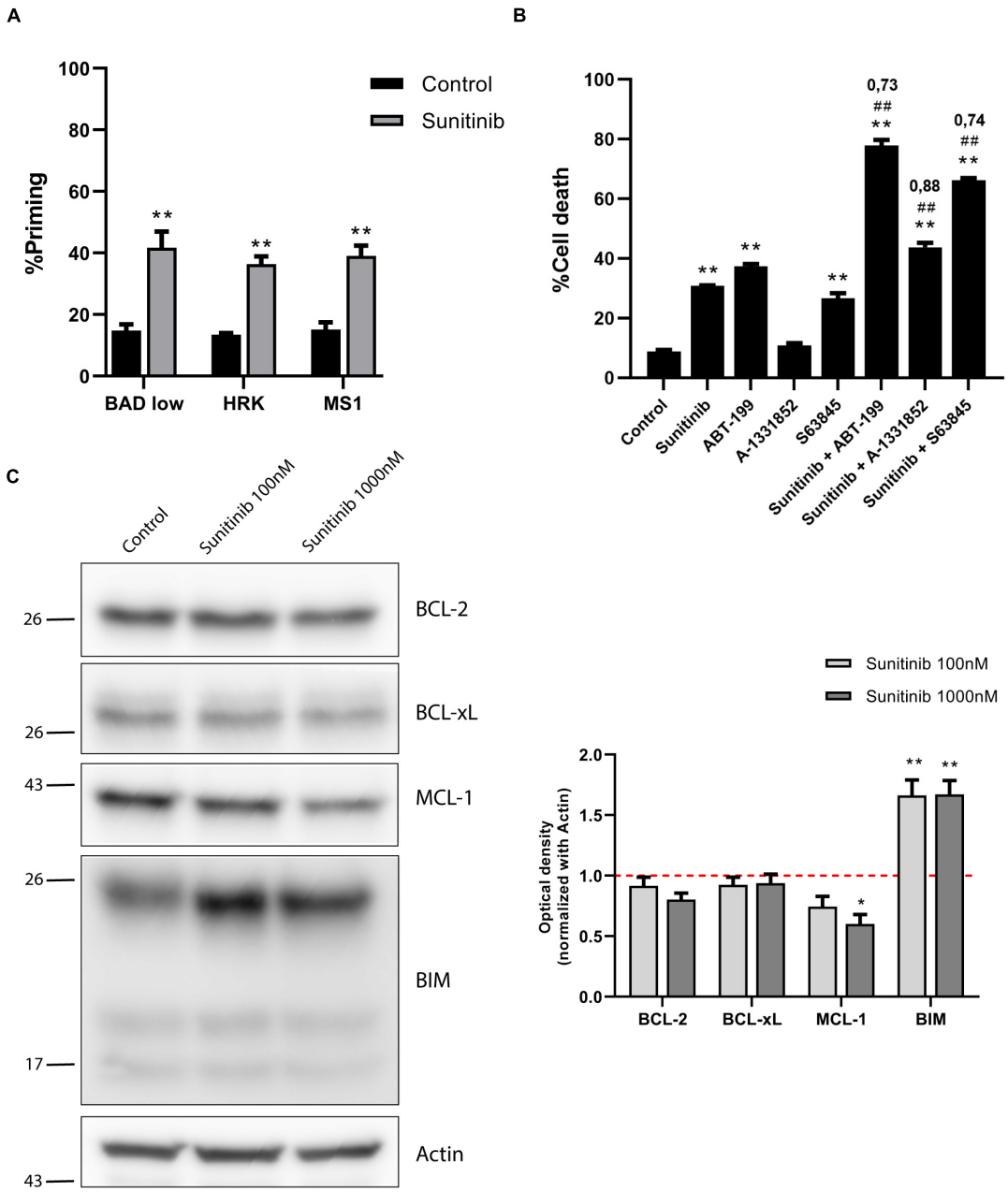

FIGURE 4 | Sunitinib synergizes with ABT-199 and S63845 in SEM cells but anti-apoptotic proteins are downregulated. **(A)** DBP results using sensitizers peptides to study anti-apoptotic dependence of BCL-2 and BCL-xL with BAD 0.1 μM, BCL-xL with HRK 100 μM and MCL-1 with MS1 10 μM after 16 h of incubation with sunitinib 1,000 nM in SEM cell line. **(B)** Cytotoxicity assessed by Annexin V/DAPI staining after 96 h of sunitinib 100 nM, ABT-199 10 nM, A-1331852 100 nM and S63845 100 nM exposure in SEM cells. BH3 mimetics in combination with sunitinib were added 16 h after treatment. **(C)** Western blot analysis for anti-apoptotic and BIM proteins in SEM cells after 16 h of treatment with sunitinib 100 nM and sunitinib 1,000 nM. Quantification of optical density for each protein was normalized to actin, and fold-change was calculated comparing to protein expression in the control condition. All results are expressed as the mean ± SEM of at least three biologically independent replicates. Statistical significance was calculated using Student's *t*-test compared to control condition and considering $^{*}p < 0.05$ and $^{**}p < 0.01$. Significance was also calculated comparing combination conditions with both single agents and considering $\#p < 0.05$ and $\#\#p < 0.01$. CI is indicated on top of every combination where CI < 1 indicates a synergistic combination.

single agent, killed around 60% of the cells (**Figure 1C**), but we aimed to improve its efficacy. By performing DBP analyses, we found that sunitinib incubation, enhanced BAD, HRK and MS1 sensitizer BH3 peptides priming, also suggesting a diversified anti-apoptotic adaptation to this targeted therapy (**Figure 4A**). We then explored reducing 10-fold the concentration of sunitinib, aiming to diminish the potential secondary effects in the clinic, and combining with BH3 mimetics to boost its anti-cancer efficacy. Two BH3 mimetics, ABT-199 and S63845, also induced high levels of cytotoxicity as single agents (**Supplementary Figure 3**), but were innocuous when lowering 10-fold their concentration (**Figure 4B**). To improve the performance of the low-dose sunitinib treatment, we combined it with three BH3 mimetics targeting different anti-apoptotic proteins. As anticipated by DBP, when blocking any of the three anti-apoptotic proteins studied following sunitinib treatment, we found a significant increase in cytotoxicity. This synergistic effect was especially notable when combining it with low-dose ABT-199 (CI = 0.73) or S63845 (CI = 0.74) (**Figure 4B**).

We hypothesized that the molecular mechanism explaining these combinations could be similar to the one found in NALM-6 after trametinib administration. Similarly, we observed a marked increase in BIM expression after sunitinib treatment (**Figure 4C**), as previously described for other types of tumors (Yang et al., 2010). Interestingly, sunitinib also reduced ERK1/2 and BIM phosphorylation (**Supplementary Figure 4A**), suggesting that this inhibitor also affects MAPK pathway, as previously described for other cancer types (Chahal et al., 2010; Fenton et al., 2010). Sunitinib clearly increases apoptotic priming in the SEM cell line; yet, it also activates the anti-apoptotic machinery to neutralize the increase of pro-apoptotic proteins. When we analyzed the BCL-2 family components, in contrast to what we observed in NALM-6, there was a minor decrease in BCL-2 and a significant reduction of MCL-1 expression (**Figure 4C**). No significant changes were observed for BAX and BAK (**Supplementary Figure 4B**). Surprisingly, these results seemed to antagonize the observed synergies with ABT-199 or S63845.

As already mentioned, when exposed to a perturbation like a cytotoxic agent, cancer cells may adapt using anti-apoptotic proteins. However, in this case, a counterintuitive decrease in these proteins was detected. To further elucidate how SEM cells survive sunitinib, we immunoprecipitated MCL-1 (**Figure 5A**) to study its interaction with BIM. As expected, cell lysates showed a significant lower expression of MCL-1 and an increase in BIM after sunitinib treatment, and the stabilization of MCL-1 after S63845 (**Figure 5B**). Interestingly, we observed that sunitinib treatment, even if the overall MCL-1 expression decreased, promoted and increase of its binding to BIM. Then, when MCL-1 was blocked with S63845, BIM was displaced and apoptosis was then restored (**Figure 5C**). These findings explain why the combination of sunitinib and S63845 synergize. Similarly as before, BCL-2 and BCL-xL could not neutralize BIM after MCL-1 inhibition to prevent cell death.

We aimed to further investigate the other significant synergy detected between sunitinib and the BCL-2 inhibitor ABT-199. In contrast to MCL-1, BCL-2 expression slightly decreased after exposing them to sunitinib (**Figure 4C**). We followed the previous approach and immunoprecipitated BCL-2, that was effectively pulled down (**Figure 6A**), and BIM increase was observed after treatment with sunitinib in the cell lysates (**Figure 6B**). BCL-2 was clearly detected in the immunoprecipitated fraction and we could observe an increased binding between BCL-2 and BIM in the SEM cells when treated; and this interaction was displaced when sequentially administering ABT-199 (**Figure 6C**). These results suggest that the increase in BIM expression and the induction of apoptosis after low-dose sunitinib treatment is neutralized preferentially by BCL-2 and MCL-1. When sequentially inhibiting BCL-2 or MCL-1 with the corresponding low-dose BH3 mimetic, BIM is then displaced and the start of the apoptotic process is inevitable – the other anti-apoptotic proteins cannot prevent it.

Pediatric BCP-ALL PDX Recapitulates SEM Anti-apoptotic Adaptation

We next aimed to confirm these anti-apoptotic adaptations using a PDX ALL sample derived from a pediatric BCP-ALL patient with the same *KMT2A*-rearrangement (*KMT2A*/AFF1) present in the SEM cell line (Benito et al., 2015). Following the same experimental conditions, we shortly incubated these cells with the same panel of targeted therapies and studied by DBP the apoptotic induction in the blast population. Similarly as previously described for the cell line, we observed a significant Δ%priming increase with the BIM peptide after sunitinib treatment but a modest increase with trametinib. The other targeted therapies did not produce any perceptible apoptotic changes (**Figure 7**). Interestingly, we also observed an increase in priming with all three sensitizer peptides (BAD, HRK and MS1) after sunitinib exposure and analogous protein expression changes (**Supplementary Figure 5**), suggesting similar anti-apoptotic adaptations as the ones observed in SEM cells (**Figure 7**), which correlates with the akin genetic background.

DISCUSSION

Pediatric and young adult BCP-ALL patients present an overall survival of 90% (Möricke et al., 2010; Pui et al., 2015). However, the minor subset of R/R cases do worse and display a poor outcome to therapy (Einsiedel et al., 2005; Ko et al., 2010), consolidating ALL as the first cause of death for pediatric cancer. Reinduction therapy for the most advanced cases often include the same treatments previously used but at a much higher concentrations (Raetz and Bhatla, 2012); which is not only ineffective but also increases detrimental secondary effects. There is a clear need for new and effective treatments to improve the survival in those patients that do not respond to actual chemotherapy regimens. Multiple targeted therapies have been proposed as potential candidates to treat different subtypes of BCP-ALL that present genetic targetable vulnerabilities (Kuhlen et al., 2019). Chemotherapy relies on the "one size fits all" concept in which all patients are treated in the same way, but the inclusion of targeted therapies requires a personalized medicine approach, where individual patient tumors are first studied to find a driving oncogene to be

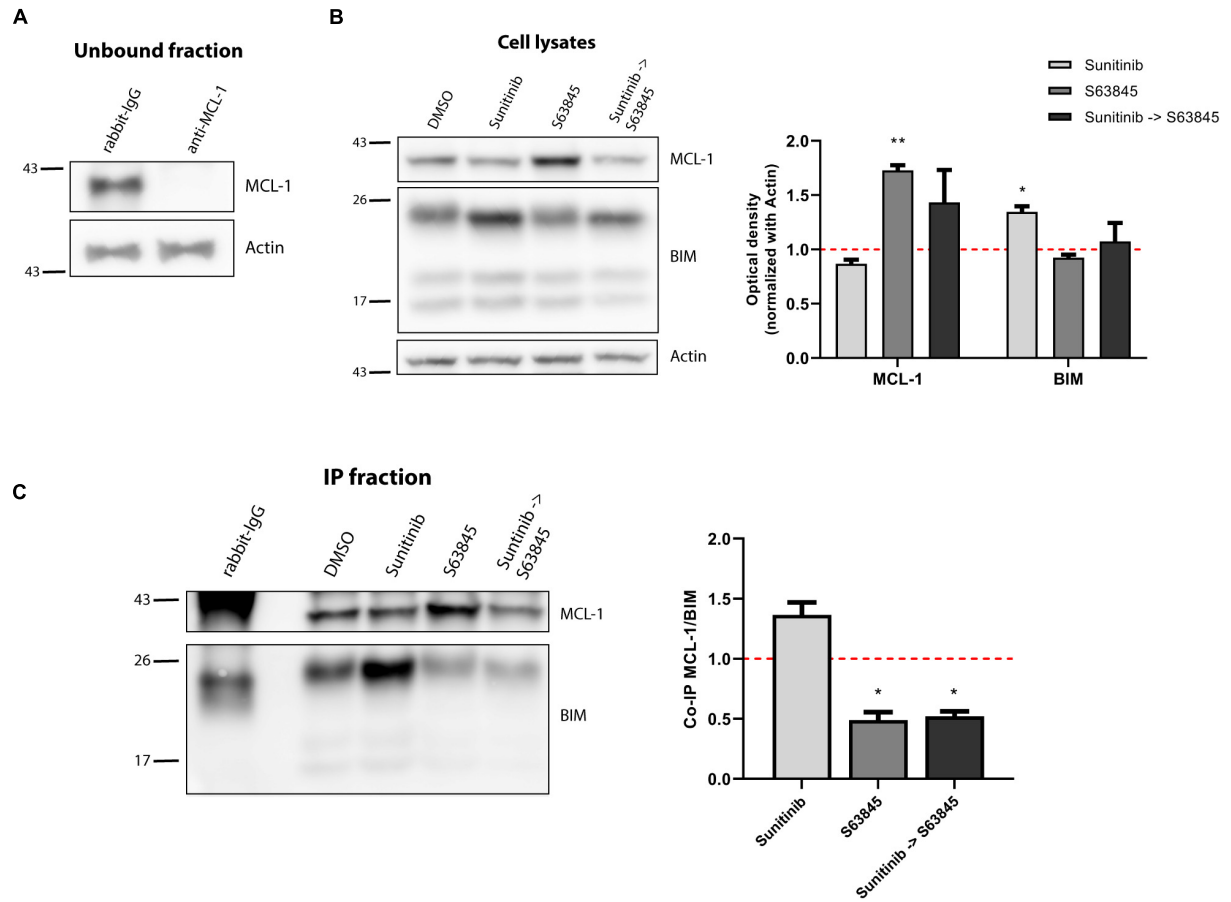

FIGURE 5 | Increased binding of BIM to MCL-1 causes sunitinib and S63845 synergism. **(A)** Western blot analysis of the unbound fraction after MCL-1 immunoprecipitation. **(B)** Immunodetection of MCL-1 and BIM initial expression in cell lysates after 16 h of incubation with sunitinib 100 nM, and 2 h incubation with S63845 100 nM in the specified conditions. Quantification of optical density for each protein was normalized to actin and fold-change was calculated comparing to protein expression in the control condition. **(C)** Western blot of the immunoprecipitated fraction was used to study the interaction between MCL-1 and BIM after treatment with sunitinib 100 nM and 2 h with S63845 100 nM. To quantify this binding, BIM optical density was normalized to MCL-1 optical density and fold-change was calculated comparing to protein expression in the control condition. All results are expressed as the mean ± SEM of at least three biologically independent replicates. Statistical significance was calculated using Student's *t*-test compared to control condition and considering $^{*}p < 0.05$ and $^{**}p < 0.01$.

exploited pharmacologically. Despite recent advances in genetic screening and current efforts to implement precision medicine to treat pediatric patients (Ginsburg and Phillips, 2018), there is a clear complication: childhood cancers present less genetic alterations compared to adults. More precisely, they present a very low frequency of somatic mutations, thus reducing the number of predictive biomarkers and novel targeted therapies (Gröbner et al., 2018).

The lack of genetic biomarkers is boosting functional assays that directly expose cancer cells to selected potential treatment to measure their efficacy. We and others have demonstrated that DBP is a useful technology to screen and identify effective treatments for many types of cancer, including pediatric (Montero et al., 2015, 2017, 2019; Townsend et al., 2016; Pallis et al., 2017; Grundy et al., 2018; Seyfried et al., 2019; Alcon et al., 2020; Foley, 2020). We performed DBP in two BCP-ALL cell lines by exposing them to potential targeted therapies for this type of leukemia. From all the treatments tested, we identified the MEK inhibitor trametinib as the most effective in the young adult NALM-6 cell line. NALM-6 presents a mutation in NRAS, and downstream activation of the MAPK pathway, that may explain its sensitivity to trametinib (Irving et al., 2014). In another pediatric BCP-ALL cell line, named SEM, DBP predicted trametinib and sunitinib effectiveness that was later confirmed by cell death measurements – the latter was particularly active as single agent. Sunitinib has been proposed as a potential candidate to treat FLT3-driven hematological malignancies (Ikezoe et al., 2006), an alteration that is present in the SEM cell line (Brown et al., 2005; Gu et al., 2011). These results demonstrate DBP's capacity to functionally identify effective targeted agents without requiring genetic information, which we believe would help personalize R/R BCP-ALL patients treatment.

Since the approval of venetoclax for chronic lymphocytic leukemia, BH3 mimetics have bloomed as potential treatments for multiple types of cancer, predominantly hematological

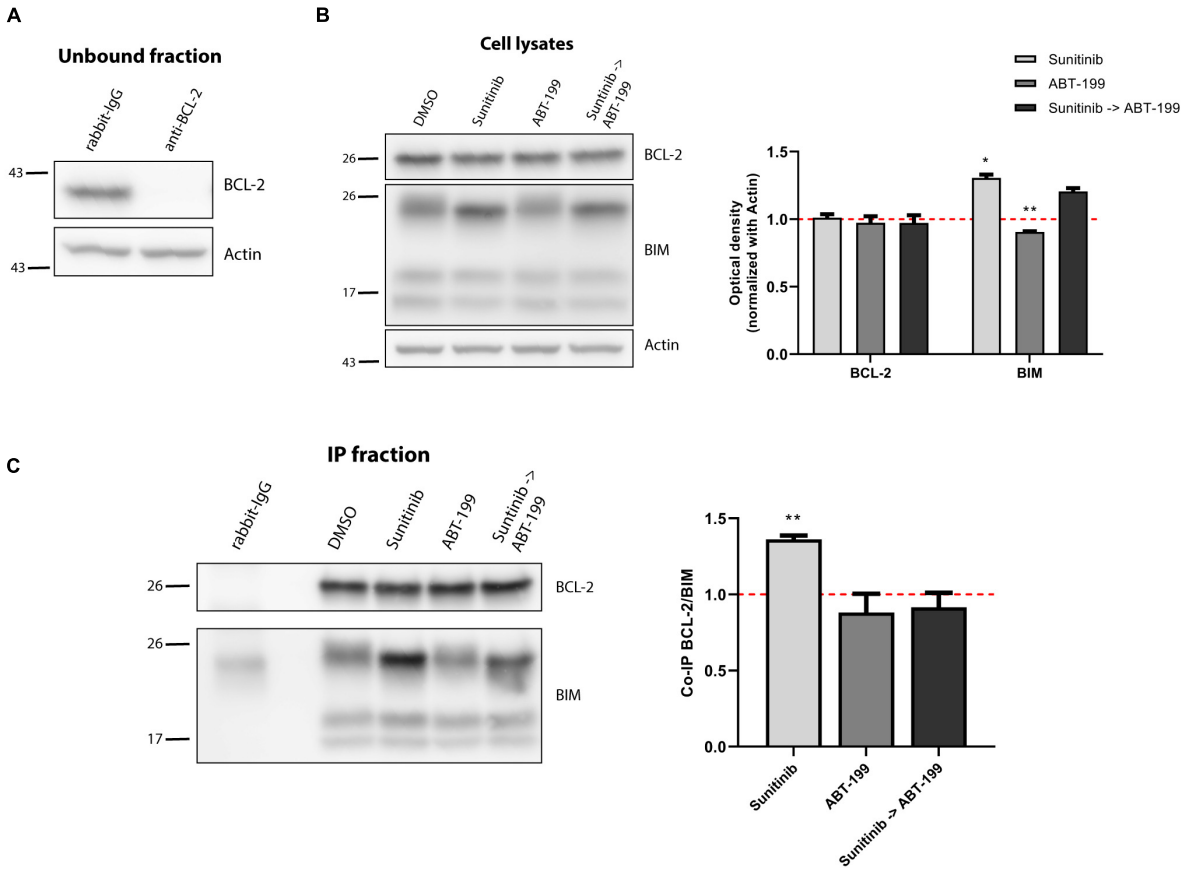

FIGURE 6 | BCL-2 binds to BIM after sunitinib treatment promoting synergy with ABT-199. **(A)** Western blot analysis of the unbound fraction after BCL-2 immunoprecipitation. **(B)** Immunodetection of BCL-2 and BIM initial expression in cell lysates after 16 h of incubation with sunitinib 100 nM, and 4 h incubation with ABT-199 10 nM. Quantification of optical density for each protein was normalized to actin and fold-change was calculated comparing to protein expression in the control condition. **(C)** Western blot of the immunoprecipitated fraction to study the interaction between BCL-2 and BIM after sunitinib 100 nM treatment, and 4 h with ABT-199 10 nM. To quantify this binding, BIM optical density was normalized to BCL-2 optical density and fold-change was calculated comparing to protein expression in the control condition. All results are expressed as the mean ± SEM of at least three biologically independent replicates. Statistical significance was calculated using Student's *t*-test compared to control condition and considering $*p < 0.05$ and $**p < 0.01$.

(Valentin et al., 2018). Despite impressive experimental and clinical results as single agents, increasing evidence showed that BH3 mimetics real potential is enhancing other anti-cancer agents, both conventional chemotherapy and targeted (Montero and Letai, 2018; Oudenaarden et al., 2018; Savona and Wei, 2019; Lin et al., 2020). Numerous studies have demonstrated that cancer cells often rely on anti-apoptotic proteins to acquire resistance to therapy, and BH3 mimetics can effectively block these adaptations (Hata et al., 2015; Maji et al., 2018). However, with these new therapeutic strategies we face the same problem described for targeted therapies: when and how to correctly use these BH3 mimetics in the clinic. We previously described that DBP can identify anti-apoptotic adaptations after treatment and guide effective combinations with BH3 mimetics to boost therapy's potency (Montero et al., 2019; Alcon et al., 2020). When we applied it to BCP-ALL, we found that trametinib as single agent only produced a modest cytotoxic effect on NALM-6 cells, but when sequentially combined with the MCL-1 inhibitor S63845, it reached an almost complete elimination of these cancer cells. Similarly, sunitinib synergized with ABT-199 and S63845 in the SEM cell line, despite reducing 10-fold its concentration. Importantly, all these combinations were anticipated by DBP after only a short incubation with the targeted therapy, demonstrating the utility of this functional assay as predictive biomarker for synergistic combinations of anti-cancer agents with BH3 mimetics.

Anti-apoptotic adaptations in response to therapy may appear by multiple cellular processes. When we analyzed the BCL-2 family of proteins after trametinib and sunitinib treatment, in both cases we observed a significant increase of pro-apoptotic BIM expression, priming cells for apoptosis. Its stabilization after kinase inhibitors use has been previously reported and related to the loss of ERK1/2 phosphorylation (Cragg et al., 2008; Tan et al., 2013; Elgendy et al., 2017), as we confirmed for both agents. Some reports also point out that sunitinib may cause its accumulation by inhibiting STAT3 and AKT (Xin et al., 2009; Yang et al., 2010). Interestingly, changes in anti-apoptotic BCL-2 family members were very different

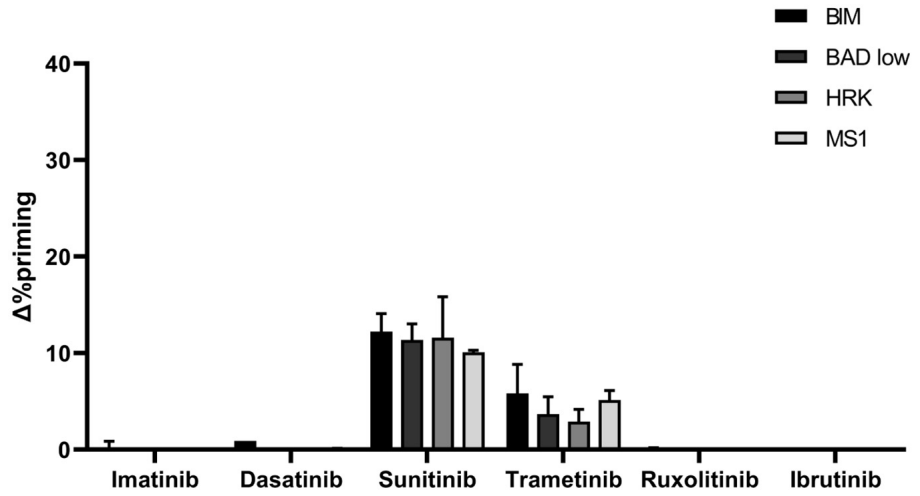

FIGURE 7 | PDX cells presenting *KMT2A* rearrangement show a similar DBP profile as the SEM cells. DBP with BIM BH3, BAD BH3, HRK BH3, and NOXA BH3 peptides after 16 h of incubation with 1,000 nM imatinib, 100 nM dasatinib, 1,000 nM sunitinib, 100 nM trametinib, 100 nM ruxolitinib and 1,000 nM ibrutinib in PDX cells. Δ%priming stands for the difference in %priming between treatment and control condition. All results are expressed as the mean ± standard deviation of two technical replicates.

when exposed to both kinase inhibitors. Trametinib increased MCL-1 expression to neutralize BIM, as previously described (Korfi et al., 2016). Although MEK inhibition was reported to enhance BCL-2/xL inhibitors cell death induction in BCP-ALL by Korfi and colleagues, as we also confirmed, as far as we know this is the first time that it is shown that trametinib strongly synergizes with MCL-1 inhibition in this disease. In contrast, sunitinib promoted BIM binding to BCL-2 and MCL-1, despite the overall expression decrease of these pro-survival proteins. Even if the adaptation mechanism was different, we could also overcome it by sequentially adding a BH3 mimetics, venetoclax or S63845, to this targeted agent, demonstrating the therapeutic potential of these molecules. We validated these results using a pediatric BCP-ALL PDX sample obtained from a patient presenting the same *KMT2A* rearrangement as the SEM cell line (Bhimani et al., 2020), detecting similar therapeutic responses. DBP identified sunitinib as the most effective agent inducing apoptotic priming; correlating with the results observed in the SEM cell line, but contrasting to NALM-6 cells that present a different genetic background. Furthermore, we observed similar anti-apoptotic adaptations when exposed to this kinase inhibitor, predicting that low-dose sunitinib combination with ABT-199 or S63845 could enhance the therapeutic effect for this patient. Altogether, these results demonstrate that DBP could be used as companion diagnostic tool to stratify R/R BCP-ALL cases and identify the optimal combination of targeted therapies with BH3 mimetics to maximize anti-cancer efficacy while decreasing undesired secondary effects. Although sunitinib was previously characterized as a potential treatment for BCP-ALL as a FLT3 inhibitor (Griffith et al., 2016), to our knowledge this is the first time that it is described in combination with BH3 mimetics to treat this disease.

In summary, these findings could represent three new potential therapeutic strategies for BCP-ALL. Taking into consideration that venetoclax is already approved for clinical use and that multiple MCL-1 inhibitors are currently explored in clinical trials, we believe that these synergistic combinations that we here describe could likely improve R/R BCP-ALL patient treatment and clinical outcomes.

DATA AVAILABILITY STATEMENT

The raw data supporting the conclusions of this article will be made available by the authors upon request without undue reservation.

ETHICS STATEMENT

The animal study was reviewed and approved by Tierversuch Nr. 1260, Regierungspräsidium Tübingen.

AUTHOR CONTRIBUTIONS

AM-M performed all experiments under supervision of CA and JM. PM provided the cell lines and important advice. FS, K-MD, and LM provided the BCP-ALL PDX cells and related relevant information. MR provided his expertise in the field. JS and JM supervised the work. AM-M and JM wrote the manuscript with the contributions from all authors. All authors contributed to the article and approved the submitted version.

FUNDING

JM acknowledges the Ramon y Cajal Program, Ministerio de Economia y Competitividad (RYC-2015-18357) and the Spanish

National Plan "Retos Investigacion" I + D + i (RTI2018-094533-A-I00) from Ministerio de Ciencia, Innovación y Universidades. This work was supported by the CELLEX foundation and the Networking Biomedical Research Center (CIBER), Spain. CIBER is an initiative funded by the VI National R&D&i Plan 2008–2011, Iniciativa Ingenio 2010, Consolider Program, CIBER Actions, and the Instituto de Salud Carlos III (RD16/0006/0012), with the support of the European Regional Development Fund (ERDF). This work was also partially funded by the CERCA Program and by the Commission for Universities and Research of the Department of Innovation, Universities, and Enterprise of the Generalitat de Catalunya (2017 SGR 1079). FS: Medical Faculty of Ulm University (Clinician Scientist Programme). K-MD and LM: German Research Foundation (DFG, SFB 1074).

ACKNOWLEDGMENTS

We would like to thank to the Cytometry Facility from the University of Barcelona for assistance with flow cytometry experiments and Virginia Rodriguez for helping with the cell lines used in this manuscript.

SUPPLEMENTARY MATERIAL

The Supplementary Material for this article can be found online at: https://www.frontiersin.org/articles/10.3389/fcell.2021.695225/full#supplementary-material

Supplementary Figure 1 | (A) ROC curve analysis using the values of Δ%priming in NALM-6 and SEM cell lines establishing 10% as the cell death threshold for responders and non-responders. **(B)** Correlation between Δ%priming and %cell death analyses.

Supplementary Figure 2 | (A) Western blot analysis of phospho-ERK1/2 and phospho-BIM in NALM-6 cell line after 16 h of treatment with trametinib 100 nM. **(B)** Western blot analysis of BAK and BAX in NALM-6 cell line after 16 h of treatment with trametinib 100 nM. Quantification of optical density for each protein was normalized to actin, and fold-change was calculated comparing to protein expression in the control condition. All results are expressed as the mean ± SEM of at least three biologically independent replicates. Statistical significance was calculated using Student's *t*-test compared to control condition and considering $*p < 0.05$ and $**p < 0.01$.

Supplementary Figure 3 | ABT-199 and S63845 induce cytotoxicity in the SEM cell line. Cytotoxicity expressed as percentage of dead cells after 72 h of treatment with 100 nM ABT-199 and 1,000 nM S63845, as assessed by an Annexin V/DAPI staining. All results are expressed as the mean ± SEM of at least three biologically independent replicates. Statistical significance was calculated using Student's *t*-test compared to control condition and considering $*p < 0.05$ and $**p < 0.01$.

Supplementary Figure 4 | (A) Western blot analysis of phospho-ERK1/2 and phospho-BIM in the SEM cell line after 16 h of treatment with sunitinib 100 nM and 1,000 nM. **(B)** Western blot analysis of BAK and BAX in SEM cell line after 16 h of treatment with sunitinib 100 nM and 1,000 nM. Quantification of optical density for each protein was normalized to actin, and fold-change was calculated comparing to protein expression in the control condition. All results are expressed as the mean ± SEM of at least three biologically independent replicates. Statistical significance was calculated using Student's *t*-test compared to control condition and considering $*p < 0.05$ and $**p < 0.01$.

Supplementary Figure 5 | BCL-2 family of proteins expression in BCP-ALL PDX cells after sunitinib treatment. Western blot analysis for anti-apoptotic and BIM proteins in BCP-ALL PDX cells after 16 h of treatment with sunitinib 100 nM and sunitinib 1,000 nM. Quantification of optical density for each protein was normalized to actin, and fold-change was calculated comparing to protein expression in the control condition.

REFERENCES

Alcon, C., Manzano-Muñoz, A., Prada, E., Mora, J., Soriano, A., Guillén, G., et al. (2020). Sequential combinations of chemotherapeutic agents with BH3 mimetics to treat rhabdomyosarcoma and avoid resistance. *Cell Death Dis.* 11:634. doi: 10.1038/s41419-020-02887-y

Benito, J. M., Godfrey, L., Kojima, K., Hogdal, L., Wunderlich, M., Geng, H., et al. (2015). MLL-rearranged acute lymphoblastic leukemias activate BCL-2 through H3K79 methylation and are sensitive to the BCL-2-specific antagonist ABT-199. *Cell Rep.* 13, 2715–2727. doi: 10.1016/j.celrep.2015.12.003

Bhimani, J., Ball, K., and Stebbing, J. (2020). Patient-derived xenograft models—the future of personalised cancer treatment. *Br. J. Cancer* 122, 601–602. doi: 10.1038/s41416-019-0678-0

Biondi, A., Schrappe, M., De Lorenzo, P., Castor, A., Lucchini, G., Gandemer, V., et al. (2012). Imatinib after induction for treatment of children and adolescents with Philadelphia-chromosome-positive acute lymphoblastic leukaemia (EsPhALL): a randomised, open-label, intergroup study. *Lancet Oncol.* 13, 936–945. doi: 10.1016/S1470-2045(12)70377-7

Brown, L. M., Hanna, D. T., Khaw, S. L., and Ekert, P. G. (2017). Dysregulation of BCL-2 family proteins by leukemia fusion genes. *J. Biol. Chem.* 292, 14325–14333. doi: 10.1074/jbc.R117.799056

Brown, P., Levis, M., Shurtleff, S., Campana, D., Downing, J., and Small, D. (2005). FLT3 inhibition selectively kills childhood acute lymphoblastic leukemia cells with high levels of FLT3 expression. *Blood* 105, 812–820. doi: 10.1182/blood-2004-06-2498

Chahal, M., Xu, Y., Lesniak, D., Graham, K., Famulski, K., Christensen, J. G., et al. (2010). MGMT modulates glioblastoma angiogenesis and response to the tyrosine kinase inhibitor sunitinib. *Neuro. Oncol.* 12, 822–833. doi: 10.1093/neuonc/noq017

Cragg, M. S., Jansen, E. S., Cook, M., Harris, C., Strasser, A., and Scott, C. L. (2008). Treatment of B-RAF mutant human tumor cells with a MEK inhibitor requires Bim and is enhanced by a BH3 mimetic. *J. Clin. Invest.* 118, 3651–3659. doi: 10.1172/JCI35437

Deininger, M. W. (2008). Milestones and monitoring in patients with CML treated with imatinib. *Hematology Am. Soc. Hematol. Educ. Program.* 2008, 419–426. doi: 10.1182/asheducation-2008.1.419

Deng, J., Isik, E., Fernandes, S. M., Brown, J. R., Letai, A., and Davids, M. S. (2017). Bruton's tyrosine kinase inhibition increases BCL-2 dependence and enhances sensitivity to venetoclax in chronic lymphocytic leukemia. *Leukemia* 31, 2075–2084. doi: 10.1038/leu.2017.32

Ding, Y. Y., Stern, J. W., Jubelirer, T. F., Wertheim, G. B., Lin, F., Chang, F., et al. (2018). Clinical efficacy of ruxolitinib and chemotherapy in a child with philadelphia chromosome-like acute lymphoblastic leukemia with GOLGA5-JAK2 fusion and induction failure. *Haematologica* 103, e427–e431. doi: 10.3324/haematol.2018.192088

Einsiedel, H. G., Von Stackelberg, A., Hartmann, R., Fengler, R., Schrappe, M., Janka-Schaub, G., et al. (2005). Long-term outcome in children with relapsed ALL by risk-stratified salvage therapy: results of trial acute lymphoblastic leukemia-relapse study of the berlin-frankfurt-Münster Group 87. *J. Clin. Oncol.* 23, 7942–7950. doi: 10.1200/JCO.2005.01.1031

Elgendy, M., Abdel-Aziz, A. K., Renne, S. L., Bornaghi, V., Procopio, G., Colecchia, M., et al. (2017). Dual modulation of MCL-1 and mTOR determines the response to sunitinib. *J. Clin. Invest.* 127, 153–168. doi: 10.1172/JCI84386

Fenton, M. S., Marion, K. M., Salem, A. K., Hogen, R., Naeim, F., and Hershman, J. M. (2010). Sunitinib inhibits MEK/ERK and SAPK/JNK pathways and increases sodium/iodide symporter expression in papillary thyroid cancer. *Thyroid* 20, 965–974. doi: 10.1089/thy.2010.0008

Foley, J. F. (2020). Revealing the plasma membrane in GPCR signaling. *Sci. Signal.* 13:eaay1451. doi: 10.1126/scisignal.aay1451

Foucquier, J., and Guedj, M. (2015). Analysis of drug combinations: current methodological landscape. *Pharmacol. Res. Perspect.* 3:e00149. doi: 10.1002/prp2.149

Frenzel, A., Grespi, F., Chmelewskij, W., and Villunger, A. (2009). Bcl2 family proteins in carcinogenesis and the treatment of cancer. *Apoptosis* 14, 584–596. doi: 10.1007/s10495-008-0300-z

Ginsburg, G. S., and Phillips, K. A. (2018). Precision medicine: from science to value. *Health Aff.* 37, 694–701. doi: 10.1377/hlthaff.2017.1624

Gore, L., Kearns, P. R., de Martino Lee, M. L., De Souza, C. A., Bertrand, Y., Hijiya, N., et al. (2018). Dasatinib in pediatric patients with chronic myeloid leukemia in chronic phase: results from a phase II trial. *J. Clin. Oncol.* 36, 1330–1338. doi: 10.1200/JCO.2017.75.9597

Griffith, M., Griffith, O. L., Krysiak, K., Skidmore, Z. L., Christopher, M. J., Klco, J. M., et al. (2016). Comprehensive genomic analysis reveals FLT3 activation and a therapeutic strategy for a patient with relapsed adult B-lymphoblastic leukemia. *Exp. Hematol.* 44, 603–613. doi: 10.1016/j.exphem.2016.04.011

Gröbner, S. N., Worst, B. C., Weischenfeldt, J., Buchhalter, I., Kleinheinz, K., Rudneva, V. A., et al. (2018). The landscape of genomic alterations across childhood cancers. *Nature* 555, 321–327. doi: 10.1038/nature25480

Grundy, M., Seedhouse, C., Jones, T., Elmi, L., Hall, M., Graham, A., et al. (2018). Predicting effective pro-apoptotic anti-leukaemic drug combinations using cooperative dynamic BH3 profiling. *PLoS One* 13:e0190682. doi: 10.1371/journal.pone.0190682

Gu, T. L., Nardone, J., Wang, Y., Loriaux, M., Villén, J., Beausoleil, S., et al. (2011). Survey of activated FLT3 signaling in leukemia. *PLoS One* 6:e19169. doi: 10.1371/journal.pone.0019169

Hata, A. N., Engelman, J. A., and Faber, A. C. (2015). The BCL2 family: key mediators of the apoptotic response to targeted anticancer therapeutics. *Cancer Discov.* 5, 475–487. doi: 10.1158/2159-8290.CD-15-0011

Howard, C. M., Valluri, J., and Claudio, P. P. (2017). Functional drug response assay for cancer stem cells in the era of precision medicine. *Transl. Med. Reports* 1, 7–10. doi: 10.4081/tmr.6421

Howlader, N., Noone, A., Krapcho, M., Miller, D., Bishop, K., Altekruse, S., et al. (2015). SEER cancer statistics review. *Natl. Cancer Inst.* Available online at: https://seer.cancer.gov/csr/1975_2017/ (accessed March 29, 2021).

Iacovelli, S., Ricciardi, M. R., Allegretti, M., Mirabilii, S., Licchetta, R., Bergamo, P., et al. (2015). Co-targeting of Bcl-2 and mTOR pathway triggers synergistic apoptosis in BH3 mimetics resistant acute lymphoblastic leukemia. *Oncotarget* 6, 32089–32103. doi: 10.18632/oncotarget.5156

Ikezoe, T., Nishioka, C., Tasaka, T., Yang, Y., Komatsu, N., Togitani, K., et al. (2006). The antitumor effects of sunitinib (formerly SU11248) against a variety of human hematologic malignancies: enhancement of growth inhibition via inhibition of mammalian target of rapamcycin signaling. *Mol. Cancer Ther.* 5, 2522–2530. doi: 10.1158/1535-7163.MCT-06-0071

Irving, J., Matheson, E., Minto, L., Blair, H., Case, M., Halsey, C., et al. (2014). Ras pathway mutations are prevalent in relapsed childhood acute lymphoblastic leukemia and confer sensitivity to MEK inhibition. *Blood* 124, 3420–3430. doi: 10.1182/blood-2014-04-531871

Jameson, J. L., and Longo, D. L. (2015). Precision medicine-personalized, problematic, and promising. *Obstet. Gynecol. Surv.* 70, 612–614. doi: 10.1097/01.ogx.0000472121.21647.38

Jerchel, I. S., Hoogkamer, A. Q., Ariës, I. M., Steeghs, E. M. P., Boer, J. M., Besselink, N. J. M., et al. (2018). RAS pathway mutations as a predictive biomarker for treatment adaptation in pediatric B-cell precursor acute lymphoblastic leukemia. *Leukemia* 32, 931–940. doi: 10.1038/leu.2017.303

Khaw, S. L., Suryani, S., Evans, K., Richmond, J., Robbins, A., Kurmasheva, R. T., et al. (2016). Venetoclax responses of pediatric all xenografts reveal sensitivity of MLL-rearranged leukemia. *Blood* 128, 1382–1395. doi: 10.1182/blood-2016-03-707414

Kim, E., Hurtz, C., Koehrer, S., Wang, Z., Balasubramanian, S., Chang, B. Y., et al. (2017). Ibrutinib inhibits pre-BCR+ B-cell acute lymphoblastic leukemia progression by targeting BTK and BLK. *Blood* 129, 1155–1165. doi: 10.1182/blood-2016-06-722900

Ko, R. H., Ji, L., Barnette, P., Bostrom, B., Hutchinson, R., Raetz, E., et al. (2010). Outcome of patients treated for relapsed or refractory acute lymphoblastic leukemia: a therapeutic advances in childhood leukemia consortium study. *J. Clin. Oncol.* 28, 648–654. doi: 10.1200/JCO.2009.22.2950

Korfi, K., Smith, M., Swan, J., Somervaille, T. C. P., Dhomen, N., and Marais, R. (2016). BIM mediates synergistic killing of B-cell acute lymphoblastic leukemia cells by BCL-2 and MEK inhibitors. *Cell Death Dis.* 7, e2177–e2177. doi: 10.1038/cddis.2016.70

Kotschy, A., Szlavik, Z., Murray, J., Davidson, J., Maragno, A. L., Le Toumelin-Braizat, G., et al. (2016). The MCL1 inhibitor S63845 is tolerable and effective in diverse cancer models. *Nature* 538, 477–482. doi: 10.1038/nature19830

Kuhlen, M., Klusmann, J. H., and Hoell, J. I. (2019). Molecular Approaches to treating pediatric leukemias. *Front. Pediatr* 7:368. doi: 10.3389/fped.2019.00368

Letai, A. (2011). The control of mitochondrial apoptosis by the BCL-2 family. *Apoptosis Physiol. Pathol.* 122, 44–50. doi: 10.1017/CBO9780511976094.005

Letai, A., Bassik, M. C., Walensky, L. D., Sorcinelli, M. D., Weiler, S., and Korsmeyer, S. J. (2002). Distinct BH3 domains either sensitize or activate mitochondrial apoptosis, serving as prototype cancer therapeutics. *Cancer Cell* 2, 183–192. doi: 10.1016/S1535-6108(02)00127-7

Li, Z., He, S., and Look, A. T. (2019). The MCL1-specific inhibitor S63845 acts synergistically with venetoclax/ABT-199 to induce apoptosis in T-cell acute lymphoblastic leukemia cells. *Leukemia* 33, 262–266. doi: 10.1038/s41375-018-0201-2

Lin, V. S., Xu, Z. F., Huang, D. C. S., and Thijssen, R. (2020). Bh3 mimetics for the treatment of b-cell malignancies—insights and lessons from the clinic. *Cancers (Basel)* 12:3353. doi: 10.3390/cancers12113353

Locatelli, F., Schrappe, M., Bernardo, M. E., and Rutella, S. (2012). How i treat relapsed childhood acute lymphoblastic leukemia. *Blood* 120, 2807–2816. doi: 10.1182/blood-2012-02-265884

Maji, S., Panda, S., Samal, S. K., Shriwas, O., Rath, R., Pellecchia, M., et al. (2018). Bcl-2 antiapoptotic family proteins and chemoresistance in Cancer. *Adv. Cancer Res.* 137, 37–75. doi: 10.1016/bs.acr.2017.11.001

Malone, E. R., Oliva, M., Sabatini, P. J. B., Stockley, T. L., and Siu, L. L. (2020). Molecular profiling for precision cancer therapies. *Genome Med.* 12:8. doi: 10.1186/s13073-019-0703-1

Mansoori, B., Mohammadi, A., Davudian, S., Shirjang, S., and Baradaran, B. (2017). The different mechanisms of cancer drug resistance: a brief review. *Adv. Pharm. Bull.* 7, 339–348. doi: 10.15171/apb.2017.041

Mathur, S., and Sutton, J. (2017). Personalized medicine could transform healthcare (Review). *Biomed. Rep.* 7, 3–5. doi: 10.3892/br.2017.922

Meijer, T. G., Naipal, K. A., Jager, A., and Van Gent, D. C. (2017). Ex vivo tumor culture systems for functional drug testing and therapy response prediction. *Future Sci. OA* 3:FSO190. doi: 10.4155/fsoa-2017-0003

Meyer, L. H., Eckhoff, S. M., Queudeville, M., Kraus, J. M., Giordan, M., Stursberg, J., et al. (2011). Early relapse in all is identified by time to leukemia in NOD/SCID mice and is characterized by a gene signature involving survival pathways. *Cancer Cell* 19, 206–217. doi: 10.1016/j.ccr.2010.11.014

Miller, D. R. (2006). A tribute to sidney farber – the father of modern chemotherapy. *Br. J. Haematol.* 134, 20–26. doi: 10.1111/j.1365-2141.2006.06119.x

Mody, R., Li, S., Dover, D. C., Sallan, S., Leisenring, W., Oeffinger, K. C., et al. (2008). Twenty-five-year follow-up among survivors of childhood acute lymphoblastic leukemia: a report from the childhood cancer survivor study. *Blood* 111, 5515–5523. doi: 10.1182/blood-2007-10-117150

Montero, J., Gstalder, C., Kim, D. J., Sadowicz, D., Miles, W., Manos, M., et al. (2019). Destabilization of NOXA mRNA as a common resistance mechanism to targeted therapies. *Nat. Commun.* 10:5157. doi: 10.1038/s41467-019-12477-y

Montero, J., and Letai, A. (2018). Why do BCL-2 inhibitorswork and where should we use them in the clinic? *Cell Death Differ.* 25, 56–64. doi: 10.1038/cdd.2017.183

Montero, J., Sarosiek, K. A., Deangelo, J. D., Maertens, O., Ryan, J., Ercan, D., et al. (2015). Drug-induced death signaling strategy rapidly predicts cancer response to chemotherapy. *Cell* 160, 977–989. doi: 10.1016/j.cell.2015.01.042

Montero, J., Stephansky, J., Cai, T., Griffin, G. K., Cabal-Hierro, L., Togami, K., et al. (2017). Blastic plasmacytoid dendritic cell neoplasm is dependent on BCL2 and sensitive to venetoclax. *Cancer Discov.* 7, 156–164. doi: 10.1158/2159-8290.CD-16-0999

Möricke, A., Zimmermann, M., Reiter, A., Henze, G., Schrauder, A., Gadner, H., et al. (2010). Long-term results of five consecutive trials in childhood acute

lymphoblastic leukemia performed by the ALL-BFM study group from 1981 to 2000. *Leukemia* 24, 265–284. doi: 10.1038/leu.2009.257

Ni Chonghaile, T., Roderick, J. E., Glenfield, C., Ryan, J., Sallan, S. E., Silverman, L. B., et al. (2014). Maturation stage of T-cell acute lymphoblastic leukemia determines BCL-2 versus BCL-XL dependence and sensitivity to ABT-199. *Cancer Discov.* 4, 1074–1087. doi: 10.1158/2159-8290.CD-14-0353

O'Brien, M. M., Seif, A. E., and Hunger, S. P. (2018). Acute lymphoblastic leukemia in children. *Wintrobes Clin. Hematol. Fourteenth Ed.* 373, 4939–5015. doi: 10.1056/nejmra1400972

O'Reilly, L. A., Kruse, E. A., Puthalakath, H., Kelly, P. N., Kaufmann, T., Huang, D. C. S., et al. (2009). MEK/ERK-mediated phosphorylation of bim is required to ensure survival of T and B lymphocytes during mitogenic stimulation. *J. Immunol.* 183, 261–269. doi: 10.4049/jimmunol.0803853

Oskarsson, T., Söderhäll, S., Arvidson, J., Forestier, E., Frandsen, T. L., Hellebostad, M., et al. (2018). Treatment-related mortality in relapsed childhood acute lymphoblastic leukemia. *Pediatr. Blood Cancer* 65:e26909. doi: 10.1002/pbc.26909

Oudenaarden, C. R. L., van de Ven, R. A. H., and Derksen, P. W. B. (2018). Re-inforcing the cell death army in the fight against breast cancer. *J. Cell Sci.* 131:jcs212563. doi: 10.1242/jcs.212563

Pallis, M., Burrows, F., Ryan, J., Grundy, M., Seedhouse, C., Abdul-Aziz, A., et al. (2017). Complementary dynamic BH3 profiles predict co-operativity between the multi-kinase inhibitor TG02 and the BH3 mimetic ABT-199 in acute myeloid leukaemia cells. *Oncotarget* 8, 16220–16232. doi: 10.18632/oncotarget.8742

PDQ Pediatric Treatment Editorial Board. (2002). *Childhood Acute Lymphoblastic Leukemia Treatment (PDQ®): Health Professional Version*. Available online at: http://www.ncbi.nlm.nih.gov/pubmed/26389206 (accessed April 14, 2021).

Pui, C. H., Yang, J. J., Hunger, S. P., Pieters, R., Schrappe, M., Biondi, A., et al. (2015). Childhood acute lymphoblastic leukemia: progress through collaboration. *J. Clin. Oncol.* 33, 2938–2948. doi: 10.1200/JCO.2014.59.1636

Raetz, E. A., and Bhatla, T. (2012). Where do we stand in the treatment of relapsed acute lymphoblastic leukemia? *Hematology Am. Soc. Hematol. Educ. Program.* 2012, 129–136. doi: 10.1182/asheducation.v2012.1.129.3800156

Reed, J. C., Miyashita, T., Takayama, S., Wang, H. G., Sato, T., Krajewski, S., et al. (1996). BCL-2 family proteins: regulators of cell death involved in the pathogenesis of cancer and resistance to therapy. *J. Cell. Biochem.* 60, 23–32. doi: 10.1002/(SICI)1097-4644(19960101)60:1<23::AID-JCB5<3.0.CO;2-5

Ryan, J., Montero, J., Rocco, J., and Letai, A. (2016). IBH3: simple, fixable BH3 profiling to determine apoptotic priming in primary tissue by flow cytometry. *Biol. Chem.* 397, 671–678. doi: 10.1515/hsz-2016-0107

Sarosiek, K. A., Fraser, C., Muthalagu, N., Bhola, P. D., Chang, W., McBrayer, S. K., et al. (2017). Developmental regulation of mitochondrial apoptosis by c-Myc Governs age- and tissue-specific sensitivity to cancer therapeutics. *Cancer Cell* 31, 142–156. doi: 10.1016/j.ccell.2016.11.011

Satti, J. (2009). The emerging low-dose therapy for advanced cancers. *Dose-Response* 7, 208–220. doi: 10.2203/dose-response.08-010.satti

Savary, C., Kim, A., Lespagnol, A., Gandemer, V., Pellier, I., Andrieu, C., et al. (2020). Depicting the genetic architecture of pediatric cancers through an integrative gene network approach. *Sci. Rep.* 10:1224. doi: 10.1038/s41598-020-58179-0

Savona, M. R., and Wei, A. H. (2019). Incorporating precision BH3 warheads into the offensive against acute myeloid leukemia. *J. Clin. Oncol.* 37, 1785–1789. doi: 10.1200/JCO.19.00400

Schwab, C., and Harrison, C. J. (2018). Advances in B-cell precursor acute lymphoblastic leukemia genomics. *HemaSphere* 2:1. doi: 10.1097/HS9.0000000000000053

Seyfried, F., Demir, S., Hörl, R. L., Stirnweiß, F. U., Ryan, J., Scheffold, A., et al. (2019). Prediction of venetoclax activity in precursor B-ALL by functional assessment of apoptosis signaling. *Cell Death Dis.* 10:571. doi: 10.1038/s41419-019-1801-0

Tan, N., Wong, M., Nannini, M. A., Hong, R., Lee, L. B., Price, S., et al. (2013). Bcl-2/Bcl-xL inhibition increases the efficacy of MEK inhibition alone and in combination with PI3 kinase inhibition in lung and pancreatic tumor models. *Mol. Cancer Ther.* 12, 853–864. doi: 10.1158/1535-7163.MCT-12-0949

Townsend, E. C., Murakami, M. A., Christodoulou, A., Christie, A. L., Köster, J., DeSouza, T. A., et al. (2016). The public repository of Xenografts enables discovery and randomized phase II-like trials in mice. *Cancer Cell* 29, 574–586. doi: 10.1016/j.ccell.2016.03.008

Valentin, R., Grabow, S., and Davids, M. S. (2018). The rise of apoptosis: targeting apoptosis in hematologic malignancies. *Blood* 132, 1248–1264. doi: 10.1182/blood-2018-02-791350

Wei, M. C., Zong, W. X., Cheng, E. H. Y., Lindsten, T., Panoutsakopoulou, V., Ross, A. J., et al. (2001). Proapoptotic BAX and BAK: a requisite gateway to mitochondrial dysfunction and death. *Science* 292, 727–730. doi: 10.1126/science.1059108

Wei, Y., Cao, Y., Sun, R., Cheng, L., Xiong, X., Jin, X., et al. (2020). Targeting Bcl-2 proteins in acute myeloid leukemia. *Front. Oncol.* 10:584974. doi: 10.3389/fonc.2020.584974

Wu, S. C., Li, L. S., Kopp, N., Montero, J., Chapuy, B., Yoda, A., et al. (2015). Activity of the type II JAK2 inhibitor CHZ868 in B cell acute lymphoblastic leukemia. *Cancer Cell* 28, 29–41. doi: 10.1016/j.ccell.2015.06.005

Xin, H., Zhang, C., Herrmann, A., Du, Y., Figlin, R., and Yu, H. (2009). Sunitinib inhibition of Stat3 induces renal cell carcinoma tumor cell apoptosis and reduces immunosuppressive cells. *Cancer Res.* 69, 2506–2513. doi: 10.1158/0008-5472.CAN-08-4323

Yang, F., Jove, V., Xin, H., Hedvat, M., Van Meter, T. E., and Yu, H. (2010). Sunitinib induces apoptosis and growth arrest of medulloblastoma tumor cells by inhibiting STAT3 and AKT signaling pathways. *Mol. Cancer Res.* 8, 35–45. doi: 10.1158/1541-7786.MCR-09-0220

Conflict of Interest: JM reports previous consulting for Vivid Biosciences and Oncoheroes Biosciences, and his laboratory is currently collaborating with AstraZeneca.

The remaining authors declare that the research was conducted in the absence of any commercial or financial relationships that could be construed as a potential conflict of interest.

Publisher's Note: All claims expressed in this article are solely those of the authors and do not necessarily represent those of their affiliated organizations, or those of the publisher, the editors and the reviewers. Any product that may be evaluated in this article, or claim that may be made by its manufacturer, is not guaranteed or endorsed by the publisher.

frontiers in Cell and Developmental Biology

ORIGINAL RESEARCH
published: 13 September 2021
doi: 10.3389/fcell.2021.662868

Recreating the Bone Marrow Microenvironment to Model Leukemic Stem Cell Quiescence

*Eimear O'Reilly[1], Hojjat Alizadeh Zeinabad[1], Caoimhe Nolan[1], Jamileh Sefy[1], Thomas Williams[2], Marina Tarunina[2], Diana Hernandez[2†], Yen Choo[2†] and Eva Szegezdi[1]**

[1] Apoptosis Research Centre, Department of Biochemistry, School of Natural Sciences, National University of Ireland Galway, Galway, Ireland, [2] Plasticell Ltd., Stevenage Bioscience Catalyst, Stevenage, United Kingdom

OPEN ACCESS

Edited by:
Triona Ni Chonghaile,
Royal College of Surgeons in Ireland, Ireland

Reviewed by:
Feng He,
Shanghai University of Traditional Chinese Medicine, China
Nehal Mohammed Eldeeb,
City of Scientific Research and Technological Applications, Egypt

***Correspondence:**
Eva Szegezdi
eva.szegezdi@nuigalway.ie

†Present address:
Diana Hernandez,
Anthony Nolan Research Institute, Royal Free Hospital, London, United Kingdom;
Cancer Institute, University College London, London, United Kingdom
Yen Choo,
Lee Kong Chian School of Medicine, Singapore, Singapore

Specialty section:
This article was submitted to Cell Death and Survival, a section of the journal Frontiers in Cell and Developmental Biology

Received: 01 February 2021
Accepted: 02 August 2021
Published: 13 September 2021

Citation:
O'Reilly E, Zeinabad HA, Nolan C, Sefy J, Williams T, Tarunina M, Hernandez D, Choo Y and Szegezdi E (2021) Recreating the Bone Marrow Microenvironment to Model Leukemic Stem Cell Quiescence. Front. Cell Dev. Biol. 9:662868. doi: 10.3389/fcell.2021.662868

The main challenge in the treatment of acute myeloid leukemia (AML) is relapse, as it has no good treatment options and 90% of relapsed patients die as a result. It is now well accepted that relapse is due to a persisting subset of AML cells known as leukemia-initiating cells or leukemic stem cells (LSCs). Hematopoietic stem cells (HSCs) reside in the bone marrow microenvironment (BMM), a specialized niche that coordinates HSC self-renewal, proliferation, and differentiation. HSCs are divided into two types: long-term HSCs (LT-HSCs) and short-term HSCs, where LT-HSCs are typically quiescent and act as a reserve of HSCs. Like LT-HSCs, a quiescent population of LSCs also exist. Like LT-HSCs, quiescent LSCs have low metabolic activity and receive pro-survival signals from the BMM, making them resistant to drugs, and upon discontinuation of therapy, they can become activated and re-establish the disease. Several studies have shown that the activation of quiescent LSCs may sensitize them to cytotoxic drugs. However, it is very difficult to experimentally model the quiescence-inducing BMM. Here we report that culturing AML cells with bone marrow stromal cells, transforming growth factor beta-1 and hypoxia in a three-dimensional system can replicate the quiescence-driving BMM. A quiescent-like state of the AML cells was confirmed by reduced cell proliferation, increased percentage of cells in the G_0 cell cycle phase and a decrease in absolute cell numbers, expression of markers of quiescence, and reduced metabolic activity. Furthermore, the culture could be established as co-axial microbeads, enabling high-throughput screening, which has been used to identify combination drug treatments that could break BMM-mediated LSC quiescence, enabling the eradication of quiescent LSCs.

Keywords: leukemic stem cell, acute myeloid leukemia, bone marrow microenvironment, quiescence, three-dimensional model

INTRODUCTION

Acute myeloid leukemia (AML) is the most common acute leukemia in adults, constituting approximately 80% of all acute leukemia cases diagnosed (Harrington, 2011). Patients are generally treated with the nucleoside analog cytarabine (AraC) in combination with anthracycline antibiotics, such as daunorubicin (Dnr) or idarubicin. While complete remission is achieved in the majority of patients, approximately two-thirds of them relapse (Lee and Muller, 2010),

resulting in an overall 4-year survival between 30 and 40% (Hanahan and Weinberg, 2017). Studies have shown that the primary cause of relapse is the presence of a treatment-resistant AML subpopulation known as leukemia-initiating cells or leukemic stem cells (LSCs) (Jonas, 2017).

Leukemic stem cells share many features with their normal counterparts, including existence in a state of quiescence which is characterized by low rate of RNA synthesis (Nakamura-Ishizu et al., 2014), low metabolic activity (Justino De Almeida et al., 2017) and a high expression of anti-apoptotic proteins, such as Bcl-2 (Sharma and Pollyea, 2018), making them resistant to cellular stress and cell death induced by chemotherapeutics. Consequently, LSCs can outcompete normal HSCs or "hijack" the bone marrow microenvironment (BMM) and occupy the HSC niches (Nwajei and Konopleva, 2013).

Studies have shown that quiescent HSCs are protected from myeloablative agents, such as 5-fluorouracil and AraC, as these agents are only effective on cycling cells. Consequently, when quiescent HSCs are forced to enter the cell cycle—for example, by cytokines—they become sensitive to myeloablative agents (Essers et al., 2009). It is thus hypothesized that LSCs may also be sensitized to chemotherapeutics in the same manner. For example, Saito et al. (2010b) have shown that priming LSCs with granulocyte colony-stimulating factor (G-CSF) resulted in their entry into the cell cycle and sensitization to AraC.

Based on these findings, there is a clinical need to identify treatments able to break LSC quiescence so that LSCs can be more effectively targeted with chemotherapeutics in order to reduce the chance of relapse. However, such studies require advanced experimental models which can replicate the quiescence-mediating BMM.

Here we report a hydrogel-based layered co-culture system which incorporates the key BMM-specific quiescence-inducing signals and is able to establish AML quiescence. The quiescent state of AML cells was confirmed by reduced cell proliferation rate, increased percentage of cells in the G_0 cell cycle phase and a substantially reduced absolute cell number, expression of quiescence markers, such as p21, and reduced metabolic activity. We translated the co-culture system into co-axial microbeads suitable for high-throughput screening. Using these beads, we were able to identify combinations of drugs that can break BMM-mediated AML quiescence, offering the potential to sensitize LSC to chemotherapeutics and eliminating the AML subpopulation responsible for patient relapse.

MATERIALS AND METHODS

Reagents

Two percent sodium alginate was prepared by dissolving sodium alginate (Sigma-Aldrich) in phosphate-buffered saline (PBS) and sterilizing by heating to 80°C in a water bath for 15 min (Leo et al., 1990). Anti-CD150-PE, anti-GRPC5C Alexa Fluor-405, and anti-Ki67-Alexa Fluor 405 antibodies for flow cytometry were purchased from R&D Systems. Anti-CD49f-PE and anti-CD90-VioBlue were purchased from Miltenyi Biotec. Transforming growth factor beta-1 (TGFβ-1) and fibroblast growth factor were obtained from PeproTech. Fms-like tyrosine kinase-3 (Flt-3), G-CSF, stem cell factor (SCF), and interferon alpha were purchased from ImmunoTools. All-*trans* retinoic acid (ATRA) was obtained from Sigma-Aldrich. Hoechst 33342, propidium iodide (PI), and pyronin Y (PY) were purchased from Sigma-Aldrich. The CountBright™ Absolute Counting Beads was purchased from Thermo Fisher Scientific. MHY1485, AZD8055, rosiglitazone, KU-55933, LEE011, roscovitine (seliciclib, CYC202), glasdegib (PF-04449913), sodium butyrate, dasatinib, BIO, plerixafor (AMD3100), quizartinib, and sorafenib were purchased from Selleckchem. Adiponectin, triglitazone LE135, PD169316, harmine, nilotinib, ethylisopropyl amiloride, anisomycin, and curcumin were purchased from Sigma-Aldrich, while prostaglandin E2 was from BioVision/Cambridge Bioscience. Cytarabine and daunorubicin were purchased from Sigma-Aldrich.

Cell Culture

KG1a cells were maintained at a density of 500,000 cells/ml in RPMI-1640 supplemented with GlutaMAX (Gibco, 2 mM), 10% HyClone fetal bovine serum (FBS, Thermo Fisher Scientific), penicillin (100 U/ml), streptomycin (100 μg/ml), and sodium pyruvate (1 mM). Bone marrow mesenchymal stromal cells (BMSCs; hTERT immortalized primary BMSCs from a healthy donor) were cultured at a density of 50,000 cells/ml in αMEM (Sigma-Aldrich) supplemented with 10% HyClone FBS, penicillin (100 U/ml)/streptomycin (100 μg/ml), sodium pyruvate (1 mM), and GlutaMAX (2 mM).

Generation of Indirect-Contact Co-culture System

BMSCs were resuspended at 500,000 cells/ml in 2% alginate solution and plated into 24-well plates (200 μl/well). Alginate was crosslinked by adding 100 mM $CaCl_2$ for 10 s, forming a layer of BMSCs trapped in the alginate scaffold. Excess $CaCl_2$ was removed with three washes of DPBS without Ca^{2+} and Mg^{2+} (Gibco). KG1a cells were labeled with the long-term cell tracker, CFSE (2.5 μM) (see section "Cell Cycle Analyses"), and seeded on top of the alginate-trapped BMSCs in IMDM medium supplemented with TGFβ-1 (10 ng/ml) or ATRA (2.5 μM) at a density of 50,000 cells/ml.

Immunophenotyping and Viability Assays

The viability of KG1a cells was determined using Annexin V staining. KG1a cells were collected from single cultures by pipetting. From alginate co-cultures, in addition to pipetting off the suspension cells, 200 μl of 1 mM ethylenediaminetetraacetic acid (EDTA) was also added to the top of the alginate to loosen the alginate Annexin V buffer (10 mM HEPES/NaOH, pH 7.5, 140 mM NaCl, 2.5 mM $CaCl_2$) containing 1.5 μl Annexin V-APC (ImmunoTools). The cells were incubated on ice in the dark for 15 min, followed by analysis by flow cytometry (BD FACSCanto II, BD Fortessa). Five microliters of CountBright™ Absolute counting beads (Molecular Probes, 0.52×10^5 beads/50 μl) were added to each sample before

analysis to enable absolute cell number determination. Data analysis was conducted using FlowJo (V10).

Cell viability in the co-axial beads was assessed using Calcein AM (Molecular Probes). The Calcein AM was diluted 1:500 in the required media. Half of the media from the beads was removed and replaced with an equal amount of the Calcein AM solution (1:1,000 dilution). This was incubated for 30 min at 37°C in the dark. The beads were visualized using fluorescent microscope under the FITC filter (Nikon Eclipse TE2000-S).

For immunophenotyping, cells were harvested and resuspended in 1% bovine serum albumin (BSA)/PBS and blocked for 10 min after which they were collected and resuspended in 100 μl 1% BSA/PBS containing 2 μl of the following antibodies: SLAMF1/CD150-PE (R&D Systems), GRPC5C Alexa Fluor-405 (R&D Systems) CD49f-PE, and CD90-VioBlue (Miltenyi Biotec). The cells were incubated on ice in the dark for 20 min, then washed with 400 μl of 1% BSA/PBS, and resuspended in 200 μl of 1% BSA/PBS for measurement.

Cell Cycle Analyses

Cell proliferation rate was monitored with CFSE dye retention assay. 5×10^6 KG1a cells were washed twice with 5 ml of Hanks' solution and the cell pellet was resuspended in 1 ml of Hanks' solution. CFSE was added to give a final concentration of 2.5 μM and incubated for 20 min at 37°C in the dark. Excess CFSE was removed by washing twice with Hanks' solution. Finally, the cells were resuspended in full IMDM growth medium to a final concentration of 50,000 cells/ml for seeding. As the CFSE content reduces by half with every division, we were able to extrapolate the drop in the CFSE signal intensity by fitting the fluorescent geometric mean read-outs on a hyperbolic curve, thus estimating the number of cell division cycles that took place (**Supplementary Figure S1**).

Cells in the G_0 phase were identified with Hoechst 33342/Pyronin Y staining or with Ki67/PI staining. For Hoechst 33342/Pyronin Y staining, 250,000 KG1a cells were harvested and resuspended in full growth medium, and Hoechst 33342 was added at a final concentration of 20 mg/ml and the cells were incubated in the dark for 45 min at 37°C with intermittent mixing. Pyronin Y (PY) was then added at a final concentration of 0.5 μg/ml, and the cells were incubated for an additional 15 min at 37°C. The samples were then analyzed immediately by flow cytometry.

For Ki67/PI staining, 1×10^6 KG1a cells were harvested and resuspended in 50 μl of PBS. The cells were fixed with 80% ice-cold ethanol (EtOH) and stored at −20°C for a minimum of 2 h. The cells were removed from EtOH and washed twice with 3 ml of PBS. A total of 250,000 cells were then resuspended in 400 μl of blocking buffer (1% BSA/PBS) and incubated for 10 min, followed by incubation in 1% BSA/PBS with Ki67 antibody for 20 min at room temperature (RT) in the dark. Excess antibody was washed off with 1% BSA/PBS, after which the cells were resuspended in the PI staining solution (10 μg/ml PI and 100 μg/ml RNAse A in 1% BSA/PBS) and incubated in the dark at RT for 30 min, with mixing, followed by analysis by flow cytometry.

Cell proliferation in the co-axial beads was assessed with EdU Click-it staining (Thermo Fisher Scientific). The EdU (component A—nucleoside analog) was added to the beads (10 μM) 1 day after the final set of drug treatments had commenced. After 3 days of treatment, the co-axial beads were collected, washed with PBS, and fixed with 4% paraformaldehyde at RT for 30 min. The beads were then incubated in permeabilization solution (0.25% Triton® X-100 in 0.1% BSA in PBS) for 20 min at RT. After washing with 3% BSA in PBS, the beads were re-suspended in Click-iT® Plus reaction cocktail (containing Alexa Fluor 480 picolyl azide) and incubated in the dark for 30 min at 37°C. After the reaction cocktail was removed, the beads were washed and visualized by microscopy (Nikon Eclipse TE2000-S).

Real-Time Quantitative PCR

Total cellular RNA was isolated using the RNeasy kit (Qiagen). cDNA was generated from 1 μg of RNA using SuperScript® IV First-Strand cDNA Synthesis Reaction kit (Invitrogen). RT-qPCR was performed in triplicate in a 96-well plate. Each reaction consisted of 4 μl of cDNA (diluted 1:10), 5 μl of 2X Brilliant III Ultra-Fast qPCR Master Mix (Agilent Technologies), and 1 μl of 10X PrimeTime qPCR Assay primer–probe (Integrated DNA Technologies). The following primer/probe sets were employed: Hs.PT.58.801316 (ABL1), Hs.PT.58.38531977 (CDK4), Hs.PT.58.344323 (CDK6), Hs.PT.58.40874346.g (CDKN1A/p21), Hs.PT.58.45564663 (CDKN1B/p27), Hs.PT.58.1677181 (CDKN1C/p57), Hs.PT.58.20045500 (CDKN2C/p18), Hs.PT.58.21147259 (GPRC5C), and Hs.PT.58.24703737 (SLAMF1/CD150). The sequences can be found in **Supplementary Table S4**. RT-qPCR was carried out using the StepOne Plus Real-Time PCR System (Applied Biosciences).

Western Blotting

Cells were lysed in whole cell lysis buffer (20 mM HEPES, 350 mM NaCl, 1 mM $MgCl_2$, 0.5 mM EDTA, 0.1 mM EGTA, and 1% Igepal-630, pH 7.5, with 0.5 mM DTT (Sigma-Aldrich) and Halt Protease inhibitor cocktail (Thermo Fisher Scientific). Proteins (20 μg) were electrophoresed and transferred onto a nitrocellulose membrane (using iBlot™ Gel Transfer and iBlot™ Transfer Stack nitrocellulose, Thermo Fisher Scientific). After blocking, the blots were incubated with rabbit monoclonal antibodies against CDK4 [Cell Signaling Technology (CST)] and p21 (Santa Cruz) and with mouse monoclonal antibodies against CDK6 (CST) and actin (Sigma-Aldrich). For detection, horseradish peroxidase-conjugated secondary antibodies were used (Pierce). The protein bands were visualized with SuperSignal® West Pico Chemiluminescent Substrate (Thermo Fisher Scientific) on X-ray film (Agfa).

Metabolic Assays

Oxidative phosphorylation and glycolysis were measured with Seahorse XFp analyzer (Agilent). The XFp Miniplate sensor cartridges were hydrated as per the instructions of the manufacturer. The KG1a cells suspended in the XFp assay

medium were collected from single cultures or alginate co-cultures as described above and were attached to the wells of Agilent Seahorse XFp Cell Culture Miniplates coated with poly-L-lysine by centrifugation as per the instructions of the manufacturer at a density of 200,000 cells/well in triplicate. The XFp Miniplate was placed in a carrier tray in a non-CO_2 incubator at 37°C for 30 min to equilibrate the temperature and pH. Analyses were performed both at basal condition as well as after the injection of oligomycin (1.5 μM), FCCP (1 μM), and rotenone plus antimycin A, both at 0.5 μM using the Seahorse XF Cell Mito Stress Test Kit (Agilent).

Generation of AML-BMSC Co-cultures in Co-axial Beads

The beads were generated with the Var-V1 encapsulator (Nisco Engineering AG) by electrostatic force. The system consisted of two syringes. One syringe contained the KG1a cells resuspended in methylcellulose, and the other syringe contained the bone marrow mesenchymal stromal cells (BMSCs) resuspended in 2% alginate which passed through the inner and outer lumen of the co-axial needle, respectively. Under a constant electric field, these two solutions combined to form droplets of 300–400 μm in diameter at the end of the co-axial needle where they were sprayed into a bath of 100 mM $CaCl_2$ (electrospraying) to ensure instant solidification of the beads before the two fluids got mixed. In the $CaCl_2$ solution, the alginate became cross-linked, and the co-axial beads were formed. The KG1a cells within the core were seeded at a density of 50,000 cells/ml. The outer shell containing the BMSCs was seeded at 500,000 cells/ml in 2% alginate.

Tagging, Flow Cytometry, and Analysis of Co-axial Beads

The co-axial beads were labeled with unique tags (intellectual property of Plasticell Ltd.) comprised of 30 unique population-inert fluorescent microspheres, which were connected to the co-axial beads through a multi-layering technique (Tarunina et al., 2016) after each drug treatment. The treatment conditions inducing KG1a cell cycling were selected based on their EdU Click-it incorporation by fluorescent microscopy. The positively selected beads were dissolved with trypsin/EDTA overnight at 37°C. The tags were analyzed by flow cytometry (BD FACSCanto II) and identified using the Ariadne Bioinformatics software (Plasticell Ltd.) to determine the sequential drug treatments that the co-axial beads were exposed to.

RESULTS

In order to replicate the quiescence-mediating bone marrow microenvironment, we tested: (1) the effect of reduced serum concentration, which has been shown to induce quiescence in multiple cell types (Gos et al., 2005; Li et al., 2019), (2) the co-culture with BMSCs known to secrete key HSC quiescence-inducing cytokines [angiopoietin-1, osteopontin, thrombopoietin, and CXC motif chemokine ligand 12 CXCL12 (data not shown)], (3) retinoic acid (Cabezas-Wallscheid et al., 2017), and (4) TGFβ-1 (Wang et al., 2018), known HSC quiescence-inducing factors within the BMM which are not produced by BMSCs, and (5) the contribution of hypoxia.

As a model of LSCs, the low-differentiation status AML cell line, KG1a, was chosen. Phenotyping by flow cytometry confirmed that KG1a cells have an LSC-like phenotype: $Lin^-/CD38^-/CD34^+/CD45RA^+/CD133^-/CD49f^+/CD90^-$ (**Supplementary Figure S2**). Cell proliferation rate was monitored with a CFSE retention assay, and the average number of cell divisions the culture underwent was calculated as described in section "Materials and Methods" (**Supplementary Figure S1**).

The Combination of BMSC and TGFβ-1 Can Induce KG1a Cell Quiescence

The first condition to induce quiescence tested was reduced serum concentration. Although it reduced KG1a proliferation rate, it also led to diminished cell viability over time; therefore, it was not used subsequently (**Supplementary Figure S3**).

To determine the ability of BMSCs to trigger quiescence, a layered, indirect co-culture system was set up by trapping BMSCs in a biocompatible, alginate-based hydrogel, providing a 3D scaffold for BMSCs and seeding the KG1a cells over the hydrogel-embedded BMSCs. Of note, direct co-culture, allowing cell–cell interaction was also tested, but it proved to be unsuitable for long-term culture as the BMSC layer quickly became overgrown and consequently the system deteriorated, indicated by diminishing KG1a cell viability (**Supplementary Figure S4**). On the contrary, in the indirect, hydrogel-based system, both BMSCs and KG1a cells survived, and the BMSCs showed little to no proliferation, minimizing the risk of BMSC overgrowth during extended culture (**Figure 1A** and **Supplementary Figure S5**).

Using the indirect co-culture, the ability of BMSCs to trigger KG1a quiescence was assessed by monitoring CFSE dye retention. Co-culture with BMSCs significantly slowed down KG1a proliferation rate by day 8, with the average division cycle reduced from 7.76 ± 0.01 in a standard culture to 6.65 ± 0.08 cycles in the presence of BMSCs ($p < 0.001$, Welch's t-test; **Figure 1A**).

TGFβ-1 and retinoic acid are also known as quiescence-inducing factors in the BMM (Cabezas-Wallscheid et al., 2017; Villeval and Vainchenker, 2020). As these factors are not produced by BMSCs, their effect on inducing KG1a cell quiescence was tested by adding them to a KG1a single culture. Both agents reduced the number of division cycles without diminishing KG1a viability (**Figure 1B**).

Because the addition of BMSCs, TGFβ-1, and ATRA could all slow down KG1a proliferation, their combined effect was tested. CFSE retention assay showed that BMSCs and TGFβ-1 had an additive effect in reducing KG1a proliferation rate (**Figure 2A**). ATRA did have a further effect but negatively impacted on KG1a viability (**Supplementary Figure S6**).

To corroborate these findings, cell cycle distribution analysis was conducted by measuring Ki67 expression combined with DNA content analysis (PI). BMSC + TGFβ-1 increased the percentage of cells in the G_0 cell cycle phase (**Figure 2B**). Additionally, by extending the culture to 20 days, CFSE retention

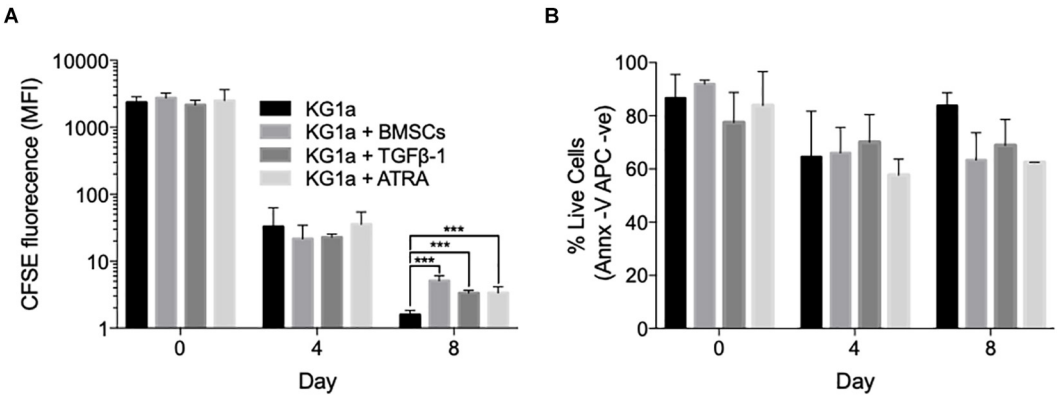

FIGURE 1 | Bone marrow mesenchymal stromal cells (BMSCs), TGFβ-1 and all-*trans* retinoic acid (ATRA) can all reduce KG1a proliferation rate. **(A)** KG1a cells were labeled with 2.5 μM carboxyfluorescein succinimidyl ester (CFSE) and cultured alone, with alginate-encapsulated BMSCs, with TGFβ-1 (10 ng/ml), or with ATRA (2.5 μM) over an 8-day period. The graph shows the mean CFSE fluorescence intensity as a measure of CFSE retention in the live KG1a cells on days 0, 4, and 8 as determined by flow cytometry. **(B)** Viability measured with Annexin V on days 0, 4, and 8 by flow cytometry. ***$p < 0.001$ (Student's *t*-test). MFI, mean fluorescence intensity.

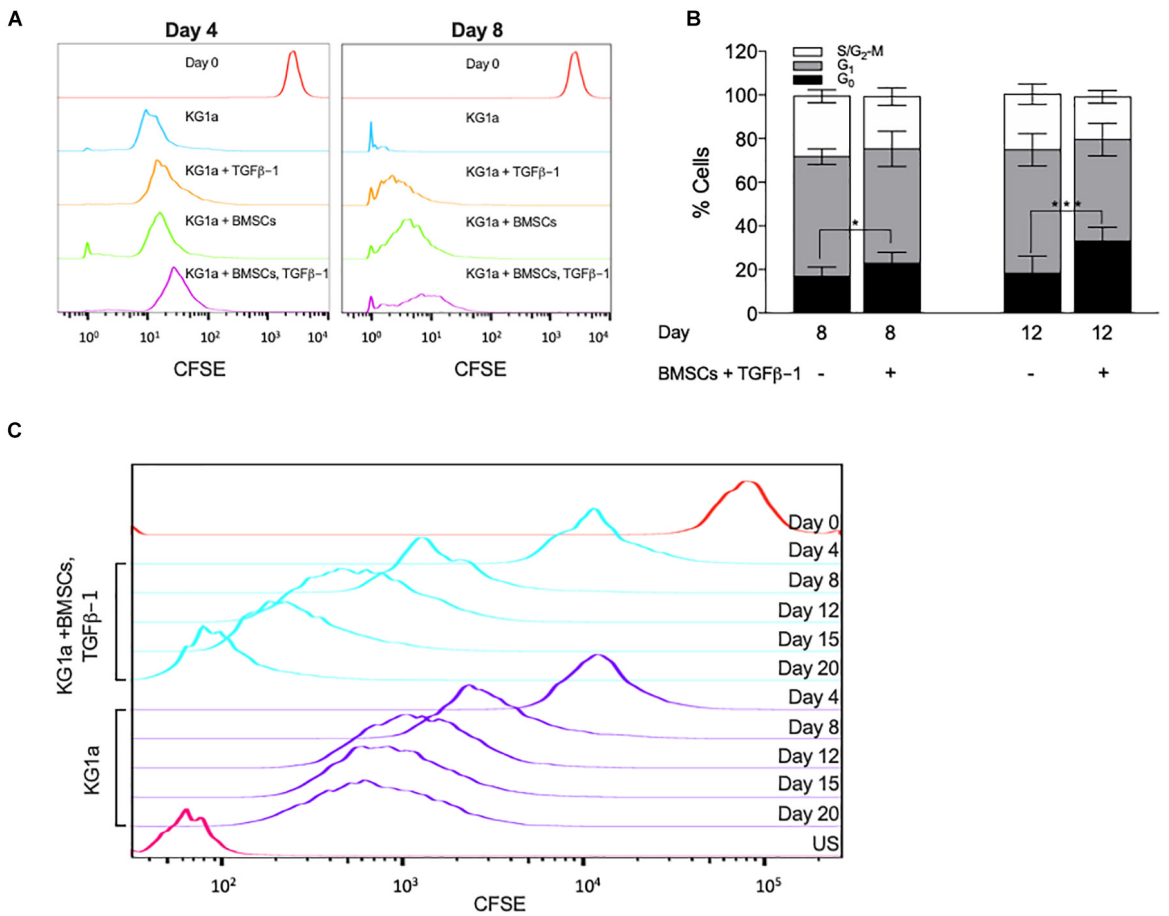

FIGURE 2 | Bone marrow mesenchymal stromal cells (BMSC) and TGFβ-1 have an additive effect on slowing KG1a proliferation and lead to the accumulation of cells in the G_0 cell cycle phase. KG1a cells were cultured with alginate-embedded BMSC with or without addition of 10 ng/ml TGFβ-1 for the times indicated. **(A)** Histogram representation of carboxyfluorescein succinimidyl ester (CFSE) retention in single culture at day 0 (red) and at day 4 or 8 (blue), culture with TGFβ-1 (orange), BMSC co-culture (green), or both (purple) on days 4 and 8. **(B)** Percentage of cells in the G_0-, G_1-, and S/G_2-M phases of the cell cycle determined by Ki67 + PI staining. **(C)** Histogram representation of CFSE retention in extended single culture (blue) vs. BMSC + TGFβ-1 co-culture (purple). Red, CFSE fluorescence on day 0; US, unstained sample. *$p < 0.05$; ***$p < 0.001$ (Student's *t*-test).

showed that, from day 12 onward, the proliferation in the co-culture got almost completely halted, corroborating that the combination of BMSCs and TGFβ-1 induced a state of quiescence (**Figure 2C**).

Hypoxia Further Enhances BMSC and TGFβ-1 Induced KG1a Quiescence

Since the hypoxic BM environment (Eliasson and Jönsson, 2010) has also been associated with HSC quiescence (Moirangthem et al., 2015), the ability of a low oxygen concentration (1% O_2) to trigger KG1a quiescence was tested. Hypoxic conditions significantly enhanced CFSE retention at day 8 (**Figure 3A**) and enhanced the effect of BMSC + TGFβ-1 without impacting on cell viability (**Figure 3B**). Absolute cell numbers monitored using counting beads confirmed the reduced cell proliferation rate by over 19-fold in the hypoxic BMSC + TGFβ-1 condition (**Figure 3C**).

Ki67 + PI staining showed that the reduced proliferation was associated with an accumulation of cells in the G_0 phase (**Figure 3D**), which was also confirmed by their reduced RNA content using Pyronin Y staining (**Supplementary Figure S7**). Collectively, the data shows that co-culture conditions incorporating BMSC, TGFβ-1, and hypoxia have a combined effect in inducing LSC quiescence as seen by dye retention, reducing the absolute cell numbers and the accumulation of cells in the G_0 cell cycle phase.

To confirm that these culture conditions trigger quiescence, we determined the expression of markers of HSC quiescence, namely, the cell surface marker CD150 (Nakamura-Ishizu et al., 2014; Cabezas-Wallscheid et al., 2017; Tajer et al., 2019) with flow cytometry, GPRC5C, CDK4, and CDK6 (Baker and Reddy, 2012), and the CKI family members p18, p21, p27, and p57 (Cheng et al., 2000; Walkley et al., 2005; Matsumoto et al., 2011; Gao et al., 2015) with quantitative RT-PCR (qRT-PCR). Of note, while CD49f and CD90 are also well recognized markers of HSC quiescence, they were both highly expressed by cycling KG1a cells and thus were deemed to be not suitable markers of KG1a quiescence (**Supplementary Figures S1, S8**).

CD150 was expressed at a low level in cycling KG1a cells, and although we detected an increase in its expression in hypoxia + BMSC + TGFβ-1 culture in comparison to the hypoxic condition alone, there was no significant difference between a normoxic single culture and a hypoxia + BMSC + TGFβ-1 culture (**Figure 4A**), which was confirmed with qRT-PCR (**Supplementary Figure S9**).

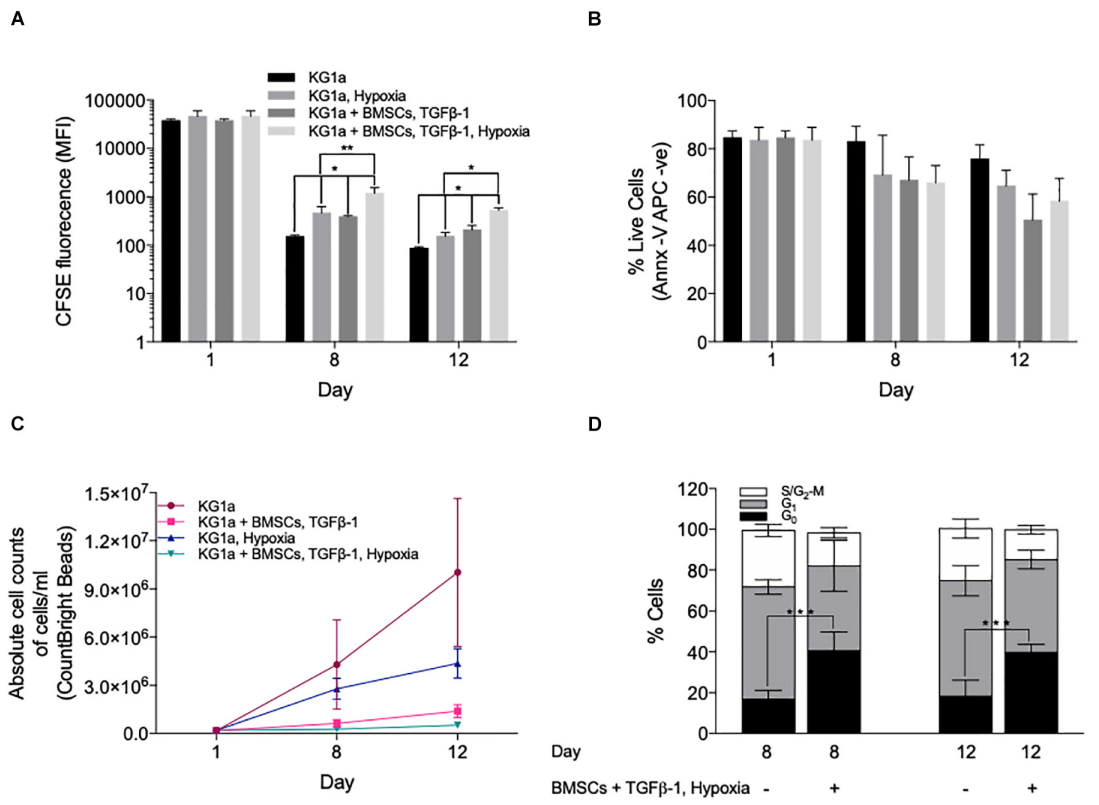

FIGURE 3 | Hypoxia enhances the quiescence-inducing effect of bone marrow mesenchymal stromal cells (BMSCs) and TGFβ-1. KG1a cells were labeled with 2.5 μM carboxyfluorescein succinimidyl ester (CFSE) and cultured alone (KG1a) or with alginate-encapsulated BMSC and TGFβ-1 (10 ng/ml) over a 12-day period in normoxia or hypoxia (1% pO_2). **(A)** CFSE retention measured in the live cell fraction on days 1, 8, and 12. **(B)** Viability measured with Annexin V on days 1, 8, and 12. **(C)** The absolute number of live cells per milliliter as determined by flow cytometry using CountBright beads on days 1, 8, and 12. **(D)** Cell cycle distribution based on Ki67 expression and DNA content (PI) on days 8 and 12. $^*p < 0.05$; $^{**}p < 0.01$; $^{***}p < 0.001$ (Student's *t*-test).

In the qRT-PCR studies, quiescence-inducing culture conditions repressed the expression of CDK4 and CDK6 and induced the expression of p21 (CDKN1A) and GPRC5C, confirming the induction of quiescence (**Figure 4**). Reduced CDK6 and induced p21 expression have also been confirmed at the protein level using Western blotting (**Figure 4G**). Reduced CDK4 protein expression was not detectable, possibly due to the technical limitations of Western blotting, which is not able to show small reductions in protein expression expected based on the level of reduction observed with the qPCR. Interestingly, the expression of p57, the highest expressed CKI in healthy HSCs and other CKIs known to play a role in HSC quiescence (p27 and p18), did not show an increase (**Supplementary Figure S9**). Overall,

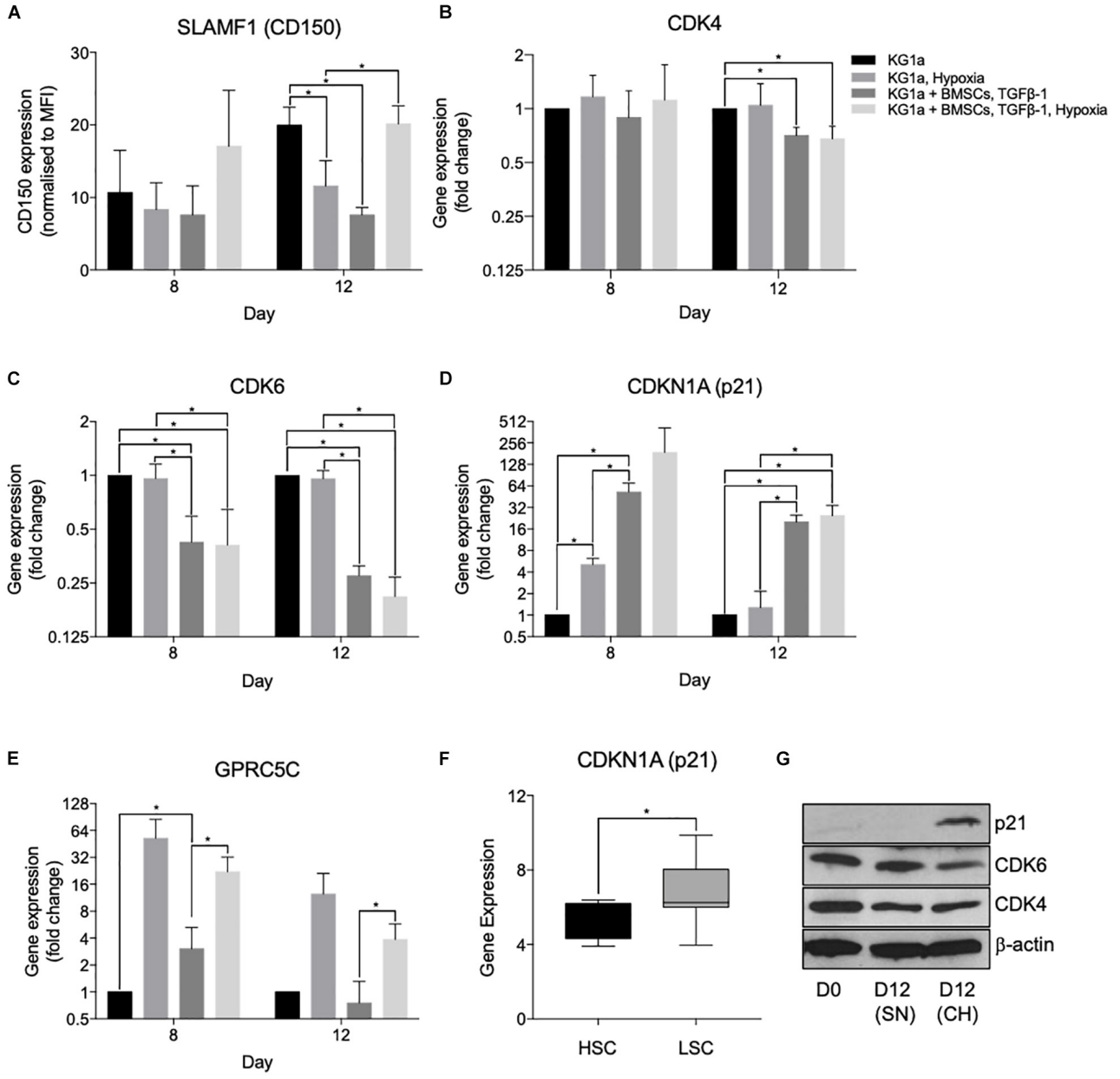

FIGURE 4 | Hypoxia and co-culture with bone marrow mesenchymal stromal cells (BMSC) + TGFβ-1 increases the expression of markers of leukemia cell quiescence. KG1a cells were cultured alone or with alginate-encapsulated BMSC and TGFβ-1 (10 ng/ml) over a 12-day period in normoxia or hypoxia (1% pO_2). **(A)** Expression of CD150 determined in the live fraction by flow cytometry. MFI, mean fluorescent intensity. *$p < 0.05$ (Student's *t*-test). **(B–E)** Results of quantitative RT-PCRs on RNA isolated on days 8 and 12. *$p < 0.05$ (one-way ANOVA). **(F)** Gene expression analysis of p21 expression conducted on the GSE17054 transcriptomic dataset. The graph represents the changes in gene expression between hematopoietic stem cells and leukemic stem cells. *$p < 0.05$ (Welch's *t*-test). **(G)** Western blot images for the expression of p21, CDK4, and CDK6 conducted on samples isolated at day 12 of culture. SN, single culture at normoxia; CH, co-culture under hypoxia.

the altered expression of these cell cycle proteins further proves the capacity of the developed system to model the quiescence-inducing bone marrow microenvironment. To further investigate that there is a differential dependence of CKIs between HSCs and LSCs, a gene expression analysis was conducted on the open-access transcriptomic analysis of patient-derived LSCs (nine samples) and healthy HSCs (four samples, GSE17054). The expression of p21 alongside p16 and p18 was higher in LSCs in comparison to HSCs (**Figure 4F** and **Supplementary Figures S10A,B**), supporting the notion that LSCs utilize different CKIs than HSCs.

To further investigate how closely the co-culture can replicate the quiescent LSC phenotype, the metabolic profile of the AML cells was studied (**Figure 5**) using the Seahorse XFp analyzer (Agilent) and the Seahorse XF Cell Mito Stress Test kit. Basal mitochondrial respiration and maximal respiration capacity were measured by determining the mitochondrial oxygen consumption rate in control conditions and after the administration of a proton uncoupler (FCCP). The rate of anaerobic glycolysis and reserved glycolytic capacity were also determined by measuring lactate production (extracellular acidification rate) in control conditions and after blocking the mitochondrial ATP production with the ATP synthase inhibitor, oligomycin. KG1a cells were cultured alone or under conditions of hypoxia + BMSC + TGFβ-1, and measurements were taken at days 8 and 12. KG1a cells in the co-culture displayed a reduced respiration rate (basal OCR) in comparison with the KG1a single cultures (**Figures 5A,B**). The rate of anaerobic glycolysis was found to be higher in the co-culture on day 8, but it reduced to a low level by day 12 (**Figures 5C,D**), suggesting that the AML cells in the co-culture stabilize in a quiescent-like state characterized by an overall substantially reduced metabolism, corroborating the proliferation profile, where cell division got almost completely halted by day 12 in the co-culture (**Figure 2C**). Maximal respiration (**Figure 5E**) and reserved glycolytic capacity (**Figure 5F**), two main indicators of the ability of a cell to respond to energy demand upon stress, were also measured. The results showed that the co-cultured cells have a much smaller maximal respiration and reserved glycolytic capacity than the cells in a single culture, which is another known characteristic of drug-resistant quiescent LSCs (Lagadinou et al., 2013).

As quiescence drives drug resistance, the ability of the co-culture system to offer protection against the mainstream AML chemotherapy was tested using the combination treatment of cytarabine + daunorubicin (AraC + Dnr). KG1a cells were cultured alone or under conditions of hypoxia + BMSC + TGFβ-1 for 8 days, after which the cultures were treated with a 3:1 molar ratio of AraC and Dnr [corresponding to the molar ratio of the two drugs used in the clinic (7 + 3 therapy)] for 48 h (Rai et al., 1981). It was found that the co-culture conditions significantly protected the KG1a cells from AraC + Dnr treatment, verifying that the quiescence-inducing co-culture also leads to protection against chemotherapeutics (**Figure 5G**).

The Quiescence-Inducing Co-culture System Can Be Translated Into Co-axial Beads Suitable for the Screening of Drugs to Revert Quiescence-Mediated Drug Resistance

In order to test the utility of the developed co-culture system to identify treatments that can re-activate quiescent leukemic cells, the indirect co-culture was developed into a high-throughput screening assay. The BMSC-KG1a co-culture was set up as co-axial beads, where an inner methylcellulose core contained the KG1a cells and an outer alginate shell encapsulated the BMSC. The cells retained their viability in the beads as determined by monitoring their viability with calcein-AM and fluorescence microscopy (**Supplementary Figure S5**). Since our pilot studies found that single treatments with individual agents had only a marginal effect on re-activating quiescent KG1a cells (**Supplementary Figure S11**), a sequential treatment matrix consisting of 1,600 different drug combinations was designed based on targeting known pathways that regulate quiescence and the proliferation of HSCs and/or LSC (**Supplementary Tables S1, S2**). The co-axial beads were exposed to these drug combinations using CombiCult, a platform that enables high-throughput sequential drug tests based on fluorescent labeling and tracking of the beads as they go through the treatment pathways (**Supplementary Figure S12**).

The co-axial beads were generated and cultured for 4 days prior to drug treatment to induce a slow cycling state, after which they were divided into 10 portions and were subjected to the first set of drug treatments (set 1, **Supplementary Table S2**) for 3 days. After the treatment, the beads were labeled with a fluorescent tag unique to the treatment that they received (Tarunina et al., 2016), and the beads from the different treatments were pooled together. The pooled beads were then split (resulting in a mixture of beads in each dish representing all possible set 1 treatments) and exposed to the second set of drugs. The labeling, pooling, and splitting process was repeated for the third set of drugs, after which all beads were pooled together, and the effect of the treatments on KG1a cell quiescence was measured with EdU Click-it labeling of cells in the S-phase of the cell cycle.

Using the Ariadne® bioinformatics software (Plasticell Ltd.), treatment sequences which reverted BMSC + TGFβ-1-induced quiescence were identified, and a deconvoluted readout of the drug combinations able to re-activate quiescent KG1a cells was generated (**Supplementary Figure S13**). From this, the most effective treatment regimens were selected for validation in the layered co-culture system (**Figure 6**).

To validate the screening results, the optimized layered co-culture was employed under conditions of hypoxia. The culture time prior to drug treatment was extended to 8 days to ensure that a quiescent-like state was established. These cultures were then exposed to the three most potent sequential treatments able to reactivate the KG1a cells identified in the CombiCult® screen. The cell cycling rate was monitored with Hoechst + PY staining (identifying quiescent cells based on low RNA content and 2N DNA). The test confirmed that sequential treatments with the hedgehog pathway inhibitor

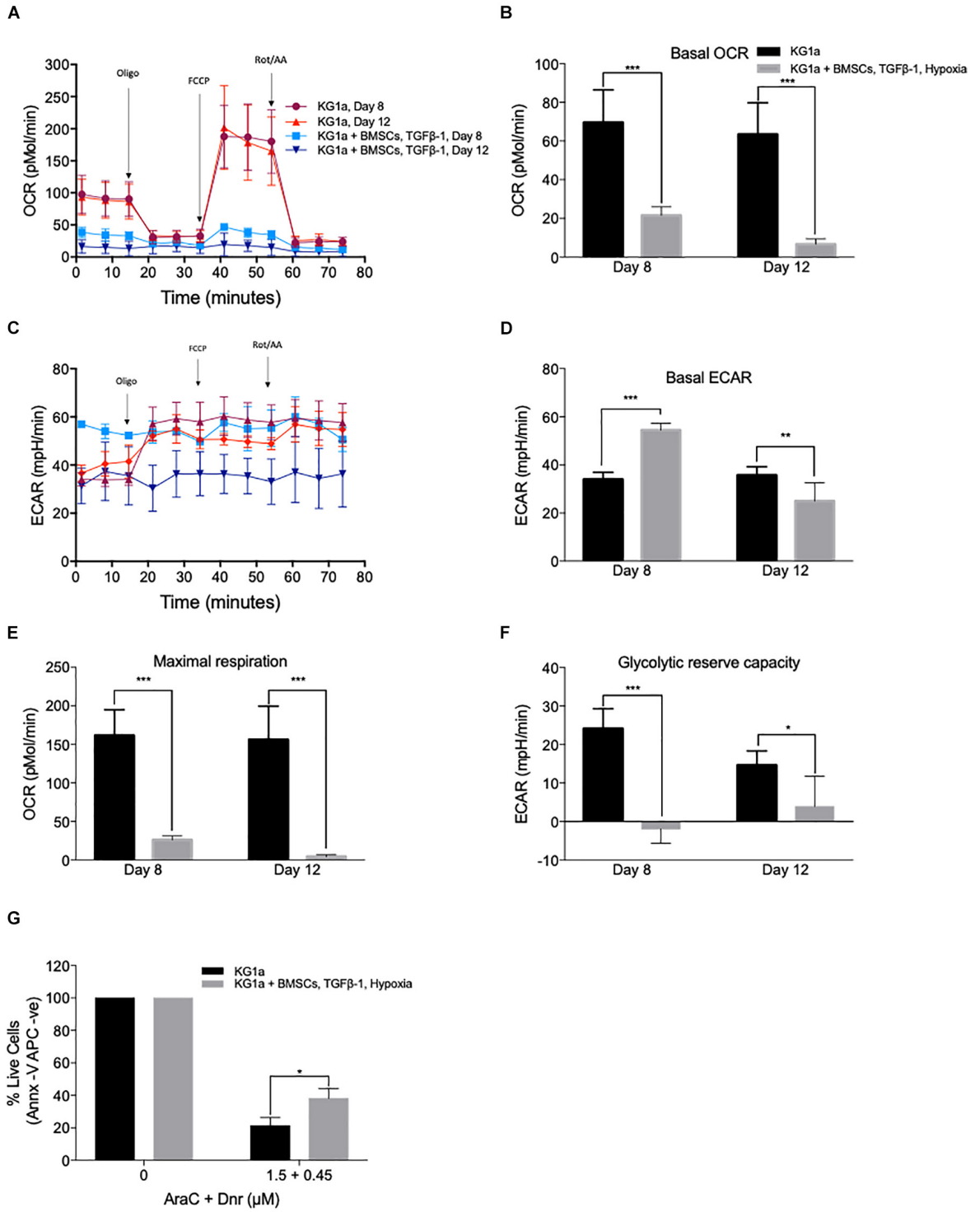

FIGURE 5 | KG1a cells in co-culture have a quiescent leukemic stem cell-like metabolic profile associated with increased drug resistance. KG1a cells were cultured alone in normoxia or with alginate-encapsulated bone marrow mesenchymal stromal cells (BMSC) and TGFβ-1 (10 ng/ml) under hypoxia (1% pO_2). Oxygen consumption rate (OCR) and extracellular acidification rate (ECAR) were analyzed using the Seahorse XFp analyzer and the Seahorse XF Cell Mito Stress Test kit in samples taken at days 8 and 12. Oligomycin, FCCP, and rotenone/antimycin A were added at the times indicated. OCR **(A)**, basal OCR **(B)**, ECAR **(C)**, basal ECAR **(D)**, maximal respiration **(E)**, and reserved glycolytic capacity **(F)** of KG1a cells alone or in co-culture. **(G)** Co-culture conditions enhance resistance to chemotherapeutics. KG1a cells were cultured alone (KG1a) or in co-culture, as described above, over an 8-day period, followed by exposure to a 3:1 molar ratio of AraC and Dnr for 48 h. The graph represents the percentage of live cells normalized to the untreated control. Viability was measured with Annexin V. $^{*}p < 0.05$; $^{**}p < 0.01$; $^{***}p < 0.001$ (Student's *t*-test).

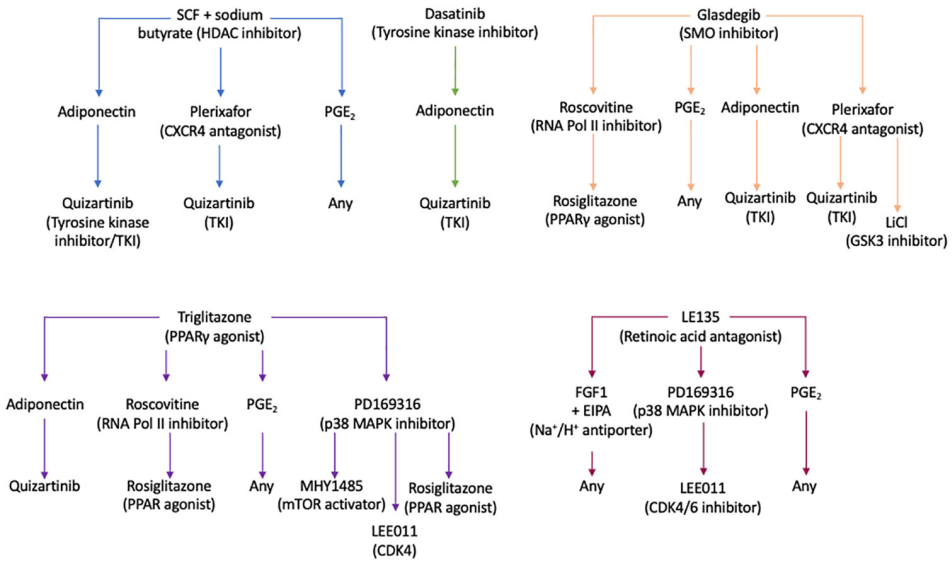

FIGURE 6 | Drug treatment pathways identified by the CombiCult screen to release leukemic stem cells from bone marrow microenvironment-mediated quiescence. The flow charts show the drug treatment sequences which could revert bone marrow mesenchymal stromal cell + TGFβ-1-induced KG1a quiescence. SCF, stem cell factor; CXCR4, CXC motif chemokine receptor type 4; PGE_2, prostaglandin E_2; SMO, smoothened; RNA Pol II, RNA polymerase II; PPARγ, peroxisome proliferator-activated receptor gamma; MAPK, mitogen-activated protein kinase; LiCl, lithium chloride; GSK, glycogen synthase kinase 3; mTOR, mammalian target or rapamycin; CDK4/6, cyclin-dependent kinase 4/6.

glasdegib-adiponectin (cytokine)-quizartinib (tyrosine kinase inhibitor), glasdegib-plerixafor (CXCR4 inhibitor)-quizartinib, and stem cell factor + sodium butyrate-adiponectin-quizartinib could induce the cycling of quiescent KG1a cells (**Figure 7**).

Collectively, we have established a layered co-culture system that can faithfully replicate BMM-mediated quiescence. This system was successfully translated into a co-axial bead-based screen used to identify possible drug combinations that could trigger the release of LSCs from quiescence.

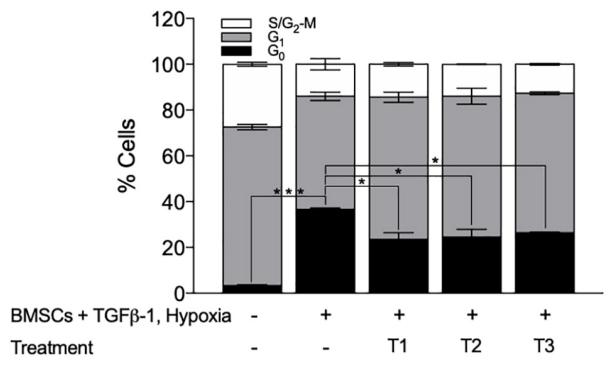

FIGURE 7 | Bone marrow mesenchymal stromal cell (BMSC) + TGFβ-1 + hypoxia co-culture system can be used to identify treatments that can break BMSC–TGFβ-1-induced quiescence. Cell cycle profile of KG1a cells exposed to the drug sequences indicated, measured by Hoechst + PY staining and flow cytometry. T1, glasdegib–adiponectin–quizartinib; T2, glasdegib, plerixafor, quizartinib; T3, stem cell factor + sodium butyrate–adiponectin–quizartinib. *$p < 0.05$; ***$p < 0.001$ (Student's t-test).

DISCUSSION

Quiescence driven by the BMM is a known mediator of drug resistance in AML (Wang et al., 2017) and it is now well accepted that a subpopulation of quiescent LSCs (or leukemia-initiating cells) resistant to chemotherapeutics is largely responsible for patient relapse (Saito et al., 2010a).

Essers et al. (2009) have shown that HSCs can be released from their quiescent state by interferon alpha (IFNα) and it makes HSCs susceptible to chemotherapeutics. In line with this, Saito et al. (2010b) have shown that pre-treatment with G-CSF triggers entry into the cell cycle and significantly enhances the response of LSCs to AraC. However, to date, there are few experimental models that can replicate the quiescence-inducing BMM *ex vivo* or *in vitro*, which hinders the identification and validation of such treatments. To address this, we developed a system to co-culture KG1a cells (LSC representative) with hydrogel-embedded BMSCs in the presence of TGFβ-1 (Blank and Karlsson, 2015) under conditions of hypoxia. This system induced quiescence in KG1a cells as seen by the increased accumulation of cells in the G_0 cell cycle phase, reduction in absolute cell number, induction the HSC/LSC quiescence markers GPRC5C and p21, and reduced expression of CDK4 and CDK6 as determined at mRNA and protein levels.

p21 is a member of the Cip/Kip CKI family (CDK2 interacting protein/kinase inhibition protein) together with p27 and p57. In normal LT-HSCs, p57 is the highest expressed member of the Cip/Kip CKI family, and of all CKIs, p57 deficiency shows the strongest developmental defects (Zhang et al., 1997; Takahashi et al., 2000) and depletion of the LT-HSC pool (Matsumoto et al., 2011). Additionally, it has been found that both p57 and p27 drive

quiescence of HSCs through interaction with the cyclin D-Hsc70 (constitutive heat shock protein 70) complex, preventing cyclin D1 nuclear translocation and inhibiting the activation of CDK4 and CDK6 (Zou et al., 2011). However, our data shows that p21, rather than p27/p57, is most highly associated with induction of quiescence in LSCs, indicating a potential differential dependence of CKIs upon leukemogenic transformation. There are other studies that support this hypothesis. Tremblay and colleagues found that in T-cell acute lymphoblastic leukemia cell cycle-restricted pre-LSCs express p21, and its deletion can revert drug resistance. The study by Viale et al. (2009) also found that p21 was essential for the maintenance of LSCs by preventing excessive DNA damage and the exhaustion of LSCs.

Another defining characteristics of quiescent LSCs is their low metabolic activity. A state of reduced metabolic activity is likely to support the persistence of LSCs in the BM niche where nutrients are limited and low metabolic activity has also been linked to drug resistance.

In line with this, we found that KG1a cells in co-culture were protected from AraC + Dnr treatment. Additionally, the study by Lagadinou et al. (2013) have shown that drug-resistant LSCs have diminished reserved ATP-producing capacity similar to the AML cells in the quiescence-inducing co-culture in our study. Importantly, they found that this lack of reserved metabolic capacity is a targetable vulnerability of LSCs, and the disruption of mitochondrial oxidative phosphorylation with the Bcl-2 inhibitor, venetoclax, sensitized LSCs to chemotherapeutics (Lagadinou et al., 2013).

By translating the co-culture to co-axial beads, a number of candidate drug combinations able to re-activate quiescent AML cells into cycling were identified. Of these, the combination of SCF with an HDAC inhibitor, such as sodium butyrate, has been employed before to expand HSPCs (Hua et al., 2019). By following this sequential treatment with adiponectin, an adipocyte-derived hormone shown to enhance the exit of HSCs from quiescence (Masamoto et al., 2017) and quizartinib, a tyrosine kinase inhibitor (TKI) that can target c-KIT (Galanis and Levis, 2015) and FLT3 (Naqvi and Ravandi, 2019), this combination could release LSCs from quiescence.

Aberrant Hedgehog signaling has also been identified in a variety of human leukemia types and LSCs. Studies have shown that the transmembrane receptor smoothened (SMO) is involved in the maintenance of LSC quiescence and drug resistance. It has been reported that inhibition of SMO by glasdegib can cause LSCs to re-enter the cell cycle (Sadarangani et al., 2015; Fukushima et al., 2016; Kakiuchi et al., 2017), and an ongoing clinical trial (phase III double-blind, BRIGHT AML 1019) investigates the combination of glasdegib with standard chemotherapy (Cortes et al., 2019) in patients with untreated AML. This corroborates that the developed co-culture model and drug screening platform can be utilized to identify drugs able to release LSCs from quiescence.

Finally, our results also highlight the importance of drug combinations as a treatment strategy. Using mathematical modeling, Glauche et al. (2012) have shown that continuous administration of TKIs with overlapping, short intervals of IFNα as opposed to continuous TKIs plus continuous IFNα or pulsed (single administration) TKI during short intervals of IFNα would be most effective at targeting the leukemic clones in chronic myeloid leukemia. It was hypothesized that the less frequent administration of IFNα may reduce the speed of eradication of leukemic clones but that this approach may prevent the possible exhaustion of normal HSCs (Glauche et al., 2012), thus decreasing possible adverse side effects of combinatorial/sequential treatments.

CONCLUSION

The co-culture systems described here can closely model BMM-mediated quiescence and be suitable for high-throughput drug screening. Although it is highly likely that other cells and components of the bone marrow also play a role in inducing quiescence, the presented co-culture model can be a beneficial tool for the identification of treatments and drug targets to reactivate quiescent LSCs and increase their sensitivity to cytotoxic drugs.

DATA AVAILABILITY STATEMENT

The dataset analyzed (GSE17054) for this study can be found in the Gene Expression Omnibus (GEO) available at https://www.ncbi.nlm.nih.gov/geo/query/acc.cgi?acc=GSE17054.

AUTHOR CONTRIBUTIONS

EO'R, ES, and DH designed the study. EO'R and ES wrote the manuscript. EO'R, ES, DH, TW, HZ, and CN preformed the wet-lab experiments. ES and JS preformed the dataset analysis. EO'R, HZ, JS, and ES carried out statistical analyses. EO'R, HZ, CN, JS, MT, TW, DH, YC, and ES contributed to data interpretation and edited and approved the manuscript. All authors contributed to the article and approved the submitted version.

FUNDING

Research in the ES lab was supported by the European Union's Horizon 2020 Research and Innovation Program DISCOVER under grant agreement no. 777995, Science Foundation Ireland (SFI/TIDA/B2388), and the Irish Cancer Society (BCNI/ICS/B3042). EO'R was funded by the Irish Research Council (EPSG/2015/91) and the Thomas Crawford Hayes fund from NUI Galway. HZ was funded by the College of Science Scholarships and Thomas Crawford Hayes fund, NUI Galway.

ACKNOWLEDGMENTS

The authors acknowledge the facilities and scientific and technical assistance of the NUI Galway Flow Cytometry

Core Facility (http://ncbes.eurhost.net/flow-cytometry-core-facility.aspx), NUI Galway Screening and Genomics Core Facility (http://ncbes.eurhost.net/screening-core-facility.aspx), and Biomaterials Equipment and Services at CÚRAM, Centre for Research in Medical Devices (13/RC/2073_P2).

SUPPLEMENTARY MATERIAL

The Supplementary Material for this article can be found online at: https://www.frontiersin.org/articles/10.3389/fcell.2021.662868/full#supplementary-material

REFERENCES

Baker, S. J., and Reddy, E. P. (2012). CDK4: a key player in the cell cycle, development, and cancer. *Genes Cancer* 3, 658–669. doi: 10.1177/1947601913478972

Blank, U., and Karlsson, S. (2015). TGF-beta signaling in the control of hematopoietic stem cells. *Blood* 125, 3542–3550. doi: 10.1182/blood-2014-12-618090

Cabezas-Wallscheid, N., Buettner, F., Sommerkamp, P., Klimmeck, D., Ladel, L., Thalheimer, F. B., et al. (2017). Vitamin A-retinoic acid signaling regulates hematopoietic stem cell dormancy. *Cell* 169, 807–823. doi: 10.1016/j.cell.2017.04.018

Cheng, T., Rodrigues, N., Shen, H., Yang, Y., Dombkowski, D., Sykes, M., et al. (2000). Hematopoietic stem cell quiescence maintained by p21cip1/waf1. *Science* 287, 1804–1808. doi: 10.1126/science.287.5459.1804

Cortes, J. E., Dombret, H., Merchant, A., Tauchi, T., DiRienzo, C. G., Sleight, B., et al. (2019). Glasdegib plus intensive/non-intensive chemotherapy in untreated acute myeloid leukemia: BRIGHT AML 1019 Phase III trials. *Futur. Oncol.* 15, 3531–3545. doi: 10.2217/fon-2019-0373

Eliasson, P., and Jönsson, J.-I. (2010). The hematopoietic stem cell niche: low in oxygen but a nice place to be. *J. Cell. Physiol.* 222, 17–22. doi: 10.1002/jcp.21908

Essers, M. A. G., Offner, S., Blanco-Bose, W. E., Waibler, Z., Kalinke, U., Duchosal, M. A., et al. (2009). IFNa activates dormant haematopoietic stem cells *in vivo*. *Nature* 458, 904–908. doi: 10.1038/nature07815

Fukushima, N., Minami, Y., Kakiuchi, S., Kuwatsuka, Y., Hayakawa, F., Jamieson, C., et al. (2016). Small-molecule Hedgehog inhibitor attenuates the leukemia-initiation potential of acute myeloid leukemia cells. *Cancer Sci.* 107, 1422–1429. doi: 10.1111/cas.13019

Galanis, A., and Levis, M. (2015). Inhibition of c-Kit by tyrosine kinase inhibitors. *Haematologica* 100, e77–e79. doi: 10.3324/haematol.2014.117028

Gao, Y., Yang, P., Shen, H., Yu, H., Song, X., Zhang, L., et al. (2015). Small-molecule inhibitors targeting INK4 protein p18(INK4C) enhance *ex vivo* expansion of haematopoietic stem cells. *Nat. Commun.* 6:6328. doi: 10.1038/ncomms7328

Glauche, I., Horn, K., Horn, M., Thielecke, L., Essers, M. A. G., Trumpp, A., et al. (2012). Therapy of chronic myeloid leukaemia can benefit from the activation of stem cells: simulation studies of different treatment combinations. *Br. J. Cancer* 106, 1742–1752. doi: 10.1038/bjc.2012.142

Gos, M., Miloszewska, J., Swoboda, P., Trembacz, H., Skierski, J., and Janik, P. (2005). Cellular quiescence induced by contact inhibition or serum withdrawal in C3H10T1/2 cells. *Cell Prolif.* 38, 107–116. doi: 10.1111/j.1365-2184.2005.00334.x

Hanahan, D., and Weinberg, R. A. (2017). "Biological hallmarks of cancer," in *Holland-Frei Cancer Medicine,* eds R. C. Bast, W. N. Hait, D. W. Kufe, R. R. Weichselbaum, J. F. Holland, C. M. Croce, et al. (Wiley). doi: 10.1002/9781119000822.hfcm002

Harrington, J. K. (2011). Biology of cancer. *Medicine* 39, 689–692. doi: 10.1016/j.mpmed.2011.09.015

Hua, P., Kronsteiner, B., van der Garde, M., Ashley, N., Hernandez, D., Tarunina, M., et al. (2019). Single-cell assessment of transcriptome alterations induced by Scriptaid in early differentiated human haematopoietic progenitors during *ex vivo* expansion. *Sci. Rep.* 9:5300. doi: 10.1038/s41598-019-41803-z

Jonas, B. A. (2017). On the origin of relapse in AML. *Sci. Transl. Med.* 9:eaan8205. doi: 10.1126/scitranslmed.aan8205

Justino De Almeida, M., Luchsinger, L. L., Corrigan, D. J., Williams, L. J., and Snoeck, H.-W. (2017). Dye-independent methods reveal elevated mitochondrial mass in hematopoietic stem cells. *Cell Stem Cell* 21, 725–729. doi: 10.1016/j.stem.2017.11.002

Kakiuchi, S., Minami, Y., Miyata, Y., Mizutani, Y., Goto, H., Kawamoto, S., et al. (2017). NANOG expression as a responsive biomarker during treatment with Hedgehog signal inhibitor in acute myeloid leukemia. *Int. J. Mol. Sci.* 18:486. doi: 10.3390/ijms18030486

Lagadinou, E. D., Sach, A., Callahan, K., Rossi, R. M., Neering, S. J., Minhajuddin, M., et al. (2013). BCL-2 inhibition targets oxidative phosphorylation and selectively eradicates quiescent human leukemia stem cells. *Cell Stem Cell* 12, 329–341. doi: 10.1016/j.stem.2012.12.013

Lee, E. Y., and Muller, W. J. (2010). Oncogenes and tumor suppressor genes. *Cold Spring Harb. Perspect. Biol.* 2:a003236. doi: 10.1101/cshperspect.a003236

Leo, W. J., Mcloughlin, A. J., and Malone, D. M. (1990). Effects of sterilization treatments on some properties of alginate solutions and gels. *Biotechnol. Prog.* 6, 51–53. doi: 10.1021/bp00001a008

Li, B., Sun, C., Sun, J., Yang, M., Zuo, R., Liu, C., et al. (2019). Autophagy mediates serum starvation-induced quiescence in nucleus pulposus stem cells by the regulation of P27. *Stem Cell Res. Ther.* 10:118. doi: 10.1186/s13287-019-1219-8

Masamoto, Y., Arai, S., Sato, T., Kubota, N., Takamoto, I., Kadowaki, T., et al. (2017). Adiponectin enhances quiescence exit of murine hematopoietic stem cells and hematopoietic recovery through mTORC1 potentiation. *Stem Cells* 35, 1835–1848. doi: 10.1002/stem.2640

Matsumoto, A., Takeishi, S., Kanie, T., Susaki, E., Onoyama, I., Tateishi, Y., et al. (2011). p57 is required for quiescence and maintenance of adult hematopoietic stem cells. *Cell Stem Cell* 9, 262–271. doi: 10.1016/j.stem.2011.06.014

Moirangthem, R. D., Singh, S., Adsul, A., Jalnapurkar, S., Limaye, L., and Kale, V. P. (2015). Hypoxic niche-mediated regeneration of hematopoiesis in the engraftment window is dominantly affected by oxygen tension in the milieu. *Stem Cells Dev.* 24, 2423–2436. doi: 10.1089/scd.2015.0112

Nakamura-Ishizu, A., Takizawa, H., and Suda, T. (2014). The analysis, roles and regulation of quiescence in hematopoietic stem cells. *Development* 141, 4656–4666. doi: 10.1242/dev.106575

Naqvi, K., and Ravandi, F. (2019). FLT3 inhibitor quizartinib (AC220). *Leuk. Lymphoma* 60, 1866–1876. doi: 10.1080/10428194.2019.1602263

Nwajei, F., and Konopleva, M. (2013). The bone marrow microenvironment as niche retreats for hematopoietic and leukemic stem cells. *Adv. Hematol.* 2013:953982. doi: 10.1155/2013/953982

Rai, K. R., Holland, J. F., Glidewell, O. J., Weinberg, V., Brunner, K., Obrecht, J. P., et al. (1981). Treatment of acute myelocytic leukemia: a study by cancer and leukemia group B. *Blood* 58, 1203–1212. doi: 10.1182/blood.V58.6.1203.1203

Sadarangani, A., Pineda, G., Lennon, K. M., Chun, H.-J., Shih, A., Schairer, A. E., et al. (2015). GLI2 inhibition abrogates human leukemia stem cell dormancy. *J. Transl. Med.* 13:98. doi: 10.1186/s12967-015-0453-9

Saito, Y., Kitamura, H., Hijikata, A., Tomizawa-Murasawa, M., Tanaka, S., Takagi, S., et al. (2010a). Identification of therapeutic targets for quiescent, chemotherapy-resistant human leukemia stem cells. *Sci. Transl. Med.* 2:17ra9. doi: 10.1126/scitranslmed.3000349

Saito, Y., Uchida, N., Tanaka, S., Suzuki, N., Tomizawa-Murasawa, M., Sone, A., et al. (2010b). Induction of cell cycle entry eliminates human leukemia stem cells in a mouse model of AML. *Nat. Biotechnol.* 28, 275–280. doi: 10.1038/nbt.1607

Sharma, P., and Pollyea, D. A. (2018). Shutting down acute myeloid leukemia and myelodysplastic syndrome with bcl-2 family protein inhibition. *Curr. Hematol. Malig. Rep.* 13, 256–264. doi: 10.1007/s11899-018-0464-8

Tajer, P., Pike-Overzet, K., Arias, S., Havenga, M., and Staal, F. J. T. (2019). *Ex vivo* expansion of hematopoietic stem cells for therapeutic purposes: lessons from development and the niche. *Cells* 8:169. doi: 10.3390/cells8020169

Takahashi, K., Nakayama, K., and Nakayama, K. (2000). Mice lacking a CDK inhibitor, p57Kip2, exhibit skeletal abnormalities and growth retardation. *J. Biochem.* 127, 73–83. doi: 10.1093/oxfordjournals.jbchem.a022586

Tarunina, M., Hernandez, D., Kronsteiner-Dobramysl, B., Pratt, P., Watson, T., Hua, P., et al. (2016). A Novel High-throughput screening platform reveals an optimized cytokine formulation for human hematopoietic progenitor cell expansion. *Stem Cells Dev.* 25, 1709–1720. doi: 10.1089/scd.2016.0216

Viale, A., De Franco, F., Orleth, A., Cambiaghi, V., Giuliani, V., Bossi, D., et al. (2009). Cell-cycle restriction limits DNA damage and maintains self-renewal of leukaemia stem cells. *Nature* 457, 51–56. doi: 10.1038/nature07618

Villeval, J.-L., and Vainchenker, W. (2020). Megakaryocytes tame erythropoiesis with TGFβ1. *Blood* 136, 1016–1017. doi: 10.1182/blood.2020006906

Walkley, C. R., Fero, M. L., Chien, W.-M., Purton, L. E., and McArthur, G. A. (2005). Negative cell-cycle regulators cooperatively control self-renewal and differentiation of haematopoietic stem cells. *Nat. Cell Biol.* 7, 172–178. doi: 10.1038/ncb1214

Wang, W., Bochtler, T., Wuchter, P., Manta, L., He, H., Eckstein, V., et al. (2017). Mesenchymal stromal cells contribute to quiescence of therapy-resistant leukemic cells in acute myeloid leukemia. *Eur. J. Haematol.* 99, 392–398. doi: 10.1111/ejh.12934

Wang, X., Dong, F., Zhang, S., Yang, W., Yu, W., Wang, Z., et al. (2018). TGF-β1 negatively regulates the number and function of hematopoietic stem cells. *Stem Cell Reports* 11, 274–287. doi: 10.1016/j.stemcr.2018.05.017

Zhang, P., Liégeois, N. J., Wong, C., Finegold, M., Hou, H., Thompson, J. C., et al. (1997). Altered cell differentiation and proliferation in mice lacking p57KIP2 indicates a role in Beckwith–Wiedemann syndrome. *Nature* 387, 151–158. doi: 10.1038/387151a0

Zou, P., Yoshihara, H., Hosokawa, K., Tai, I., Shinmyozu, K., Tsukahara, F., et al. (2011). $p57^{Kip2}$ and $p27^{Kip1}$ cooperate to maintain hematopoietic stem cell quiescence through interactions with Hsc70. *Cell Stem Cell* 9, 247–261. doi: 10.1016/j.stem.2011.07.003

Conflict of Interest: MT, TW, DH, and YC were employed by Plasticell Ltd., is the owner of the CombiCult® technology.

The remaining authors declare that the research was conducted in the absence of any commercial or financial relationships that could be construed as a potential conflict of interest.

Publisher's Note: All claims expressed in this article are solely those of the authors and do not necessarily represent those of their affiliated organizations, or those of the publisher, the editors and the reviewers. Any product that may be evaluated in this article, or claim that may be made by its manufacturer, is not guaranteed or endorsed by the publisher.

frontiers in Cell and Developmental Biology

ORIGINAL RESEARCH
published: 14 October 2021
doi: 10.3389/fcell.2021.705828

A Pyroptosis-Related Gene Panel in Prognosis Prediction and Immune Microenvironment of Human Endometrial Cancer

*Xiaocui Zhang and Qing Yang**

Department of Obstetrics and Gynecology, Shengjing Hospital of China Medical University, Shenyang, China

OPEN ACCESS

Edited by:
Tugba Bagci-Onder, Koç University, Turkey

Reviewed by:
Ivarne L. S. Tersariol, Federal University of São Paulo, Brazil
Triona Ni Chonghaile, Royal College of Surgeons in Ireland, Ireland
Zongqiang Huang, First Affiliated Hospital of Zhengzhou University, China
Runju Zhang, Zhejiang University, China

***Correspondence:**
Qing Yang
yangqing_sj@126.com

Specialty section:
This article was submitted to Cell Death and Survival, a section of the journal Frontiers in Cell and Developmental Biology

Received: *06 May 2021*
Accepted: *22 September 2021*
Published: *14 October 2021*

Citation:
Zhang X and Yang Q (2021) A Pyroptosis-Related Gene Panel in Prognosis Prediction and Immune Microenvironment of Human Endometrial Cancer. Front. Cell Dev. Biol. 9:705828. doi: 10.3389/fcell.2021.705828

As the second common diagnosed cancer among gynecological tumors, endometrial cancer (EC) has heterogeneous pathogenesis and clinical manifestations. Therefore, prognosis prediction that considers gene expression value and clinical characteristics, is helpful to patients with EC. We downloaded RNA expression and clinical data from the TCGA database. We achieved 4 DEPRGs and constructed the PRG panel by univariate, lasso and multivariate Cox analysis. Based on the median value of the risk score, patients were divided into two groups. The Kaplan–Meier curve suggested that the patients with lower risk scores had better clinical outcomes of EC. AUC of ROC curves suggested the panel can be used as an independent predictor. Future analysis indicated the positive correlations between risk score and clinical characteristics. What's more, we performed GO and KEGG functional analysis and immune environment exploration to get an understanding of the potential molecular mechanism and immunotherapeutic target. To future validate the panel, we found that the relapse-free and overall survival probability of 4 prognostic DEPRGs between high-expression group and low-expression group were different through the Kaplan–Meier plotter in UCEC. In addition, GEPIA database and RT-PCR experiment indicated GPX4 and GSDMD were highly expressed in UCEC compared to normal endometrial tissue, and TIRAP and ELANE were downregulated. This study identified a PRG panel to predict the prognosis immune microenvironment in human EC. Then, Kaplan–Meier analysis and AUC below the ROC curves was used to validate the panel. In addition, Chi-square was used to show the clinical significance. GO, KEGG and GSEA were used to show the functional differences. Different immune-related databases were used to analyze the immune characteristics. The Kaplan–Meier plotter website was used to assess the effect of genes on survival. GEPIA and RT-PCR were used to analyze the expression level. In summary, we identified 4 prognosis-associated pyroptosis-related genes (ELANE, GPX4, GSDMD, and TIRAP). The panel can also predict prognosis prediction and immune microenvironment in human endometrial cancer.

Keywords: endometrial cancer, pyroptosis-related genes, overall survival, panel, tumor immune environment

INTRODUCTION

There were 417267 new cases and 97370 new cancer deaths reported in 2020, endometrial cancer (EC) was ranked in the top 10 most common cancers in female patients across the world, and is the second most commonly diagnosed cancer among gynecological tumors (Sung et al., 2021). Most cases are diagnosed in the late stage of life, but there are increasing numbers being diagnosed at an early stage, meaning the onset of EC is younger (Amant et al., 2005; Moore and Brewer, 2017). Though the mortality is relatively lower than other gynecological tumors, the pathogenesis and clinical manifestations of EC are heterogeneous (Gupta, 2017). Therefore, prognosis prediction considering the gene expression value and clinical characteristics is helpful for patients with EC.

Pyroptosis mediated by gasdermin is a kind of programmed cell death, which is characterized by cell swelling until cell membrane rupture, leading to the release of cell contents and then activating a strong inflammatory response (Bergsbaken et al., 2009; He et al., 2015; Vande Walle and Lamkanfi, 2016; Kovacs and Miao, 2017; Man et al., 2017; Shi et al., 2017). For morphology, pyroptosis cells showed swelling under a light microscope, and there were many bubble-like protrusions. Compared with necrotic cells, the swelling degree of focal death is lower. Under the electron microscope, it can be seen that before the rupture of the membrane, the pyroptosis cells form a large number of vesicles, namely focal apoptotic bodies. The cell membrane then forms pores and breaks, meaning the content flows out. The biochemical characteristics of pyroptosis involve the formation of inflammatory bodies, the activation of caspase and gasdermin, and the release of a large number of inflammatory factors. Pyroptosis is also an important innate immune response and plays an important role in the fight against infection (Bergsbaken et al., 2009; Man et al., 2017; Robinson et al., 2019). Pyroptosis has been reported to be involved in different processes in different diseases, including cardiovascular diseases (Jia et al., 2019; Zhaolin et al., 2019), Parkinson's disease (Wang S. et al., 2019), Alzheimer's disease (Han et al., 2020), diabetic kidney disease (Wang Y. et al., 2019; Lin et al., 2020), inflammatory bowel disease (Chen et al., 2019), cancers (Pizato et al., 2018; Cui et al., 2019; Qiao et al., 2019; Yu et al., 2019; Zhang C. C. et al., 2019; Zhang T. et al., 2019; Teng et al., 2020), and so on.

Recently, many reports have outlined that pyroptosis-related genes and processes play an important role in cancers. For breast cancer, DRD2 which promotes macrophage M1 polarization, triggers gasdermin E (GSDME) and induces pyroptosis, which is then downregulated (Tan et al., 2021), and through increased levels of caspase-1, caspase-3, gasdermin D and E (GSDMD and GSDME), docosahexaenoic acid (DHA) and tetraarsenic hexoxide could promote pyroptosis and thus inhibit breast cancer progress (Pizato et al., 2018; An et al., 2021; Li, 2021). For colorectal cancer, lobaplatin (Yu et al., 2019), liver X receptors (LXPs) (Derangère et al., 2014), and arsenic trioxide (ATO) combined with ascorbic acid (AA) (Tian et al., 2020) could be used to better treat colorectal cancers through inducing pyroptosis. For hepatocellular carcinoma, Hage et al. (2019) reported that sorafenib could induce the pyroptosis of macrophages which were the key mediators of antitumor effect. Zhang X. et al. (2020) reported that miltirone, a phenanthraquinone derivative isolated from Radix Salviae Miltiorrhizae, could inhibit hepatocellular carcinoma cells proliferation and induce the proteolysis of GSDME and cleavage of caspase 3. Furthermore, gasdermin also attaches importance to gastric, lung, skin, and esophageal squamous cancer (Xia et al., 2019). Yang et al. (2020) have reported that NLRP3, caspase-1, and GSDMD were upregulated in EC, and activation in pyroptosis could lead to an anti-tumor effect. Since pyroptosis plays such an important role in cancers and to date there have been few studies exploring its role in EC, combined analysis of pyroptosis and EC is imminent.

This study used TCGA, a large-scale open database, for analyzing pyroptosis-related genes (PRGs) in EC and constructed a novel PRG panel to predict the overall survival and immune microenvironment in EC. This research confirmed that the panel can be used to predict the clinical outcomes of EC independently and could eventually instruct immunotherapy of EC in the future.

MATERIALS AND METHODS

The process of data analysis is shown in the flow chart in **Figure 1**.

Data Acquisition

The RNA expression and clinical data of UCEC patients were downloaded from the TCGA website on April 2, 2021[1]. After removing the cases with incomplete clinical information, 526 cases were remained, as shown in **Table 1**. The "limma" R package was used to normalize the RNA expression profiles. A total of 34 pyroptosis-related genes were achieved through literature mining and are provided in **Table 2** (Man and Kanneganti, 2015; Wang and Yin, 2017; Karki and Kanneganti, 2019; Xia et al., 2019; Ye et al., 2021).

Identification of Prognostic Differentially Expressed Pyroptosis-Related Genes

Differential expression genes (DEGs) were searched for with the "limma" R package by comparing tumor tissues with

Abbreviations: EC, endometrial cancer; UCEC, uterine Corpus Endometrial Carcinoma; GSDMD, gasdermin D; GSDME, gasdermin E; DHA, docosahexaenoic acid; LXPs, liver X receptors; ATO, arsenic trioxide; AA, ascorbic acid; NLRP3, NACHT Domain-, Leucine-Rich Repeat-, and PYD-Containing Protein 3; PRGs, pyroptosis-related genes; DEGs, Differential expression genes; DEPRGs, differentially expressed PRGs; OS, overall survival; RFS, relapse-free survival; BH, Benjamini and Hochberg; PCA, principal components analysis; ROC, operating characteristic curve; DCA, decision curve analysis; GO, Gene ontology; KEGG, Kyoto Encyclopedia of Genes and Genomes; GSEA, Gene Set Enrichment Analysis; GEPIA, Gene Expression Profiling Interactive Analysis; T, tumor; N, normal; FDR, false discovery rate.

[1]https://portal.gdc.cancer.gov/repository

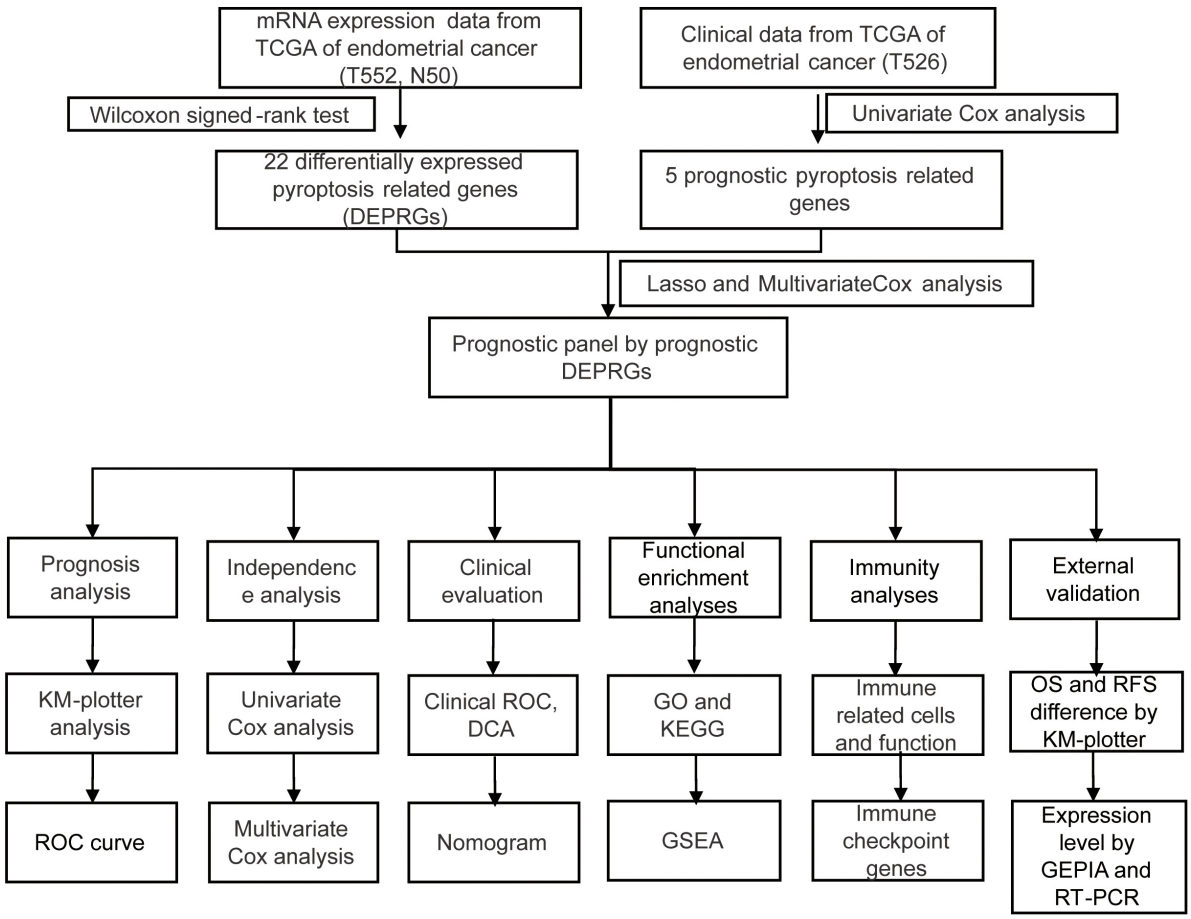

FIGURE 1 | The flow chart of whole process of data analysis.

TABLE 1 | Clinical characteristics of the UCEC patients in TCGA.

No. of patients		526
Age (median,range)		64 (31–90)
Grade (%)	Grade1	98
	Grade2	119
	Grade3	309
Stage (%)	I	330
	II	51
	III	119
	IV	26
Survival status	OS days (median)	847.5

TABLE 2 | 34 pyroptosis-related genes, 22 differentially expressed PRGs, 5 prognostic PRGs, and 4 DEPRGs.

34 pyroptosis-related genes	AIM2 CASP1 CASP3 CASP4 CASP5 CASP6 CASP8 CASP9 ELANE GPX4 GSDMA GSDMB GSDMC GSDMD GSDME IL18 IL1B IL6 NLRC4 NLRP1 NLRP2 NLRP3 NLRP6 NLRP7 NOD1 NOD2 PJVK PLCG1 PRKACA PYCARD SCAF11 TIRAP TNF
22 differentially expressed PRGs	AIM2 CASP CASP5 CASP6 CASP8 ELANE GPX4 GSDMB GSDMC GSDMD GSDME IL18 IL6 NLRP1 NLRP2 NLRP3 NLRP7 NOD1 NOD2 PYCARD TIRAP TNF
5 prognostic PRGs	CASP9 ELANE GPX4 GSDMD TIRAP
4 DEPRGs	ELANE GPX4 GSDMD TIRAP

normal tissues. We screened DEGs by a Wilcoxon signed-rank test (false discovery rate, FDR < 0.05). The intersection of DEGs and pyroptosis-related genes (PRGs) was considered as significant differentially expressed PRGs (DEPRGs). We conducted a univariate Cox analysis of overall survival (OS) to screen prognostic DEPRGs. Benjamini and Hochberg (BH) correction was used to adjust *p* values. The expression condition of these prognostic DEPRGs were shown with the "pheatmap" R package (1.0.12).

Construction and Confirmation of a Prognostic Panel by Differentially Expressed Pyroptosis-Related Genes

The "glmnet" R package was used for constructing the DEPRGs panel by lasso regression analysis, and 10-fold cross confirmation and a *P* value of less than 0.05 were used to simplify and rectify the model (Liang et al., 2020). The gene expression levels should be corrected by demographics in multivariate regression models.

At the same time, the risk score of patients was generated [risk score = Σ(expression value of each gene × and its coefficient)]. We used the median risk score to divide patients into two groups and visualized the results with the "Rtsne" R package. We then used the "stats" R package to conduct a principal components analysis (PCA) to study the different gene expression patterns of samples.

To validate this panel, we conducted a Kaplan-Meier analysis to show the clinical outcome differences between two groups with or without other clinical characteristics and visualized the survival curve using the "survive" and "survminer" R packages. The 1-, 2-, 3-, 4-, and 5-year ROC curves and the ROC curves compared with panels were drawn to predict the survival status with the "survivalROC" R packages. Univariate and multivariate Cox regression analyses then showed whether our panel could predict the prognosis of endometrial cancer independently.

A Chi-square test was then used to analyze the relationship between the panel and clinicopathological characteristics. These were shown in a strip chart and labeled as follows: $p < 0.001$ = ***, $p < 0.01$ = **,

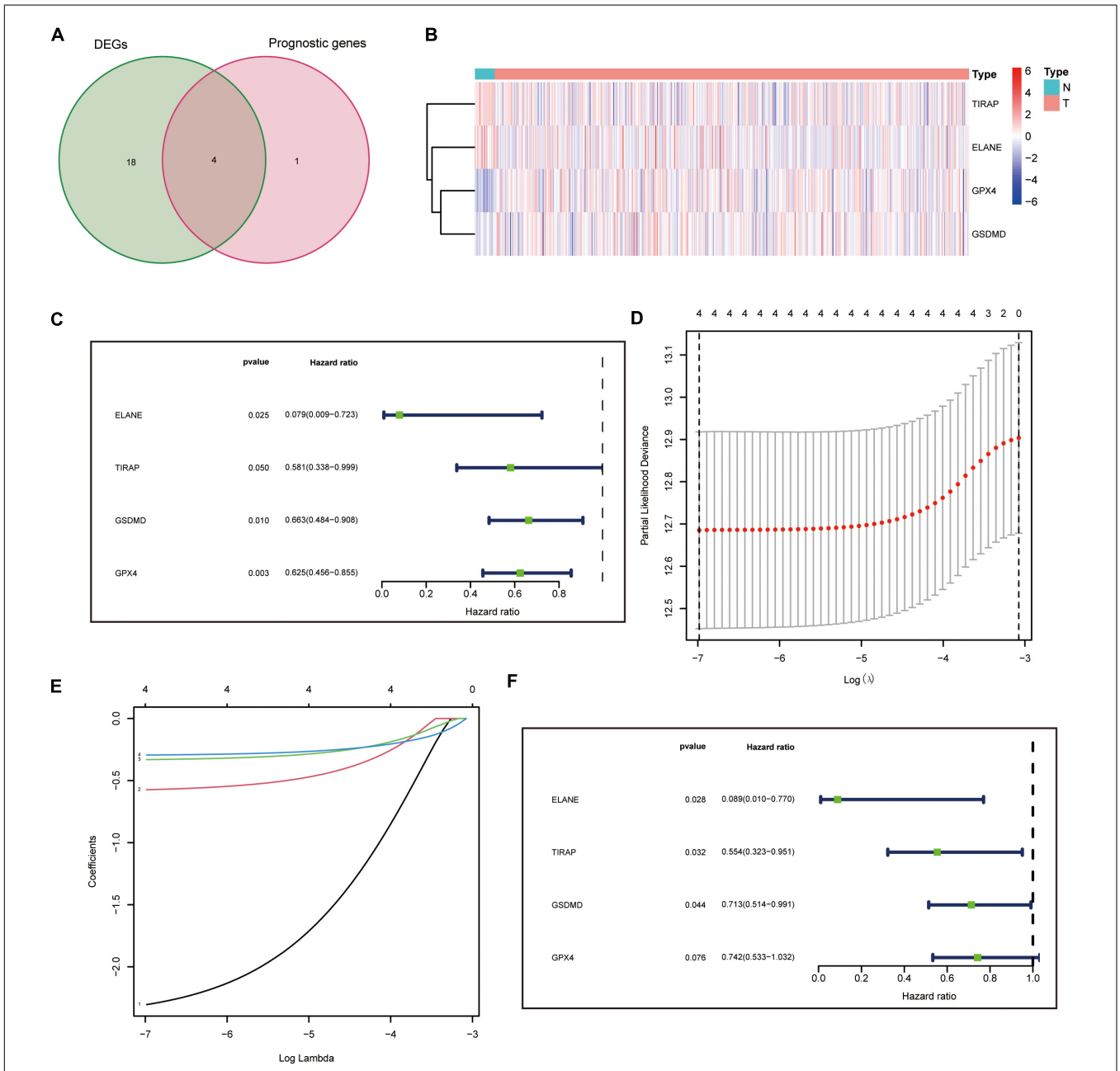

FIGURE 2 | Identification and analysis of prognostic DEPRGs. **(A)** 4 identified prognostic DEPRGs, and their expression condition **(B)**. Univariate **(C)**, lasso Cox **(D,E)**, and multivariate **(F)** analysis of prognostic DEPRGs.

and $p < 0.05$ = * by "ComplexHeatmap" R package. Wilcoxon signed-rank test compared the risk scores among different groups of these clinicopathological characteristics. The scatter diagram showed the analysis results.

We then conducted operating characteristic curve (ROC) and decision curve analysis (DCA) to assess the sensitivity and specificity of the prognostic panel for UCEC in comparison to other clinicopathological factors (Vickers and Elkin, 2006).

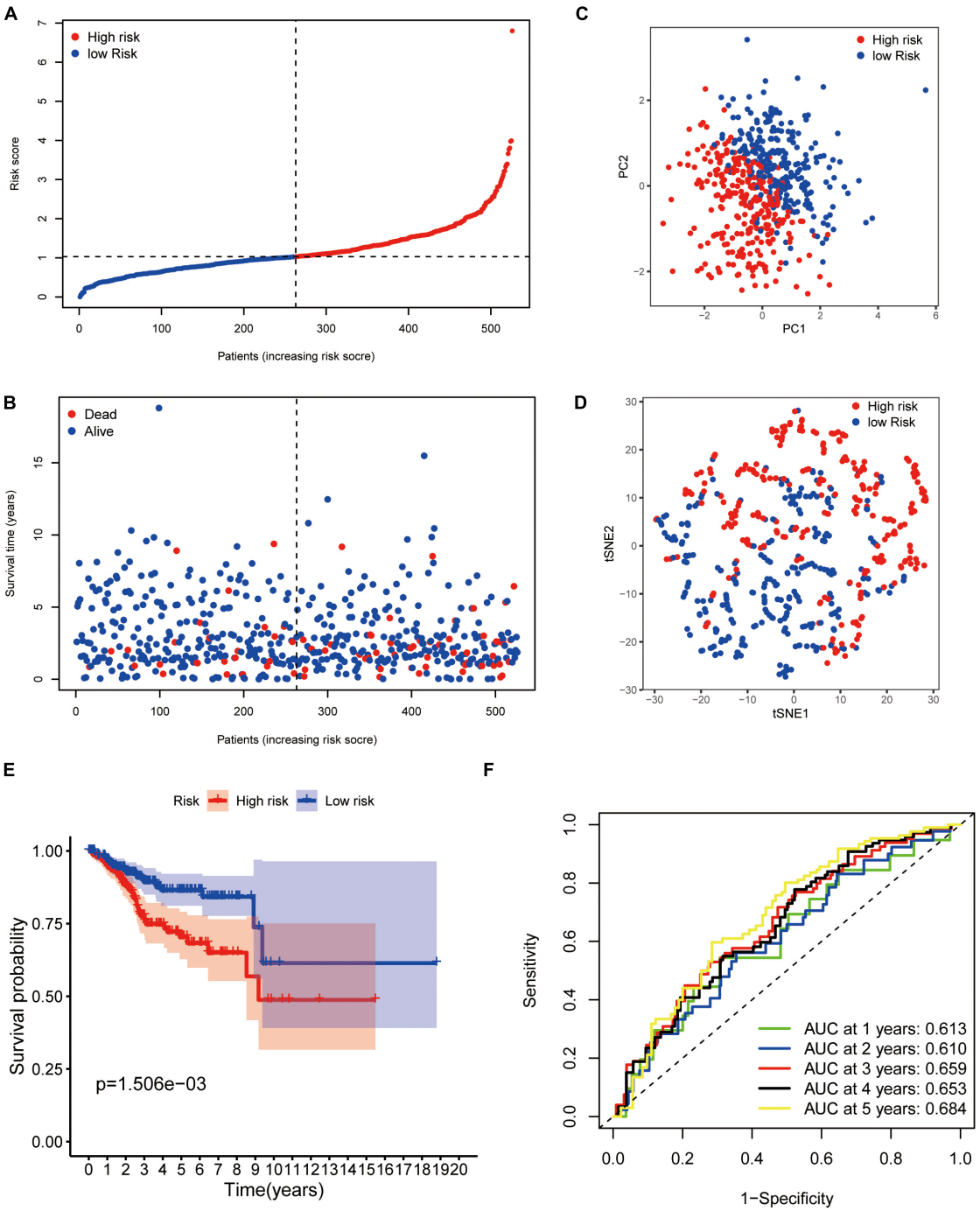

FIGURE 3 | Prognostic confirmation of the panel by DEPRGs. **(A)** Risk scores and **(B)** survival status of EC patients. **(C)** PCA, **(D)** t-SNE studying the different gene expression patterns of samples. **(E)** Kaplan-Meier plot showing patients in the low-risk group survived longer than patients in the high-risk group. **(F)** The 1-, 2-, 3-, 4-, and 5-year ROC curve to predict the survival status.

A nomogram was constructed, integrating the prognostic panel, for prediction of 1, 3, and 5-year OS of UCEC patients.

Gene Ontology, Kyoto Encyclopedia of Genes and Genomes Functional Enrichment, and Gene Set Enrichment Analysis Analysis Between High-Risk Versus Low-Risk Groups

Gene ontology (GO) and Kyoto Encyclopedia of Genes and Genomes (KEGG) pathway enrichment analyses predicted the potential functions of DEPRGs using the "clusterProfiler" R package. We then sorted and presented the top items of GO and KEGG pathways based on *P*-value < 0.05 through the statistical software R (version 4.0.2) and visualized the results in barplots using the "ggplot2" R package. Gene Set Enrichment Analysis (GSEA) software (Version 4.0.3)[2] was also used to explore the potential biological function difference between the two groups. GSEA (version 3.0) was run for the "c2.cp.kegg.v.7.2.symbols.gmt" gene sets. The number of permutations was set to 1,000 and the phenotype labels were high-risk and low risk. FDR < 0.25 and NOM $P < 0.05$ indicated statistical significance.

Immune Characteristics Analysis

Using TIMER, CIBERSORT, CIBERSORT-ABS, QUANTISEQ, MCPcounter, XCELL, and EPIC, we analyzed the correlation

[2]http://www.broad.mit.edu/gsea

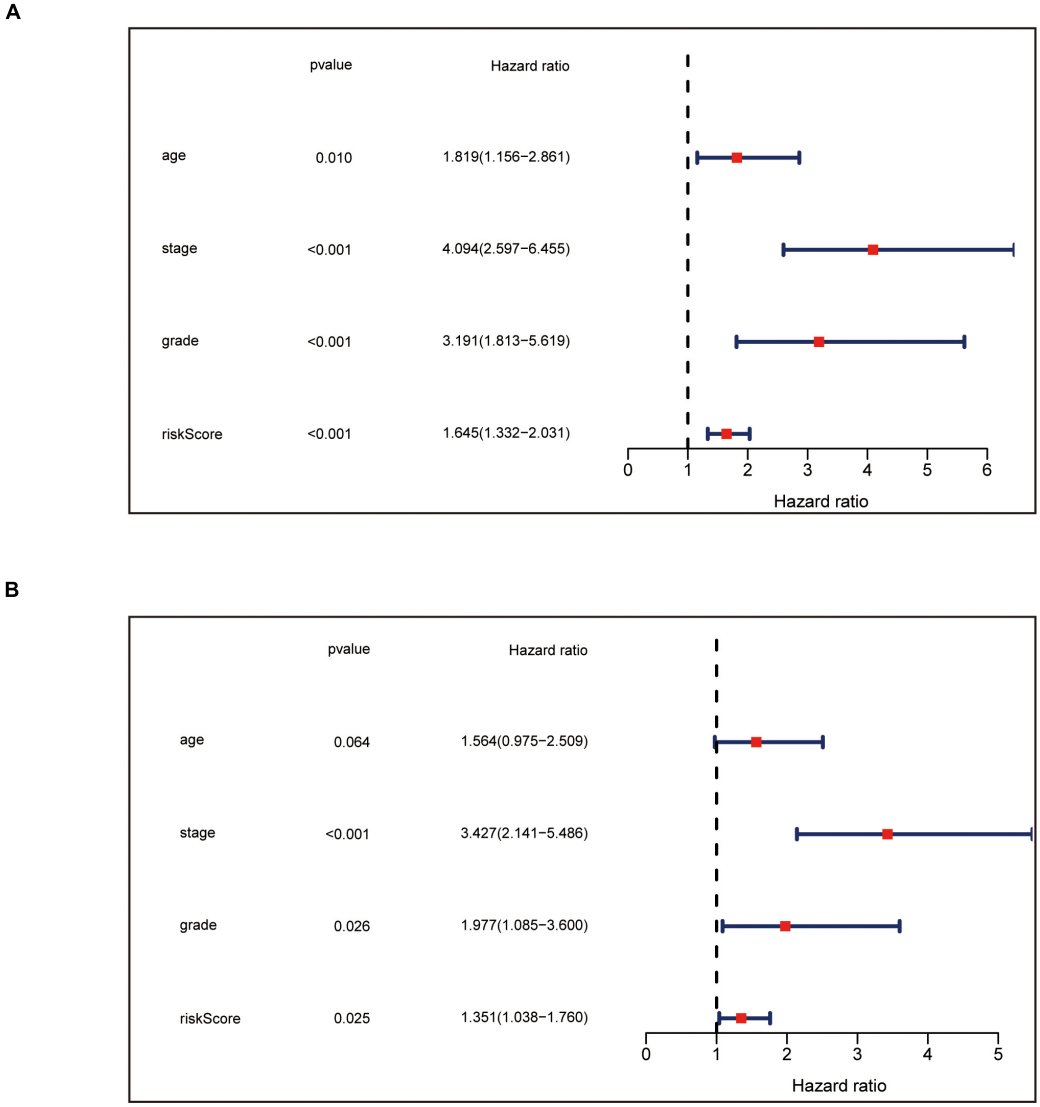

FIGURE 4 | Independence confirmation of the panel by DEPRGs. **(A)** Univariate and **(B)** Multivariate Cox regression analysis of the panel and other clinical characteristics associated with OS.

between the riskScore and immune-cell characteristics in UCEC patients of TCGA database by Spearman correlation analysis, and the results were visualized in a diagram. A p value < 0.05 was considered as statistically significant.

The "gsva" R package compared normalized gene expression data with the gene sets that had common biological functions, chromosomal localization, and physiological regulation in ssGSEA (Subramanian et al., 2005). The infiltrating score of 16 types of immune cells and the activity of 13 immune-related pathways were concluded. To study the expression value of immune checkpoint-related genes in two groups, we performed a "ggstatsplot" R package and violin plot visualization.

Survival Analysis of Four Prognostic Differentially Expressed Pyroptosis-Related Genes

The Kaplan–Meier plotter[3] could assess the effect of 54,675 genes on survival using 18,674 cancer samples (Győrffy et al., 2013). These cover 543 UCEC cancer patients with relapse-free and overall survival information (Nagy et al., 2021). Our study analyzed the relapse-free and overall survival of four prognostic DEPRGs through the Kaplan–Meier plotter in UCEC. Patients were classified into two groups according to the median of each prognostic DEPRG expression in the Kaplan–Meier plotter for relapse-free and overall survival. This classification method could show the survival probability differences between the high-expression group and the low-expression group.

[3]http://kmplot.com/analysis/

Gene Expression Profiling Interactive Analysis Database Analysis of Four Prognostic Differentially Expressed Pyroptosis-Related Genes

GEPIA is an online database that facilitates the standardized analysis of a tremendous amount of RNA sequencing data in the TCGA and GTEx data sets(Tang et al., 2017)[4]. The expression level of 4 prognostic DEPRGs was validated in GEPIA (Gene Expression Profiling Interactive Analysis) based on TCGA data [num(T) = 174; num(N) = 13].

Ethics Statement

This study was carried out in accordance with the standards of the Helsinki Declaration of the World Medical Association and approved by the Ethics Committee of China Medical University. All clinical samples were collected from the Shengjing Hospital of China Medical University, with informed consent from all patients.

Tissue Collection

There were 56 clinical samples used in this study, including 33 cases of primary UCEC tissue and 23 cases of normal endometrial tissue. All samples were collected from the patients undergoing surgical excision at the Department of Obstetrics and Gynecology, Shengjing Hospital of China Medical University. No patient received radiotherapy, chemotherapy, or hormone therapy before surgery.

[4]http://gepia.cancer-pku.cn/

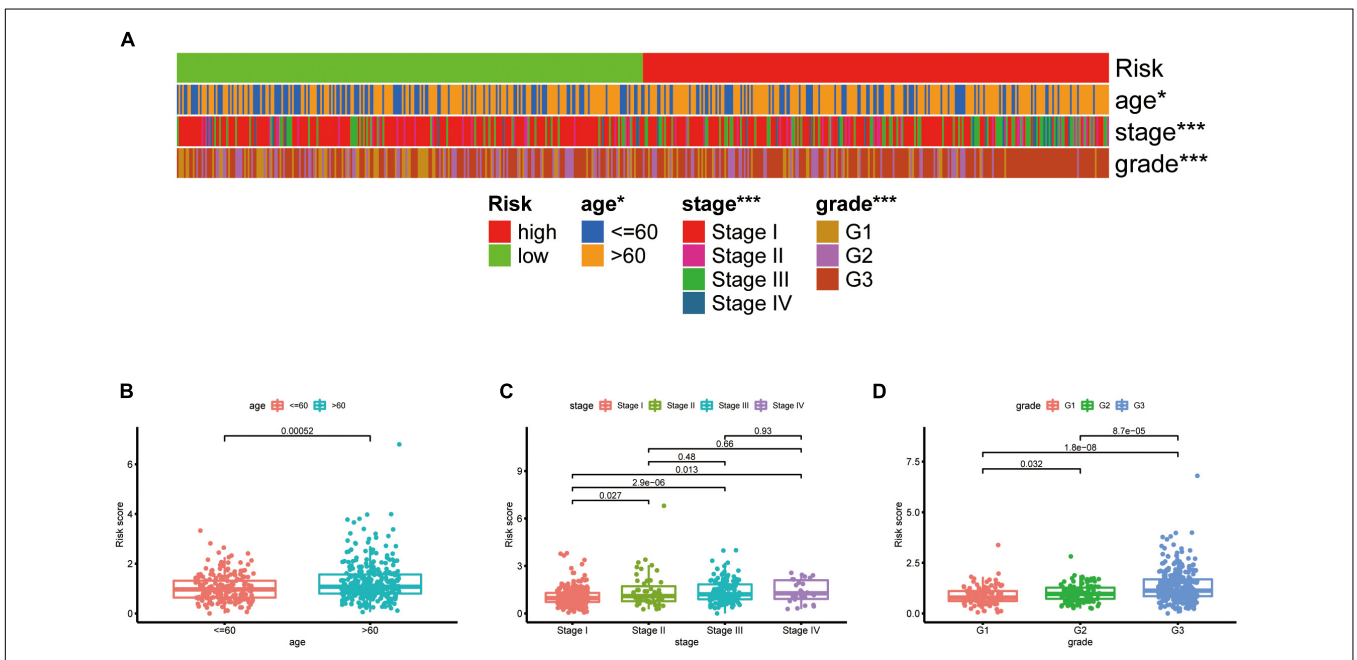

FIGURE 5 | Clinical evaluation of the panel by DEPRGs. A band chart **(A)** and the scatter diagram indicating that **(B)** age, **(C)** clinical stage, and **(D)** tumor grade were significantly associated with the risk score.

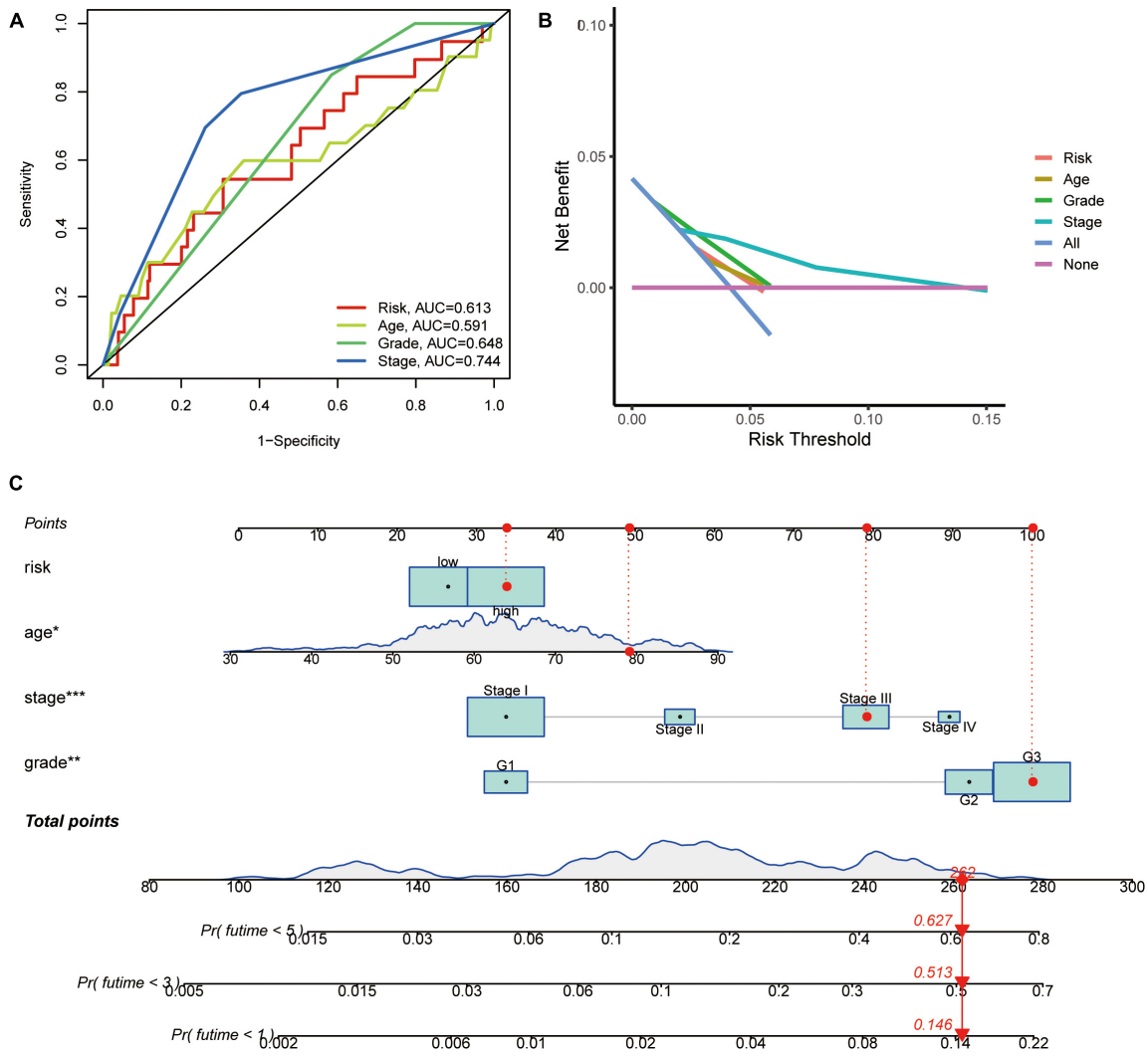

FIGURE 6 | Indicators of the panel diagnosis by DEPRGs. **(A)** The clinical ROC curve, **(B)** decision curve analysis, and **(C)** c-index of the nomogram of the panel.

The histopathological diagnosis was obtained from the Pathology Department according to the criteria of the World Health Organization.

Total RNA Extraction and Quantitative Real-Time RT-PCR

RNA isolation of endometrial tissue samples was conducted through TRIzol Reagent (Invitrogen, United States). The synthesis of complementary DNA (cDNA) was conducted using PrimeScriptTM RT reagent Kit with gDNA Eraser (Takara), through reverse transcription reaction. Quantitative polymerase chain reactions for TIRAP, ELANE, GPX4, GSDMD, and GAPDH were conducted in a volume of 20 μL using SYBR Premix Ex Taq (Takara) in the ABI 7500 Fast (Life Technologies, Carlsbad, CA, United States). GAPDH was selected as the internal reference gene. The primer sequences were as follows: TIRAP forward 5- CAGGAGGCATTGCTGATGAT-3; TIRAP reverse 5-GGGTAGTGGGCTGTCCTGTGAG-3; ELANE forward 5-GGAGCCCATAACCTCTCGC-3; ELANE reverse 5-GAGCAAGTTTACGGGGTCGT-3; GPX4 forward 5-GAGG CAAGACCGAAGTAAACTAC-3; GPX4 reverse 5-CCGAACT GGTTACACGGGAA-3; GSDMD forward 5- GTGTGTCAA CCTGTCTATCAAGG-3; GSDMD reverse 5-CATGGCATC GTAGAAGTGGAAG-3; GAPDH forward 5- CAGGAGGCA TTGCTGATGAT-3; GAPDH reverse 5-GAAGGCTG GGGCTCATTT-3. The relative levels of gene expression were evaluated by the $2^{-\Delta\Delta CT}$ method using GAPDH as the control.

Statistical Analysis

Statistical analysis was conducted using the R package and Graphpad Prism 8. Variance homogeneous and normal distributed continuous variables were analyzed using the unpaired student's *t*-test, otherwise, the Mann-Whitney *U*-test or Kruskal-Wallis *H*-test was used. DEGs were

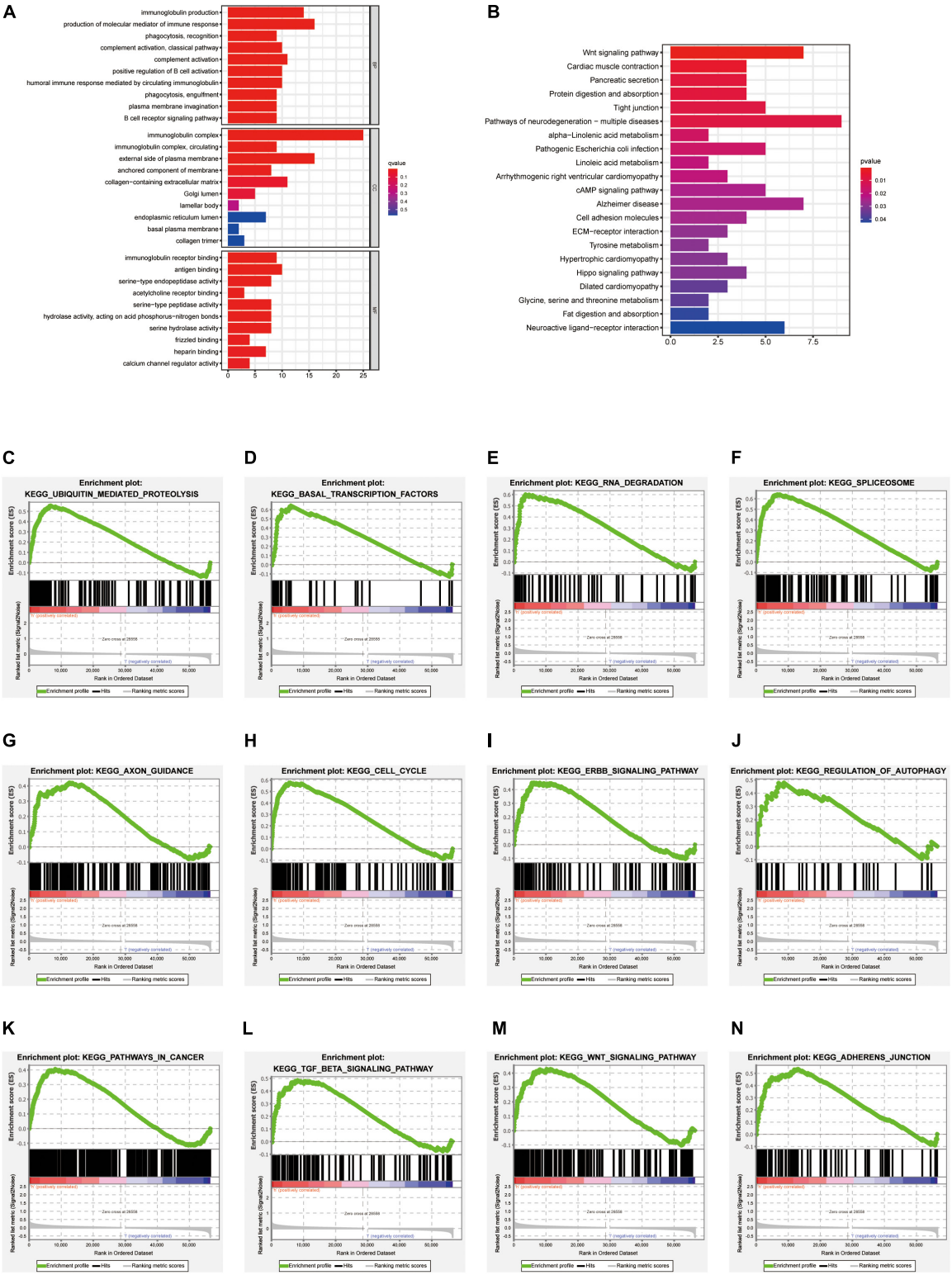

FIGURE 7 | GO, KEGG functional enrichment, and GSEA analysis between high-risk versus low-risk groups. Top 10 results of **(A)** GO functional and **(B)** KEGG pathway enrichment of DEGs between the two groups. **(C–N)** The pathway enriched in the high-risk group based on GSEA.

TABLE 3 | The whole results of GO functional analysis.

Ontology	ID	Description	*q* value	Count
BP	GO:0002377	immunoglobulin production	5.35E-06	14
BP	GO:0002440	production of molecular mediator of immune response	8.19E-06	16
BP	GO:0006910	phagocytosis, recognition	4.59E-05	9
BP	GO:0006958	complement activation, classical pathway	0.000229	10
BP	GO:0006956	complement activation	0.000229	11
BP	GO:0050871	positive regulation of B cell activation	0.000229	10
BP	GO:0002455	humoral immune response mediated by circulating immunoglobulin	0.000321	10
BP	GO:0006911	phagocytosis, engulfment	0.000321	9
BP	GO:0099024	plasma membrane invagination	0.000527	9
BP	GO:0050853	B cell receptor signaling pathway	0.00054	9
BP	GO:0010324	membrane invagination	0.000714	9
BP	GO:0006959	humoral immune response	0.000778	14
BP	GO:0016064	immunoglobulin mediated immune response	0.000778	11
BP	GO:0019724	B cell mediated immunity	0.000823	11
BP	GO:0050864	regulation of B cell activation	0.000949	10
BP	GO:0002449	lymphocyte mediated immunity	0.002587	13
BP	GO:0007409	axonogenesis	0.002863	15
BP	GO:0008037	cell recognition	0.002863	10
BP	GO:0002429	immune response-activating cell surface receptor signaling pathway	0.002863	15
BP	GO:0002757	immune response-activating signal transduction	0.002863	15
BP	GO:0007411	axon guidance	0.004257	11
BP	GO:0097485	neuron projection guidance	0.004257	11
BP	GO:0042742	defense response to bacterium	0.004348	12
BP	GO:0002460	adaptive immune response based on somatic recombination of immune receptors built from immunoglobulin superfamily domains	0.009757	12
BP	GO:0051249	regulation of lymphocyte activation	0.011431	14
BP	GO:0002920	regulation of humoral immune response	0.016708	7
BP	GO:0042113	B cell activation	0.040074	10
BP	GO:0006909	phagocytosis	0.040074	11
BP	GO:0050851	antigen receptor-mediated signaling pathway	0.043343	10
CC	GO:0019814	immunoglobulin complex	1.39E-21	25
CC	GO:0042571	immunoglobulin complex, circulating	1.90E-06	9
CC	GO:0009897	external side of plasma membrane	4.75E-05	16
CC	GO:0031225	anchored component of membrane	0.008656	8
MF	GO:0034987	immunoglobulin receptor binding	6.33E-06	9
MF	GO:0003823	antigen binding	0.000225	10
MF	GO:0004252	serine-type endopeptidase activity	0.008426	8
MF	GO:0033130	acetylcholine receptor binding	0.010056	3
MF	GO:0008236	serine-type peptidase activity	0.010191	8
MF	GO:0016825	hydrolase activity, acting on acid phosphorus-nitrogen bonds	0.010191	8
MF	GO:0017171	serine hydrolase activity	0.010191	8
MF	GO:0005109	frizzled binding	0.013552	4
MF	GO:0008201	heparin binding	0.024119	7
MF	GO:0005246	calcium channel regulator activity	0.024119	4
MF	GO:0004175	endopeptidase activity	0.035063	11
MF	GO:0004867	serine-type endopeptidase inhibitor activity	0.035063	5
MF	GO:1901681	sulfur compound binding	0.037929	8

screened by a Wilcoxon signed-rank test (false discovery rate, FDR < 0.05), and Benjamini and Hochberg (BH) corrections were used to adjust p values. The relationship between DEPRGS and clinicopathological manifestations were evaluated using logistic regression analyses and a heatmap graph. The survival analysis of UCEC patients based on the DEPRG panel was assessed using Kaplan–Meier survival analysis. A P-value of less than 0.05 was considered to be statistically significant ($p < 0.001 = ***$, $p < 0.01 = **$, and $p < 0.05 = *$).

RESULTS

Identification of Prognostic Differentially Expressed Pyroptosis-Related Genes of TCGA Database

In total, 5 of the 34 pyroptosis-related genes were related to prognosis and four of them (ELANE, GPX4, GSDMD, and TIRAP) had different expression values between tumor and normal tissues, which were, thus, chosen as prognostic DEPRGs (**Figure 2A**). The heatmap in endometrial cancer showed that

TABLE 4 | The whole results of KEGG functional analysis.

hsa04310	Wnt signaling pathway	0.030193	7
hsa04260	Cardiac muscle contraction	0.191447	4
hsa04972	Pancreatic secretion	0.191447	4
hsa04974	Protein digestion and absorption	0.191447	4
hsa04530	Tight junction	0.191447	5
hsa05022	Pathways of neurodegeneration - multiple diseases	0.191447	9
hsa00592	alpha-Linolenic acid metabolism	0.232448	2
hsa05130	Pathogenic Escherichia coli infection	0.232448	5
hsa00591	Linoleic acid metabolism	0.232448	2
hsa05412	Arrhythmogenic right ventricular cardiomyopathy	0.232448	3
hsa04024	cAMP signaling pathway	0.232448	5
hsa05010	Alzheimer's disease	0.232448	7
hsa04514	Cell adhesion molecules	0.232448	4
hsa04512	ECM-receptor interaction	0.232448	3
hsa00350	Tyrosine metabolism	0.232448	2
hsa05410	Hypertrophic cardiomyopathy	0.232448	3
hsa04390	Hippo signaling pathway	0.232448	4
hsa05414	Dilated cardiomyopathy	0.249298	3
hsa00260	Glycine, serine and threonine metabolism	0.249298	2
hsa04975	Fat digestion and absorption	0.264308	2
hsa04080	Neuroactive ligand-receptor interaction	0.264308	6

ELANE and GSDMD were upregulated and GPX4 and TIRAP were downregulated (**Figure 2B**). The univariate Cox analysis of OS of the prognostic pyroptosis-related DEGs indicated that the four genes were low-risk factors ($HR < 1$) (**Figure 2C**). Therefore, these four genes were constituted into the optimal prognostic risk model of DEPRGs. The details of the genes are shown in **Table 2**.

Construction of a Prognostic Panel by Differentially Expressed Pyroptosis-Related Genes

A prognostic panel was constructed using the four DEPRGs by lasso regression analysis (**Figures 2D,E**) and multivariate Cox analysis (**Figure 2F**). The risk score of each patient was calculated according to the formula: risk score = expression value of ELANE $\times$ (-2.41387833412429) + expression value of GPX4 $\times$ (-0.298331831704336) + expression value of GSDMD $\times$ (-0.337701574941294) + expression value of TIRAP $\times$ (-0.58979182292574).

Prognostic Confirmation of the Prognostic Panel by Differentially Expressed Pyroptosis-Related Genes

The median risk score was taken for dividing patients into two groups (high- and low-risk group) and visualizing the results, as seen in **Figure 3A**. The survival status of each group was also visualized, as seen in **Figure 3B**. Patients in the two groups were distributed in different directions according to the PCA and t-SNE analysis (**Figures 3C,D**). Then, KM analysis showed that the patients with lower risk scores had higher survival potential with a p value < 0.01 (**Figure 3E**). The 1-, 2-, 3-, 4-, and 5-year ROC curves showed all areas under the curve (AUC) were over 0.6, and AUC under 5-year ROC curve was 0.692 (**Figure 3F**).

Independence Confirmation and Clinical Evaluation of the Panel by Differentially Expressed Pyroptosis-Related Genes

We carried univariate Cox analyses among the common clinical features first, and multivariate Cox analysis next, which showed our panel can predict the prognosis of endometrial cancer independently (**Figures 4A,B**).

The chi-square test, analyzing the relationship between the panel and clinicopathological characteristics, suggested that age, clinical stage, and tumor grade were significantly associated with the risk Score ($p < 0.001$) (**Figure 5A**). Wilcoxon signed-rank test comparing the risk score differences among different groups of these clinicopathological characteristics indicated age clinical stage, and tumor grade showed a positive relationship to risk scores (**Figures 5B–D**). The AUC of the panel, traditional clinicopathological characteristics, and DCA are shown in **Figures 6A,B**. There was also a nomogram incorporating the panel and clinicopathological characteristics in **Figure 6C**.

Gene Ontology, Kyoto Encyclopedia of Genes and Genomes Functional Enrichment, and Gene Set Enrichment Analysis Analysis Between High-Risk Versus Low-Risk Groups

To understand the molecular mechanism related to the risk score, the DEGs between two groups were used for GO and KEGG pathway analysis (**Figures 7A,B**). GO functional enrichment indicated that processes related to immunoglobin, immune response, and phagocytosis were enriched (**Figure 7A**). KEGG pathways analysis also indicated DEGs are enriched in some classic pathways including Wnt and cAMP signaling pathways and some necessary substance metabolism (**Figure 7B**). The details are shown in **Tables 3**, **4**. The pathways enriched in the high-risk group based on GSEA are shown in **Figures 7C–N**.

Immune Characteristics Analysis

Through TIMER, CIBERSORT, CIBERSORT-ABS, QUANTISEQ, MCPcounter, XCELL, and EPIC conjoint analysis, we indicated that patients with high riskScore accumulated tumor-infiltrating immune cells such as macrophage, NK cells, B cells, and T cells (**Figure 8A**). In addition, we quantified the scores of different immune cell subsets, related functions, or pathways with ssGSEA for analyzing the relationship between risk scores and immune status. Interestingly, the immune function of CCR, check point, cytolytic activity, T cell co inhibition, T cell co stimulation, type I IFN response, type II IFN response and immune cell proportion of CD8+ T cells, DCs, neutrophils, pDCs, T helper cells, Th1 cells, and TIL were significantly different among the two groups (**Figures 8B,C**). Furthermore, patients with high-risk scores had low expression of immune checkpoint related genes (**Figure 8D**).

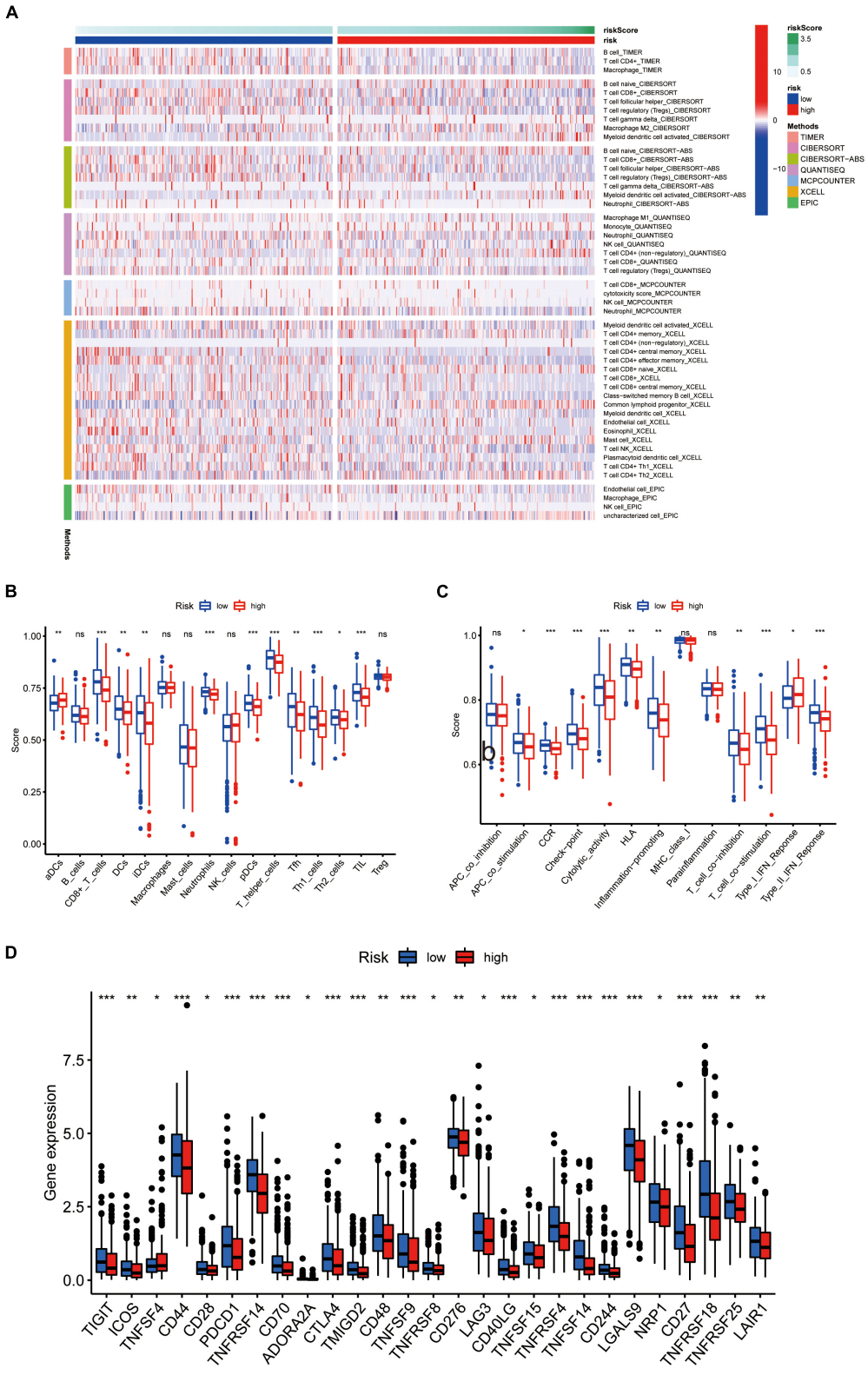

FIGURE 8 | Immune characteristics analysis. **(A)** Heatmap for immune responses based on TIMER, CIBERSORT, CIBERSORT-ABS, QUANTISEQ, MCPcounter, XCELL, and EPIC algorithms among high and the low risk group. The differences of **(B)** immune cells, **(C)** related pathways between two groups based on ssGSEA. **(D)** Expression difference of immune checkpoint related genes between the two groups.

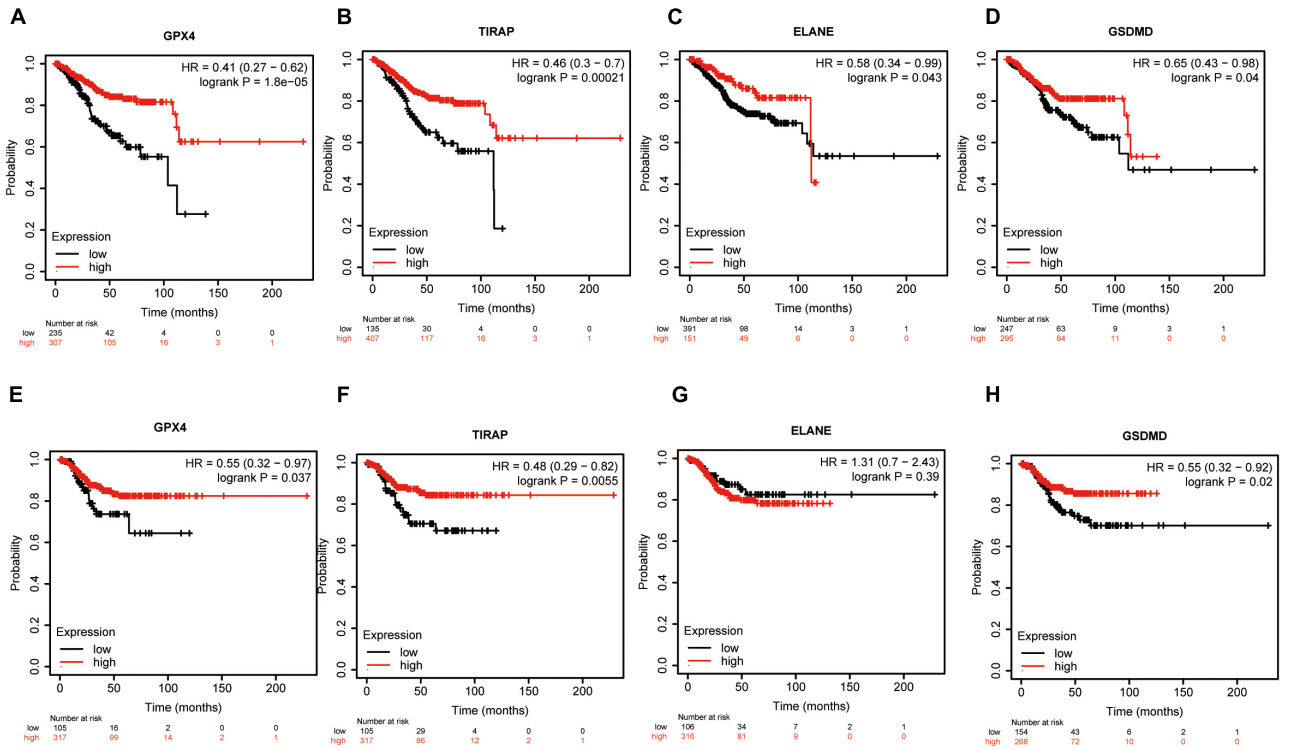

FIGURE 9 | Survival Analysis of four prognostic DEPRGs. The OS **(A–D)** and RFS **(E–H)** difference in groups with high or low expression of prognostic DEPRGs.

External Validation of the Four Prognostic Differentially Expressed Pyroptosis-Related Gene Panel

We first analyzed the relapse-free and overall survival of four prognostic DEPRGs through the Kaplan–Meier plotter in UCEC. The results showed that the survival probability differences between the high-expression group and the low-expression group were consistent with the former analysis (**Figures 9A–H**). We then used the GEPIA database and RT-PCR experiment to analyze the expression levels of the four prognostic DEPRGs, which indicated that GPX4 and GSDMD were highly expressed in UCEC compared to normal endometrial tissue, and TIRAP and ELANE were downregulated (**Figures 10A–H**).

DISCUSSION

Recently, pyroptosis related genes, proteins, and related molecular processes in carcinogenesis, cancer novel therapy have attracted much attention in the research. There is a correlation with EC, as reported in another previous study (Yang et al., 2020). There is also another PRG panel that can help predict the overall survival and immune microenvironment in gastric and ovarian cancer (Shao et al., 2021; Ye et al., 2021). However, a PRG panel in EC has never been reported.

We used the TAGA database and 34 PRGs were analyzed in cases of UCEC and healthy people. We found four PRGs (ELANE, GPX4, GSDMD, and TIRAP) were significantly differentially expressed and related to overall survival in EC. As a member of the gasdermin family, GSDMD cleaved by caspase-1 and caspase-11/4/5 can trigger pyroptosis (Kayagaki et al., 2015; Shi et al., 2015, 2017). The role of GSDMD has been reported in EC (Yang et al., 2020). As a member of serine protease, ELANE can hydrolyze many proteins besides elastin. As Kambara et al. (2018) have reported, ELANE could mediate GSDMD cleavage and activation in a caspase-independent manner in neutrophils, and could in the future be used to promote macrophage pyroptosis. GPX4, an enzyme that can effectively reduce lipid peroxidation, regulates lipid peroxidation-dependent caspase-11 activation and GSDMD cleavage (Kang et al., 2018). TIRAP regulates the expression of caspase-11, a caspase-1-related protease, which is crucial for the activation of inflammatory bodies (Gurung et al., 2012). All in all, these 4 PRGs are included in pyroptosis and affect cancer cell progression, but whether it takes action in EC needs more exploration due to a few being reported in EC.

These four PRGs were used to construct the prediction panel. In univariate Cox analysis, there may be some false correlation or indirect correlation between the independent variable and the dependent variable. For example, factor A has no impact on the outcome event, while factor B is an influencing factor for the outcome event. However,

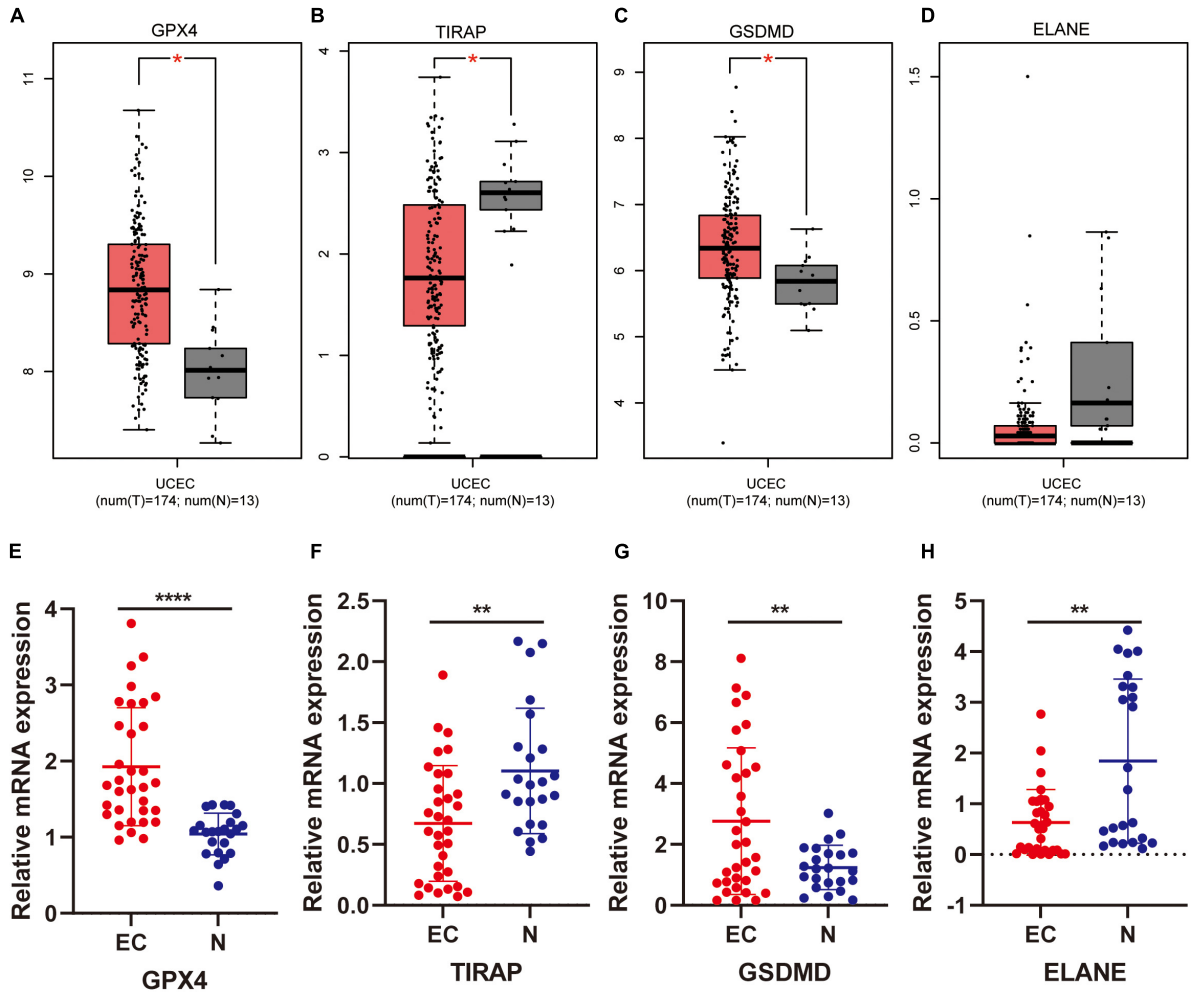

FIGURE 10 | Expression validation of four prognostic DEPRGs. The expression difference between EC and normal endometrial tissues based on the GEPIA database **(A–D)** and RT-PCR **(E–H)**.

since factor A is only simple and has a strong correlation with factor B, there is collinearity between them, so in univariate Cox analysis, there may be significant differences in factor A, which leads to factor a being mistaken as an influencing factor and included in the multi-factor analysis. In multivariate analysis, by adjusting the influence of factor B, the "false correlation" between factor A and the dependent variable disappears. At this time, it can be considered that factor A is not an influencing factor for the outcome event. Therefore, we conducted univariate, lasso, and multivariate Cox analyses to create the panel and avoid bias. KM plotter analysis, AUC of ROC curves, and univariate and multivariate cox analysis suggest that it can be used to predict the overall survival of EC patients independently. In addition, the risk score calculated by this panel in each patient was positively related to clinical characteristics, such as age, stage, and grade. The DEGs between two groups then conducted functional enrichment in GO, KEGG, GSEA, and immune characteristics analysis. In GO analysis, "phagocytosis," "immunoglobin," and "immune response" had the most frequent occurrences among the top 10 results, which suggested that the immune microenvironment may play a part in EC progression. In KEGG analysis, popular pathways, such as the Wnt signaling pathway, and cAMP signaling pathway, and some necessary substant metabolism, stressed the roles of PRGs in endometrial cancer. In GSEA analysis, pathways related to carcinogeneses such as ubiquitin-mediated proteolysis, basal transcription factors, cell cycle, regulation of autophagy, ERBB, TGFβ, Wnt pathways, and pathways in cancer were enriched. We next undertook immune function and immune cell distribution among the two groups. The results indicated that antigen-presenting cells, including DCs, pDCs, and T helper cells can help present pyroptosis cells to the T cells, and costimulate T cells and para secretion interferon to trigger a subsequent reaction. As reported, gasdermin-mediated cell pyroptosis was related to T cells, dendritic cells, neutrophils, and NK cells. Natural killer cells and cytolytic T cells release granzyme A or B mediating caspase activation and

gasdermin family protein cleavage in macrophages, which increases pore-forming activity and formation of pore-forming protein, and thus cell pyroptosis (Wang et al., 2013; Jorgensen et al., 2016; Kambara et al., 2018; Xi et al., 2019; Liu et al., 2020; Zhang Z. et al., 2020; Zhou et al., 2020). However, how the pyroptosis-related immune system plays a role in EC needs more exploration and confirmation *in vitro* and *in vivo*.

Finally, we used an external database and low-throughput experiments to validate the four prognostic DEPRGs in EC. The results of the KM-plotter showed that low expression of these four prognostic DEPRGs had a longer survival time, which is consistent with the former analysis. Furthermore, the results of the GEPIA and RT-PCR experiment showed the expression level difference in EC and normal endometrial tissues.

In summary, we identified fpur prognosis-associated pyroptosis-related genes (ELANE, GPX4, GSDMD, and TIRAP). The model can also predict prognosis prediction and microenvironment in human endometrial cancer. However, to date, there have been few studies in the molecular mechanisms in pyroptosis related pathways and immunotherapy, and future large-scale clinical cohorts need to be undertaken to correct this panel.

DATA AVAILABILITY STATEMENT

The original contributions presented in the study are included in the article/**Supplementary Material**, further inquiries can be directed to the corresponding author.

ETHICS STATEMENT

The studies involving human participants were reviewed and approved by This study was carried out in accordance with the standards of the Helsinki Declaration of the World Medical Association, and approved by the Ethics Committee of China Medical University. The patients/participants provided their written informed consent to participate in this study.

AUTHOR CONTRIBUTIONS

XZ downloaded the dataset, analyzed the data, and was a major contributor in writing the manuscript. QY reviewed the manuscript. Both authors read and approved the final manuscript.

FUNDING

This work was supported by the National Natural Science Foundation of China (No. 81872125) and the Outstanding Scientific Fund of Shengjing Hospital (No. 201704).

SUPPLEMENTARY MATERIAL

The Supplementary Material for this article can be found online at: https://www.frontiersin.org/articles/10.3389/fcell.2021.705828/full#supplementary-material

REFERENCES

Amant, F., Moerman, P., Neven, P., Timmerman, D., Van Limbergen, E., and Vergote, I. (2005). Endometrial cancer. *Lancet* 366, 491–505.

An, H., Heo, J. S., Kim, P., Lian, Z., Lee, S., Park, J., et al. (2021). Tetraarsenic hexoxide enhances generation of mitochondrial ROS to promote pyroptosis by inducing the activation of caspase-3/GSDME in triple-negative breast cancer cells. *Cell Death Dis* 12:159.

Bergsbaken, T., Fink, S. L., and Cookson, B. T. (2009). Pyroptosis: host cell death and inflammation. *Nat. Rev. Microbiol.* 7, 99–109. doi: 10.1038/nrmicro2070

Chen, X., Liu, G., Liu, Y., Wu, G., Wang, S., and Yuan, L. (2019). NEK7 interacts with NLRP3 to modulate the pyroptosis in inflammatory bowel disease via NF-κB signaling. *Cell Death Dis.* 10:906.

Cui, J., Zhou, Z., Yang, H., Jiao, F., Li, N., Gao, Y., et al. (2019). MST1 suppresses pancreatic cancer progression via ros-induced pyroptosis. *Mol. Cancer Res.* 17, 1316–1325. doi: 10.1158/1541-7786.mcr-18-0910

Derangère, V., Chevriaux, A., Courtaut, F., Bruchard, M., Berger, H., Chalmin, F., et al. (2014). Liver X receptor β activation induces pyroptosis of human and murine colon cancer cells. *Cell Death Differ.* 21, 1914–1924. doi: 10.1038/cdd.2014.117

Gupta, D. (2017). Clinical behavior and treatment of endometrial cancer. *Adv. Exp. Med. Biol.* 943, 47–74. doi: 10.1007/978-3-319-43139-0_2

Gurung, P., Malireddi, R. K., Anand, P. K., Demon, D., Vande Walle, L., Liu, Z., et al. (2012). Toll or interleukin-1 receptor (TIR) domain-containing adaptor inducing interferon-β (TRIF)-mediated caspase-11 protease production integrates Toll-like receptor 4 (TLR4) protein- and Nlrp3 inflammasome-mediated host defense against enteropathogens. *J. Biol. Chem.* 287, 34474–34483. doi: 10.1074/jbc.m112.401406

Győrffy, B., Surowiak, P., Budczies, J., and Lánczky, A. (2013). Online survival analysis software to assess the prognostic value of biomarkers using transcriptomic data in non-small-cell lung cancer. *PLoS One* 8:e82241. doi: 10.1371/journal.pone.0082241

Hage, C., Hoves, S., Strauss, L., Bissinger, S., Prinz, Y., Pöschinger, T., et al. (2019). Sorafenib induces pyroptosis in macrophages and triggers natural killer cell-mediated cytotoxicity against hepatocellular carcinoma. *Hepatology* 70, 1280–1297. doi: 10.1002/hep.30666

Han, C., Yang, Y., Guan, Q., Zhang, X., Shen, H., and Sheng, Y. (2020). New mechanism of nerve injury in Alzheimer's disease: β-amyloid-induced neuronal pyroptosis. *J. Cell Mol. Med.* 24, 8078–8090. doi: 10.1111/jcmm.15439

He, W. T., Wan, H., Hu, L., Chen, P., Wang, X., Huang, Z., et al. (2015). Gasdermin D is an executor of pyroptosis and required for interleukin-1β secretion. *Cell Res.* 25, 1285–1298. doi: 10.1038/cr.2015.139

Jia, C., Chen, H., Zhang, J., Zhou, K., Zhuge, Y., Niu, C., et al. (2019). Role of pyroptosis in cardiovascular diseases. *Int. Immunopharmacol.* 67, 311–318. doi: 10.1016/s0939-4753(03)80058-3

Jorgensen, I., Lopez, J. P., Laufer, S. A., and Miao, E. A. (2016). IL-1β, IL-18, and eicosanoids promote neutrophil recruitment to pore-induced intracellular traps following pyroptosis. *Eur. J. Immunol.* 46, 2761–2766. doi: 10.1002/eji.201646647

Kambara, H., Liu, F., Zhang, X., Liu, P., Bajrami, B., Teng, Y., et al. (2018). Gasdermin D exerts anti-inflammatory effects by promoting neutrophil death. *Cell Rep.* 22, 2924–2936. doi: 10.1016/j.celrep.2018.02.067

Kang, R., Zeng, L., Zhu, S., Xie, Y., Liu, J., Wen, Q., et al. (2018). Lipid peroxidation drives gasdermin D-mediated pyroptosis in lethal polymicrobial sepsis. *Cell Host Microbe* 24, 97–108.e4.

Karki, R., and Kanneganti, T. D. (2019). Diverging inflammasome signals in tumorigenesis and potential targeting. *Nat. Rev. Cancer* 19, 197–214. doi: 10.1038/s41568-019-0123-y

Kayagaki, N., Stowe, I. B., Lee, B. L., O'Rourke, K., Anderson, K., Warming, S., et al. (2015). Caspase-11 cleaves gasdermin D for non-canonical inflammasome signalling. *Nature* 526, 666–671. doi: 10.1038/nature15541

Kovacs, S. B., and Miao, E. A. (2017). Gasdermins: effectors of pyroptosis. *Trends Cell Biol.* 27, 673–684. doi: 10.1016/j.tcb.2017.05.005

Li, Y. (2021). Dihydroartemisinin induces pyroptosis by promoting the AIM2/caspase-3/DFNA5 axis in breast cancer cells. *Chem. Biol. Interact.* 340:109434. doi: 10.1016/j.cbi.2021.109434

Liang, J. Y., Wang, D. S., Lin, H. C., Chen, X. X., Yang, H., Zheng, Y., et al. (2020). A novel ferroptosis-related gene signature for overall survival prediction in patients with hepatocellular carcinoma. *Int. J. Biol. Sci.* 16, 2430–2441. doi: 10.7150/ijbs.45050

Lin, J., Cheng, A., Cheng, K., Deng, Q., Zhang, S., Lan, Z., et al. (2020). New insights into the mechanisms of pyroptosis and implications for diabetic kidney disease. *Int. J. Mol. Sci.* 21:7057. doi: 10.3390/ijms21197057

Liu, Y., Fang, Y., Chen, X., Wang, Z., Liang, X., Zhang, T., et al. (2020). Gasdermin E-mediated target cell pyroptosis by CAR T cells triggers cytokine release syndrome. *Sci. Immunol.* 5:eaax7969. doi: 10.1126/sciimmunol.aax7969

Man, S. M., and Kanneganti, T. D. (2015). Regulation of inflammasome activation. *Immunol. Rev.* 265, 6–21. doi: 10.1111/imr.12296

Man, S. M., Karki, R., and Kanneganti, T. D. (2017). Molecular mechanisms and functions of pyroptosis, inflammatory caspases and inflammasomes in infectious diseases. *Immunol. Rev.* 277, 61–75. doi: 10.1111/imr.12534

Moore, K., and Brewer, M. A. (2017). Endometrial cancer: is this a new disease? *Am. Soc. Clin. Oncol. Educ. Book* 37, 435–442. doi: 10.14694/edbk_175666

Nagy, Á, Munkácsy, G., and Győrffy, B. (2021). Pancancer survival analysis of cancer hallmark genes. *Sci. Rep.* 11:6047.

Pizato, N., Luzete, B. C., Kiffer, L. F. M. V., Corrêa, L. H., de Oliveira Santos, I., Assumpção, J. A. F., et al. (2018). Omega-3 docosahexaenoic acid induces pyroptosis cell death in triple-negative breast cancer cells. *Sci. Rep.* 8:1952.

Qiao, L., Wu, X., Zhang, J., Liu, L., Sui, X., Zhang, R., et al. (2019). α-NETA induces pyroptosis of epithelial ovarian cancer cells through the GSDMD/caspase-4 pathway. *FASEB J.* 33, 12760–12767. doi: 10.1096/fj.201900483rr

Robinson, N., Ganesan, R., Hegedûs, C., Kovács, K., Kufer, T. A., and Virág, L. (2019). Programmed necrotic cell death of macrophages: focus on pyroptosis, necroptosis, and parthanatos. *Redox Biol.* 26:101239. doi: 10.1016/j.redox.2019.101239

Shao, W., Yang, Z., Fu, Y., Zheng, L., Liu, F., Chai, L., et al. (2021). The pyroptosis-related signature predicts prognosis and indicates immune microenvironment infiltration in gastric cancer. *Front. Cell Dev. Biol.* 9:676485.

Shi, J., Gao, W., and Shao, F. (2017). Pyroptosis: gasdermin-mediated programmed necrotic cell death. *Trends Biochem. Sci.* 42, 245–254. doi: 10.1016/j.tibs.2016.10.004

Shi, J., Zhao, Y., Wang, K., Shi, X., Wang, Y., Huang, H., et al. (2015). Cleavage of GSDMD by inflammatory caspases determines pyroptotic cell death. *Nature* 526, 660–665. doi: 10.1038/nature15514

Subramanian, A., Tamayo, P., Mootha, V. K., Mukherjee, S., Ebert, B. L., Gillette, M. A., et al. (2005). Gene set enrichment analysis: a knowledge-based approach for interpreting genome-wide expression profiles. *Proc. Natl. Acad. Sci. U.S.A.* 102, 15545–15550. doi: 10.1073/pnas.0506580102

Sung, H., Ferlay, J., Siegel, R. L., Laversanne, M., Soerjomataram, I., Jemal, A., et al. (2021). Global cancer statistics 2020: GLOBOCAN estimates of incidence and mortality worldwide for 36 cancers in 185 countries. *CA Cancer J. Clin.* 71, 209–249. doi: 10.3322/caac.21660

Tan, Y., Sun, R., Liu, L., Yang, D., Xiang, Q., Li, L., et al. (2021). Tumor suppressor DRD2 facilitates M1 macrophages and restricts NF-κB signaling to trigger pyroptosis in breast cancer. *Theranostics* 11, 5214–5231. doi: 10.7150/thno.58322

Tang, Z., Li, C., Kang, B., Gao, G., Li, C., and Zhang, Z. (2017). GEPIA: a web server for cancer and normal gene expression profiling and interactive analyses. *Nucleic Acids Res.* 45, W98–W102.

Teng, J. F., Mei, Q. B., Zhou, X. G., Tang, Y., Xiong, R., Qiu, W. Q., et al. (2020). Polyphyllin VI Induces caspase-1-mediated pyroptosis via the induction of ROS/NF-κB/NLRP3/GSDMD signal axis in non-small cell lung cancer. *Cancers (Basel)* 12:193. doi: 10.3390/cancers12010193

Tian, W., Wang, Z., Tang, N. N., Li, J. T., Liu, Y., Chu, W. F., et al. (2020). Ascorbic acid sensitizes colorectal carcinoma to the cytotoxicity of arsenic trioxide via promoting reactive oxygen species-dependent apoptosis and pyroptosis. *Front. Pharmacol.* 11:123.

Vande Walle, L., and Lamkanfi, M. (2016). Pyroptosis. *Curr. Biol* 26, R568–R572.

Vickers, A. J., and Elkin, E. B. (2006). Decision curve analysis: a novel method for evaluating prediction models. *Med. Decis Making* 26, 565–574. doi: 10.1177/0272989x06295361

Wang, B., and Yin, Q. (2017). AIM2 inflammasome activation and regulation: a structural perspective. *J Struct. Biol.* 200, 279–282. doi: 10.1016/j.jsb.2017.08.001

Wang, Q., Imamura, R., Motani, K., Kushiyama, H., Nagata, S., and Suda, T. (2013). Pyroptotic cells externalize eat-me and release find-me signals and are efficiently engulfed by macrophages. *Int. Immunol.* 25, 363–372. doi: 10.1093/intimm/dxs161

Wang, S., Yuan, Y. H., Chen, N. H., and Wang, H. B. (2019). The mechanisms of NLRP3 inflammasome/pyroptosis activation and their role in Parkinson's disease. *Int. Immunopharmacol.* 67, 458–464. doi: 10.1016/j.intimp.2018.12.019

Wang, Y., Zhu, X., Yuan, S., Wen, S., Liu, X., Wang, C., et al. (2019). TLR4/NF-κB signaling induces gsdmd-related pyroptosis in tubular cells in diabetic kidney disease. *Front. Endocrinol. (Lausanne)* 10:603.

Xi, G., Gao, J., Wan, B., Zhan, P., Xu, W., Lv, T., et al. (2019). GSDMD is required for effector CD8(+) T cell responses to lung cancer cells. *Int. Immunopharmacol.* 74, 105713. doi: 10.1016/j.intimp.2019.105713

Xia, X., Wang, X., Cheng, Z., Qin, W., Lei, L., Jiang, J., et al. (2019). The role of pyroptosis in cancer: pro-cancer or pro-"host"? *Cell Death Dis.* 10:650.

Yang, Y., Liu, P. Y., Bao, W., Chen, S. J., Wu, F. S., and Zhu, P. Y. (2020). Hydrogen inhibits endometrial cancer growth via a ROS/NLRP3/caspase-1/GSDMD-mediated pyroptotic pathway. *BMC Cancer* 20:28.

Ye, Y., Dai, Q., and Qi, H. (2021). A novel defined pyroptosis-related gene signature for predicting the prognosis of ovarian cancer. *Cell Death Discov .*7:71.

Yu, J., Li, S., Qi, J., Chen, Z., Wu, Y., Guo, J., et al. (2019). Cleavage of GSDME by caspase-3 determines lobaplatin-induced pyroptosis in colon cancer cells. *Cell Death Dis.* 10:193.

Zhang, C. C., Li, C. G., Wang, Y. F., Xu, L. H., He, X. H., Zeng, Q. Z., et al. (2019). Chemotherapeutic paclitaxel and cisplatin differentially induce pyroptosis in A549 lung cancer cells via caspase-3/GSDME activation. *Apoptosis* 24, 312–325. doi: 10.1007/s10495-019-01515-1

Zhang, T., Li, Y., Zhu, R., Song, P., Wei, Y., Liang, T., et al. (2019). Transcription factor p53 suppresses tumor growth by prompting pyroptosis in non-small-cell lung cancer. *Oxid. Med. Cell. Longev.* 2019:8746895.

Zhang, X., Zhang, P., An, L., Sun, N., Peng, L., Tang, W., et al. (2020). Miltirone induces cell death in hepatocellular carcinoma cell through GSDME-dependent pyroptosis. *Acta Pharm. Sin. B* 10, 1397–1413. doi: 10.1016/j.apsb.2020.06.015

Zhang, Z., Zhang, Y., Xia, S., Kong, Q., Li, S., Liu, X., et al. (2020). Gasdermin E suppresses tumour growth by activating anti-tumour immunity. *Nature* 579, 415–420. doi: 10.1038/s41586-020-2071-9

Zhaolin, Z., Guohua, L., Shiyuan, W., and Zuo, W. (2019). Role of pyroptosis in cardiovascular disease. *Cell Prolif.* 52, e12563. doi: 10.1111/cpr.12563

Zhou, Z., He, H., Wang, K., Shi, X., Wang, Y., Su, Y., et al. (2020). Granzyme A from cytotoxic lymphocytes cleaves GSDMB to trigger pyroptosis in target cells. *Science* 368:eaaz7548. doi: 10.1126/science.aaz7548

Conflict of Interest: The authors declare that the research was conducted in the absence of any commercial or financial relationships that could be construed as a potential conflict of interest.

Publisher's Note: All claims expressed in this article are solely those of the authors and do not necessarily represent those of their affiliated organizations, or those of the publisher, the editors and the reviewers. Any product that may be evaluated in this article, or claim that may be made by its manufacturer, is not guaranteed or endorsed by the publisher.

frontiers in Cell and Developmental Biology

ORIGINAL RESEARCH
published: 26 November 2021
doi: 10.3389/fcell.2021.761350

Construction and Validation of a Novel Pyroptosis-Related Gene Signature to Predict the Prognosis of Uveal Melanoma

*Yuan Cao[1†], Jiaheng Xie[2†], Liang Chen[3†], Yiming Hu[4], Leili Zhai[1], Jin Yuan[1], Long Suo[1], Yaming Shen[1], Rong Ye[1], Jiajun Li[1], Zixuan Gong[5], Yunfan Dong[6], Wei Bao[7], Huan Li[1] and Ming Wang[2]**

[1]The Fourth Clinical Medical College, Nanjing Medical University, Nanjing, China, [2]Department of Burn and Plastic Surgery, The First Affiliated Hospital of Nanjing Medical University, Nanjing, China, [3]Department of General Surgery, Fuyang Hospital Affiliated to Anhui Medical University, Fuyang, China, [4]College of Pharmacy, Jiangsu Ocean University, Lianyungang, China, [5]Urology Department, The First Affiliated Hospital of Nanjing Medical University, Nanjing, China, [6]Department of Gastroenterology, Nanjing First Hospital, Nanjing Medical University, Nanjing, China, [7]Urology Department, The Second Affiliated Hospital of Nanjing Medical University, Nanjing, China

OPEN ACCESS

Edited by:
Tugba Bagci-Onder,
Koç University, Turkey

Reviewed by:
Ibrahim Kulac,
Koç University, Turkey
Xingyu Chen,
Central South University, China
Li Li,
Peking Union Medical College, China

***Correspondence:**
Ming Wang
wangming@jsph.org.cn

†These authors share first authorship

Specialty section:
This article was submitted to Cell Death and Survival, a section of the journal Frontiers in Cell and Developmental Biology

Received: 19 August 2021
Accepted: 05 November 2021
Published: 26 November 2021

Citation:
Cao Y, Xie J, Chen L, Hu Y, Zhai L, Yuan J, Suo L, Shen Y, Ye R, Li J, Gong Z, Dong Y, Bao W, Li H and Wang M (2021) Construction and Validation of a Novel Pyroptosis-Related Gene Signature to Predict the Prognosis of Uveal Melanoma. Front. Cell Dev. Biol. 9:761350. doi: 10.3389/fcell.2021.761350

Uveal melanoma is the most common primary intraocular tumor with a poor prognosis. Currently, treatment for UVM is limited, and the development of drug resistance and tumor recurrence are common. Therefore, it is important to identify new prognostic biomarkers of UVM and explore their role in the tumor microenvironment. Pyroptosis is a way of cell programmed death, and related research is in full throttle. However, the role of pyroptosis in UVM is unclear. In this study, we constructed the prognosis model of pyroptosis-related genes of UVM. This model can accurately guide the prognosis of UVM, and different groups differ in immune infiltration. We further verified our results in cell experiments. To some extent, our study can provide new ideas for the diagnosis and treatment of UVM.

Keywords: uveal melanoma, pyroptosis, signature, immune microenvironment, programmed cell death

INTRODUCTION

Uveal melanoma is a general term for melanoma that occurs in the choroid, iris, and ciliary body (Chattopadhyay et al., 2016; Kaliki and Shields, 2017). The number of new UVM cases in the United States is 1,500 per year (Smit et al., 2020). Although the total number of cases is small, UVM is the most common primary intraocular malignancy whose most common clinical manifestation is painless vision loss (Luke et al., 2020). When the tumor is large, serous retinal detachment is often associated (Kaliki and Shields, 2017). Once metastasis has occurred, the prognosis for UVM is often poor and treatment options are limited (Carvajal et al., 2018). Treatment options for advanced cutaneous melanoma, such as targeted therapy and immunotherapy, seem to be attractive options for advanced UVM (Jager et al., 2020). Although these treatments are often effective, these treatments are also limited (Jager et al., 2020). It is because that a significant proportion of UVM patients develop drug resistance during treatment, which often leads to tumor recurrence and patient death. Hence, it is time to look for new prognostic indicators of UVM and explore its implications for cancer treatment.

Recently, programmed cell death has become a hot topic in biology (Kovacs and Miao, 2017; Chen et al., 2021a). Pyroptosis is a mode of programmed cell death that plays an important role in homeostasis regulation as well as disease occurrence (Tang et al., 2020; Chen et al., 2021b; Chen et al., 2021c). Pyroptosis is a gasdermin (GSDM) dependent process of membrane perforation

accompanied by exudation of inflammatory contents (Xie et al., 2021a). In cancer, pyroptosis has a dual effect. On the one hand, we can reduce tumor load by inducing cancer cells pyroptosis (Xia et al., 2019; Ruan et al., 2020); On the other hand, inflammatory substances released by pyroptosis are involved in the formation of the tumor microenvironment (Jiang et al., 2020). Our current understanding of pyroptosis is far from sufficient, especially in UVM. Pyroptosis is a promising research field.

Here, we combine bioinformatics with cellular experiments to provide a prognostic signature of genes associated with pyroptosis for UVM. Our findings can provide some new ideas for the diagnosis and treatment of UVM.

MATERIALS AND METHODS

Information Extraction of Datasets

We downloaded uveal melanoma RNA sequencing data from TCGA database (https://portal.gdc.cancer.gov/). Data inclusion criteria were: 1) patients diagnosed with uveal melanoma; 2) Patients had detailed mRNA expression and clinical information. Collectively, 80 patients met the inclusion criteria, the gene expression of whom were downloaded for further analysis. (Those with a follow-up of fewer than 30 days were excluded).

Identification of Genes Associated With Cell Pyroptosis

81 pyroptosis-related genes were extracted from GENECARDS (https://www.genecards.org/). Setting "pyroptosis" as a key word, we searched for pyroptosis-related protein coding genes in the Genecard database. Protein coding genes with correlation score >0.6 were included in our subsequent analysis. A total of 81 genes were eventually included in our analysis.

Identification of Prognostic Pyroptosis-Related Genes

We initially performed a univariate Cox regression to screen for those potentially prognostic pyroptosis-related genes derived from the TCGA data using R software (version 4.1.0). Packages "survival" were utilized for cox regression analysis. Using R packages "glmnet", Lasso regression was subsequently performed with those genes that are significantly correlated with patient survival (with $p < 0.05$).

Risk scores were calculated based on the LASSO regression results. The scoring formula is: risk score = $\sum_{i=1}^{n} \beta_i$*(expression of pyroptosis associated gene$_i$). Using a median risk score, patients were divided into high-risk and low-risk groups. The defined groups were respectively analyzed during further studies.

Construction of the Prognostic Model

After the division of patients into high-risk and low-risk groups, survival analysis was performed for both groups to identify the prognostic value of the model. Survival analysis was performed within various subgroups, such as gender, age, and conditions of tumor staging. The accuracy of the established prognosis model was verified by the calibration curve and ROC curve on 1, 3, and 5 years basis.

Clinical Prediction Value of the Established Prognostic Model

We used univariate and multivariate Cox regressions, respectively, to test whether risk score and clinical characteristics (age, sex, stage) were effective prognostic indicators for uveal melanoma patients. Using R package "forestplot", the results of cox regression were visualized to see whether the risk score model we previously established was an independent prognostic factor.

Gene Ontology and Kyoto Encyclopedia of Genes and Genomes Analysis

Differential genes from high-risk and low-risk groups were then subjected to Gene Ontology (GO) and Kyoto Encyclopedia of Genes and Genomes (KEGG) enrichment analysis using R packages "ClusterProfiler" (version 3.0.4), the significantly enriched pathways and ontologies and the associated genes of which were illustrated. Gene Set Enrichment analysis (GSEA) was used as the next enrichment analysis. GSEA required a preexisting set of biologically significant genes (like genes in a pathway), and then the genes in the set (with the same meaning/function) were calculated and summarized into a single enrichment score. This analytical approach added to the interpretability and was used in this study to assess changes in the activity of the pathway/function of the gene set and to select the gene set with $p < 0.05$. Gene Set Variation Analysis (GSVA) was one of the GSEA algorithms. In this study, we collected genes related to immune function and obtained the score of each sample's immune function Gene Set by GSVA calculation.

Analysis of Immune Microenvironment

By enquiry into TIMER database (http://timer.cistrome.org/), we downloaded 7 kinds of algorithms of each patient's immune infiltration situation. Then we analyzed the expression of immune cells in the high and low-risk groups, and isolated the cells with differential expression ($p < 0.05$), before developing a heatmap, At the same time, we studied the expression of immune checkpoint genes between the high and low-risk groups. Similarly, immune checkpoint genes with different expressions ($p < 0.05$) were extracted and the boxplot was made. In DREIMT database (http://www.dreimt.org/), we further analyzed the correlation between the model and immune cells by inputting 80 down-regulated genes and the first 199 up-regulated genes in ascending order of p-value into the website. Patients with UVM were scored using the "ESTIMATE" R package to obtain tumor purity score, immune score, stromal score, and total score for each patient.

Potential Drug Candidate Prediction Using R Software and *the Construction of a Nomogram*

Using the "pRRophetic" package and the expression matrix of gastric cancer patients, we predicted the minimum drug

inhibition concentration (IC_{50}) of drugs in uveal melanoma patients of high-risk and low-risk groups, and finally obtained drugs that have statistically different IC_{50} values and may become candidates for the treatment of uveal melanoma. A nomogram of the patient "TCGA-VD-A8KH" was plotted using the "Regplot" package to integrate risk groups with clinical features.

Cell Culture and Transfection

The human invasive uveal melanoma cell line (MuM2B) was purchased from Fuheng Biology Inc. (Fuheng, Shanghai, China). MUM2B cells were cultured in Roswell Park Memorial Institute 1,640 (RPMI1640, Gibco, Carlsbad, CA, United States), supplemented with 10% Fetal Bovine Serum (Gibco), along with 100 U/mL penicillin and 100 μg/ml streptomycin (Gibco). The cells were cultured in an atmosphere of 5% CO_2 and at a temperature of 37°C. 24 h prior to transfection, MUM2Bs were seeded onto six-well tissue culture plates at a density of 50,000 cells per well. Cells were starved in 0.5% FBS medium for 6 h before any further treatment.

The small interfering RNA (siRNA) probe for ANO6 and GAPDH positive control oligonucleotides and its control siRNAs were synthesized by Shanghai GenePharma Inc. (Shanghai, China). The sequence of the siRNAs were illustrated in (**Supplementary Table S1**). Lipo6000™ Transfection reagent (Beyotime, Nanjing, China) was used for the transfection of siRNA according to the manufacturer's instructions.

Quantitative Real-Time Polymerase Chain Reaction (qRT-PCR)

Total cellular RNAs were isolated from cells using Trizol Reagent (Invitrogen, Carlsbad, CA, United States) according to the manufacturer's instructions. The reverse transcription was conducted using the reverse transcription kit provided by Takara (Otsu, Shiga, Japan). Real-time polymerase chain reaction (RT-PCR) was performed using a QuantiTect SYBR Green PCR Kit (Takara), and on a Applied Biosystems QuantStudio 1 (Thermo, Waltham, MA, United States). Relative quantification was determined using the $-2\Delta\Delta Ct$ method. The relative expression of messenger RNA (mRNA) for each gene was normalized to the level of glyceraldehyde-3-phosphate dehydrogenase (GAPDH) mRNA. The primers were synthesized by GenePharma Inc. (Shanghai, China), the sequence of which were listed in (**Supplementary Table S2**).

Cell Proliferation and Cell Cycle Analysis

5-ethynyl-2 deoxyuridine (EdU) assay was performed according to the manufacturer's instructions (Beyotime, Shanghai, China), MUM2B cells were incubated with EdU for 2 h. The number of proliferating cells were analyzed under an Olympus confocal microscope (Olympus, Tokyo, Japan).

Cell Migration Assay

A scratch wound-healing migration assay was performed in transfected and non-transfected uveal melanoma cell lines to validate the relationship between the prognostic genes and the tumor cell migration ability. When the MUM2Bs reached 90–100% confluence in the 6-well culture plate, cells were subjected to serum-free RPMI1640 medium for 24 h. After serum starvation, one line within the MUM2Bs were scraped using a sterile plastic pipette tip in each cultured well. The cells were washed twice in warm serum-free medium to remove cellular debris After 0, 6, and 12 h the scratch wounds were subjected to microscope photography. Images were acquired using a microscope (Olympus, Tokyo, Japan), and cell migration was determined by the percentage of the wound closure area in five independent experiments using the Image J software.

Data Processing and Statistical Analysis

The quantification of the experiment data was conducted using Image J software (version 1.0.3). All experimental data were analyzed using IBM SPSS software (version 16.0.0) multiple comparisons were conducted using one-way ANOVA and Student- Newman-Keuls (SNK) multiple comparison method, and $p < 0.05$ was considered statistically significant.

RESULTS

5 Pyroptosis-Related Genes Were Identified to Calculate the Risk Score

The flow diagram of our present study is illustrated in **Figure 1**. Based on the previously described inclusion criteria, 80 UVM patients were treated as the training cohort. Using univariate Cox regression, we screened for the genes which are potentially related to the patient's prognosis (with p-value <0.05), both in the training cohort and in the validation cohort as well. An intersection was performed subsequently to achieve a higher confidence level, which included nine potentially prognostic genes. The forestplot which contained the Hazard Ratio (HR) and its 95% confidence interval can be seen in **Figure 2A**. The potential prognostic genes were subsequently subjected to LASSO-Cox regression in the training cohort to generate a Prognostic signature (**Figures 2B,C**). 5 pyroptosis-related genes with prognostic value were eventually obtained. The names and the coefficients of the prognostic genes were listed in **Table1**. The risk score was calculated according to the formula which was previously described.

Based on the Median Risk Score, 80 Melanoma Patients in TCGA Were Divided Into High-Risk and Low-Risk Groups

The group model based on risk score effectively predicted the prognosis of melanoma patients.

To further test the confidence of the risk model, a survival analysis was performed between high-risk group and low risk groups between the training cohort (**Figure 3A**) and the validation cohort (**Figure 3B**). Meanwhile, a further, more specifically classified survival analysis was performed in different subgroups in the training cohort. The survival rate of patients in the high-risk group suffered a more drastic decrease, regardless of the age, gender, and tumor stages. The differences

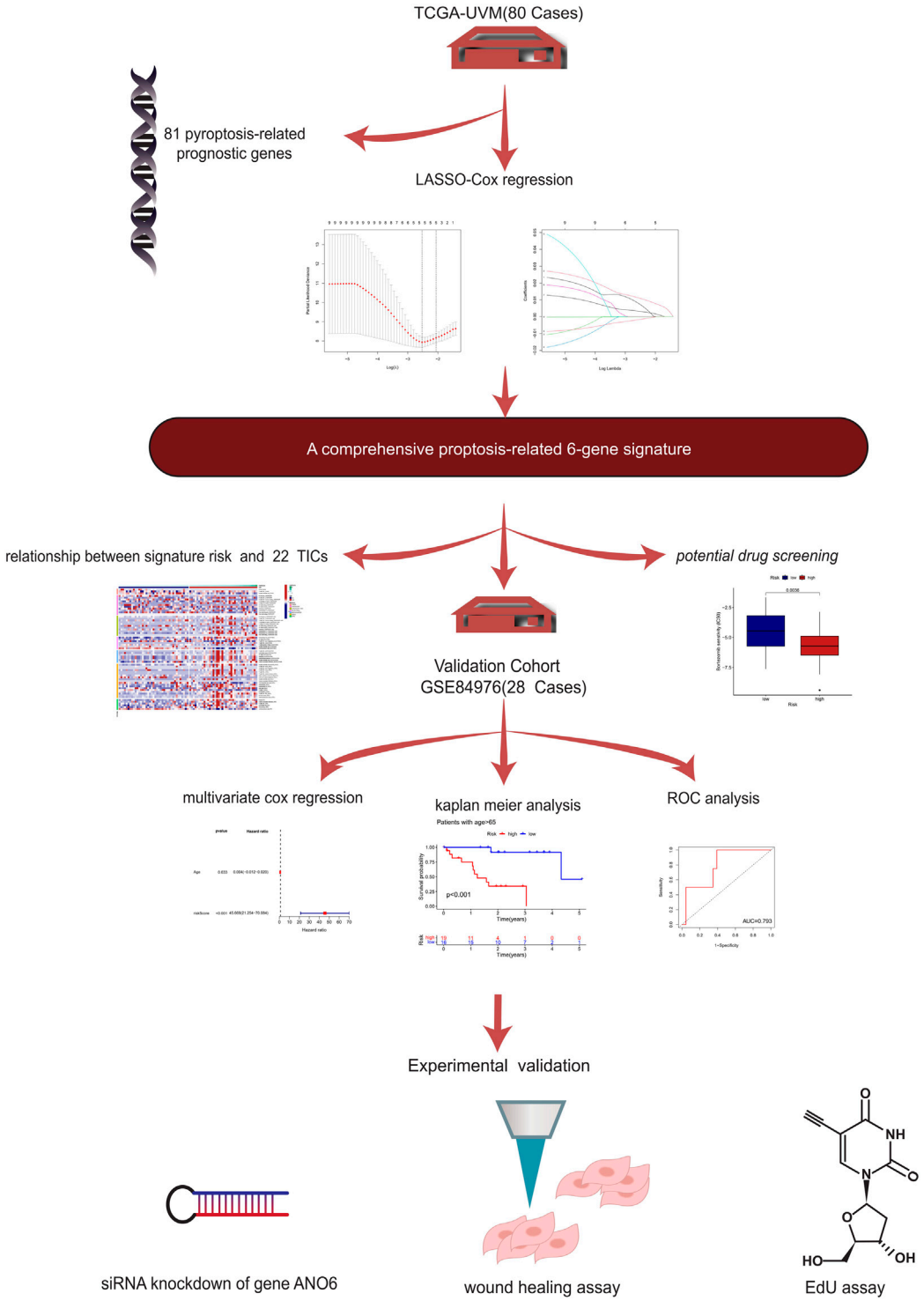

FIGURE 1 | The flow chart.

were statistically significant ($p < 0.001$) (**Figures Figure3C–J**). The ROC curve of patient's survival of different years in the training cohort and the validation cohort showed that the model had a potent predicting ability, with the 1-year, 2-years, 3-years and 5-years AUC being 0.79, 0.83, 0.854, 0.886 respectively in the training cohort, and the 2-years, 3-years, and 5-years AUC being 0.856, 0.846, 0.873 respectively in the validation cohort. (**Figures 4A,B**). The findings revealed that the model was effective in predicting patient's survival. The distribution of the risk scores, outcome status, and gene profiles of the gene signature in the

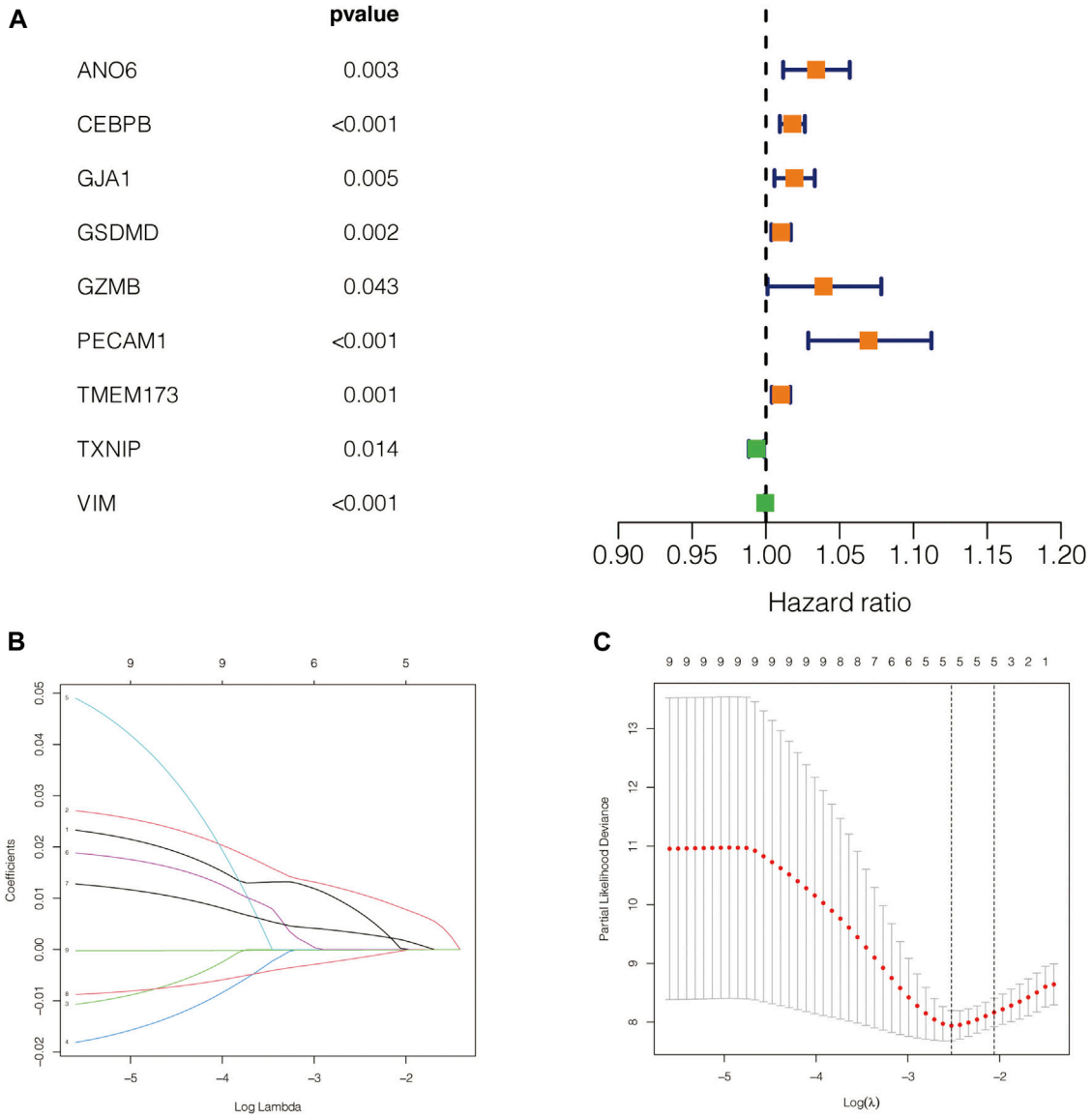

FIGURE 2 | Construction of the prognostic model. **(A)** The forestplot which contained the Hazard Ratio (HR) and its 95% confidence interval. **(B,C)** The potential prognostic genes were subsequently subjected to LASSO-Cox regression in the training cohort to generate a Prognostic signature.

TABLE 1 | The names and the coefficients of the prognostic genes.

Gene	Coef
ANO6	0.00750335379446634
CEBPB	0.0110094507963823
TMEM173	0.00320430405522329
TXNIP	−0.00165919015758192
VIM	−9.89378996691334e-05

training and validation cohort were shown in **Figures 4C,D**. The risk group successfully predicted the outcomes of the patients in both the training cohort and the validation cohort, with significantly more events found in the high-risk group. Moreover, the expression of genes ANO6, CEBPB and TMEM173 were upregulated, while genes VIM, TXNIP were seen downregulated in the high-risk group both in the training cohort and in the validation cohort, which was in accordance with our previous risk model (**Figures 4C,D**).

Univariate and Multivariate Cox Regression Revealed That the Risk Score Was an Independent Prognostic Factor in UVM Patients

In order to explore whether risk score was an independent influencing factor for melanoma patients, univariate and multivariate Cox regression were performed for risk score, age,

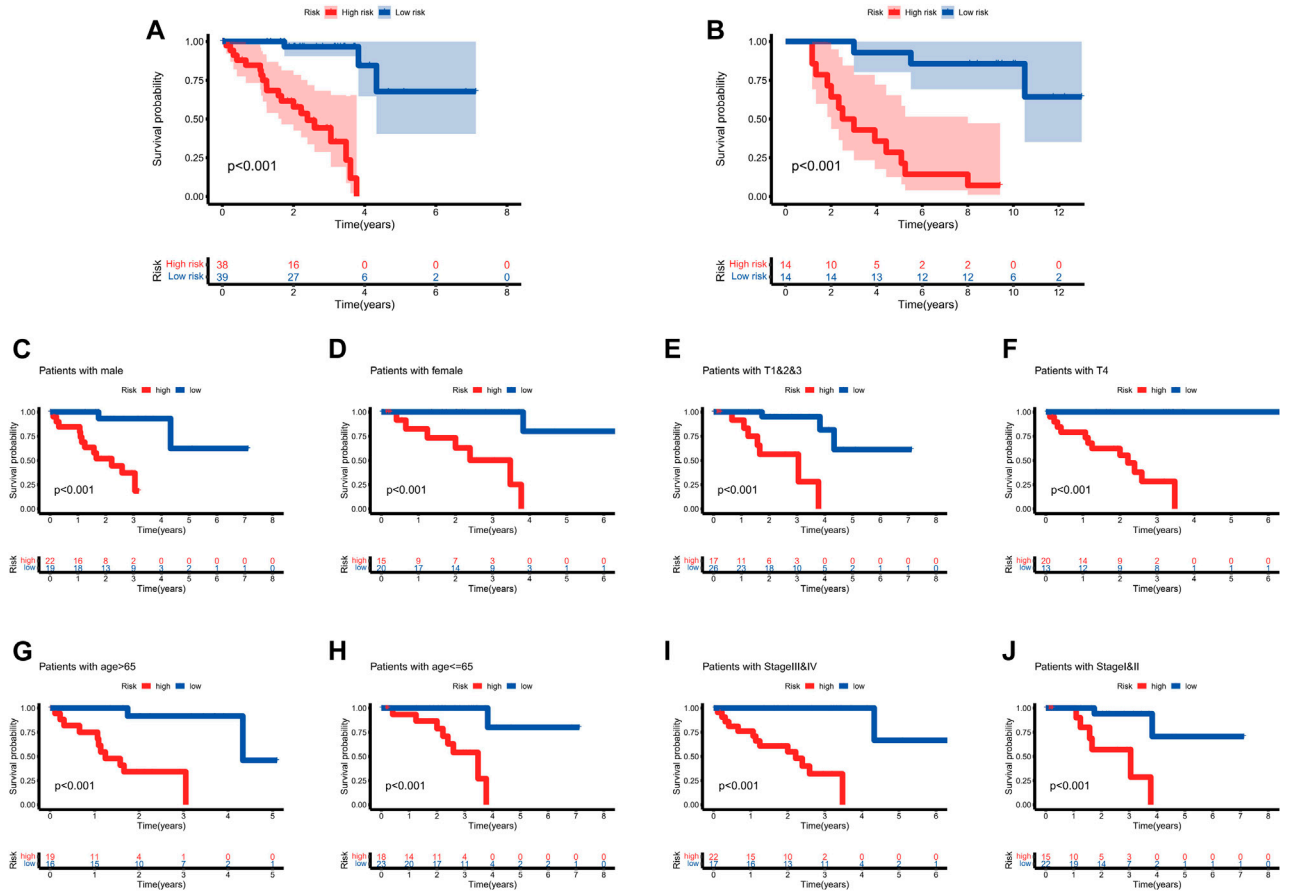

FIGURE 3 | The survival analysis based on the prognostic model. **(A,B)** To further test the confidence of the risk model, a survival analysis was performed between high-risk group and low risk groups between the training cohort (**Figure 3A**) and the validation cohort (**Figure 3B**). **(C–J)** The survival rate of patients in the high-risk group suffered a more drastic decrease, regardless of the age, gender, and tumor stages. The differences were statistically significant ($p < 0.001$).

gender, TNM stage and other factors in both the training cohort and the validation cohort. Cox regression showed that risk score was a independent prognostic factor using univariate cox regression using both univariate and multivariate regression (**Figures 5A,B**), despite the fact that tumor stage could also be considered as an independent prognostic factor by means of univariate cox regression. Likewise, risk score was also an independent prognostic factor with statistical significance in validation cohort (**Figures 5C,D**).

Gene Ontology and Kyoto Encyclopedia of Genes and Genomes Enrichment Analysis Revealed That the Differential Genes Between High Risk and Low Risk Groups Were Strongly Correlated With Immune Response

GO Enrichment analysis revealed that, biological processes like T cell activation and differentiation, lymphocyte differentiation and leukocyte cell-cell adhesion; molecular functions such as chemokine activity, cytokine activity, immune receptor activity, as well as cytokine receptor activity were enriched in differential genes between the high-risk group and the low-risk group. The enriched genes were mainly concentrated in the external side of the plasma membrane, which was in line with our findings that the differential genes were correlated immune response. (**Figures 6A,B**). KEGG analysis revealed a more specific picture of which pathways were enriched between the two groups. Not only was Th1 and Th2 cell differentiation related to the risk model, but PD-1 and PD-L1 activity was also concerned (**Figures 6C,D**). GSEA showed that immune-related functional gene sets were mainly enriched in the high-risk group, including allograft rejection, IL6-JAK-STAT3 signaling pathway, inflammatory response, interferon-alpha response, interferon-gamma response (**Figure 6E**). Next, 2,483 immune-related genes were downloaded from IMMPORT database. Through GSEA analysis, we found that these immune-related genes are mainly enriched in antigen processing and presentation, cell adhesion molecules, cytokine receptor interactions, and cytotoxicity mediated by natural killer cells in the high-risk group. Axon guidance was the main enrichment pathway in the low-risk group (**Figure 6F**).

Analysis of Immune Microenvironment

To further analyze the relationship between tumor immune response and the risk model we previously constructed,

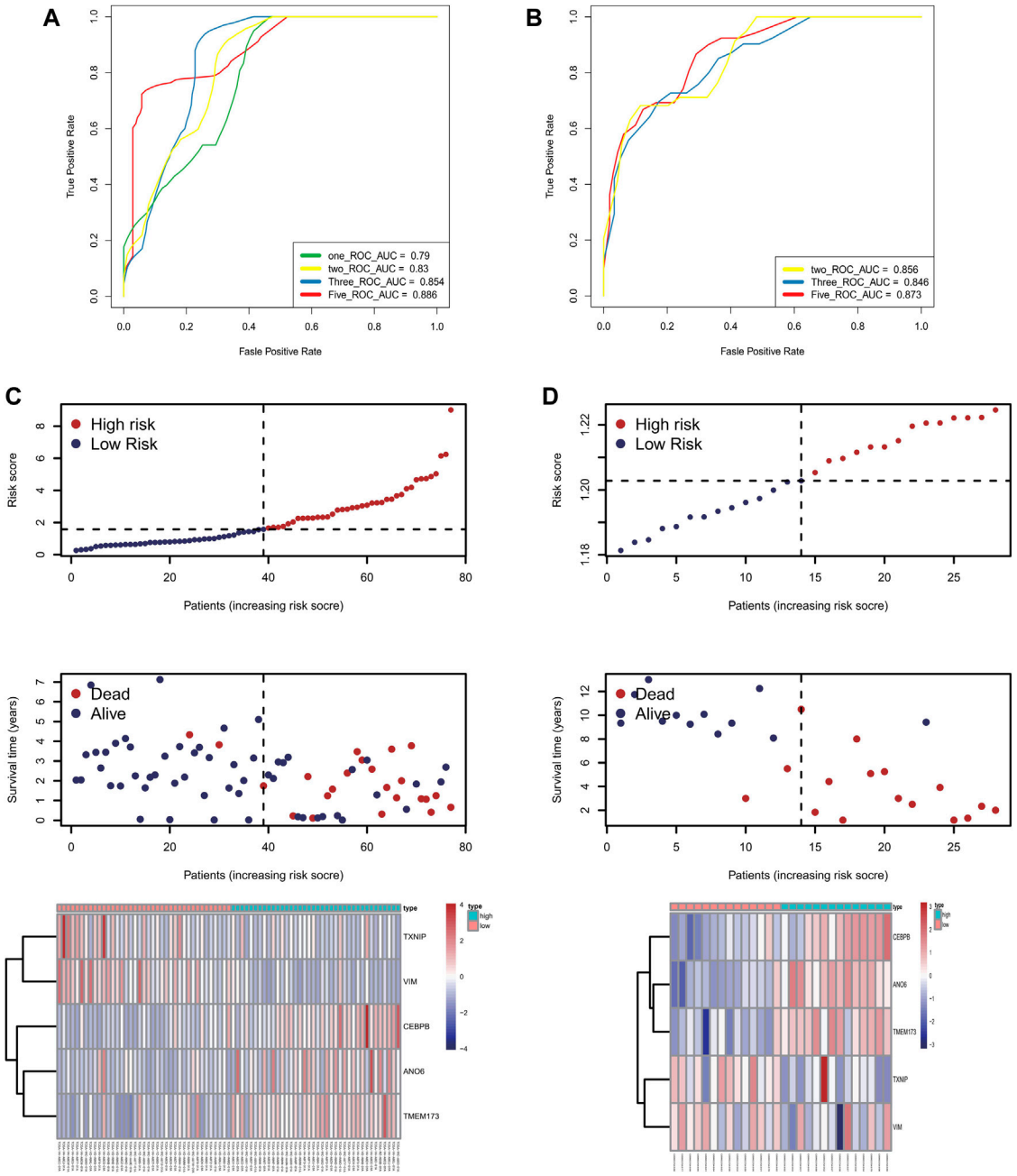

FIGURE 4 | The accuracy of this prognostic model. **(A,B)** The ROC curve of patient's survival of different years in the training cohort and the validation cohort showed that the model had a potent predicting ability, with the 1-year, 2-years, 3-years and 5-years AUC being 0.79, 0.83, 0.854, 0.886 respectively in the training cohort (Panel 4A), and the 2-years, 3-years and 5-years AUC being 0.856, 0.846, 0.873 respectively in the validation cohort (Panel 4B). (**C,D**) The distribution of the risk scores, outcome status, and gene profiles of the gene signature in the training and validation cohort were shown. The risk group successfully predicted the outcomes of the patients in both the training cohort and the validation cohort, with significantly more events found in the high-risk group. Moreover, the expression of genes ANO6, CEBPB and TMEM173 were upregulated, while genes VIM, TXNIP were seen downregulated in the high-risk group both in the training cohort and in the validation cohort, which was in accordance with our previous risk model.

immune infiltration analysis using various methods was conducted. The levels of immune infiltration differed between different risk groups. In **Figure 7A**, the samples in the training cohort were displayed according to ascending risk scores, while the levels of immune infiltration in high-risk and low-risk groups were calculated by algorithm such as TIMER, CIBERSORT, Quantiseq and other methods, which were marked in different colors. The heatmap showed the level of each immune cell infiltration in the tumor microenvironment of the two groups of patients under different algorithms. We could see that the

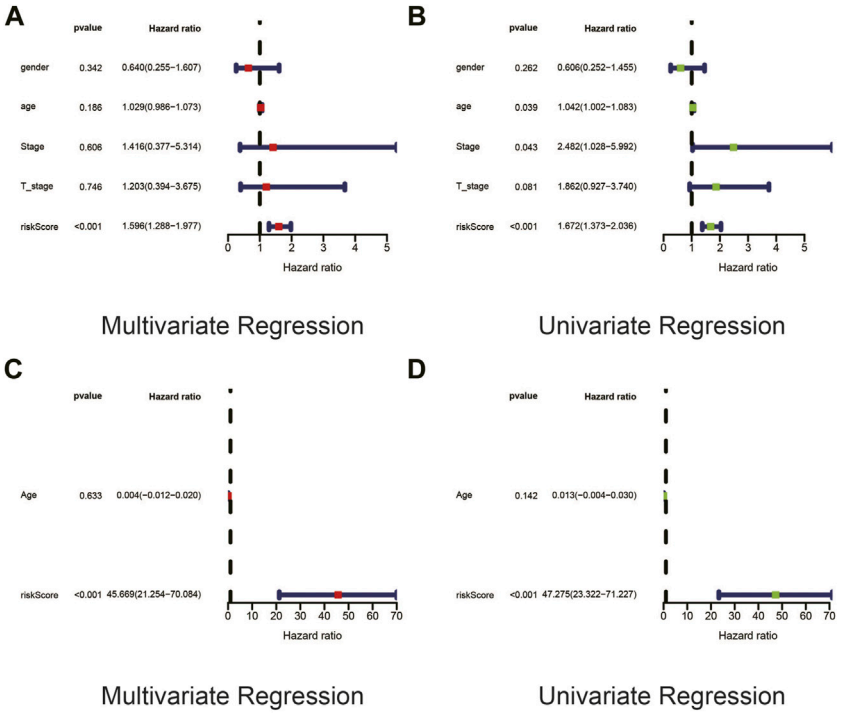

FIGURE 5 | Univariate and Multivariate Cox regression revealed that the risk score was an independent prognostic factor in UVM patients. **(A,B)** In order to explore whether risk score was an independent influencing factor for melanoma patients, univariate and multivariate Cox regression were performed for risk score, age, gender, TNM stage and other factors in both the training cohort and the validation cohort. Cox regression showed that risk score was a independent prognostic factor using univariate cox regression using both univariate (Panel 5A) and multivariate (Panel 5B) regression, despite the fact that tumor stage could also be considered as an independent prognostic factor by means of univariate cox regression. (**C,D**) Likewise, risk score was also an independent prognostic factor with statistical significance in validation cohort.

high-risk group tended to have higher levels of immune cells in the tumor microenvironment. Likewise, The immune checkpoint genes were expressed differently in the two groups and gene tended to be higher in the high-risk group (***$p < 0.001$) (**Figure 7B**). In **Figures 8A–D**, we can see the differences in stromal score, tumor purity, ESTIMATE score and total score between the two groups (***$p < 0.001$). The stromal score and ESTIMATE score were higher in the high-risk group than in the low-risk group ($p < 0.001$). Patients in the high-risk group had lower tumor purity scores than those in the low-risk group ($p < 0.001$). In terms of total score, the score of patients in the high-risk group showed a higher trend.

Analysis of Sensitivity Difference of Antitumor Drugs in Different Groups and the Construction of a Nomogram

The study of the sensitivity of different groups of patients to antitumor drugs can provide help for the formulation of future treatment regimens. Boxplot showed the differential IC_{50} of our previously established high-risk and low risk groups in the TCGA cohort. The high-risk group was more sensitive to antitumor drugs like Rapamycin, Pazopanib, Bortezomib, Cisplatin, Methotrexate, Mitomycin. C, Bortezomib and Imatinib. Those antitumor drugs were potentially more capable of inhibiting high-risk uveal melanoma with relatively minor dosage. However, further investigations are required to understand their mechanisms in Uveal Melanoma inhibition. (**Figures 9A–H**). To further evaluate the survival of UVM patients, we drew a Nomogram combining the risk value and clinical characteristics of the model. As shown in **Figure 10**, we found that the 1-, 3-, and 5-years mortality rates of patient "TCGA-VD-A8KH" were 0.00272, 0.0339 and 0.555, respectively.

ANO6 Knockdown Slows Down Uveal Melanoma Cell Proliferation *in vitro*

We further performed the experimental analysis of genes that are in the prognostic signature to validate their functions in uveal melanoma cell growth and migration. Because gene ANO6 had a relatively higher level of hazard ratio, and tended to be robust in our previously constructed models, the oncogenic role of ANO6 was tested in further experiments. Firstly, RT-qPCR analysis was performed to validate the knockdown of gene ANO6 mRNA. **Figure 11A** showed that the level of ANO6 mRNA expression was significantly downregulated after ANO6 siRNA transfection in MUM2B cell lines, which is valid for further investigation ($p < 0.001$).

5-ethynyl-2 deoxyuridine (EdU) assay was performed to test whether the knockdown of gene ANO6 could influence uveal melanoma cell proliferation *in vitro*. After knockdown of ANO6 gene, the in MUM2B cell lines showed a significant decrease in

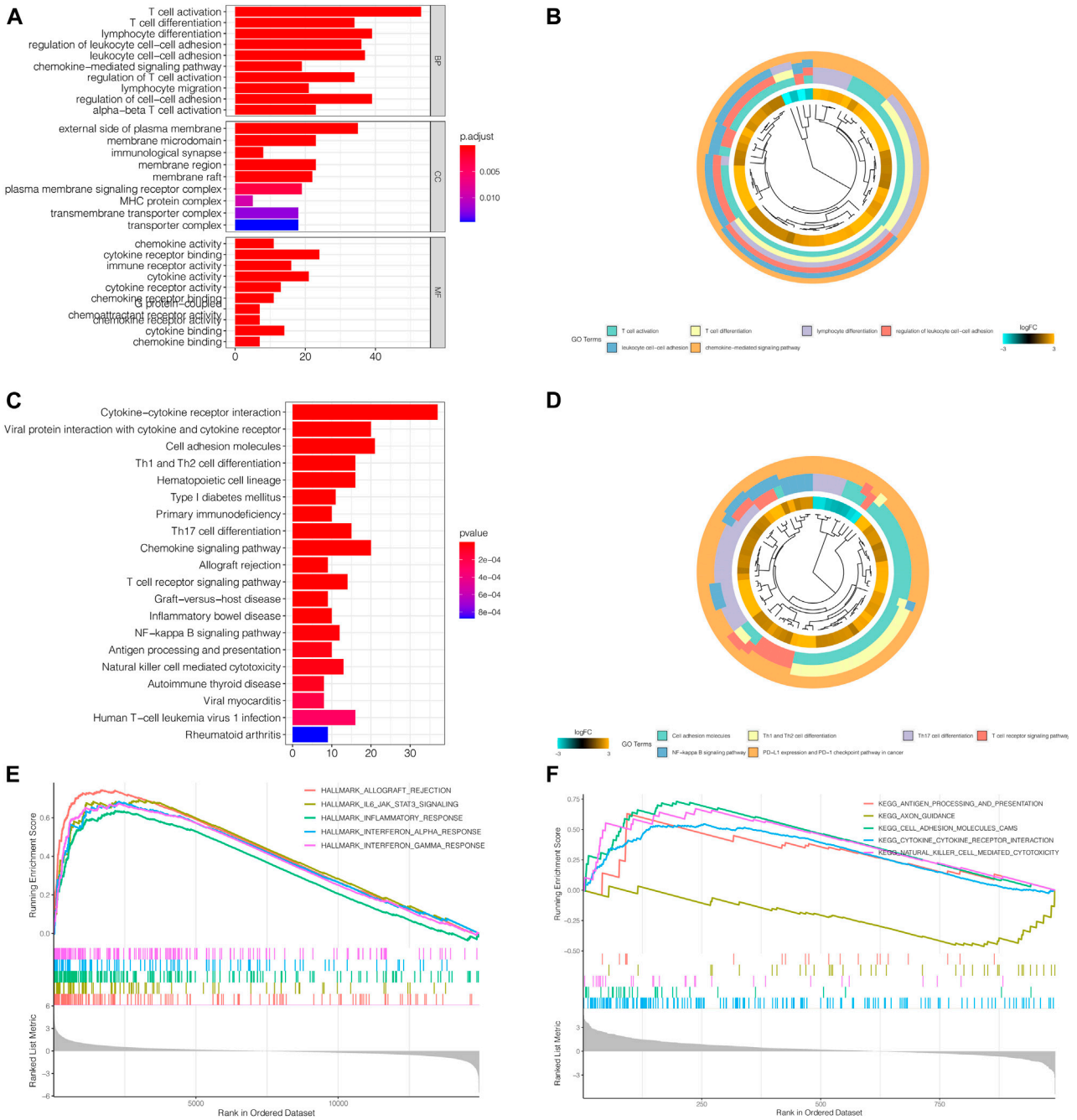

FIGURE 6 | GO and KEGG Enrichment Analysis revealed that the differential genes between high risk and low risk groups were strongly correlated with immune response. **(A,B)** GO Enrichment analysis revealed that, biological processes like T cell activation and differentiation, lymphocyte differentiation and leukocyte cell-cell adhesion; molecular functions such as chemokine activity, cytokine activity, immune receptor activity, as well as cytokine receptor activity were enriched in differential genes between the high-risk group and the low-risk group. The enriched genes were mainly concentrated in the external side of the plasma membrane, which was in line with our findings that the differential genes were correlated immune response. **(C,D)** KEGG analysis revealed a more specific picture of which pathways were enriched between the two groups. Not only was Th1 and Th2 cell differentiation related to the risk model, but PD-1 and PD-L1 activity was also concerned. However, further studied are still needed to validate the relationship between the relationship with our model and immune response. **(E)** GSEA showed that immune-related functional gene sets were mainly enriched in the high-risk group, including allograft rejection, IL6-JAK-STAT3 signaling pathway, inflammatory response, interferon-alpha response, interferon-gamma response. **(F)** 2,483 immune-related genes were downloaded from IMMPORT database. Through GSEA analysis, we found that these immune-related genes are mainly enriched in antigen processing and presentation, cell adhesion molecules, cytokine receptor interactions, and ccytotoxicity mediated by natural killer cells in the high-risk group. Axon guidance was the main enrichment pathway in the low-risk group.

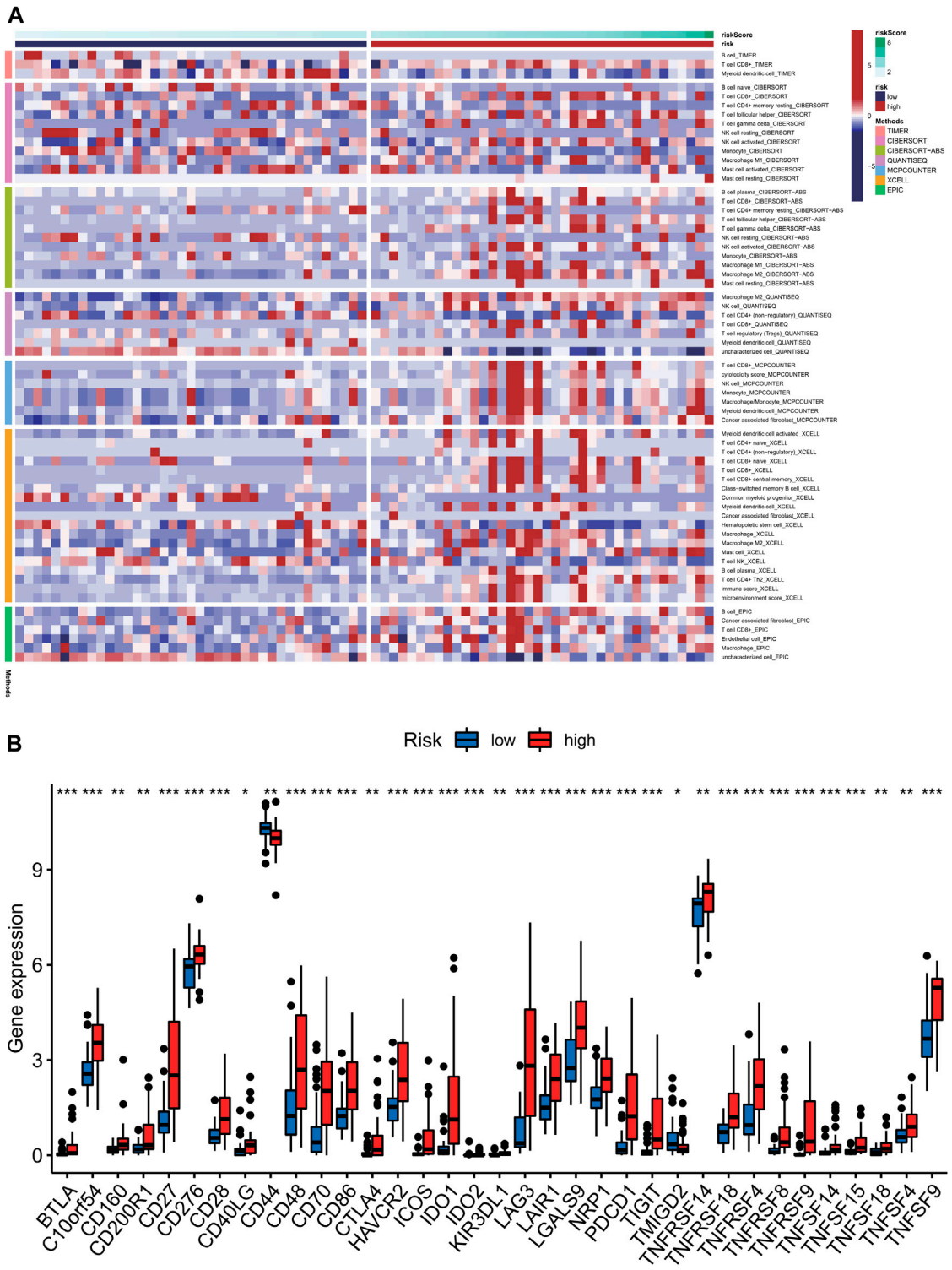

FIGURE 7 | Analysis of immune cell infiltration levels correlation analysis of immune checkpoint and in different risk groups. **(A)** The samples in the training cohort were displayed according to ascending risk scores, while the levels of immune infiltration in high-risk and low-risk groups were calculated by algorithm such as TIMER, CIBERSORT, Quantiseq and other methods, which were marked in different colors. The heatmap showed the level of each immune cell infiltration in the tumor microenvironment of the two groups of patients under different algorithms. **(B)** We could see that the high-risk group tended to have higher levels of immune cells in the tumor microenvironment. Likewise, The immune checkpoint genes were expressed differently in the two groups and gene tended to be higher in the high-risk group (***$p < 0.001$).

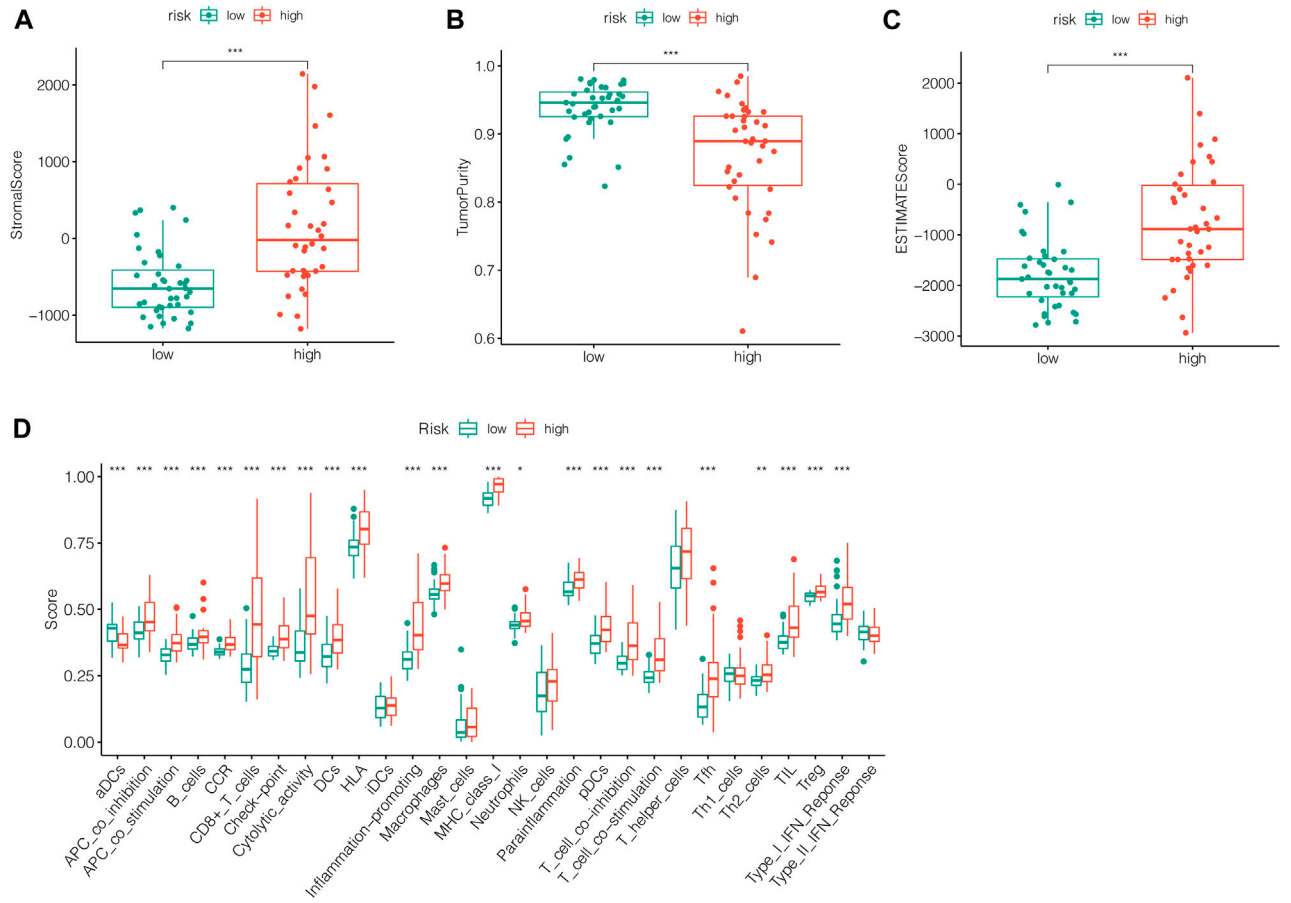

FIGURE 8 | Analysis of immune score between two groups. **(A)** The stromal score was higher in the high-risk group than in the low-risk group ($p < 0.001$). **(B)** Patients in the high-risk group had lower tumor purity scores than those in the low-risk group ($p < 0.001$). **(C)** The ESTIMATE score was higher in the high-risk group than in the low-risk group ($p < 0.001$). **(D)** The total immune score of patients in the high-risk group showed a higher trend.

nuclear DNA synthesis, indicating the ANO6 gene may progress the proliferation of uveal melanoma cell lines (**Figure 11B**), which sheds light on further study. The results were statistically significant ($p < 0.05$).

ANO6 Knockdown Attenuates Uveal Melanoma Cell Migration *in vitro*

Scratch assays in **Figure 11C** showed that after the knockdown of ANO6 mRNA, MUM2B cells migrated slower than scrambled siRNA or mock-treated control cells, which means that ANO6 knockdown may attenuate the migration of uveal melanoma cells. The results were of statistical significance ($p < 0.05$).

The Prognostic Value of This Pyroptosis-Related Gene Signature in Other Cancers

Finally, we explored whether this signature also has prognostic significance in other tumors (gastric cancer, liver cancer, skin melanoma). The same method was used to calculate the risk scores of patients with gastric cancer, liver cancer and cutaneous melanoma in the TCGA database, and the patients were divided into the high-risk group and the low-risk group according to the median score value. Then we performed survival analysis between the two groups. As shown in **Figures 12A–C**, this signature has no prognostic significance in gastric cancer, liver cancer and skin melanoma. This indicates that the model has a certain degree of specificity for predicting the prognosis of UVM.

DISCUSSION

The idea that cell death is guided by internal instructions was first suggested in 1961 in a study of insects (Tower, 2015). This landmark discovery opens the door to the study of cell death. Since then, the concept of programmed cell death has been proposed, and its significance and mechanism are being intensively explored (Nagata and Tanaka, 2017). According to existing studies, cell apoptosis, cell necrosis, and cell pyroptosis constitute the three main parts of programmed death, and relevant studies are in full bloom (Bedoui et al., 2020).

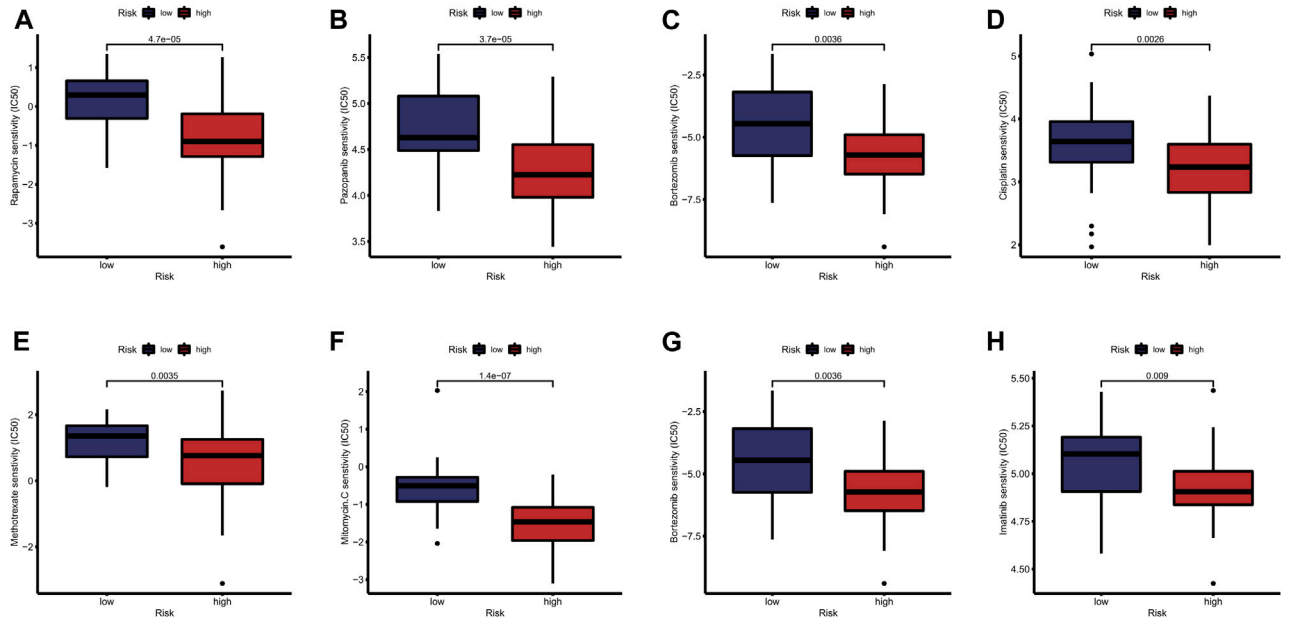

FIGURE 9 | Analysis of sensitivity difference of antitumor drugs in different groups. **(A–H)** The study of the sensitivity of different groups of patients to anti-tumor drugs can provide help for the formulation of future treatment regimens. Boxplot showed the differential IC_{50} of our previously established high-risk and low risk groups in the TCGA cohort. The high-risk group was more sensitive to antitumor drugs like Rapamycin, Pazopanib, Bortezomib, Cisplatin, Methotrexate, Mitomycin. C, Bortezomib and Imatinib. Those antitumor drugs were potentially more capable of inhibiting high-risk uveal melanoma with relatively minor dosage. However, further investigations are required to understand their mechanisms in Uveal Melanoma inhibition.

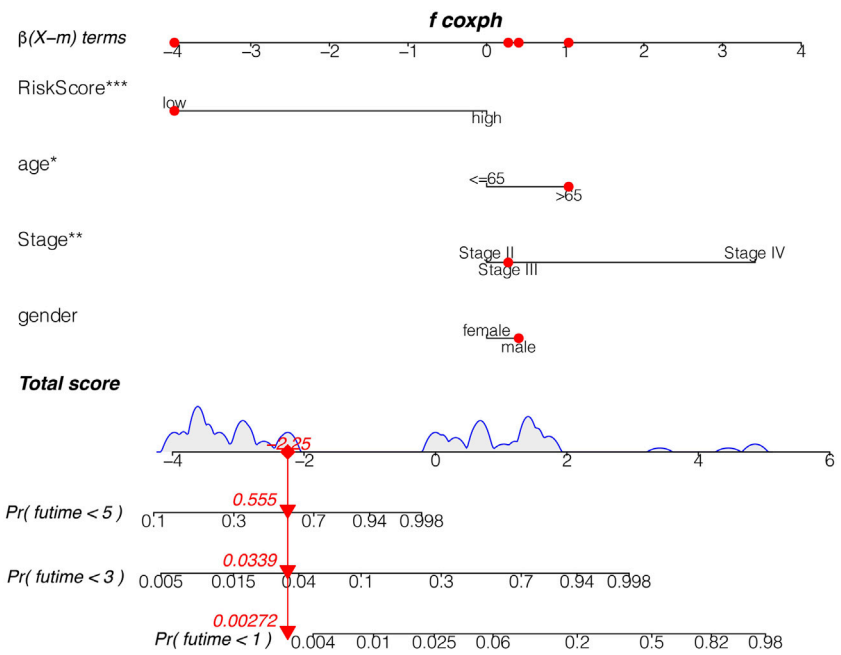

FIGURE 10 | The nomogram. The 1, 3, and 5 mortality rates of patient "TCGA-VD-A8KH" were 0.00272, 0.0339 and 0.555, respectively.

Uveal Melanoma, as one of the most harmful diseases to human vision, has seriously hindered the development of the social economy (Souto et al., 2019). Exploring the biological potential of this kind of cancer is primed and poised (Kashyap et al., 2016). Hallmarks of cancer mainly include excessive activation of growth signals, unrestricted replication, inhibition

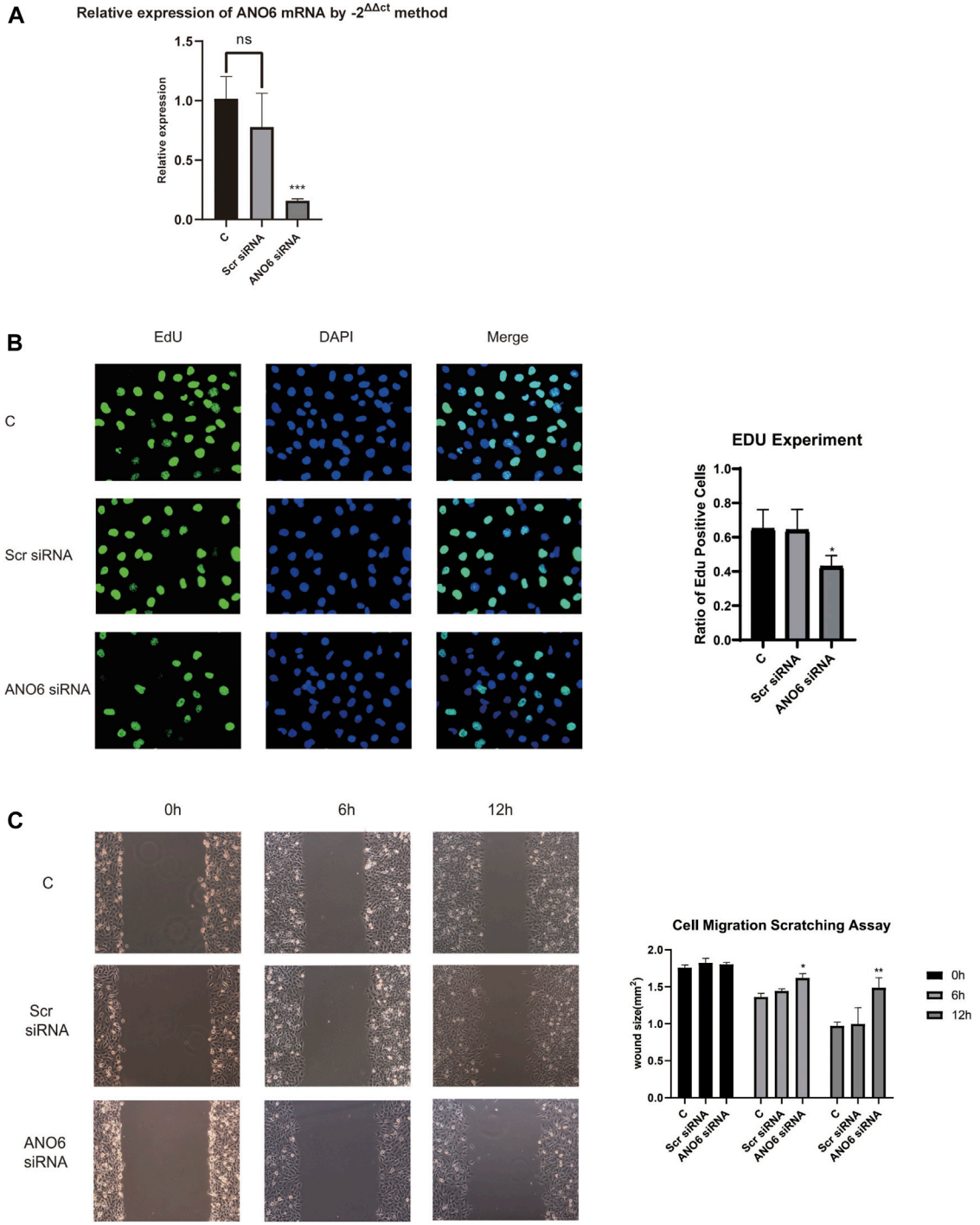

FIGURE 11 | Cell experiments of gene ANO6 to verify our results. **(A)** Firstly, RT-qPCR analysis was performed to validate the knockdown of gene ANO6 mRNA. The level of ANO6 mRNA expression was significantly downregulated after ANO6 siRNA transfection in MUM2B cell lines, which is valid for further investigation ($p < 0.001$). **(B)** 5-ethynyl-2 deoxyuridine (EdU) assay was performed to test whether the knockdown of gene ANO6 could influence uveal melanoma cell proliferation *in vitro*. After knockdown of ANO6 gene, the in MUM2B cell lines showed a significant decrease in nuclear DNA synthesis, indicating the ANO6 gene may progress the proliferation of uveal melanoma cell lines, which sheds light on further study. The results were statistically significant ($p < 0.05$). **(C)** Scratch assays showed that after the knockdown of ANO6 mRNA, MUM2B cells migrated slower than scrambled siRNA or mock-treated control cells, which means that ANO6 knockdown may attenuate the migration of uveal melanoma cells. The results were of statistical significance ($p < 0.05$).

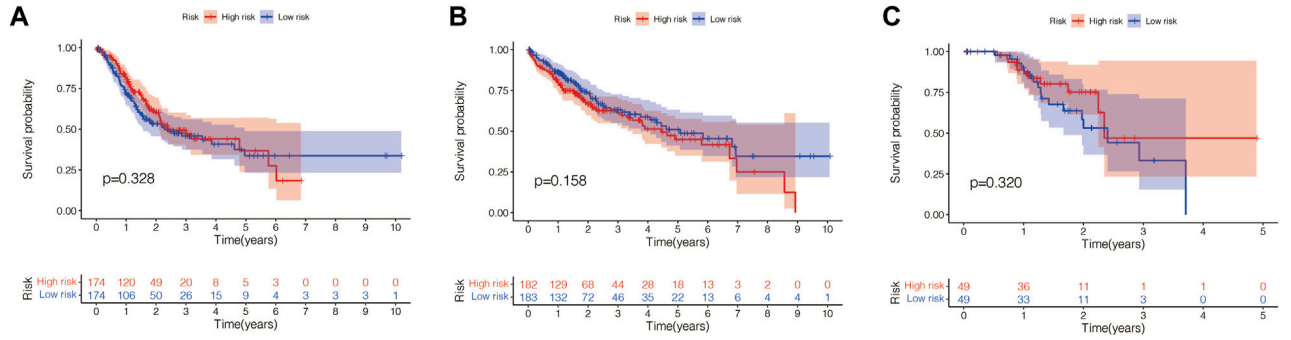

FIGURE 12 | The prognostic value of this pyroptosis-related gene signature in other cancers. (**A**) This signature has no prognostic significance in gastric cancer (p = 0.328). (**B**) This signature has no prognostic significance in liver cancer (p = 0.158). (**C**) This signature has no prognostic significance in skin melanoma (p = 0.320).

of cell death, immune re-editing, and metabolic reprogramming (Xie et al., 2021b; Xie et al., 2021c). As a kind of programmed death, cell pyroptosis plays an indelible role in both normal homeostasis regulation and cancer occurrence (Zhaolin et al., 2019). In cancer, pyroptosis has a dual effect. On the one hand, inducing pyroptosis of cancer cells can reduce tumor load in some cancers (Kesavardhana et al., 2020). Adversely, in other cancers, inflammatory substances released by cell rupture during pyroptosis can activate multiple cancer signals and may cause changes in the immune microenvironment that are beneficial for cancer proliferation (Hou et al., 2020). Hence, it's particularly important to explore the implications of char death in particular cancer types.

In this study, we built a prognosis model related to pyroptosis in UVM. According to the risk score, UVM patients can be divided into high-risk and low-risk groups, with differences in prognosis, immune infiltration, signaling pathways, and drug sensitivity between the two groups. It can be seen that our prognostic model can accurately assess the prognosis of UVM patients. In addition, we further verified our results in cell experiments.

At present, although multi-disciplinary and multi-protocol therapies have been applied to UVM, and the research on UVM is increasing, the understanding of the pathophysiology mechanism and tumor microenvironment of UVM is far from sufficient (Li et al., 2020). Moreover, the prognosis for UVM in the current context is still poor. Early diagnosis, early treatment, and the search for new prognostic markers are urgent (Zheng and Li, 2020). We constructed the prognosis model of UVM through pyroptosis-related genes and divided UVM patients into the high-risk group and low-risk group by calculating risk scores. Such a grouping pattern can accurately predict the prognosis of UVM patients. This is beneficial for the diagnosis and treatment of UVM.

The tumor immune microenvironment is still a research focus in oncology (Junttila and de Sauvage, 2013). In this complex environment, there are interactions between multiple cells and multiple signaling molecules to promote tumor growth (Wu and Dai, 2017). The degree of infiltration of immune cells in the tumor microenvironment provides a reference for us to understand tumor immunity and tumor pathogenesis (Kim and Bae, 2016). Inflammatory substances released by pyroptosis are involved in the formation of the immune microenvironment. It can be seen that after the prognosis model of UVM was constructed by pyroptosis-related genes, there was a difference in the degree of immune infiltration between the high-risk group and the low-risk group. This not only helps us to understand the immune regulatory role of pyroptosis in UVM but also provides a reference for us to explore the differences in the immune microenvironment of UVM.

Immune checkpoint inhibitors are a major discovery in the history of cancer therapy and have been successfully used in a variety of solid tumors (Dolladille et al., 2020). Cutaneous melanoma is a typical case. Although there are differences in the pathophysiology between UVM and cutaneous melanoma, the treatment of cutaneous melanoma can provide a reference for the treatment of UVM because they both originate from melanocytes (Alavi et al., 2018). Therefore, the significance of immunotherapy in UVM is also being explored in this study. We found that the high-risk group had a higher propensity to express genes associated with immune checkpoints than the low-risk group. This may suggest that UVM patients in the high-risk group may benefit more from immune checkpoint inhibitor therapy.

In our study, ANO6 is a significant gene in the pyroptosis-related prognosis model. In addition, we verified the expression and functional effects of ANO6 in UVM through cell experiments. ANO6 has also been preliminarily described for its role in immunity. Szteyn et al. found that ANO6 is a Ca (2+) activated Cl (-) channel in mouse dendritic cells (DCs) and plays an important role in chemokine-induced DC migration (Szteyn et al., 2012). Ousingsawat et al. found that ANO6 is involved in bacterial phagocytosis and promotes THP1 macrophages to kill bacteria (Ousingsawat et al., 2015). Their study demonstrated the role of ANO6 in macrophage-associated immune defense. Seidel et al. found that ANO6 may be involved in the regulation of CD137/CD137L immune response and may have an impact on immunotherapy approaches targeting CD137 (Seidel et al., 2021). Therefore, ANO6 has potential significance in tumor immunity.

All in all, our study provides a new idea for the diagnosis, treatment, and prognosis of UVM. This has significant implications for UVM, a tumor with a poor prognosis. Future studies are expected to explore the tumor microenvironment of UVM.

CONCLUSION

We constructed the prognosis model of pyroptosis related genes in UVM. Our model can accurately assess the prognosis of UVM patients. In addition, our model provides some ideas for exploring the tumor microenvironment of UVM.

DATA AVAILABILITY STATEMENT

The raw data supporting the conclusion of this article will be made available by the authors, without undue reservation.

AUTHOR CONTRIBUTIONS

YC and JX designed the study. LC and YH were involved in database search and statistical analyses. JX, YC, and MW were involved in the writing of manuscript and its critical revision. MW was responsible for the submission of the final version of the paper. All authors approved the final version. All authors agree to be accountable for all aspects of the work.

ACKNOWLEDGMENTS

We are very grateful for data provided by databases such as TCGA, GEO.

SUPPLEMENTARY MATERIAL

The Supplementary Material for this article can be found online at: https://www.frontiersin.org/articles/10.3389/fcell.2021.761350/full#supplementary-material

REFERENCES

Alavi, S., Stewart, A. J., Kefford, R. F., Lim, S. Y., Shklovskaya, E., and Rizos, H. (2018). Interferon Signaling Is Frequently Downregulated in Melanoma. *Front. Immunol.* 9, 1414, 2018 . 2018 Jun 21. doi:10.3389/fimmu.2018.01414

Bedoui, S., Herold, M. J., and Strasser, A. (2020). Emerging Connectivity of Programmed Cell Death Pathways and its Physiological Implications. *Nat. Rev. Mol. Cel Biol* 21 (11), 678–695. doi:10.1038/s41580-020-0270-8

Carvajal, R. D., Piperno-Neumann, S., Kapiteijn, E., Chapman, P. B., Frank, S., Joshua, A. M., et al. (2018). Selumetinib in Combination with Dacarbazine in Patients with Metastatic Uveal Melanoma: A Phase III, Multicenter, Randomized Trial (SUMIT). *Jco* 36 (12), 1232–1239. doi:10.1200/jco.2017.74.1090

Chattopadhyay, C., Kim, D. W., Gombos, D. S., Oba, J., Qin, Y., Williams, M. D., et al. (2016). Uveal Melanoma: From Diagnosis to Treatment and the Science in between. *Cancer* 122 (15), 2299–2312. doi:10.1002/cncr.29727

Chen, X., Chen, H., Yao, H., Li, R., Zhao, H., Wang, X., et al. (2021). Turning up the Heat on Non-immunoreactive Tumors: Pyroptosis Influences the Tumor Immune Microenvironment in Bladder Cancer, [published online ahead of print, 2021 Sep 29]. *Oncogene* 29. doi:10.1038/s41388-021-02024-9

Chen, X., Chen, H., He, D., Cheng, Y., Zhu, Y., Xiao, M., et al. (2021). Analysis of Tumor Microenvironment Characteristics in Bladder Cancer: Implications for Immune Checkpoint Inhibitor Therapy. *Front. Immunol.* 12, 672158, 2021 . 2021 Apr 15. doi:10.3389/fimmu.2021.672158

Chen, X., Xu, R., He, D., Zhang, Y., Chen, H., Zhu, Y., et al. (2021). CD8+ T Effector and Immune Checkpoint Signatures Predict Prognosis and Responsiveness to Immunotherapy in Bladder Cancer. *Oncogene* 40, 6223–6234. doi:10.1038/s41388-021-02019-6

Dolladille, C., Ederhy, S., Sassier, M., Cautela, J., Thuny, F., Cohen, A. A., et al. (2020). Immune Checkpoint Inhibitor Rechallenge after Immune-Related Adverse Events in Patients with Cancer. *JAMA Oncol.* 6 (6), 865–871. doi:10.1001/jamaoncol.2020.0726

Hou, J., Zhao, R., Xia, W., Chang, C.-W., You, Y., Hsu, J.-M., et al. (2020). PD-L1-mediated Gasdermin C Expression Switches Apoptosis to Pyroptosis in Cancer Cells and Facilitates Tumour Necrosis. *Nat. Cel Biol* 22 (10), 1264–1275. doi:10.1038/s41556-020-0575-z

Jager, M. J., Shields, C. L., Cebulla, C. M., Abdel-Rahman, M. H., Grossniklaus, H. E., Stern, M.-H., et al. (2020). Uveal Melanoma. *Nat. Rev. Dis. Primers* 6 (1), 24, 2020 . 2020 Apr 9. doi:10.1038/s41572-020-0158-0

Jiang, M., Qi, L., Li, L., and Li, Y. (2020). The Caspase-3/GSDME Signal Pathway as a Switch between Apoptosis and Pyroptosis in Cancer. *Cell Death Discov.* 6, 112, 2020 . 2020 Oct 28. doi:10.1038/s41420-020-00349-0

Junttila, M. R., and de Sauvage, F. J. (2013). Influence of Tumour Microenvironment Heterogeneity on Therapeutic Response. *Nature* 501 (7467), 346–354. doi:10.1038/nature12626

Kaliki, S., and Shields, C. L. (2017). Uveal Melanoma: Relatively Rare but Deadly Cancer. *Eye* 31 (2), 241–257. doi:10.1038/eye.2016.275

Kashyap, S., Meel, R., Singh, L., and Singh, M. (2016). Uveal Melanoma. *Semin. Diagn. Pathol.* 33 (3), 141–147. doi:10.1053/j.semdp.2015.10.005

Kesavardhana, S., Malireddi, R. K. S., and Kanneganti, T.-D. (2020). Caspases in Cell Death, Inflammation, and Pyroptosis. *Annu. Rev. Immunol.* 38, 567–595. doi:10.1146/annurev-immunol-073119-095439

Kim, J., and Bae, J. S. (2016). Tumor-Associated Macrophages and Neutrophils in Tumor Microenvironment. *Mediators Inflamm.* 2016, 6058147. doi:10.1155/2016/6058147

Kovacs, S. B., and Miao, E. A. (2017). Gasdermins: Effectors of Pyroptosis. *Trends Cel Biol.* 27 (9), 673–684. doi:10.1016/j.tcb.2017.05.005

Li, L., Li, Y., and Bai, Y. (2020). Role of GSDMB in Pyroptosis and Cancer. *Cmar* Vol. 12, 3033–3043. Published 2020 Apr 30. doi:10.2147/cmar.s246948

Luke, J. J., Olson, D. J., Allred, J. B., Strand, C. A., Bao, R., Zha, Y., et al. (2020). Randomized Phase II Trial and Tumor Mutational Spectrum Analysis from Cabozantinib versus Chemotherapy in Metastatic Uveal Melanoma (Alliance A091201). *Clin. Cancer Res.* 26 (4), 804–811. doi:10.1158/1078-0432.ccr-19-1223

Nagata, S., and Tanaka, M. (2017). Programmed Cell Death and the Immune System. *Nat. Rev. Immunol.* 17 (5), 333–340. doi:10.1038/nri.2016.153

Ousingsawat, J., Wanitchakool, P., Kmit, A., Romao, A. M., Jantarajit, W., Schreiber, R., et al. (2015). Anoctamin 6 Mediates Effects Essential for Innate Immunity Downstream of P2X7 Receptors in Macrophages. *Nat. Commun.* 6, 6245, 2015 . 2015 Feb 5. doi:10.1038/ncomms7245

Ruan, J., Wang, S., and Wang, J. (2020). Mechanism and Regulation of Pyroptosis-Mediated in Cancer Cell Death. *Chemico-Biological Interactions* 323, 109052. doi:10.1016/j.cbi.2020.109052

Seidel, J., Leitzke, S., Ahrens, B., Sperrhacke, M., Bhakdi, S., and Reiss, K. (2021). Role of ADAM10 and ADAM17 in Regulating CD137 Function. *Ijms* 22 (5), 2730, 2021 . Mar 8. doi:10.3390/ijms22052730

Smit, K. N., Jager, M. J., de Klein, A., and Kiliç, E. (2020). Uveal Melanoma: Towards a Molecular Understanding. *Prog. Retin. Eye Res.* 75, 100800. doi:10.1016/j.preteyeres.2019.100800

Souto, E. B., Zielinska, A., Luis, M., Carbone, C., Martins-Gomes, C., Souto, S. B., et al. (2019). Uveal Melanoma: Physiopathology and New In Situ-specific Therapies. *Cancer Chemother. Pharmacol.* 84 (1), 15–32. doi:10.1007/s00280-019-03860-z

Szteyn, K., Schmid, E., Nurbaeva, M. K., Yang, W., Münzer, P., Kunzelmann, K., et al. (2012). Expression and Functional Significance of the Ca2+-Activated Cl- Channel ANO6 in Dendritic Cells. *Cell Physiol Biochem* 30 (5), 1319–1332. doi:10.1159/000343321

Tang, R., Xu, J., Zhang, B., Liu, J., Liang, C., Hua, J., et al. (2020). Ferroptosis, Necroptosis, and Pyroptosis in Anticancer Immunity. *J. Hematol. Oncol.* 13 (1), 110, 2020 . 2020 Aug 10. doi:10.1186/s13045-020-00946-7

Tower, J. (2015). Programmed Cell Death in Aging. *Ageing Res. Rev.* 23 (Pt A), 90–100. doi:10.1016/j.arr.2015.04.002

Wu, T., and Dai, Y. (2017). Tumor Microenvironment and Therapeutic Response. *Cancer Lett.* 387, 61–68. doi:10.1016/j.canlet.2016.01.043

Xia, X., Wang, X., Cheng, Z., Qin, W., Lei, L., Jiang, J., et al. (2019). The Role of Pyroptosis in Cancer: Pro-cancer or Pro-"host". *Cell Death Dis* 10 (9), 650, 2019 . 2019 Sep 9. doi:10.1038/s41419-019-1883-8

Xie, J., Li, H., Chen, L., Cao, Y., Hu, Y., Zhu, Z., et al. (2021). A Novel Pyroptosis-Related lncRNA Signature for Predicting the Prognosis of Skin Cutaneous Melanoma. *Ijgm* 14, 6517–6527. 2021 Oct 8. doi:10.2147/ijgm.s335396

Xie, J., Ruan, S., Zhu, Z., Wang, M., Cao, Y., Ou, M., et al. (2021). Database Mining Analysis Revealed the Role of the Putative H+/sugar Transporter Solute Carrier Family 45 in Skin Cutaneous Melanoma. *Channels* 15 (1), 496–506. doi:10.1080/19336950.2021.1956226

Xie, J., Zhu, Z., Cao, Y., Ruan, S., Wang, M., and Shi, J. (2021). Solute Carrier Transporter Superfamily Member SLC16A1 Is a Potential Prognostic Biomarker and Associated with Immune Infiltration in Skin Cutaneous Melanoma. *Channels* 15 (1), 483–495. doi:10.1080/19336950.2021.1953322

Zhaolin, Z., Guohua, L., Shiyuan, W., and Zuo, W. (2019). Role of Pyroptosis in Cardiovascular Disease. *Cell Prolif* 52 (2), e12563. doi:10.1111/cpr.12563

Zheng, Z., and Li, G. (2020). Mechanisms and Therapeutic Regulation of Pyroptosis in Inflammatory Diseases and Cancer. *Ijms* 21 (4), 1456, 2020 . 2020 Feb 20. doi:10.3390/ijms21041456

Conflict of Interest: The authors declare that the research was conducted in the absence of any commercial or financial relationships that could be construed as a potential conflict of interest.

Publisher's Note: All claims expressed in this article are solely those of the authors and do not necessarily represent those of their affiliated organizations, or those of the publisher, the editors and the reviewers. Any product that may be evaluated in this article, or claim that may be made by its manufacturer, is not guaranteed or endorsed by the publisher.

frontiers in Cell and Developmental Biology

ORIGINAL RESEARCH
published: 26 November 2021
doi: 10.3389/fcell.2021.734699

ONC201/TIC10 Is Empowered by 2-Deoxyglucose and Causes Metabolic Reprogramming in Medulloblastoma Cells *in Vitro* Independent of C-Myc Expression

*Annika Dwucet[1], Maximilian Pruss[1], Qiyu Cao[1], Mine Tanriover[1], Varun V. Prabhu[2], Joshua E. Allen[2], Aurelia Peraud[1], Mike-Andrew Westhoff[3], Markus D. Siegelin[4], Christian Rainer Wirtz[1] and Georg Karpel-Massler[1]**

[1]Department of Neurosurgery, Ulm University Medical Center, Ulm, Germany, [2]Chimerix Inc., Durham, NC, United States, [3]Department of Pediatric and Adolescent Medicine, Ulm University Medical Center, Ulm, Germany, [4]Department of Pathology and Cell Biology, Columbia University Medical Center, New York, NY, United States

OPEN ACCESS

Edited by:
Uwe Knippschild,
University of Ulm, Germany

Reviewed by:
Angela Mastronuzzi,
Bambino Gesù Children Hospital (IRCCS), Italy
Kun Qian,
Shanghai Jiao Tong University, China

***Correspondence:**
Georg Karpel-Massler
georg.karpel-massler@uniklinik-ulm.de
georg.karpel@gmail.com

Specialty section:
This article was submitted to Cell Death and Survival, a section of the journal Frontiers in Cell and Developmental Biology

Received: *01 July 2021*
Accepted: *21 October 2021*
Published: *26 November 2021*

Citation:
Dwucet A, Pruss M, Cao Q, Tanriover M, Prabhu VV, Allen JE, Peraud A, Westhoff M-A, Siegelin MD, Wirtz CR and Karpel-Massler G (2021) ONC201/TIC10 Is Empowered by 2-Deoxyglucose and Causes Metabolic Reprogramming in Medulloblastoma Cells in Vitro *Independent of C-Myc Expression. Front. Cell Dev. Biol. 9:734699. doi: 10.3389/fcell.2021.734699*

The purpose of this study was to examine whether the imipridone ONC201/TIC10 affects the metabolic and proliferative activity of medulloblastoma cells *in vitro*. Preclinical drug testing including extracellular flux analyses (agilent seahorse), MTT assays and Western blot analyses were performed in high and low c-myc-expressing medulloblastoma cells. Our data show that treatment with the imipridone ONC201/TIC10 leads to a significant inihibitory effect on the cellular viability of different medulloblastoma cells independent of c-myc expression. This effect is enhanced by glucose starvation. While ONC201/TIC10 decreases the oxidative consumption rates in D458 (c-myc high) and DAOY (c-myc low) cells extracellular acidification rates experienced an increase in D458 and a decrease in DAOY cells. Combined treatment with ONC201/TIC10 and the glycolysis inhibitor 2-Deoxyglucose led to a synergistic inhibitory effect on the cellular viability of medulloblastoma cells including spheroid models. In conclusion, our data suggest that ONC201/TIC10 has a profound anti-proliferative activity against medulloblastoma cells independent of c-myc expression. Metabolic targeting of medulloblastoma cells by ONC201/TIC10 can be significantly enhanced by an additional treatment with the glycolysis inhibitor 2-Deoxyglucose. Further investigations are warranted.

Keywords: medulloblastoma, ONC201/TIC10, 2-Deoxyglucose, seahorse, metabolism

INTRODUCTION

Medulloblastoma represents a heterogenous tumor entity that constitutes more than 60% of embryonal brain tumors in children (Khanna et al., 2017; Northcott et al., 2019). This disease is mostly localized in the cerebellum and the majority of medulloblastomas occur in pediatric patients with a median age of 9 years (Roberts et al., 1991; Orr, 2020). Despite the fact that the majority of these tumors arise in children, adults are also rarely affected by this disease (Giordana et al., 1999). Based on distinct molecular characteristics, medulloblastomas can be divided into the WNT, sonic hedgehog (SHH), group 3 and group 4 subgroups (Taylor et al., 2011). While current first-line therapy is associated with a 5-year overall survival greater than 70% in standard-risk

patients, high-risk patients face a significantly inferior clinical course (Oyharcabal-Bourden et al., 2005; Gajjar et al., 2006; Packer et al., 2006; Cavalli et al., 2017; Khanna et al., 2017). In addition, first-line therapy is associated with an important side-effect burden including neurocognitive and endocrinological deficits as well as a strong psychosocial impairment. Notably, patients with group 3 myc-amplified or myc-overexpressing tumors were identified to be of high-risk facing a worse clinical outcome (Cavalli et al., 2017; Northcott et al., 2019). As a consequence, novel strategies need to be developed that are taking in account the characteristics of the individual disease in order to increase the therapeutic efficacy and to lower the toxicity.

Alterations with respect to the metabolic activity of cancer cells have already been described in the 1920s (Warburg et al., 1927). Otto Warburg was the first to report that cancer cells preferentially metabolize glucose through glycolysis instead of oxidative phosphorylation despite an abundant presence of oxygen. This metabolic feature is tailored to cope with a great need in biomass in order to maintain a high proliferative activity as typically seen in malignancies (Venneti and Thompson, 2017). Nowadays, it is known that the specific features of the tumor cell metabolism are much more complex and exceed by far the sole phenomenon of aerobic glycolysis (Pavlova and Thompson, 2016). The facts that 1) the cell metabolism represents a center node to maintain the cellular function and 2) cancer cell-specific metabolic features offer potential vulnerabilities support efforts to target the tumor cell metabolism to develop therapeutic strategies against cancer.

ONC201/TIC10, belongs to a class of substances termed imipridones and was discovered to have an anti-cancer activity through a drug screen searching for compounds that induce Tumor Necrosis Factor-related apoptosis-inducing ligand (TRAIL) (Allen et al., 2013). One of the main mechanisms of action of ONC201/TIC10 was discovered to rely on the hyperactivation of the mitochondrial caseinolytic protease P (CIpP) (Ishizawa et al., 2019). In turn, ONC201/TIC10-mediated activation of CIpP was shown to induce a decreased expression of respiratory chain proteins and subsequently, an impaired oxidative phosphorylation. Notably, recent preclinical studies reported that ONC201/TIC10 offers a strong antineoplastic activity against pediatric tumor cells such as diffuse intrinsic pontine glioma or MYCN-amplified neuroblastoma cells (El-Soussi et al., 2021; Zhang et al., 2021). Moreover, high expression of c-myc was shown to be associated with an improved response towards ONC201/TIC10 in glioblastoma models (Ishida et al., 2018). We therefore formed the hypothesis that this forementioned observation may prove favorable to patients with group 3 medulloblastomas in which myc amplification relates to a worse prognosis. From a translational perspective, ONC201/TIC10 has been clinically applied and is currently tested in trials including children with gliomas (NCT02525692, NCT03416530) (Arrillaga-Romany et al., 2017; Stein et al., 2017; Arrillaga et al., 2018; Karpel-Massler and Siegelin, 2018; Chi et al., 2019).

In this study, we provide evidence that ONC201/TIC10 has a strong antiproliferative activity on medulloblastoma cells with IC_{50}-values in the lower micromolar range. We also show that this effect is enhanced by glucose deprivation and that its anti-proliferative activity seemed not to be overly affected by c-myc expression. At baseline, extracellular flux analyses showed a consistent down-regulation of oxygen consumption rates following treatment with ONC201/TIC10 among DAOY and D458 cells. In contrast, the response in glycolytic rates varied among the two cell lines tested. Notably, additional treatment with 2-Deoxyglucose led to a synergistic anti-proliferative activity.

MATERIALS AND METHODS

Reagents

ONC201/TIC10 was kindly provided by Oncoceutics, Inc. (Philadelphia, PA, United States). 2-Deoxyglucose was purchased from Sigma Aldrich (St. Louis, MO, United States). A 10 mM stock solution was prepared for ONC201/TIC10 with dimethylsulfoxide (DMSO). For 2-Deoxyglucose a 500 mM stock solution was prepared with sterile water. All stock solutions were stored at −20°C. For all experiments, final concentrations of DMSO were below 0.1% (v/v).

Cell Cultures and Growth Conditions

D425, D458, and DAOY human medulloblastoma cells were obtained from the American Type Culture Collection (Manassas, VA, United States). HD-MB03 cells were purchased from the German Collection of Microorganisms and Cell Cultures (DSMZ, Braunschweig, Germany). The identities of the medulloblastoma cell lines were confirmed by the source of purchase. MB-PC322 cells were cultivated from tumor tissue obtained from a patient that was operated on at our hospital. The procedure was approved by the ethics committee of the University of Ulm (No.162/10) and consent was granted by next of kin. The initial stocks were expanded, frozen and stored in liquid nitrogen. Fresh aliquots were thawed every 6 weeks. DAOY cells were cultured in Minimum Essential Medium (MEM, Gibco, Grand Island, NY, United States) supplemented with 20% FBS (Gibco, Grand Island, NY, United States), 1% Penicillin/Streptomycin (Gibco, Grand Island, NY, United States), 1% L-glutamine (Gibco, Grand Island, NY, United States), 1% MEM non-essential amino acids (Gibco, Grand Island, NY, United States), 1% sodium pyruvate (Gibco, Grand Island, NY, United States) and 25 mM HEPES (Bioand Sell, Feucht, Germany). D425 and D458 cells were cultured in Improved MEM Zinc Option (IMEMZO, Gibco, Grand Island, NY, United States) supplemented with 20% FBS (Gibco, Grand Island, NY, United States), 1% Penicilline/Streptomycine (Gibco, Grand Island, NY, United States), 1% MEM non-essential amino acids (Gibco, Grand Island, NY, United States) and 25 mM HEPES (Biochrom, Feucht, Germany). HD-MB03 cells were cultured in Roswell Park Memorial Institute Medium (RPMI, Gibco, Grand Island, NY, United States) supplemented with 10% FBS (Gibco, Grand Island, NY, United States) and 1% Penicilline/Streptomycine (Gibco, Grand Island, NY, United States). MB-PC322 cells were cultured in Dulbecco's

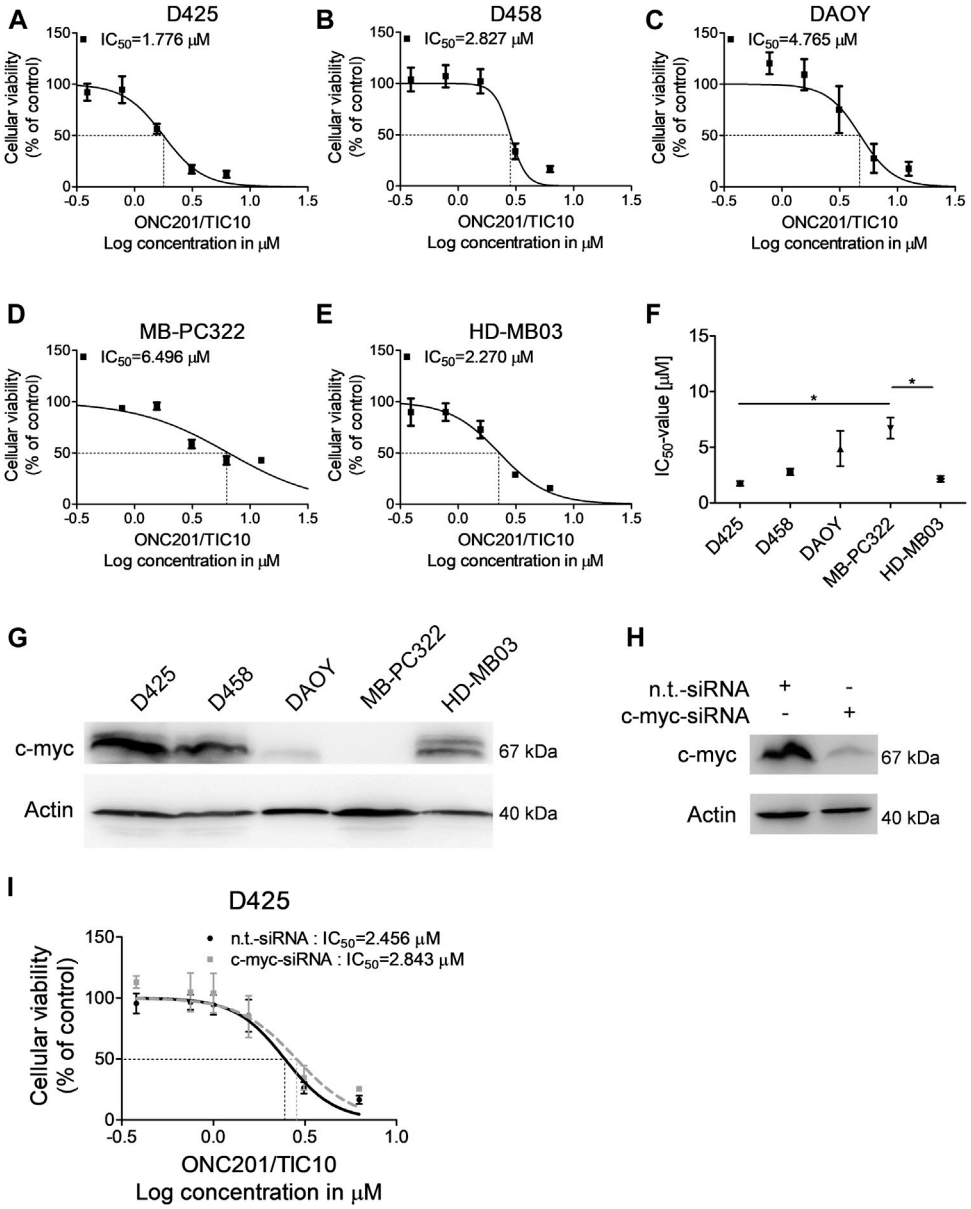

FIGURE 1 | ONC201/TIC10 has a dose-dependent anti-proliferative effect on medulloblastoma cells. **(A–E)**, D425, D458, DAOY, MB-PC322 and HD-MB03 cells were treated with solvent or increasing concentrations of ONC201/TIC10 under serum starvation (1.5%FBS). Non-linear regression was performed and IC_{50}-values were calculated. Data are presented as mean and SEM of three independent experiments. **(F)**, Quantitative representation of the IC_{50}-values for indicated cells treated as described for **(A–E)**. Mean, SEM and $n = 3$. *$p < 0.05$. **(G)**, Whole cell extracts of D425, D458, DAOY, MD-PC322 and HD-MB03 cells were collected and subjected to Western blot analysis for c-myc and Actin. **(H)**, D425 cells were transfected with non-targeting (n.t.)-siRNA or c-myc-siRNA. Cell lysates were collected and Western blot analysis for c-myc and Actin was performed. **(I)**, D425 cells were treated as described for H prior to treatment with solvent or increasing concentrations of ONC201/TIC10. Non-linear regression was performed and IC_{50}-values were calculated. Data are presented as mean and SD of three independent experiments.

Modified Eagle's Medium (DMEM, Gibco, Grand Island, NY, United States) supplemented with 10% FBS (Gibco, Grand Island, NY, United States) and 1% Penicillin/Streptomycin (Gibco, Grand Island, NY, United States). All cells were cultivated humidified at 37°C and 5% CO_2.

Cell Viability Assays

In order to examine cellular proliferation, 3-(4, 5-dimethylthiazol-2-yl)-2, 5-diphenyltetrazolium bromide (MTT) assays were performed as previously described (Karpel-Massler et al., 2015; Pruss et al., 2020).

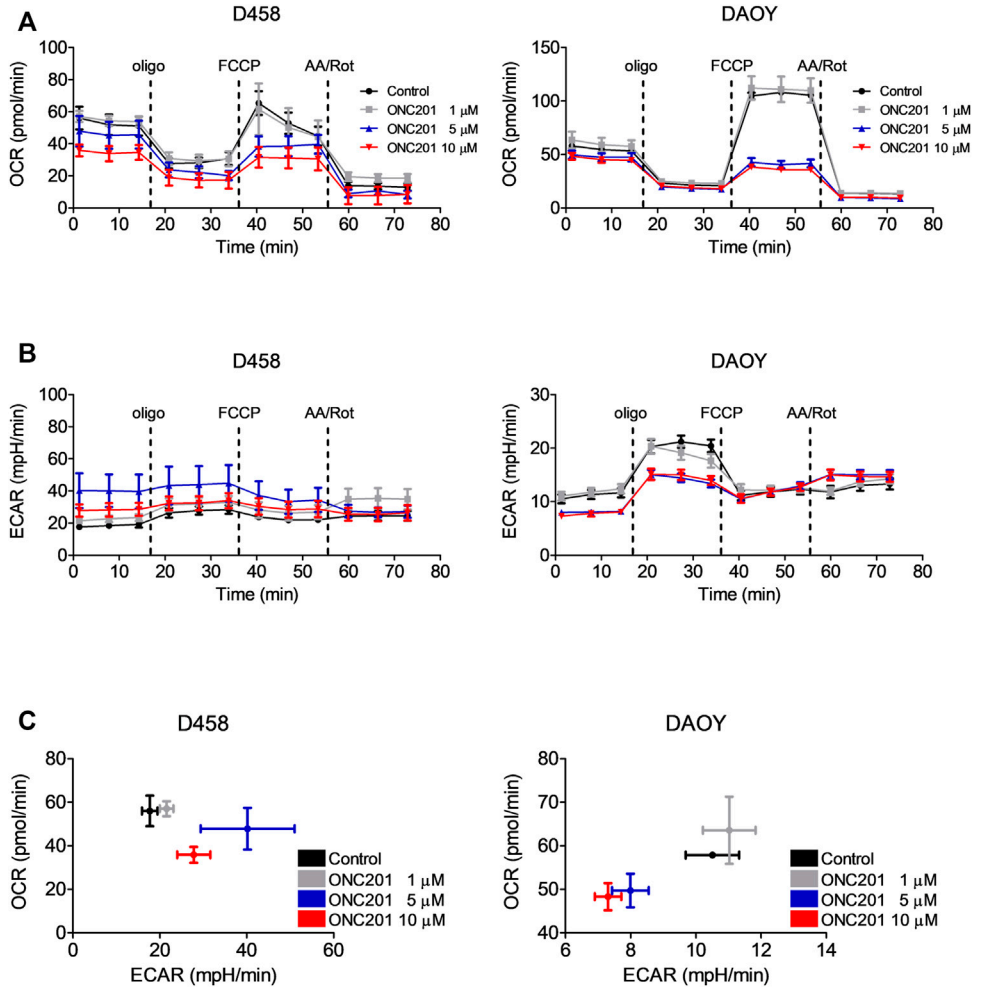

FIGURE 2 | ONC201/TIC10 suppresses OXPHOS and differentially modulates the glycolytic rates in D458 an DAOY cells. **(A)**, D458 and DAOY cells were treated for 24 h with indicated concentrations of ONC201/TIC10. Mitochondrial stress tests were performed. Oxygen consumption rates (OCR) were continuously recorded while oligomycin (olig), FCCP and antimycin A/rotenone (AA/Rot) were sequentially injected into the wells. Mean and SD of four technical replicates representative for two independent experiments. **(B)**, Extracellular acidification rates (ECAR) for cells treated as described for A. Mean and SD of four technical replicates representative for two independent experiments. **(C)**, D458 and DAOY cells were treated for 24 h with indicated concentrations of ONC201/TIC10. Graphical representation of baseline OCR/ECAR-values. Mean and SD of four technical replicates representative for two independent experiments.

Transfections of siRNAs

For siRNA transfections, lipofectamine 3000 (Invitrogen, Carlsbad, CA, United States) was used according to the manufacturer's instructions. Briefly, 5000 cells/well were seeded in 96 well plates. After 24 h, the siRNA-lipid complex was added to the cells followed by an incubation for 24 h. Then, treatments were performed for 72 h prior to analysis of the cellular viability by MTT assays or protein expression by Western blot. siRNA targeting c-myc was purchased from CST (#6552, c-myc siRNA II, SignalSilence®; Cell Signaling Technology, Danvers, MA, United States). Non-targeting siRNA was obtained from Dharmacon (D-001810-03-05, ON-TARGETplus; Lafayette, CO, United States).

Western Blot Analysis

Specific protein expression in cell lines was determined by Western blot analysis as described before (Hlavac et al., 2019; Pruss et al., 2020) using the following primary antibodies: Total OXPHOS human WB antibody cocktail (1:1,000, #ab110411, Abcam, Cambridge, U.K.), c-myc (1:1,000, #18583, clone E5Q6W; Cell Signaling Technology, Danvers, MA, United States), c-myc/n-myc (1:1,000, #13987, clone D3N8F; Cell Signaling Technology, Danvers, MA, United States) and β-actin (1:2,000, clone AC15; Sigma Aldrich, St. Louis, MO). Secondary HRP-linked antibodies were purchased from Cell Signaling Technology (#7076S, #7074S).

Extracellular Flux Analysis

1×10^4 cells were seeded on XF96 V3 PS cell culture microplates (Agilent Technologies Inc., Wilmington, DE, United States). After 24 h cells subjected to the indicated treatments for 24 h followed by washes with XF assay medium containing 5 mM glucose (pH adjusted to 7.5). Afterwards the mito stress test kit

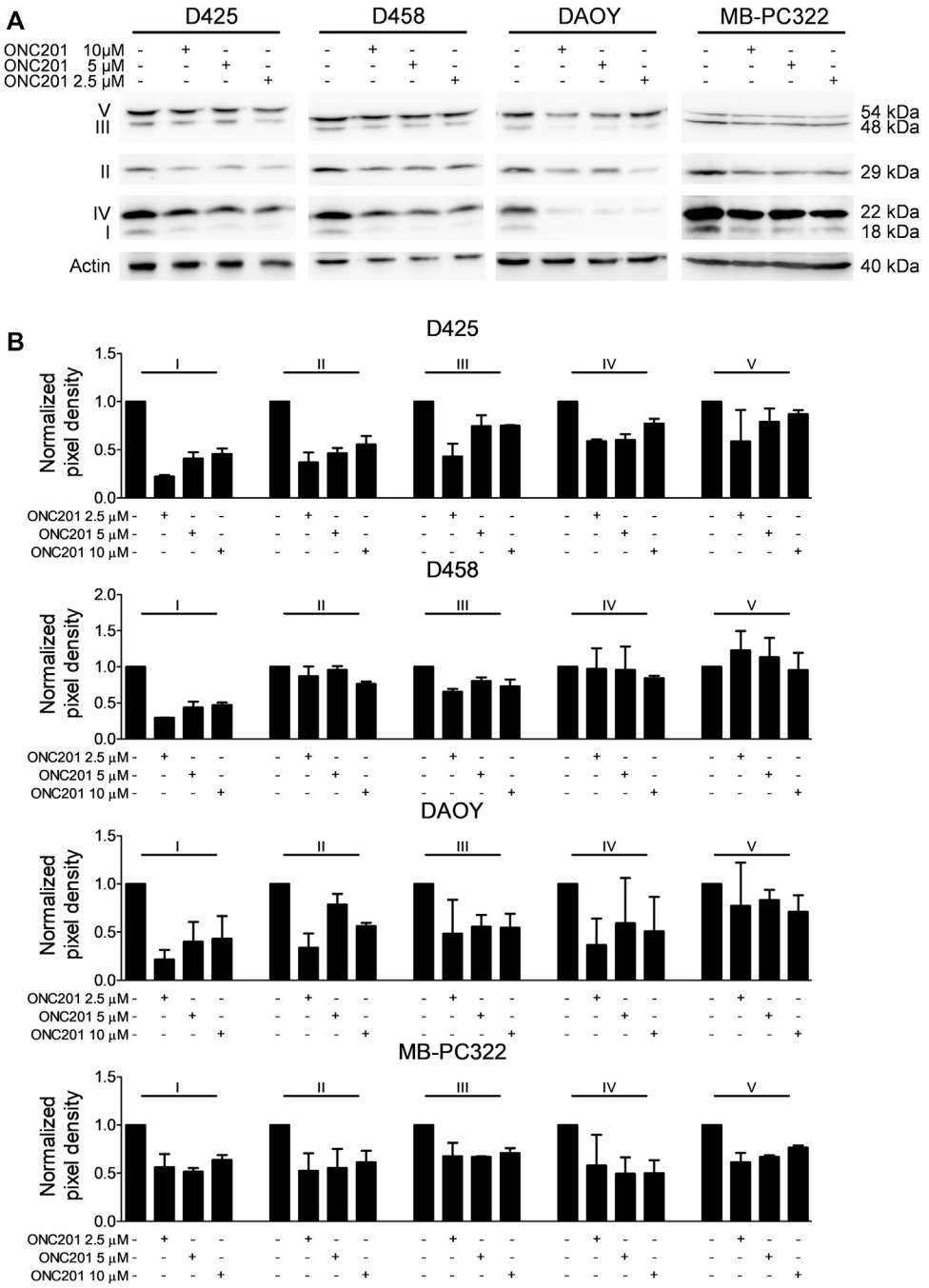

FIGURE 3 | ONC201/TIC10 reduces the expression of respiratory chain complexes. **(A)**, D425, D458, DAOY and MB-PC322 cells were treated for 24 h as indicated. Cell lysates were collected and analysed by Western blot for the expression of respiratory chain complexes I-V. Equal loading was confirmed by analysis for Actin expression. **(B)**, Quantitative representation of cells treated as described for A. Densitometric analysis was performed using ImageJ (NIH, Bethesda, MD; http://imagej.nih.gov/ij). Data were normalized to control. Columns: mean. Error bars: SD. *N* = 2.

(Agilent Technologies Inc., Wilmington, DE, United States) was used as described by the manufacturer applying serial injections of oligomycin at a final concentration of 2 μM, FCCP at a final concentration of 2 μM and rotenone/antimycin A at a final concentration of 0.5 μM. All analyses were performed on an Agilent Seahorse XFe96 analyzer.

Spheroid Assay

Spheroids were established to assess the effects of ONC201/2-Deoxyglucose in a 3-dimensional setting. In 96-well plates, 0.35×10^5 cells/well were resuspended in 20 μL of a mixture of 80% Matrigel and 20% DMEM prior to incubation for 1 h at 37°C. Afterwards, the cell/Matrigel matrix was gently transferred

to 12-well plates containing DMEM (10% FBS). Then, spheroids were allowed to grow for 7 days prior to changing the medium to DMEM containing 1.5% FBS and starting treatments. For quantification, CellTiter-Glo® assays were performed. To this purpose, spheroids suspended in 100 µL of medium were transferred to opaque-walled 96-well plates prior to adding 100 µL of the CellTiter-Glo® solution followed by incubation for 10 min at RT and measurement of luminescence.

Statistical Analysis

Statistical significance was assessed by one-way ANOVA followed by Newman-Keuls post hoc analysis using GraphPad Prism version 5.04 (La Jolla, CA). A $p \leq 0.05$ was considered statistically significant. Combination indices and isobolograms were calculated using the CompuSyn software (ComboSyn, Inc., Paramus, NJ) as described before (Karpel-Massler et al., 2017). For BLISS analysis, the expected total response was calculated as fractional response to drug A (Fa) + fractional response to drug B (Fb)—Fa x Fb. A ratio of the actual total response and the expected total response of 0.9–1.1 was considered as additive, a ratio <0.9 as antagonistic and a ratio >1.1 as synergistic (Golla et al., 2021).

RESULTS

ONC201/TIC10 Inhibits the Cellular Viability of Medulloblastoma Cells Independent of C-Myc Expression

Imipridones such as ONC201/TIC10 have been shown before to impair the cellular viability of different malignancies including glioblastoma, colorectal cancer, or ovarian cancer. In glioblastoma, a direct correlation was found between the response towards ONC201/TIC10 and c-myc expression (Ishida et al., 2018). Notably, upregulation of myc represents a molecular feature that has been shown to be associated with a worse outcome in medulloblastoma (Cavalli et al., 2017; Northcott et al., 2019). We therefore sought to examine whether ONC201/TIC10 has the ability to inhibit the cellular viability of medulloblastoma cells expressing varying levels of c-myc. D425, metastatic D458, DAOY, and HD-MB03 medulloblastoma cell lines as well as MB-PC322 primary cultured medulloblastoma cells were treated with increasing concentrations of ONC201/TIC10 prior to performing MTT assays (**Figures 1A–E**). As shown in **Figures 1A–E**, a sigmoid dose response was noted in all cells with IC_{50}-values ranging from approximately 1.8–6.5 µM. Notably, c-myc expression was high in D425, D458, and HD-MB03 cells but low in DAOY and MB-PC322 cells (**Figure 1G**). While the IC_{50}-value of ONC201/TIC10 in MB-PC322 cells was statisticallysignificant different from D425 and HD-MB03 cells no significant difference regarding the response towards ONC201/TIC10 was found when comparing the IC_{50}-value for DAOY cells with the IC_{50}-values for the other cells (**Figure 1F**).

Therefore, in order to further assess whether c-myc expression affects the response of medulloblastoma cells towards ONC201/TIC10, specific knock down of c-myc was performed in D425 cells (**Figure 1H**). As shown in **Figure 1I**, the IC_{50}-value for ONC201/TIC10 in D425 cells that were silenced for c-myc was not markedly different when compared to cells treated with non-targeting siRNA.

ONC201/TIC10 Suppresses OXPHOS in Medulloblastoma Cells

In other malignancies, the anti-cancer activity of ONC201/TIC10 has been linked to an impairment of oxidative phosphorylation and ATP depletion resulting from a hyperactivation of the mitochondrial protease CIpP and an increased depletion of respiratory chain complexes. To address the question whether ONC201/TIC10 affects oxidative phosphorylation in medulloblastoma cells, we performed extracellular flux analyses in D458 and DAOY cells. As shown in **Figure 2A**, treatment with increasing concentrations of ONC201/TIC10 results in a marked decrease in oxidative consumption rates in both cell lines at baseline and throughout the mitochondrial stress test.

ONC201/TIC10 Reduces the Expression of Complexes of the Respiratory Chain in Medulloblastoma Cells

A reduction in oxidative phosphorylation following treatment with ONC201/TIC10 has been shown in other models to go along with changes in the expression of respiratory chain proteins. To verify, whether this proposed part of the mechanism of action of ONC201/TIC10 also holds true for this setting, Western blot analysis for respiratory enzymes was performed. Treatment with increasing concentrations of ONC201/TIC10 resulted in a reduced expression of various respiratory chain complexes but did not follow a dose response under these conditions (**Figures 3A,B**). The most consistent observation was an ONC201/TIC10-mediated reduced expression of complexes I and III (**Figure 3B**). While treatment with ONC201/TIC10 decreased the expression of complexes II and IV in D425 and DAOY cells, it was not altered in metastatic D458 cells (**Figure 3B**). Complex V (ATP synthase) levels were only slightly reduced in D425 and DAOY cells when treated with ONC201/TIC10. In MB-PC322 cells, treatment with ONC201/TIC10 led to a reduced expression of all complexes of the respiratory chain.

ONC201/TIC10 Differentially Affects the Basic Glycolytic Rate in Medulloblastoma Cells

We next analysed the effects of ONC201/TIC10 on the glycolytic rates of D458 and DAOY medulloblastoma cells using the extracellular acidification rates (ECAR) as a surrogate. While treatment with ONC201/TIC10 induced a decrease in OXPHOS in both cell lines, the glycolytic rates were inversely altered by this drug (**Figures 2B,C**). At base-line, ECAR was upregulated following treatment with ONC201/TIC10 in D458 cells. In contrast, in DAOY a decrease of the ECAR was observed.

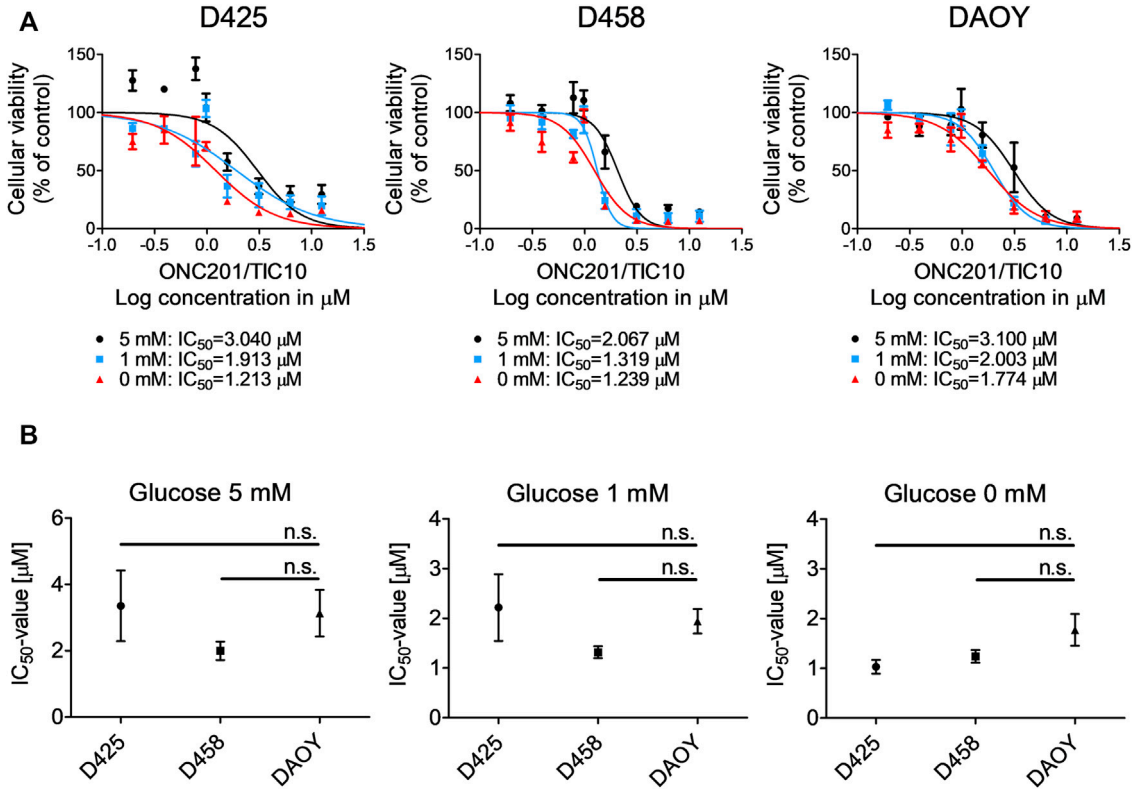

FIGURE 4 | Glucose starvation sensitizes for ONC201/TIC10. **(A)**, D425, D458 and DAOY cells were treated with solvent or increasing concentrations of ONC201/TIC10 under serum starvation (1.5%FBS) and indicated glucose concentrations. Non-linear regression was performed and IC_{50}-values were calculated. Data are presented as mean and SEM of three independent experiments. **(B)**, Quantitative representation of the IC_{50}-values for indicated cells treated as described for A. Mean, SEM and $n = 3$.

Glucose Deprivation Sensitizes Medulloblastoma Cells Towards ONC201/TIC10

Given our observation that ONC201/TIC10 modifies core metabolic pathways in different medulloblastoma cells, we formed the hypothesis that this compound creates a metabolically vulnerable cellular state which may be further destabilized by deprivation of glucose as a major energy substrate. To test this hypothesis, we exposed medulloblastoma cells to increasing concentrations of ONC201/TIC10 in the presence of decreasing levels of glucose (**Figure 4A**). Our data show that the lower the glucose concentrations are, the more the dose response curves are shifted to the left side and the more the IC_{50}-values decrease. Notably, the IC_{50}-values did not significantly vary among the three cell lines tested even under glucose-starved conditions despite varying expression of c-myc (**Figure 4B**).

ONC201/TIC10 Combined With 2-Deoxyglucose Synergistically Impairs the Cell Viability of Medulloblastoma Cells

Based on our observations that 1) glucose deprivation sensitizes for ONC201/TIC10 and 2) ONC201/TIC10 upregulates the glycolytic rate in D458 cells, we decided to assess whether the anti-neoplastic activity of ONC201/TIC10 can be significantly enhanced by a concomitant treatment with the glycolysis inhibitor 2-Deoxyglucose. To this end, we performed cell viability assays in medulloblastoma cells treated with ONC201/TIC10 and 2-Deoxyglucose alone or combined. As shown in **Figure 5A**, D425, D458, DAOY and MB-PC322 cells treated with the combination of ONC201/TIC10 and 2-Deoxyglucose displayed a statistically significant reduction of the cell viability when compared to cells receiving treatment with the single agents or solvent. Moreover, isobolograms and combination index-plots were calculated and revealed that ONC201/TIC10 and 2-Deoxyglucose act predominantly in a synergistic manner with respect to their anti-medulloblastoma activity (**Figures 5B,C**).

ONC201/TIC10 Combined With 2-Deoxyglucose Synergistically Inhibits the Growth of Spheroids

Next, we examined how the combination treatment with ONC201/TIC10 and 2-Deoxyglucose affects the growth of medulloblastoma cells in a 3-dimensional setting. For this purpose, spheroids were established prior to treatment with

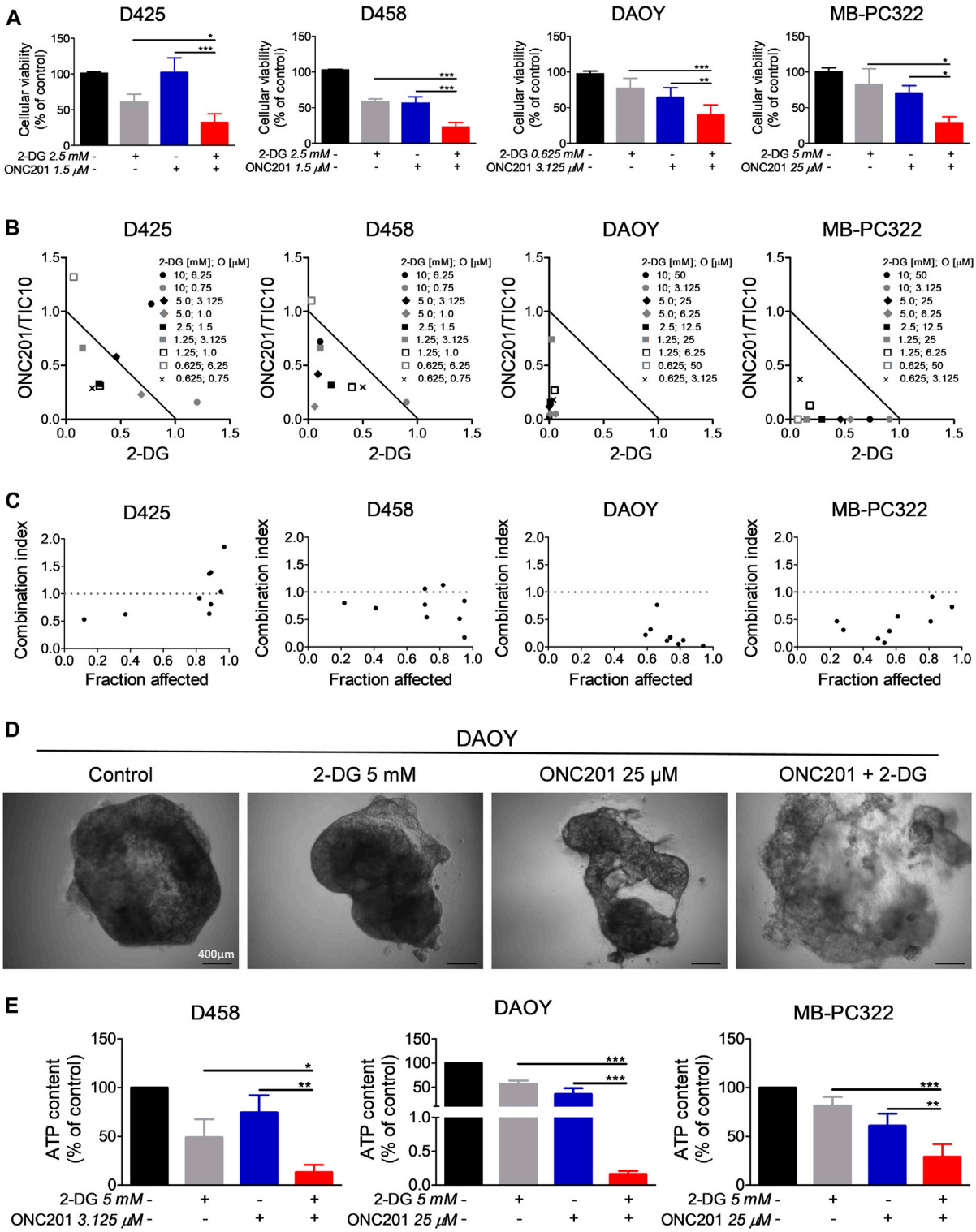

FIGURE 5 | 2-Deoxyglucose and ONC201/TC10 synergistically inhibit the cellular viability and the growth of spheroids in medulloblastoma. **(A)**, D425, D458, DAOY and MB-PC322 cells were treated with solvent or indicated concentrations of 2-Deoxyglucose and/or ONC201/TIC10 under serum starvation (1.5%FBS) for 72 h prior to performing MTT assays. Columns: mean. Error bars: SD. $N = 3$. $^{*}p < 0.05$, $^{**}p < 0.01$, $^{***}p < 0.005$. **(B)**, D425, D458, DAOY and MB-PC322 cells were treated for 72 h as indicated. MTT assays were performed and normalized isobolograms were calculated. Data points within the triangle are indicative for a synergistic, data points outside of the triangle point towards an antagonistic and data points on the diagonal line indicate an additive drug-drug interaction. Data are representative for three independent experiments. **(C)**, Combination index (CI)-plots for medulloblastoma cells treated as described for B. A CI < 1 signifies a synergistic, a CI = 1 an additive and a CI > 1 an antagonistic drug-drug interaction. **(D)**, Microphotographs of DAOY spheroids that were grown for 14 days. Treatment as indicated was performed on d 7, d 9, and d 12. Magnification, × 4. **(E)**, D458, DAOY and MB-PC322 spheroids were treated as described for D. CellTiter-Glo® assays were performed to determine the ATP content. Columns: mean. Error bars: SD. $N = 3$. $^{*}p < 0.05$, $^{**}p < 0.01$, $^{***}p < 0.005$.

the two drugs. Microscopic imaging showed that spheroids treated with the combination developed a reduced cellular density and experienced a disruption of the spheroid structure (**Figure 5D**). In line with this finding, the ATP content of D458, DAOY and MB-PC322 spheroids treated with the combination therapy was significantly reduced in comparison with the single agent treatments and control (**Figure 5E**). Furthermore, BLISS analysis revealed that ONC201/TIC10 and 2-Deoxyglucose did act in a synergistic manner in spheroids derived from D458 (BLISS index = 1.37), DAOY (BLISS index = 1.26) and MB-PC322 (BLISS index = 1.41) cells.

DISCUSSION

Medulloblastoma represents one of the most common childhood brain tumors and while we have learned a lot regarding the molecular characteristics of this disease within the past years more efficient and less toxic therapeutics are greatly needed (Northcott et al., 2019; Orr, 2020). Patients with medulloblastomas harboring amplified myc were reported to face a worse prognosis (Cavalli et al., 2017). It was on these grounds, that we formed the hypothesis that the imipridone ONC201/TIC10, which was shown before to be more potent in c-myc high expressing glioblastomas (Ishida et al., 2018), might have a pronounced anti-medulloblastoma efficacy in this subtype.

Our data showed that ONC201/TIC10 had strong anti-neoplastic activity across multiple medulloblastoma cell models. However, we did not find a statistically significant difference between c-myc low-expressing DAOY cells and c-myc high-expressing D425, D458, and HD-MB03 cells. In addition, silencing of c-myc in D425 cells did not significantly alter the response towards ONC201/TIC10. These data suggest that c-myc expression does not predict the response towards ONC201/TIC10 in this setting. In contrast to our findings, Ishida et al. reported that c-myc high-expressing glioblastoma cells were significantly more responsive towards a treatment with ONC201/TIC10 (Ishida et al., 2018). Moreover, silencing of c-myc using shRNA markedly increased DNA fragmentation following ONC201/TIC10 treatment. The discrepancy between the results of this study and the study by Ishida et al. are likely due to differences in the genetic background of these two different tumor entities. Taken together, it also suggests that c-myc might not be as important with respect to the mechanism that underlies the activity of ONC201/TIC10 in medulloblastoma when compared to glioblastoma.

Another controversy, is represented by the fact that while OXPHOS seems to be consistently suppressed by ONC201/TIC10, ECARs as an outread for the glycolytic rate show a varying response. Treatment of U87 and SF188 glioblastoma cells with ONC201/TIC10 was reported to result in significantly decreased ECARs (Ishida et al., 2018). In contrast, in U251 and A172 glioblastoma cells ECARs at baseline were markedly increased when cells were subjected to ONC201/TIC10 (Pruss et al., 2020). In all these cells, OXPHOS was consistently shown to be suppressed by ONC201/TIC10 independent of differences in experimental conditions. Similarly, in the present study ONC201/TIC10 led to a strong down-regulation of OXPHOS in all medulloblastoma cell lines tested. However, while ONC201/TIC10 up-regulated ECAR in D458 cells, a decrease was observed in DAOY cells. The origin of this discrepancy is presently not identified. Differences in experimental conditions, genetic or metabolic background are likely to be involved and need further elucidation.

We have shown before that 2-Deoxyglucose synergistically enhanced the inhibitory activity of ONC201/TIC10 on the cellular viability and tumor growth in glioblastoma (Pruss et al., 2020). These biological effects are in line with the observations we made in the current study. Interestingly, in this setting, a differing response regarding glycolytic rates following treatment with ONC201/TIC10 did not seem to translate into markedly different responses towards an additional treatment with the glycolysis inhibitor 2-Deoxyglucose. Regardless whether ONC201/TIC10 led to an increase of the ECAR as seen in D458 or to a decrease of the ECAR as seen in DAOY, a predominantly synergistic anti-neoplastic activity of the combination was observed. As a consequence, the hypothesis that the mechanistic basis of the synergistic effect of the combination therapy relies only on an additional inhibition of glycolysis needs to be at least questioned and indicates that other molecular or metabolic alterations might be involved. Further analyses of the transcriptome and the metabolome of D458 and DAOY cells subjected to the combination therapy are planned and will likely aid at uncovering additional modes of mechanism.

Our data provide evidence that interference with OXPHOS and glycolysis might represent a useful instrument for the treatment of medulloblastoma patients. In order to guide therapeutic measures, novel technologies are in development to facilitate a metabolic fingerprinting. As an example, varying substrates were developed such as ferric or magnetic particles covered with a Pd-Au shell to improve the analysis of metabolites in body fluids by laser desorption/ionization mass spectrometry (Cao et al., 2020; Huang et al., 2020; Pei et al., 2020). These analyses combined with machine learning tools allowed for the identification of specific metabolic patterns in patients with early stage lung adenocarcinoma (Huang et al., 2020), medulloblastoma (Cao et al., 2020) and gynecological cancers (Pei et al., 2020). In the future, this technology may allow for a high-throughput and cost-efficient way of identifying patients with tumors showing specific metabolic signatures that may predict a response towards drugs targeting the tumor cell metabolism such as ONC201/TIC10 or 2-Deoxyglucose. In addition, changes in metabolic signatures following therapy could be monitored and used to adapt the therapeutic interventions in a dynamic fashion.

The development of therapeutic resistance represents a major problem for the treatment of malignant diseases such as medulloblastoma and will very likely also extend to anti-metabolic approaches. Therefore, preventive strategies should be considered. For instance the use of nanodrugs or Janus particles have been described to allow for a better drug delivery and drug distribution across tumor tissue to avoid

suboptimal local drug dosing and a subsequent selection of resistant clones (Su et al., 2019; Ma et al., 2020). In addition, the combination of anti-metabolic strategies with treatment modalities such as photodynamic or sonodynamic therapy using a different anti-neoplastic mechanism may add further therapeutic benefits and counteract therapeutic resistance (Wu et al., 2020).

There are certainly a number of limitations that need to be carefully considered when interpreting the results of this study. One limitation is presented by the fact that we included only five different medulloblastoma cells in our analyses. Moreover, we did not verify our findings in an *in vivo* model. However, to our knowledge, this study provides first evidence for ONC201/TIC10 as a potentially valuable therapeutic in medulloblastoma. In addition, proof of principle is provided for a multi-targeted anti-metabolic therapeutic strategy resulting in a synergistic anti-neoplastic activity in this setting. This approach is supported by the fact that both, ONC201/TIC10 and 2-Deoxyglucose are known to cross the blood brain barrier reaching concentrations that are in the same range as the ones used in this study. Moreover, both drugs were used in clinical trials with a good safety profile (Singh et al., 2005; Raez et al., 2013; Arrillaga-Romany et al., 2017; Arrillaga et al., 2018; Chi et al., 2019). Of course, a combined treatment with multiple drugs that target core metabolic pathways holds the risk for unforeseen toxicity and needs further critical validation. However, the results of this study suggest that translation of ONC201/TIC10 into the clinics for the treatment of patients with medulloblastoma—independent of myc status—might hold promise and legitimate further studies.

DATA AVAILABILITY STATEMENT

The raw data supporting the conclusion of this article will be made available by the authors, without undue reservation.

ETHICS STATEMENT

The studies involving human participants were reviewed and approved by the ethics committee of the University of Ulm (No.162/10). Written informed consent to participate in this study was provided by the participants' legal guardian/next of kin.

AUTHOR CONTRIBUTIONS

Conceptualization, GK-M; methodology, AD, GK-M, MP and M-AW; formal analysis, AD, GK-M and MP; investigation, AD, GK-M, MP, and MT; resources, GK-M, AP, M-AW and CRW; data curation, AD and GK-M; writing—original draft preparation, GK-M; writing—review and editing, JA, AD, GK-M, AP, VP, MP, MDS, M-AW and CRW; supervision, GK-M; project administration, GK-M All authors have read and agreed to the published version of the manuscript.

FUNDING

National Institutes of Health, National Institute of Neurological Disorders and Stroke (K08 NS083732, R01 NS095848, and R01 NS102366) to MDS.

ACKNOWLEDGMENTS

We would like to express our gratitude to the Core Facility "Extracellular Flux Analyzer" at Ulm University for excellent help and assistance. We also thank Ms. Nika Koshnevis for excellent technical support.

REFERENCES

Allen, J. E., Krigsfeld, G., Mayes, P. A., Patel, L., Dicker, D. T., Patel, A. S., et al. (2013). Dual Inactivation of Akt and ERK by TIC10 Signals Foxo3a Nuclear Translocation, TRAIL Gene Induction, and Potent Antitumor Effects. *Sci. Transl. Med.* 5, 171ra17. doi:10.1126/scitranslmed.3004828

Arrillaga, I., Odia, Y., Allen, J. E., Prabhu, V. V., Tarapore, R., Oster, W., et al. (2018). Intratumoral Activity of ONC201 in Adult Recurrent Glioblastoma Patients. *Jco* 36 (15_Suppl. l), e14034. doi:10.1200/jco.2018.36.15_suppl.e14034

Arrillaga-Romany, I., Chi, A. S., Allen, J. E., Oster, W., Wen, P. Y., and Batchelor, T. T. (2017). A Phase 2 Study of the First Imipridone ONC201, a Selective DRD2 Antagonist for Oncology, Administered Every Three Weeks in Recurrent Glioblastoma. *Oncotarget* 8, 79298–79304. doi:10.18632/oncotarget.17837

Cao, J., Shi, X., Gurav, D. D., Huang, L., Su, H., Li, K., et al. (2020). Metabolic Fingerprinting on Synthetic Alloys for Medulloblastoma Diagnosis and Radiotherapy Evaluation. *Adv. Mater.* 32, 2000906. doi:10.1002/adma.202000906

Cavalli, F. M. G., Remke, M., Rampasek, L., Peacock, J., Shih, D. J. H., Luu, B., et al. (2017). Intertumoral Heterogeneity within Medulloblastoma Subgroups. *Cancer Cell* 31, 737–e6. doi:10.1016/j.ccell.2017.05.005

Chi, A. S., Tarapore, R. S., Hall, M. D., Shonka, N., Gardner, S., Umemura, Y., et al. (2019). Pediatric and Adult H3 K27M-Mutant Diffuse Midline Glioma Treated with the Selective DRD2 Antagonist ONC201. *J. Neurooncol.* 145, 97–105. doi:10.1007/s11060-019-03271-3

El-Soussi, S., Hanna, R., Semaan, H., Khater, A.-R., Abdallah, J., Abou-Kheir, W., et al. (2021). A Novel Therapeutic Mechanism of Imipridones ONC201/ONC206 in MYCN-Amplified Neuroblastoma Cells via Differential Expression of Tumorigenic Proteins. *Front. Pediatr.* 9, 693145. doi:10.3389/fped.2021.693145

Gajjar, A., Chintagumpala, M., Ashley, D., Kellie, S., Kun, L. E., Merchant, T. E., et al. (2006). Risk-adapted Craniospinal Radiotherapy Followed by High-Dose Chemotherapy and Stem-Cell rescue in Children with Newly Diagnosed Medulloblastoma (St Jude Medulloblastoma-96): Long-Term Results from a Prospective, Multicentre Trial. *Lancet Oncol.* 7, 813–820. doi:10.1016/s1470-2045(06)70867-1

Giordana, M. T., Schiffer, P., Lanotte, M., Girardi, P., and Chio, A. (1999). Epidemiology of Adult Medulloblastoma. *Int. J. Cancer* 80, 689–692. doi:10.1002/(sici)1097-0215(19990301)80:5<689:aid-ijc10>3.0.co;2-g

Golla, C., Bilal, M., Dwucet, A., Bader, N., Anthonymuthu, J., Heiland, T., et al. (2021). Photodynamic Therapy Combined with Bcl-2/Bcl-xL Inhibition Increases the Noxa/Mcl-1 Ratio Independent of Usp9X and Synergistically Enhances Apoptosis in Glioblastoma. *Cancers* 13, 4123. doi:10.3390/cancers13164123

Hlavac, M., Dwucet, A., Kast, R. E., Engelke, J., Westhoff, M.-A., Siegelin, M. D., et al. (2019). Combined Inhibition of RAC1 and Bcl-2/Bcl-xL Synergistically Induces Glioblastoma Cell Death through Down-Regulation of the Usp9X/Mcl-1 axis. *Cell Oncol.* 42, 287–301. doi:10.1007/s13402-019-00425-3

Huang, L., Wang, L., Hu, X., Chen, S., Tao, Y., Su, H., et al. (2020). Machine Learning of Serum Metabolic Patterns Encodes Early-Stage Lung Adenocarcinoma. *Nat. Commun.* 11, 3556. doi:10.1038/s41467-020-17347-6

Ishida, C. T., Zhang, Y., Bianchetti, E., Shu, C., Nguyen, T. T. T., Kleiner, G., et al. (2018). Metabolic Reprogramming by Dual AKT/ERK Inhibition through Imipridones Elicits Unique Vulnerabilities in Glioblastoma. *Clin. Cancer Res.* 24, 5392–5406. doi:10.1158/1078-0432.ccr-18-1040

Ishizawa, J., Zarabi, S. F., Davis, R. E., Halgas, O., Nii, T., Jitkova, Y., et al. (2019). Mitochondrial ClpP-Mediated Proteolysis Induces Selective Cancer Cell Lethality. *Cancer Cell* 35, 721–737. doi:10.1016/j.ccell.2019.03.014

Karpel-Massler, G., and Siegelin, M. D. (2018). TIC10/ONC201-a Potential Therapeutic in Glioblastoma. *Transl. Cancer Res.* 6, S1439–S1440. doi:10.21037/tcr.2017.10.51

Karpel-Massler, G., Bâ, M., Shu, C., Halatsch, M.-E., Westhoff, M.-A., Bruce, J. N., et al. (2015). TIC10/ONC201 Synergizes with Bcl-2/Bcl-xL Inhibition in Glioblastoma by Suppression of Mcl-1 and its Binding Partners *In Vitro* and *In Vivo*. *Oncotarget* 6, 36456–36471. doi:10.18632/oncotarget.5505

Karpel-Massler, G., Ishida, C. T., Bianchetti, E., Zhang, Y., Shu, C., Tsujiuchi, T., et al. (2017). Induction of Synthetic Lethality in IDH1-Mutated Gliomas through Inhibition of Bcl-xL. *Nat. Commun.* 8, 1067. doi:10.1038/s41467-017-00984-9

Khanna, V., Achey, R. L., Ostrom, Q. T., Block-Beach, H., Kruchko, C., Barnholtz-Sloan, J. S., et al. (2017). Incidence and Survival Trends for Medulloblastomas in the United States from 2001 to 2013. *J. Neurooncol.* 135, 433–441. doi:10.1007/s11060-017-2594-6

Ma, Y., Mou, Q., Yan, D., and Zhu, X. (2020). Engineering Small Molecule Nanodrugs to Overcome Barriers for Cancer Therapy. *View* 1, 2020062. doi:10.1002/viw.20200062

Northcott, P. A., Robinson, G. W., Kratz, C. P., Mabbott, D. J., Pomeroy, S. L., Clifford, S. C., et al. (2019). Medulloblastoma. *Nat. Rev. Dis. Primers* 5, 11. doi:10.1038/s41572-019-0063-6

Orr, B. A. (2020). Pathology, Diagnostics, and Classification of Medulloblastoma. *Brain Pathol.* 30, 664–678. doi:10.1111/bpa.12837

Oyharcabal-Bourden, V., Kalifa, C., Gentet, J. C., Frappaz, D., Edan, C., Chastagner, P., et al. (2005). Standard-risk Medulloblastoma Treated by Adjuvant Chemotherapy Followed by Reduced-Dose Craniospinal Radiation Therapy: a French Society of Pediatric Oncology Study. *Jco* 23, 4726–4734. doi:10.1200/jco.2005.00.760

Packer, R. J., Gajjar, A., Vezina, G., Rorke-Adams, L., Burger, P. C., Robertson, P. L., et al. (2006). Phase III Study of Craniospinal Radiation Therapy Followed by Adjuvant Chemotherapy for Newly Diagnosed Average-Risk Medulloblastoma. *Jco* 24, 4202–4208. doi:10.1200/jco.2006.06.4980

Pavlova, N. N., and Thompson, C. B. (2016). The Emerging Hallmarks of Cancer Metabolism. *Cel. Metab.* 23, 27–47. doi:10.1016/j.cmet.2015.12.006

Pei, C., Liu, C., Wang, Y., Cheng, D., Li, R., Shu, W., et al. (2020). FeOOH@Metal-Organic Framework Core-Satellite Nanocomposites for the Serum Metabolic Fingerprinting of Gynecological Cancers. *Angew. Chem. Int. Ed.* 59, 10831–10835. doi:10.1002/anie.202001135

Pruss, M., Dwucet, A., Tanriover, M., Hlavac, M., Kast, R. E., Debatin, K.-M., et al. (2020). Dual Metabolic Reprogramming by ONC201/TIC10 and 2-Deoxyglucose Induces Energy Depletion and Synergistic Anti-cancer Activity in Glioblastoma. *Br. J. Cancer* 122, 1146–1157. doi:10.1038/s41416-020-0759-0

Raez, L. E., Papadopoulos, K., Ricart, A. D., Chiorean, E. G., DiPaola, R. S., Stein, M. N., et al. (2013). A Phase I Dose-Escalation Trial of 2-Deoxy-D-Glucose Alone or Combined with Docetaxel in Patients with Advanced Solid Tumors. *Cancer Chemother. Pharmacol.* 71, 523–530. doi:10.1007/s00280-012-2045-1

Roberts, R. O., Lynch, C. F., Jones, M. P., and Hart, M. N. (1991). Medulloblastoma: a Population-Based Study of 532 Cases. *J. Neuropathol. Exp. Neurol.* 50, 134–144. doi:10.1097/00005072-199103000-00005

Singh, D., Banerji, A. K., Dwarakanath, B. S., Tripathi, R. P., Gupta, J. P., Mathew, T. L., et al. (2005). Optimizing Cancer Radiotherapy with 2-Deoxy-D-Glucose. *Strahlenther. Onkol.* 181, 507–514. doi:10.1007/s00066-005-1320-z

Stein, M. N., Bertino, J. R., Kaufman, H. L., Mayer, T., Moss, R., Silk, A., et al. (2017). First-in-human Clinical Trial of Oral ONC201 in Patients with Refractory Solid Tumors. *Clin. Cancer Res.* 23, 4163–4169. doi:10.1158/1078-0432.ccr-16-2658

Su, H., Hurd Price, C.-A., Jing, L., Tian, Q., Liu, J., and Qian, K. (2019). Janus Particles: Design, Preparation, and Biomedical Applications. *Mater. Today Bio.* 4, 100033. doi:10.1016/j.mtbio.2019.100033

Taylor, M. D., Northcott, P. A., Korshunov, A., Remke, M., Cho, Y.-J., Clifford, S. C., et al. (2011). Molecular Subgroups of Medulloblastoma: the Current Consensus. *Acta Neuropathol.* 123, 465–472. doi:10.1007/s00401-011-0922-z

Venneti, S., and Thompson, C. B. (2017). Metabolic Reprogramming in Brain Tumors. *Annu. Rev. Pathol. Mech. Dis.* 12, 515–545. doi:10.1146/annurev-pathol-012615-044329

Warburg, O., Wind, F., and Negelein, E. (1927). The Metabolism of Tumors in the Body. *J. Gen. Physiol.* 8, 519–530. doi:10.1085/jgp.8.6.519

Wu, J., Sha, J., Zhang, C., Liu, W., Zheng, X., and Wang, P. (2020). Recent Advances in Theranostic Agents Based on Natural Products for Photodynamic and Sonodynamic Therapy. *View* 1, 2020090. doi:10.1002/viw.20200090

Zhang, Y., Zhou, L., Safran, H., Borsuk, R., Lulla, R., Tapinos, N., et al. (2021). EZH2i EPZ-6438 and HDACi Vorinostat Synergize with ONC201/TIC10 to Activate Integrated Stress Response, DR5, Reduce H3K27 Methylation, ClpX and Promote Apoptosis of Multiple Tumor Types Including DIPG. *Neoplasia* 23, 792–810. doi:10.1016/j.neo.2021.06.007

Conflict of Interest: Authors JA and VP were employed and shareholders of Chimerix Inc./Oncoceutics Inc.

The remaining authors declare that the research was conducted in the absence of any commercial or financial relationships that could be construed as a potential conflict of interest.

The handling editor declared a shared affiliation with one of the authors GK-M at time of review.

Publisher's Note: All claims expressed in this article are solely those of the authors and do not necessarily represent those of their affiliated organizations, or those of the publisher, the editors and the reviewers. Any product that may be evaluated in this article, or claim that may be made by its manufacturer, is not guaranteed or endorsed by the publisher.

frontiers in Cell and Developmental Biology

REVIEW
published: 29 November 2021
doi: 10.3389/fcell.2021.765859

Ferroptosis: The Silver Lining of Cancer Therapy

Zhengming Tang[1†], Zhijie Huang[1†], Yisheng Huang[1], Yuanxin Chen[1], Mingshu Huang[1], Hongyu Liu[1], Q. Adam Ye[2,3], Jianjiang Zhao[4]* and Bo Jia[1]**

[1]Department of Oral and Maxillofacial Surgery, Stomatological Hospital, Southern Medical University, Guangzhou, China, [2]School of Stomatology and Medicine, Foshan University, Foshan, China, [3]Center of Regenerative Medicine, Renmin Hospital of Wuhan University, Wuhan University, Wuhan, China, [4]Shenzhen Stomatological Hospital, Southern Medical University, Shenzhen, China

OPEN ACCESS

Edited by:
Tugba Bagci-Onder,
Koç University, Turkey

Reviewed by:
Ilknur Sur Erdem,
University of Oxford, United Kingdom
Yansheng Feng,
The University of Texas Health Science Center at San Antonio, United States

***Correspondence:**
Q. Adam Ye
qingsongye@hotmail.com
Jianjiang Zhao
zjj2521@sina.com
Bo Jia
dentist-jia@163.com

†These authors share first authorship

Specialty section:
This article was submitted to Gastrointestinal and Hepatic Pharmacology, a section of the journal Frontiers in Pharmacology

Specialty section:
This article was submitted to Cell Death and Survival, a section of the journal Frontiers in Cell and Developmental Biology

Received: 27 August 2021
Accepted: 25 October 2021
Published: 29 November 2021

Citation:
Tang Z, Huang Z, Huang Y, Chen Y, Huang M, Liu H, Ye QA, Zhao J and Jia B (2021) Ferroptosis: The Silver Lining of Cancer Therapy. Front. Cell Dev. Biol. 9:765859. doi: 10.3389/fcell.2021.765859

Regulatory cell death has been a major focus area of cancer therapy research to improve conventional clinical cancer treatment (e.g. chemotherapy and radiotherapy). Ferroptosis, a novel form of regulated cell death mediated by iron-dependent lipid peroxidation, has been receiving increasing attention since its discovery in 2012. Owing to the highly iron-dependent physiological properties of cancer cells, targeting ferroptosis is a promising approach in cancer therapy. In this review, we summarised the characteristics of ferroptotic cells, associated mechanisms of ferroptosis occurrence and regulation and application of the ferroptotic pathway in cancer therapy, including the use of ferroptosis in combination with other therapeutic modalities. In addition, we presented the challenges of using ferroptosis in cancer therapy and future perspectives that may provide a basis for further research.

Keywords: ferroptosis, cancer therapy, lipid peroxidation, regulatory cell death, reactive oxygen species

INTRODUCTION

Cancer is one of the biggest problems plaguing the human life and health. Despite the availability of diverse cancer treatment modalities and the development of modern medicine, cancer therapy faces challenges in selectively killing cancer cells and not damaging normal cells as much as possible to minimise the toxic side effects of treatment. Therefore, targeting regulated cell death (RCD) has become a major focus area of cancer treatment research. A conventional treatment modality was previously used to induce apoptosis in tumour cells using antitumour drugs; however, the therapeutic effect was often limited because tumour cells developed acquired resistance-induced apoptosis (Holohan et al., 2013). Ferroptosis has been increasingly investigated for cancer therapy owing to its specific regulatory mechanism on antitumour-related signalling pathways and its potential target drugs. Increasing studies have demonstrated the therapeutic effects of inducing ferroptosis in cancer cells. In addition to cancer treatment, the ferroptosis process is also associated with many other diseases including ischemia-reperfusion (I/R) injury diseases, neurodegenerative diseases, stroke, myocarditis (**Figure 1**).

Unlike necrosis and apoptosis, ferroptosis is a form of RCD characterised by iron ion accumulation and substantial lipid peroxidation-mediated membrane damage (Dixon et al., 2012; Stockwell et al., 2017). The concept of ferroptosis was initially proposed in 2012 by Dixon when he used erastin to kill RAS-mutant cancer cells in his study (Dixon et al., 2012). To the best of our knowledge, this is the first review to describe the characteristics of ferroptosis along with its regulatory mechanisms, potential applications in cancer therapy, future perspectives, and challenges.

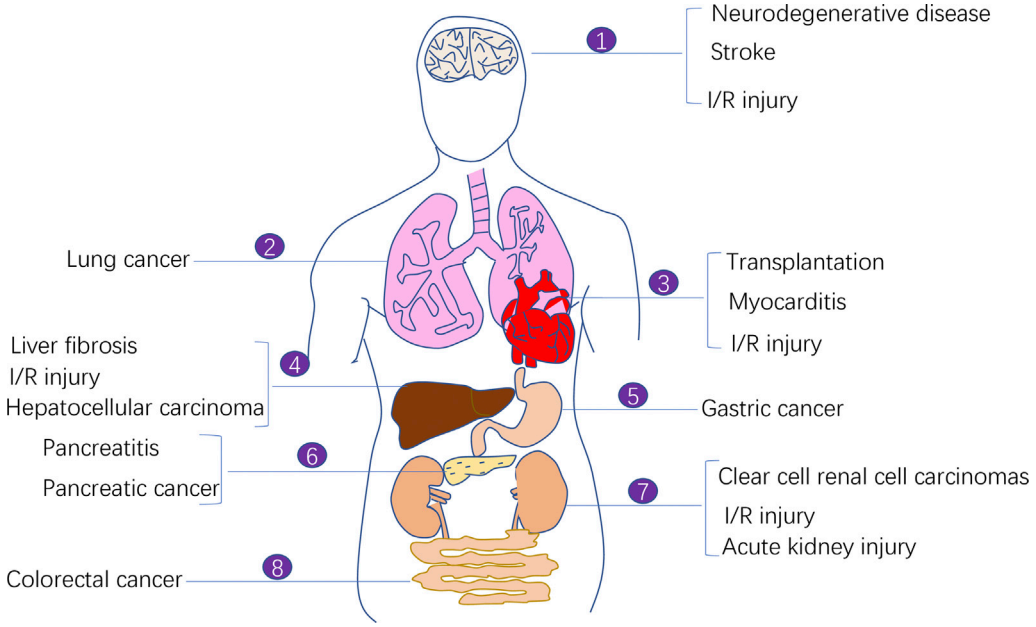

FIGURE 1 | The involvement of ferroptosis in various human diseases. Ferroptosis process is implicated in the pathogenesis of a variety of human diseases including ischemia-reperfusion (I/R) injury diseases, neurodegenerative diseases, stroke, myocarditis, and malignant diseases (e.g., lung cancer, pancreatic cancer, colorectal cancer, clear cell renal cell carcinoma, and gastric cancer).

TABLE 1 | Features of different regulated cell death.

RCD	Necroptosis	Apoptosis	Autophagy	Pyroptosis	Ferrroptosis
Morphological Features	Organelle swelling; moderate chromatin condensation	Plasma membrane blebbing; nucler fragmentation	Formation of double-membraned autolysosomes	Cell edema and membrane rupture	Small mitochondria with membrane densities
Biochemical Features	Drop in ATP level; Activation of RIP3	Activation of caspases oligonucleosomal DNA fragmentation	Increased lysosomal activity	Dependent on caspase-1 and proinflammatory cytokine releases	Inhibition of GPX4; Iron ac cumulation; lipid peroxidation
Immune Features	Pro-inflammatory	Anti-inflammatory	Anti-inflammatory	Pro-inflammatoy	Pro-inflammatory
DAMP	DNA and IL6	Ecto-CRT; HMGB1 and ATP	HMGB1	HMGB1 ATP, IL-1β	HMGB1
Regulatory gene	IEF1, RIP1, RIP3	Caspase; P53; Fas; Bcl-2; Bax	ATG5, ATG7, DRAM3, TFEB	IL-18, IL-1β, Caspase-1	GPX4, Nrf2, LSH, TFR1

CHARACTERISTICS OF FERROPTOSIS

Ferroptosis is characterised by intracellular iron ion accumulation and reactive oxygen species (ROS)-induced lipid peroxidation (Dixon et al., 2012). As a novel form of cell death, ferroptosis is significantly distinct from other types of cell death in morphology, biological function, genetic mechanism and immunological regulation (**Table 1**). Ferroptotic cells lead to various cellular morphological alterations, including the loss of cell membrane integrity, partial release of cell contents (e.g. damage-associated molecular patterns [DAMPs]) (Wen et al., 2019), marked reduction in mitochondrial volume, marked loss of mitochondrial cristae and chromatin condensation (Yagoda et al., 2007; Dixon et al., 2012; Friedmann Angeli et al., 2014). Iron chelators (desferrioxamine) have been reported to effectively prevent the occurrence of ferroptosis (Yagoda et al., 2007; Yang and Stockwell, 2008). Furthermore, dysregulation of various genes has been reported to be involved in the biological process of ferroptosis. Various studies have reported the abundant expression of ferroptosis-related genetic biomarkers, including genes related to iron metabolism (e.g. the transferrin receptor [TFR1] and iron-responsive element-binding protein [IREB2]) and lipid synthesis (such as acetyl coenzyme A [CoA] synthase long-chain family member 4 [ACLS4]) (Xie et al., 2016; Mou et al., 2019). In addition, ferroptosis has been found to regulate tumour immunity, and a typical example is HMGB1, a type of DAMP that is released by ferroptotic cells in an autophagy-dependent manner. The released HMGB1 can bind its receptors (e.g. toll-like receptor 4 [TLR4] and advanced glycosylation end-product-specific receptor

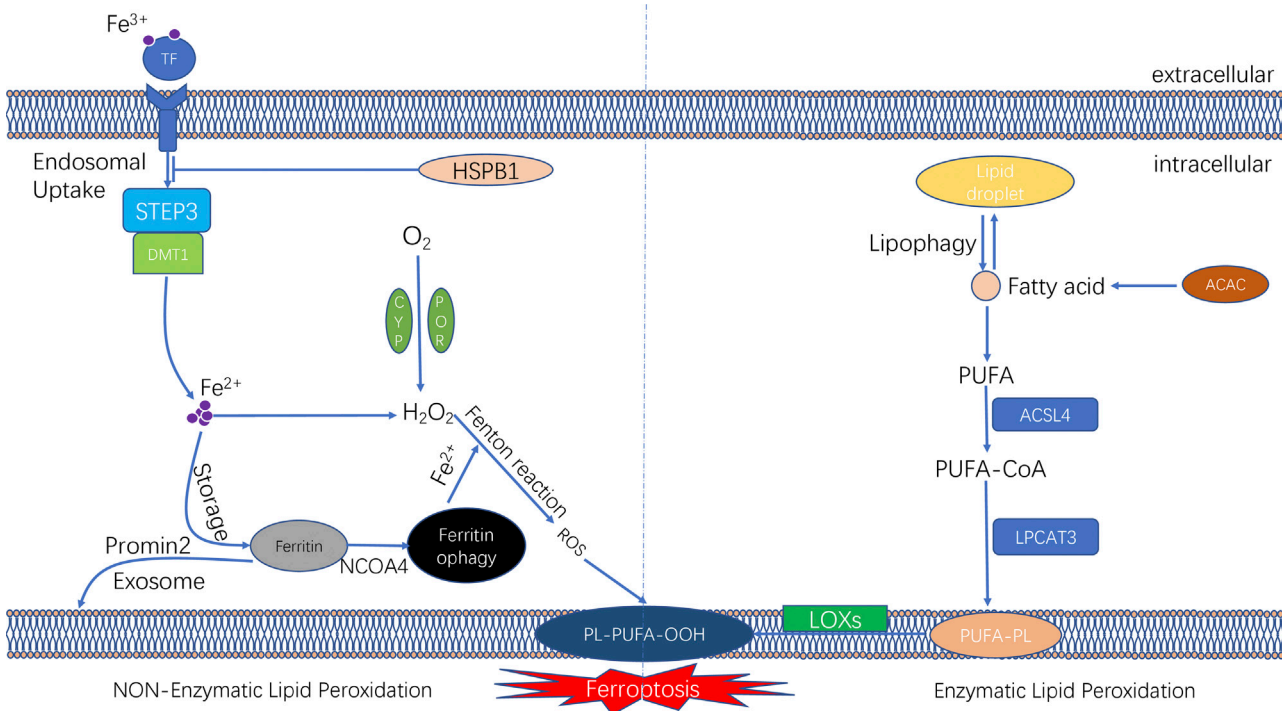

FIGURE 2 | The molecular mechanisms underlying the initiation of ferroptosis. The unique feature of ferroptosis is the iron-dependent lipid peroxide accumulation. The lipid peroxidation can be divided into non-enzymatic lipid peroxidation and enzymatic lipid peroxidation. During the process of non-enzymatic lipid peroxidation, iron ion was transported into cells by transferrinl; the fention reaction between iron ion and H_2O_2 lead to the production of lipid ROS. During the process of enzymatic lipid peroxidation, ACSL4 and LPCAT3 promote PUFAs to form PUFA-PLs; and PUFA-PLs undergo lipid peroxidation by lipoxygenases (ALOXs).

[AGER]) to mediate the antitumour immune response by stimulating T cells and activating antigen-presenting cells (Wen et al., 2019; Zheng and Conrad, 2020).

MOLECULAR MECHANISMS ASSOCIATED WITH FERROPTOSIS

The core molecular mechanism of ferroptosis involves the imbalance between oxidative damage generated by intracellular free radicals and the intracellular antioxidant system (Kuang et al., 2020). Ferroptosis involves oxidative damage to the cell membrane, leading to cell death, and iron ion accumulation and lipid peroxidation are the important markers of oxidative damage.

Role of Iron in Ferroptosis

Iron is an essential redox-active metal in the cell that is involved in various necessary biological activities. The process of iron ion metabolism in an organism and its role in ferroptosis will be summarised in this section. The trivalent iron ions ($Fe3^+$) in the peripheral circulation bind to transferrin (TF) to form a complex and then enter the cellular endosome by binding to the TF receptor (TFR1) on the cell membrane. Simultaneously, $Fe3^+$ is reduced to $Fe2^+$ (divalent iron ions) by the iron oxygen reductase six-transmembrane epithelial antigen of the prostate (STEAP3). Subsequently, $Fe2^+$ is released from the endosome into the cytoplasm, mediated by divalent metal ion transporter protein 1 (DMT1). Some $Fe2^+$ released into the cytoplasm is stored in the unstable iron pool (labile iron pool [LIP]). Excess iron is stored as ferritin, and the remaining $Fe2^+$ is oxidised to $Fe3^+$, which is transported outside the cell by ferroportin (FPN) and participates in iron recirculation *in vivo*. LIP and $Fe2^+$ formed by the degradation of ferritin can participate in the intracellular Fenton reaction, which is involved in oxidative stress (Li et al., 2020) (**Figure 2**).

Iron ions in the intracellular LIP can react with hydrogen peroxide in a Fenton reaction, which lead to the overproduction of reactive oxygen radicals, such as hydroxyl radicals.

The peroxide reaction between hydroxyl radicals and phospholipids containing polyunsaturated fatty acids (PUFAs) occured on the cell membrane can lead to the a series of changes of cell membrane, such as the thinning of cell membrane and formation of protein pores. Such changes of cell membrane affects the balance of the intracellular environment and further causes cell damage (Magtanong et al., 2016). Therefore, changes in the intracellular iron levels through various pathways can impact ferroptosis. Ferritin, another intracellular iron storage, also plays a vital role in the onset of ferroptosis. Nuclear receptor coactivator-4 (NCOA4) mediates the phagocytic degradation of ferritin. NCOA4 overexpression enhances ferritin degradation by binding to ferritin and transporting it from the cytosol to lysosome, leading to increased release of free $Fe2^+$ and eventually increased lysosomal ROS production (Torii et al.,

2016; Santana-Codina and Mancias, 2018; Battaglia et al., 2020). In addition, indirectly enhancing intracellular ferric ion concentration by increasing the expression of TF and TFR1 can also promote the occurrence of ferroptosis in cells (Shen Y. et al., 2018). However, various interventions that lead to intracellular iron ion depletion can inhibit the occurrence of ferroptosis. Heat shock protein beta-1 (HSPB1) was recently found to inhibit ferroptosis by suppressing the expression of TRF1 to reduce intracellular iron ion concentration (Sun et al., 2015) (**Figure 2**). A study reported that in iron ion regulation of ferroptosis, intracellular protrusion protein 2 inhibited ferroptosis by promoting iron-containing multivesicular bodies (MVBs) and exosomes to transport iron ions outside the cell, thereby reducing the intracellular iron ion concentration (Brown et al., 2019).

Lipid Peroxidation and the Antioxidant System

Lipid peroxidation is an essential mechanism of ferroptosis and can be classified as enzymatic and non-enzymatic. The intracellular antioxidant system also plays an essential regulatory role in ferroptosis. In the following sections, we have systematically summarised the involvement of lipid peroxidation and the antioxidant system in the mechanism of ferroptosis (**Figure 2**).

Non-Enzymatic Lipid Peroxidation

Non-Enzymatic lipid peroxidation is a chain reaction driven by free radicals. It is essentially the ROS-induced lipid peroxidation of PUFAs on cell membranes (Hassannia et al., 2019). Intracellular ROS are formed mainly through three modalities: intracellular mitochondrial oxidative phosphorylation; the transmembrane transfer of electrons by nicotinamide adenine dinucleotide phosphate oxidase (NOX); and the Fenton reaction (Kuang et al., 2020). Hydroxyl radicals are one of the most dominant ROS and are mainly derived from the Fenton reaction between iron and hydrogen peroxide.

Recent studies have found that hydrogen peroxide, which undergoes the Fenton reaction, may be associated with intracellular enzymes. Nicotinamide adenine dinucleotide phosphate (NADPH)–cytochrome P450 oxidoreductase (POR) is an oxidoreductase located on the endoplasmic reticulum that transfers electrons from NADPH to microsomal cytochrome P450, cytochrome b5 and haeme oxygenase (HO), thus maintaining the intracellular redox homeostasis (Riddick et al., 2013). NADH–cytochrome b5 reductase 1 (CYB5R1) is another oxidoreductase whose deletion inhibits lipid peroxidation and ferroptosis. It was found that POR bound to CYB5R1 can induce lipid peroxidation in cells. The specific mechanism involves the binding of POR to CYB5R1 to form hydrogen peroxide, followed by the Fenton reaction of hydrogen peroxide with $Fe2^{+}$ to generate hydroxyl radicals (Koppula et al., 2021; Yan et al., 2021).

The first step in non-enzymatic lipid peroxidation is the extraction of hydrogen by hydroxyl radicals from PUFAs in the cell membrane, thereby generating carb-centric lipid radicals (L•). Subsequently, oxygen molecules (O_2) react with carbon-centred lipid radicals to form lipid peroxide radicals (LOO), which can take up hydrogen from adjacent PUFAs to form lipid hydroperoxide (LOOH) and new lipid radicals to complete the lipid radical chain reaction. In addition, lipid hydroperoxides (LOOH) are converted to alkoxides (LO•) via Fe^{2+}, which then react with adjacent PUFAs to induce another lipid radical chain reaction. These processes occur when there is an imbalance between lipid oxidation and the antioxidant system, leading to cell rupture and death and eventually ferroptosis (Hassannia et al., 2019).

Enzymatic Lipid Peroxidation

Enzymatic lipid peroxidation is mainly mediated by the lipoxygenase (LOX) family, which is a group of haeme-type iron-containing enzymes that catalyse PUFAs, primarily adrenergic acid (Ada) and arachidonic acid (AA). The first step in enzymatic lipid peroxidation involves that Acetyl-CoA carboxylase (ACAC)-mediated fatty acid synthesis or lipophagy-mediated fatty acid release induces the accumulation of intracellular free fatty acids. The next step in enzymatic lipid peroxidation involves the formation of the corresponding derivatives AA-CoA and Ada-CoA catalysed by ACSL4 (Hassannia et al., 2019). Subsequently, lysophosphatidylcholine group transferase 3 (LPCAT3) catalyses the reaction of AA-CoA and Ada-CoA with phosphatidylethanolamine (PE) to form AA/PE and Ada/PE, respectively (Dixon et al., 2015; Doll et al., 2017). Finally, LOX promotes the peroxidation of AA/PE and Ada/PE to form AA/Ada-PE-OOH, leading to oxidative damage to the cell membrane. Therefore, the ACSL4–LPCAT3–LOX signalling axis is an intracellular pathway that promotes lipid peroxidation in ferroptosis, and inhibition of this pathway may inhibit ferroptosis.

Antioxidant System

It is now known that ferroptosis can be regulated by multiple parallel antioxidant pathways, for example, Cysteine/GSH/GPX4 axis, FSP1/DHODH/CoQ10 axis, and GCH1/BH4/DHFR axis. The implication of these three signaling axes in ferroptosis will be summarized in this section (**Figure 3**).

Cysteine/GSH/GPX4 Axis

The glutathione (GSH) peroxidase (GPX) family is a group of essential enzymes that intracellularly inhibit antioxidants. GPX4 is considered the most important antioxidant enzyme. It uses GSH as a substrate to reduce intracellular peroxides to non-toxic lipid alcohols. Therefore, once GPX activity is inhibited by inhibiting GSH synthesis or by directly inhibiting GPX, inhibition of peroxides can be directly reduced, thus achieving increased intracellular lipid peroxide accumulation and cellular ferroptosis.

GSH is synthesised by cysteine in the presence of r-glutamylcysteine synthetase, and GSH synthetase (GSS). Cysteine synthesis depends on the cystine/glutamate reverse transporter (system XC^{-}), which is a membrane Na^{+}-dependent amino acid reverse transporter widely distributed in the phospholipid bilayer of biological cells. The transporter system XC^{-} is also a heterodimer composed of a light chain

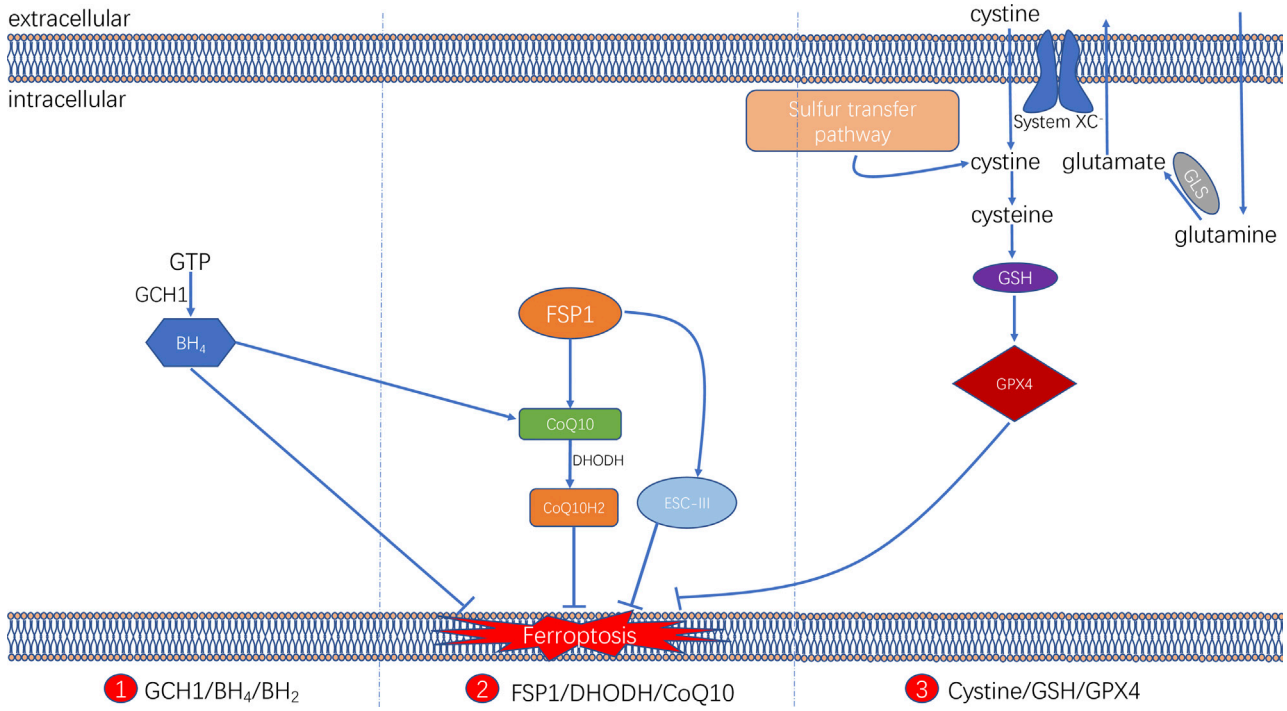

FIGURE 3 | Three signaling axes in the ferroptosis-regulating antioxidant systems, including GTP/GCH1/BH4 axis, FSP1/DHODH/CoQ10 axis, and Cysteine/GSH/GPX4 axis.

solute carrier family 7 member 11 (SLC7A11) and a heavy solute carrier family three members 2 (SLC3A2). This transporter system excretes a molecule of cystine whenever a molecule of cystine is taken up into the cell (Pitman et al., 2019). Intracellular cystine is reduced to cysteine mediated by thioredoxin reductase 1 (TXNRD1) (Mandal et al., 2010). Followed by this, glutathione (GSH) was synthesized by using cysteine as the substrate. Cysteine–GSH–GPX4 signalling axis is considered the most classical pathway in the regulation of ferroptosis. Inhibiting the system XC^- transporter reduces intracellular GSH synthesis and further inhibit GPX4 activity directly, which affects the capacity of the intracellular antioxidant system and thereby leading to the development of ferroptosis. Extracellular glutamate and glutamine levels can affect the occurrence of ferroptosis by affecting system XC^-. When extracellular glutamate levels are elevated, system XC^- can be prevented from performing glutamate/cystine exchange, thereby reducing GSH synthesis and subsequently triggering ferroptosis (Hirschhorn and Stockwell, 2019; Battaglia et al., 2020).

FSP1/DHODH/CoQ10 Axis

Two recent studies have identified a regulatory protein similar to GPX4 that is involved in the onset of cellular ferroptosis, namely ferroptosis suppressor protein 1 (FSP1) (Bersuker et al., 2019; Doll et al., 2019). FSP1 was previously known as apoptosis-inducing factor mitochondrial 2 (AIFM2) and has significant homology to apoptosis-inducing factor (AIF) (Wu et al., 2002), a flavoprotein described initially as a P53-responsive gene (Horikoshi et al., 1999) that induces apoptosis.

FSP1 is recruited to the cell membrane via myristoylation and can subsequently reduce ubiquinone (i.e. coenzyme Q [CoQ10]) to ubiquinol in the form of an oxidoreductase. By such reaction, FSP1, acts as a lipophilic radical trap and inhibits cell membrane lipid peroxidation (Bersuker et al., 2019; Doll et al., 2019). In addition, FSP1, as an AIF family protein, can catalyse the regeneration of CoQ10 in reaction with NAD(P)H [31]. In some cases, FSP1 can also inhibit ferroptosis in a pathway parallel to that of CoQ10, such as through the membrane repair mechanism of ESCRT-III (a protein complex). However, the exact mechanism remains unknown (Dai et al., 2020). The FSP1 inhibitor iFSP1, which induced ferroptosis in GPX4-knockdown cells and FSP1-overexpressing cells, was found to exert the intracellular antioxidant effect of FSP1 (Doll et al., 2019).

In addition, a recent study revealed that an antioxidant system might exist in cellular mitochondria (Mao et al., 2021). Dihydroorotate dehydrogenase (DHODH) is located in the inner mitochondrial membrane and is responsible for catalysing the fourth step of pyrimidine nucleotide synthesis, that is, the oxidation of dihydroorotate (DHO) to orotate (OA) and the reduction of CoQ in the inner membrane to ubiquinol (CoH_2) by receiving electrons. CoH_2 can act as a trapping antioxidant to prevent intracellular lipid peroxidation (Vasan et al., 2020).

The DHODH inhibitor brequinar was found to induce ferroptosis in GPX4-low cells and enhance the susceptibility of GPX4-high cells to ferroptosis. The results were further validated in an *in vivo* assay via tumour formation in a nude mouse. The assay identified an alternative oxidative pathway to GPX4 in the cytosol and mitochondria and FSP1 in the cell membrane. DHODH in the inner mitochondrial membrane inhibits lipid peroxidation in the mitochondria by reducing CoQ_{10} to $CoQ_{10}H_2$, indicating that DHODH can be a novel therapeutic target in cancer therapy by inducing ferroptosis.

GCH1/BH4/DHFR Axis

In addition, a study demonstrated that a CRISPR/dCas9 overexpression screening using a genome-wide activation library identified the genes signature that inhibit ferroptosis, among which GTP cyclic hydrolase 1 (GCH1) and its metabolic derivative tetrahydrobiopterin/dihydrobiopterin (BH_4/BH_2) are shown to be the most prominent (Kraft et al., 2020). In cells, GTP can be hydrolysed by GCH1 to generate BH_4 and mediates its role in cellular lipid remodelling, thus acting as an antioxidant. It was further found that, unlike the antioxidant mechanism of GPX4, the antioxidant effect of GCH1–BH_4/BH2 did not protect all PUFA-containing phosphates (PUFA-PLs) from oxidation; instead, it can selectively protect specific phosphates containing two PUFA acyl chains from oxidative degradation, thereby inhibiting ferroptosis. In addition, under oxidative stress following ferroptosis induction, BH_4 inhibited ferroptosis by increasing CoQ10 levels. Therefore, the implication of GCH1–BH_4/BH_2 axis in inhibiting ferroptosis can be either by directly playing the intracellular antioxidant role in protecting cell membrane phospholipids, or by promoting CoQ10 synthesis and further regulating oxidative stress levels. The combination of these two regulating approaches can together form an antioxidant system independent of Cysteine/GSH/GPX4 axis (Kraft et al., 2020).

Role of Tumour Suppressor Genes in Ferroptosis

Previous investigation have reported that two tumour suppressor genes [p53 and BRCA1-associated protein 1 (BAP1)] played significant roles in regulating tumour by targeting ferroptosis. For example, p53 is an important tumour suppressor gene that regulates cellular responses such as transient cell cycle arrest and apoptosis (Bieging et al., 2014). P53 inactivation plays a crucial role in the initiation and progression of several tumours (Berkers et al., 2013). It has been found that p53 sensitises cells to ferroptosis by inhibiting the expression of SLC7A11, a vital component of system XC^-, which in turn inhibits cellular uptake of cystine and reduces intracellular GSH synthesis (Jiang et al., 2015). In addition, p53 can reduce GSH depletion and lipid ROS aggregation through the P53–P21 axis, thus inhibiting lipid peroxidation and delaying the onset of ferroptosis caused by cystine deficiency (Tarangelo et al., 2018). Therefore, p53 gene seems to play dual regulating role in ferroptosis, depending on different circumstances. Another tumour suppressor gene-BAP1 can reduce GSH synthesis and induce ferroptosis by suppressing the level of H2A-K119ub on the SLC7A11 gene and the transcription of its mRNA, thereby inhibiting the ability of SLC7A11 to transport cysteine into the cell (Zhang et al., 2018).

Role of Ferroptosis in Cancer Therapy

Owing to the rapid growth and proliferation of cancer cells, they are more iron-dependent as compared with normal cells. TFR1 upregulation and FPN downregulation have been reported in various cancer cell lines (Gao et al., 2015; Torti and Torti, 2019); therefore, ferroptosis-related genetic biomarkers may be considered potential therapeutic biomarkers for cancer treatment. Ferroptosis-related anticancer drugs and ferroptosis inhibitors are also widely studied in the field of cancer treatment (**Table 2**).

Anti-Tumour Drugs Associated With Ferroptosis

Various mechanisms can induce cellular ferroptosis, for instance, inhibition of system XC^- transport and GPX4 activity or GPX4 degradation. Different antitumour drugs associated with ferroptosis have been developed, including iron activators, NRF2 inhibitors and GSH inhibitors (Su et al., 2020). These drugs have been demonstrated to inhibit tumour growth and exert antitumour effects by inducing ferroptosis. The currently developed ferroptosis-related drug agents are summarised in this section (**Figure 4**) (**Table 3**).

Iron Activators

Artesunate, a semisynthetic derivative of the artemisinin group of drugs, has been commonly used as a frontline drug for treating malaria. In addition, it was also reported to exhibit great potential for cancer treatment. Previous studies have found that artemisinin and its derivatives can exert antitumour effects by inducing cell cycle arrest (Willoughby et al., 2009; Chen et al., 2010), promoting cell invasion and facilitating tumour angiogenesis and metastasis (Zhang et al., 2017). The signalling pathways that mediate the antitumour effects of artemisinin were identified to be the mitochondrial and classic MAPK pathways. A recent study demonstrated that in addition to the conventional mechanism of inducing antitumour effects, artesunate influenced the phenotype of mutationally active KRAS pancreatic ductal adenocarcinoma (PDAC) cells by inducing ferroptosis (Eling et al., 2015). Artesunate induces ferroptosis in tumour cells by enhancing lysosomal activity and increasing lysosomal iron concentration (Yang et al., 2014). A previous study investigated the antitumour role of artesunate by inducing ferroptosis and found that artesunate can alter the mRNA expression level of iron-related genes in tumour cells and further induce cell death in an iron-dependent manner (Ooko et al., 2015). Artesunate regulates ferroptosis by promoting ferritinophagy by regulating the gene expression of NCOA4, which leads to an increase in the iron levels (Kong et al., 2019). The overproduction of ROS triggered by the Fenton reaction between iron ion and hydrogen peroxide is a crucial factor for inducing ferroptosis. Several clinical trials have shown

TABLE 2 | Ferroptosis inhibitors and mode of action.

Ferroptosis inhibitors	Mechanism
Alpha-tocopherol, Vitamin E, trolox	Block LOX PUFA oxygenation
CoQ10, idenbenone	Target lipid peroxyl radicals
Deferoxamine, deferiprone, ciclopirox	Deplete intracellular iron
Cycloheximide	Block system XC^- protein synthesis
Ferrotatins, liproxstatins	Inhibit lipid peroxidation
Butylated hydroxytolune butylated hydroxyanisole	Inhibit lipid peroxidation
Dihydrobiopterin (BH2)	Antioxiant effect
Tetrahydrobiopterin (BH4)	—
Glutaminolysis inhibitor	Hinder mitochondrial TCA cycle
Deuterated PUFAs, MUFAs	Inhibit lipid peroxidation

the therapeutic efficacy of targeting ferroptosis in cancer therapy. In a clinical trial regarding metastatic uveal melanoma, patients treated with artesunate had higher survival rates than those of patients in the control group, suggesting that using artesunate to target ferroptosis was beneficial for the prognosis of patients with cancer (Berger et al., 2005). Although several studies have demonstrated the anti-tumour effects of artesunate in cancer treatment, its underlying genetic mechanisms warrant investigation using advanced gene sequencing technology.

Furthermore, two other iron activators are siramesine, which has been commonly used for treating depression, and lapatinib, which is a tyrosine kinase inhibitor. Recent studies have found that siramesine can cause cell death by rupturing cellular lysosomal membranes and can subsequently increase intracellular ROS production. Lapatinib is a potent inhibitor of the epidermal growth factor receptor (EGFR, ErbB-1) and ErbB-2(Wood et al., 2004) The combination of siramesine and lapatinib exerts antitumour effects by inducing ferroptosis, which can be reversed via iron chelators (Ma et al., 2017). A study reported that the combination of siramesine and lapatinib induced intracellular ROS overproduction and ferroptosis by elevating the intracellular free iron levels in breast cancer cells (MDA-MB-231, MCF-7, ZR-75 and SKBr3). In addition, these drugs induced aberrant expression of ferroptosis-related genes, for instance, FPN downregulation and TF upregulation (Ma et al., 2016). Therefore, the study provided a new idea for treating breast cancer through ferroptosis, providing a basis for subsequent clinical cancer treatment. Although these studies have demonstrated evident antitumour effects of using siramesine and lapatinib in treating cancer cells *in vitro*, the *in vivo* application of these drugs requires further research.

NRF2 Inhibitors

Sorafenib, as a multi-kinase inhibitor, has been acknowledged as a standard therapeutic drug for treating advanced hepatocellular carcinoma (Wilhelm et al., 2006). The underlying mechanism of the antitumour action of sorafenib involves inhibition of tumour angiogenesis and downregulation of the RAF/MEK/ERK pathway (Su et al., 2020). In addition, sorafenib was also reported to exert antitumour effects in various types of tumour cells by triggering ferroptosis (Wang and Lippard, 2005). Sorafenib was reported to induce ferroptosis by activating two signalling pathways

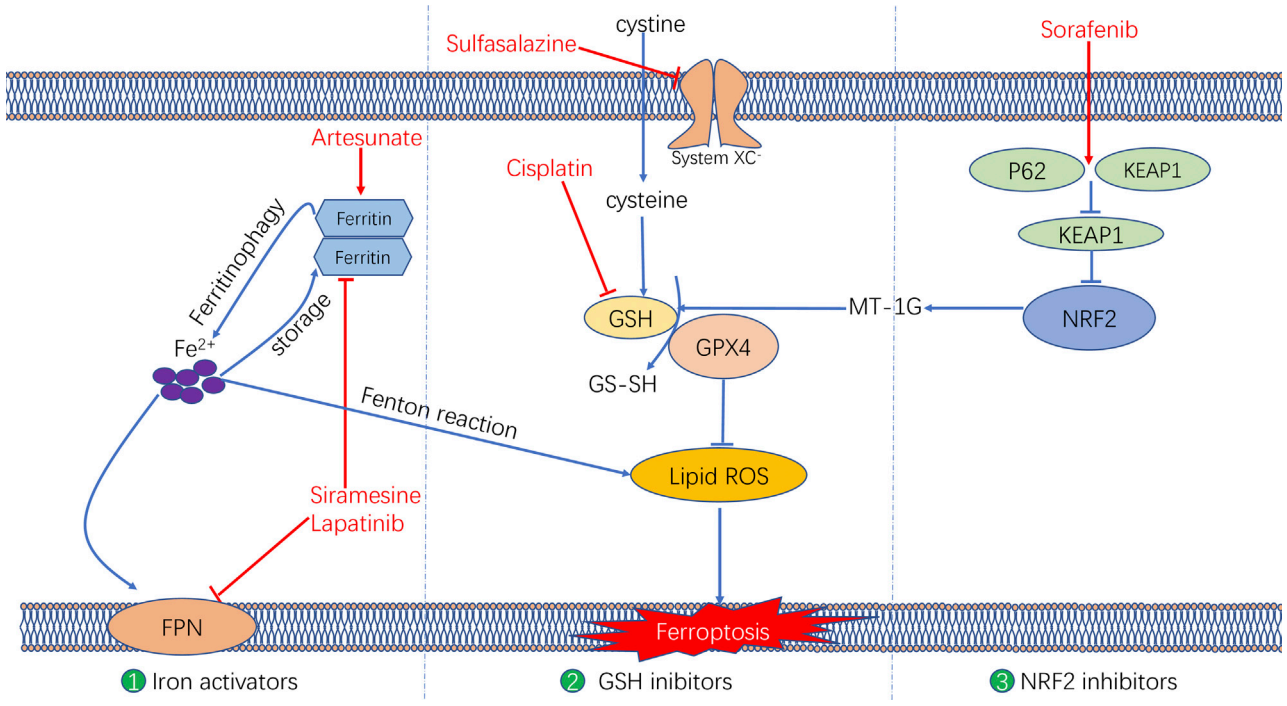

FIGURE 4 | The molecular mechanisms underlying the ferroptosis targeting role of three types of anti-tumor drugs (i.e., Iron activators, NRF2 inhibitors, as well as System XC^- and GSH inhibitors).

TABLE 3 | Anti-tumor drugs associated with ferroptosis.

Agent	Targets	Possible mechanisms of ferroptosis	Cancer type
Iron activators			
Artesunate	Iron	Promotes ferritin degradation	pancreatic ductal adenocarcinoma
Ferumoxytol	Iron	Iron overproduction	Leukemia
Siramesine	Iron	Inhibit ferroportin and ferritin	Breast cancer
Lapatinib	Iron	Promote the expression of transferrin	Breast cancer
Salinomycin	Iron	Promote the expression of IREB2 and TFRC	Tumour stem cell
Neratinib	Iron	increase the level of iron	Breast cancer, CRC
NRF2 inhibitors			
Sorafenib	SlC7A11, NRF2	activates NRF2 and inhibit system XC^-	Hepatocellular Carcinoma
Fenugreek	NRF2	inhibit NRF2	head and neck cancer
System $XC^-$and GSH inhibitors			
Sulfasalazine	System XC^-	inhibit the production of GSH	small-cell lung cancer; Prostate Cancer
Cisplatin	GSH	Decrese the level of GSH	Ovarian cancer; pancreatic cancer
Lanperisome	System XC^-	Inhibit the absorption of cystine	Kras-mutant tumor

including the GSH and p62–Kelch-like ECH-associated protein 1 (Keap1)–NRF2 pathways. Regarding the GSH signalling pathway, sorafenib was found to inhibit the transport function of system XC^-, which leads to GSH depletion and decrease in the antioxidant capacity (Dixon et al., 2014). With regard to the p62–Keap1–NRF2 pathway, sorafenib was shown to activate the gene function of NRF2 by inhibiting the degradation of Keap1, which is an important component of the p62–Keap1–NRF2 signalling axis. Activated NRF2 regulates ferroptosis by dysregulating the expression of quinone oxidoreductase 1 (NQO1), HO1 and ferritin heavy chain 1 (FTH1). As the first approved antitumour drug targeting ferroptosis, sorafenib faces major challenges regarding drug resistance that should be overcome before its safe application in clinical treatment. An important target causing sorafenib resistance is metallothionein (MT), which is a class of high-level small-molecule reactive proteins that can effectively scavenge ROS (Datta et al., 2007). After being treated by sorafenib, MT1G expression was reported to be upregulated, which inhibited ferroptosis and led to drug resistance by inhibiting the GPX4 gene expression. Therefore, MT1G knockdown via RNA interference technology may be a potential strategy to avoid drug resistance caused by sorafenib in cancer treatment (Sun et al., 2016). In addition, studies have also reported that sorafenib can work synergistically with the ferroptosis inducer erastin in drug-resistant tumour cells, suggesting that the combined use of sorafenib and erastin provides a novel therapeutic strategy for cancer treatment (Lu et al., 2017).

GSH Inhibitors

The anti-tumour effects of two GSH inhibitors (sulfasalazine and cisplatin) that target ferroptosis will be described in this section. Sulfasalazine is an oral anti-inflammatory drug widely used in clinical practice for treating rheumatoid arthritis or ulcerative colitis (Fleig et al., 1988; Combe et al., 2009). As an inhibitor of the antiporter system XC^-, sulfasalazine induces ferroptosis in tumour cells (e.g. lymphoma) by suppressing the intracellular antioxidant capacity (Gout et al., 2001). The application of sulfasalazine drug was shown to enhance the treatment efficacy of gamma radiation therapy in glioma treatment, indicating its role in promoting the treatment sensitivity of tumour cells (Sleire et al., 2015). In studies regarding breast and lung cancers, sulfasalazine was found to inhibit drug resistance and reduce side effects of chemotherapy when used in combination with conventional chemotherapeutic drugs (Lay et al., 2007; Narang et al., 2007; Guan et al., 2009). Although various studies have reported the beneficial treatment effects of sulfasalazine in many cancers, whether its anticancer effects are mediated by targeting ferroptosis remains unclear.

Another GSH inhibitor—cisplatin—is a key chemotherapeutic drug agent that has been widely used in the clinical treatment of various solid tumours. It exerts its anti-tumour effects mainly through DNA damage in the cell nucleus, followed by apoptosis (Wang and Lippard, 2005). However, recent studies have reported a novel regulatory mechanism of cisplatin in cancer treatment by demonstrating its ferroptosis-inducing role via GSH depletion and its promoting role in ferritin autophagy (Guo et al., 2018; Zhang et al., 2020). Owing to DNA damage and apoptosis, the anticancer effect of cisplatin often results in drug resistance. Compared with apoptosis, ferroptosis-mediated cell death may not easily lead to drug resistance because ferroptosis as a form of RCD is independent of apoptosis. Therefore, ferroptosis may be a promising pathway to overcome cisplatin resistance. In addition, a recent study demonstrated that cisplatin can synergistically act with the ferroptosis inducer erastin, and the combined use of both drugs was found to enhance antitumour effects when compared with the use of either drug alone (Guo et al., 2018).

Gene Technology-Induced Ferroptosis

Genes are essential in life processes and can encode proteins involved in various cellular activities. Some genes have recently been found to play a crucial role in the occurrence of ferroptosis. Therefore, gene technology targeting ferroptosis can be used to treat cancer. The primary gene technologies include gene transfection and gene knockout.The P53 pathway, a classical tumour suppression pathway, has recently been found to sensitise cells to ferroptosis by inhibiting SLC7A11 (Berkers et al., 2013), a positive regulatory gene of ferroptosis. However, ACSL4 is an essential pro-ferroptosis gene (Shen Z. et al., 2018), and ACSL4-mediated production of 5-

hydroxyeicosatetraenoic acid (5-HETE) contributes to ferroptosis and is significantly downregulated in ferroptosis-resistant cells, thus positively regulating ferroptosis (Shen Z. et al., 2018). Therefore, by transfecting target cells with ferroptosis-positive regulatory genes such as P53 and ACSL4, ferroptosis can be induced for cancer treatment (Shen Z. et al., 2018). HSPB1 is a negative regulator of ferroptosis. HSPB1 knockdown in cells enhances erastin-induced ferroptosis, whereas HSPB1 overexpression inhibits erastin-induced death (Sun et al., 2015). Ferroptosis-negative regulatory genes can be knocked down in tumour cells using RNA interference technology, which induces cellular ferroptosis and increases anticancer activity. Therefore, gene technology (e.g. gene transfection or gene knockout) can be used in cancer therapy to introduce a relevant regulatory gene into a cell or to silence a gene, thereby regulating cellular ferroptosis (Shen Z. et al., 2018).

Ferroptosis in Combination With Other Treatments

Despite the efficacy of several clinical modalities for cancer treatment, increasing studies have shown that a single tumour treatment modality is often limited by multiple factors in clinical practice, resulting in unsatisfactory treatment outcomes. However, a combination of various modalities may offer advantages (Lang et al., 2019). Studies have demonstrated that ferroptosis can be associated with multiple cancer treatment modalities, such as radiotherapy and immunotherapy, with promising results (Lang et al., 2019). Therefore, combining ferroptosis with other cancer treatment modalities is also a major focus area for cancer therapy research.

Ferroptosis in Combination With Immunotherapy

The traditional treatment modalities often fail to achieve good results in clinical practice owing to various drawbacks. Immunotherapy has gradually become an essential strategy for tumour treatment, in which immune-blocking agents exert their antitumour effects mainly by promoting the clearance function of cytotoxic T cells and preventing the escape of tumour cells (Khalil et al., 2016). Cancer immunotherapy is effective in treating some solid tumours including breast cancer, lung cancer, gastric carcinoma. However, compared with other conventional treatment modalities, immunotherapy is less effective in treating some tumours (Pham et al., 2018). Therefore, it is necessary to combine immunotherapy with other treatment modalities to improve its therapeutic effects (Adams et al., 2019). Recent studies have revealed a close relationship between activated $CD8^+$ T cells in tumour immunotherapy and ferroptosis. The underlying mechanism involves the downregulation of SLC3A2 and SLC7A11, the two subunits system XC^-, by interferon-gamma released from immunotherapy-activated $CD8^+$ T cells, thus reducing intracellular cysteine synthesis, decreasing antioxidant capacity and promoting lipid peroxidation and ferroptosis in tumour cells (Wang et al., 2019). In addition, it was found in an *in vivo* study in mice that when an immunosuppressant was combined with cysteine proteases (which degrade intracellular cysteine and cystine), they induced ferroptosis in tumour cells and simultaneously enhanced the efficacy of the immunosuppressant, achieving a synergistic effect (Wang et al., 2019) (**Figure 5**).

Ferroptosis interacts with the immune system through various mechanisms. In addition to the activation of $CD8^+$ T cells by immunotherapy to promote ferroptosis, it has been demonstrated that ferroptosis is a form of immunogenic cell death (ICD) (Efimova et al., 2020). Therefore, ferroptotic cells can release a range of DAMPS, including high-mobility group protein B1 (HMGB1) and calreticulin (CRT), which may interact with pattern recognition receptors (PRRs) and phagocytic receptors on immune cells to activate the immune response and adaptive immune system (Shi et al., 2021). Therefore, it is of great clinical significance to study the immunogenicity of ferroptotic cancer cells and investigate their therapeutic effects.

Furthermore, the excellent biological properties of nanomaterials can be used to improve therapeutic effects by combining ferroptosis with tumour immunotherapy. In a study, a bionic magnetic cyst was constructed, in which Fe_3O_4 magnetic nanoclusters (NCs) as the core and leukocyte membrane as the shell were combined with transforming growth factor-β inhibitor (Ti) and PD-1 antibody (Pa) to promote the synergistic effect of ferroptosis and immunomodulation. Under magnetic resonance imaging (MRI)-guided drug delivery, Pa and Ti in bionic magnetic vesicles created an immunogenic environment after entering the tumour interior, which increased the concentration of hydrogen peroxide in polarised M1 macrophages, promoting a Fenton reaction with iron ions released from NCs. Hydroxyl radicals generated from the Fenton reaction subsequently induced ferroptosis in tumour cells, and the tumour antigens released by the dead cells subsequently promoted ferroptosis. The tumour antigens released by the dead cells, in turn, enhanced the immunogenicity of the microenvironment. Therefore, immunotherapy and ferroptosis exert a powerful synergistic effect (Zhang et al., 2019).

Although the relationship between ferroptosis and immunotherapy is not well understood, preliminary studies have been conducted on immunotherapy and ferroptosis in animal models. A study developed an iron oxide-loaded nanovaccine (IONV) for combined ferroptosis–immunotherapy treatment (Ruiz-de-Angulo et al., 2020). The principle of this nanovaccine was based on chemically integrated iron catalysts and drug delivery systems by exploiting the properties of the tumour microenvironment. IONV activation in the tumour microenvironment increased oxidative stress in tumour cells, which in turn promoted ferritin deposition, activated M1 macrophages, improved tumour antigen cross-presentation and enhanced the immunotherapeutic efficacy. The findings from the above-mentioned studies suggest that the combination of ferroptosis and immunotherapy is a promising cancer treatment strategy, which requires in-depth research.

Combined Application of Ferroptosis and Chemotherapy

Chemotherapy is a common clinical approach to cancer treatment, and the commonly used chemical agents include

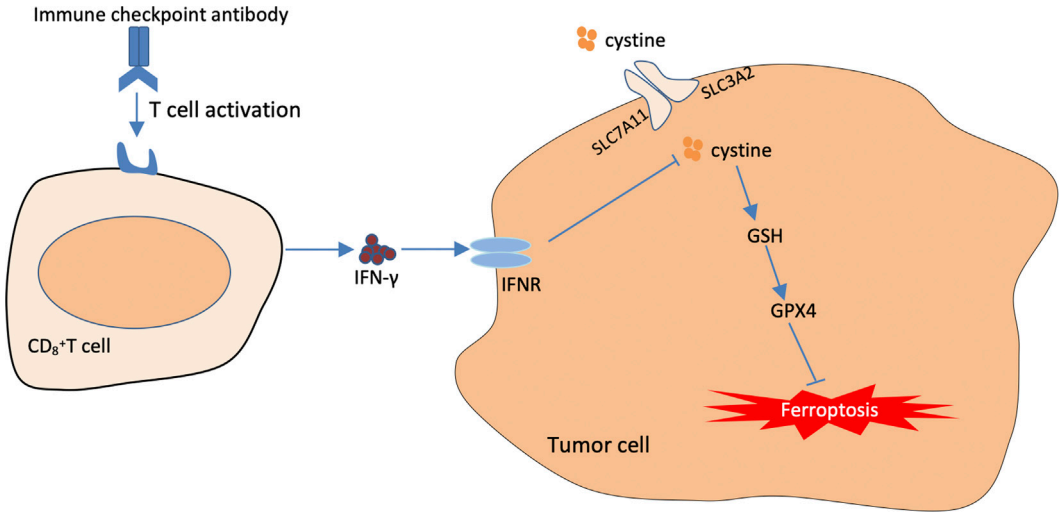

FIGURE 5 | The Mechanisms underlying the promoting role of immunotherapy in targeting cellular ferroptosis. T cells activated by immunotherapy treatment induce ferroptosis by secreting interferon-γ (IFN-γ). IFN-γ can further inhibit cystine uptake by tumor cells, thus further weakening the capacity of intracellular GPX4.

methotrexate, cyclophosphamide and vincristine. Although chemotherapy has made significant progress in clinical cancer treatment, the epithelial-to-mesenchymal transition, in which tumour cells can metastasise and become resistant to drugs, has limited the effectiveness of anticancer therapies (van Staalduinen et al., 2018; Yang et al., 2020). Epithelial-to-mesenchymal transition is a process wherein epithelial cells lose polarity and intercellular adhesion and gradually transform into invasive and metastatic mesenchymal cells (Yang et al., 2020). However, it has been found that mesenchymal cells formed after epithelial-to-mesenchymal transition have a higher susceptibility to ferroptosis (Hangauer et al., 2017; Viswanathan et al., 2017). Therefore, the use of ferroptosis appears to be one of the strategies to address tumour drug resistance and metastasis (Xu et al., 2021).

Inducing ferroptosis in drug-resistant tumour cells can overcome drug resistance, and varied underlying mechanisms have been proposed. Ferroptosis inducers can reverse tumour drug resistance by promoting intracellular ROS accumulation, thereby inducing ferroptosis in drug-resistant tumour cells (Friedmann Angeli et al., 2019). Furthermore, NRF2 can reduce intracellular ROS accumulation via the P62–Keap1–NRF2 pathway, which in turn is involved in the resistance of cancer cells to sorafenib; however, NRF2 inhibitors can reverse the resistance of cancer cells by increasing intracellular ROS accumulation (Roh et al., 2017).

Furthermore, ferroptosis inducers can induce ferroptosis in drug-resistant tumour cells by decreasing cellular TF levels and increasing intracellular iron transfer. For example, artesunate can induce ferroptosis in Adriamycin-resistant leukaemia cells by decreasing TF levels and promoting the therapeutic effect of Adriamycin on leukaemia (Wang et al., 2017; Park et al., 2018).

Ferroptosis agonists that act by inhibiting the system XC^- transport function can also lead to lipid peroxidation in resistant cells, thereby reversing drug resistance in tumour cells (Lim et al., 2005). For example, erastin can reverse cisplatin resistance in ovarian cancer cells by inhibiting the transport function of system XC^- (Sato et al., 2018).

In addition to reversing tumour cell resistance, the use of ferroptosis agonists in combination with chemotherapeutic agents for non-drug-resistant cancer cells can also achieve more desirable results. Ferroptosis can adopt the mechanism of action of traditional chemotherapeutic drugs, such as cisplatin, which function by reducing intracellular GSH by inhibiting GPX4 activity to induce cellular ferroptosis (Guo et al., 2018). Therefore, a combination of the chemotherapeutic drug cisplatin and ferroptosis inducers may enhance therapeutic efficacy. For example, erastin combined with cisplatin provides better results than when cisplatin is used alone (Guo et al., 2018). Another ferroptosis inducer, RSL3, exerts its induction effect by inhibiting GPX4 when combined with cisplatin, which enhances the therapeutic influence of cisplatin both *in vitro* and *in vivo* (Zhang et al., 2020). In addition to cisplatin, other classical chemotherapeutic agents can also exert better effects when used along with ferroptosis inducers. For example, the classical chemotherapeutic drug paclitaxel can further regulate glutamate catabolism (one of the pathways through which ferroptosis occurs) in colorectal cancer cells by reducing the expression of intracellular glutamate-catabolism-related genes such as SLC7A11 and SLC1A5 and inducing an increased expression of P53 and P21, which altogether inhibit tumour growth (Lv et al., 2017). In mutant-P53 pharyngeal squamous carcinoma, when low doses of paclitaxel were combined with the ferroptosis inducer RSL3, paclitaxel upregulated mutant P53 and promoted RLS3-induced ferroptosis, providing a synergistic therapeutic effect (Ye et al., 2019).

Therefore, the emergence of ferroptosis combined with chemotherapy as a new treatment modality offers a new strategy for tumour treatment.

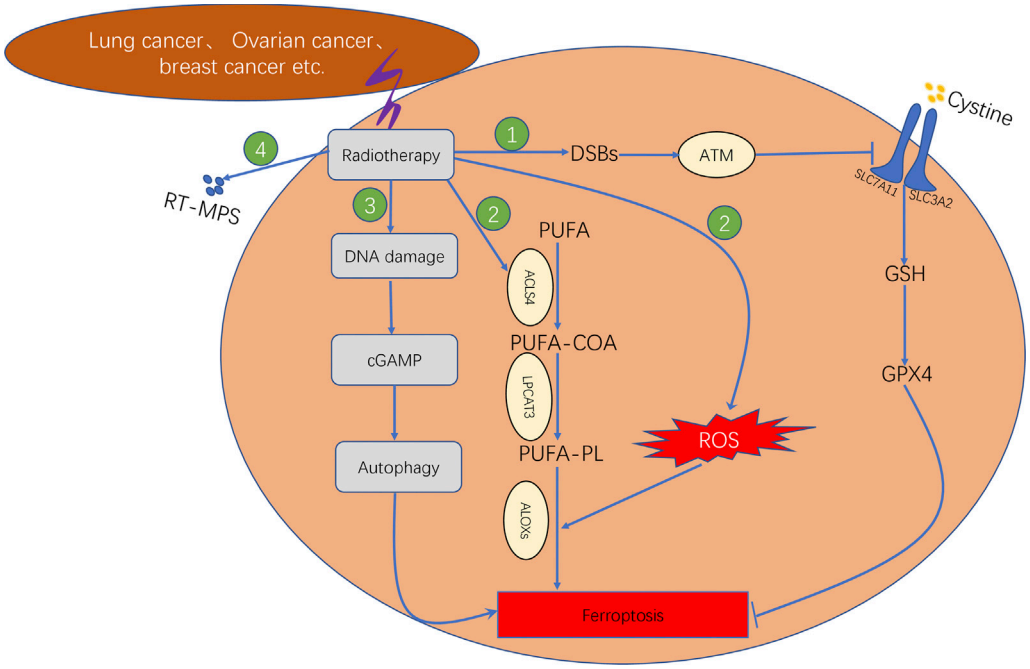

FIGURE 6 | Mechanism underlying ferroptosis induced by radiotherapy, which consisted of four steps. First step: Radiotherapy affects GSH synthesis by affecting system XC^- transport via ATM. Second step: Radiotherapy promotes lipid biosynthesis by upregulating ACSL4 expression. Third step: Radiotherapy induces autophagy-dependent ferroptosis by causing DNA damage. Fourth step: Radiotherapy facilitates the production of RT-MPs; thereby causing lipid peroxidation in neighbouring cells.

Combination of Ferroptosis and Radiotherapy

Radiotherapy is one of the therapeutic modalities for the clinical treatment of tumours, which involves direct and indirect mechanisms of action. Regarding its direct mechanism, high-energy ionising radiation disrupts the double-stranded structure of cellular DNA and leads to cell cycle arrest. Regarding its indirect mechanism, radiation leads to cellular alterations including radiolysis of intracellular water and stimulation of oxidative enzymes. These alterations can generate ROS such as hydroxyl radicals and hydrogen peroxide. ROS overproduction can further damage nucleic acids, proteins and lipids, thereby inducing cell death (Lei et al., 2020). A recent study demonstrated that radiotherapy can exert therapeutic effects by inducing ferroptosis in cells, and the combination of radiotherapy and ferroptosis inducers results in enhanced antitumour effects when compared with the use of either treatment alone. The results of the study indicated that the combination of ferroptosis and radiotherapy might provide a promising strategy for treating tumours (Lang et al., 2019).

In addition, recent studies have reported that radiotherapy can induce ferroptosis in tumour cells. The four primary underlying mechanisms can be summarised as follows (**Figure 6**: First, radiotherapy can upregulate the expression ofataxia–telangiectasia mutated (ATM) gene and further inhibit the transport function of system XC–through inducing DNA double strand breaks (DBSs), which leads to the inhibition of antioxidant activity of GSH and GPX4, therebyresulting in lipid peroxidation (Lang et al., 2019). Second, radiotherapy can either increase the production of ROS or upregulate the gene expression of ACSL4. The conversion of PUFA to PUFA-CoA is catalysed by ACSL4. Subsequently, the PUFA-CoA enzyme is converted to PUFA-PL, which is catalysed by LPCAT3. The PUFA-PL product can induce lipid peroxidation owing to the catalysis of arachidonate lipoxygenases (ALOXs). Therefore, radiotherapy can promote intracellular lipid peroxidation and induce ferroptosis (Lei et al., 2020; Lei et al., 2021). Third, tumour cells treated with radiation can release tumour cell-released microparticles (RT-MPs) into the extracellular environment, which can promote the effect of radiotherapy by inducing ferroptosis in other tumour cells (Wan et al., 2020). Fourth, radiotherapy induces intracellular DNA damage, thereby activating the CGAS–cGAMP signalling pathway and subsequently inducing autophagy-dependent ferroptosis (Li et al., 2021).

Regarding the application of ferroptosis in radiotherapy, the combination of radiotherapy and the ferroptosis inducer (FIN) was found to act synergistically in tumour treatment by increasing lipid peroxidation and upregulating PTGS2 expression, with FINS exerting significant radio-sensitising effects *in vitro* and *in vivo* (Lei et al., 2020). Another study reported similar results by demonstrating that the ferroptosis inducer sulfasalazine acted as a radiosensitiser and increased the sensitivity of gliomas to Gamma Knife radiosurgery. The underlying mechanism involves blocking the uptake of cystine by system XC^-, leading to GSH depletion (Sleire et al., 2015). Another study investigating lung adenocarcinoma and glioma established a murine xenograft model and human patient-derived models to analyse the beneficial effects of combining radiotherapy with the ferroptosis

inducer sorafenib *in vivo*, resulting in the improved efficacy of radiotherapy and inhibition of tumour growth (Ye et al., 2020).

Furthermore, a study reported that ferroptosis was also involved in radiotherapy-induced cellular damage in normal cells instead of only affecting tumour cells (Li et al., 2019). Based on this study, the combined application of ferroptosis inducers and radiotherapy in cancer treatment needs to be considered with caution. Whether the combination causes less harm to normal tissues than to tumour tissues needs to be investigated. Further studies to address this issue are warranted, and nanomaterials may be a future research direction. Altogether, these studies demonstrate that the combination of radiotherapy and ferroptosis may be considered a novel therapeutic strategy and also provides directions for future cancer research.

Combined Application of Ferroptosis and Photodynamic Therapy

Photodynamic therapy (PDT) is a non-invasive cancer treatment modality. The action mechanism of PDT involves absorbing energy from ionising radiation and generating cytotoxic singlet oxygen (Dolmans et al., 2003). However, the efficacy of PDT in tumour treatment is limited owing to the inherent hypoxic nature of the tumour microenvironment. Therefore, oxygen supplementation in the tumour microenvironment is an essential measure to improve the efficacy of PDT (Cui et al., 2018). Because ferroptosis can generate lipid ROS, it is an excellent strategy to synergise with PDT.

Some studies have reported the applications of ferroptosis-related drugs in PDT therapy. A previous study designed a co-assembled nanosystem using the combination of erastin (ferroptosis inducer) and chlorin e6 (photosensitiser Ce6). This nanosystem was formed via intermolecular interactions of hydrogen bonding and π–π stacking. Erastin increased the concentration of intracellular oxygen and significantly improved the therapeutic efficiency of PDT by generating ROS (Zhu et al., 2019). Another example of the combined use of oxygen-enhanced PDT and ferroptosis is a 2-in-1 nanoplatform (SRF@HB-Ce6), which was designed by piggybacking the photosensitiser Ce6 on sorafenib (ferroptosis inducer) attached to the haemoglobin (Hb) (Xu et al., 2020). As for this nanoplatform, the capacity of Hb in providing endogenous iron and carrying oxygen provided the conditions for photodynamic-type therapy by enhancing ferroptosis (Xu et al., 2020). In addition, PDT can enhance ferroptosis and sensitise tumour cells to ferroptosis by recruiting immune cells to secrete interferon-gamma. Such 2-in-1 nanosystems combine the therapeutic advantage of both ferroptosis-related drugs and PDT and play a significant role in promoting antitumour effects (Xu et al., 2020). In addition to these nanosystems established by incorporating specialised photodynamic sensitisers (e.g. ferroptosis inducers), another design method has recently emerged based on the ability of some nanomaterials to generate ROS under certain conditions. For example, graphene oxide was recently found to release ROS under near-infrared (NIR) irradiation (He et al., 2017). Based on this theory, a research group prepared a new graphene oxide-based NIR-absorbing nanoparticle agent that was decorated with iron hydroxide/oxide (GO-FeO xH). *In vitro* experiments on this nanomaterial demonstrated that GO-FeO x H released oxygen upon exposure to NIR, which improved the treatment outcome of PDT (He et al., 2017).

Ferroptosis and Nano-Therapy

Owing to the unique physicochemical properties of nanomaterials, bio-nanotechnology has become a focused research topic in the field of cancer treatment. Drug treatment can be improved by delivering anticancer drugs via nano-drug delivery systems (nano-DDS), which can significantly reduce the toxic side effects of drugs.

Recent studies have reported the use of nanomaterials to efficiently deliver ferroptosis targeting drugs (Shen Z. et al., 2018). Because ferroptosis is cell death caused by intracellular iron ion-dependent lipid peroxidation and lipid ROS accumulation, nanomedicines developed for ferroptosis are mainly used for intracellular ROS assembly. Therefore, based on the action mechanism of ferroptosis, ferroptosis-related nanodrugs can be classified into the following three categories: first, ferroptosis-related nanodrugs that can promote intracellular Fenton reaction; second, nanodrugs that can inhibit intracellular GPX4 activity, thus reducing intracellular antioxidant capacity; third, nanodrugs that can be used for exogenous regulation of lipid peroxidation in tumour cells (Shan et al., 2020). The regulatory role and application of these three categories of ferroptosis-related nano-drugs will be discussed in this section.

The first category of ferroptosis-related nanodrugs (for promoting intracellular Fenton reaction): The Fenton reaction is defined as the reaction between intracellular iron ions and hydrogen peroxide, leading to the production of the harmful hydroxyl radicals. Ferroptosis can induce cell death by promoting the intracellular Fenton reaction (Qian et al., 2019). Compared with normal cells, tumour cells possess more hydrogen peroxide and hence served as a substrate for the Fenton reaction, further facilitating the induction of ferroptosis. In addition, the tumour microenvironment is slightly acidic compared with the normal cell environment, and such Fenton reactions generally do not occur in the relatively neutral normal cells/tissues. Therefore, based on the Fenton reaction, ferroptosis-related drugs can accurately target tumour cells instead of destroying normal cells, which is a major advantage, especially involving less toxic side effects.

The Fenton reaction can be induced in tumour cells by enhancing the substrate of intracellular Fenton reaction (e.g. Fe^{+} and H_2O_2) via sustained release by a nano-delivery system. A typical example is nanocatalysts, which are prepared by adding ultrafine Fe_3O_4 nanoparticles and natural glucose oxidase (GOD) to silica nanoparticles with large pore size. GOD can effectively consume glucose in tumour cells, thus generating a large amount of hydrogen peroxide. Furthermore, Fe_3O_4 reacts with hydrogen peroxide, leading to a Fenton reaction, followed by the overproduction of hydroxyl radicals, which increases ROS levels and further induces ferroptosis in cells (Huo et al., 2017).

The second category of ferroptosis-related nanodrugs (for inhibiting intracellular GPX4 activity): In addition to promoting the intracellular Fenton reaction, these nanodrugs can inhibit GPX4 activity, thus reducing intracellular GSH levels.

Currently, there are two primary modes of combining inhibition of GPX4 activity with nanomaterials: mode 1, intracellular administration of GPX4 inhibitors via nano-delivery systems; mode 2, direct GPX4 inhibition using nanomaterials or nanodrugs (Shan et al., 2020).

Mode 1 (direct administration of GPX4 inhibitors via nano-delivery systems): In a study, a nanomaterial scaffold was incorporated with three components (small molecule GPX4 inhibitor sorafenib, Fe^{3+} and tannic acid). Such nanodrugs can not only inhibit GPX4 activity but also convert Fe^{3+} to Fe^{2+} via tannic acid. These alterations eventually induce ferroptosis in cancer cells (Liu et al., 2018).

Mode 2 (nanosystems with GPX4 inhibition): This mode involves designing nanomaterials or drugs with GPX4 inhibition. A typical example is low-density lipoprotein (LDL) nanoparticles reconstituted with the natural omega-3 fatty acid docosahexaenoic acid (LDL-DHA), which were reported to induce ferroptosis in hepatocellular carcinoma cells by inhibiting intracellular GPX4 expression and reducing GSH levels (Ou et al., 2017). Another example is arginine-rich manganese silicate nanobubbles (AMSNs), which were found to induce iron sagging by inactivating GPX4, leading to an efficient GSH depletion capacity. The surface coating of arginine and the nanobubble structure improved the GSH depletion efficiency of manganese silicate nanobubbles when compared with the conventional nanoparticles (Wang et al., 2018).

The third category of ferroptosis-related nanodrugs (for regulating exogenous lipid peroxidation): Ferroptosis is mainly caused by lipid peroxidation, and the primary substrates of lipid peroxidation are PUFAs present in the phospholipid membranes. Therefore, increasing PUFA concentration exogenously may be a reasonable strategy for regulating lipid peroxidation and effectively inducing ferroptosis. This drug design strategy can efficiently improve the antitumour activity of ferroptosis inducers. To verify this hypothesis, some studies have been recently conducted using nano-delivery systems to exogenously modulate lipid peroxidation. A typical example is the nanosystem design based on Fenton-like reactions wherein linoleic acid hydroperoxide (LAHP) was incorporated into iron oxide nanoparticles (IONPs) using sub-stable FeO and Fe_3O_4 as iron sources to achieve on-demand Fe^{2+} release from the nanosystem under acidic conditions in tumours. The released Fe^{2+} generated tumor-specific $^1O_2$ using LAHP, ultimately inducing ferroptosis in tumour cells (Zhou et al., 2017).

FUTURE PERSPECTIVES AND CHALLENGES

Ferroptosis was initially discovered as a novel form of RCD in 2012, and its underlying transduction mechanisms have recently gained increasing attention in cancer research (Hassannia et al., 2019; Mou et al., 2019). Based on the currently known pathways of ferroptosis (e.g. system XC^-, GPX4, FSP1 and BH1), various ferroptosis inducers and techniques have been discovered and potentially applied in cancer treatment (Liang et al., 2019). In addition to the sole application of ferroptosis in treating cancer cells, ferroptosis can also be combined with other conventional therapeutic modalities, such as the combination of ferroptosis inducers and chemotherapeutic drugs based on nano-DDS. Such combinational modalities may significantly improve therapeutic efficacy as compared with the effects of either treatment alone and may be a promising strategy for cancer treatment (Shan et al., 2020) (**Figure 7**).

Despite the leaps and bounds in ferroptosis-based cancer treatment, it still faces several challenges, especially in terms of regulatory mechanisms and its potential application in clinical cancer therapy (**Figure 7**). The action mechanism of iron-dependent cell death remains unclear and requires extensive investigation. Other regulated cell deaths are executed mainly through proteins and proteases (such as caspases). Whether ferroptosis is caused by the products of lipid peroxidation or by the products downstream of lipid peroxidation remains unclear. In addition, there are insufficient studies regarding the physiological function of ferroptosis during growth and development. Therefore, understanding the role of ferroptosis in growth and development is important for using ferroptosis for further development of cancer therapy.

In addition, there are some unaddressed issues regarding the potential application of ferroptosis in cancer therapy. The first unsolved research question is whether the specific ferroptosis inhibitors and inducers can be applied *in vivo* more safely. Sorafenib, sulfasalazine, statins and artemisinin mentioned in previous sections are currently being investigated as ferroptosis inducers; however, their application in clinical practice requires further investigation. In addition, controlling the toxic effects of ferroptosis inducers on normal tissues is a major concern. Another problem is the selection of tumour types or patients more likely to be treated with ferroptosis-related regimens (Chen et al., 2021). Different tumour types and patients may have different sensitivity to ferroptosis owing to differences in iron levels and expression levels of ferroptosis-related genes. Therefore, iron levels, gene expression and mutations can be used as criteria for judging populations more likely to benefit from ferroptosis-promoting therapies. In addition, ferroptosis-inducing agents need to be significantly improved, especially regarding their pharmacokinetic and physicochemical properties. Currently used ferroptosis inducers have several physical and chemical drawbacks that prevent their rational use in clinical practice. Nanosystems can be improved to some extent in this regard. However, when combining ferroptosis with nanosystem therapies, it should be noted that outcome differences may exist between animals and humans because ferroptosis is non-apoptotic death, which should be further validated. Furthermore, effective combinational strategies that can synergistically work with ferroptosis induction in cancer therapy may provide an experimental direction for future research. Although the combination of ferroptosis with other treatments has been shown to improve the clinical outcomes of cancers, an optimal combination strategy involving ferroptosis and other treatments has not yet been identified. Moreover, there exists neither an accurate method nor an indicator for detecting ferroptosis. Various features of ferroptosis have been identified;

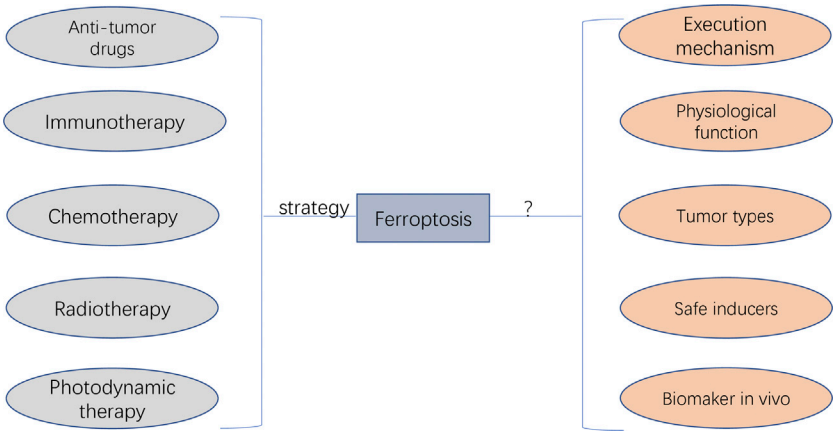

FIGURE 7 | The potential application and faced challenges of ferroptosis in clinical cancer therapy. The anti-tumour drug agents targeting ferroptosis can be developed, which can be applied by the combination of other therapeutic approaches (i.e., immunotherapy, chemotherapy, radiotherapy, and photodynamic therapy). The unaddressed concerns before clinical transfer include unknown execution mechanism, unexplored physiological function, unexpected regulating roles depending on cancer types, undiscovered ferrpotosis inducers applied safely in human, and undetected specific biomarkers for diagnosing the initiation of ferropotosis *in vivo*.

however, a specific biomarker of ferroptosis has not yet been identified. At the level of lipid peroxidation, the BODIPY 581/591 C11 fluorescent probe can be used to detect the degree of intracellular lipid peroxidation and hence ferroptosis. At the iron level, ferroptosis can be detected indirectly by using an iron kit to detect the intracellular iron concentration. At the genetic level, PTGS2, ACSL4, CHAC1 and TFRC170 are considered ferroptosis-associated genetic biomarkers based on preclinical models. Although these genes are well known to be significantly involved in ferroptosis, further studies should focus on discovering more specific biomarkers and detection tools for ferroptosis, which will be beneficial for providing meaningful guidance to clinical practitioners.

CONCLUSION

Ferroptosis is a promising strategy for cancer therapy; however, further research is required for evaluating its clinical applications.

AUTHORS CONTRIBUTIONS

ZT and ZH conceptualized the research, conducted the current review, and wrote the manuscript; YH, YC, MH, and HL participated in the figure plotting and revised the manuscript; QY, JZ, and BJ administrated and supervised the whole research project. All authors read and approved the final manuscript.

REFERENCE

Adams, S., Gatti-Mays, M. E., Kalinsky, K., Korde, L. A., Sharon, E., Amiri-Kordestani, L., et al.fnm . (2019). Current Landscape of Immunotherapy in Breast Cancer: A Review. *JAMA Oncol.* 5(8), 1205–1214. doi:10.1001/jamaoncol.2018.7147

Battaglia, A. M., Chirillo, R., Aversa, I., Sacco, A., Costanzo, F., and Biamonte, F. (2020). Ferroptosis and Cancer: Mitochondria Meet the "Iron Maiden" Cell Death. *Cells* 9. doi:10.3390/cells9061505

Berger, T. G., Dieckmann, D., Efferth, T., Schultz, E. S., Funk, J. O., Baur, A., et al. (2005). Artesunate in the Treatment of Metastatic Uveal Melanoma–First Experiences. *Oncol. Rep.* 14 (6), 1599–1603. doi:10.3892/or.14.6.1599

Berkers, C. R., Maddocks, O. D., Cheung, E. C., Mor, I., and Vousden, K. H. (2013). Metabolic Regulation by P53 Family Members. *Cell Metab* 18 (5), 617–633. doi:10.1016/j.cmet.2013.06.019

Bersuker, K., Hendricks, J. M., Li, Z., Magtanong, L., Ford, B., Tang, P. H., et al. (2019). The CoQ Oxidoreductase FSP1 Acts Parallel to GPX4 to Inhibit Ferroptosis. *Nature* 575 (7784), 688–692. doi:10.1038/s41586-019-1705-2

Bieging, K. T., Mello, S. S., and Attardi, L. D. (2014). Unravelling Mechanisms of P53-Mediated Tumour Suppression. *Nat. Rev. Cancer* 14 (5), 359–370. doi:10.1038/nrc3711

Brown, C. W., Amante, J. J., Chhoy, P., Elaimy, A. L., Liu, H., Zhu, L. J., et al. (2019). Prominin2 Drives Ferroptosis Resistance by Stimulating Iron Export. *Dev. Cel* 51 (5), 575–586. doi:10.1016/j.devcel.2019.10.007

Chen, H., Sun, B., Wang, S., Pan, S., Gao, Y., Bai, X., et al. (2010). Growth Inhibitory Effects of Dihydroartemisinin on Pancreatic Cancer Cells: Involvement of Cell Cycle Arrest and Inactivation of Nuclear Factor-kappaB. *J. Cancer Res. Clin. Oncol.* 136 (6), 897–903. doi:10.1007/s00432-009-0731-0

Chen, X., Kang, R., Kroemer, G., and Tang, D. (2021). Broadening Horizons: the Role of Ferroptosis in Cancer. *Nat. Rev. Clin. Oncol.* 18 (5), 280–296. doi:10.1038/s41571-020-00462-0

Combe, B., Codreanu, C., Fiocco, U., Gaubitz, M., Geusens, P. P., Kvien, T. K., et al. (2009). Efficacy, Safety and Patient-Reported Outcomes of Combination Etanercept and Sulfasalazine versus Etanercept Alone in Patients with Rheumatoid Arthritis: a Double-Blind Randomised 2-year Study. *Ann. Rheum. Dis.* 68 (7), 1146–1152. doi:10.1136/ard.2007.087106

Cui, Q., Wang, J. Q., Assaraf, Y. G., Ren, L., Gupta, P., Wei, L., et al. (2018). Modulating ROS to Overcome Multidrug Resistance in Cancer. *Drug Resist. Updat* 41, 1–25. doi:10.1016/j.drup.2018.11.001

Dai, E., Zhang, W., Cong, D., Kang, R., Wang, J., and Tang, D. (2020). AIFM2 Blocks Ferroptosis Independent of Ubiquinol Metabolism. *Biochem. Biophys. Res. Commun.* 523 (4), 966–971. doi:10.1016/j.bbrc.2020.01.066

Datta, J., Majumder, S., Kutay, H., Motiwala, T., Frankel, W., Costa, R., et al. (2007). Metallothionein Expression Is Suppressed in Primary Human Hepatocellular Carcinomas and Is Mediated through Inactivation of CCAAT/enhancer Binding Protein Alpha by Phosphatidylinositol 3-kinase Signaling cascade. *Cancer Res.* 67 (6), 2736–2746. doi:10.1158/0008-5472.CAN-06-4433

Dixon, S. J., Lemberg, K. M., Lamprecht, M. R., Skouta, R., Zaitsev, E. M., Gleason, C. E., et al. (2012). Ferroptosis: an Iron-dependent Form of Nonapoptotic Cell Death. *Cell* 149 (5), 1060–1072. doi:10.1016/j.cell.2012.03.042

Dixon, S. J., Patel, D. N., Welsch, M., Skouta, R., Lee, E. D., Hayano, M., et al. (2014). Pharmacological Inhibition of Cystine-Glutamate Exchange Induces Endoplasmic Reticulum Stress and Ferroptosis. *Elife* 3, e02523. doi:10.7554/eLife.02523

Dixon, S. J., Winter, G. E., Musavi, L. S., Lee, E. D., Snijder, B., Rebsamen, M., et al. (2015). Human Haploid Cell Genetics Reveals Roles for Lipid Metabolism Genes in Nonapoptotic Cell Death. *ACS Chem. Biol.* 10 (7), 1604–1609. doi:10.1021/acschembio.5b00245

Doll, S., Freitas, F. P., Shah, R., Aldrovandi, M., da Silva, M. C., Ingold, I., et al. (2019). FSP1 Is a Glutathione-independent Ferroptosis Suppressor. *Nature* 575 (7784), 693–698. doi:10.1038/s41586-019-1707-0

Doll, S., Proneth, B., Tyurina, Y. Y., Panzilius, E., Kobayashi, S., Ingold, I., et al. (2017). ACSL4 Dictates Ferroptosis Sensitivity by Shaping Cellular Lipid Composition. *Nat. Chem. Biol.* 13 (1), 91–98. doi:10.1038/nchembio.2239

Dolmans, D. E., Fukumura, D., and Jain, R. K. (2003). Photodynamic Therapy for Cancer. *Nat. Rev. Cancer* 3 (5), 380–387. doi:10.1038/nrc1071

Efimova, I., Catanzaro, E., Van der Meeren, L., Turubanova, V. D., Hammad, H., Mishchenko, T. A., et al. (2020). Vaccination with Early Ferroptotic Cancer Cells Induces Efficient Antitumor Immunity. *J. Immunother. Cancer* 8. doi:10.1136/jitc-2020-001369

Eling, N., Reuter, L., Hazin, J., Hamacher-Brady, A., and Brady, N. R. (2015). Identification of Artesunate as a Specific Activator of Ferroptosis in Pancreatic Cancer Cells. *Oncoscience* 2 (5), 517–532. doi:10.18632/oncoscience.160

Fleig, W. E., Laudage, G., Sommer, H., Wellmann, W., Stange, E. F., and Riemann, J. (1988). Prospective, Randomized, Double-Blind Comparison of Benzalazine and Sulfasalazine in the Treatment of Active Ulcerative Colitis. *Digestion* 40 (3), 173–180. doi:10.1159/000199652

Friedmann Angeli, J. P., Krysko, D. V., and Conrad, M. (2019). Ferroptosis at the Crossroads of Cancer-Acquired Drug Resistance and Immune Evasion. *Nat. Rev. Cancer* 19 (7), 405–414. doi:10.1038/s41568-019-0149-1

Friedmann Angeli, J. P., Schneider, M., Proneth, B., Tyurina, Y. Y., Tyurin, V. A., Hammond, V. J., et al. (2014). Inactivation of the Ferroptosis Regulator Gpx4 Triggers Acute Renal Failure in Mice. *Nat. Cel Biol* 16 (12), 1180–1191. doi:10.1038/ncb3064

Gao, M., Monian, P., Quadri, N., Ramasamy, R., and Jiang, X. (2015). Glutaminolysis and Transferrin Regulate Ferroptosis. *Mol. Cel* 59 (2), 298–308. doi:10.1016/j.molcel.2015.06.011

Gout, P. W., Buckley, A. R., Simms, C. R., and Bruchovsky, N. (2001). Sulfasalazine, a Potent Suppressor of Lymphoma Growth by Inhibition of the X(c)- Cystine Transporter: a New Action for an Old Drug. *Leukemia* 15 (10), 1633–1640. doi:10.1038/sj.leu.2402238

Guan, J., Lo, M., Dockery, P., Mahon, S., Karp, C. M., Buckley, A. R., et al. (2009). The Xc- Cystine/glutamate Antiporter as a Potential Therapeutic Target for Small-Cell Lung Cancer: Use of Sulfasalazine. *Cancer Chemother. Pharmacol.* 64 (3), 463–472. doi:10.1007/s00280-008-0894-4

Guo, J., Xu, B., Han, Q., Zhou, H., Xia, Y., Gong, C., et al. (2018). Ferroptosis: A Novel Anti-tumor Action for Cisplatin. *Cancer Res. Treat.* 50 (2), 445–460. doi:10.4143/crt.2016.572

Hangauer, M. J., Viswanathan, V. S., Ryan, M. J., Bole, D., Eaton, J. K., Matov, A., et al. (2017). Drug-tolerant Persister Cancer Cells Are Vulnerable to GPX4 Inhibition. *Nature* 551 (7679), 247–250. doi:10.1038/nature24297

Hassannia, B., Vandenabeele, P., and Vanden Berghe, T. (2019). Targeting Ferroptosis to Iron Out Cancer. *Cancer Cell* 35 (6), 830–849. doi:10.1016/j.ccell.2019.04.002

He, Y., Del Valle, A., Qian, Y., and Huang, Y. F. (2017). Near Infrared Light-Mediated Enhancement of Reactive Oxygen Species Generation through Electron Transfer from Graphene Oxide to Iron Hydroxide/oxide. *Nanoscale* 9 (4), 1559–1566. doi:10.1039/c6nr08784a

Hirschhorn, T., and Stockwell, B. R. (2019). The Development of the Concept of Ferroptosis. *Free Radic. Biol. Med.* 133, 130–143. doi:10.1016/j.freeradbiomed.2018.09.043

Holohan, C., Van Schaeybroeck, S., Longley, D. B., and Johnston, P. G. (2013). Cancer Drug Resistance: an Evolving Paradigm. *Nat. Rev. Cancer* 13 (10), 714–726. doi:10.1038/nrc3599

Horikoshi, N., Cong, J., Kley, N., and Shenk, T. (1999). Isolation of Differentially Expressed cDNAs from P53-dependent Apoptotic Cells: Activation of the Human Homologue of the Drosophila Peroxidasin Gene. *Biochem. Biophys. Res. Commun.* 261 (3), 864–869. doi:10.1006/bbrc.1999.1123

Huo, M., Wang, L., Chen, Y., and Shi, J. (2017). Tumor-selective Catalytic Nanomedicine by Nanocatalyst Delivery. *Nat. Commun.* 8 (1), 357. doi:10.1038/s41467-017-00424-8

Jiang, L., Kon, N., Li, T., Wang, S. J., Su, T., Hibshoosh, H., et al. (2015). Ferroptosis as a P53-Mediated Activity during Tumour Suppression. *Nature* 520 (7545), 57–62. doi:10.1038/nature14344

Khalil, D. N., Smith, E. L., Brentjens, R. J., and Wolchok, J. D. (2016). The Future of Cancer Treatment: Immunomodulation, CARs and Combination Immunotherapy. *Nat. Rev. Clin. Oncol.* 13 (5), 273–290. doi:10.1038/nrclinonc.2016.25

Kong, Z., Liu, R., and Cheng, Y. (2019). Artesunate Alleviates Liver Fibrosis by Regulating Ferroptosis Signaling Pathway. *Biomed. Pharmacother.* 109, 2043–2053. doi:10.1016/j.biopha.2018.11.030

Koppula, P., Zhuang, L., and Gan, B. (2021). Cytochrome P450 Reductase (POR) as a Ferroptosis Fuel. *Protein Cell*. doi:10.1007/s13238-021-00823-0

Kraft, V. A. N., Bezjian, C. T., Pfeiffer, S., Ringelstetter, L., Müller, C., Zandkarimi, F., et al. (2020). GTP Cyclohydrolase 1/Tetrahydrobiopterin Counteract Ferroptosis through Lipid Remodeling. *ACS Cent. Sci.* 6 (1), 41–53. doi:10.1021/acscentsci.9b01063

Kuang, F., Liu, J., Tang, D., and Kang, R. (2020). Oxidative Damage and Antioxidant Defense in Ferroptosis. *Front Cel Dev Biol* 8, 586578. doi:10.3389/fcell.2020.586578

Lang, X., Green, M. D., Wang, W., Yu, J., Choi, J. E., Jiang, L., et al. (2019). Radiotherapy and Immunotherapy Promote Tumoral Lipid Oxidation and Ferroptosis via Synergistic Repression of SLC7A11. *Cancer Discov.* 9 (12), 1673–1685. doi:10.1158/2159-8290.Cd-19-0338

Lay, J. D., Hong, C. C., Huang, J. S., Yang, Y. Y., Pao, C. Y., Liu, C. H., et al. (2007). Sulfasalazine Suppresses Drug Resistance and Invasiveness of Lung Adenocarcinoma Cells Expressing AXL. *Cancer Res.* 67 (8), 3878–3887. doi:10.1158/0008-5472.CAN-06-3191

Lei, G., Mao, C., Yan, Y., Zhuang, L., and Gan, B. (2021). Ferroptosis, Radiotherapy, and Combination Therapeutic Strategies. *Protein Cell*. doi:10.1007/s13238-021-00841-y

Lei, G., Zhang, Y., Koppula, P., Liu, X., Zhang, J., Lin, S. H., et al. (2020). The Role of Ferroptosis in Ionizing Radiation-Induced Cell Death and Tumor Suppression. *Cell Res* 30 (2), 146–162. doi:10.1038/s41422-019-0263-3

Li, C., Zhang, Y., Liu, J., Kang, R., Klionsky, D. J., and Tang, D. (2021). Mitochondrial DNA Stress Triggers Autophagy-dependent Ferroptotic Death. *Autophagy* 17 (4), 948–960. doi:10.1080/15548627.2020.1739447

Li, J., Cao, F., Yin, H. L., Huang, Z. J., Lin, Z. T., Mao, N., et al. (2020). Ferroptosis: Past, Present and Future. *Cell Death Dis* 11 (2), 88. doi:10.1038/s41419-020-2298-2

Li, X., Duan, L., Yuan, S., Zhuang, X., Qiao, T., and He, J. (2019). Ferroptosis Inhibitor Alleviates Radiation-Induced Lung Fibrosis (RILF) via Down-Regulation of TGF-Beta1. *J. Inflamm. (Lond)* 16, 11. doi:10.1186/s12950-019-0216-0

Liang, C., Zhang, X., Yang, M., and Dong, X. (2019). Recent Progress in Ferroptosis Inducers for Cancer Therapy. *Adv. Mater.* 31 (51), e1904197. doi:10.1002/adma.201904197

Lim, J., Lam, Y. C., Kistler, J., and Donaldson, P. J. (2005). Molecular Characterization of the Cystine/glutamate Exchanger and the Excitatory Amino Acid Transporters in the Rat Lens. *Invest. Ophthalmol. Vis. Sci.* 46 (8), 2869–2877. doi:10.1167/iovs.05-0156

Liu, T., Liu, W., Zhang, M., Yu, W., Gao, F., Li, C., et al. (2018). Ferrous-Supply-Regeneration Nanoengineering for Cancer-cell-specific Ferroptosis in Combination with Imaging-Guided Photodynamic Therapy. *ACS Nano* 12 (12), 12181–12192. doi:10.1021/acsnano.8b05860

Lu, B., Chen, X. B., Ying, M. D., He, Q. J., Cao, J., and Yang, B. (2017). The Role of Ferroptosis in Cancer Development and Treatment Response. *Front. Pharmacol.* 8, 992. doi:10.3389/fphar.2017.00992

Lv, C., Qu, H., Zhu, W., Xu, K., Xu, A., Jia, B., et al. (2017). Low-Dose Paclitaxel Inhibits Tumor Cell Growth by Regulating Glutaminolysis in Colorectal Carcinoma Cells. *Front. Pharmacol.* 8, 244. doi:10.3389/fphar.2017.00244

Ma, S., Dielschneider, R. F., Henson, E. S., Xiao, W., Choquette, T. R., Blankstein, A. R., et al. (2017). Ferroptosis and Autophagy Induced Cell Death Occur Independently after Siramesine and Lapatinib Treatment in Breast Cancer Cells. *PLoS One* 12, e0182921. doi:10.1371/journal.pone.0182921

Ma, S., Henson, E. S., Chen, Y., and Gibson, S. B. (2016). Ferroptosis Is Induced Following Siramesine and Lapatinib Treatment of Breast Cancer Cells. *Cel Death Dis* 7, e2307. doi:10.1038/cddis.2016.208

Magtanong, L., Ko, P. J., and Dixon, S. J. (2016). Emerging Roles for Lipids in Non-apoptotic Cell Death. *Cell Death Differ* 23 (7), 1099–1109. doi:10.1038/cdd.2016.25

Mandal, P. K., Seiler, A., Perisic, T., Kölle, P., Banjac Canak, A., Förster, H., et al. (2010). System X(c)- and Thioredoxin Reductase 1 Cooperatively rescue Glutathione Deficiency. *J. Biol. Chem.* 285 (29), 22244–22253. doi:10.1074/jbc.M110.121327

Mao, C., Liu, X., Zhang, Y., Lei, G., Yan, Y., Lee, H., et al. (2021). DHODH-mediated Ferroptosis Defence Is a Targetable Vulnerability in Cancer. *Nature* 593 (7860), 586–590. doi:10.1038/s41586-021-03539-7

Mou, Y., Wang, J., Wu, J., He, D., Zhang, C., Duan, C., et al. (2019). Ferroptosis, a New Form of Cell Death: Opportunities and Challenges in Cancer. *J. Hematol. Oncol.* 12 (1), 34. doi:10.1186/s13045-019-0720-y

Narang, V. S., Pauletti, G. M., Gout, P. W., Buckley, D. J., and Buckley, A. R. (2007). Sulfasalazine-induced Reduction of Glutathione Levels in Breast Cancer Cells: Enhancement of Growth-Inhibitory Activity of Doxorubicin. *Chemotherapy* 53 (3), 210–217. doi:10.1159/000100812

Ooko, E., Saeed, M. E., Kadioglu, O., Sarvi, S., Colak, M., Elmasaoudi, K., et al. (2015). Artemisinin Derivatives Induce Iron-dependent Cell Death (Ferroptosis) in Tumor Cells. *Phytomedicine* 22 (11), 1045–1054. doi:10.1016/j.phymed.2015.08.002

Ou, W., Mulik, R. S., Anwar, A., McDonald, J. G., He, X., and Corbin, I. R. (2017). Low-density Lipoprotein Docosahexaenoic Acid Nanoparticles Induce Ferroptotic Cell Death in Hepatocellular Carcinoma. *Free Radic. Biol. Med.* 112, 597–607. doi:10.1016/j.freeradbiomed.2017.09.002

Park, S., Oh, J., Kim, M., and Jin, E. J. (2018). Bromelain Effectively Suppresses Kras-Mutant Colorectal Cancer by Stimulating Ferroptosis. *Anim. Cell Syst (Seoul)* 22 (5), 334–340. doi:10.1080/19768354.2018.1512521

Pham, T., Roth, S., Kong, J., Guerra, G., Narasimhan, V., Pereira, L., et al. (2018). An Update on Immunotherapy for Solid Tumors: A Review. *Ann. Surg. Oncol.* 25 (11), 3404–3412. doi:10.1245/s10434-018-6658-4

Pitman, K. E., Alluri, S. R., Kristian, A., Aarnes, E. K., Lyng, H., Riss, P. J., et al. (2019). Influx Rate of (18)F-Fluoroaminosuberic Acid Reflects Cystine/glutamate Antiporter Expression in Tumour Xenografts. *Eur. J. Nucl. Med. Mol. Imaging* 46 (10), 2190–2198. doi:10.1007/s00259-019-04375-8

Qian, X., Zhang, J., Gu, Z., and Chen, Y. (2019). Nanocatalysts-augmented Fenton Chemical Reaction for Nanocatalytic Tumor Therapy. *Biomaterials* 211, 1–13. doi:10.1016/j.biomaterials.2019.04.023

Riddick, D. S., Ding, X., Wolf, C. R., Porter, T. D., Pandey, A. V., Zhang, Q. Y., et al. (2013). NADPH-cytochrome P450 Oxidoreductase: Roles in Physiology, Pharmacology, and Toxicology. *Drug Metab. Dispos* 41 (1), 12–23. doi:10.1124/dmd.112.048991

Roh, J. L., Kim, E. H., Jang, H., and Shin, D. (2017). Nrf2 Inhibition Reverses the Resistance of Cisplatin-Resistant Head and Neck Cancer Cells to Artesunate-Induced Ferroptosis. *Redox Biol.* 11, 254–262. doi:10.1016/j.redox.2016.12.010

Ruiz-de-Angulo, A., Bilbao-Asensio, M., Cronin, J., Evans, S. J., Clift, M. J. D., Llop, J., et al. (2020). Chemically Programmed Vaccines: Iron Catalysis in Nanoparticles Enhances Combination Immunotherapy and Immunotherapy-Promoted Tumor Ferroptosis. *iScience* 23 (9), 101499. doi:10.1016/j.isci.2020.101499

Santana-Codina, N., and Mancias, J. D. (2018). The Role of NCOA4-Mediated Ferritinophagy in Health and Disease. *Pharmaceuticals (Basel) 11(4).* doi:10.3390/ph11040114

Sato, M., Kusumi, R., Hamashima, S., Kobayashi, S., Sasaki, S., Komiyama, Y., et al. (2018). The Ferroptosis Inducer Erastin Irreversibly Inhibits System Xc- and Synergizes with Cisplatin to Increase Cisplatin's Cytotoxicity in Cancer Cells. *Sci. Rep.* 8 (1), 968. doi:10.1038/s41598-018-19213-4

Shan, X., Li, S., Sun, B., Chen, Q., Sun, J., He, Z., et al. (2020). Ferroptosis-driven Nanotherapeutics for Cancer Treatment. *J. Control. Release* 319, 322–332. doi:10.1016/j.jconrel.2020.01.008

Shen, Y., Li, X., Dong, D., Zhang, B., Xue, Y., and Shang, P. (2018a). Transferrin Receptor 1 in Cancer: a New Sight for Cancer Therapy. *Am. J. Cancer Res.* 8 (6), 916–931.

Shen, Z., Song, J., Yung, B. C., Zhou, Z., Wu, A., and Chen, X. (2018b). Emerging Strategies of Cancer Therapy Based on Ferroptosis. *Adv. Mater.* 30 (12), e1704007. doi:10.1002/adma.201704007

Shi, L., Liu, Y., Li, M., and Luo, Z. (2021). Emerging Roles of Ferroptosis in the Tumor Immune Landscape: from Danger Signals to Anti-tumor Immunity. *FEBS J.* doi:10.1111/febs.16034

Sleire, L., Skeie, B. S., Netland, I. A., Førde, H. E., Dodoo, E., Selheim, F., et al. (2015). Drug Repurposing: Sulfasalazine Sensitizes Gliomas to Gamma Knife Radiosurgery by Blocking Cystine Uptake through System Xc-, Leading to Glutathione Depletion. *Oncogene* 34 (49), 5951–5959. doi:10.1038/onc.2015.60

Stockwell, B. R., Friedmann Angeli, J. P., Bayir, H., Bush, A. I., Conrad, M., Dixon, S. J., et al. (2017). Ferroptosis: A Regulated Cell Death Nexus Linking Metabolism, Redox Biology, and Disease. *Cell* 171 (2), 273–285. doi:10.1016/j.cell.2017.09.021

Su, Y., Zhao, B., Zhou, L., Zhang, Z., Shen, Y., Lv, H., et al. (2020). Ferroptosis, a Novel Pharmacological Mechanism of Anti-cancer Drugs. *Cancer Lett.* 483, 127–136. doi:10.1016/j.canlet.2020.02.015

Sun, X., Niu, X., Chen, R., He, W., Chen, D., Kang, R., et al. (2016). Metallothionein-1G Facilitates Sorafenib Resistance through Inhibition of Ferroptosis. *Hepatology* 64 (2), 488–500. doi:10.1002/hep.28574

Sun, X., Ou, Z., Xie, M., Kang, R., Fan, Y., Niu, X., et al. (2015). HSPB1 as a Novel Regulator of Ferroptotic Cancer Cell Death. *Oncogene* 34 (45), 5617–5625. doi:10.1038/onc.2015.32

Tarangelo, A., Magtanong, L., Bieging-Rolett, K. T., Li, Y., Ye, J., Attardi, L. D., et al. (2018). p53 Suppresses Metabolic Stress-Induced Ferroptosis in Cancer Cells. *Cell Rep* 22 (3), 569–575. doi:10.1016/j.celrep.2017.12.077

Torii, S., Shintoku, R., Kubota, C., Yaegashi, M., Torii, R., Sasaki, M., et al. (2016). An Essential Role for Functional Lysosomes in Ferroptosis of Cancer Cells. *Biochem. J.* 473 (6), 769–777. doi:10.1042/BJ20150658

Torti, S. V., and Torti, F. M. (2019). Winning the War with Iron. *Nat. Nanotechnol* 14 (6), 499–500. doi:10.1038/s41565-019-0419-9

van Staalduinen, J., Baker, D., Ten Dijke, P., and van Dam, H. (2018). Epithelial-mesenchymal-transition-inducing Transcription Factors: New Targets for Tackling Chemoresistance in Cancer? *Oncogene* 37 (48), 6195–6211. doi:10.1038/s41388-018-0378-x

Vasan, K., Werner, M., and Chandel, N. S. (2020). Mitochondrial Metabolism as a Target for Cancer Therapy. *Cel Metab* 32 (3), 341–352. doi:10.1016/j.cmet.2020.06.019

Viswanathan, V. S., Ryan, M. J., Dhruv, H. D., Gill, S., Eichhoff, O. M., Seashore-Ludlow, B., et al. (2017). Dependency of a Therapy-Resistant State of Cancer Cells on a Lipid Peroxidase Pathway. *Nature* 547 (7664), 453–457. doi:10.1038/nature23007

Wan, C., Sun, Y., Tian, Y., Lu, L., Dai, X., Meng, J., et al. (2020). Irradiated Tumor Cell-Derived Microparticles Mediate Tumor Eradication via Cell Killing and Immune Reprogramming. *Sci. Adv. 6(13), Eaay9789.* doi:10.1126/sciadv.aay9789

Wang, D., and Lippard, S. J. (2005). Cellular Processing of Platinum Anticancer Drugs. *Nat. Rev. Drug Discov.* 4 (4), 307–320. doi:10.1038/nrd1691

Wang, S., Li, F., Qiao, R., Hu, X., Liao, H., Chen, L., et al. (2018). Arginine-Rich Manganese Silicate Nanobubbles as a Ferroptosis-Inducing Agent for Tumor-Targeted Theranostics. *ACS Nano* 12 (12), 12380–12392. doi:10.1021/acsnano.8b06399

Wang, W., Green, M., Choi, J. E., Gijon, M., Kennedy, P. D., Johnson, J. K., et al. (2019). CD8(+) T Cells Regulate Tumour Ferroptosis during Cancer Immunotherapy. *Nature* 569 (7755), 270–274. doi:10.1038/s41586-019-1170-y

Wang, Y. J., Zhao, H. D., Zhu, C. F., Li, J., Xie, H. J., and Chen, Y. X. (2017). Tuberostemonine Reverses Multidrug Resistance in Chronic Myelogenous Leukemia Cells K562/ADR. *J. Cancer* 8 (6), 1103–1112. doi:10.7150/jca.17688

Wen, Q., Liu, J., Kang, R., Zhou, B., and Tang, D. (2019). The Release and Activity of HMGB1 in Ferroptosis. *Biochem. Biophys. Res. Commun.* 510 (2), 278–283. doi:10.1016/j.bbrc.2019.01.090

Wilhelm, S., Carter, C., Lynch, M., Lowinger, T., Dumas, J., Smith, R. A., et al. (2006). Discovery and Development of Sorafenib: a Multikinase Inhibitor for Treating Cancer. *Nat. Rev. Drug Discov.* 5 (10), 835–844. doi:10.1038/nrd2130

Willoughby, J. A., Sr., Sundar, S. N., Cheung, M., Tin, A. S., Modiano, J., and Firestone, G. L. (2009). Artemisinin Blocks Prostate Cancer Growth and Cell Cycle Progression by Disrupting Sp1 Interactions with the Cyclin-dependent Kinase-4 (CDK4) Promoter and Inhibiting CDK4 Gene Expression. *J. Biol. Chem.* 284 (4), 2203–2213. doi:10.1074/jbc.M804491200

Wood, E. R., Truesdale, A. T., McDonald, O. B., Yuan, D., Hassell, A., Dickerson, S. H., et al. (2004). A Unique Structure for Epidermal Growth Factor Receptor Bound to GW572016 (Lapatinib): Relationships Among Protein Conformation, Inhibitor Off-Rate, and Receptor Activity in Tumor Cells. *Cancer Res.* 64 (18), 6652–6659. doi:10.1158/0008-5472.Can-04-1168

Wu, M., Xu, L. G., Li, X., Zhai, Z., and Shu, H. B. (2002). AMID, an Apoptosis-Inducing Factor-Homologous Mitochondrion-Associated Protein, Induces Caspase-independent Apoptosis. *J. Biol. Chem.* 277 (28), 25617–25623. doi:10.1074/jbc.M202285200

Xie, Y., Hou, W., Song, X., Yu, Y., Huang, J., Sun, X., et al. (2016). Ferroptosis: Process and Function. *Cel Death Differ* 23 (3), 369–379. doi:10.1038/cdd.2015.158

Xu, G., Wang, H., Li, X., Huang, R., and Luo, L. (2021). Recent Progress on Targeting Ferroptosis for Cancer Therapy. *Biochem. Pharmacol.* 190, 114584. doi:10.1016/j.bcp.2021.114584

Xu, T., Ma, Y., Yuan, Q., Hu, H., Hu, X., Qian, Z., et al. (2020). Enhanced Ferroptosis by Oxygen-Boosted Phototherapy Based on a 2-in-1 Nanoplatform of Ferrous Hemoglobin for Tumor Synergistic Therapy. *ACS Nano* 14 (3), 3414–3425. doi:10.1021/acsnano.9b09426

Yagoda, N., von Rechenberg, M., Zaganjor, E., Bauer, A. J., Yang, W. S., Fridman, D. J., et al. (2007). RAS-RAF-MEK-dependent Oxidative Cell Death Involving Voltage-dependent Anion Channels. *Nature* 447 (7146), 864–868. doi:10.1038/nature05859

Yan, B., Ai, Y., Sun, Q., Ma, Y., Cao, Y., Wang, J., et al. (2021). Membrane Damage during Ferroptosis Is Caused by Oxidation of Phospholipids Catalyzed by the Oxidoreductases POR and CYB5R1. *Mol. Cel* 81 (2), 355–369. doi:10.1016/j.molcel.2020.11.024

Yang, J., Antin, P., Berx, G., Blanpain, C., Brabletz, T., Bronner, M., et al. (2020). Guidelines and Definitions for Research on Epithelial-Mesenchymal Transition. *Nat. Rev. Mol. Cel Biol* 21 (6), 341–352. doi:10.1038/s41580-020-0237-9

Yang, N. D., Tan, S. H., Ng, S., Shi, Y., Zhou, J., Tan, K. S., et al. (2014). Artesunate Induces Cell Death in Human Cancer Cells via Enhancing Lysosomal Function and Lysosomal Degradation of Ferritin. *J. Biol. Chem.* 289 (48), 33425–33441. doi:10.1074/jbc.M114.564567

Yang, W. S., and Stockwell, B. R. (2008). Synthetic Lethal Screening Identifies Compounds Activating Iron-dependent, Nonapoptotic Cell Death in Oncogenic-RAS-Harboring Cancer Cells. *Chem. Biol.* 15 (3), 234–245. doi:10.1016/j.chembiol.2008.02.010

Ye, J., Jiang, X., Dong, Z., Hu, S., and Xiao, M. (2019). Low-Concentration PTX and RSL3 Inhibits Tumor Cell Growth Synergistically by Inducing Ferroptosis in Mutant P53 Hypopharyngeal Squamous Carcinoma. *Cancer Manag. Res.* 11, 9783–9792. doi:10.2147/CMAR.S217944

Ye, L. F., Chaudhary, K. R., Zandkarimi, F., Harken, A. D., Kinslow, C. J., Upadhyayula, P. S., et al. (2020). Radiation-Induced Lipid Peroxidation Triggers Ferroptosis and Synergizes with Ferroptosis Inducers. *ACS Chem. Biol.* 15 (2), 469–484. doi:10.1021/acschembio.9b00939

Zhang, F., Li, F., Lu, G. H., Nie, W., Zhang, L., Lv, Y., et al. (2019). Engineering Magnetosomes for Ferroptosis/Immunomodulation Synergism in Cancer. *ACS Nano* 13 (5), 5662–5673. doi:10.1021/acsnano.9b00892

Zhang, F., Ma, Q., Xu, Z., Liang, H., Li, H., Ye, Y., et al. (2017). Dihydroartemisinin Inhibits TCTP-dependent Metastasis in Gallbladder Cancer. *J. Exp. Clin. Cancer Res.* 36 (1), 68. doi:10.1186/s13046-017-0531-3

Zhang, X., Sui, S., Wang, L., Li, H., Zhang, L., Xu, S., et al. (2020). Inhibition of Tumor Propellant Glutathione Peroxidase 4 Induces Ferroptosis in Cancer Cells and Enhances Anticancer Effect of Cisplatin. *J. Cel Physiol* 235 (4), 3425–3437. doi:10.1002/jcp.29232

Zhang, Y., Shi, J., Liu, X., Feng, L., Gong, Z., Koppula, P., et al. (2018). BAP1 Links Metabolic Regulation of Ferroptosis to Tumour Suppression. *Nat. Cel Biol* 20 (10), 1181–1192. doi:10.1038/s41556-018-0178-0

Zheng, J., and Conrad, M. (2020). The Metabolic Underpinnings of Ferroptosis. *Cel Metab* 32 (6), 920–937. doi:10.1016/j.cmet.2020.10.011

Zhou, Z., Song, J., Tian, R., Yang, Z., Yu, G., Lin, L., et al. (2017). Activatable Singlet Oxygen Generation from Lipid Hydroperoxide Nanoparticles for Cancer Therapy. *Angew. Chem. Int. Ed. Engl.* 56 (23), 6492–6496. doi:10.1002/anie.201701181

Zhu, T., Shi, L., Yu, C., Dong, Y., Qiu, F., Shen, L., et al. (2019). Ferroptosis Promotes Photodynamic Therapy: Supramolecular Photosensitizer-Inducer Nanodrug for Enhanced Cancer Treatment. *Theranostics* 9 (11), 3293–3307. doi:10.7150/thno.32867

Conflict of Interest: The authors declare that the research was conducted in the absence of any commercial or financial relationships that could be construed as a potential conflict of interest.

Publisher's Note: All claims expressed in this article are solely those of the authors and do not necessarily represent those of their affiliated organizations, or those of the publisher, the editors and the reviewers. Any product that may be evaluated in this article, or claim that may be made by its manufacturer, is not guaranteed or endorsed by the publisher.

frontiers in Cell and Developmental Biology

ORIGINAL RESEARCH
published: 04 January 2022
doi: 10.3389/fcell.2021.738916

Pyruvate Dehydrogenase Contributes to Drug Resistance of Lung Cancer Cells Through Epithelial Mesenchymal Transition

*Buse Cevatemre[1,2], Engin Ulukaya[3], Egemen Dere[2], Sukru Dilege[4] and Ceyda Acilan[1,4]**

[1]Research Center for Translational Medicine, Koc University, Istanbul, Turkey, [2]Department of Biology, Uludag University, Bursa, Turkey, [3]Department of Clinical Biochemistry, Istinye University Faculty of Medicine, Istanbul, Turkey, [4]School of Medicine, Koc University, Istanbul, Turkey

Recently, there has been a growing interest on the role of mitochondria in metastatic cascade. Several reports have shown the preferential utilization of glycolytic pathway instead of mitochondrial respiration for energy production and the pyruvate dehydrogenase (PDH) has been considered to be a contributor to this switch in some cancers. Since epithelial mesenchymal transition (EMT) is proposed to be one of the significant mediators of metastasis, the molecular connections between cancer cell metabolism and EMT may reveal underlying mechanisms and improve our understanding on metastasis. In order to explore a potential role for PDH inhibition on EMT and associated drug resistance, we took both pharmacological and genetic approaches, and selectively inhibited or knocked down PDHA1 by using Cpi613 and shPDHA1, respectively. We found that both approaches triggered morphological changes and characteristics of EMT (increase in mesenchymal markers). This change was accompanied by enhanced wound healing and an increase in migration. Interestingly, cells were more resistant to many of the clinically used chemotherapeutics following PDH inhibition or PDHA1 knockdown. Furthermore, the TGFβRI (known as a major inducer of the EMT) inhibitor (SB-431542) together with the PDHi, was effective in reversing EMT. In conclusion, interfering with PDH induced EMT, and more importantly resulted in chemoresistance. Therefore, our study demonstrates the need for careful consideration of PDH-targeting approaches in cancer treatment.

Keywords: epithelial mesenchymal transition, lung cancer, drug resistance, pyruvate dehydrogenase complex, cancer metabolism

OPEN ACCESS

Edited by:
Ozgur Kutuk,
Başkent University, Turkey

Reviewed by:
Anamaria Brozovic,
Rudjer Boskovic Institute, Croatia
Varisa Pongrakhananon,
Chulalongkorn University, Thailand

****Correspondence:***
Ceyda Acilan
cayhan@ku.edu.tr

Specialty section:
This article was submitted to Cell Death and Survival, a section of the journal Frontiers in Cell and Developmental Biology

Received: *09 July 2021*
Accepted: *13 December 2021*
Published: *04 January 2022*

Citation:
Cevatemre B, Ulukaya E, Dere E, Dilege S and Acilan C (2022) Pyruvate Dehydrogenase Contributes to Drug Resistance of Lung Cancer Cells Through Epithelial Mesenchymal Transition. Front. Cell Dev. Biol. 9:738916. doi: 10.3389/fcell.2021.738916

1 INTRODUCTION

The survival and growth of cancer cells usually involve changes in the metabolic pathways and reprogramming, in various cancer types, therefore dysregulated metabolism is considered as an important hallmark (Hanahan and Weinberg, 2011). Cancer cells have unique metabolic properties and there is a growing interest in elucidating the relationship between abnormal metabolic pathways and the progressive behaviors of cancer cells (Wei et al., 2020). The most well-described phenomenon is the Warburg effect (also known as aerobic glycolysis), in which glucose utilization becomes a priority for cancer cells even in the presence of sufficient oxygen

(Warburg, 1956a; Warburg, 1956b). This unique aerobic glycolysis might provide several selective advantages, including resistance to apoptosis and therapeutic strategies, acidification of the tumor microenvironment and thus increased tumor invasion and metastasis ability (Gatenby and Gillies, 2004).

The pyruvate dehydrogenase (PDH), the gatekeeper enzyme in glucose metabolism, produces acetyl-CoA by oxidatively decarboxylating pyruvate to fuel mitochondrial tricarboxylic acid cycle (TCA). It plays a critical role in the metabolic axis by separating pyruvate between glycolysis and the TCA. Inhibition of PDH in cancer cells promotes the Warburg effect, and confers aggressive properties to cells (McFate et al., 2008; Luo et al., 2019). Decarboxylation of pyruvate is considered to be the rate-limiting step and catalyzed by the pyruvate dehydrogenase E1 (PDHA1) which is the catalytic component of PDH (Rajagopalan et al., 2015). E1 is a heterotetramer of two α and two β subunits and the active site containing-E1α is encoded by the *PDHA1* gene (Patel and Korotchkina, 2001). PDHA1 dysregulation has been implicated in metabolic reprogramming (Liu F. et al., 2015; Li et al., 2016a; Liu et al., 2018; Liu et al., 2019). Decreased expression of PDHA1 was found to be an unfavorable prognostic factor in various types of cancer including ovarian (Li et al., 2016b), gastric (Liu et al., 2018), prostate (Zhong et al., 2017), lung (Cao et al., 2017), liver (Sun et al., 2019), and esophageal cancer (Zhong et al., 2015). Furthermore, knockout of PDHA1 resulted in higher stemness phenotype in prostate cancer (Zhong et al., 2017) and led to Warburg effect with aggressive traits in esophageal squamous cancer *in vitro* and *in vivo* (Liu et al., 2019).

PDHA1 activity can be inhibited by the pyruvate dehydrogenase kinases (PDKs). Not surprisingly, it has been reported that the upregulation of PDK activity may contribute, in part, to the Warburg effect, resulting in inactivation of PDH (Kim et al., 2007). In a study of Zhang et al. (2019), PDK1 was found to be elevated in cisplatin-resistant cells (ovarian cancer) compared to cisplatin naïve-parental cells. Silencing PDK1 in resistant cells resulted in increased sensitivity against cisplatin, reversal of epithelial mesenchymal transition (EMT) and decreased cell motility, suggesting that the enhanced aerobic glycolysis not only drives tumor growth, but also provides metastatic advantage to cancer cells by EMT.

EMT is an important process with a predominant role in multiple conditions (physiological and pathophysiological) and known to be associated with drug resistance (Shibue and Weinberg., 2017). The oncogenic EMT process enables epithelial cells to acquire mesenchymal characters (through up- and down-regulation of mesenchymal and epithelial markers, respectively), thus providing cancer cells with increased invasive and migratory capacities, and resistance to chemotherapy. Indeed, these features are important drivers of cancer progression (Derynck and Weinberg, 2019). EMT is considered to be a key process for the initiation of metastatic cascade by allowing epithelial cancer cells to invade the extracellular matrix, enter the blood stream and eventually grow in a different tissue. In this cascade, a continuous nutritional supplement is required, which is provided by blood flow and metabolic reprogramming of cells (Sciacovelli and Frezza, 2017). Currently, there is accumulating evidence supporting that transcription factors that play an essential role in the EMT process also have regulatory functions in metabolic reprogramming (Kang et al., 2019). Metastasis is responsible for 90% of cancer-related mortalities (Chaffer and Weinberg, 2011), reinforcing the significance of blocking EMT. Therefore, providing knowledge on metabolic players in this process might be exploited for improved cancer therapy.

Although a number of studies have highlighted the significance of PDH activity or PDHA1 to promote metabolism and growth in cancer cells, the relationship between PDH and EMT has not been elucidated. Specifically, we hypothesized that PDH inhibition or PDHA1 knockdown might play a role in EMT and chemoresistance and investigated how disruption of PDH activity influenced the molecular events triggering these changes using lung cancer cells as a model.

2 MATERIALS AND METHODS

2.1 Cell Culture

A549 cells were maintained in RPMI-1640 (Gibco, 21875-034) supplemented with 10% fetal bovine serum (Gibco, 10270-106) and 1% penicillin/streptomycin (Gibco, 15140-122). Cells were grown at 37°C in a humidified atmosphere with 5% CO_2.

2.2 Knockdown of PDHA1 Using shRNA

PDHA1 human shRNA lentiviral vector plasmid and the corresponding control backbone (PDHA1 Human shRNA Plasmid Kit, TL310532) was obtained from OriGene Technologies. Lentivirus was produced by co-transfecting the lentiviral vector, the packaging plasmid (PAX2), and the envelope plasmid (pMD2.G) into HEK-293T cells using Lipofectamine™ 3000 (Thermo Fisher Scientific, L3000015). Supernatants were collected 48 h after transfection and filtered through a 0.45 µm membrane. A549 cells were transduced with lentiviral supernatant (with 8 µg/ml polybrene, Sigma, TR-1003-G) and then selected with 2 µg/mL puromycin (Sigma, 540411) to obtain cells with stable knockdown of PDHA1.

2.3 Cell Proliferation Analysis

2.3.1 Sulforhodamine B (SRB) Assay

Cells were seeded on 96-well plates (3.5×10^3 per well) the day prior to drug exposure. At the end of the treatment, cells were fixed by using trichloroacetic acid (10%, Sigma, T6399) at 4°C for 1 h. Plates were washed with ddH_2O and allowed to dry at room temperature (RT). SRB (0.4%, Santa Cruz, sc-253615A) was used to stain the cells for 30 min and subsequently washed with 1% acetic acid (Sigma, 100063). The bound SRB dye was solubilized by using Tris base (10 mM, BioShop, TRS001). The optical density was measured at 564 nm with a microplate reader (FLASH Scan S12, Analytical Jena).

2.3.2 ATP Assay

Cell were seeded and treated as depicted in 2.3.1. ATP assay was performed as described previously (Karakas et al., 2015) and the content of ATP was measured by using a luminometer with a

measuring time of 1 s (FLx800, BioTek). The cell viability for both SRB (Abs) and ATP (RLU) assays was calculated by using the formula:

$$\%\text{Viability} = 100 \times \text{Treatment}_{(\text{Abs/RLU})} / \text{Control}_{(\text{Abs/RLU})}$$

2.3.3 xCELLigence Real Time Cell Analyzer (RTCA)

Cells were seeded on E-plates (3.5×10^3 per well, Roche) the day prior to drug exposure. Cell growth was monitored at 1 h intervals for 72–96 h by using xCELLigence real time cell analyzer (Roche). Cell index (CI) graphs were generated by using the RTCA software of the manufacturer.

2.3.4 Colony Formation Assay

A549 cells were seeded on 6-well plates (1×10^3) and cultured for additional 15 days. Culture media was changed every 3 days. After this period, cells were washed with PBS and fixed by using ice cold methanol at −20°C for 10 min. Crystal violet (0.05%, Sigma, C6158) was used to stain the cells for 15 min and subsequently washed twice with ddH_2O. Images of the colonies were taken by using an Olympus CKX41 inverted microscope.

2.4 Wound Healing

A549 cells were seeded on 12-well plates (1.2×10^5 per well) and after a day cells were wounded by scratching with a 10 µL tip. Wells were rinsed with PBS and fresh culture medium containing Cpi613/Devimistat (BioVision, 9464) was added on cells. The movement of untreated and treated (6.25–25 µM) cells in the wounded area were photographed by using an inverted microscope (Olympus CKX41) at 0, 12, 24, and 30 h.

2.5 Transwell Invasion Assay

Transwell assay was performed using the cell culture inserts (pore size 8 µm, BD353097). Briefly, inserts were coated with matrigel (0.4 mg/ml, Corning, 356234). After incubating at 37°C overnight, the Matrigel solidified and coated inserts were placed on 24-well plates. Harvested cells were seeded on the upper well in 1% FBS containing media and the lower wells were filled with complete media. After 24 h, insides of the inserts were brushed with wet cotton swab to remove non-invaded cells and invaded cells on the outside were fixed by using methanol, stained with crystal violet (0.05%). Bound violet as solubilized with acetic acid (10%) and the optical density was measured at 570 nm with a microplate reader (FLASH Scan S12, Analytical Jena).

2.6 Phalloidin Staining

A549 cells were seeded (1×10^4) on 8-well chamber slides (Corning, 354630). A day after cells were fixed by using 4% formaldehyde (Thermo Fisher Scientific, 28906) for 15 min at RT, permeabilized with 0.1% Triton X-100 for 10 min, and blocked with 3% BSA (Cell Signaling Technology, 9998) for 1 h. DyLight™ 554 phalloidin (Cell Signaling Technology, 13054) was used to stain F-actin (1:200 dilution in PBS) for 15 min at RT. Chamber slides then incubated with Prolong Gold Antifade Mountant containing DAPI (Thermo Fisher Scientific, P36931).

2.7 Annexin-V Staining

A549 cells were seeded on 6-well plates (1×10^5) the day prior to Cpi613 exposure (24, 48 and 72 h). After the treatment period, cells were detached by trypsinization and stained by using Annexin V/7-aminoactinomycin D at RT in the dark for 20 min (Annexin V & Dead Cell kit, Luminex, MCH100105). The percentage of apoptotic cells was calculated by Muse™ Cell Analyzer (Luminex).

2.8 qRT-PCR

RNA samples were extracted from cells using Total RNA Purification Kit (Jena Bioscience, PP-210L) and cDNA was synthesized from 500 ng total RNA using the SCRIPT cDNA Synthesis Kit (Jena Bioscience, PCR-511S). Subsequently 10 ng cDNA template was amplified using qPCR GreenMaster with UNG (Jena Bioscience, PCR-369L). β-Actin was used as reference control and real-time quantitative PCR was run on LightCycler 480 (Roche). The relative fold change in gene expressions were measured with the $2^{(-\Delta\Delta CT)}$ method.

2.9 SDS-PAGE and Western Blotting

Total proteins were extracted by using RIPA lysis buffer (Santa Cruz, sc-24948) containing protease inhibitor cocktail and sodium orthovanadate. PMSF was added at a final concentration of 2 mM (Sigma, P7626). Cells were lysed on ice for 30 min and subsequently the lysate was centrifuged to separate proteins (4°C, 15 min, 13.000 g). The resulting supernatant was quantified using BCA assay (Thermo Fisher Scientific, 23227). Samples were boiled (95°C, 7 min) after mixing with NuPAGE LDS sample buffer (Thermo Fisher Scientific, NP0007) and NuPAGE Sample reducing agent (Thermo Fisher Scientific, NP0004). Twenty µg of total protein were subjected to 12% SDS-PAGE (150 V, 50 min) and transferred onto a nitrocellulose membrane using the iBlot (Thermo Fisher Scientific, IB301001). After blocking the membranes with 5% non-fat dry milk (BioShop, SKI400) at RT for 1 h, primary antibodies (1:1000) were applied and incubated at 4°C overnight. Antibodies against e-cadherin (3195S), vimentin (5741S), actin (4970S), n-cadherin (13116), α-sma (14968S), mdrp-1 (72202S), mdr-1 (13978S), histone H3 (9715S), α-tubulin (2144S), p44/42-MAPK (4695), p38-MAPK (9212), p-c-jun (9164S), and glut1 (12939) were from Cell Signaling Technology and pdha1 (ab67592) from Abcam. Following washes in TBST, membranes were incubated with HRP-linked secondary antibody (1:2000, Cell Signaling Technology, 7074) at RT for 1 h and probed with Immobilon Forte Western HRP substrate (Merck, WBLUF0100), and imaged by Fusion FX-7 imaging system (Vilber Lourmat, France).

3 RESULTS

3.1 PDHi Inhibits the Growth of Cancer Cells

In order to examine the effect of PDHi (Cpi613/Devimistat) on cancer cell growth, its cytotoxicity was evaluated on a number of cells of different origins such as lung (A549), breast (MCF7) and colorectal (HT29) cancers. The viability of each cell line was significantly decreased in a time (24, 48 and 72 h) and concentration dependent (6.25–200 µM) manner in response to PDHi exposure

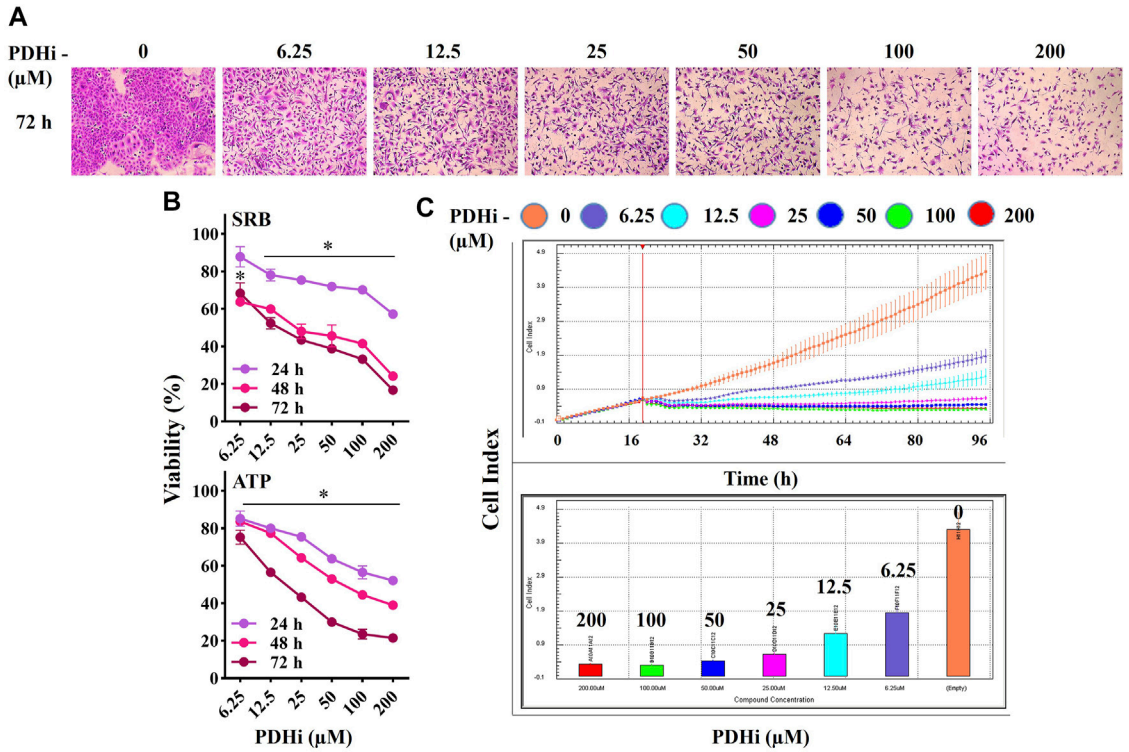

FIGURE 1 | PDHi treatment resulted in growth inhibition. **(A)** A549 cells were treated (72 h) with PDHi at indicated doses and after staining with SRB dye, cells were photographed under phase contrast microscope (magnification 100×). **(B)** The effect of PDHi on the growth of A549 cells was quantified by SRB and ATP viability assays. Data are presented as mean ± SEM. **(C)** The cell index (CI) values for 0–200 μM (represented by different colours) of PDHi on A549 cells was generated by real time cell analyzer (RTCA). * Significantly difference compared to untreated cells ($p < 0.0001$).

(**Figure 1**) (**Supplementary Figures S1–S3**). The IC_{50} values at 72 h (based on ATP assay) were 18.6, 99.2, and 54.5 μM against A549, MCF7, and HT29, respectively. To differentiate PDHi-induced cytotoxic, cytostatic and antiproliferative effects, real time cell monitoring was used for all of the cells. While lower doses (25–100 μM) were mostly cytostatic, higher doses (200 μM) led to cytotoxicity in all cell lines tested (**Figure 1C**; **Supplementary Figures S2C, S3C**). The most responsive of these lines (A549) was chosen for further functional studies. Indeed, PDHi-induced growth inhibition correlated with apoptosis induction as evidenced by DNA fragmentation, Annexin-V staining, and rescue of cell death *via* pretreatment with z-VAD-FMK, a pan-caspase inhibitor, in A549 cells (**Supplementary Figure S4**). Based on these observations, sublethal doses of PDHi (6.25, 12.5 and 25 μM) were chosen to analyze EMT-related phenotypes for further studies. At these selected doses of PDHi, flow cytometric analysis revealed G_2/M-phase cell accumulation in A549 cells, suggesting a mechanism for the growth suppressive effect of PDHi (**Supplementary Figures S5A–C**).

3.2 PDHi Induces Epithelial Mesenchymal Transition-Like Phenotype in A549 Lung Cancer Cells

To explore the effect of PDHi on cell morphology, PDHi-treated A549, HT29, MCF7 cells were monitored using phase contrast microscopy. Interestingly, while untreated cells grew in tight clumps and have the cobblestone appearance that is a characteristic of epithelial cells, inhibition of PDH resulted in elongated/irregular fibroblastic appearance, suggesting mesenchymal-like phenotypes may have been triggered in response to PDHi (**Figure 2**; **Supplementary Figure S6**). Since cells need to acquire additional cell-matrix contact points during EMT, the remodeling of actin cytoskeleton was evaluated following inhibition of PDH *via* phalloidin staining (**Figure 2B**). As expected, untreated epithelial cells were organized in cortical thin bundles. In contrast, PDHi treatment induced bundling of actin filaments into thick and elongated contractile stress fibers at the cell attachment sites, as typically seen in transdifferentiated mesenchymal cells (**Figure 2B**). Therefore, our morphological observations led us to inquire whether other molecular or biological changes associated with EMT could also be observed following PDH inhibition. In order to pursue this aim, we investigated the expressions of e-cadherin and vimentin (epithelial and mesenchymal markers, respectively) using western blotting. Consistent with morphological observations, inhibition of PDH resulted in increased vimentin expression and decreased e-cadherin expression, supporting induction of EMT-like phenotypes (**Figure 3A**; **Supplementary Figure S7**). We determined the expressions of kinases (PDK1-4) that play an important role in the regulation of the PDH complex. Among these inactivating kinases, we found that expression of PDK4 was significantly

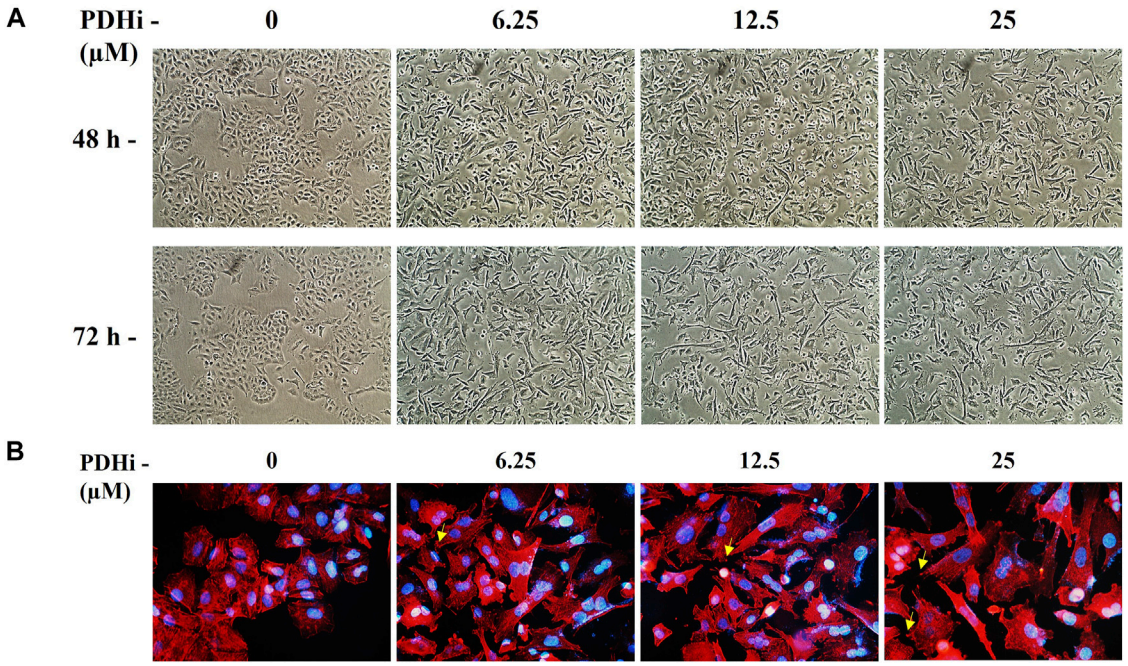

FIGURE 2 | PDHi-induced morphological changes in A549 cancer cells. **(A)** Cells treated with PDHi for 48–72 h (**Supplementary Figure S6** for morphological changes in HT29 and MCF7 cancer cells) at indicated doses and were photographed under phase contrast microscope (magnification 100×). **(B)**. Phalloidin staining indicated F-actin (red) reorganization in PDHi treated A549 cells. DAPI was used to stain DNA (blue, magnification 400×).

increased (at all the time points tested, 6–24 h) in a dose-dependent manner (**Supplementary Figure S8**). High expression of PDK4 can have both oncogenic or tumor suppressive properties, and has been previously associated with EMT, albeit with controversial results (Atas et al., 2020). Our findings support an oncogenic role for PDK4 in response to PDH suppression. Indeed, more work should be performed to determine the exact molecular mechanisms as to how these cellular events are linked.

It has been well demonstrated that EMT confers migratory and metastatic properties to cancer cells (Yang and Weinberg, 2008). Therefore, we performed wound healing and invasion assays to investigate the ability of lung cancer cells to migrate/invade after they were subjected to different concentrations of PDHi. As expected, greater migration was observed in PDHi-treated cell to untreated cells in wound healing migration assays (**Figure 3B**). PDHi-treated A549 cells showed approximately 2-fold increase in invasion compared to untreated cells (**Figure 3C**). These results demonstrate that the PDHi-induced EMT phenotype significantly accelerates cancer cell migration and invasion *in vitro*.

3.3 TGF-β Signaling May Be Involved in PDHi-Induced Epithelial Mesenchymal Transition

Among the cues in the extracellular microenvironment, transforming growth factor β (TGFβ) is known to be a prominent inducer of EMT through cellular pathways involving several transcription factors. To understand whether TGFβ pathway is important for the EMT related changes seen in response to PDHi, we used an inhibitor targeting TGFβRI, SB-431542 (TGFβRI-i) and determined whether PDHi-induced EMT can be reversed *via* TGFβ inhibition. Supporting involvement of the TGFβ pathway, addition of TGFβRI-i was sufficient to significantly reduce vimentin expression (**Figure 4A**). Next, we then examined the ability of TGFβRI-i to block the PDHi-mediated inhibition of cell proliferation. PDHi efficiently suppressed the growth of A549 cells, whereas TGFβRI-i significantly blocked PDHi-induced growth inhibition as determined by both SRB and ATP cell viability assays (**Figure 4B**). Furthermore, TGFβRI-i reverted PDHi-induced elongated/irregular fibroblastic morphology to an epithelial-like morphology (**Figure 4C**).

We hypothesized that if PDHA1 inhibition leads to drug resistance *via* triggering EMT, suppressing EMT may result in reversion of the drug resistance. Since TGFβ is a well-known inducer of EMT, we used RepSox (TGFβRI) to suppress it. shPDHA1-induced cells were subjected to cisplatin in combination with RepSox and then cell death was measured to determine whether cells were more sensitive to cisplatin. Consistent with our model, PDH inhibition did not lead to cisplatin resistance when EMT was inhibited *via* TGFβ inhibitor (**Supplementary Figure S9**).

This data prompted us to consider whether there is a PDH-related regulation when EMT is stimulated. For this purpose, we induced EMT in A549 cells by applying TGFβI and then

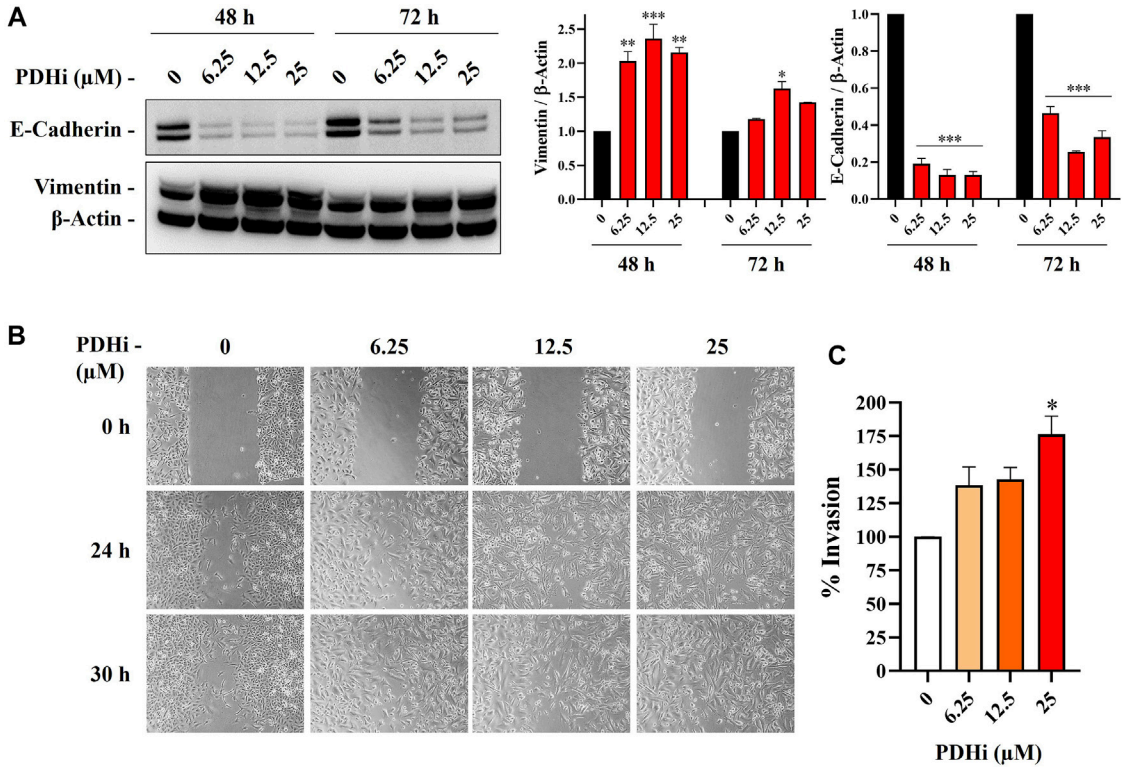

FIGURE 3 | PDHi led to the induction of EMT phenotype. **(A)** Western blot analysis showing the decrease of E-cadherin (epithelial marker) and increase in vimentin (mesenchymal marker) in PDHi treated A549 cells. **(B)** Wound healing assay was performed in A549 cells when cultured with PDHi at indicated doses and time points. The results are shown at 100× magnification. **(C)** Transwell invasion assay was conducted on PDHi treated (24 h) A549 cells. The invaded cells were stained and counted. *Significantly difference compared to untreated cells (*$p < 0.01$, **$p < 0.001$, ***$p < 0.0001$).

determined the expression levels of PDH genes (namely, PDHA1, PDHB, and PDHX) by qRT-PCR. Interestingly, we observed a reduction in transcript levels in these genes upon TGFβI treatment (**Supplementary Figure S10**). Therefore, apparently there is two sided feedback between PDH and EMT. However, it is not clear whether this is a direct effect or through other molecular players.

Furthermore, among the SMAD proteins of the canonical TGFβ signaling pathway, we looked at the expressions of SMAD2, 3, and 4 following PDH inhibition. We found that only SMAD4 expression decreased in a dose- and time-dependent manner (**Supplementary Figure S11**). Consistent with our data, previous research has shown that SMAD4 reduction is associated with phenotypes such as tumor progression and metastasis in some cancers including lung cancer (Fukuchi et al., 2002; He et al., 2011; Tan et al., 2021), therefore is supportive with our findings of PDH inhibition leading to a more aggressive phenotype.

3.4 PDHi Confers Resistance to Chemotherapeutic Drug-Induced Cell Death

Since the acquisition of EMT phenotype generally correlates with chemoresistance, we measured the survival of PDHi-pretreated cells in response to treatment with commonly used chemotherapeutic drugs. Consistent with EMT-like changes, inhibition of PDH increased resistance of cancer cells to all of the drugs tested in this study, while cell viability was drastically reduced in non-treated cells upon treatment with the cytotoxic agents (cisplatin, doxorubicin, etoposide, 5-FU, and gemcitabine) (**Figure 5**; **Supplementary Figure S12**). Since the mechanism of action of these drugs are different from each other, this finding suggested a more general mechanism for cellular protection such as increase in survival signals or inhibition of apoptotic pathways, which will be examined further.

3.5 Knockdown of PDHA1 Induces Epithelial Mesenchymal Transition-Like Morphological Changes

To explore whether observed effect is directly a result of PDH inhibition or a consequence of some off-target phenotype, we established a number of PDHA1 knockdown clones derived from A549 cells. We validated our cells by showing the significant reduction in protein expression levels of PDHA1 in shPDHA1 group of A549 cells compared with the control (shCtrl) cells (**Figure 6A**). When grown to confluence,

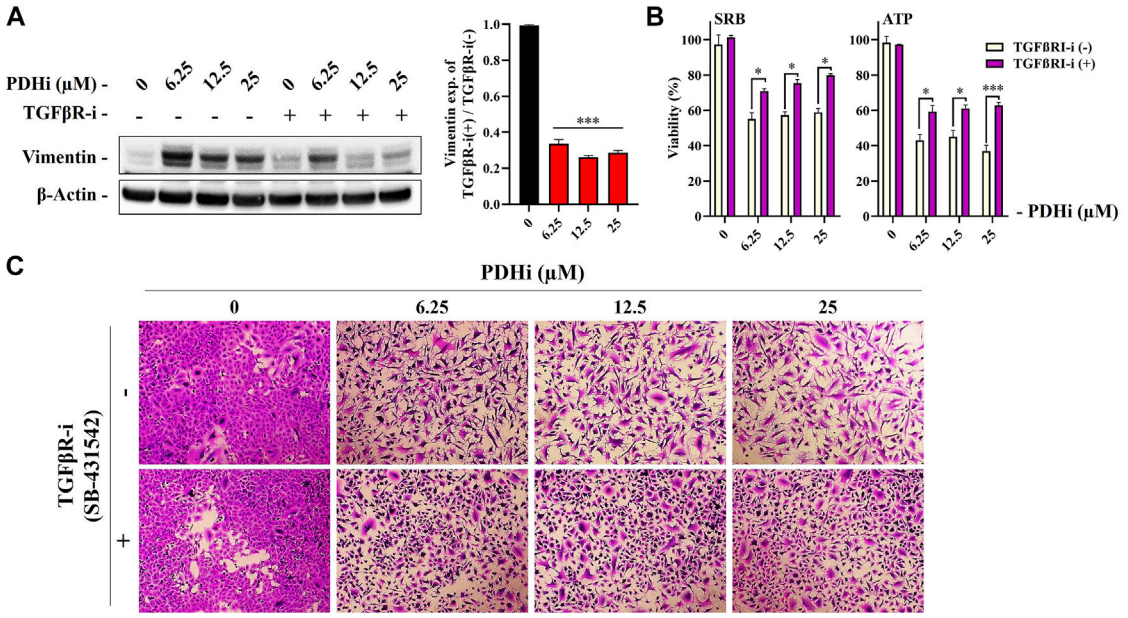

FIGURE 4 | Treatment with a TGFβRI inhibitor (SB-431542) reversed PDHi-induced vimentin expression and morphological changes. The cells were co-incubated with 2.5 μM of TGFβRI-i and PDHi for 72 h. **(A)** Treated cells were analyzed by western blot for the expression levels of Vimentin and β-Actin was used as a loading control. Data are presented as mean ± SEM. *Significantly difference compared to PDHi-alone (***$p < 0.0001$) **(B)** Rescue of growth inhibition was analyzed by SRB and ATP viability assays. Data are presented as mean ± SEM. *Significantly difference compared to PDHi-alone (*$p < 0.01$, ***$p < 0.0001$). **(C)** Morphology of PDHi and/or TGFβRI-i treated cells for 72 h and cells were visualized by using the SRB dye (magnification 100×).

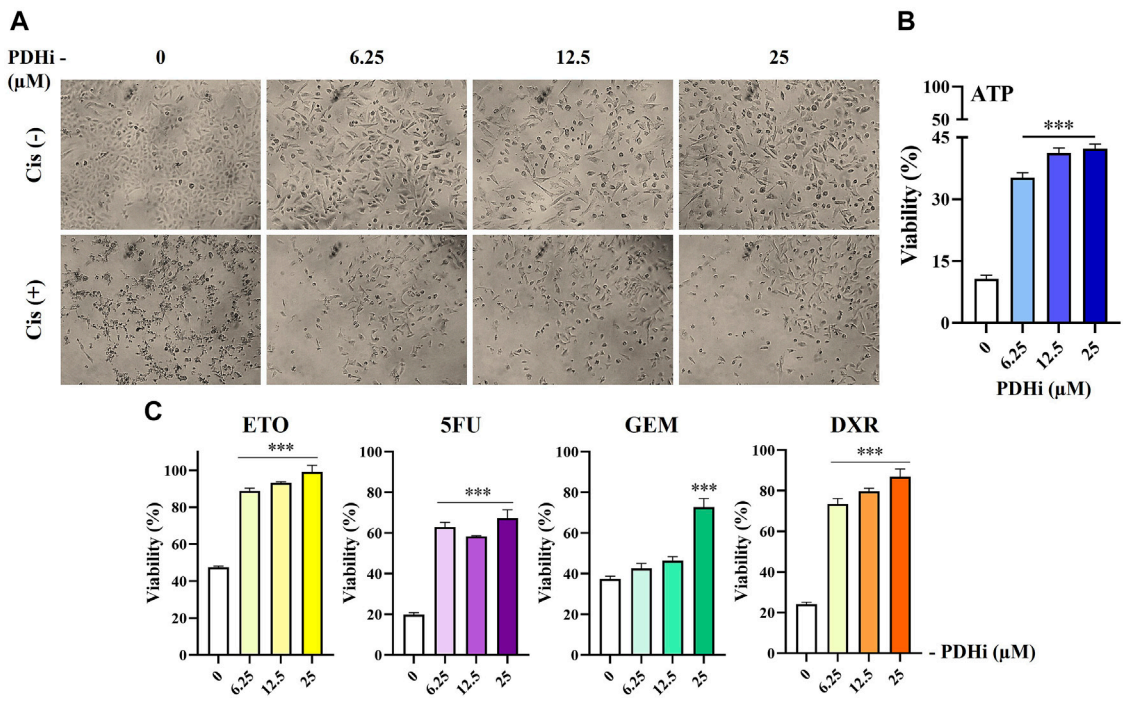

FIGURE 5 | PDHi treatment decreased the chemotherapeutic drug sensitivity of A549 cells. **(A–C)** PDHi pretreated (6.25, 12, 25 μM) or non-pretreated (0 μM) A549 cells were exposed to Cisplatin (25 μM) for 72 h, and **(B,C)** the cell viability was examined by ATP assay. Data are presented as mean ± SEM. *Significantly difference compared to 0 μM, one-way ANOVA with subsequent Tukey test (***$p < 0.0001$).

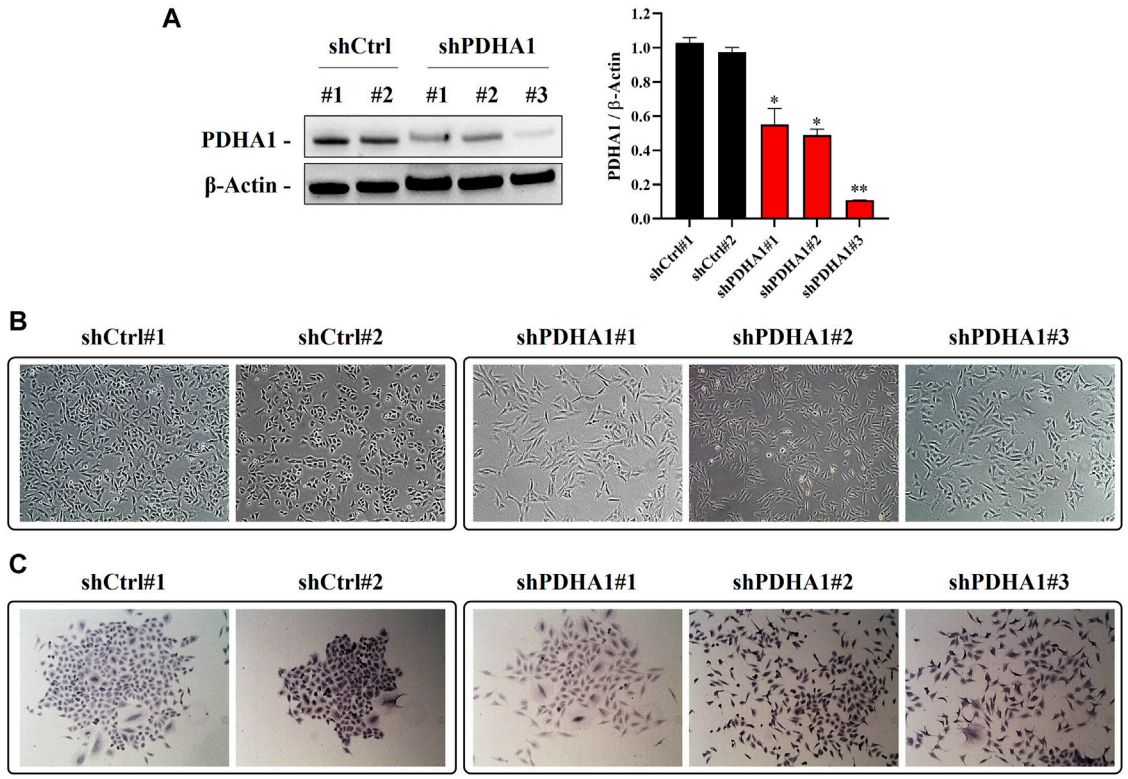

FIGURE 6 | PDHA1-silenced lung cancer cells exhibited morphological changes. **(A)** Knockdown (stable) efficiency of shPDHA1 and the control (shCtrl) vectors in A549 lung cancer cells was determined *via* western blotting to confirm PDHA1 protein expression. Data are presented as mean ± SEM. *Significantly difference compared to shCtrl cells (*$p < 0.01$, **$p < 0.001$) **(B)** ShCtrl cells showed an epithelioid, cobblestone rounded appearance. On the contrary, the phenotypic changes in shPDHA1 cells includes loss of cell polarity and a spindle-like morphology (magnification 100×). **(C)** shPDHA1 cells showed scattered morphology as compared with the control backbone transfected shCtrl cells (magnification 200×).

shPDHA1 cells did neither form a monolayer nor exhibited epithelial, cobblestone-like morphology as seen in shCtrl cells, but rather displayed a spindle-shaped mesenchymal phenotype and acquired a spread morphology (**Figures 6B,C**). The effect of PDHA1 silencing on lung cancer cell growth/proliferation was also explored by performing doubling assays. As indicated in **Supplementary Figure S13**, the doubling of cells was significantly slower in PDHA1 knockdown group compared with those in the shCtrl group.

To confirm if the cytoskeletal changes observed after treatment with the PDHi is also valid following silencing of PDHA1, the stress fibers resulted from F-actin reorganization was examined by phalloidin staining. As seen before, shCtrl cells showed cortical actin staining, whereas the shPDHA1 cells exhibited elongated F-actin stress fibers (**Figure 7A**). Similar to PDHi, expression of e-cadherin was found to be downregulated, whereas mesenchymal proteins, n-cadherin, vimentin and α-SMA, were upregulated after PDHA1 knockdown as compared to shCtrl cells (**Figure 7B**). Once again, a greater migration capacity was observed in PDHA1 knockdown cells as compared to shCtrl cells in wound healing assay (**Figure 7C**). Furthermore, transwell invasion assay showed increased number of invading cells following PDHA1 silencing (approximately 1.5 fold) compared to that of shCtrl cells (**Figure 7D**). Cumulatively, these results favor phenotypes associated with EMT in response to inhibition or silencing of PDHA1 activity.

3.6 Knockdown of PDHA1 Expression Confers Chemoresistance

We next elucidated whether PDHA1 accounts for chemoresistance. For this purpose, ATP viability assay was used to evaluate the chemoresistance between shCtrl and shPDHA1 cells. Cells were exposed to chemotherapeutic drugs (paclitaxel, docetaxel, pemetrexed, and 5FU) that are commonly used for the treatment for lung cancer. The results demonstrated that cells treated with shPDHA1 displayed significantly better survival ability than shCtrl cells (**Figure 8A**).

Aberrant activation of signaling pathways of Erk MAPK and p38 MAPK was shown to be essential for drug resistance, EMT and growth of cancer cells (Li et al., 2016c). Abnormalities in MAPK signaling have been implicated to be required in cancer development and progression (Dhillon et al., 2007). To identify which signaling pathway was mediated, the phosphorylation

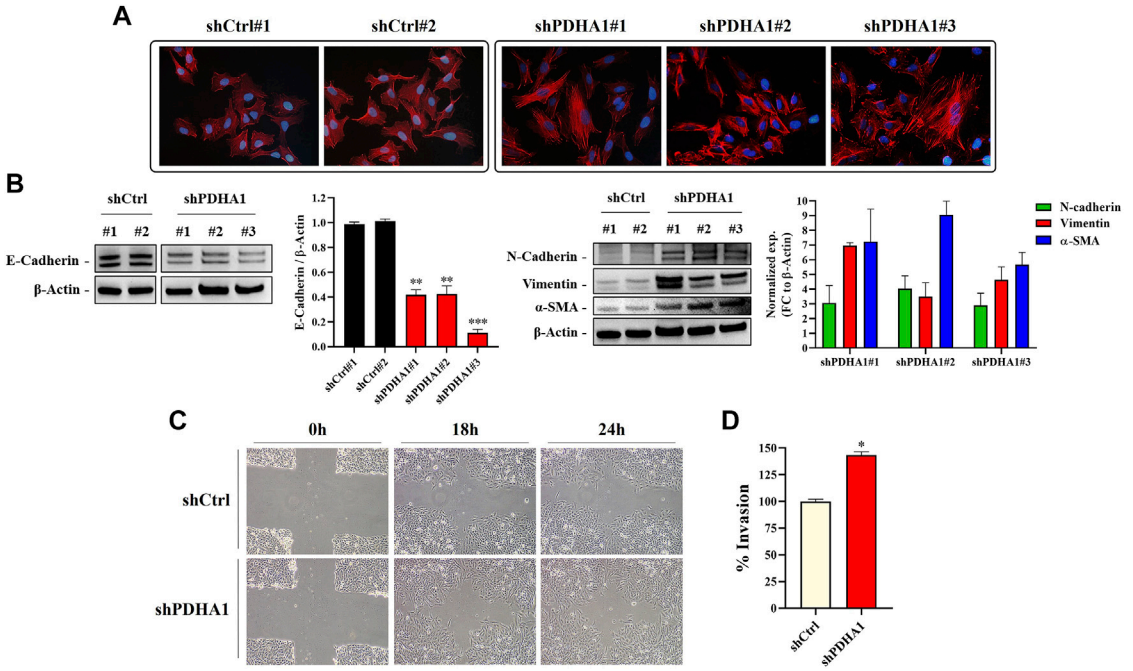

FIGURE 7 | PDHA1 knockdown induced EMT features in human lung cancer cells. **(A)** Phalloidin staining indicated F-actin (red) reorganization in shPDHA1 and shCtrl cells. DAPI was used to stain DNA (blue, magnification 400×). **(B)** Western blot analysis showing the loss of E-cadherin (epithelial marker) and the increase in N-cadherin, vimentin, and α-SMA (mesenchymal markers) in shPDHA1 cells. *Significantly difference compared to shCtrl cells (**$p < 0.001$, ***$p < 0.0001$) **(C)** Wound healing assay was performed in shPDHA1 and shCtrl cells. The results are shown at 100× magnification. **(D)** Transwell invasion assay was conducted on shPDHA1 and shCtrl cells for 24 h. The invaded cells were stained and counted. *Significantly difference compared to shCtrl cells (*$p < 0.01$).

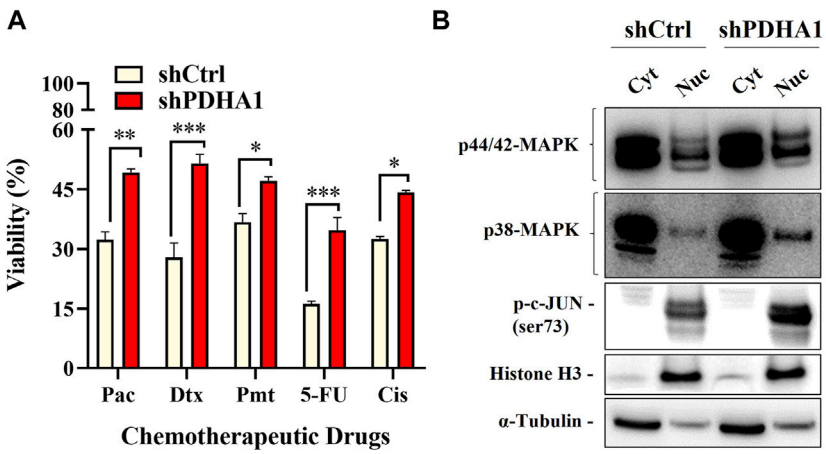

FIGURE 8 | PDHA1 knockdown induced chemoresistance in lung cancer cells. **(A)** shPDHA1 cells are more chemoresistant than shCtrl cells at individual doses of paclitaxel, docetaxel, pemetrexed, and 5FU, as shown by ATP viability assay. *Significantly difference compared to shCtrl cells (*$p < 0.05$, **$p < 0.001$, ***$p < 0.0001$) **(B)** p44/42 MAPK (Erk1/2), p38-MAPK, p-c-JUN proteins in shCtrl and shPDHA1 cells were determined by western blotting.

levels of p44/42 MAPK (Erk1/2) and p38 were examined in shPDHA1 cells. Interestingly, the phosphorylation levels of these proteins were elevated remarkably in PDHA1 knockdown cells, suggesting that in addition to increase in drug efflux, proliferative signals are also stimulated in response to inhibition of PDHA1 (**Figure 8B**).

4 DISCUSSION

The goal of this study was to investigate whether PDH, the gate-keeper of mitochondria, is involved in EMT. Mitochondrial dysfunction is shown to be positively correlated with increased aggressiveness and metastatic

potential in cancer (Lunetti et al., 2019). mtDNA depletion induced-mitochondrial dysfunction induced EMT in human mammary epithelial cells (MCF7 and MCF10A) (Guha et al., 2014). In support of this finding, downregulation of mitochondrial genes was found to be associated with poor clinical outcome across 20 different types of solid cancers (TCGA) and correlates with the expression of EMT-gene signature (Gaude and Frezza, 2016). Furthermore, EMT has been reported as a prominent phenotype in tumors harboring mutations in enzymes of the TCA cycle. For instance, accumulation of fumarate caused by the loss of fumarate hydratase (FH), resulted in EMT signatures (Sciacovelli et al., 2016). Similarly, silencing FH increased the clonogenicity and enhanced the migratory and invasive potentials of nasopharyngeal cancer cells (He et al., 2016). Cells deficient in succinate dehydrogenase (SDH), another enzyme that functions in TCA, displayed an EMT-associated metastatic phenotype (Loriot et al., 2015). The relationship between SDHB loss and EMT was also shown in colon (Wang et al., 2016) and ovarian cancer (Aspuria et al., 2014). The mutations in isocitrate dehydrogenase mutations can lead to the production and accumulation of produce 2-hydroxyglutarate (2-HG), which was shown to induce EMT. Grassian et al. (2012) reported a direct correlation between intracellular 2-HG levels and EMT characteristics. Citrate synthase (CS) is another TCA cycle enzyme that is associated with EMT. CS knockdown induced morphological changes consistent with EMT features in cervical cancer and resulted in enhanced metastasis and proliferation in *in vitro* and *in vivo* models. (Lin et al., 2012).

In accordance with these studies, we demonstrated that PDH inhibition or PDHA1 knockdown resulted in morphological and molecular changes (increase in the expression of vimentin and a decrease in the expression of E-cadherin) consistent with the mesenchymal phenotype. The present study also demonstrated that administration of PDHi may promote these EMT-like changes in A549 lung cancer cells, in part *via* the activation of TGFβ signaling, as TGFβRI-i was sufficient to significantly reduce vimentin expression and revert PDHi-induced elongated/irregular fibroblastic morphology to an epithelial-like morphology. The observation of increased cell migration and invasion of PDHi-treated or shPDHA1 cells was also consistent with these results. Although the underlying mechanism is not clear, it is most likely due to the activation of TGFβ pathway. In addition, these cells grew more slowly compared to the untreated/shCtrl cells. Mechanisms underlying EMT-induced drug resistance may include slow growth rate (Zhang and Weinberg, 2018). It was shown that slowly dividing pancreatic cell subpopulations show an expression profile consistent with CSC (cancer stem cell) and EMT signatures (Dembinski and Krauss, 2009). In another study, cell proliferation has been shown to be impaired when Snail (an EMT-inducing transcription factor) was expressed in cells (Vega et al., 2004). The reported Snail-driven mechanism includes the impairment of transition from early to late G_1 by maintaining low levels of Cyclins D and the blockage of G_1/S transition by maintaining high levels of p21. While the drug resistance phenotype observed in our study might be a result of EMT trigger through PDH inhibition, we cannot rule out the fact that G_2/M accumulation (**Supplementary Figure S5**) could have also contributed to the resistance outcome.

It has been shown that EMT conferred to drug resistance of NSCLC (Thomson et al., 2005; Rho et al., 2009) and TGFβ is a pivotal driver of these multistep process (Hua et al., 2020). Accordingly, we hypothesized whether PDH could contribute to the chemoresistance in cancer cells. Consistent with their EMT characteristics, PDHi or shPDHA1 treated cells showed less sensitivity to cisplatin (compared with untreated/shCtrl cells) and to other chemotherapeutic drugs used in this study. The previous reports and our observations together confirmed that the NSCLC with the EMT phenotype is prone to develop resistance to various drugs, including cisplatin (Wang et al., 2018). Although the underlying mechanism was not clear, our study has confirmed the relationship between drug resistance and EMT in A549 cells.

In cells, the mitogen-activated protein kinase (MAPK) signaling cascade allows cells to transduce extracellular signals into appropriate adaptive intracellular responses and this network is considered to be associated with EMT (Gui et al., 2012). In addition to Smad signaling pathways, TGFβ can also activate a variety of non-Smad signaling pathways (Ras, MAPKs, PI3K/Akt) which are shown to be also associated with TGFβ-induced EMT (Bakin et al., 2002; Xie et al., 2004; Tavares et al., 2006). In addition, studies have found Erk1/2 to be involved in tumour chemoresistance (Liu Q.-H. et al., 2015). Aberrant activation of Erk signaling (triggered by Erk2 amplification) was shown to be the underlying mechanism for acquired resistance against EGFR inhibitors in NSCLC (Ercan et al., 2012). Zheng et al. (2013) showed that gemcitabine resistant pancreatic cancer cells (Panc1) constitutively produced high levels of pERK1/2 (p44/42 MAPK). Likewise, when we manipulated PDHA1 in A549 cells, p44/42 and p38 signaling pathways were also triggered. With regard to whether PDHA1-induced EMT dependent on these pathways, subsequent research is necessary to confirm these findings.

In the study by Cao et al., 196 of NSCLC tissues and adjacent normal tissues were immunohistochemically detected and the correlation between PDHA1 expression and the pathological characteristics of NSCLC was examined. Their results suggested that expression of PDHA1 was related to differentiation degree of tissues, lymphatic metastasis and TNM staging. Specifically, the expression of PDHA1 protein in patients with high and intermediate differentiation was higher compared with low differentiated ones. Patients without lymphatic metastasis showed higher expression of PHDA1 protein than those with it. Additionally, patients in stage I and II had higher expression of PDHA1 protein compared to those in stage III and IV, suggesting that the lower expression of PDHA1 was associated with poor prognosis in NSCLC patients. In the same study, the overall survival rate was significantly different with a reported survival of 78.9% in the PDHA1-positive group, and 60.0% in the PDHA1-negative group.

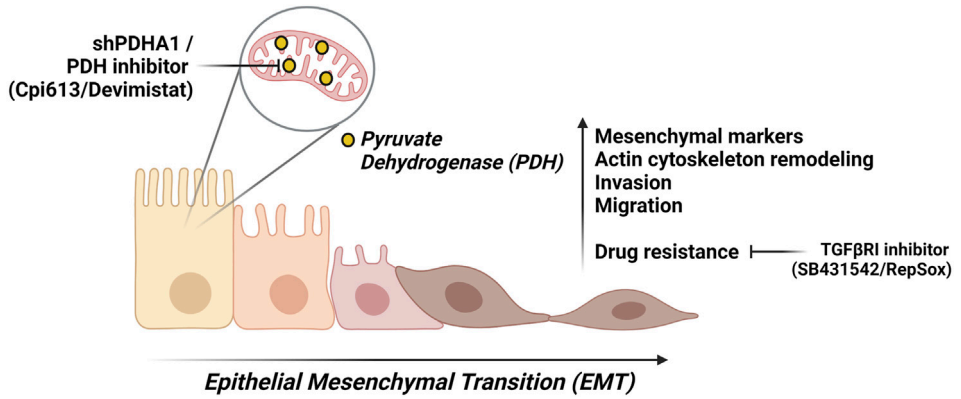

FIGURE 9 | A summary of this study. We suggest that PDH inhibition either through chemical inhibitor (Devimistat) or shPDHA1, leads to EMT-like phenotypes in lung cancer cells. These phenotypes include an increase in migration capability and invasion. Furthermore, PDH inhibition confers to resistance to several chemotherapeutic drugs, and this can be reverted *via* inhibition TGFβ pathway. Created with BioRender.

Our results suggest that PDHA1 may affect the lung cancer cell proliferation, invasion, migration, and chemoresistance, thereby affecting lung cancer progression. Although the precise role of PDHA1 in EMT process remains to be elucidated, the results from our study support that loss of PDHA1 or inhibition of PDH may act as an EMT-inducer. We cannot refer to a single molecule that is responsible for our observations. However, it is probably a cumulative series of events that lead to EMT upon PDH inhibition. Additionally, our finding proposes a mechanism by which cells treated with PDHi or shPDHA1 may acquire chemoresistance by undergoing EMT (**Figure 9**). Inhibiting or reversing the EMT process may cause re-sensitization of chemoresistant cells. Collectively, the above results suggest that the use of EMT-inhibitors in combination with PDHi's could become a rational strategy for the treatment of solid tumors especially lung cancer.

DATA AVAILABILITY STATEMENT

The original contributions presented in the study are included in the article/**Supplementary Material**, further inquiries can be directed to the corresponding author.

AUTHOR CONTRIBUTIONS

BC, EU, and AC contributed to the study conception and design. BC performed the experiments and wrote the manuscript. All authors read and approved the submitted version.

FUNDING

This study was funded by the Research Fund of TUBITAK (The Scientific and Technological Research Council of Turkey) and Research Fund of Uludag University under grant numbers of 115Z124 and DD(F)_2016/8, respectively. We also appreciate the Scientific Research Projects Coordination Unit of Uludag University for the financial support (grant number: BUAP(T)-2016/4). This work was also supported by Koç University School of Medicine (KUSOM).

ACKNOWLEDGMENTS

The authors gratefully acknowledge that they have benefited from the services and facilities of Koç University Research Center for Translational Medicine (KUTTAM), funded by Republic of Turkey Ministry of Development (Presidency of Strategy and Budget). The content is solely the responsibility of the authors and does not reflect the official views of the Ministry of Development. The figure created using BioRender.com is licensed for publication (**Figure 9**: ZS23ADRU67).

SUPPLEMENTARY MATERIAL

The Supplementary Material for this article can be found online at: https://www.frontiersin.org/articles/10.3389/fcell.2021.738916/full#supplementary-material

REFERENCES

Aspuria, P. P., Lunt, S. Y., Väremo, L., Vergnes, L., Gozo, M., Beach, J. A., et al. (2014). Succinate Dehydrogenase Inhibition Leads to Epithelial-Mesenchymal Transition and Reprogrammed Carbon Metabolism. *Cancer Metab.* 2 (1), 21–15. doi:10.1186/2049-3002-2-21

Atas, E., Oberhuber, M., and Kenner, L. (2020). The Implications of PDK1-4 on Tumor Energy Metabolism, Aggressiveness and Therapy Resistance. *Front. Oncol.* 10, 583217. doi:10.3389/fonc.2020.583217

Bakin, A. V., Rinehart, C., Tomlinson, A. K., and Arteaga, C. L. (2002). p38 Mitogen-Activated Protein Kinase Is Required for TGFβ-Mediated Fibroblastic Transdifferentiation and Cell Migration. *J. cell Sci.* 115 (15), 3193–3206. doi:10.1242/jcs.115.15.3193

Cao, J., Wu, Q., Lv, Z., Zeng, X., Dang, Q., and Suo, Z. (2017). Studies on the PDHA1 Protein Expression and its Correlation with Clinicopathological Characteristics and Prognosis in NSCLC. *Int. J. Clin. Exp. Med.* 10 (6), 9771–9778.

Chaffer, C. L., and Weinberg, R. A. (2011). A Perspective on Cancer Cell Metastasis. *Science* 331 (6024), 1559–1564. doi:10.1126/science.1203543

Dembinski, J. L., and Krauss, S. (2009). Characterization and Functional Analysis of a Slow Cycling Stem Cell-like Subpopulation in Pancreas Adenocarcinoma. *Clin. Exp. Metastasis* 26 (7), 611–623. doi:10.1007/s10585-009-9260-0

Derynck, R., and Weinberg, R. A. (2019). EMT and Cancer: More Than Meets the Eye. *Dev. cell* 49 (3), 313–316. doi:10.1016/j.devcel.2019.04.026

Dhillon, A. S., Hagan, S., Rath, O., and Kolch, W. (2007). MAP Kinase Signalling Pathways in Cancer. *Oncogene* 26 (22), 3279–3290. doi:10.1038/sj.onc.1210421

Ercan, D., Xu, C., Yanagita, M., Monast, C. S., Pratilas, C. A., Montero, J., et al. (2012). Reactivation of ERK Signaling Causes Resistance to EGFR Kinase Inhibitors. *Cancer Discov.* 2 (10), 934–947. doi:10.1158/2159-8290.cd-12-0103

Fukuchi, M., Masuda, N., Miyazaki, T., Nakajima, M., Osawa, H., Kato, H., et al. (2002). Decreased Smad4 Expression in the Transforming Growth Factor-β Signaling Pathway during Progression of Esophageal Squamous Cell Carcinoma. *Cancer* 95 (4), 737–743. doi:10.1002/cncr.10727

Gatenby, R. A., and Gillies, R. J. (2004). Why Do Cancers Have High Aerobic Glycolysis? *Nat. Rev. Cancer* 4 (11), 891–899. doi:10.1038/nrc1478

Gaude, E., and Frezza, C. (2016). Tissue-specific and Convergent Metabolic Transformation of Cancer Correlates with Metastatic Potential and Patient Survival. *Nat. Commun.* 7 (1), 13041–13049. doi:10.1038/ncomms13041

Grassian, A. R., Lin, F., Barrett, R., Liu, Y., Jiang, W., Korpal, M., et al. (2012). Isocitrate Dehydrogenase (IDH) Mutations Promote a Reversible ZEB1/microRNA (miR)-200-dependent Epithelial-Mesenchymal Transition (EMT). *J. Biol. Chem.* 287 (50), 42180–42194. doi:10.1074/jbc.m112.417832

Guha, M., Srinivasan, S., Ruthel, G., Kashina, A. K., Carstens, R. P., Mendoza, A., et al. (2014). Mitochondrial Retrograde Signaling Induces Epithelial-Mesenchymal Transition and Generates Breast Cancer Stem Cells. *Oncogene* 33 (45), 5238–5250. doi:10.1038/onc.2013.467

Gui, T., Sun, Y., Shimokado, A., and Muragaki, Y. (2012). The Roles of Mitogen-Activated Protein Kinase Pathways in TGF-β-Induced Epithelial-Mesenchymal Transition. *J. signal transduction* 2012, 1–10. doi:10.1155/2012/289243

Hanahan, D., and Weinberg, R. A. (2011). Hallmarks of Cancer: the Next Generation. *Cell* 144 (5), 646–674. doi:10.1016/j.cell.2011.02.013

He, S. M., Zhao, Z. W., Wang, Y., Zhao, J. P., Wang, L., Hou, F., et al. (2011). Reduced Expression of SMAD4 in Gliomas Correlates with Progression and Survival of Patients. *J. Exp. Clin. Cancer Res.* 30 (1), 70–77. doi:10.1186/1756-9966-30-70

He, X., Yan, B., Liu, S., Jia, J., Lai, W., Xin, X., et al. (2016). Chromatin Remodeling Factor LSH Drives Cancer Progression by Suppressing the Activity of Fumarate Hydratase. *Cancer Res.* 76 (19), 5743–5755. doi:10.1158/0008-5472.can-16-0268

Hua, W., Ten Dijke, P., Kostidis, S., Giera, M., and Hornsveld, M. (2020). Tgfβ-induced Metabolic Reprogramming during Epithelial-To-Mesenchymal Transition in Cancer. *Cell. Mol. Life Sci.* 77 (11), 2103–2123. doi:10.1007/s00018-019-03398-6

Kang, H., Kim, H., Lee, S., Youn, H., and Youn, B. (2019). Role of Metabolic Reprogramming in Epithelial-Mesenchymal Transition (EMT). *Ijms* 20 (8), 2042. doi:10.3390/ijms20082042

Karakas, D., Cevatemre, B., Aztopal, N., Ari, F., Yilmaz, V. T., and Ulukaya, E. (2015). Addition of Niclosamide to Palladium(II) Saccharinate Complex of Terpyridine Results in Enhanced Cytotoxic Activity Inducing Apoptosis on Cancer Stem Cells of Breast Cancer. *Bioorg. Med. Chem.* 23 (17), 5580–5586. doi:10.1016/j.bmc.2015.07.026

Kim, J.-w., Gao, P., Liu, Y.-C., Semenza, G. L., and Dang, C. V. (2007). Hypoxia-inducible Factor 1 and Dysregulated C-Myc Cooperatively Induce Vascular Endothelial Growth Factor and Metabolic Switches Hexokinase 2 and Pyruvate Dehydrogenase Kinase 1. *Mol. Cell Biol* 27 (21), 7381–7393. doi:10.1128/mcb.00440-07

Li, Y., Huang, R., Li, X., Li, X., Yu, D., Zhang, M., et al. (2016b). Decreased Expression of Pyruvate Dehydrogenase A1 Predicts an Unfavorable Prognosis in Ovarian Carcinoma. *Am. J. Cancer Res.* 6 (9), 2076–2087.

Li, Y., Huang, S., Li, Y., Zhang, W., He, K., Zhao, M., et al. (2016c). Decreased Expression of LncRNA SLC25A25-AS1 Promotes Proliferation, Chemoresistance, and EMT in Colorectal Cancer Cells. *Tumor Biol.* 37 (10), 14205–14215. doi:10.1007/s13277-016-5254-0

Li, Y., Li, X., Li, X., Zhong, Y., Ji, Y., Yu, D., et al. (2016a). PDHA1 Gene Knockout in Prostate Cancer Cells Results in Metabolic Reprogramming towards Greater Glutamine Dependence. *Oncotarget* 7 (33), 53837–53852. doi:10.18632/oncotarget.10782

Lin, C. C., Cheng, T. L., Tsai, W. H., Tsai, H. J., Hu, K. H., Chang, H. C., et al. (2012). Loss of the Respiratory Enzyme Citrate Synthase Directly Links the Warburg Effect to Tumor Malignancy. *Sci. Rep.* 2 (1), 1–12. doi:10.1038/srep00785

Liu, F., Zhang, W., You, X., Liu, Y., Li, Y., Wang, Z., et al. (2015a). The Oncoprotein HBXIP Promotes Glucose Metabolism Reprogramming via Downregulating SCO2 and PDHA1 in Breast Cancer. *Oncotarget* 6 (29), 27199–27213. doi:10.18632/oncotarget.4508

Liu, L., Cao, J., Zhao, J., Li, X., Suo, Z., and Li, H. (2019). PDHA1 Gene Knockout in Human Esophageal Squamous Cancer Cells Resulted in Greater Warburg Effect and Aggressive Features *In Vitro* and *In Vivo*. *Ott* 12, 9899–9913. doi:10.2147/ott.s226851

Liu, Q.-H., Shi, M.-L., Sun, C., Bai, J., and Zheng, J.-N. (2015b). Role of the ERK1/2 Pathway in Tumor Chemoresistance and Tumor Therapy. *Bioorg. Med. Chem. Lett.* 25 (2), 192–197. doi:10.1016/j.bmcl.2014.11.076

Liu, Z., Yu, M., Fei, B., Fang, X., Ma, T., and Wang, D. (2018). miR-21-5p T-argets PDHA1 to R-egulate G-lycolysis and C-ancer P-rogression in G-astric C-ancer. *Oncol. Rep.* 40 (5), 2955–2963. doi:10.3892/or.2018.6695

Loriot, C., Domingues, M., Berger, A., Menara, M., Ruel, M., Morin, A., et al. (2015). Deciphering the Molecular Basis of Invasiveness in Sdhb-Deficient Cells. *Oncotarget* 6 (32), 32955–32965. doi:10.18632/oncotarget.5106

Lunetti, P., Di Giacomo, M., Vergara, D., De Domenico, S., Maffia, M., Zara, V., et al. (2019). Metabolic Reprogramming in Breast Cancer Results in Distinct Mitochondrial Bioenergetics between Luminal and Basal Subtypes. *Febs J.* 286 (4), 688–709. doi:10.1111/febs.14756

Luo, F., Li, Y., Li, Y., Yuan, F., and Zuo, J. (2019). Hexokinase II Promotes the Warburg Effect by Phosphorylating Alpha Subunit of Pyruvate Dehydrogenase. *Chin. J. Cancer Res.* 31 (3), 521–532. doi:10.21147/j.issn.1000-9604.2019.03.14

McFate, T., Mohyeldin, A., Lu, H., Thakar, J., Henriques, J., Halim, N. D., et al. (2008). Pyruvate Dehydrogenase Complex Activity Controls Metabolic and Malignant Phenotype in Cancer Cells. *J. Biol. Chem.* 283 (33), 22700–22708. doi:10.1074/jbc.m801765200

Patel, M. S., and Korotchkina, L. G. (2001). Regulation of Mammalian Pyruvate Dehydrogenase Complex by Phosphorylation: Complexity of Multiple Phosphorylation Sites and Kinases. *Exp. Mol. Med.* 33 (4), 191–197. doi:10.1038/emm.2001.32

Rajagopalan, K. N., Egnatchik, R. A., Calvaruso, M. A., Wasti, A. T., Padanad, M. S., Boroughs, L. K., et al. (2015). Metabolic Plasticity Maintains Proliferation in Pyruvate Dehydrogenase Deficient Cells. *Cancer Metab.* 3 (1), 7–12. doi:10.1186/s40170-015-0134-4

Rho, J. K., Choi, Y. J., Lee, J. K., Ryoo, B.-Y., Na, I. I., Yang, S. H., et al. (2009). Epithelial to Mesenchymal Transition Derived from Repeated Exposure to Gefitinib Determines the Sensitivity to EGFR Inhibitors in A549, a Non-small Cell Lung Cancer Cell Line. *Lung cancer* 63 (2), 219–226. doi:10.1016/j.lungcan.2008.05.017

Sciacovelli, M., and Frezza, C. (2017). Metabolic Reprogramming and Epithelial-To-Mesenchymal Transition in Cancer. *Febs J.* 284 (19), 3132–3144. doi:10.1111/febs.14090

Sciacovelli, M., Gonçalves, E., Johnson, T. I., Zecchini, V. R., Da Costa, A. S. H., Gaude, E., et al. (2016). Fumarate Is an Epigenetic Modifier that Elicits Epithelial-To-Mesenchymal Transition. *Nature* 537 (7621), 544–547. doi:10.1038/nature19353

Shibue, T., and Weinberg, R. A. (2017). EMT, CSCs, and Drug Resistance: the Mechanistic Link and Clinical Implications. *Nat. Rev. Clin. Oncol.* 14 (10), 611–629. doi:10.1038/nrclinonc.2017.44

Sun, J., Li, J., Guo, Z., Sun, L., Juan, C., Zhou, Y., et al. (2019). Overexpression of Pyruvate Dehydrogenase E1α Subunit Inhibits Warburg Effect and Induces Cell Apoptosis through Mitochondria-Mediated Pathway in Hepatocellular Carcinoma. *Oncol. Res.* 27 (4), 407–414. doi:10.3727/096504018x15180451872087

Tan, X., Tong, L., Li, L., Xu, J., Xie, S., Ji, L., et al. (2021). Loss of Smad4 Promotes Aggressive Lung Cancer Metastasis by De-repression of PAK3 *via* miRNA Regulation. *Nat. Commun.* 12, 4853. doi:10.1038/s41467-021-24898-9

Tavares, A. L. P., Mercado-Pimentel, M. E., Runyan, R. B., and Kitten, G. T. (2006). Tgfβ-mediated RhoA Expression Is Necessary for Epithelial-Mesenchymal Transition in the Embryonic Chick Heart. *Dev. Dyn.* 235 (6), 1589–1598. doi:10.1002/dvdy.20771

Thomson, S., Buck, E., Petti, F., Griffin, G., Brown, E., Ramnarine, N., et al. (2005). Epithelial to Mesenchymal Transition Is a Determinant of Sensitivity of Non-small-cell Lung Carcinoma Cell Lines and Xenografts to Epidermal Growth Factor Receptor Inhibition. *Cancer Res.* 65 (20), 9455–9462. doi:10.1158/0008-5472.can-05-1058

Vega, S., Morales, A. V., Ocaña, O. H., Valdés, F., Fabregat, I., and Nieto, M. A. (2004). Snail Blocks the Cell Cycle and Confers Resistance to Cell Death. *Genes Dev.* 18 (10), 1131–1143. doi:10.1101/gad.294104

Wang, H., Chen, Y., and Wu, G. (2016). SDHB Deficiency Promotes TGFβ-Mediated Invasion and Metastasis of Colorectal Cancer through Transcriptional Repression Complex SNAIL1-Smad3/4. *Translational Oncol.* 9 (6), 512–520. doi:10.1016/j.tranon.2016.09.009

Wang, J., Chen, Y., Xiang, F., Li, M., Li, H., Chi, J., et al. (2018). Suppression of TGF-B1 Enhances Chemosensitivity of Cisplatin-Resistant Lung Cancer Cells through the Inhibition of Drug-Resistant Proteins. *Artif. Cell nanomedicine, Biotechnol.* 46 (7), 1505–1512. doi:10.1080/21691401.2017.1374285

Warburg, O. (1956a). On Respiratory Impairment in Cancer Cells. *Science* 124, 269–270. doi:10.1126/science.124.3215.269

Warburg, O. (1956b). On the Origin of Cancer Cells. *Science* 123 (3191), 309–314. doi:10.1126/science.123.3191.309

Wei, Q., Qian, Y., Yu, J., and Wong, C. C. (2020). Metabolic Rewiring in the Promotion of Cancer Metastasis: Mechanisms and Therapeutic Implications. *Oncogene* 39 (39), 6139–6156. doi:10.1038/s41388-020-01432-7

Xie, L., Law, B. K., Chytil, A. M., Brown, K. A., Aakre, M. E., and Moses, H. L. (2004). Activation of the Erk Pathway Is Required for TGF-B1-Induced EMT *In Vitro*. *Neoplasia* 6 (5), 603–610. doi:10.1593/neo.04241

Yang, J., and Weinberg, R. A. (2008). Epithelial-mesenchymal Transition: at the Crossroads of Development and Tumor Metastasis. *Dev. cell* 14 (6), 818–829. doi:10.1016/j.devcel.2008.05.009

Zhang, M., Cong, Q., Zhang, X. Y., Zhang, M. X., Lu, Y. Y., and Xu, C. J. (2019). Pyruvate Dehydrogenase Kinase 1 Contributes to Cisplatin Resistance of Ovarian Cancer through EGFR Activation. *J. Cell Physiol* 234 (5), 6361–6370. doi:10.1002/jcp.27369

Zhang, Y., and Weinberg, R. A. (2018). Epithelial-to-mesenchymal Transition in Cancer: Complexity and Opportunities. *Front. Med.* 12 (4), 361–373. doi:10.1007/s11684-018-0656-6

Zheng, C., Jiao, X., Jiang, Y., and Sun, S. (2013). ERK1/2 Activity Contributes to Gemcitabine Resistance in Pancreatic Cancer Cells. *J. Int. Med. Res.* 41 (2), 300–306. doi:10.1177/0300060512474128

Zhong, Y., Huang, R., Li, X., Xu, R., Zhou, F., Wang, J., et al. (2015). Decreased Expression of PDHE1α Predicts Worse Clinical Outcome in Esophageal Squamous Cell Carcinoma. *Anticancer Res.* 35 (10), 5533–5538.

Zhong, Y., Li, X., Ji, Y., Li, X., Li, Y., Yu, D., et al. (2017). Pyruvate Dehydrogenase Expression Is Negatively Associated with Cell Stemness and Worse Clinical Outcome in Prostate Cancers. *Oncotarget* 8 (8), 13344–13356. doi:10.18632/oncotarget.14527

Conflict of Interest: The authors declare that the research was conducted in the absence of any commercial or financial relationships that could be construed as a potential conflict of interest.

Publisher's Note: All claims expressed in this article are solely those of the authors and do not necessarily represent those of their affiliated organizations, or those of the publisher, the editors and the reviewers. Any product that may be evaluated in this article, or claim that may be made by its manufacturer, is not guaranteed or endorsed by the publisher.

frontiers in Cell and Developmental Biology

REVIEW
published: 18 January 2022
doi: 10.3389/fcell.2021.789948

Targeting Cell Death: Pyroptosis, Ferroptosis, Apoptosis and Necroptosis in Osteoarthritis

*Jian Yang[1,2,3†], Shasha Hu[4†], Yangyang Bian[1,2,3], Jiangling Yao[1,2,3], Dong Wang[1], Xiaoqian Liu[1], Zhengdong Guo[1,2], Siyuan Zhang[1] and Lei Peng[1,2,3]**

[1]Trauma Center, The First Affiliated Hospital of Hainan Medical University, Hainan Medical University, Haikou, China, [2]Key Laboratory of Emergency and Trauma Ministry of Education, Hainan Medical University, Haikou, China, [3]Hainan Provincial Biomaterials and Medical Device Engineering Technology Research Center, Hainan Medical University, Haikou, China, [4]Department of Pathology, Hainan General Hospital, Hainan Medical University, Haikou, China

New research has shown that the development of osteoarthritis (OA) is regulated by different mechanisms of cell death and types of cytokines. Therefore, elucidating the mechanism of action among various cytokines, cell death processes and OA is important towards better understanding the pathogenesis and progression of the disease. This paper reviews the pathogenesis of OA in relation to different types of cytokine-triggered cell death. We describe the cell morphological features and molecular mechanisms of pyroptosis, apoptosis, necroptosis, and ferroptosis, and summarize the current research findings defining the molecular mechanisms of action between different cell death types and OA.

Keywords: pyroptosis, ferroptosis, apoptosis, necroptosis, osteoarthritis, molecular mechanism, signal pathway

OPEN ACCESS

Edited by:
Tugba Bagci-Onder, Koç University, Turkey

Reviewed by:
Qian Chen, Warren Alpert Medical School of Brown University, United States
Csaba Matta, University of Debrecen, Hungary

****Correspondence:***
Lei Peng
xiaobo197518@163.com

†These authors have contributed equally to this work and share first authorship

Specialty section:
This article was submitted to Cell Death and Survival, a section of the journal Frontiers in Cell and Developmental Biology

Received: *05 October 2021*
Accepted: *21 December 2021*
Published: *18 January 2022*

Citation:
Yang J, Hu S, Bian Y, Yao J, Wang D, Liu X, Guo Z, Zhang S and Peng L (2022) Targeting Cell Death: Pyroptosis, Ferroptosis, Apoptosis and Necroptosis in Osteoarthritis. Front. Cell Dev. Biol. 9:789948. doi: 10.3389/fcell.2021.789948

INTRODUCTION

Cell death plays a key role in the development of the body and maintains homeostasis to prevent the development of diseases. Classically, apoptosis and necrosis were viewed as the main types of cell death, however, this paradigm continues to evolve (Walker et al., 1988). Cell death can be defined as programmed and non-programmed forms based on the regulation of the processes involved.

Programmed cell death (PCD) can be divided into lytic and non-lytic cell death (Jorgensen et al., 2017). Non-lytic cell death mainly refers to apoptosis which can produce apoptotic bodies that are cleared by phagocytes and does not involve the inflammatory response (Fuchs and Steller, 2011). Lytic forms of cell death include necroptosis and pyroptosis (Christofferson and Yuan, 2010; Jorgensen and Miao, 2015). These forms of cell death lead to leakage of intracellular components including damage-associated molecular pattern molecules (DAMPs) which in turn activate a strong inflammatory response also known as inflammatory death (Jorgensen and Miao, 2015).

Non-programmed cell death (Non-PCD) generally refers to necrosis which describes the process of irreversible cell damage and final cell death caused by physical or chemical stimulation in extreme environments (Majno and Joris, 1995). The main characteristics of necrosis include the destruction of cell membranes, edema of cells and organelles (cytoplasmic vesicles), and the release of cell contents, however, chromatin does not agglutinate during necrosis (Dondelinger et al., 2017).

A new type of cell death termed ferroptosis, was proposed by Stockwell in 2012 (Dixon et al., 2012). Ferroptosis is a form of programmed cell death driven by iron-dependent lipid peroxidation. The ferroptosis is characterized by changes in the mitochondrial phenotype, mitochondrial atrophy, and an increase of membrane density (Dixon and Stockwell, 2014; Cao and Dixon, 2016). Different

types of cell death have been shown to regulate the development of multiple chronic diseases (Zhou et al., 2016; Anderton et al., 2020).

Osteoarthritis (OA) is a chronic degenerative disease with progressive features. OA involves structures all parts of the joints in which undergo structural damage and functional imbalances occur as a result of multiple factors (Loeser et al., 2016). The influence of different types of cell death on the development of OA has become a new research hotspot (Hosseinzadeh et al., 2016; Loeser et al., 2016). The purpose of this review is to summarize the pathogenesis of OA and to explore research opportunities focusing on mechanisms of cell death including pyroptosis, apoptosis and ferroptosis.

Osteoarthritis

OA is a common and complex chronic disease that affects 250 million people worldwide (Hunter and Bierma-Zeinstra, 2019). Due to an aging population and a rise in obesity, OA has become the fourth largest disabling disease in the world (Woolf and Pfleger, 2003). It is estimated that the medical cost of OA accounts for 1–2.5% of GDP in different high-income countries (Hunter et al., 2014). OA is associated with all parts of the joints and involves structural changes in hyaline articular cartilage, subchondral bone, ligaments, joint capsule, synovium and muscles around the joint (Martel-Pelletier et al., 2016). OA involves metabolic, inflammatory, mechanical and other factors leading to structural damage and repair imbalances. Currently, the main risk factors associated with OA are age, female sex, obesity, hip deformities, weight-bearing work, exercise, diabetes, hypertension, cardiovascular disease, depression and hereditary factors (Hunter and Bierma-Zeinstra, 2019).

Chondrogenic progenitor cells (CPCs) are mesenchymal stem cells that differentiate into chondrocytes and are also known as cartilage precursor cells (Koelling et al., 2009). Chondrocytes and the extracellular matrix are the main components of articular cartilage. No blood vessels or nerves are present in the cartilage matrix, and chondrocytes are the only cellular components present in the articular cartilage matrix. Under physiological conditions, chondrocytes maintain the lowest level of collagen turnover and do not show mitotic activity (Houard et al., 2013). Collagen turnover gradually increases with risk factors such as age, mechanical stress, diabetes and hypertension. Subsequently, the composition and structure of the cartilage matrix change resulting in the formation of fibrous tissue. As this pathological process progresses, deep fissures develop that are related to the shedding of cartilage fragments and eventually lead to the delamination and exposure of calcified cartilage and bone (Hunter and Bierma-Zeinstra, 2019). In the early stages of this process, the surface receptors of chondrocytes inhibit the low collagen turnover rate of chondrocytes through integrins and other related factors. The synthetic activity of chondrocytes also increases significantly due to the repair of the perichondrial matrix which finally develops to invade the collagen network (Xu et al., 2014). This marks the irreversible progression of OA. Also, increases in chondrocyte activity result in the increased production of inflammatory reactive proteins including interleukin-1β (IL-1β), interleukin-6, tumor necrosis factor-α (TNF-α) and matrix metalloproteinases (MMP1, 3 and 13).

Injury to the bone and cartilage around the joint is an important factor in OA. The subchondral bone tissue is composed of cortical and cancellous bone (Burr, 2004; Goldring and Goldring, 2010). As AO progresses, the volume, thickness and outline of the cortical bone gradually increase. Also, the trabecular structure and bone mass of the subchondral bone change as bone cysts form along with the appearance of osteophytes (Goldring, 2008; Xu et al., 2014). A characteristic feature of the OA is the gradual thickening of the subchondral plate that reflects changes in mechanical loading owing to cartilage damage and properties of the subchondral bone (Martel-Pelletier et al., 2016). Shanchez et al., reported that osteoblasts can express inflammatory cytokines and degrading enzymes in response to mechanical stimulation and chondrocytes (Sanchez et al., 2012) that can in turn act on cartilage or subchondral bone to increase the severity of OA.

Synovitis is a common feature of OA (Scanzello and Goldring, 2012). The synovium includes the synovial membrane and the fluid. The synovium is a thin cell layer arranged in the joint cavity that contains macrophages and fibroblasts that regulate the trafficking of molecules through the joint (Shiozawa et al., 2020). The release of inflammatory factors and the secretion of degrading enzymes in the synovial tissue are correlated with the severity of OA (Scanzello and Goldring, 2012). Proteases released by chondrocytes increase the production of pro-inflammatory cartilage degradation products that interact with DAMPs, Toll-like receptors (TLRs) and integrin. These changes further aggravate inflammation and catabolic products to increase the severity of OA (Loeser et al., 2012; Houard et al., 2013; Martel-Pelletier et al., 2016). Baker and Roemer et al. reported that the risk of synovitis progression and OA was positively correlated with joint symptoms through MRI analysis (Baker et al., 2010; Roemer et al., 2011). IL-1, IL-6, IL-15, tumor necrosis factor (TNF), prostaglandin E2, matrix metalloproteinases (MMP1, 3 and 13) and collagenase (coLI, II) have also been detected in the synovial fluid, cartilage and the synovium of patients with OA (Kapoor et al., 2011; Scanzello and Goldring, 2012).

Pyroptosis

The first experimental observations of lytic death were made over 30 years ago when it was reported that Shigella fowleri could induce lytic death in infected host macrophages. This form of lytic death has characteristics that are common to apoptosis such as chromatin agglutination, DNA fragmentation and cysteinyl aspartate specific proteinase (Caspase) activity dependence (Zychlinsky et al., 1992). This mode of death was initially considered to be apoptosis, yet, it was not until 2001 that Cookson et al. showed that this form of cell death depends on Caspase-1 activity which is different from Caspase-3 activity-dependent apoptosis (Cookson and Brennan, 2001). For the first time, the authors defined pyroptosis as a form of Caspase-1-dependent cell death. The term originates from “pyro” meaning fire, indicating that this kind of programmed cell death causes inflammation, and “ptosis” means falling (Gao et al., 2018), indicating the nature of programmed cell death. When cells

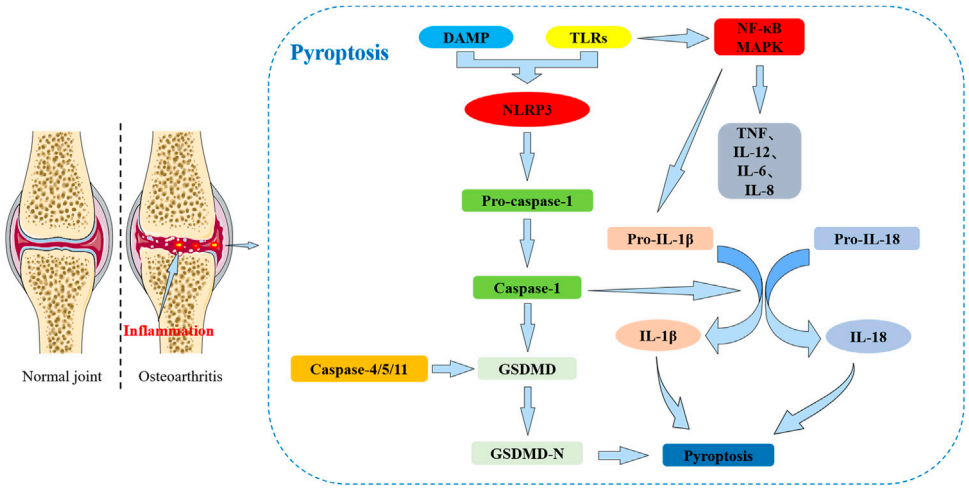

FIGURE 1 | The relationship between pyroptosis and osteoarthritis (OA). Pyroptosis: DAMPs and TLRs can interact to exacerbate the inflammatory response. TLRs initiate a signaling cascade leading to cell activation, increased release of the NLRP3 inflammasome, activation of NF-κB and MAPK signaling pathway, and production of associated inflammatory factors (including TNF, IL-12, IL-6, IL-8 and pro-IL-1β) that in turn activate a strong inflammatory response. The inflammatory response promotes the increased release of IL-1β and IL-18 on the cartilage surface exacerbating cartilage damage and also enhancing pyroptosis signaling. The NLRP3 inflammasome can activate caspase-1 which further activates GSDMD to undergo shearing to form the N-terminal end. The N-terminal end of GSDMD leads to cell membrane perforation and ultimately induces pyroptosis. Caspases-4/5/11 are also able to activate GSDMD and can induce pyroptosis.

undergo pyroptosis, the nucleus becomes concentrated and the chromatin DNA is randomly broken and degraded. Pores in the cell membrane regulate the trafficking of substances to and from cells. As this process becomes imbalanced, osmotic swelling occurs and the membrane breaks (Hersh et al., 1999) releasing the cell contents that contain molecules to stimulate the immune response. During the process of cell death, the nucleus becomes condensed and rounded (Fernandes-Alnemri et al., 2007) yet the nuclear integrity remains unchanged (Santos et al., 2001; Mariathasan et al., 2005).

Pyroptosis mainly leads to the splicing and polymerization of members of the Gasdermin family (such as GSDMD). It can also activate cell perforation and death through inflammatory corpuscle activation and caspases. Based on the different mechanisms of caspase-mediated cell death, pyroptosis can be defined as caspase-1 and caspase-4/5/11 types (**Figure 1**). Pyroptosis induced by caspase-1 activation mainly occurs in macrophages and dendritic cells (Fink et al., 2008; Broz et al., 2010). Caspase-4/5/11 activation can also cause pyroptosis in macrophages and other non-macrophage cell types (Kayagaki, Warming et al., 2011).

Gasdermin proteins are a family that has multiple functions and are expressed in a variety of cell types and tissues. Human gasdermin proteins are composed of Gasdermin A (GSDMA), Gasdermin B (GSDMB), Gasdermin C (GSDMC), Gasdermin D (GSDMD), Gasdermin E (GSDME, also known as DFNA5) and Pejvakin (PJVK, also known as DFNB59) (Feng et al., 2018). Except for PJVK, all gasdermin proteins have conserved double domain arrangements including a C-terminal (GSDM-C) and N-terminal domains (GSDM-N). The N terminal has a pore-forming activity and can induce pyroptosis (Yang et al., 2018). GSDMD can be specifically activated by caspases-1, 4, 5, 11, and can be cut by caspase-1 and 11 into GSDMD-N (p30 fragment) and GSDMD-C (p20 fragment) (Zhao L. R. et al., 2018; Kayagaki et al., 2015). The activated GSDMD-N domain has lipophilic characteristics and can be transported from the cytoplasm to the cell membrane (Liu et al., 2016; Shi et al., 2017). The N-terminus of gasdermin can directly interact with membrane lipids and oligomerize to form 10–33 nm pores (Aglietti et al., 2016; Sborgi et al., 2016; Shi et al., 2017). New research has shown that intracellular IL-1β can be released outside the cell through channels formed by GSDMD. When exposed to inflammation or hyperactivating stimuli, GSDMD and caspase-11 can form larger pores in the liposomes of cell membranes leading to a massive release of IL-1β which in turn causes pyroptosis (Evavold et al., 2018). Recently, it has been demonstrated that when GSDME is stimulated by chemotherapeutic agents, tumor necrosis factor (TNF) and viral infection, it is activated by caspase-3 which is involved in apoptotic signaling. GSDME then releases the activated N-terminal end causing perforation of the cell membrane which converts cells that should undergo apoptosis into pyroptosis (Wang et al., 2018). These data further suggest that the regulation of cell death is highly complex and dependent on the mode of death.

The main types of inflammasomes include NLRP3, NLRP1, NLRC4 and AIM2. The basic structure of inflammasomes consists of pattern recognition receptors (PRRs), apoptosis-associated speck-like protein containing a CARD (ASC) and pro-caspase-1 (CASP1) (Man and Kanneganti, 2015; von Moltke et al., 2013). Inflammasomes are multimeric protein complexes that assemble in the cytosol and act as platforms for caspase activation (An et al., 2020). When cells sense inflammation or the invasion of viral microbes, they respond by damaging tissues (Matzinger, 2002). A series of cascade reactions mediated by the TLRs are initiated to activate nuclear factor-κB (NF-κB), mitogen-activated protein kinase (MAPK) and interferon signaling pathways leading to cell activation and the production of related inflammatory cytokines. These include tumor necrosis factor (TNF),

TABLE 1 | Summary of the main areas of research and potential applications of pyroptosis in osteoarthritis (Wang et al., 2021; Li et al., 2021a; Li C. et al., 2021; Liu et al., 2020; Yu et al., 2021; Yan et al., 2020; Hu et al., 2020; Zu et al., 2019; Zhao L. R. et al., 2018; Liu et al., 2019; Zhang and Xing, 2019; Xiao et al., 2021; Zhang et al., 2019b; Qian et al., 2021).

Important targets	Disease	Experimental subjects	Intervention factors	Cytokines	Biological function	Activation pathway
NLRP1, NLRP3	KOA	Human FLSs	**LPS**, ATP	IL-1β, uricacid, IL-18	Promote pyroptosis	Inflammasome, Caspase-l
NLRP3	OA	Male Wistar mice chondrocytes	**Icariin (ICA)**, LPS	MMP-1, MMP-13, NRLP3, IL-1β, IL-18, Col II	Inhibits pyroptosis	Inflammasome, Caspase-l
NRF2, NLRP3	OA	C57BL/6 male mice chondrocytes	**Lico A**, LPS	NLRP3, ASC, GSDMD, caspase-1, IL-1β, IL-18, Col II, aggrecan	Inhibits pyroptosis	NRF2/HO-1/NF-κB, Inflammasome, Caspase-l, p65, IκB-α
NLRP3	OA	C57BL/6 male mice	**Loganin**	MMP-3, MMP-13, Col II, Col X, CD31, cryopyrin, caspase-1, endomucin	Inhibits pyroptosis	NF-κB, Inflammasome, Caspase-l, p65, IκB-α
NLRP1, NLRP3	OA	C57BL/6J mice chondrocytes	**Morroniside,** DMM	MMP13, NLRP3, Caspase-1, Caspase-3, Ki67	Inhibits pyroptosis	NF-κB, Inflammasome, Caspase-l, p65, IκB-α
Hedgehog	OA	C57BL/6 male mice, Human chondrocyte cell (C28/I2)	**GANT-61**, Indomethacin, LPS	TNF-α, IL-2, IL-6, IL-1β, IL-18, caspase-1	Inhibits pyroptosis	Caspase-l, Hedgehog, Inflammasome
NLRP3	OA	C57BL/6 male mice, Human FLSs	**SDF-1** aka **CXCL12**	NLRP3, Caspase-1, ASC, IL-1β, GSDMD	Inhibits pyroptosis	AMPK, PI3K–mTOR, Caspase-l, Inflammasome
NLRP3	KOA	SD male rats, fibroblasts, synovial macrophage	**LPS**, ATP	IL-1β, IL-18, HMGB1, Caspase1, NLRP3, ASC, TGF-β, PLOD2, COL1A1, TIMP1, GSDMD	Inhibits pyroptosis	Inflammasome, Caspase-l
NLRP1, NLRP3	KOA	SD male rats, FLSs	**HMGB1**, LPS, ATP	IL-1β, HMGB1, Caspase1, NLRP3, NLRP1, GSDMD	Promote pyroptosis	Inflammasome, Caspase-l
NLRP1, NLRP3	KOA	SD female rats, FLSs	**HIF-1α**, LPS, ATP	IL-1β, IL-18, TGF-β, ASC, PLOD2, COL1A1, TIMP1, GSDMD, caspase-11	Promote pyroptosis	Inflammasome, Caspase-l
NLRP3	OA	SD rats, Chondrocytes	**USP7**, NOX4, H_2O_2	Caspase1, MMP-1, MMP-13, GSDMD, NLRP3	Promote pyroptosis	Inflammasome, Ubiquitinylation, Caspase-l, NOX4, ROS, NLPR3
NLRP3	OA	SD male rats, Chondrocytes	**P2X7 Receptor**, MIA, BzATP	MMP13, NF-κB, Col II, NLRP3, Caspase-1, p65, P2X7, IL-1β	Promote pyroptosis	NF-κB, NLPR3, Caspase-l, Inflammasome
NLRP1, NLRP3	OA	C28/I2 chondrocytes	**LPS**, ATP, Disulfiram, Glycyrrhizic acid	Caspase-1, GSDMD, NLRP3, IL-1β, IL-18, HMGB1	Inhibits pyroptosis	Inflammasome, Caspase-l, NLPR3
NLRP3, miR-107	KOA	Chondrocytes	**LPS**, ATP, miR-107	IL-1β, HMGB1, IL-18, Caspase-1, Col II, MMP13, GSDMD, TLR4	Inhibits pyroptosis	Inflammasome, Caspase-l, NLPR3

interleukin-6 (IL-6), interleukin-8 (IL-8) and type I interferons (IFNs) in response to extracellular inflammatory stimulation signals (Kawai and Akira, 2007). Nod-like receptors (NLRs) also play an important role in the perception of inflammation or viral invasion. Oligonucleotide binding of NLRs to domain-containing protein 1 (NOD1) and NOD2 triggers a signaling cascade after ligand recognition that is similar to the cascade initiated by TLRs and which leads to the production of inflammatory cytokines (Kufer and Sansonetti, 2007). The other part of the NLR mediates the activation of caspase 1 which triggers caspase 1-dependent pyroptosis and releases inflammatory cytokines IL-18 and IL-1β (Martinon and Tschopp, 2007; Wang and Zhang, 2020). TLR, NOD1 and NOD2 coactivate caspase1 and produce large amounts of IL-1β (Kufer and Sansonetti, 2007).

Research Related to Osteoarthritis and Pyroptosis

Currently, only a few studies have investigated the mechanism of interaction between OA and pyroptosis and most studies have focused on the role of the NLRP3 inflammasome (**Table 1**). NLRP3 inflammasomes have an important role in the pathogenesis of autoinflammation, cancer and degenerative diseases. In OA, perichondral synovial cells stimulated by DAMPs lead to the increased release of the NLRP3 inflammasomes, IL-1β and IL-18 on the cartilage surface to further exacerbate inflammatory cytokine production and promote pyroptosis (Man and Kanneganti, 2015). Shuya Wang et al. reported that activation of the AMPK signaling pathway by exogenous stromal cell-derived factor-1 (SDF-1) inhibits the NLRP3 inflammasome which in turn inhibits the scorching process of osteoarthritic synovial cells (Wang et al., 2021). P2X7R is a purinoceptor that is a non-selective cation channel gated by adenosine triphosphate. P2X7R mediates Na and Ca influx and K efflux, and is involved in a variety of inflammatory responses and different mechanisms of cell death (Surprenant et al., 1996; Bartlett et al., 2014). P2X7R participates in NLRP3 and caspase-11 distinct pathway-mediated pyroptosis and produces cartilage degrading enzymes to activate inflammatory factors in synovial tissue (Haseeb and Haqqi, 2013; Viganò and Mortellaro, 2013; Li et al., 2021a). Activated P2X7 promotes

extracellular matrix degradation and pyroptotic inflammation in OA chondrocytes through NF-κB/NLRP3 crosstalk to aggravate the symptoms of OA (Li et al., 2021b).

Recent studies have shown that the combined effect of disulfiram and glycyrrhizic acid at standard concentrations protects chondrocytes, inhibits the inflammatory responses and reduces pyroptosis (Li C. et al., 2021). Ubiquitin (Ub)-specific proteases (USPs), also known as deubiquitinating enzymes, remove Ub from Ub conjugates and regulate a variety of cellular processes (Ovaa et al., 2004). USP7 is a member of the ubiquitin-specific proteases. USP7 inhibitors attenuate H2O2-induced chondrocyte damage and pyroptosis by inhibiting the NOX4/NLRP3 signaling pathway (Liu et al., 2020).

The therapeutic role of Chinese medicine in the management of OA is gaining increasing attention. For example, Morroniside significantly inhibits the NF-κB signaling pathway, decreases the expression of NLRP3 and Caspase-1, and reduces the nuclear translocation of p65, thereby inhibiting the onset of pyroptosis and delaying the progression of OA (Yu et al., 2021). Chondrocyte pyroptosis is inhibited by licochalcone A (Lico A) through inhibition of the NLRP3 inflammasome (Yan et al., 2020). Jiaming Hu et al. reported that loganin ameliorates cartilage degeneration and the development of OA in a mouse model through inhibition of NF-κB activity and pyroptosis in chondrocytes (Hu et al., 2020). In animal models, Icariin (ICA) attenuates chondrocyte damage and OA by inhibiting the NLRP3 signaling-mediated caspase-1 pathway to reduce pyroptosis (Zu et al., 2019). NLRP1 and NLRP3 inflammasomes mediate the onset of pyroptosis in knee OA (KOA) via the Caspase-l/IL-1β inflammatory pathway (Zhao Y. et al., 2018). Shi et al. showed that increased lipopolysaccharide (LPS) and ATP in joint-space may promote KOA by NLRP3 Inflammasome (Shi et al., 2018). Overall, the role of inflammasomes such as NLRP3 and its regulators in pyroptosis suggests that NLRP3 may be a promising biomarker for the diagnosis and monitoring of OA. Therapeutic targeting of NLRP3 may be a potential strategy for the treatment of OA.

Ferroptosis

Ferroptosis is a newly discovered form of regulated cell death that differs from the traditional cell death programs of necrosis, apoptosis, and pyroptosis that are caused by iron-dependent and lethal lipid peroxidation. Ferroptosis was first proposed by Dixon in 2012 (Dixon et al., 2012) and describes a form of cell death induced by the small molecule Erastin which inhibits cystine import leading to glutathione depletion and inactivation of the phospholipid peroxidase glutathione peroxidase 4 (Gpx4) (Yang et al., 2014; Stockwell et al., 2017). GPX4 converts potentially toxic lipid hydroperoxides (L-OOH) to non-toxic lipid alcohols (L-OH) (Ursini et al., 1982; Stockwell et al., 2017). Inactivation of Gpx4 by depletion of GSH with Erastin or with a direct Gpx4 inhibitor, (1S,3R)-RSL3, ultimately leads to overwhelming lipid peroxidation and cell death.

Inactivation of GPX4-RSL3 directly induces ferroptosis. Erastin and RSL3 were first identified as ferroptosis-inducing compounds (Dolma et al., 2003; Yang and Stockwell, 2008). Erastin inhibits the transfer of cysteine causing loss. Cysteine is an essential component of glutathione and so indirectly induces ferroptosis (Latunde-Dada, 2017). Ferroptosis can be suppressed by iron chelators, lipophilic antioxidants, inhibitors of lipid peroxidation, and depletion of polyunsaturated fatty acids. This process also correlates with the accumulation of markers of lipid peroxidation (Stockwell et al., 2017). Recent studies suggest that mobilization and upregulation of the transferrin receptor (TfR) can be a potential marker of iron death (Stockwell et al., 2017; Kajarabille and Latunde-Dada, 2019). In contrast to other forms of programmed cell death, ferroptosis exhibits specific morphological and biological features (**Table2**).

The Relationship Between Ferroptosis and Disease

The mechanisms of interaction between ferroptosis-inducing compounds and ferroptosis signaling pathways remain to be fully elucidated. A growing body of experimental evidence suggests that excessive iron contributes to oxidative tissue damage and organ dysfunction resulting in the development of cirrhosis (Yu et al., 2020), cardiomyopathy (Fang et al., 2020), diabetes and other diseases (Stockwell et al., 2020; Sha et al., 2021). In an animal model of traumatic brain injury (TBI), ferroptosis was shown to be involved in acute central nervous system (CNS) trauma based on glutathione peroxidase activity, lipid-responsive oxygen species and observations of mitochondrial shrinking (Xie et al., 2019). The characteristic products of ferroptosis have also been demonstrated in spinal cord injury and the source of iron is closely related to red blood cell rupture, hemolysis (Yao et al., 2019).

The role of ferroptosis in the treatment of hepatocellular carcinoma has also been a research focus. Urano et al. showed that the combination of iron inhibitors and anti-angiogenic drugs enhanced the tumor-killing effects of sorafenib by inducing cell cycle arrest and apoptosis (Urano et al., 2016). Studies from as early as 1992 have observed selective accumulation of iron in Aβ aggregation areas and neurofibrillary tangles in the brain in Alzheimer's disease (Good et al., 1992). Ayton et al. showed that excessive accumulation of iron in the brains of Alzheimer's patients may be associated with accelerated cognitive decompensation (Ayton et al., 2020).

Currently, very few studies have focused on the role of ferroptosis in OA. Recent research findings from the past 2 years are summarized in **Figure 2**. Yao X et al. used chondrocytes extracted from the knee joints of C57BL/6J mice as an *in vitro* experimental model of OA using interleukin-1β and ferric ammonium citrate to mimic the inflammatory response and iron overload (Yao et al., 2021). The study demonstrated that ferrostatin-1 attenuates IL-1β and Fac induced cytotoxicity, the accumulation of reactive oxygen species (ROS) and lipid-ROS, and the expression of ferroptosis-related proteins to promote activation of the NRF2 antioxidant system. This was the first study to demonstrate that chondrocytes underwent ferroptosis *in vitro*.

TABLE 2 | The main morphological, biochemical, and signaling pathways involved in the regulation of pyroptosis, apoptosis, necroptosis, and ferroptosis (Kerr et al., 1972; Xu and Shi, 2007; Charlier et al., 2016; Newton and Manning, 2016; Xie et al., 2016; Yang and Stockwell, 2016; Zargarian et al., 2017; Jiang and Stockwell, 2021).

Cell Components/ Events	Cell Death Types			
	Pyroptosis	**Apoptosis**	**Necroptosis**	**Ferroptosis**
Cell morphology	Gradual flattening	Shrinkage	Swelling	Smaller and rounder
Nucleus	Enrichment	Condensation and rupture	Nuclear condensation (pyknosis)	Normal nuclear size
Cytoplasm	Osmotic swelling	Retraction of pseudopods, reduction of cellular volume	Cytoplasmic swelling, swelling of cytoplasmic organelles	Mitochondrial membrane rupture and atrophy
Cell membrane	Formation of membrane pores, loss of integrity	Plasma membrane blebbing	Rupture of plasma membrane	Lack of rupture and blebbing of the plasma membrane
Chromatine	Random breakage degradation	Condensation	Fragmented	Lack of condensation
DNA	Random breakage degradation	Intranucleosomal cleavage-DNA laddering	Random cleavage DNA Smear	None
Lysosomial enzyme	Damage	Inside apoptotic bodies	Leakage	None
Special microstructure	Pyroptotic bodies	Apoptotic bodies	Necroptotic bodies	Mitochondrial membrane rupture
Inflammation	Yes	No	Yes	Yes
Key role	Caspase-1, Caspase-4/ 5/11	Caspase-3, Caspase-6, Caspase-7	RIP1, RIP3, TNF-α, Fas, Necrostatin-1, MLKL	GPX4, Phospholipid peroxidation, Iron
signal pathway	Gasdermin, NLRs	Fas-FasL, TRAIL-DR, TNFa-TNFR1, mitochondrial pathway	IKKα/IKKβ, NF-□b, TNF-α	Mevalonate, AMPK, Hypoxia, glutathione depletion, Glutaminolysis, Transsulfuration, Heat shock protein beta 1
ATP requirement	Yes	Yes	No	Yes

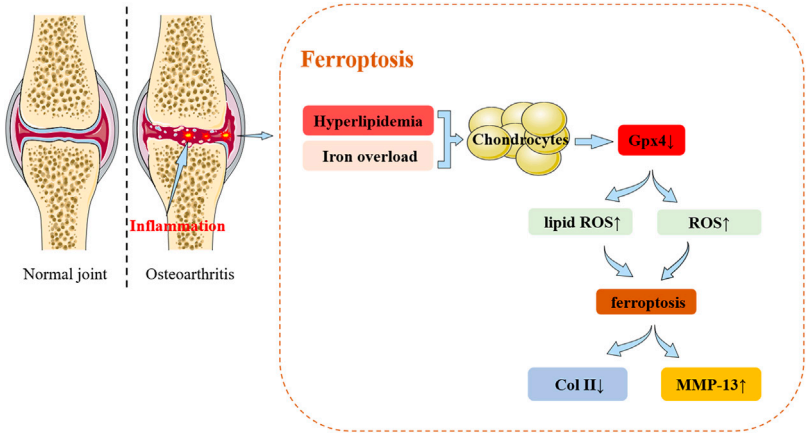

FIGURE 2 | The relationship between ferroptosis and osteoarthritis (OA). Ferroptosis: In cellular environments stimulated by iron overload, hyperlipidemia, inflammation, the expression of Gpx4 in chondrocytes decreases. These changes lead to the accumulation of reactive oxygen species and lipid peroxides to ultimately induce ferroptosis. Ferroptosis in turn can progressively exacerbate the inflammatory response leading to the increased expression of MMP-13 and decreased expression of collagen II in chondrocytes to accelerate the progression of OA.

In a lipopolysaccharide (LPS)-induced OA cell model, icariin (ICA) reduced the expression of iron transport factor TFR1. ICA activated the Xc-/Gpx4 axis to exert an inhibitory effect on the expression of Gpx4, SLC7A11 and SLC3A2L which acted to significantly reduce cell death in induced cells and inhibit ferroptosis (Luo and Zhang, 2021). Zhang et al. identified a new subpopulation of chondrocytes located in the nucleus pulposus of the intervertebral disc using single-cell RNA-seq analysis. The study revealed the presence of ferroptosis during disc degeneration (Zhang et al., 2021).

Ferroptosis has also been shown to have an important role in the development of cancer and inflammatory and chronic diseases. In OA, high concentrations of iron can promote joint degeneration and facilitate the development of OA. However,

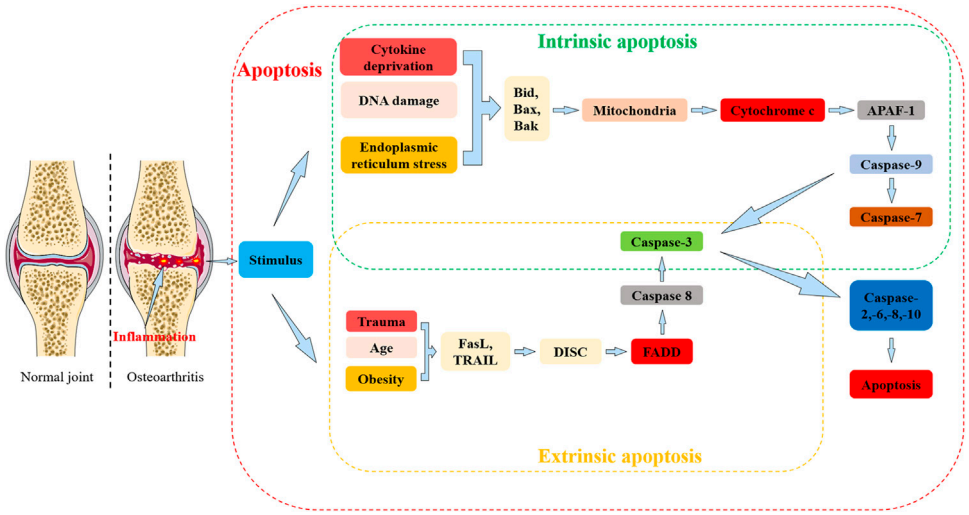

FIGURE 3 | The relationship between apoptosis and osteoarthritis (OA). Apoptosis: Apoptosis is can be divided into extrinsic and intrinsic pathways. In the extrinsic pathway, death receptors (including Fas, TRAIL) are activated and bind to corresponding ligands (including FasL) in response to stimulation by risk factors for OA (including trauma, age, obesity, etc.) to form a multi-protein complex, also known as the DISC. Activation of Caspase-8 is mediated by FADD, and Caspase-8 further activates Caspase-3 to propagate apoptotic signals. In the intrinsic pathway, intracellular damage, DNA damage and endoplasmic reticulum stress lead to activation mainly in the mitochondria and endoplasmic reticulum BCL2 protein family members (including Bid, Bax, and Bak). Bcl2 protein family members can activate cytochrome c which can further activate apoptosis protease activating factor-1 (APAF-1) and caspase-9. Activated caspase-9 further activates caspases-3 and -7 which in turn activate caspases-2,-6,-8,-10 to create a positive feedback loop that amplifies the apoptotic signal and induces apoptosis.

evidence from relevant studies is lacking and the detailed molecular mechanisms by which iron compromises to cartilage remains to be understood.

Apoptosis

Apoptosis is the active, physiological process of cell death that is activated under specific physiological or pathological conditions. Apoptosis is regulated by intrinsic genetic mechanisms of autologous damage to the organism (Rathmell and Thompson, 2002). Apoptosis is regulated by apoptosis-related genes and so the process is also known as programmed cell death (PCD) or type I cell death.

The concept of apoptosis was first introduced by Kerr, Wyllie and Currie in 1972 (Kerr et al., 1972). "Apoptosis" is a Greek word meaning "to leave or fall" implying that apoptosis occurs when a cell dies similar to the natural withering of leaves or flowers. This metaphor emphasizes that apoptosis is an important part of the normal life cycle of an organism, and that it is an active process under strict genetic control. Apoptosis has a wide range of biological functions during the development and differentiation of the organisms, in immune regulation, and the maintenance of tissue stability. The process is also involved in the removal of redundant or harmful cells and the prevention of cancer (Honarpour et al., 2001; Luke et al., 2003; Ke et al., 2018).

Apoptosis is morphologically characterized by reductions in cell size, loss of connections, and detachment from surrounding cells. The cytoplasmic density gradually increases and the mitochondrial membrane potential disappears. During apoptosis, the nucleoplasm becomes concentrated in the nucleus, the nucleolus becomes broken, and DNA is degraded into 180–200 bp fragments (Enari et al., 1998). The entire cell has an intact cytosolic structure with vesicle formation which eventually divides and wraps the apoptotic cell into several apoptotic vesicles. This process does not involve the release of cellular contents and the inflammatory response is not activated (Mariño and Kroemer, 2013).

Apoptosis can be defined as either extrinsic or intrinsic depending on the stimulus (**Figure 3**). Extrinsic apoptosis is also known as the death receptor apoptotic pathway and intrinsic apoptosis refers to the mitochondrial apoptotic pathway (Elmore, 2007). Death receptors refer to Fas (also known as DR2, APO-1, or CD95), tumor necrosis factor receptor 1 (TNFR1) or tumor necrosis factor-associated apoptosis-inducing ligand receptor (TRAILR), all of which are members of the Tumor Necrosis Factor Receptor Superfamily (TNFRSF) (Lavrik et al., 2005).

Death receptors are transmembrane glycoproteins located on the surface of cell membranes that cause conformational changes in cell membrane delivery when receiving death ligands from extrinsic apoptotic signaling pathways and rapidly activate caspase ultimately leading to apoptosis (Mariño and Kroemer, 2013). The engagement of the death receptor, Fas, binds to its ligand FasL to assembly a typical multiprotein complex called the death-inducing signaling complex (DISC). DISC formation allows the recruitment and activation of initiator caspase-8, mediated by the Fas-associated protein with death domain (FADD) adaptor molecule (Charlier et al., 2016). The recruitment of caspase-8 leads to autoproteolytic cleavage and subsequent activation (Medema et al., 1997; Charlier et al., 2016). The active fragment of caspase-8 propagates apoptotic signals by activating caspase-3 fragment activity which further catabolizes cellular components (Fuentes-Prior and Salvesen, 2004).

Fas is involved in regulating the DISC-mediated production of active caspase-8 and activates caspase-9 prior to activation of caspase-3 (Scaffidi et al., 1998). Intrinsic apoptosis triggers include intracellular damage, cytokine withdrawal, DNA damage, oxidative or endoplasmic reticulum (ER) stress, and cytosolic Ca^{2+} overload (Vanden Berghe et al., 2015). These stimuli ultimately activate members of the BCL2 family of proteins located primarily in the mitochondria and endoplasmic reticulum and have contrasting effects on cell fate. For example, Bcl-xs (Boise et al., 1993), Bcl-GL (Guo et al., 2001), Bok (Hsu and Hsueh, 1998), Bax (Oltvai et al., 1993), and Bak can promote apoptosis (Chittenden et al., 1995), whilst A1 (Lin et al., 1996), Mcl-1 (Kozopas et al., 1993), Bcl-B (Ke et al., 2001), Bcl-2 (Tsujimoto et al., 1985), Bcl-x (Boise et al., 1993), and Bcl-w can prevent apoptosis (Gibson et al., 1996; Kroemer and Reed, 2000).

The proteins that lead to apoptosis can be functionally classified based on whether they can function independently of caspases (i.e., Omi/HtrA2, apoptosis-inducing factor AIF) or activate caspases either directly or indirectly (e.g., Smac/DIABLO, cytochrome c) (van Loo et al., 2002a; van Loo et al., 2002b; Charlier et al., 2016). Apoptosis protease-activating factor-1 (APAF-1) is a key component of the apoptosome (Green, 2003). Cytochrome c can activate APAF-1 whilst forming an activation platform for the caspase-9 promoter in the mitochondrial pathway by oligomerization with APAF-1 (Bao and Shi, 2007). Activated caspase-9 further activates caspases-3 and -7, which in turn activate caspases-2,-6,-8,-10 forming a positive feedback loop that amplifies apoptosis signals and induces apoptosis (Slee et al., 1999; Van de Craen et al., 1999).

Signaling Pathways Involved in Osteoarthritis and Apoptosis

Recent studies focused on apoptosis of articular chondrocytes in OA involve the inflammatory response, signaling pathways and target modulation. Interleukin-1β (IL-1β) is an important inflammatory factor that belongs to the interleukin-1 (IL-1) family and plays a key role in the pathogenesis of OA (López-Armada et al., 2006; Chevalier et al., 2011). IL-1β increases apoptosis in articular chondrocytes by stimulating the expression of TNF, Fas-associated death region protein, and Caspases-3, and -8 (Qin et al., 2013).

Current research has focused on the role of non-coding RNAs regulating IL-1β-mediated apoptosis in chondrocytes. Recent studies demonstrate that the LINC00623/miR-101/HRAS axis modulates chondrocyte apoptosis, senescence and extracellular matrix (ECM) degradation in OA through MAPK signaling (Lü et al., 2020). Also, it has been shown that miR-27a is a regulator of the PI3K-Akt-mTOR axis in human chondrocytes that could be involved in OA (Cai et al., 2019). Junkui Xu et al. reported that LncRNA SNHG7 alleviates IL-1β-induced OA by inhibiting miR-214-5p-mediated PPARGC1B signaling pathways (Xu et al., 2021).

The tumor necrosis factor (TNF) superfamily is a group of cytokines produced by a variety of cell types including macrophages (Baud and Karin, 2001; Wajant et al., 2003). TNF plays a key role in immunity, inflammation, and the control of cell differentiation, proliferation, and apoptosis (Wajant et al., 2003). TNF-α is one of the most important signaling molecules in this family. TNF-R1 mediates most of the biological functions of TNF-α and contains a death structural domain. TNF-R1 can induce apoptosis by activating the NF-κB, JNK and MAPKs signaling pathways (Chen and Goeddel, 2002).

The combination of long-stranded non-coding RNA (LncRNA) and microRNA (MiRNA) has gradually replaced single, localized research approaches as the main approach to study the roles of these molecules in OA today. Xu Kai et al. reported that LncRNA PVT1 induces chondrocyte apoptosis through upregulation of TNF-α in synoviocytes by sponging miR-211-3p (Xu K. et al., 2020). Wang Yingjie et al. reported that MiR-140-5p inhibits the PI3K/AKT signaling pathway and suppresses the progression of OA by targeting HMGB1 (Wang et al., 2020).

Mitogen-activated protein kinases (MAPKs) are a class of serine/threonine protein kinases that are widely present in eukaryotic cells. MAPKs are activated by extracellular signals, physical stimuli, and inflammatory cytokines. They also regulate the activity of transcription factors to control the expression of related genes and elicit cellular responses (Wang et al., 2016). The MAPK subfamily includes p38mapk, extracellular regulated protein kinases (ERK) and c-Jun N-terminal kinase (JNK) (Davis, 2000; Tang et al., 2012). JNK can promote the expression of apoptotic genes by phosphorylating c-jun and by increasing the expression of proteins related to the Fas/FasL signaling pathway. Conversely, JNK induces phosphorylation and inactivation of related anti-apoptotic proteins to promote apoptosis in OA (Shajahan et al., 2012; Zhou et al., 2019). Fas signaling can initiate apoptosis by activating caspase-8 which in turn can activate the downstream effector caspase-3 (Xue et al., 2017).

Notch signaling is an evolutionarily conserved pathway that plays an important regulatory role in cell fate determination, proliferation, differentiation, and dynamic homeostasis. The Notch signaling pathway also plays an important role in proliferation and differentiation during chondrogenesis and in the development of cartilage (Kohn et al., 2012; Mirando et al., 2013). The Notch pathway consists primarily of Notch receptors, Notch ligands, and downstream target genes. In post-traumatic OA, the Notch pathway is highly activated in human and mouse joint tissues (Karlsson et al., 2008). Notch1, JAG1 and other downstream target genes are overexpressed in OA tissue biopsies (Karlsson et al., 2008). However, in a mouse model, loss of Notch signaling in OA indicated an important role in maintaining osteoarticular cartilage growth (Liu et al., 2015). Also, intra-articular injection of the Notch complex inhibits cartilage degeneration in a mouse OA model (Hosaka et al., 2013). Overall, a dual role for Notch signaling in maintaining the normal physiological function of articular cartilage and promoting the progression of OA has been observed. In short, Notch signaling plays a complex role in cartilage homeostasis and transient or physiological Notch signaling in chondrocytes favors a balanced anabolic and catabolic response. In contrast, sustained or enhanced Notch activity elicits a pathological response

through the simultaneous suppression of chondrogenic genes and the induction of genes encoding catabolic factors (Zieba et al., 2020).

Melatonin (N-acetyl-5-methoxytryptamine) is a molecule that is produced primarily by the pineal gland and other organs that acts to reduce peroxidative damage in the body (Acuña-Castroviejo et al., 2014; Reiter et al., 2016). Melatonin plays an important role in inflammation, apoptosis, proliferation, and metastasis. It has also been shown to have a protective role in chronic diseases including OA, osteoporosis, COVID-19, Parkinson's, Alzheimer's, cancer, and sepsis (Zhang R. et al., 2020; Luo et al., 2020; Xu et al., 2018; Hosseinzadeh et al., 2016).

Melatonin prevents apoptosis and promotes cell survival by inhibiting p38, phosphorylation of JNK MAPKs, and p53 activation by limiting cytochrome c release and activating procaspases proteases (Tomás-Zapico and Coto-Montes, 2005). LIM et al. investigated the effects of melatonin on human chondrocytes and rabbit OA models (Lim et al., 2012). The study showed that melatonin inhibits H_2O_2-induced cytotoxicity, suppresses the production of NO and PEG2 production, and blocks the H_2O_2-induced release of TNF- α, IL- 1β, and IL- 8. Animal experiments have shown that intra-articular injection of melatonin protects articular cartilage by targeting miR-140. This acts to prevent the disruption of cartilage matrix homeostasis and slows the progression of surgically induced OA in mice (Zhang Y. et al., 2019).

Currently, apoptosis is an important focus of OA research as an increasing number of signaling pathways have been shown to be involved. The interaction between non-coding RNA and OA is subject to ongoing investigations. Further elucidation of the respective roles of apoptosis and non-coding RNAs may facilitate the development of novel gene therapy and targeted approaches for the treatment of OA.

Necroptosis

It was more than 2 centuries ago that pathologists determined that necrosis was a cause and consequence of disease (Linkermann, 2014). 100 years later, apoptosis was first discovered. Previous studies identified the pathophysiological importance of necroptosis in myocardial infarction and stroke (Smith et al., 2007), atherosclerosis (Lin et al., 2013), ischemia-reperfusion injury (Linkermann et al., 2012), pancreatitis (Wu et al., 2013), inflammatory bowel disease (Welz et al., 2011), and several other common clinical disorders (Linkermann, 2014).

Necrosis has long been described as the exposure of cells to extreme physicochemical stresses resulting in rapid cell death. However, necrosis can be induced under different stimulatory conditions (e.g., inflammatory factors, interferon-g (IFN-g), ATP depletion, ischemia-reperfusion injury, and pathogens) with steps and signaling events similar to the cell death program (Vanlangenakker et al., 2012; Kaczmarek et al., 2013). This process of regulated necrosis is referred to as necroptosis. Morphological changes during necroptosis include a translucent cytoplasm, swelling of the organelles, permeabilization of the lysosomal and plasma membranes, increased cell volume (oncosis), and mild chromatin condensation (Pasparakis and Vandenabeele, 2015) (**Table 2**).

In contrast to apoptosis and pyroptosis, necroptosis is a caspase-independent death program. Necroptosis is programmed necrotic cell death caused by RIP1/RIP3 and MLKL under various pathological conditions (Han et al., 2011; Chan et al., 2015; Yoon et al., 2017). Apoptosis and necroptosis are closely related, and TNF can determine the final fate of cells (Van Herreweghe et al., 2010). Once TNF binds to TNF receptor 1, TNF induces receptor trimerization and recruits the death domain (DD)-containing adaptor proteins TRADD, TRAF2, and RIP1 to form the so-called complex I (Zhang et al., 2018). Several components of complex I recombine to form a cytosolic complex (complex II) that recruits FADD (Fas-associated via DD) via DD-mediated interactions. In complex II, FADD recruits procaspase-8, whilst RIP1 recruits RIP3. When RIP3 is absent or present at low levels, caspase-8 can activate automatically and the cell undergoes apoptosis (Zhang et al., 2018).

In contrast, in the presence of high concentrations of RIP3, complex II tends to recruit large amounts of this protein and turns itself into a so-called necrosome (Silke et al., 2015). Procaspase-8 in the necrosome cleaves RIP1 and RIP3 preventing the initiation of the necroptosis (Zhang et al., 2018). Therefore, the development of necroptosis requires inhibition of caspase-8 activity (Zhang et al., 2009). RIP3 can be auto-phosphorylated in response to homo-interactions (Chen et al., 2013). Auto-phosphorylated RIP3 recruits and phosphorylates the mixed-lineage kinase domain-like protein (MLKL) (Sun et al., 2012). Phosphorylated RIP3 recruits and phosphorylates MLKL leading to MLKL oligomerization and translocation to the plasma membrane. MLKL oligomers execute necroptosis by generating cation channels causing plasma membrane rupture (Zhang et al., 2018). Recent studies have identified MLKL as the most important working protein for plasma membrane rupture (Chen et al., 2014).

In summary, RIP1 deubiquitination is critical for necrosome assembly and activation (Hitomi et al., 2008), whilst RIP3 determines the susceptibility of cells to move towards necroptosis (Linkermann, 2014) which is ultimately executed by phosphorylated MLKL (Cai et al., 2014).

Necroptosis and Orthopaedic-Related Diseases

Emerging studies have focused on the link between necrosis and orthopaedic-related diseases. Osteoporosis is a systemic bone disease characterized by low bone mass and degenerative damage to the ultrastructure of bone trabeculae resulting in increased bone fragility and susceptibility to fractures (Ensrud and Crandall, 2017). In 2016, Cui et al. constructed an ovariectomy-induced osteoporosis rat model and found that the levels of RIP1, RIP3, and MLKL proteins were significantly elevated in rat femurs and a large number of necrotic osteocytes with positive TUNEL staining but negative caspase-3 staining were seen. The study also showed that administration of necrostatin-1 (Nec-1) significantly reduced the expression of RIP1, RIP3 levels and inhibited programmed necrosis of osteoblasts to reverse bone loss (Cui et al., 2016a; Cui et al., 2016b). Studies have found that excessive alcohol consumption leads to activation of RIPK1/RIPK3/MLKL signaling which

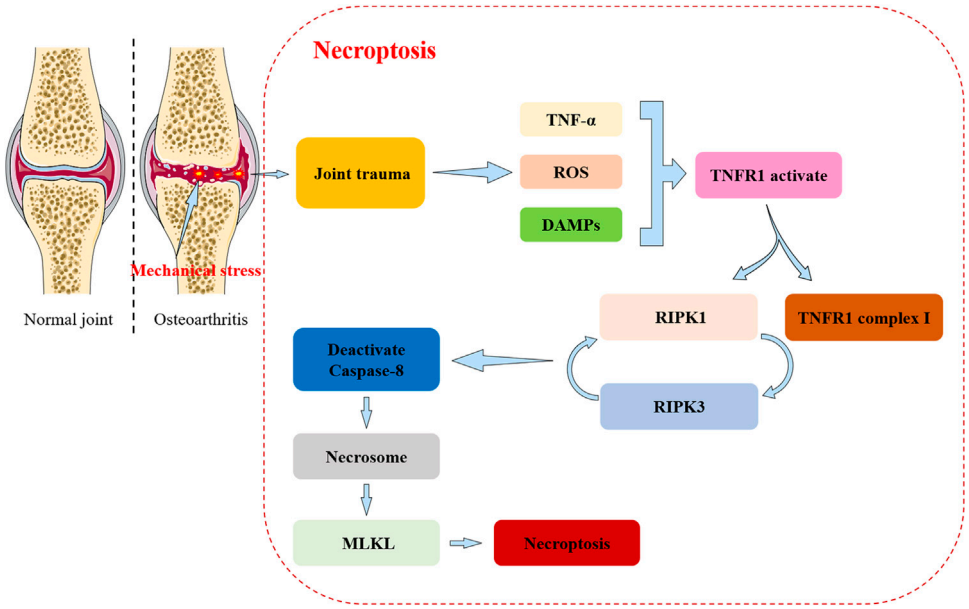

FIGURE 4 | The relationship between necroptosis and osteoarthritis (OA). Necroptosis: Joint trauma leads to the release of death-related triggers including tumor necrosis factor alpha (TNF-α), reactive oxygen/nitrogen species (ROS/RNS), and damage associated molecular patterns (DAMPs). These factors subsequently lead to TNF receptor 1 (TNFR1) activation, forming the TNFR1 complex I and the receptor interacting protein kinase 1 (RIPK1). RIPK1 and RIPK3 interact to activate caspase-8. When caspase8 is inactivated it leads to the appearance of necrosomes which cause the recruitment and phosphorylation of mixed-lineage kinase domain-like protein (MLKL), ultimately leading to disruption of membrane integrity. This leads to the formation of necroptosis.

TABLE 3 | Summary of the pathogenesis of osteoarthritis (OA) and the relationship with different types of cell death (Hunter and Bierma-Zeinstra, 2019; An et al., 2020; Riegger and Brenner, 2019; Shi et al., 2019; Royce et al., 2019; Zhou et al., 2021; Yao et al., 2021; Li et al., 2020; Tang et al., 2018; Xu et al., 2019; Sun et al., 2021; Xu L. et al., 2020; Tian et al., 2020; Aluganti Narasimhulu and Singla, 2021; Zu et al., 2019; Zhao Y. et al., 2018).

Osteoarthritis pathogenesis	**Cell Death Types**			
	Pyroptosis	**Apoptosis**	**Necroptosis**	**Ferroptosis**
Increased inflammatory component	IL-1β↑, IL-18↑, Caspase-1↑, NLRP3↑, MMP-1↑, MMP-13↑, NLRP3↑, NLRP1↑	IL-1β↑, IL-6↑, IL-8↑, TNF-α↑, Bax↑, Bcl-2↑, ROS↑, MMP2↑, MMP9↑	MLKL↑, Cleaved caspase8↑, *p*-MLKL↑	Expression of catabolic genes Mmp3↑, Mmp13↑, Adamts5↑, Ptsg2↑, Col10a1↑
Mechanical overload	IL-1β↑, IL-18↑, Caspase-1↑, NLRP3↑, MMP-1↑, MMP-13↑	Cleaved caspase-3, -6, -7, and -8↑, actin polymerization↑	RIP1↑, RIP3↑, Caspase-8↑, ROS↑, Mitochondrial membrane potential↓	MMP13↑, collagen II↓
Metabolic alterations	Caspase-1↑, IL-1β↑, IL-18↑, Gasdermin-D↑	Phospho-fructose kinase 1 (Pfk1) I↓, hexokinase II (Hk2) I↓, ATP I↓, mitochondrial fusion	Inhibits necroptosis through the hypermethylation of the promoter	Reactive oxygen species (ROS) ↑, lipid ROS↑, MMP13↑, collagen II↓
Cell senescence	IL-1β↑, IL-18↑, activation caspase-1 or caspase-11	COL10A1↑, IL-1↑, TNF-α↑, MMP-13↑, ADAMTS5↑, COL2A1↓	Oxidative stress↑, mTOR signaling↑, DAMPs↑	Mmp3↑, Mmp13↑, Adamts5↑, Ptsg2↑, Col10a1↑

increases necrotrophic apoptosis of osteoblasts and reduces osteogenic differentiation and bone formation *in vivo* and *in vitro*, leading to the development of osteoporosis (Guo et al., 2021).

Lumbar disc herniation (LDH) is a syndrome in which the lumbar disc degenerates and the nucleus pulposus protrudes outwards either alone or together with the fibrous ring and cartilage endplates. This causes irritation or compression of the sinus nerve and nerve roots with lumbar and leg pain as the main symptom (Deyo and Mirza, 2016). The pathogenesis of lumbar disc herniation includes disc degeneration, mechanical stress injury, immune inflammation, and imbalance of extracellular matrix metabolism (Deyo and Mirza, 2016). Necroptosis and lumbar disc herniation are closely associated processes. Recent studies have shown that necrosulfonamide (NSA) protects intervertebral disc degeneration via necroptosis and apoptosis inhibition (Zhang QX. et al., 2020). Chen et al. demonstrated in an *in vivo* model that RIPK1-mediated mitochondrial dysfunction and oxidative stress play a crucial role in NP cell necroptosis and apoptosis during compression

injury. The synergistic regulation of necroptosis and apoptosis may exert more beneficial effects on NP cell survival to ultimately delay or prevent intervertebral disc degeneration (Chen et al., 2018).

Research on the role and mechanisms of necroptosis in OA is becoming an area of increasing interest. Recent evidence suggests that oxidative and mechanical stresses can contribute to the development of necroptosis in OA (Riegger and Brenner, 2019) (**Figure 4**). Mechanical stress also mediates apoptosis and necroptosis in mandibular cartilage via RIP1 (Zhang et al., 2017). Cheng et al. demonstrate that upregulation of RIP1 contributions to OA pathogenesis by mediating chondrocyte necroptosis and ECM destruction via BMP7, a newly identified downstream target of RIP1, in addition to MLKL (Cheng et al., 2021). Chen et al. reported that PLCγ1 inhibition combined with inhibition of apoptosis and necroptosis increases cartilage matrix synthesis in IL-1β treated rat chondrocytes (Chen et al., 2021). Also, recent evidence has shown that perturbation of the TRIM24-RIP3 axis regulates mouse osteoarticular pathogenesis by activating RIP3 kinase and regulating the expression of catabolic factors (Jeon et al., 2020).

In summary, the development and progression of OA is closely related to RIP1 and RIP3. Recent studies have suggested that necroptosis has an important position in inflammation-related diseases. Necroptosis and apoptosis are closely related highlighting the complexity and diversity of mechanisms of disease.

DISCUSSION AND PERSPECTIVES

OA is a complex chronic disease that is affected by age, gender, weight, mechanical injury and joint deformity. The number of people affected and the cost of medical treatment are increasing every year, hence there is a need for improved OA treatment options. The current pharmacological approach to treating OA is mostly palliative and surgery remains the ultimate option for patients. As the understanding of the etiology and pathogenesis of OA improves, more and more potential targets are being used to prevent the development and progression of the disease. The relationship between the pathogenesis of OA and different cell death types is likely to remain a future research focus.

During the development of OA, inflammatory mediators such as ROS, interleukins, NO, and MMP are closely related to chondrocyte apoptosis that involves the mitochondrial, death receptor and JNK signaling pathways. These signaling pathways are directly related to apoptosis in chondrocytes and regulate gene targets, proteins and miRNAs (**Table 3**).

The relationship between pyroptosis and OA has recently attracted attention. Pyroptosis produced during cell scorch death promotes the development of OA which contributes to pain associated with OA. The current focus of research remains on NLRP3 inflammatory vesicles. Undeniably, current experimental evidence *in vivo* and *in vitro* strongly suggests a close relationship between pyroptosis and OA. However, the molecular regulatory mechanisms of the relevant signaling pathways and the interconnections between these factors have not been fully elucidated. Few studies have reported on the link between pyroptosis, non-coding RNAs and OA.

Ferroptosis is an iron-dependent, non-apoptotic form of cell death that is distinct from apoptosis, pyroptosis, or necrosis. The main features of ferroptosis are lipid peroxidation and iron overload. New mechanisms and novel targets have been identified in studies of tumors (including hepatocellular carcinoma, pancreatic cancer, breast cancer, renal clear cell carcinoma), neurological diseases (including Alzheimer's disease, Parkinson's disease), cardiovascular diseases (including myocardial injury, ischemia-reperfusion, hemorrhagic stroke), and chronic diseases (including OA, rheumatoid arthritis). This provides novel perspectives and strategies for the treatment of related diseases. The occurrence of ferroptosis involves the expression and regulation of multiple genes, with complex signaling pathways and mechanisms that have not been fully elucidated. Currently available studies cannot fully reveal the relationship between ferroptosis and disease, and more research is needed in this area.

In conclusion, apoptosis, ferroptosis and pyroptosis have important roles in the development of OA, but deeper studies are needed. Exploring the relationship between OA and cell death can provide a theoretical basis and enable the development of translational strategies towards curing OA Kayagaki et al., 2011.

AUTHOR CONTRIBUTIONS

LP conceived the scope and schemes of this review manuscript. JY and SH wrote the first draft. JY, and SH revised and finalized the manuscript. Others proofread the content of the article. all authors read and approved the submitted version.

FUNDING

This work was supported by the National Natural Science Foundation of China (NSFC No. 82060347), the Natural Science Foundation of Hainan Province (820QN387), The Innovative Research Projects for Postgraduates in Higher Education Institutions in Hainan Province (Hys 2020-342), Hainan General Hospital Hospital-level Youth Fund Project (QN202016).

ACKNOWLEDGMENTS

We thank the members of Peng's research group for providing feedback and help in preparing the manuscript.

REFERENCES

Acuña-Castroviejo, D., Escames, G., Venegas, C., Díaz-Casado, M. E., Lima-Cabello, E., López, L. C., et al. (2014). Extrapineal Melatonin: Sources, Regulation, and Potential Functions. *Cell. Mol. Life Sci.* 71 (16), 2997–3025. doi:10.1007/s00018-014-1579-2

Aglietti, R. A., Estevez, A., Gupta, A., Ramirez, M. G., Liu, P. S., Kayagaki, N., et al. (2016). GsdmD P30 Elicited by Caspase-11 during Pyroptosis Forms Pores in Membranes. *Proc. Natl. Acad. Sci. USA* 113 (28), 7858–7863. doi:10.1073/pnas.1607769113

Aluganti Narasimhulu, C., and Singla, D. K. (2021). Amelioration of Diabetes-Induced Inflammation Mediated Pyroptosis, Sarcopenia, and Adverse Muscle Remodelling by Bone Morphogenetic Protein-7. *J. cachexia, sarcopenia Muscle* 12 (2), 403–420. doi:10.1002/jcsm.12662

An, S., Hu, H., Li, Y., and Hu, Y. (2020). Pyroptosis Plays a Role in Osteoarthritis. *Aging Dis.* 11 (5), 1146–1157. doi:10.14336/ad.2019.1127

Anderton, H., Wicks, I. P., and Silke, J. (2020). Cell Death in Chronic Inflammation: Breaking the Cycle to Treat Rheumatic Disease. *Nat. Rev. Rheumatol.* 16 (9), 496–513. doi:10.1038/s41584-020-0455-8

Ayton, S., Wang, Y., Diouf, I., Schneider, J. A., Brockman, J., Morris, M. C., et al. (2020). Brain Iron Is Associated with Accelerated Cognitive Decline in People with Alzheimer Pathology. *Mol. Psychiatry* 25 (11), 2932–2941. doi:10.1038/s41380-019-0375-7

Baker, K., Grainger, A., Niu, J., Clancy, M., Guermazi, A., Crema, M., et al. (2010). Relation of Synovitis to Knee Pain Using Contrast-Enhanced MRIs. *Ann. Rheum. Dis.* 69 (10), 1779–1783. doi:10.1136/ard.2009.121426

Bao, Q., and Shi, Y. (2007). Apoptosome: a Platform for the Activation of Initiator Caspases. *Cell Death Differ* 14 (1), 56–65. doi:10.1038/sj.cdd.4402028

Bartlett, R., Stokes, L., and Sluyter, R. (2014). The P2X7 Receptor Channel: Recent Developments and the Use of P2X7 Antagonists in Models of Disease. *Pharmacol. Rev.* 66 (3), 638–675. doi:10.1124/pr.113.008003

Baud, V., and Karin, M. (2001). Signal Transduction by Tumor Necrosis Factor and its Relatives. *Trends Cel Biol.* 11 (9), 372–377. doi:10.1016/s0962-8924(01)02064-5

Boise, L. H., González-García, M., Postema, C. E., Ding, L., Lindsten, T., Turka, L. A., et al. (1993). Bcl-X, a Bcl-2-Related Gene that Functions as a Dominant Regulator of Apoptotic Cell Death. *Cell* 74 (4), 597–608. doi:10.1016/0092-8674(93)90508-n

Broz, P., von Moltke, J., Jones, J. W., Vance, R. E., and Monack, D. M. (2010). Differential Requirement for Caspase-1 Autoproteolysis in Pathogen-Induced Cell Death and Cytokine Processing. *Cell Host & Microbe* 8 (6), 471–483. doi:10.1016/j.chom.2010.11.007

Burr, D. B. (2004). Anatomy and Physiology of the Mineralized Tissues: Role in the Pathogenesis of Osteoarthrosis. *Osteoarthritis and Cartilage* 12, 20–30. doi:10.1016/j.joca.2003.09.016

Cai, C., Min, S., Yan, B., Liu, W., Yang, X., Li, L., et al. (2019). MiR-27a Promotes the Autophagy and Apoptosis of IL-1β Treated-Articular Chondrocytes in Osteoarthritis through PI3K/AKT/mTOR Signaling. *Aging* 11 (16), 6371–6384. doi:10.18632/aging.102194

Cai, Z., Jitkaew, S., Zhao, J., Chiang, H.-C., Choksi, S., Liu, J., et al. (2014). Plasma Membrane Translocation of Trimerized MLKL Protein Is Required for TNF-Induced Necroptosis. *Nat. Cel Biol* 16 (1), 55–65. doi:10.1038/ncb2883

Cao, J. Y., and Dixon, S. J. (2016). Mechanisms of Ferroptosis. *Cel. Mol. Life Sci.* 73, 2195–2209. doi:10.1007/s00018-016-2194-1

Chan, F. K.-M., Luz, N. F., and Moriwaki, K. (2015). Programmed Necrosis in the Cross Talk of Cell Death and Inflammation. *Annu. Rev. Immunol.* 33, 79–106. doi:10.1146/annurev-immunol-032414-112248

Charlier, E., Relic, B., Deroyer, C., Malaise, O., Neuville, S., Collée, J., et al. (2016). Insights on Molecular Mechanisms of Chondrocytes Death in Osteoarthritis. *Int. J. Mol. Sci.* 17 (12), 2146. doi:10.3390/ijms17122146

Chen, G., and Goeddel, D. V. (2002). TNF-R1 Signaling: a Beautiful Pathway. *Science* 296 (5573), 1634–1635. doi:10.1126/science.1071924

Chen, S., Lv, X., Hu, B., Zhao, L., Li, S., Li, Z., et al. (2018). Critical Contribution of RIPK1 Mediated Mitochondrial Dysfunction and Oxidative Stress to Compression-Induced Rat Nucleus Pulposus Cells Necroptosis and Apoptosis. *Apoptosis* 23, 299–313. doi:10.1007/s10495-018-1455-x

Chen, W., Zhou, Z., Li, L., Zhong, C.-Q., Zheng, X., Wu, X., et al. (2013). Diverse Sequence Determinants Control Human and Mouse Receptor Interacting Protein 3 (RIP3) and Mixed Lineage Kinase Domain-like (MLKL) Interaction in Necroptotic Signaling. *J. Biol. Chem.* 288 (23), 16247–16261. doi:10.1074/jbc.M112.435545

Chen, X., Chen, R., Xu, Y., and Xia, C. (2021). PLCγ1 Inhibition Combined with Inhibition of Apoptosis and Necroptosis Increases Cartilage Matrix Synthesis in IL-1β-treated Rat Chondrocytes. *FEBS open bio* 11 (2), 435–445. doi:10.1002/2211-5463.13064

Chen, X., Li, W., Ren, J., Huang, D., He, W.-t., Song, Y., et al. (2014). Translocation of Mixed Lineage Kinase Domain-like Protein to Plasma Membrane Leads to Necrotic Cell Death. *Cell Res* 24 (1), 105–121. doi:10.1038/cr.2013.171

Cheng, J., Duan, X., Fu, X., Jiang, Y., Yang, P., Cao, C., et al. (2021). RIP1 Perturbation Induces Chondrocyte Necroptosis and Promotes Osteoarthritis Pathogenesis via Targeting BMP7. *Front. Cel Dev. Biol.* 9, 638382. doi:10.3389/fcell.2021.638382

Chevalier, X., Conrozier, T., and Richette, P. (2011). Desperately Looking for the Right Target in Osteoarthritis: the anti-IL-1 Strategy. *Arthritis Res. Ther.* 13 (4), 124. doi:10.1186/ar3436

Chittenden, T., Flemington, C., Houghton, A. B., Ebb, R. G., Gallo, G. J., Elangovan, B., et al. (1995). A Conserved Domain in Bak, Distinct from BH1 and BH2, Mediates Cell Death and Protein Binding Functions. *EMBO J.* 14 (22), 5589–5596. doi:10.1002/j.1460-2075.1995.tb00246.x

Christofferson, D. E., and Yuan, J. (2010). Necroptosis as an Alternative Form of Programmed Cell Death. *Curr. Opin. Cel Biol.* 22 (2), 263–268. doi:10.1016/j.ceb.2009.12.003

Cookson, B. T., and Brennan, M. A. (2001). Pro-inflammatory Programmed Cell Death. *Trends Microbiol.* 9 (3), 113–114. doi:10.1016/s0966-842x(00)01936-3

Cui, H., Zhu, Y., and Jiang, D. (2016b). The RIP1-RIP3 Complex Mediates Osteocyte Necroptosis after Ovariectomy in Rats. *PLoS One* 11 (3), e0150805. doi:10.1371/journal.pone.0150805

Cui, H., Zhu, Y., Yang, Q., Zhao, W., Zhang, S., Zhou, A., et al. (2016a). Necrostatin-1 Treatment Inhibits Osteocyte Necroptosis and Trabecular Deterioration in Ovariectomized Rats. *Sci. Rep.* 6, 33803. doi:10.1038/srep33803

Davis, R. J. (2000). Signal Transduction by the JNK Group of MAP Kinases. *Cell* 103 (2), 239–252. doi:10.1016/s0092-8674(00)00116-1

Deyo, R. A., and Mirza, S. K. (2016). Herniated Lumbar Intervertebral Disk. *N. Engl. J. Med.* 374 (18), 1763–1772. doi:10.1056/NEJMcp1512658

Dixon, S. J., Lemberg, K. M., Lamprecht, M. R., Skouta, R., Zaitsev, E. M., Gleason, C. E., et al. (2012a). Ferroptosis: an Iron-dependent Form of Nonapoptotic Cell Death. *Cell* 149 (5), 1060–1072. doi:10.1016/j.cell.2012.03.042

Dixon, S. J., and Stockwell, B. R. (2014). The Role of Iron and Reactive Oxygen Species in Cell Death. *Nat. Chem. Biol.* 10 (1), 9–17. doi:10.1038/nchembio.1416

Dolma, S., Lessnick, S. L., Hahn, W. C., and Stockwell, B. R. (2003). Identification of Genotype-Selective Antitumor Agents Using Synthetic Lethal Chemical Screening in Engineered Human Tumor Cells. *Cancer Cell* 3 (3), 285–296. doi:10.1016/s1535-6108(03)00050-3

Dondelinger, Y., Delanghe, T., Rojas-Rivera, D., Priem, D., Delvaeye, T., Bruggeman, I., et al. (2017). MK2 Phosphorylation of RIPK1 Regulates TNF-Mediated Cell Death. *Nat. Cel Biol* 19 (10), 1237–1247. doi:10.1038/ncb3608

Elmore, S. (2007). Apoptosis: a Review of Programmed Cell Death. *Toxicol. Pathol.* 35 (4), 495–516. doi:10.1080/01926230701320337

Enari, M., Sakahira, H., Yokoyama, H., Okawa, K., Iwamatsu, A., and Nagata, S. (1998). A Caspase-Activated DNase that Degrades DNA during Apoptosis, and its Inhibitor ICAD. *Nature* 391 (6662), 43–50. doi:10.1038/34112

Ensrud, K. E., and Crandall, C. J. (2017). Osteoporosis. *Ann. Intern. Med.* 167 (3), ITC17–ITC32. doi:10.7326/aitc201708010

Evavold, C. L., Ruan, J., Tan, Y., Xia, S., Wu, H., and Kagan, J. C. (2018). The Pore-Forming Protein Gasdermin D Regulates Interleukin-1 Secretion from Living Macrophages. *Immunity* 48 (1), 35–44. e6. doi:10.1016/j.immuni.2017.11.013

Fang, X., Cai, Z., Wang, H., Han, D., Cheng, Q., Zhang, P., et al. (2020). Loss of Cardiac Ferritin H Facilitates Cardiomyopathy via Slc7a11-Mediated Ferroptosis. *Circ. Res.* 127 (4), 486–501. doi:10.1161/circresaha.120.316509

Feng, S.-Q., Yao, X., Zhang, Y., Hao, J., Duan, H.-Q., Zhao, C.-X., et al. (2019). Deferoxamine Promotes Recovery of Traumatic Spinal Cord Injury by

Inhibiting Ferroptosis. *Neural Regen. Res.* 14 (3), 532–541. doi:10.4103/1673-5374.245480

Feng, S., Fox, D., and Man, S. M. (2018). Mechanisms of Gasdermin Family Members in Inflammasome Signaling and Cell Death. *J. Mol. Biol.* 430, 3068–3080. doi:10.1016/j.jmb.2018.07.002

Fernandes-Alnemri, T., Wu, J., Yu, J.-W., Datta, P., Miller, B., Jankowski, W., et al. (2007). The Pyroptosome: a Supramolecular Assembly of ASC Dimers Mediating Inflammatory Cell Death via Caspase-1 Activation. *Cel Death Differ* 14 (9), 1590–1604. doi:10.1038/sj.cdd.4402194

Fink, S. L., Bergsbaken, T., and Cookson, B. T. (2008). Anthrax Lethal Toxin and Salmonella Elicit the Common Cell Death Pathway of Caspase-1-dependent Pyroptosis via Distinct Mechanisms. *Proc. Natl. Acad. Sci.* 105 (11), 4312–4317. doi:10.1073/pnas.0707370105

Fuchs, Y., and Steller, H. (2011). Programmed Cell Death in Animal Development and Disease. *Cell* 147 (4), 742–758. doi:10.1016/j.cell.2011.10.033

Fuentes-Prior, P., and Salvesen, G. S. (2004). The Protein Structures that Shape Caspase Activity, Specificity, Activation and Inhibition. *Biochem. J.* 384 (Pt 2), 201–232. doi:10.1042/bj20041142

Gao, Y.-L., Zhai, J.-H., and Chai, Y.-F. (2018). Recent Advances in the Molecular Mechanisms Underlying Pyroptosis in Sepsis. *Mediators Inflamm.* 2018, 1–7. doi:10.1155/2018/5823823

Gibson, L., Holmgreen, S. P., Huang, D. C., Bernard, O., Copeland, N. G., Jenkins, N. A., et al. (1996). Bcl-W, a Novel Member of the Bcl-2 Family, Promotes Cell Survival. *Oncogene* 13 (4), 665–675.

Goldring, M. B., and Goldring, S. R. (2010). Articular Cartilage and Subchondral Bone in the Pathogenesis of Osteoarthritis. *Ann. N. Y Acad. Sci.* 1192, 230–237. doi:10.1111/j.1749-6632.2009.05240.x

Goldring, S. R. (2008). The Role of Bone in Osteoarthritis Pathogenesis. *Rheum. Dis. Clin. North America* 34 (3), 561–571. doi:10.1016/j.rdc.2008.07.001

Good, P. F., Perl, D. P., Bierer, L. M., and Schmeidler, J. (1992). Selective Accumulation of Aluminum and Iron in the Neurofibrillary Tangles of Alzheimer's Disease: a Laser Microprobe (LAMMA) Study. *Ann. Neurol.* 31 (3), 286–292. doi:10.1002/ana.410310310

Green, D. R. (2003). Overview: Apoptotic Signaling Pathways in the Immune System. *Immunol. Rev.* 193, 5–9. doi:10.1034/j.1600-065x.2003.00045.x

Guo, B., Godzik, A., and Reed, J. C. (2001). Bcl-G, a Novel Pro-apoptotic Member of the Bcl-2 Family. *J. Biol. Chem.* 276 (4), 2780–2785. doi:10.1074/jbc.M005889200

Guo, M., Huang, Y.-L., Wu, Q., Chai, L., Jiang, Z.-Z., Zeng, Y., et al. (2021). Chronic Ethanol Consumption Induces Osteopenia via Activation of Osteoblast Necroptosis. *Oxidative Med. Cell Longevity* 2021, 1–24. doi:10.1155/2021/3027954

Han, J., Zhong, C.-Q., and Zhang, D.-W. (2011). Programmed Necrosis: Backup to and Competitor with Apoptosis in the Immune System. *Nat. Immunol.* 12 (12), 1143–1149. doi:10.1038/ni.2159

Haseeb, A., and Haqqi, T. M. (2013). Immunopathogenesis of Osteoarthritis. *Clin. Immunol.* 146 (3), 185–196. doi:10.1016/j.clim.2012.12.011

Hersh, D., Monack, D. M., Smith, M. R., Ghori, N., Falkow, S., and Zychlinsky, A. (1999). The Salmonella Invasin SipB Induces Macrophage Apoptosis by Binding to Caspase-1. *Proc. Natl. Acad. Sci.* 96 (5), 2396–2401. doi:10.1073/pnas.96.5.2396

Hitomi, J., Christofferson, D. E., Ng, A., Yao, J., Degterev, A., Xavier, R. J., et al. (2008). Identification of a Molecular Signaling Network that Regulates a Cellular Necrotic Cell Death Pathway. *Cell* 135 (7), 1311–1323. doi:10.1016/j.cell.2008.10.044

Honarpour, N., Gilbert, S. L., Lahn, B. T., Wang, X., and Herz, J. (2001). Apaf-1 Deficiency and Neural Tube Closure Defects Are Found in Fog Mice. *Proc. Natl. Acad. Sci.* 98 (17), 9683–9687. doi:10.1073/pnas.171283198

Hosaka, Y., Saito, T., Sugita, S., Hikata, T., Kobayashi, H., Fukai, A., et al. (2013). Notch Signaling in Chondrocytes Modulates Endochondral Ossification and Osteoarthritis Development. *Proc. Natl. Acad. Sci.* 110 (5), 1875–1880. doi:10.1073/pnas.1207458110

Hosseinzadeh, A., Kamrava, S. K., Joghataei, M. T., Darabi, R., Shakeri-Zadeh, A., Shahriari, M., et al. (2016). Apoptosis Signaling Pathways in Osteoarthritis and Possible Protective Role of Melatonin. *J. Pineal Res.* 61 (4), 411–425. doi:10.1111/jpi.12362

Houard, X., Goldring, M. B., and Berenbaum, F. (2013). Homeostatic Mechanisms in Articular Cartilage and Role of Inflammation in Osteoarthritis. *Curr. Rheumatol. Rep.* 15 (11), 375. doi:10.1007/s11926-013-0375-6

Hsu, S. Y., and Hsueh, A. J. W. (1998). A Splicing Variant of the Bcl-2 Member Bok with a Truncated BH3 Domain Induces Apoptosis but Does Not Dimerize with Antiapoptotic Bcl-2 Proteins *In Vitro*. *J. Biol. Chem.* 273 (46), 30139–30146. doi:10.1074/jbc.273.46.30139

Hu, J., Zhou, J., Wu, J., Chen, Q., Du, W., Fu, F., et al. (2020). Loganin Ameliorates Cartilage Degeneration and Osteoarthritis Development in an Osteoarthritis Mouse Model through Inhibition of NF-Kb Activity and Pyroptosis in Chondrocytes. *J. Ethnopharmacology* 247, 112261. doi:10.1016/j.jep.2019.112261

Hunter, D. J., and Bierma-Zeinstra, S. (2019). Osteoarthritis. *The Lancet* 393 (10182), 1745–1759. doi:10.1016/s0140-6736(19)30417-9

Hunter, D. J., Schofield, D., and Callander, E. (2014). The Individual and Socioeconomic Impact of Osteoarthritis. *Nat. Rev. Rheumatol.* 10 (7), 437–441. doi:10.1038/nrrheum.2014.44

Jeon, J., Noh, H.-J., Lee, H., Park, H.-H., Ha, Y.-J., Park, S. H., et al. (2020). TRIM24-RIP3 axis Perturbation Accelerates Osteoarthritis Pathogenesis. *Ann. Rheum. Dis.* 79 (12), 1635–1643. doi:10.1136/annrheumdis-2020-217904

Jiang, X., Stockwell, B. R., and Conrad, M. (2021). Ferroptosis: Mechanisms, Biology and Role in Disease. *Nat. Rev. Mol. Cel Biol* 22 (4), 266–282. doi:10.1038/s41580-020-00324-8

Jorgensen, I., and Miao, E. A. (2015). Pyroptotic Cell Death Defends against Intracellular Pathogens. *Immunol. Rev.* 265 (1), 130–142. doi:10.1111/imr.12287

Jorgensen, I., Rayamajhi, M., and Miao, E. A. (2017). Programmed Cell Death as a Defence against Infection. *Nat. Rev. Immunol.* 17 (3), 151–164. doi:10.1038/nri.2016.147

Kaczmarek, A., Vandenabeele, P., and Krysko, D. V. (2013). Necroptosis: the Release of Damage-Associated Molecular Patterns and its Physiological Relevance. *Immunity* 38 (2), 209–223. doi:10.1016/j.immuni.2013.02.003

Kajarabille, N., and Latunde-Dada, G. O. (2019). Programmed Cell-Death by Ferroptosis: Antioxidants as Mitigators. *Int. J. Mol. Sci.* 20 (19), 4968. doi:10.3390/ijms20194968

Kapoor, M., Martel-Pelletier, J., Lajeunesse, D., Pelletier, J.-P., and Fahmi, H. (2011). Role of Proinflammatory Cytokines in the Pathophysiology of Osteoarthritis. *Nat. Rev. Rheumatol.* 7 (1), 33–42. doi:10.1038/nrrheum.2010.196

Karlsson, C., Brantsing, C., Egell, S., and Lindahl, A. (2008). Notch1, Jagged1, and HES5 Are Abundantly Expressed in Osteoarthritis. *Cells Tissues Organs* 188 (3), 287–298. doi:10.1159/000121610

Kawai, T., and Akira, S. (2007). TLR Signaling. *Semin. Immunol.* 19 (1), 24–32. doi:10.1016/j.smim.2006.12.004

Kayagaki, N., Stowe, I. B., Lee, B. L., O'Rourke, K., Anderson, K., Warming, S., et al. (2015). Caspase-11 Cleaves Gasdermin D for Non-canonical Inflammasome Signalling. *Nature* 526 (7575), 666–671. doi:10.1038/nature15541

Kayagaki, N., Warming, S., Lamkanfi, M., Walle, L. V., Louie, S., Dong, J., et al. (2011). Non-canonical Inflammasome Activation Targets Caspase-11. *Nature* 479 (7371), 117–121. doi:10.1038/nature10558

Ke, F. F. S., Vanyai, H. K., Cowan, A. D., Delbridge, A. R. D., Whitehead, L., Grabow, S., et al. (2018). Embryogenesis and Adult Life in the Absence of Intrinsic Apoptosis Effectors BAX, BAK, and BOK. *Cell* 173 (5), 1217–1230. e17. doi:10.1016/j.cell.2018.04.036

Ke, N., Godzik, A., and Reed, J. C. (2001). Bcl-B, a Novel Bcl-2 Family Member that Differentially Binds and Regulates Bax and Bak. *J. Biol. Chem.* 276 (16), 12481–12484. doi:10.1074/jbc.C000871200

Kerr, J. F. R., Wyllie, A. H., and Currie, A. R. (1972). Apoptosis: A Basic Biological Phenomenon with Wideranging Implications in Tissue Kinetics. *Br. J. Cancer* 26 (4), 239–257. doi:10.1038/bjc.1972.33

Koelling, S., Kruegel, J., Irmer, M., Path, J. R., Sadowski, B., Miro, X., et al. (2009). Migratory Chondrogenic Progenitor Cells from Repair Tissue during the Later Stages of Human Osteoarthritis. *Cell stem cell* 4 (4), 324–335. doi:10.1016/j.stem.2009.01.015

Kohn, A., Dong, Y., Mirando, A. J., Jesse, A. M., Honjo, T., Zuscik, M. J., et al. (2012). Cartilage-specific RBPjκ-dependent and -independent Notch Signals Regulate Cartilage and Bone Development. *Development* 139 (6), 1198–1212. doi:10.1242/dev.070649

Kozopas, K. M., Yang, T., Buchan, H. L., Zhou, P., and Craig, R. W. (1993). MCL1, a Gene Expressed in Programmed Myeloid Cell Differentiation, Has Sequence Similarity to BCL2. *Proc. Natl. Acad. Sci.* 90 (8), 3516–3520. doi:10.1073/pnas.90.8.3516

Kroemer, G., and Reed, J. C. (2000). Mitochondrial Control of Cell Death. *Nat. Med.* 6 (5), 513–519. doi:10.1038/74994

Kufer, T. A., and Sansonetti, P. J. (2007). Sensing of Bacteria: NOD a Lonely Job. *Curr. Opin. Microbiol.* 10 (1), 62–69. doi:10.1016/j.mib.2006.11.003

Latunde-Dada, G. O. (2017). Ferroptosis: Role of Lipid Peroxidation, Iron and Ferritinophagy. *Biochim. Biophys. Acta (Bba) - Gen. Subjects* 1861 (8), 1893–1900. doi:10.1016/j.bbagen.2017.05.019

Lavrik, I., Golks, A., and Krammer, P. H. (2005). Death Receptor Signaling. *J. Cel Sci* 118 (Pt 2), 265–267. doi:10.1242/jcs.01610

Li, C., Li, L., and Lan, T. (2021c). Co-treatment with Disulfiram and Glycyrrhizic Acid Suppresses the Inflammatory Response of Chondrocytes. *J. Orthop. Surg. Res.* 16 (1), 132. doi:10.1186/s13018-021-02262-3

Li, Z., Cheng, J., and Liu, J. (2020). Baicalin Protects Human OA Chondrocytes against IL-1β-Induced Apoptosis and ECM Degradation by Activating Autophagy via MiR-766-3p/AIFM1 Axis. *Drug Des. Dev. Ther.* 14, 2645–2655. doi:10.2147/dddt.s255823

Li, Z., Huang, Z., and Bai, L. (2021a). The P2X7 Receptor in Osteoarthritis. *Front. Cel Dev. Biol.* 9, 628330. doi:10.3389/fcell.2021.628330

Li, Z., Huang, Z., Zhang, H., Lu, J., Tian, Y., Wei, Y., et al. (2021b). P2X7 Receptor Induces Pyroptotic Inflammation and Cartilage Degradation in Osteoarthritis via NF-Kb/nlrp3 Crosstalk. *Oxidative Med. Cell Longevity* 2021, 1–16. doi:10.1155/2021/8868361

Lim, H.-D., Kim, Y.-S., Ko, S.-H., Yoon, I.-J., Cho, S.-G., Chun, Y.-H., et al. (2012). Cytoprotective and Anti-inflammatory Effects of Melatonin in Hydrogen Peroxide-Stimulated CHON-001 Human Chondrocyte Cell Line and Rabbit Model of Osteoarthritis via the SIRT1 Pathway. *J. Pineal Res.* 53 (3), 225–237. doi:10.1111/j.1600-079X.2012.00991.x

Lin, E., Orlofsky, A., Wang, H., Reed, J., and Prystowsky, M. (1996). A1, a Bcl-2 Family Member, Prolongs Cell Survival and Permits Myeloid Differentiation. *Blood* 87 (3), 983–992. doi:10.1182/blood.v87.3.983.bloodjournal873983

Lin, J., Li, H., Yang, M., Ren, J., Huang, Z., Han, F., et al. (2013). A Role of RIP3-Mediated Macrophage Necrosis in Atherosclerosis Development. *Cel Rep.* 3 (1), 200–210. doi:10.1016/j.celrep.2012.12.012

Linkermann, A., Bräsen, J. H., Himmerkus, N., Liu, S., Huber, T. B., Kunzendorf, U., et al. (2012). Rip1 (Receptor-interacting Protein Kinase 1) Mediates Necroptosis and Contributes to Renal Ischemia/reperfusion Injury. *Kidney Int.* 81 (8), 751–761. doi:10.1038/ki.2011.450

Linkermann, A., and Green, D. R. (2014). Necroptosis. *N. Engl. J. Med.* 370 (5), 455–465. doi:10.1056/NEJMra1310050

Liu, G., Liu, Q., Yan, B., Zhu, Z., and Xu, Y. (2020). USP7 Inhibition Alleviates H2O2-Induced Injury in Chondrocytes via Inhibiting NOX4/NLRP3 Pathway. *Front. Pharmacol.* 11, 617270. doi:10.3389/fphar.2020.617270

Liu, Q., Wu, Z., Hu, D., Zhang, L., Wang, L., and Liu, G. (2019). Low Dose of Indomethacin and Hedgehog Signaling Inhibitor Administration Synergistically Attenuates Cartilage Damage in Osteoarthritis by Controlling Chondrocytes Pyroptosis. *Gene* 712, 143959. doi:10.1016/j.gene.2019.143959

Liu, X., Zhang, Z., Ruan, J., Pan, Y., Magupalli, V. G., Wu, H., et al. (2016). Inflammasome-activated Gasdermin D Causes Pyroptosis by Forming Membrane Pores. *Nature* 535 (7610), 153–158. doi:10.1038/nature18629

Liu, Z., Chen, J., Mirando, A. J., Wang, C., Zuscik, M. J., O'Keefe, R. J., et al. (2015). A Dual Role for NOTCH Signaling in Joint Cartilage Maintenance and Osteoarthritis. *Sci. Signal.* 8 (386), ra71. doi:10.1126/scisignal.aaa3792

Loeser, R. F., Collins, J. A., and Diekman, B. O. (2016). Ageing and the Pathogenesis of Osteoarthritis. *Nat. Rev. Rheumatol.* 12 (7), 412–420. doi:10.1038/nrrheum.2016.65

Loeser, R. F., Goldring, S. R., Scanzello, C. R., and Goldring, M. B. (2012). Osteoarthritis: a Disease of the Joint as an Organ. *Arthritis Rheum.* 64 (6), 1697–1707. doi:10.1002/art.34453

López-Armada, M. J., Caramés, B., Lires-Deán, M., Cillero-Pastor, B., Ruiz-Romero, C., Galdo, F., et al. (2006). Cytokines, Tumor Necrosis Factor-α and Interleukin-1β, Differentially Regulate Apoptosis in Osteoarthritis Cultured Human Chondrocytes. *Osteoarthritis and Cartilage* 14 (7), 660–669. doi:10.1016/j.joca.2006.01.005

Lü, G., Li, L., Wang, B., and Kuang, L. (2020). LINC00623/miR-101/HRAS axis Modulates IL-1β-mediated ECM Degradation, Apoptosis and Senescence of Osteoarthritis Chondrocytes. *Aging* 12 (4), 3218–3237. doi:10.18632/aging.102801

Luke, J. J., Van De Wetering, C. I., and Knudson, C. M. (2003). Lymphoma Development in Bax Transgenic Mice Is Inhibited by Bcl-2 and Associated with Chromosomal Instability. *Cel Death Differ* 10 (6), 740–748. doi:10.1038/sj.cdd.4401233

Luo, F., Sandhu, A. F., Rungratanawanich, W., Williams, G. E., Akbar, M., Zhou, S., et al. (2020). Melatonin and Autophagy in Aging-Related Neurodegenerative Diseases. *Int. J. Mol. Sci.* 21 (19), 7174. doi:10.3390/ijms21197174

Luo, H., and Zhang, R. (2021). Icariin Enhances Cell Survival in Lipopolysaccharide-Induced Synoviocytes by Suppressing Ferroptosis via the Xc-/GPX4 axis. *Exp. Ther. Med.* 21 (1), 72. doi:10.3892/etm.2020.9504

Majno, G., and Joris, I. (1995). Apoptosis, Oncosis, and Necrosis. An Overview of Cell Death. *Am. J. Pathol.* 146 (1), 3–15.

Man, S. M., and Kanneganti, T.-D. (2015). Regulation of Inflammasome Activation. *Immunol. Rev.* 265 (1), 6–21. doi:10.1111/imr.12296

Mariathasan, S., Weiss, D. S., Dixit, V. M., and Monack, D. M. (2005). Innate Immunity against Francisella Tularensis Is Dependent on the ASC/caspase-1 axis. *J. Exp. Med.* 202 (8), 1043–1049. doi:10.1084/jem.20050977

Mariño, G., and Kroemer, G. (2013). Mechanisms of Apoptotic Phosphatidylserine Exposure. *Cel Res* 23 (11), 1247–1248. doi:10.1038/cr.2013.115

Martel-Pelletier, J., Barr, A. J., Cicuttini, F. M., Conaghan, P. G., Cooper, C., Goldring, M. B., et al. (2016). Osteoarthritis. *Nat. Rev. Dis. Primers* 2, 16072. doi:10.1038/nrdp.2016.72

Martinon, F., and Tschopp, J. (2007). Inflammatory Caspases and Inflammasomes: Master Switches of Inflammation. *Cel Death Differ* 14 (1), 10–22. doi:10.1038/sj.cdd.4402038

Matzinger, P. (2002). The Danger Model: a Renewed Sense of Self. *Science* 296 (5566), 301–305. doi:10.1126/science.1071059

Medema, J. P., Scaffidi, C., Kischkel, F. C., Shevchenko, A., Mann, M., Krammer, P. H., et al. (1997). FLICE Is Activated by Association with the CD95 Death-Inducing Signaling Complex (DISC). *EMBO J.* 16 (10), 2794–2804. doi:10.1093/emboj/16.10.2794

Mirando, A. J., Liu, Z., Moore, T., Lang, A., Kohn, A., Osinski, A. M., et al. (2013). RBPjκ-Dependent Notch Signaling Is Required for Articular Cartilage and Joint Maintenance. *Arthritis Rheum.* 65 (10), a–n. doi:10.1002/art.38076

Newton, K., and Manning, G. (2016). Necroptosis and Inflammation. *Annu. Rev. Biochem.* 85, 743–763. doi:10.1146/annurev-biochem-060815-014830

Oltvai, Z. N., Milliman, C. L., and Korsmeyer, S. J. (1993). Bcl-2 Heterodimerizes *In Vivo* with a Conserved Homolog, Bax, that Accelerates Programmed Cell Death. *Cell* 74 (4), 609–619. doi:10.1016/0092-8674(93)90509-o

Ovaa, H., Kessler, B. M., Rolén, U., Galardy, P. J., Ploegh, H. L., and Masucci, M. G. (2004). Activity-based Ubiquitin-specific Protease (USP) Profiling of Virus-Infected and Malignant Human Cells. *Proc. Natl. Acad. Sci.* 101 (8), 2253–2258. doi:10.1073/pnas.0308411100

Pasparakis, M., and Vandenabeele, P. (2015). Necroptosis and its Role in Inflammation. *Nature* 517 (7534), 311–320. doi:10.1038/nature14191

Qian, J., Fu, P., Li, S., Li, X., Chen, Y., and Lin, Z. (2021). miR-107 Affects Cartilage Matrix Degradation in the Pathogenesis of Knee Osteoarthritis by Regulating Caspase-1. *J. Orthop. Surg. Res.* 16 (1), 40. doi:10.1186/s13018-020-02121-7

Qin, J., Shang, L., Ping, A.-s., Li, J., Li, X.-j., Yu, H., et al. (2013). Response to 'TNF/TNFR Signal Transduction Pathway-Mediated Anti-apoptosis and Anti-inflammatory Effects of Sodium Ferulate on IL-1β-induced Rat Osteoarthritis Chondrocytes *In Vitro*' - Authors' Reply. *Arthritis Res. Ther.* 15 (3), 409. doi:10.1186/ar4227

Rathmell, J. C., and Thompson, C. B. (2002). Pathways of Apoptosis in Lymphocyte Development, Homeostasis, and Disease. *Cell* 109 (Suppl. l), S97–S107. doi:10.1016/s0092-8674(02)00704-3

Reiter, R. J., Mayo, J. C., Tan, D.-X., Sainz, R. M., Alatorre-Jimenez, M., and Qin, L. (2016). Melatonin as an Antioxidant: under Promises but over Delivers. *J. Pineal Res.* 61 (3), 253–278. doi:10.1111/jpi.12360

Riegger, J., and Brenner, R. E. (2019). Evidence of Necroptosis in Osteoarthritic Disease: Investigation of blunt Mechanical Impact as Possible Trigger in Regulated Necrosis. *Cell Death Dis* 10 (10), 683. doi:10.1038/s41419-019-1930-5

Roemer, F. W., Guermazi, A., Felson, D. T., Niu, J., Nevitt, M. C., Crema, M. D., et al. (2011). Presence of MRI-Detected Joint Effusion and Synovitis Increases the Risk of Cartilage Loss in Knees without Osteoarthritis at 30-month Follow-Up: the MOST Study. *Ann. Rheum. Dis.* 70 (10), 1804–1809. doi:10.1136/ard.2011.150243

Royce, G. H., Brown-Borg, H. M., and Deepa, S. S. (2019). The Potential Role of Necroptosis in Inflammaging and Aging. *GeroScience* 41 (6), 795–811. doi:10.1007/s11357-019-00131-w

Sanchez, C., Pesesse, L., Gabay, O., Delcour, J.-P., Msika, P., Baudouin, C., et al. (2012). Regulation of Subchondral Bone Osteoblast Metabolism by Cyclic Compression. *Arthritis Rheum.* 64 (4), 1193–1203. doi:10.1002/art.33445

Santos, R. L., Tsolis, R. M., Zhang, S., Ficht, T. A., Bäumler, A. J., and Adams, L. G. (2001). Salmonella -Induced Cell Death Is Not Required for Enteritis in Calves. *Infect. Immun.* 69 (7), 4610–4617. doi:10.1128/iai.69.7.4610-4617.2001

Sborgi, L., Rühl, S., Mulvihill, E., Pipercevic, J., Heilig, R., Stahlberg, H., et al. (2016). GSDMD Membrane Pore Formation Constitutes the Mechanism of Pyroptotic Cell Death. *Embo J.* 35 (16), 1766–1778. doi:10.15252/embj.201694696

Scaffidi, C., Fulda, S., Srinivasan, A., Friesen, C., Li, F., Tomaselli, K. J., et al. (1998). Two CD95 (APO-1/Fas) Signaling Pathways. *EMBO J.* 17 (6), 1675–1687. doi:10.1093/emboj/17.6.1675

Scanzello, C. R., and Goldring, S. R. (2012). The Role of Synovitis in Osteoarthritis Pathogenesis. *Bone* 51 (2), 249–257. doi:10.1016/j.bone.2012.02.012

Sha, W., Hu, F., Xi, Y., Chu, Y., and Bu, S. (2021). Mechanism of Ferroptosis and its Role in Type 2 Diabetes Mellitus. *J. Diabetes Res.* 2021, 1–10. doi:10.1155/2021/9999612

Shajahan, A. N., Dobbin, Z. C., Hickman, F. E., Dakshanamurthy, S., and Clarke, R. (2012). Tyrosine-phosphorylated Caveolin-1 (Tyr-14) Increases Sensitivity to Paclitaxel by Inhibiting BCL2 and BCLxL Proteins via C-Jun N-Terminal Kinase (JNK). *J. Biol. Chem.* 287 (21), 17682–17692. doi:10.1074/jbc.M111.304022

Shi, F., Zhou, M., Shang, L., Du, Q., Li, Y., Xie, L., et al. (2019). EBV(LMP1)-induced Metabolic Reprogramming Inhibits Necroptosis through the Hypermethylation of the RIP3 Promoter. *Theranostics* 9 (9), 2424–2438. doi:10.7150/thno.30941

Shi, J., Gao, W., and Shao, F. (2017). Pyroptosis: Gasdermin-Mediated Programmed Necrotic Cell Death. *Trends Biochem. Sci.* 42 (4), 245–254. doi:10.1016/j.tibs.2016.10.004

Shi, J., Zhao, W., Ying, H., Zhang, Y., Du, J., Chen, S., et al. (2018). Estradiol Inhibits NLRP 3 Inflammasome in Fibroblast-like Synoviocytes Activated by Lipopolysaccharide and Adenosine Triphosphate. *Int. J. Rheum. Dis.* 21 (11), 2002–2010. doi:10.1111/1756-185x.13198

Shiozawa, J., de Vega, S., Cilek, M. Z., Yoshinaga, C., Nakamura, T., Kasamatsu, S., et al. (2020). Implication of HYBID (Hyaluronan-Binding Protein Involved in Hyaluronan Depolymerization) in Hyaluronan Degradation by Synovial Fibroblasts in Patients with Knee Osteoarthritis. *Am. J. Pathol.* 190 (5), 1046–1058. doi:10.1016/j.ajpath.2020.01.003

Silke, J., Rickard, J. A., and Gerlic, M. (2015). The Diverse Role of RIP Kinases in Necroptosis and Inflammation. *Nat. Immunol.* 16 (7), 689–697. doi:10.1038/ni.3206

Slee, E. A., Harte, M. T., Kluck, R. M., Wolf, B. B., Casiano, C. A., Newmeyer, D. D., et al. (1999). Ordering the Cytochrome C-Initiated Caspase cascade: Hierarchical Activation of Caspases-2, -3, -6, -7, -8, and -10 in a Caspase-9-dependent Manner. *J. Cel Biol* 144 (2), 281–292. doi:10.1083/jcb.144.2.281

Smith, C. C. T., Davidson, S. M., Lim, S. Y., Simpkin, J. C., Hothersall, J. S., and Yellon, D. M. (2007). Necrostatin: a Potentially Novel Cardioprotective Agent? *Cardiovasc. Drugs Ther.* 21 (4), 227–233. doi:10.1007/s10557-007-6035-1

Stockwell, B. R., Friedmann Angeli, J. P., Bayir, H., Bush, A. I., Conrad, M., Dixon, S. J., et al. (2017). Ferroptosis: A Regulated Cell Death Nexus Linking Metabolism, Redox Biology, and Disease. *Cell* 171 (2), 273–285. doi:10.1016/j.cell.2017.09.021

Stockwell, B. R., Jiang, X., and Gu, W. (2020). Emerging Mechanisms and Disease Relevance of Ferroptosis. *Trends Cel Biol.* 30 (6), 478–490. doi:10.1016/j.tcb.2020.02.009

Sun, L., Wang, H., Wang, Z., He, S., Chen, S., Liao, D., et al. (2012). Mixed Lineage Kinase Domain-like Protein Mediates Necrosis Signaling Downstream of RIP3 Kinase. *Cell* 148 (1-2), 213–227. doi:10.1016/j.cell.2011.11.031

Sun, Y., Leng, P., Guo, P., Gao, H., Liu, Y., Li, C., et al. (2021). G Protein Coupled Estrogen Receptor Attenuates Mechanical Stress-Mediated Apoptosis of Chondrocyte in Osteoarthritis via Suppression of Piezo1. *Mol. Med.* 27 (1), 96. doi:10.1186/s10020-021-00360-w

Surprenant, A., Rassendren, F., Kawashima, E., North, R. A., and Buell, G. (1996). The Cytolytic P 2Z Receptor for Extracellular ATP Identified as a P 2X Receptor (P2X 7). *Science* 272 (5262), 735–738. doi:10.1126/science.272.5262.735

Tang, R.-X., Kong, F. Y., Fan, B. F., Liu, X. M., You, H. J., Zhang, P., et al. (2012). HBx Activates FasL and Mediates HepG2 Cell Apoptosis through MLK3-MKK7-JNKs Signal Module. *World J. Gastroenterol.* 18 (13), 1485–1495. doi:10.3748/wjg.v18.i13.1485

Tang, Y.-h., Yue, Z.-s., Zheng, W.-j., Shen, H.-f., Zeng, L.-r., Hu, Z.-q., et al. (2018). 4-Phenylbutyric Acid Presents Therapeutic Effect on Osteoarthritis via Inhibiting Cell Apoptosis and Inflammatory Response Induced by Endoplasmic Reticulum Stress. *Biotechnol. Appl. Biochem.* 65 (4), 540–546. doi:10.1002/bab.1642

Tian, J., Cheng, C., Kuang, S.-D., Su, C., Zhao, X., Xiong, Y.-l., et al. (2020). OPN Deficiency Increases the Severity of Osteoarthritis Associated with Aberrant Chondrocyte Senescence and Apoptosis and Upregulates the Expression of Osteoarthritis-Associated Genes. *Pain Res. Manag.* 2020, 1–9. doi:10.1155/2020/3428587

Tomás-Zapico, C., and Coto-Montes, A. (2005). A Proposed Mechanism to Explain the Stimulatory Effect of Melatonin on Antioxidative Enzymes. *J. Pineal Res.* 39 (2), 99–104. doi:10.1111/j.1600-079X.2005.00248.x

Tsujimoto, Y., Cossman, J., Jaffe, E., and Croce, C. M. (1985). Involvement of the Bcl -2 Gene in Human Follicular Lymphoma. *Science* 228 (4706), 1440–1443. doi:10.1126/science.3874430

Urano, S., Ohara, T., Noma, K., Katsube, R., Ninomiya, T., Tomono, Y., et al. (2016). Iron Depletion Enhances the Effect of Sorafenib in Hepatocarcinoma. *Cancer Biol. Ther.* 17 (6), 648–656. doi:10.1080/15384047.2016.1177677

Ursini, F., Maiorino, M., Valente, M., Ferri, L., and Gregolin, C. (1982). Purification from Pig Liver of a Protein Which Protects Liposomes and Biomembranes from Peroxidative Degradation and Exhibits Glutathione Peroxidase Activity on Phosphatidylcholine Hydroperoxides. *Biochim. Biophys. Acta (Bba) - Lipids Lipid Metab.* 710 (2), 197–211. doi:10.1016/0005-2760(82)90150-3

Van de Craen, M., Declercq, W., Van den brande, I., Fiers, W., and Vandenabeele, P. (1999). The Proteolytic Procaspase Activation Network: an *In Vitro* Analysis. *Cel Death Differ* 6 (11), 1117–1124. doi:10.1038/sj.cdd.4400589

Van Herreweghe, F., Festjens, N., Declercq, W., and Vandenabeele, P. (2010). Tumor Necrosis Factor-Mediated Cell Death: to Break or to Burst, That's the Question. *Cel. Mol. Life Sci.* 67 (10), 1567–1579. doi:10.1007/s00018-010-0283-0

Van Loo, G., Demol, H., van Gurp, M., Hoorelbeke, B., Schotte, P., Beyaert, R., et al. (2002b). A Matrix-Assisted Laser Desorption Ionization post-source Decay (MALDI-PSD) Analysis of Proteins Released from Isolated Liver Mitochondria Treated with Recombinant Truncated Bid. *Cel Death Differ* 9 (3), 301–308. doi:10.1038/sj.cdd.4400966

van Loo, G., van Gurp, M., Depuydt, B., Srinivasula, S. M., Rodriguez, I., Alnemri, E. S., et al. (2002a). The Serine Protease Omi/HtrA2 Is Released from Mitochondria during Apoptosis. Omi Interacts with Caspase-Inhibitor XIAP and Induces Enhanced Caspase Activity. *Cel Death Differ* 9 (1), 20–26. doi:10.1038/sj.cdd.4400970

Vanden Berghe, T., Kaiser, W. J., Bertrand, M. J., and Vandenabeele, P. (2015). Molecular Crosstalk between Apoptosis, Necroptosis, and Survival Signaling. *Mol. Cell Oncol.* 2 (4), e975093. doi:10.4161/23723556.2014.975093

Vanlangenakker, N., Vanden Berghe, T., and Vandenabeele, P. (2012). Many Stimuli Pull the Necrotic Trigger, an Overview. *Cel Death Differ* 19 (1), 75–86. doi:10.1038/cdd.2011.164

Viganò, E., and Mortellaro, A. (2013). Caspase-11: the Driving Factor for Noncanonical Inflammasomes. *Eur. J. Immunol.* 43 (9), 2240–2245. doi:10.1002/eji.201343800

von Moltke, J., Ayres, J. S., Kofoed, E. M., Chavarría-Smith, J., and Vance, R. E. (2013). Recognition of Bacteria by Inflammasomes. *Annu. Rev. Immunol.* 31, 73–106. doi:10.1146/annurev-immunol-032712-095944

Wajant, H., Pfizenmaier, K., and Scheurich, P. (2003). Tumor Necrosis Factor Signaling. *Cel Death Differ* 10 (1), 45–65. doi:10.1038/sj.cdd.4401189

Walker, N. I., Harmon, B. V., Gobé, G. C., and Kerr, J. F. (1988). Patterns of Cell Death. *Methods Achiev Exp. Pathol.* 13, 18–54.

Wang, J., Chen, H., Cao, P., Wu, X., Zang, F., Shi, L., et al. (2016). Inflammatory Cytokines Induce Caveolin-1/β-Catenin Signalling in Rat Nucleus Pulposus

Cell Apoptosis through the P38 MAPK Pathway. *Cell Prolif.* 49 (3), 362–372. doi:10.1111/cpr.12254

Wang, S., Mobasheri, A., Zhang, Y., Wang, Y., Dai, T., and Zhang, Z. (2021). Exogenous Stromal Cell-Derived Factor-1 (SDF-1) Suppresses the NLRP3 Inflammasome and Inhibits Pyroptosis in Synoviocytes from Osteoarthritic Joints via Activation of the AMPK Signaling Pathway. *Inflammopharmacol* 29, 695–704. doi:10.1007/s10787-021-00814-x

Wang, Y., Shen, S., Li, Z., Li, W., and Weng, X. (2020). MIR-140-5p Affects Chondrocyte Proliferation, Apoptosis, and Inflammation by Targeting HMGB1 in Osteoarthritis. *Inflamm. Res.* 69 (1), 63–73. doi:10.1007/s00011-019-01294-0

Wang, Y., Yin, B., Li, D., Wang, G., Han, X., and Sun, X. (2018). GSDME Mediates Caspase-3-dependent Pyroptosis in Gastric Cancer. *Biochem. Biophysical Res. Commun.* 495 (1), 1418–1425. doi:10.1016/j.bbrc.2017.11.156

Wang, Y., Zhang, H., Chen, Q., Jiao, F., Shi, C., Pei, M., et al. (2020). TNF-α/HMGB1 Inflammation Signalling Pathway Regulates Pyroptosis during Liver Failure and Acute Kidney Injury. *Cell Prolif* 53 (6), e12829. doi:10.1111/cpr.12829

Welz, P.-S., Wullaert, A., Vlantis, K., Kondylis, V., Fernández-Majada, V., Ermolaeva, M., et al. (2011). FADD Prevents RIP3-Mediated Epithelial Cell Necrosis and Chronic Intestinal Inflammation. *Nature* 477 (7364), 330–334. doi:10.1038/nature10273

Woolf, A. D., and Pfleger, B. (2003). Burden of Major Musculoskeletal Conditions. *Bull. World Health Organ.* 81 (9), 646–656.

Wu, J., Huang, Z., Ren, J., Zhang, Z., He, P., Li, Y., et al. (2013). Mlkl Knockout Mice Demonstrate the Indispensable Role of Mlkl in Necroptosis. *Cel Res* 23 (8), 994–1006. doi:10.1038/cr.2013.91

Xiao, Y., Ding, L., Yin, S., Huang, Z., Zhang, L., Mei, W., et al. (2021). Relationship between the Pyroptosis of Fibroblast-like Synoviocytes and HMGB1 Secretion in Knee Osteoarthritis. *Mol. Med. Rep.* 23 (2). doi:10.3892/mmr.2020.11736

Xie, B. S., Wang, Y. Q., Lin, Y., Mao, Q., Feng, J. F., Gao, G. Y., et al. (2019). Inhibition of Ferroptosis Attenuates Tissue Damage and Improves Long-Term Outcomes after Traumatic Brain Injury in Mice. *CNS Neurosci. Ther.* 25 (4), 465–475. doi:10.1111/cns.13069

Xie, Y., Hou, W., Song, X., Yu, Y., Huang, J., Sun, X., et al. (2016). Ferroptosis: Process and Function. *Cel Death Differ* 23 (3), 369–379. doi:10.1038/cdd.2015.158

Xu, B., Xing, R., Huang, Z., Yin, S., Li, X., Zhang, L., et al. (2019). Excessive Mechanical Stress Induces Chondrocyte Apoptosis through TRPV4 in an Anterior Cruciate Ligament-Transected Rat Osteoarthritis Model. *Life Sci.* 228, 158–166. doi:10.1016/j.lfs.2019.05.003

Xu, G., and Shi, Y. (2007). Apoptosis Signaling Pathways and Lymphocyte Homeostasis. *Cel Res* 17 (9), 759–771. doi:10.1038/cr.2007.52

Xu, J., Pei, Y., Lu, J., Liang, X., Li, Y., Wang, J., et al. (2021). LncRNA SNHG7 Alleviates IL-1β-induced Osteoarthritis by Inhibiting miR-214-5p-Mediated PPARGC1B Signaling Pathways. *Int. Immunopharmacology* 90, 107150. doi:10.1016/j.intimp.2020.107150

Xu, K., Meng, Z., Xian, X.-m., Deng, M.-h., Meng, Q.-g., Fang, W., et al. (2020a). LncRNA PVT1 Induces Chondrocyte Apoptosis through Upregulation of TNF-α in Synoviocytes by Sponging miR-211-3p. *Mol. Cell Probes* 52, 101560. doi:10.1016/j.mcp.2020.101560

Xu, L., Golshirazian, I., Asbury, B. J., and Li, Y. (2014). Induction of High Temperature Requirement A1, a Serine Protease, by TGF-Beta1 in Articular Chondrocytes of Mouse Models of OA. *Histol. Histopathol* 29 (5), 609–618. doi:10.14670/hh-29.10.609

Xu, L., Wu, Z., He, Y., Chen, Z., Xu, K., Yu, W., et al. (2020b). MFN2 Contributes to Metabolic Disorders and Inflammation in the Aging of Rat Chondrocytes and Osteoarthritis. *Osteoarthritis and Cartilage* 28 (8), 1079–1091. doi:10.1016/j.joca.2019.11.011

Xu, L., Zhang, L., Wang, Z., Li, C., Li, S., Li, L., et al. (2018). Melatonin Suppresses Estrogen Deficiency-Induced Osteoporosis and Promotes Osteoblastogenesis by Inactivating the NLRP3 Inflammasome. *Calcif Tissue Int.* 103 (4), 400–410. doi:10.1007/s00223-018-0428-y

Xue, L., Borné, Y., Mattisson, I. Y., Wigren, M., Melander, O., Ohro-Melander, M., et al. (2017). FADD, Caspase-3, and Caspase-8 and Incidence of Coronary Events. *Arteriosclerosis, Thromb. Vasc. Biol.* 37 (5), 983–989. doi:10.1161/atvbaha.117.308995

Yan, Z., Qi, W., Zhan, J., Lin, Z., Lin, J., Xue, X., et al. (2020). Activating Nrf2 Signalling Alleviates Osteoarthritis Development by Inhibiting Inflammasome Activation. *J. Cel. Mol. Med.* 24 (22), 13046–13057. doi:10.1111/jcmm.15905

Yang, J., Liu, Z., Wang, C., Yang, R., Rathkey, J. K., Pinkard, O. W., et al. (2018). Mechanism of Gasdermin D Recognition by Inflammatory Caspases and Their Inhibition by a Gasdermin D-Derived Peptide Inhibitor. *Proc. Natl. Acad. Sci. USA* 115 (26), 6792–6797. doi:10.1073/pnas.1800562115

Yang, W. S., SriRamaratnam, R., Welsch, M. E., Shimada, K., Skouta, R., Viswanathan, V. S., et al. (2014). Regulation of Ferroptotic Cancer Cell Death by GPX4. *Cell* 156 (1-2), 317–331. doi:10.1016/j.cell.2013.12.010

Yang, W. S., and Stockwell, B. R. (2016). Ferroptosis: Death by Lipid Peroxidation. *Trends Cel Biol.* 26 (3), 165–176. doi:10.1016/j.tcb.2015.10.014

Yang, W. S., and Stockwell, B. R. (2008). Synthetic Lethal Screening Identifies Compounds Activating Iron-dependent, Nonapoptotic Cell Death in Oncogenic-RAS-Harboring Cancer Cells. *Chem. Biol.* 15 (3), 234–245. doi:10.1016/j.chembiol.2008.02.010

Yao, X., Sun, K., Yu, S., Luo, J., Guo, J., Lin, J., et al. (2021). Chondrocyte Ferroptosis Contribute to the Progression of Osteoarthritis. *J. Orthopaedic Translation* 27, 33–43. doi:10.1016/j.jot.2020.09.006

Yoon, S., Kovalenko, A., Bogdanov, K., and Wallach, D. (2017). MLKL, the Protein that Mediates Necroptosis, Also Regulates Endosomal Trafficking and Extracellular Vesicle Generation. *Immunity* 47 (1), 51–65. e7. doi:10.1016/j.immuni.2017.06.001

Yu, H., Yao, S., Zhou, C., Fu, F., Luo, H., Du, W., et al. (2021). Morroniside Attenuates Apoptosis and Pyroptosis of Chondrocytes and Ameliorates Osteoarthritic Development by Inhibiting NF-Kb Signaling. *J. Ethnopharmacology* 266, 113447. doi:10.1016/j.jep.2020.113447

Yu, Y., Jiang, L., Wang, H., Shen, Z., Cheng, Q., Zhang, P., et al. (2020). Hepatic Transferrin Plays a Role in Systemic Iron Homeostasis and Liver Ferroptosis. *Blood* 136 (6), 726–739. doi:10.1182/blood.2019002907

Zargarian, S., Shlomovitz, I., Erlich, Z., Hourizadeh, A., Ofir-Birin, Y., Croker, B. A., et al. (2017). Phosphatidylserine Externalization, "necroptotic Bodies" Release, and Phagocytosis during Necroptosis. *Plos Biol.* 15 (6), e2002711. doi:10.1371/journal.pbio.2002711

Zhang, C., Lin, S., Li, T., Jiang, Y., Huang, Z., Wen, J., et al. (2017). Mechanical Force-Mediated Pathological Cartilage Thinning Is Regulated by Necroptosis and Apoptosis. *Osteoarthritis and Cartilage* 25 (8), 1324–1334. doi:10.1016/j.joca.2017.03.018

Zhang, D.-W., Shao, J., Lin, J., Zhang, N., Lu, B.-J., Lin, S.-C., et al. (2009). RIP3, an Energy Metabolism Regulator that Switches TNF-Induced Cell Death from Apoptosis to Necrosis. *Science* 325 (5938), 332–336. doi:10.1126/science.1172308

Zhang, L., Xing, R., Huang, Z., Zhang, N., Zhang, L., Li, X., et al. (2019). Inhibition of Synovial Macrophage Pyroptosis Alleviates Synovitis and Fibrosis in Knee Osteoarthritis. *Mediators Inflamm.* 2019, 1–11. doi:10.1155/2019/2165918

Zhang, L., Zhang, L., Huang, Z., Xing, R., Li, X., Yin, S., et al. (2019b). Increased HIF-1α in Knee Osteoarthritis Aggravate Synovial Fibrosis via Fibroblast-like Synoviocyte Pyroptosis. *Oxidative Med. Cell Longevity* 2019, 1–11. doi:10.1155/2019/6326517

Zhang, Q. X., Guo, D., Wang, F. C., and Ding, W. Y. (2020b). Necrosulfonamide (NSA) Protects Intervertebral Disc Degeneration via Necroptosis and Apoptosis Inhibition. *Eur. Rev. Med. Pharmacol. Sci.* 24 (5), 2683–2691. doi:10.26355/eurrev_202003_20538

Zhang, R., Wang, X., Ni, L., Di, X., Ma, B., Niu, S., et al. (2020a). COVID-19: Melatonin as a Potential Adjuvant Treatment. *Life Sci.* 250, 117583. doi:10.1016/j.lfs.2020.117583

Zhang, Y., Chen, X., Gueydan, C., and Han, J. (2018). Plasma Membrane Changes during Programmed Cell Deaths. *Cel Res* 28 (1), 9–21. doi:10.1038/cr.2017.133

Zhang, Y., Han, S., Kong, M., Tu, Q., Zhang, L., and Ma, X. (2021). Single-cell RNA-Seq Analysis Identifies Unique Chondrocyte Subsets and Reveals Involvement of Ferroptosis in Human Intervertebral Disc Degeneration. *Osteoarthritis and Cartilage* 29 (9), 1324–1334. doi:10.1016/j.joca.2021.06.010

Zhang, Y., Lin, J., Zhou, X., Chen, X., Chen, A. C., Pi, B., et al. (2019a). Melatonin Prevents Osteoarthritis-Induced Cartilage Degradation via Targeting MicroRNA-140. *Oxidative Med. Cell Longevity* 2019, 1–16. doi:10.1155/2019/9705929

Zhao, L. R., Xing, R. L., Wang, P. M., Zhang, N. S., Yin, S. J., Li, X. C., et al. (2018a). NLRP1 and NLRP3 Inflammasomes Mediate LPS/ATP-induced Pyroptosis in Knee Osteoarthritis. *Mol. Med. Rep.* 17 (4), 5463–5469. doi:10.3892/mmr.2018.8520

Zhao, Y., Shi, J., and Shao, F. (2018b). Inflammatory Caspases: Activation and Cleavage of Gasdermin-D *In Vitro* and during Pyroptosis. *Methods Mol. Biol. (Clifton, NJ)* 1714, 131–148. doi:10.1007/978-1-4939-7519-8_9

Zhou, H., Yu, M., Zhao, J., Martin, B. N., Roychowdhury, S., McMullen, M. R., et al. (2016). IRAKM-mincle axis Links Cell Death to Inflammation: Pathophysiological Implications for Chronic Alcoholic Liver Disease. *Hepatology* 64 (6), 1978–1993. doi:10.1002/hep.28811

Zhou, X., Zheng, Y., Sun, W., Zhang, Z., Liu, J., Yang, W., et al. (2021). D-mannose Alleviates Osteoarthritis Progression by Inhibiting Chondrocyte Ferroptosis in a HIF-2α-dependent Manner. *Cel Prolif* 54, e13134. doi:10.1111/cpr.13134

Zhou, Y., Ming, J., Li, Y., Deng, M., Chen, Q., Ma, Y., et al. (2019). Ligustilide Attenuates Nitric Oxide-Induced Apoptosis in Rat Chondrocytes and Cartilage Degradation via Inhibiting JNK and P38 MAPK Pathways. *J. Cel Mol Med* 23 (5), 3357–3368. doi:10.1111/jcmm.14226

Zieba, J. T., Chen, Y.-T., Lee, B. H., and Bae, Y. (2020). Notch Signaling in Skeletal Development, Homeostasis and Pathogenesis. *Biomolecules* 10 (2), 332. doi:10.3390/biom10020332

Zu, Y., Mu, Y., Li, Q., Zhang, S.-T., and Yan, H.-J. (2019). Icariin Alleviates Osteoarthritis by Inhibiting NLRP3-Mediated Pyroptosis. *J. Orthop. Surg. Res.* 14 (1), 307. doi:10.1186/s13018-019-1307-6

Zychlinsky, A., Prevost, M. C., and Sansonetti, P. J. (1992). Shigella Flexneri Induces Apoptosis in Infected Macrophages. *Nature* 358 (6382), 167–169. doi:10.1038/358167a0

Conflict of Interest: The authors declare that the research was conducted in the absence of any commercial or financial relationships that could be construed as a potential conflict of interest.

Publisher's Note: All claims expressed in this article are solely those of the authors and do not necessarily represent those of their affiliated organizations, or those of the publisher, the editors and the reviewers. Any product that may be evaluated in this article, or claim that may be made by its manufacturer, is not guaranteed or endorsed by the publisher.

GLOSSARY

OA Osteoarthritis
KOA Knee osteoarthritis
DAMPs Damage associated molecular pattern molecules
TLRs Toll-like receptors
PRRs Particular pattern recognition receptors
ASC Apoptosis-associated speck-like protein containing a CARD
FADD Fas-associated protein with death domain
DISC Death-inducing signaling complex
NF-κB Nuclear factor-κB
MAPK Mitogen-activated protein kinase
FLS Fibroblast-like synoviocytes
NLRP Nod-like receptor protein
ASC Apoptosis-associated speck-like protein with a caspase-recruitment domain
GSDMD Gasdermin D
LPS Lipopolysaccharide
Lico A Licochalcone A
SDF-1 Stromal cell-derived factor-1
ATP Adenosine triphosphate
MMP-1 Matrix metalloproteinases 1
MMP-13 Matrix metalloproteinases 13
MMP-3 Matrix metalloproteinases 3
TGF-β Transforming growth factor-β
PLOD2 Procollagen-lysine, 2-oxoglutarate 5-dioxygenase 2
COL1A1 Collagen type Iα1 chain
TIMP1 Tissue inhibitor of metalloproteinase 1.
DMM Destabilization of the medial meniscus
HMGB1 High mobility group box 1
SD rats Sprague-dawley rats
Human FLSs Human fibroblast-like synoviocytes
HIF-1α Hypoxia-inducible factor-1α
USP7 Ubiquitin-specific protease 7
ROS Reactive oxygen species
Lipid-ROS Lipid reactive oxygen species
NOXs NAD(P)H oxidases
NOX4 One of the members of the NOX family
Gpx4 Glutathione peroxidase 4
H2O2 Hydrogen peroxide
MIA Monosodium iodoacetate
BzATP An ATP analog with greater potency than ATP
Col II Collagen II
Col X Collagen X
CNS trauma Central nervous system trauma.
RIP1 Receptor interacting protein kinase-1
RIP3 Receptor interacting protein kinase-3
MLKL Mixed-lineage kinase domain-like protein
TRADD TNF-receptor associated via DD
TRAF2 TNF receptor-associated factor 2

frontiers in Cell and Developmental Biology

ORIGINAL RESEARCH
published: 24 February 2022
doi: 10.3389/fcell.2022.768579

Impact of Extracellular pH on Apoptotic and Non-Apoptotic TRAIL-Induced Signaling in Pancreatic Ductal Adenocarcinoma Cells

*Sofie Hagelund and Anna Trauzold**

Institute for Experimental Cancer Research, University of Kiel, Kiel, Germany

Tumor necrosis factor-related apoptosis-inducing ligand (TRAIL) is an important mediator of tumor immune surveillance. In addition, its potential to kill cancer cells without harming healthy cells led to the development of TRAIL receptor agonists, which however did not show the desired effects in clinical trials. This is caused mainly by apoptosis resistance mechanisms operating in primary cancer cells. Meanwhile, it has been realized that in addition to cell death, TRAIL also induces non-apoptotic pro-inflammatory pathways that may enhance tumor malignancy. Due to its late detection and resistance to current therapeutic options, pancreatic ductal adenocarcinoma (PDAC) is still one of the deadliest types of cancer worldwide. A dysregulated pH microenvironment contributes to PDAC development, in which the cancer cells become highly dependent on to maintain their metabolism. The impact of extracellular pH (pH_e) on TRAIL-induced signaling in PDAC cells is poorly understood so far. To close this gap, we analyzed the effects of acidic and alkaline pH_e, both in short-term and long-term settings, on apoptotic and non-apoptotic TRAIL-induced signaling. We found that acidic and alkaline pH_e differentially impact TRAIL-induced responses, and in addition, the duration of the pH_e exposition also represents an important parameter. Thus, adaptation to acidic pH_e increases TRAIL sensitivity in two different PDAC cell lines, Colo357 and Panc1, one already TRAIL-sensitive and the other TRAIL-resistant, respectively. However, the latter became highly TRAIL-sensitive only by concomitant inhibition of Bcl-xL. None of these effects was observed under other pH_e conditions studied. Both TRAIL-induced non-apoptotic signaling pathways, as well as constitutively expressed anti-apoptotic proteins, were regulated by acidic pH_e. Whereas the non-apoptotic pathways were differently affected in Colo357 than in Panc1 cells, the impact on the anti-apoptotic protein levels was similar in both cell lines. In Panc1 cells, adaptation to either acidic or alkaline pH_e blocked the activation of the most of TRAIL-induced non-apoptotic pathways. Interestingly, under these conditions, significant downregulation of the plasma membrane levels of TRAIL-R1 and TRAIL-R2 was observed. Summing up, extracellular pH influences PDAC cells' response to TRAIL with acidic pH_e adaptation, showing the ability to strongly increase TRAIL sensitivity and in addition to inhibit TRAIL-induced pro-inflammatory signaling.

Keywords: TRAIL, TRAIL receptor, apoptosis, non-apoptotic signaling, extracellular pH, pancreatic ductal adenocarcinoma

OPEN ACCESS

Edited by:
Triona Ni Chonghaile, Royal College of Surgeons in Ireland, Ireland

Reviewed by:
Alvaro De Mingo Pulido, Moffitt Cancer Center, United States
Jungsun Kim, Oregon Health and Science University, United States

****Correspondence:***
Anna Trauzold
atrauzold@email.uni-kiel.de

Specialty section:
This article was submitted to Cell Death and Survival, a section of the journal Frontiers in Cell and Developmental Biology

Received: *31 August 2021*
Accepted: *20 January 2022*
Published: *24 February 2022*

Citation:
Hagelund S and Trauzold A (2022) Impact of Extracellular pH on Apoptotic and Non-Apoptotic TRAIL-Induced Signaling in Pancreatic Ductal Adenocarcinoma Cells. Front. Cell Dev. Biol. 10:768579. doi: 10.3389/fcell.2022.768579

INTRODUCTION

Pancreatic cancer is currently the seventh leading cause of cancer deaths worldwide, despite being relatively infrequent (Bray et al., 2018; Rawla et al., 2019; Christopher et al., 2020). The 5-year survival rate remains low (9%–10%), due to poor early detection, inadequate therapy options, and no available screening tests (Christopher et al., 2020; American-Cancer-Society, 2021). Pancreatic ductal adenocarcinoma (PDAC) accounts for more than 90% of all pancreatic cancer cases and occurs in the exocrine pancreas (Christopher et al., 2020; American-Cancer-Society, 2021). Both acini and ductal cells, comprising the exocrine pancreas, have a structured network of ion channels that enables them to regulate pH in the lumen and interstitium, as well as an intracellular pH (pH_i) (Novak et al., 2013; Chii et al., 2014; Pallagi et al., 2015). Thus, pancreatic epithelial cells form a unique and dynamic pH microenvironment (Pedersen, Novak, et al., 2017), and dysregulation of this particular microenvironment can contribute to PDAC development (Chii et al., 2014; Pedersen et al., 2017; Schnipper et al., 2020). Here, the cancer cells become highly dependent on the altered pH regulation to maintain their metabolism (Swietach 2019). The majority of cancers have a dysregulated extracellular pH (pH_e) microenvironment due to a change in glucose metabolism known as the "Warburg effect," where they produce high amounts of lactate and protons even in the presence of oxygen (Vander Heiden et al., 2009; Kato et al., 2018). The accumulation of lactate and protons contributes to tumor acidosis through ion channels, while at the same time, pH_i is maintained (Chii et al., 2014). Ultimately, this favors tumor progression and therapy resistance (Chii et al., 2014; Vaupel et al., 2019).

Though pH_i is generally well-maintained at a neutral state, it responds to changes in pH_e, meaning that pH_e can influence cellular physiology through pH_i regulation achieved by signaling proteins sensitive to changes in pH_e (Boron, 2004; Michl et al., 2019; Swietach, 2019). Cells exposed to acidic stress will generally not demonstrate ideal pH_i homeostasis, and steady-state pH_i drops when (even well-perfused single) cells are exposed to acidic pH_e (Boron, 2004; Kato et al., 2013; Swietach, 2019). This could be the consequence of cancer cells trying to protect themselves from lactate retention, which would alternatively take place if the pH_i was considerably higher than pH_e (Swietach, 2019). Moreover is it well-known that intracellular acidification (a decrease of 0.3–0.4 pH_i values) occurs in mammalian cells during apoptosis (Matsuyama et al., 2000; Lagadic-Gossmann et al., 2004; Sergeeva et al., 2017) and has been observed after multiple types of apoptotic stimuli such as UV exposure, growth factor deprivation, death receptor-mediated and mitochondria-mediated apoptosis (Lagadic-Gossmann et al., 2004). To that extent, intracellular acidification has been shown to be either caspase-independent or caspase-dependent (Lagadic-Gossmann et al., 2004). Due to this knowledge, pH_e could affect the apoptotic response.

Tumor necrosis factor-related apoptosis-inducing ligand (TRAIL), a member of the TNF superfamily (TNFSF), can bind to four different plasma membrane receptors in humans: TRAIL-receptors 1, 2, 3, and 4 (TRAIL-R1, 2, 3, and 4). While TRAIL-R1 and TRAIL-R2 can induce apoptosis through their death domains, TRAIL-R3 and TRAIL-R4 are lacking this ability since they miss or have a truncated death domain, respectively. Although the function of TRAIL-R3 and TRAIL-R4 is still not well understood, it is likely that they can work as decoys and regulatory receptors (von Karstedt et al., 2017). Following the binding of TRAIL, the formation of the death-inducing signaling complex (DISC) is initiated. Within the DISC, the adapter protein FADD is recruited, which in turn leads to recruitment and activation of caspases-8 and/or -10 (Dickens et al., 2012). In so-called type I cells, sufficient levels of activated caspase-8/10 are generated at the DISC for direct activation of the effector caspases required for the activation of the caspase cascade. In contrast, type II cells require the engagement of the mitochondrial apoptosis pathway for the efficient activation of caspases (Ozören and El-Deiry, 2002; Jost et al., 2009). In these cells, activation of small amounts of caspase-8 in DISC leads to the cleavage of Bid, which in turn leads to Bax/Bak-mediated mitochondrial outer membrane permeabilization (MOMP) (Luo et al., 1998; Antonsson et al., 2001; Dewson et al., 2009; Huang et al., 2016). Upon MOMP, the second mitochondrial activator of caspases/direct inhibitor of apoptosis-binding protein with a low isoelectric point (pI) (SMAC/DIABLO) is released to the cytosol for counteracting protein X-linked inhibitor of apoptosis protein (XIAP) (Ozören and El-Deiry, 2002; Jost et al., 2009), an inhibitor of effector caspases (Deveraux et al., 1998; Bratton et al., 2001; Holcik and Korneluk, 2001). In addition, cytochrome c is released, the step which is a prerequisite for the formation of the apoptosome. In apoptosome, another initiator caspase, caspase-9, is activated, which in turn is able to fully activate the effector caspase-3 to trigger apoptosis in type II cells (Riedl and Salvesen, 2007; Kalkavan and Green, 2018). Of note, PDAC cells have been shown to employ a type II apoptotic signaling pathway upon death receptor stimulation (Hinz et al., 2000). The observations that TRAIL death receptors are frequently overexpressed in cancer and that TRAIL induces apoptosis in tumor cells and not normal healthy cells led to the development of TRAIL/TRAIL-R-based therapeutic drugs and their testing in clinical trials (Lemke et al., 2014; de Miguel et al., 2016). However, despite promising pre-clinical findings, none of these drugs showed the desired effects in cancer patients. These disappointing results can be attributed to the apoptosis resistance mechanisms present in many primary tumor cells and may comprise the constitutive upregulation of the anti-apoptotic proteins operating at different levels of the TRAIL/TRAIL-R signaling cascades like decoy/regulatory receptors, FLIP, Bcl-xL, and IAP (Hinz et al., 2000; Trauzold et al., 2001; Trauzold et al., 2003; Lemke et al., 2010). It also becomes obvious that cancer cells frequently misuse TRAIL death receptors as an inducer of pro-inflammatory pathways, like NF-κB, ERK1/2, Akt, Src, p38, and JNK. These non-canonical TRAIL-induced pathways become visible in apoptosis-resistant tumors and by enhancing cell proliferation, migration, and invasion may lead to cancer progression (Trauzold et al., 2001; Ehrenschwender

et al., 2010; von Karstedt et al., 2015; Azijli et al., 2013; Trauzold et al., 2006; Hoogwater et al., 2010).

Importantly, the TRAIL/TRAIL-R system represents one of the mechanisms by which the immune system contributes to the surveillance of developing tumors (Falschlehner et al., 2009). In addition, cancer cells themselves frequently express TRAIL. Consequently, in the (patho)physiological context, the importance of TRAIL/TRAIL-R signaling cannot be underestimated. Since PDAC cells originate from cells naturally exposed to acidic and alkaline pH and an acidic environment is observed often in tumors, it is very likely that pH_e influences the response to TRAIL in these cells. Yet, such data are not available so far. Therefore, in the present study, we sought to investigate the impact of both the short-term and long-term exposition to alkaline (7.6) and acidic (6.5) pH_e compared to control (pH_e 7.4) on TRAIL-induced apoptotic and non-apoptotic signaling in PDAC cells.

MATERIALS AND METHODS

Cell Culture and Reagents

Human pancreatic ductal adenocarcinoma cell lines Panc1 and Colo357 were cultured in RPMI-1640 medium (Sigma-Aldrich, Hamburg, Germany) supplemented with 10% FCS (Pan BioTech, Aidenbach, Germany), 10 mM D-glucose (Sigma-Aldrich), 5% GlutaMax (Gibco, Darmstadt, Germany), and 5% sodium pyruvate (Gibco) under standard cell culture conditions (37°C, 5% CO_2) up to 70%–85% confluence. The pH medium 7.6 and 6.5 were obtained by using the Henderson–Hasselbalch equation [for further information, we refer to Michl et al. (2019)] and done similarly to Czaplinska et al. (2020), Yao et al. (2020), and Flinck et al. (2018) by adjusting the HCO_3 concentration by adding a proper amount of $NaHCO_3$ (Sigma-Aldrich) and NaCl to ensure equal osmolarity. Panc1 pH_e (7.6 and 6.5)-adapted cell lines were established and kindly provided by Stine Pedersen (University of Copenhagen, Denmark). Colo357 pH_e (7.6 and 6.5)-adapted cell lines were generated internally. Human sTRAIL/Apo2L (Peprotech, Hamburg, Germany) was used to treat (200 ng/ml) PDAC cells. Trypsin (Pan BioTech) was used to detach cells when passaged, while Accutase (Sigma-Aldrich) was used to detach cells before experiments. PBS (Gibco) was used during washing steps. Cell lines were authenticated by STR profiling and tested regularly for *Mycoplasma* contamination.

Experimental pH_e Setup

Cells were either exposed to an "acute" pH_e setup, with a different pH_e and exposure times between 24 h and a maximum of 7 days depending on the experiment, or they were cultured for a period of minimum 30 days in a certain pH_e value and stocked for future use as pH_e "adapted" cells.

Colony Formation Assay

For each cell line and each pH_e condition, 1×10^3 cells/well were seeded in six-well plates. Twenty-four hours later, cells were treated with TRAIL (200 ng/ml) for another 24 h, and after removing the medium and replacing it with a fresh one, they were allowed to grow for additional 5–7 days. The colonies were quantified by NyOne (Synentec, Elmshorn, Germany) live-cell imager. Finally, the cells were stained with 0.5% crystal violet (Sigma-Aldrich)/20% MeOH (ROTH, Karlsruhe, Germany) to visualize the colonies. Crystal violet was thoroughly washed away with ddH_2O, and plates were left to dry.

Live-Cell Imaging Staining

The cells (1.5×10^4 per well) were seeded in 96-well plates for 24 h, followed by TRAIL treatment (200 ng/ml) for another 24 h. The inhibitors Navitoclax (Selleck Chemicals, Distributor Absource Diagnostics GmbH, München, Germany) and Venetoclax (Selleck Chemicals) were added in a concentration of 5 μM to the cells 2 h prior to TRAIL (200 ng/ml) treatment. Hoechst "Bisbenzimid H 33342" (2.5 μg/ml, Sigma-Aldrich), Calcein-AM (1 μg/ml, BioLegend, San Diego, United States), and propidium iodide (PI) (Invitrogen, Karlsruhe, Germany) (10 μg/ml) mixed in PBS were added to the wells and incubated for 20 min in the cell incubator (37°C, 5% CO_2). Pictures were obtained and quantified by NyOne (Synentec). Quantification of both, dead cells and live cells, at the same time was used to clarify whether the decreased number of viable cells results from enhanced cell death or decreased cell proliferation.

Flow Cytometry

Flow cytometry was performed on either BD FACSCalibur™ (Becton Dickinson, Heidelberg, Germany) or MACSQuantify™ (Miltenyi Biotec, Bergisch Gladbach, Germany) and evaluated with CellQuest Pro (Becton Dickinson) or MACSQuantify™ software (Miltenyi Biotec), respectively.

Cell Surface TRAIL Receptor Expression

Cell surface expression levels of TRAIL receptors were analyzed by flow cytometry. Briefly, 4.5×10^5 cells were seeded per well in six-well plates for 24 h. Then, cells were detached from culture dishes by treatment with Accutase (Sigma-Aldrich), re-suspended in 0.05% NaN_3/PBS, transferred to a plate with V-shaped wells (Nerbe plus, Winsen, Germany), and centrifuged at 300 × *g* for 10 min at 4°C. The supernatant was discarded, and cells were incubated for 30 min with the following APC-conjugated antibodies with the concentration 1:3 in 0.6% BSA/PBS: TRAIL-R1 (FAB347A), TRAIL-R2 (FAB6311A), TRAIL-R3 (FAB6302A), and TRAIL-R4 (FAB633A) all purchased from R&D Systems GmbH, Wiesbaden, Germany. Respective isotype control stainings were performed with APC-conjugated mouse IgG1 Control (IC002A) and mouse IgG2B (IC0041A) (both from R&D Systems GmbH). Finally, cells were washed in 0.05% NaN3/PBS, re-suspended in 1% PFA (Morphisto, Offenbach am Main, Germany)/PBS, and the staining was measured within 24 h by flow cytometry. A population size of 10,000 cells was regarded as representative for data evaluation.

Crystal Violet Assay

Cells (1.5×10^4 per well) were seeded in 96-well plates for 24 h, followed by TRAIL treatment (200 ng/ml) for another 24 h. The supernatant was discarded, and adherent cells were incubated

with crystal violet as already described in the *Colony Formation Assay* section. After wells were dried, they were filled with 200 µl of 100% MeOH and incubated for 20 min at room temperature with gentle shaking. Finally, absorption was measured on either Tecan Sunrise or Tecan Infinite M200 Pro with wavelength at 590 nm and reference at 700 nm.

Western Blotting

Cells were lysed in RIPA buffer supplemented with Complete Protease Inhibitor Cocktail and PhosphoStop (both from Roche, Mannheim, Germany), and western blot analyses were performed as described previously (Trauzold et al., 2003). Primary antibodies were purchased from the following: Cell Signaling, Frankfurt, Germany [anti-ERK1/2 (9102), anti-phospho-ERK1/2 (9106), anti-JNK (9252), anti-phospho-JNK (9255), anti-p38 (9212), anti-phospho-p38 (9216), anti-Akt (2920), ant-phospho-Akt (4058), anti-IκBα (4814), anti-phospho-IκBα (2859), anti-Src (2110), anti-phospho-Src (2101), anti-TRAIL-R2 (3696), anti-caspase-8 (9746), anti-caspase-3 (9668), anti-Survivin (2802), anti-XIAP (2045), anti-cIAP2 (3130), and anti-Mcl-1 (94296)]; Santa Cruz Biotechnology, Heidelberg, Germany [anti-cIAP1 (sc-7943) and anti-HSP90 (sc-7947)]; BD Pharmingen, Heidelberg, Germany [anti-Bcl-x (516446)]; Merck Millipore, Darmstadt, Germany [anti-TRAIL-R1 (AB16955)]; Enzo Life Sciences, Lörrach, Germany [anti-FLIP (ALX-804961)]; and from Sigma-Aldrich [anti-β-actin (A5441)]. Bound primary antibodies were detected by using HRP-linked secondary antibodies [Cell Signaling, anti-mouse IgG (7076) and anti-rabbit IgG (7074)]. Membranes were developed using Pierce™ ECL (Thermo Fisher), Pierce™ ECL plus (Thermo Fisher), Radiance Chemiluminescence Subtrat (Azure), Radiance Q (Azure), or Radiance Plus (Azure) and the machines AGFA curix50 (with CL-X Posure Film from Thermo Fisher; developer and fixer from AGFA) or Azure Imaging Systems 300Q. Densitometric analyses were carried out using ImageJ software (Schneider et al., 2012).

Statistics

Data are presented as mean ± S.E.M of at least three independent experiments unless otherwise mentioned. Data analyses were performed using GraphPad Prism 7.0. When several groups were analyzed, one-way or two-way ANOVA with either Tukey's or Sidak's multiple comparison tests was used, which was dependent on whether pH conditions or treatment conditions were compared, respectively. p-values of <0.05 were considered statistically significant; $^{*}p < 0.05$, $^{**}p < 0.01$, $^{***}p < 0.001$, and $^{****}p < 0.0001$.

RESULTS

Acidic pH_e Increases TRAIL-Induced Cell Death in PDAC Cells

To study the impact of pH_e on TRAIL-induced signaling in PDAC cells, we established Colo357 and Panc1 cell lines adapted for a longer period of time to either of the three pH_e conditions: pH_e 6.5 (simulating pH_e in the tumor microenvironment), pH_e 7.6 (corresponding to the luminal pH_e in the exocrine pancreas), or pH_e 7.4 (control). Following adaptation, cells were exposed to TRAIL for 24 h, and cell viability and cell death were studied by live-cell staining with Hoechst, Calcein-AM, and PI, followed by quantification of the living and dead cells by the NyOne live-cell imager. In agreement with previous data (Hinz, Trauzold et al., 2000; Trauzold et al., 2003), Colo357 cells were re-proven to be sensitive (**Figure 1**) while Panc1 cells to be resistant to TRAIL-mediated cell death (**Figure 2**). Interestingly, acidic pH_e adaptation strongly sensitized Colo357 cells to TRAIL treatment, decreasing cell viability (**Figure 1C**; pH_e 7.4: 65.1%, pH_e 6.5 adapted: 38.0%) and correspondingly increasing cell death (**Figures 1A,B**; pH_e 7.4: 32.7%, pH_e 6.5 adapted: 59.3%). In contrast, under these conditions, only a slight enhancement of TRAIL-induced cell death was detectable in Panc1 cells (**Figures 2A,B**; pH_e 7.4: 10.8%, pH_e 6.5 adapted: 21.7%). No significant difference in TRAIL sensitivity could be detected between cells adapted to pH_e 7.6 and 7.4 (**Figures 1**, **2**). In addition, we investigated the impact of acutely changed pH_e on TRAIL-mediated cell death. For this purpose, we exposed cells to different pH_e shortly before (24 h) and during the treatment with TRAIL. Short-term exposition of cells to pH_e of either 7.6 or 6.5 did not have an impact on TRAIL sensitivity neither in Colo357 (**Figure 1**) nor Panc1 cells with the only exception of acute pH 7.6 exposure, which still exhibited lower TRAIL sensitivity than cells adapted to acidic pH_e (**Figure 2**). Similar results for both pH_e settings (adapted and acute) have been obtained using crystal violet staining as an indicator of cell viability (**Figures 1D**, **2D**).

Western blot analyses of apoptotic caspases revealed that in Colo357 pH_e-adapted cells, TRAIL induced strong caspase-8 and caspase-3 activation, irrespective of the culture conditions (**Figure 1E**). In agreement with the results of cell death-quantifying assays (**Figure 1B**), acidic pH_e adaptation potentiated TRAIL-induced cleavage of both caspases in these cells (**Figures 1E,F**). Again, the effects observed in TRAIL-treated Panc1 cells were less pronounced than those in Colo357 cells (**Figures 2E,F**).

Next, we studied the clonogenic survival of both PDAC cell lines under different pH_e conditions with and without TRAIL treatment. As shown in **Figure 3**, in this aspect, Colo357 cells (**Figures 3A,C**) and Panc1 cells (**Figures 3B,D**) respond differently to pH_e. Thus, whereas acute and long-term adaptation to acidic pH_e as well as adaptation to pH_e of 7.6 resulted in a robustly reduced clonogenic survival of Panc1 cells, none of these conditions did affect Colo357 cells. In Colo357 cells, solely the acute exposition to pH_e 7.6 decreased the number of colonies, an effect which was not observed in Panc1 cells. Consistent with previous data (Legler, Hauser et al., 2018), treatment with TRAIL for 24 h significantly reduced clonogenic survival of Colo357 cells cultured under normal pH_e conditions of 7.4. In contrast, TRAIL did not affect clonogenic survival in Panc1 cells, when each pH_e condition was compared to their respective pH_e control.

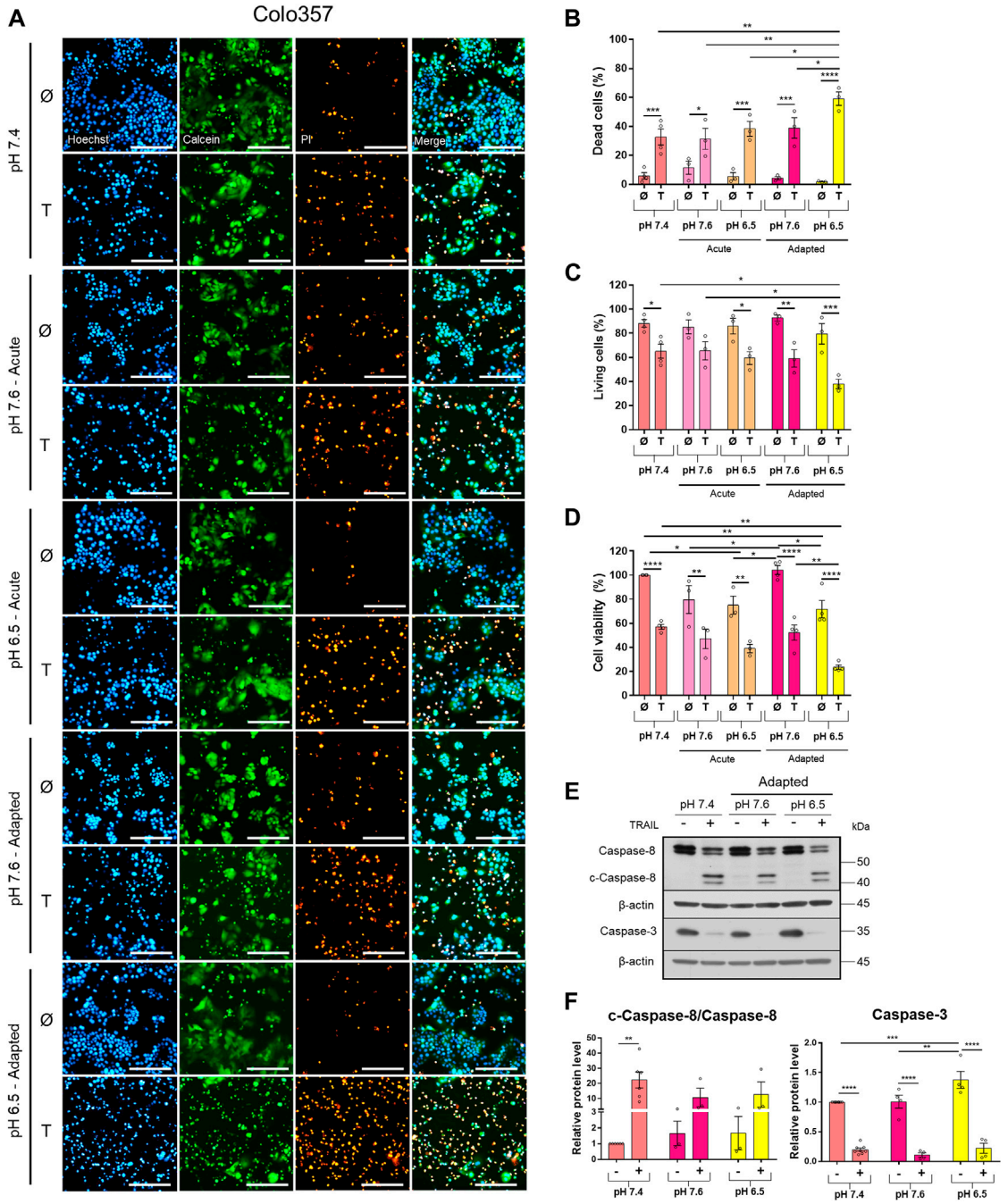

FIGURE 1 | Acidic pH_e increases TRAIL-induced cell death in the TRAIL-sensitive cell line Colo357. Twenty-four hours after seeding, cells were treated for additional 24 h with TRAIL. Cell death/viability was determined by live-cell staining. **(A)** Colo357 cells were live-stained with Hoechst, Calcein-AM, and propidium iodide (PI), and all measurements were processed by NyOne. Scale bar = 200 µm. **(B)** Quantification of PI-positive dead cells. **(C)** Quantification of Calcein-positive living cells. Hoechst was used to stain the nuclei. **(D)** Cell viability measured by crystal violet staining. Data are normalized to untreated cells cultured under pH_e 7.4 conditions and presented as cell viability in percentage without (Ø) or with 200 ng/ml TRAIL (T) for 24 h. Data are shown as mean with S.E.M error bars, of at least three independent experiments per cell line. *p < 0.05, ** < 0.01, *** < 0.001, **** < 0.0001: Significant difference between untreated and treated using two-way ANOVA with Sidak's multiple-comparisons test or between pH_e conditions using two-way ANOVA with Tukey's multiple comparisons test. **(E)** Colo357 cells were grown for 24 h, then either not treated (–) or treated (+) with 200 ng/ml TRAIL for 24 h, lysed, and subjected to western blot analyses for caspase-8 (c-caspase-8 = cleaved-caspase-8) and caspase-3. Blots are representatives of at least three independent experiments. **(F)** Densitometric quantification normalized to loading control and the respective level of untreated cells cultured under pH_e 7.4 conditions. Data are shown as mean with S.E.M error bars, of at least three independent experiments per cell line. ** < 0.01, *** < 0.001, and **** < 0.0001: significant difference of the results was calculated between untreated and treated samples using two-way ANOVA with Sidak's multiple-comparison test or between pH_e conditions using two-way ANOVA with Tukey's multiple-comparison test.

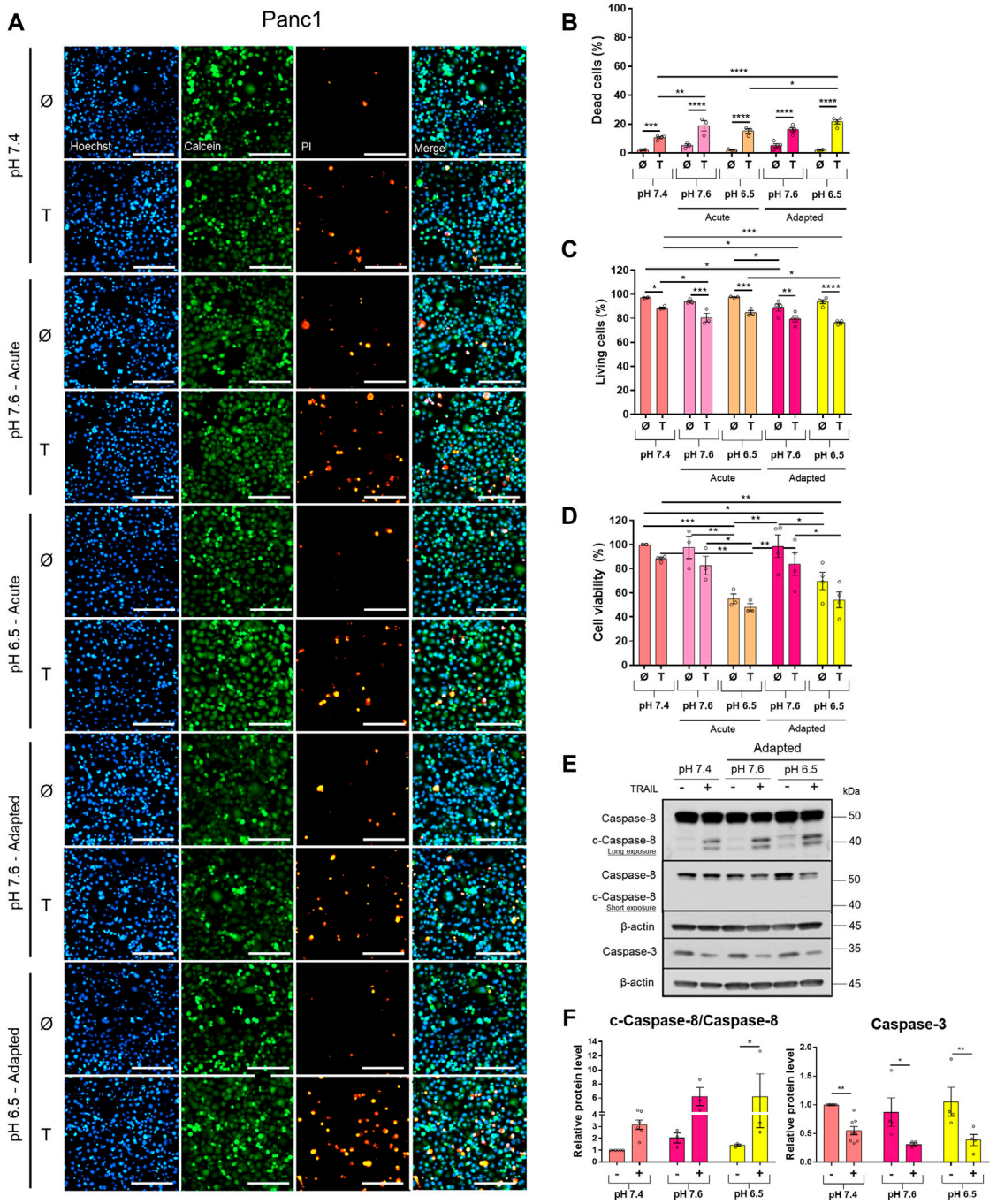

FIGURE 2 | Acidic pH_e increases TRAIL-induced cell death only slightly in the TRAIL-resistant cell line Panc1. Twenty-four hours after seeding, cells were treated for additional 24 h with TRAIL. Cell death/viability was determined by live-cell staining. **(A)** Panc1 cells were live-stained with Hoechst, Calcein-AM, and propidium iodide (PI), and all measurements were processed by NyOne. Scale bar = 200 µm. **(B)** Quantification of PI-positive dead cells. **(C)** Quantification of Calcein-positive living cells. Hoechst was used to stain the nuclei. **(D)** Cell viability measured by crystal violet staining. Data are normalized to untreated cells cultured under pH_e 7.4 conditions and presented as cell viability in percentage without (Ø) or with 200 ng/ml TRAIL (T) for 24 h. Data are shown as mean with S.E.M error bars, of at least three independent experiments per cell line. *p < 0.05, ** < 0.01, *** < 0.001, **** < 0.0001: significant difference between untreated and treated using two-way ANOVA with Sidak's multiple-comparison test or between pH_e conditions using two-way ANOVA with Tukey's multiple-comparison test. **(E)** Panc1 cells were grown for 24 h, then either not treated (–) or treated (+) with 200 ng/ml TRAIL for 24 h, lysed, and subjected to western blot analyses for caspase-8 (c-caspase-8 = cleaved-caspase-8) and caspase-3. Blots are representatives of at least three independent experiments. **(F)** Densitometric quantification normalized to loading control and the respective level of untreated cells cultured under pH_e 7.4 conditions. Data are shown as mean with S.E.M error bars of at least three independent experiments per cell line. *p < 0.05 and **<0.01: significant difference of the results was calculated between untreated and treated samples using two-way ANOVA with Sidak's multiple comparisons test or between pH_e conditions using two-way ANOVA with Tukey's multiple-comparison test.

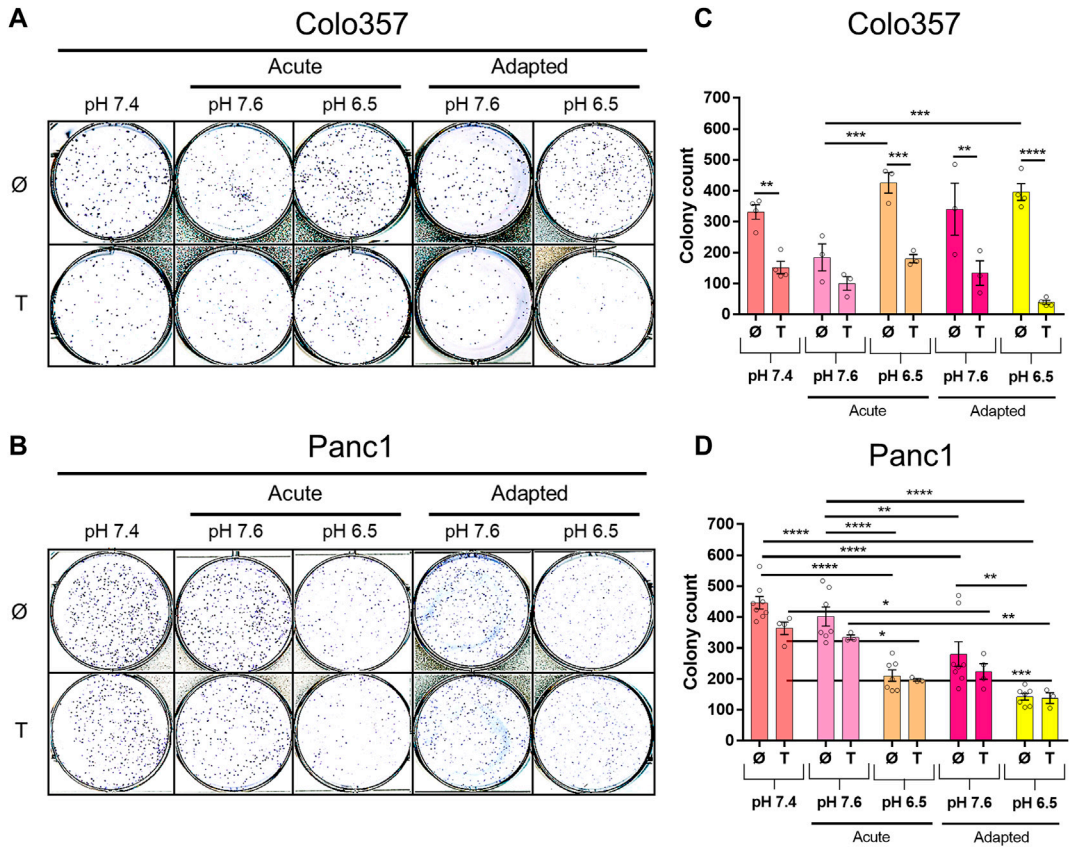

FIGURE 3 | pH_e and TRAIL affect colony formation in PDAC cells. Cells (1×10^3 per well) were seeded to six-well plates for 24 h, treated with TRAIL for 24 h, and following medium change let to grow for additional 5–7 [Colo357; **(A,C)**] or 5–6 days [Panc1, **(B,D)**]. The colonies were counted by live-cell imager NyOne. **(A,B)** Representative crystal violet-stained plates and **(C,D)** quantified data shown as mean with S.E.M error bars of at least three independent experiments per cell line. *$p < 0.05$, ** <0.01, *** <0.001, **** < 0.0001: Significant difference between untreated and treated cells using two-way ANOVA with Sidak's multiple-comparison test or between pH_e conditions using two-way ANOVA with Tukey's multiple-comparison test.

Acidic pH_e Affects Non-Apoptotic TRAIL-R Signaling in PDAC Cells

The TRAIL-induced apoptotic pathway is frequently inhibited in cancer cells leading to the de-masking of the potential of TRAIL death receptors to induce several pro-inflammatory signaling pathways, which may ultimately result in tumor progression (von Karstedt et al., 2017; Trauzold et al., 2001; Trauzold et al., 2006; Hoogwater et al., 2010; Azijli et al., 2010). To study the impact of pH_e on the activation of these non-canonical TRAIL-induced pathways, cells grown under different pH_e conditions were exposed to TRAIL for 3 h. Subsequently, the phosphorylation/activity of Akt, Src, and MAP kinases, as well as the phosphorylation of the Iκbα as an indicator for the activation of NFκB, was analyzed by western blot using phospho-specific antibodies. As a control, the overall cellular expression levels of these proteins were analyzed in parallel. Under normal pH_e conditions, TRAIL treatment resulted, in both PDAC cell lines, in strong activation-related phosphorylation of p38, JNK, and IκBα (**Figure 4**; **Supplementary Figure S1**). In addition, in Colo357 cells, TRAIL also led to the activation of ERK1/2 in pH_e 7.4 and especially in acidic pH_e compared to their respective pH_e controls (**Figure 4A, C**; **Supplementary Figures S1A,C**). Neither in Colo357 cells nor Panc1 cells, changes in Src or Akt activity could be observed following exposure to TRAIL (**Figure 4**; **Supplementary Figure S1**). Of note, these proteins became significantly more active in Colo357 cells adapted to acidic pH_e compared to control cells or cells adapted to pH_e of 7.6 (**Figures 4A,C**). No such effects were seen in Panc1 cells (**Figures 4B,D**). Regarding the impact of pH_e on TRAIL-induced non-canonical pathways, the adaptation of Colo357 cells to acidic pH_e did not change their response to TRAIL (**Figures 4A,C**). Also, no significant TRAIL-mediated phosphorylation of ERK1/2, p38, or IκBα was observed in these cells when adapted to pH_e of 7.6 (**Figures 4A,C**). Importantly, the adaptation of Panc1 cells to either pH_e 7.6 or 6.5 strongly reduced their ability to activate the non-canonical signal transduction pathways in response to TRAIL (**Figures 4B,D**). The activity of the non-canonical TRAIL-induced signaling pathways was also investigated in acute pH_e exposure (**Supplementary Figure S1**). In general, a stronger response to TRAIL treatment was observed in Panc1

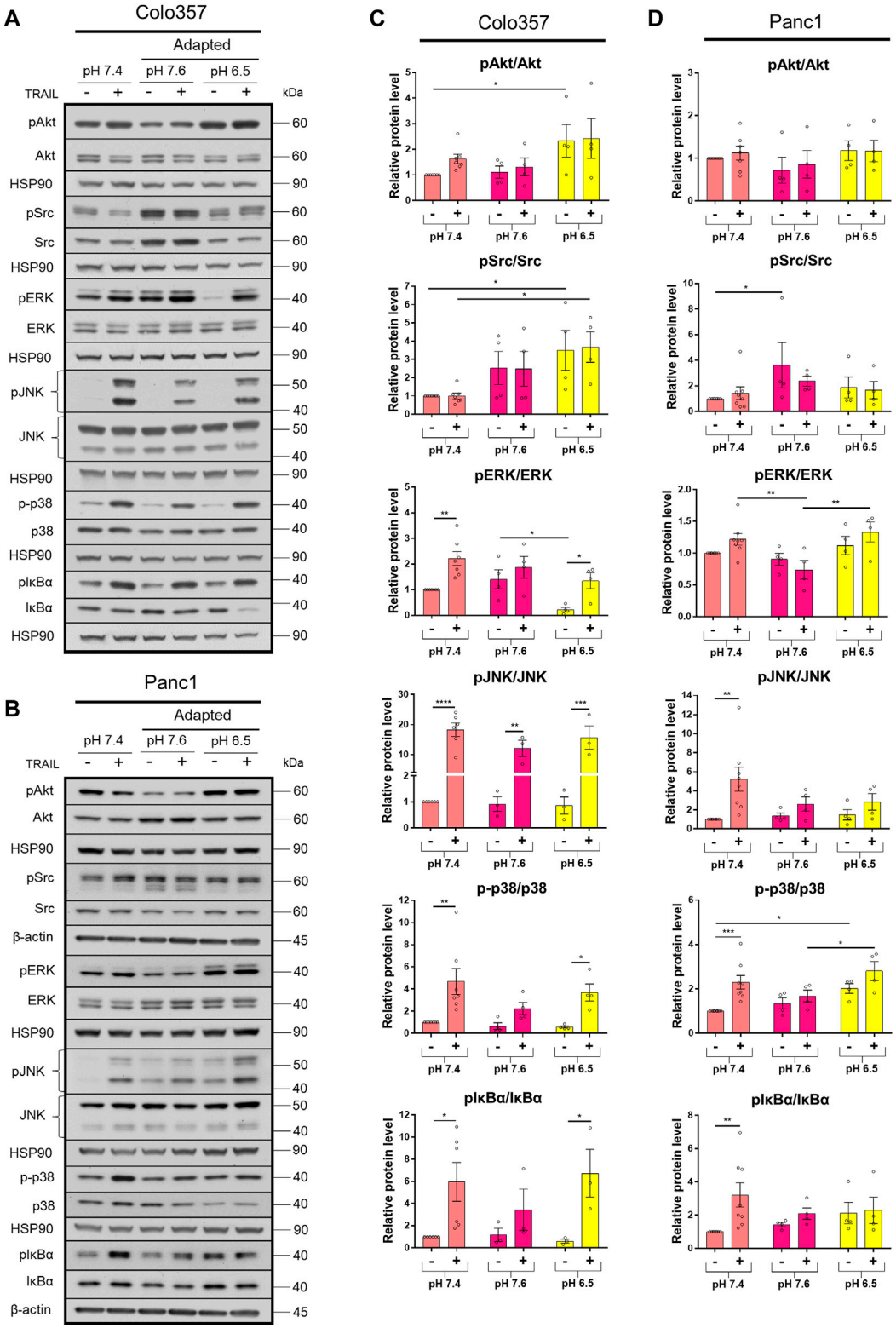

FIGURE 4 | Acidic pH_e affects non-apoptotic TRAIL-R signaling in PDAC cells. **(A,B)** PDAC cells were grown for 24 h, then either not treated (–) or treated (+) with 200 ng/ml TRAIL for 3 h, lysed, and subjected to western blot analyses for pAkt, Akt, pSrc, Src, pERK, ERK, pJNK, JNK, p-p38, p38, pIκBα, and IκBα. Blots are representative and show **(C,D)** densitometric quantification normalized to loading control and the respective level of untreated cells cultured under pH_e 7.4 conditions. Phosphorylated (p) proteins were normalized to non-phosphorylated proteins. Data are shown as mean with S.E.M error bars, of at least three independent experiments per cell line. *$p < 0.05$, **<0.01, ***<0.001, and ****<0.0001: significant difference between untreated and treated cells using two-way ANOVA with Sidak's multiple-comparison test or between pH_e conditions using two-way ANOVA with Tukey's multiple-comparison test.

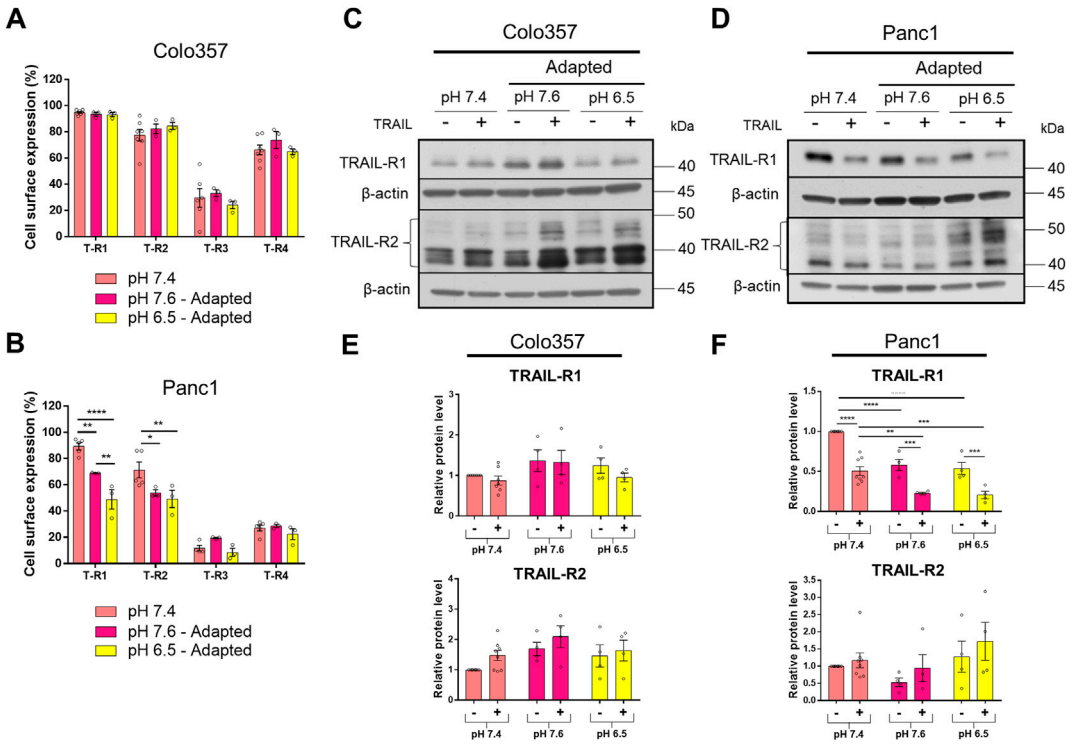

FIGURE 5 | pH_e influences the expression of TRAIL death receptors. **(A,B)** PDAC cells were grown for 24 h, then stained with APC-conjugated anti-TRAIL-Rs antibodies to measure their cell surface expression by flow cytometry. **(C,D)** PDAC cells were grown for 24 h, then either not treated (–) or treated (+) with 200 ng/ml TRAIL for 24 h, lysed, and subjected to western blot analyses for TRAIL-R1 and TRAIL-R2. Blots are representative and **(E,F)** show densitometric quantification normalized to loading control and the respective level of untreated cells cultured under pH_e 7.4 conditions. Data are shown as mean with S.E.M error bars, of at least three independent experiments per cell line. **<0.01, ***<0.001, and ****<0.0001: significant difference between untreated and treated cells using two-way ANOVA with Sidak's multiple-comparison test or between pH_e conditions using two-way ANOVA with Tukey's multiple-comparison test.

cells compared to their pH_e-adapted counterparts (**Supplementary Figures S1B,D**), whereas more similar response patterns, at least for the acidic pH_e were detected in Colo357 cells (**Supplementary Figures S1A,C**). In these cells, alkaline acute pH_e exposure resulted in higher non-apoptotic activity compared to alkaline adapted Colo357 cells (**Supplementary Figures S1A,C**).

pH_e Influences the Expression of TRAIL Death Receptors

The data presented so far show that PDAC cells adapted to acidic pH_e became more sensitive to TRAIL compared to those cultured at pH_e 7.4 or 7.6. Yet, this holds true non-restrictive only for Colo357 cells, while Panc1 cells were only marginally affected and stayed largely TRAIL-resistant. To gain insights into the potential mechanisms behind these effects, we next investigated the expression of TRAIL-Rs as well as several anti-apoptotic proteins in cells adapted to different pH_e conditions and treated or not with recombinant TRAIL for 24 h. Flow cytometric analyses revealed no impact of pH_e on the cell surface expression of TRAIL death receptors in Colo357 cells (**Figure 5A**). Likewise, no differences in the cell surface expression of TRAIL-R3 or TRAIL-R4 were detected neither in Colo357 cells nor in Panc1 cells (**Figures 5A,B**).

Intriguingly, in Panc1 cells, both TRAIL-R1 and TRAIL-R2 were significantly decreased at the plasma membrane following their adaptation to either pH_e 7.6 or 6.5 (**Figure 5B**). Of note, TRAIL-R1 appeared to be stronger influenced by pH_e than TRAIL-R2. In addition, acidic adaptation reduced the plasma membrane levels of TRAIL-R1 significantly stronger than adaptation to pH_e of 7.6 (**Figure 5B**).

Western blot analyses of whole-cell lysates were mostly congruent with the results obtained for the cell surface-expressed TRAIL-R1 and TRAIL-R2. Thus, no pH_e-dependent changes in the levels of these receptors were observed in Colo357 cells (**Figures 5C,E**) while cellular levels of TRAIL-R1 in Panc1 cells were significantly reduced in cells adapted to both pH_e 7.6 and 6.5 (**Figures 5D,F**). However, and contrary to the data showed for the cell surface expression, no impact of pH_e on cellular levels of TRAIL-R2 could be detected by western blot (**Figures 5D,F**).

Besides differences in the impact of pH_e on TRAIL-Rs levels, treatment with TRAIL also differentially influenced these receptors in Colo357 cells and Panc1 cells. Concretely, TRAIL had no effects on the overall levels of TRAIL-R1 or TRAIL-R2 in Colo357 cells in none of the studied pH_e conditions (**Figures 5C,E**). In contrast, in Panc1 cells treatment with TRAIL led to a

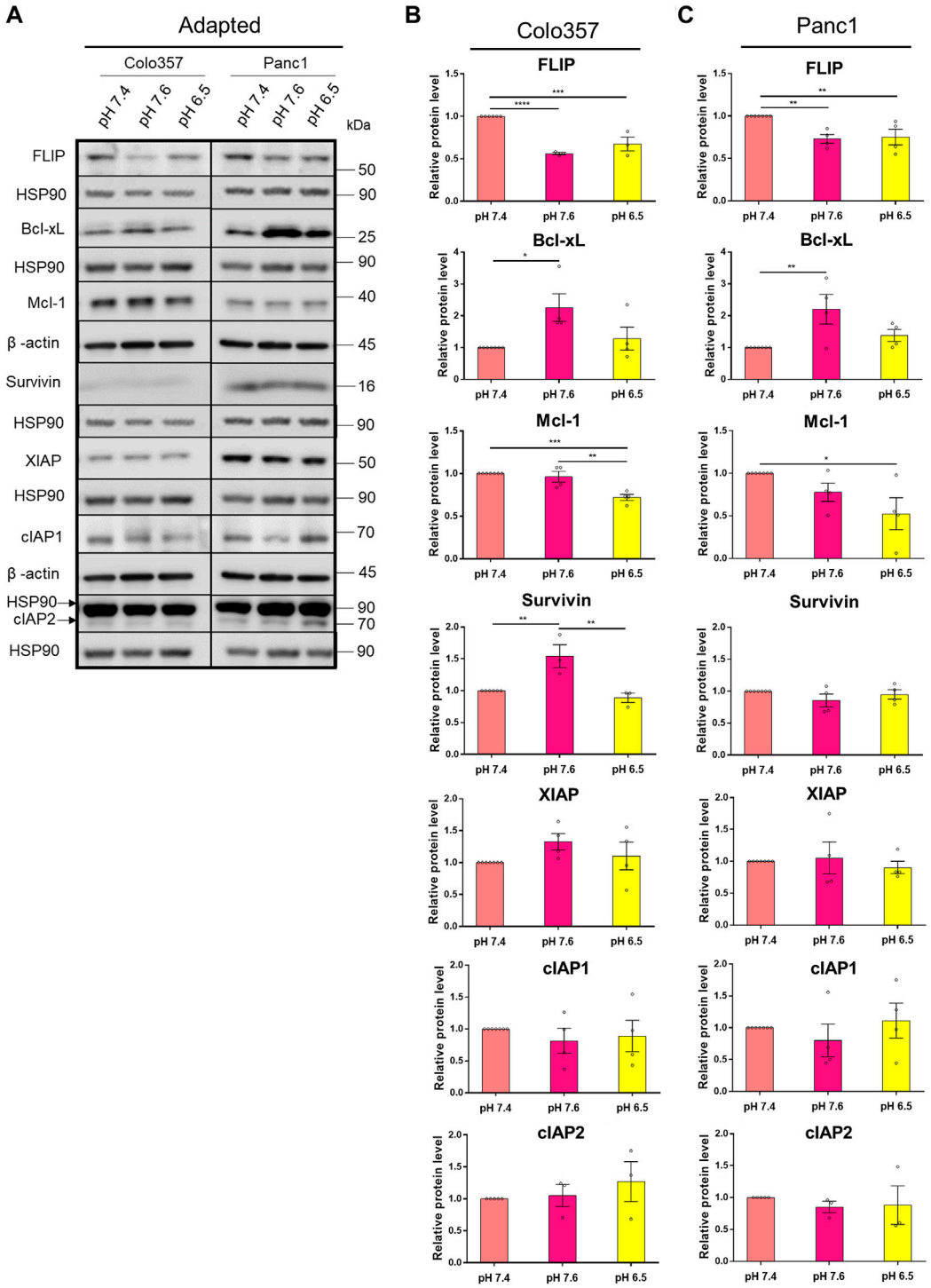

FIGURE 6 | pH_e affects the expression levels of anti-apoptotic proteins. **(A)** PDAC cells were grown for 27 h, then lysed and subjected to western blot analyses for FLIP, Bcl-xL, Mcl-1, Survivin, XIAP, cIAP1, and cIAP2. Blots are representative, where Colo357 cells and Panc1 cells were compared side by side. **(B,C)** Densitometric quantification normalized to loading control and the respective level of untreated cells cultured under pH_e 7.4 conditions. Data are shown as mean with S.E.M error bars, of at least three independent experiments per cell line. *$p < 0.05$, **<0.01, ***<0.001, and ****<0.0001: significant difference between pH_e conditions using one-way ANOVA with Tukey's multiple-comparison test.

strong reduction of TRAIL-R1 levels, but interestingly did not affect the levels of TRAIL-R2 (**Figures 5D,F**).

The expression of TRAIL-Rs was also investigated following the acute pH_e exposure (**Supplementary Figure S2**) and delivered almost completely contrary results. Thus, instead of being downregulated, the levels of TRAIL-R1 were increased in Panc1 cells acutely exposed to either 7.6 or 6.5 (**Supplementary Figures S2B,D**). Similar effects were observed in Colo357 cells in which in acidic pH_e additionally TRAIL-R2 levels were significantly upregulated (**Supplementary Figures S2A,C**). Moreover, upon TRAIL-treatment TRAIL-R1 levels decreased not only in Panc1 cells but also in Colo357 cells, an effect which was not seen in pH_e adapted Colo357 cells (**Supplementary Figure S2**). However, whereas in Panc1 cells this effect was observed under all pH_e conditions, TRAIL-induced downregulation of TRAIL-R1 could be detected only under acidic pH_e (**Supplementary Figures S2A,C**).

pH_e Affects the Expression Levels of Anti-Apoptotic Proteins

Apoptosis resistance due to an overexpression of anti-apoptotic proteins is a known hallmark of cancer (Hanahan and Weinberg, 2011). Concerted upregulation of proteins operating at different steps of the apoptotic signal transduction pathway was shown to assure TRAIL resistance in PDAC cells (Hinz et al., 2000; Trauzold et al., 2003). However, to the best of our knowledge, the effects of pH_e on the expression levels of these proteins in PDAC cells are unknown so far. To close this gap, we next analyzed by western blot the levels of FLIP, Mcl-1, Bcl-xL, and the members of the inhibitor of apoptosis (IAP) family Survivin, XIAP, cIAP1, and cIAP2 in whole-cell lysates of Colo357 and Panc1 cells cultured in different pH_e conditions. As shown in **Figure 6**, in both cell lines, albeit stronger in Colo357 than in Panc1 cells, FLIP was significantly decreased in both pH_e 7.6 and 6.5 adapted cell lines compared to control (**Figures 6A–C**). In both pH_e 6.5 adapted cell lines, Mcl-1 was also significantly decreased compared to control, and again stronger in Colo357 cells (**Figures 6A–C**). Interestingly, Bcl-xL significantly increased in both pH_e 7.6 adapted cells lines compared to control (**Figures 6A–C**). Regarding the expression levels of IAPs, only Survivin and only in Colo357 cells showed pH_e-dependence being significantly increased in pH_e 7.6 adapted cells (**Figures 6A,B**; **Supplementary Figure S3**). None of the remaining analyzed IAP proteins (XIAP, cIAP1, and cIAP2) show any significant changes due to changes in pH_e either in Colo357 or in Panc1 cells (**Figures 6A–C**). In agreement with already published data (Hinz, Trauzold, et al., 2000; Trauzold, Schmiedel, et al., 2003), and with the apoptosis-resistant phenotype of Panc1 cells, these cells showed higher expression of most of the analyzed anti-apoptotic proteins (FLIP, Bcl-xL, Survivin, and XIAP) as compared to Colo357 cells except for Mcl-1, which was higher in Colo357 cells (**Figure 6A**).

The expression of the anti-apoptotic proteins has been also studied in cells acutely exposed to different pH_e (**Supplementary Figure S4**). Interestingly, the expression pattern was not the same as for the cells adapted to pH_e. Thus, the levels of the studied proteins in cells acutely exposed to different pH_e were either the same or even slightly increased compared to control (**Supplementary Figure S4**). These results show again that cells react differently to long-time and acute pH_e exposure.

Inhibition of Bcl-xL Highly Sensitizes Acidic pH_e-Adapted Panc1 Cells to TRAIL-Induced Cell Death

Our results revealed that under acidic pH_e, Colo357 cells become highly sensitive to TRAIL, while this effect was only marginal in Panc1 cells. Since the latter overexpress Bcl-xL, we wonder whether inhibition of Bcl-xL could sensitize these cells to TRAIL under acidic pH_e conditions. Recently, the so-called BH3-mimetics have been developed, which bind to and neutralize the activity of anti-apoptotic members of the Bcl-2-family. Among several generated and pre-clinically evaluated BH3-mimetics, Navitoclax (ABT-263) and Venetoclax (ABT-199) have successfully entered clinical trial testing. Navitoclax potently antagonizes Bcl-2 and Bcl-xL, whereas Venetoclax selectively inhibits Bcl-2. We set out to investigate whether BH3-mimetics may harbor the potential to sensitize Panc1 cells to TRAIL and to study their potentially synergistic effects with acidic pH_e. Panc1 cells adapted to different pH_e were pre-treated for 2 h with inhibitors prior to treatment with TRAIL for an additional 24 h. Cell viability and cell death were analyzed by staining the cells with Hoechst, Calcein-AM, and PI followed by measurement and quantification on the live-cell imager NyOne. As shown in **Figures 7A–C**, under normal pH_e conditions, Navitoclax only marginally increased TRAIL-mediated cell death. Likewise, it did not show synergizing effects with TRAIL in cells adapted to pH_e 7.6 (**Figures 7A–C**). Intriguingly, Navitoclax robustly enhanced the death-inducing capacity of TRAIL in Panc1 cells adapted to acidic pH_e. In contrast, pre-treatment with Venetoclax did not enhance TRAIL-induced apoptosis further, highlighting the pivotal role of Bcl-xL in mediating apoptosis resistance in Panc1 cells (**Figures 7A–C**). The same patterns were obtained when analyzing cell viability using cell staining with Calcein-AM (**Figures 7A,D,E**), except that a combination of Navitoclax with TRAIL was also able to significantly decrease the cell viability in alkaline pH_e-adapted cells compared to TRAIL treatment only (**Figures 7A,D,E**). Again, no decrease in cell viability could be observed when combining TRAIL with Venetoclax compared to TRAIL alone (**Figures 7A,E**). Similar results were generated by studying cell viability using crystal violet staining (**Supplementary Figure S5**).

Summing up, we provide here a comprehensive analysis of the effects of pH_e on TRAIL-induced apoptotic and non-apoptotic signaling in PDAC cells. We show that these pathways are differentially affected by alkaline and acidic pH_e. Most importantly, we found that cells adapted to acidic pH_e become highly sensitive to TRAIL-induced cell death either when treated with TRAIL as a single agent or in combination with the already clinically approved drug Navitoclax (ABT-263).

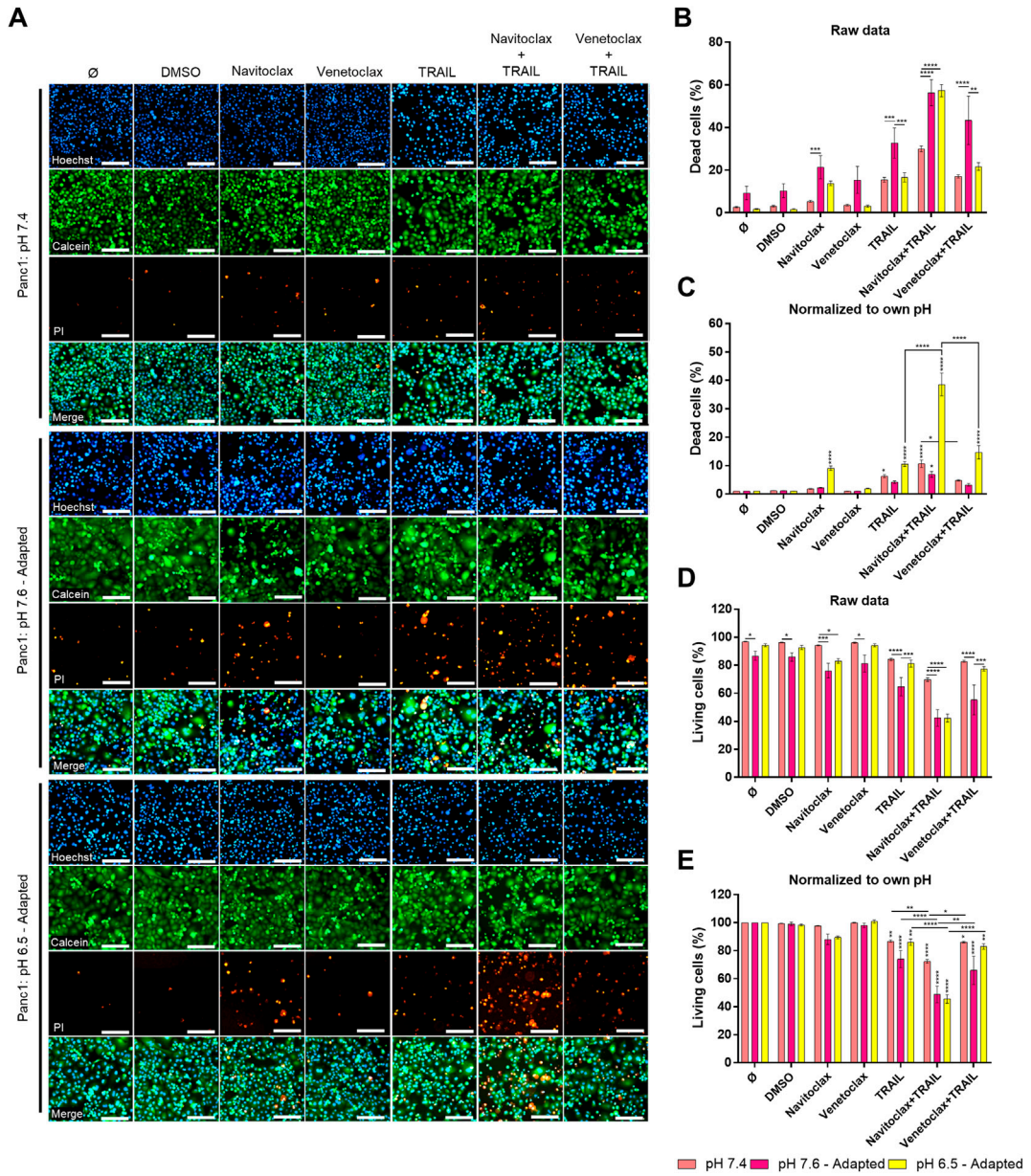

FIGURE 7 | Navitoclax (Bcl-xL inhibitor) sensitizes Panc1 cells to TRAIL-induced cell death in acidic pH_e. **(A)** Panc1 cells were grown for 24 h, then either not treated (Ø) or treated with DMSO, 5 μM inhibitor (Navitoclax or Venetoclax) for 26 h, TRAIL treatment (200 ng/ml) for 24 h, or a combination of pre-treated 5 μM inhibitor for 2 h prior to TRAIL treatment for an additional 24 h. Cells were finally live-stained with Hoechst, Calcein-AM, and propidium iodide (PI), and all measurements were processed by NyOne. Scale bar = 200 μm. **(B,C)** Cell death quantification of PI-positive cells, either showed as raw data or normalized to respective pH_e control. **(D,E)** Living cells quantified from Calcein-positive cells, either showed as raw data or normalized to respective pH_e control. Hoechst was used to stain the nuclei. Data are shown as mean with S.E.M error bars, of at least three independent experiments per cell line. *$p < 0.05$, **<0.01, ***<0.001, and ****<0.0001: significant difference between untreated and treated cells using two-way ANOVA with Sidak's multiple-comparison test or between pH_e conditions using two-way ANOVA with Tukey's multiple-comparison test. Significant differences in "raw data" are only shown between different pH conditions within each treatment. Significant differences in "normalized to own pH" are only shown between different treatments within the same pH, where vertical stars are significant differences to respective controls (Ø or DMSO).

DISCUSSION

Dysregulated pH_e microenvironment, commonly observed in PDAC, influences many physiological and cellular processes in tumor cells (Kato et al., 2018). pH_e in tumors is generally more acidic than in normal tissue and can decrease to as low as 5.8 (Tannock and Rotin, 1989). In our study, we included both cells acutely exposed and adapted to either alkaline or acidic pH_e. We consider selecting and adapting cells to a specific pH_e to be a highly relevant biological setup, in order to determine how cancer

pH_e microenvironment influences cell signaling. Additionally, we compared both pH_e setups, as we speculated that this would be affecting PDAC cells differently. To our knowledge, most studies have focused exclusively on acute pH_e exposure and acidic pH_e, and the latter is presumably because acidic pH_e has been observed in many tumors (Tannock and Rotin, 1989). In our study, we included alkaline pH_e as well, because this is particularly interesting concerning PDAC due to the fact that the pancreas normally produces a high amount of bicarbonate into the lumen (Pallagi et al., 2015).

\We found that when PDAC cells were either exposed acutely or adapted to acidic pH_e, the colony formation decreased in Panc1 cells but was unaffected in Colo357 cells. For the alkaline pH_e setups, there were differences between acute and adapted pH_e conditions for both cell lines. In Panc1 cells, colony formation remained unchanged in acute alkaline pH_e exposure but decreased when adapted and was the complete opposite for Colo357 cells. No studies concerning the influence of pH_e on colony formation in PDAC have been conducted according to our knowledge, but in equivalence to our study, one study showed that Panc1 cells, but not Colo357 cells, decreased in growth significantly after acute pH_e 6.5 exposure (Kumar et al., 2010). Similar to Panc1 cells, lung carcinoma decreased in growth under acute acidic pH_e exposure (Sutoo et al., 2020). Another study showed that very short exposure (10–30 min) of alkaline pH_e decreased cell area in breast cancer (Khajah et al., 2013), similar to Colo357 cells (data not shown).

Acidic pH_e has been shown to be able to potentiate TRAIL-induced cell death in some cancer types such as prostate carcinoma (Lee et al., 2004), colorectal carcinoma (Lee et al., 2004), gastric carcinoma (Hong and Han 2018), colon carcinoma (Meurette et al., 2007), hepatocarcinoma (Meurette et al., 2007), and lung cancer (Valiahdi et al., 2013). According to our knowledge, corresponding studies have not yet been performed with PDAC cells. Likewise, no data on the impact of alkaline pH_e on TRAIL-induced signaling is available so far. Therefore, in the present study, we addressed this issue and compared side by side the TRAIL-induced death and pro-inflammatory signaling in TRAIL-sensitive and TRAIL-resistant PDAC cell lines Colo357 and Panc1 cells, respectively. We observed increased cell death particularly in acid-adapted Colo357 cells, but only slightly in Panc1 cells, which stayed highly resistant even in acidic pH_e. In agreement, increased activity of pro-apoptotic proteins was observed in acid-adapted Colo357 cells, but to a much lower degree in acid-adapted Panc1 cells, correlating well with cell death observations in both cell lines. Interestingly, both cell lines became more vulnerable when grown in alkaline pH_e, where a higher number of dead cells were observed even without treatment with TRAIL. Cancer cells need to maintain an optimal pH_i value, which is often kept slightly more alkaline or the same as in healthy cells (Chii et al., 2014). A sudden change in pH_e can disrupt pH_i (Boron, 2004; Kato et al., 2013; Michl et al., 2019; Swietach 2019), which could last either shortly or for a longer period, usually reflected by the cells' ability to regulate metabolism, ion channels, and metabolite transporters (Vander Heiden et al., 2009; Chii et al., 2014; Vaupel et al., 2019). Thus, growing cells in alkaline pH_e may disrupt important cellular processes making them more vulnerable. Especially, PDAC is known to be highly dependent on autophagy, a nutrient-scavenging process (Yang et al., 2011; Flinck et al., 2020), where lysosomes, a compartment with a pH_i as low as 4.7 for optimal hydrolytic enzyme activity, play an important role in this process (Casey et al., 2010; Halcrow et al., 2021).

TRAIL sensitivity can be altered at many different cellular levels. The protein expression of TRAIL-Rs has already been seen to be regulated in gastric cancer cells acutely exposed to acidic pH_e, where both TRAIL-R1 and TRAIL-R2 increased (Hong and Han, 2018), similar to our results with acutely exposed Panc1 cells. Interestingly, adaptation to acidic pH_e had the opposite effect on TRAIL-R1 in Panc1 cells. To this extent, both TRAIL-R1 and TRAIL-R2 significantly decreased at the cell surface in acid-adapted Panc1 cells. Thus, it is worth noting that Panc1 cells exhibit lower cell surface expression of TRAIL-R2 than TRAIL-R1 and that they have a preference for TRAIL-R2 compared to TRAIL-R1 for the induction of apoptosis (Nahacka et al., 2018). In our study, the protein level and cell surface expression of TRAIL-R1 in Panc1 cells correlated, suggesting that it was not a change in cellular location but rather a lower expression of TRAIL-R1. Alternatively, enhanced constitutive receptor internalization and subsequent degradation could account for the lower levels of TRAIL-R1 in pH_e-adapted cells. Specific degradation of TRAIL-R1 has already been described as an effect of steady-state receptor internalization and modification by the membrane-associated RING-CH ubiquitin ligase (March-8) (van de Kooij, et al., 2013). Ultimately, this outcome would contribute to TRAIL resistance. Ligand-induced endocytosis and subsequent degradation of TRAIL-R1 could also account for the observed lower levels of this receptor in Panc1 cells following TRAIL treatment. Interestingly, we also found that TRAIL-R2 decreased at the cell surface in both acidic and alkaline pH_e-adapted Panc1 cells, and while this correlated well with the total cellular protein level in alkaline-adapted Panc1 cells (mean decrease of ~50%), it did not in the acid-adapted Panc1 cells. This suggests that TRAIL-R2 showed changed intracellular distribution in acid-adapted Panc1 cells, an effect that has already been demonstrated to occur to a high degree in Panc1 cells under normal pH_e conditions (Haselmann et al., 2014). Summing up, the relocation of TRAIL-R1 and TRAIL-R2 may be one of the mechanisms Panc1 cells utilize to maintain TRAIL resistance. Furthermore, we clearly show that the exposure time to pH_e (acute or adapted) influences the overall and the plasma membrane level of TRAIL-Rs.

In cancer cells, TRAIL death receptors regularly induce a non-canonical signaling pathway, which becomes of high relevance especially in apoptosis-resistant cells (Trauzold et al., 2001; Ehrenschwender et al., 2010; von Karstedt et al., 2015; Azijli et al., 2013; Trauzold et al., 2006; Hoogwater et al., 2010). Here, we observed a generally higher activity of these pathways in Colo357 cells upon TRAIL treatment compared to Panc1 cells. In particular, in Panc1 cells adapted to either alkaline or acidic pH_e, almost no differences in the TRAIL-induced activation of IκBα, p38, and JNK were observed. This could be due to the much lower cell surface expression of both TRAIL-R1 and TRAIL-R2 in pH_e-adapted Panc1 cells, which ultimately would cause a general lower activation of all pathways these two receptors may induce upon triggering. Because TRAIL can initiate both the pro-apoptotic and non-apoptotic pathways, it may not be surprising to see the non-apoptotic proteins increase significantly more in acid-adapted Colo357 cells. Alkaline-adapted

Colo357 cells showed mostly decreased or the same activity upon TRAIL treatment compared to control or acid-adapted Colo357 cells. Similar tendencies were seen in breast cancer cells where acute alkaline pH_e conditions reduced the levels of activated p38, Akt, and ERK1/2 (Khajah et al., 2013). Even though acidic pH_e increases TRAIL-induced cell death, it is worth noting that the non-apoptotic pathway might be activated to a higher degree as well. Hence, if the apoptotic pathway is not superior, TRAIL treatment can induce and select for malignant progression.

Anti-apoptotic proteins can be responsible for decreased cell death while keeping non-apoptotic signaling ongoing, which contributes to malignant aggressiveness (Hinz et al., 2000; Trauzold et al., 2001; Trauzold et al., 2003; Lemke et al., 2010). In our study, we showed that some of these proteins are influenced by pH_e. TRAIL-induced cytochrome c release has been seen to increase in acute acidic pH_e compared to normal pH_e in prostate carcinoma, while multiple anti-apoptotic proteins (cFLIP, cIAP1, cIAP2, and Bcl-2) remained overall unchanged (Lee et al., 2004). In contrast, in our study, we observed an upregulation of XIAP and Bcl-xL in both PDAC cells acutely exposed to acidic pH_e but a decrease of the cellular levels of FLIP and Mcl-1 following acidic pH_e adaptation. These results again display that cell signaling in cancer cells is affected very differently upon short-term and long-term pH_e exposure. Diverse dependencies towards pH_i acidification to induce apoptosis have been seen in type I and type II cells (Matsuyama and Reed, 2000). In type I cells, apoptosis was overall unaffected upon changed pH_i when treated with Fas, while apoptosis was partially suppressed in type II cells when pH_i was kept neutral instead of acidic after Fas treatment (Matsuyama and Reed, 2000). This indicates that cytosol acidification may be important to TRAIL-induced apoptosis in PDAC cells, which are known to be type II cells (Hinz et al., 2000; Trauzold et al., 2001). Cytosolic acidification can be blocked by Bcl-2/Bcl-xL (Matsuyama et al., 2000), while we have now shown that acidic extracellular pH lowers the levels of FLIP and Mcl-1, indicating that pH and anti-apoptotic proteins both can regulate each other. Another study showed that overexpressed Bcl-2 in colorectal carcinoma cells was able to lower TRAIL-induced cell death in acute acidic pH_e and did not differ highly from pH_e 7.4 (Lee et al., 2004). This indicates that cancer cells that already have a high overexpression of anti-apoptotic proteins can escape the TRAIL-sensitizing effect from acidic pH_e. Panc1 cells show a generally higher expression of anti-apoptotic proteins than Colo357 cells (Trauzold et al., 2003), and this can be partly responsible for the ongoing TRAIL resistance of these cells also in acidic pH_e. Using orally bioavailable small molecular inhibitors of Bcl-2 family proteins, we have shown that the resistance of Panc1 cells under acidic pH_e-adapted conditions is highly dependent on Bcl-xL and can be overcome by the treatment with Bcl-xL/Bcl-2 inhibitor Navitoclax. Such effects were much less pronounced in the other pH_e conditions. Since the specific Bcl-2 inhibitor Venetoclax did not show the same effects in our current study and also in other studies analyzing TRAIL responses under normal pH_e conditions in PDAC cells (Hari et al., 2015; Legler et al., 2018), this confirms that Bcl-xL and not Bcl-2 is responsible for the apoptosis resistance in PDAC cells.

In conclusion, our study has shown that long-term exposition to acidic pH_e alone increases TRAIL sensitivity in PDAC, but mainly in already TRAIL-sensitive PDAC cells. The TRAIL-resistant cell line Panc1 decreased both TRAIL-R1 and TRAIL-R2 at the cell surface under long-term acidic pH_e conditions, which partly explains their ongoing resistance to TRAIL. Different capacities to quickly adapt and respond to altered pH_e in TRAIL-sensitive and TRAIL-resistant PDAC cells could also be observed in the change of TRAIL-induced signaling pathways and the expression of anti-apoptotic proteins. Importantly, acid-adapted Panc1 cells could be sensitized to TRAIL by using an inhibitor of Bcl-xL, again pointing to the decisive role of the mitochondrial amplification loop in these cells. The chosen cell lines, Colo357 and Panc1, have been extensively studied by us and others and are widely accepted models for studying PDAC. Yet, since only two PDAC cell lines were analyzed, the generalization of the conclusions may be limited. Nevertheless, our study gives important insights into the effect of pH_e on TRAIL-induced signaling in PDAC cells, improving our understanding of the function of TRAIL receptors in this particularly aggressive cancer.

DATA AVAILABILITY STATEMENT

The original contributions presented in the study are included in the article/**Supplementary Material**, further inquiries can be directed to the corresponding author.

AUTHOR CONTRIBUTIONS

SH performed all experiments, data analysis, and design. AT supervised the project and was in charge of the overall direction and planning. All authors contributed to the article and approved the submitted version.

ACKNOWLEDGMENTS

This work was supported and funded by the European Marie Skłodowska-Curie Innovative Training Network (ITN) pH and Ion Transport in Pancreatic Cancer-pHioniC (Grant Agreement number: 813834; H2020-MSCAITN-2018). We also acknowledge financial support by Land Schleswig-Holstein within the funding programme Open Access Publikationsfonds.

SUPPLEMENTARY MATERIAL

The Supplementary Material for this article can be found online at: https://www.frontiersin.org/articles/10.3389/fcell.2022.768579/full#supplementary-material

REFERENCES

American-Cancer-Society (2021). *Cancer Facts & Figures 2021*. Atlanta.

Antonsson, B., Montessuit, S., Sanchez, B., and Martinou, J.-C. (2001). Bax Is Present as a High Molecular Weight Oligomer/complex in the Mitochondrial Membrane of Apoptotic Cells. *J. Biol. Chem.* 276, 11615–11623. doi:10.1074/jbc.M010810200

Azijli, K., Dekker, H., Joore, J., Peters, G. J., de Jong, S., and Kruyt, F. A. (2010). Abstract 1261: TRAIL-Induced Pro- and Antiapoptotic Kinase Activation in Non-small Cell Lung Cancer Cells. *Cancer Res.* 70, 8. doi:10.1158/1538-7445.am10-1261

Azijli, K., Weyhenmeyer, B., Peters, G. J., de Jong, S., and Kruyt, F. A. E. (2013). Non-canonical Kinase Signaling by the Death Ligand TRAIL in Cancer Cells: Discord in the Death Receptor Family. *Cell Death Differ* 20, 858–868. doi:10.1038/cdd.2013.28

Boron, W. F. (2004). Regulation of Intracellular pH. *Adv. Physiol. Educ.* 28, 160–179. doi:10.1152/advan.00045.2004

Bratton, S. B., Walker, G., Srinivasula, S. M., Sun, X. M., Butterworth, M., Alnemri, E. S., et al. (2001). Recruitment, Activation and Retention of Caspases-9 and -3 by Apaf-1 Apoptosome and Associated XIAP Complexes. *Embo j* 20, 998–1009. doi:10.1093/emboj/20.5.998

Bray, F., Ferlay, J., Soerjomataram, I., Siegel, R. L., Torre, L. A., and Jemal, A. (2018). Global Cancer Statistics 2018: GLOBOCAN Estimates of Incidence and Mortality Worldwide for 36 Cancers in 185 Countries. *CA: a Cancer J. clinicians* 68, 394–424. doi:10.3322/caac.21492

Casey, J. R., Grinstein, S., and Orlowski, J. (2010). Sensors and Regulators of Intracellular pH. *Nat. Rev. Mol. Cel Biol* 11, 50–61. doi:10.1038/nrm2820

Chii, K. S., Andrea, G., Ivana, N., and Falsig, P. S. (2014). Acid-base Transport in Pancreatic Cancer: Molecular Mechanisms and Clinical Potential. *Biochem. Cel Biol.* 92, 6. doi:10.1139/bcb-2014-0078%M25372771

Christopher, P. W., Elisabete, W., and Stewart, B. W. (2020). *World Cancer Report: Cancer Research for Cancer Prevention*. Lyon, France: International Agency for Research on Cancer.

de Miguel, D., Lemke, J., Anel, A., Walczak, H., and Martinez-Lostao, L. (2016). Onto Better TRAILs for Cancer Treatment. *Cel Death Differ* 23, 733–747. doi:10.1038/cdd.2015.174

Deveraux, Q. L., Roy, N., Stennicke, H. R., Van Arsdale, T., Zhou, Q., Srinivasula, S. M., et al. (1998). IAPs Block Apoptotic Events Induced by Caspase-8 and Cytochrome C by Direct Inhibition of Distinct Caspases. *EMBO J.* 17, 2215–2223. doi:10.1093/emboj/17.8.2215

Dewson, G., Kratina, T., Czabotar, P., Day, C. L., Adams, J. M., and Kluck, R. M. (2009). Bak Activation for Apoptosis Involves Oligomerization of Dimers via Their α6 Helices. *Mol. Cel* 36, 696–703. doi:10.1016/j.molcel.2009.11.008

Dickens, L. S., Boyd, R. S., Jukes-Jones, R., Hughes, M. A., Robinson, G. L., Fairall, L., et al. (2012). A Death Effector Domain Chain DISC Model Reveals a Crucial Role for Caspase-8 Chain Assembly in Mediating Apoptotic Cell Death. *Mol. Cel* 47, 291–305. doi:10.1016/j.molcel.2012.05.004

Ehrenschwender, M., Siegmund, D., Wicovsky, A., Kracht, M., Dittrich-Breiholz, O., Spindler, V., et al. (2010). Mutant PIK3CA Licenses TRAIL and CD95L to Induce Non-apoptotic Caspase-8-Mediated ROCK Activation. *Cel Death Differ* 17, 1435–1447. doi:10.1038/cdd.2010.36

Falschlehner, C., Schaefer, U., and Walczak, H. (2009). Following TRAIL's Path in the Immune System. *Immunology* 127, 145–154. doi:10.1111/j.1365-2567.2009.03058.x

Flinck, M., Hagelund, S., Gorbatenko, A., Severin, M., Pedraz-Cuesta, E., Novak, I., et al. (2020). The Vacuolar H+ ATPase α3 Subunit Negatively Regulates Migration and Invasion of Human Pancreatic Ductal Adenocarcinoma Cells. *Cells* 9, 465. doi:10.3390/cells9020465

Flinck, M., Kramer, S. H., Schnipper, J., Andersen, A. P., and Pedersen, S. F. (2018). The Acid-Base Transport Proteins NHE1 and NBCn1 Regulate Cell Cycle Progression in Human Breast Cancer Cells. *Cell Cycle* 17, 1056–1067. doi:10.1080/15384101.2018.1464850

Halcrow, P. W., Geiger, J. D., and Chen, X. (2021). Overcoming Chemoresistance: Altering pH of Cellular Compartments by Chloroquine and Hydroxychloroquine. *Front. Cel Dev. Biol.* 9, 170. doi:10.3389/fcell.2021.627639

Hanahan, D., and Weinberg, R. A. (2011). Hallmarks of Cancer: The Next Generation. *Cell* 144, 646–674. doi:10.1016/j.cell.2011.02.013

Hari, Y., Harashima, N., Tajima, Y., and Harada, M. (2015). Bcl-xL Inhibition by Molecular-Targeting Drugs Sensitizes Human Pancreatic Cancer Cells to TRAIL. *Oncotarget* 6, 41902–41915. doi:10.18632/oncotarget.5881

Haselmann, V., Kurz, A., Bertsch, U., Hübner, S., Olempska–MüllerMüller, M. M., Fritsch, J., et al. (2014). Nuclear Death Receptor TRAIL-R2 Inhibits Maturation of Let-7 and Promotes Proliferation of Pancreatic and Other Tumor Cells. *Gastroenterology* 146, 278–290. doi:10.1053/j.gastro.2013.10.009

Hinz, S., Trauzold, A., Boenicke, L., Sandberg, C., Beckmann, S., Bayer, E., et al. (2000). Bcl-XL Protects Pancreatic Adenocarcinoma Cells against CD95- and TRAIL-Receptor-Mediated Apoptosis. *Oncogene* 19, 5477–5486. doi:10.1038/sj.onc.1203936

Holcik, M., and Korneluk, R. G. (2001). XIAP, the Guardian Angel. *Nat. Rev. Mol. Cel Biol* 2, 550–556. doi:10.1038/35080103

Hong, R., and Han, S. I. (2018). Extracellular Acidity Enhances Tumor Necrosis Factor-Related Apoptosis-Inducing Ligand (TRAIL)-mediated Apoptosis via DR5 in Gastric Cancer Cells. *Korean J. Physiol. Pharmacol.* 22, 513. doi:10.4196/kjpp.2018.22.5.513

Hoogwater, F. J. H., Nijkamp, M. W., Smakman, N., Steller, E. J. A., Emmink, B. L., Westendorp, B. F., et al. (2010). Oncogenic K-Ras Turns Death Receptors into Metastasis-Promoting Receptors in Human and Mouse Colorectal Cancer Cells. *Gastroenterology* 138, 2357–2367. doi:10.1053/j.gastro.2010.02.046

Huang, K., Zhang, J., O'Neill, K. L., Gurumurthy, C. B., Quadros, R. M., Tu, Y., et al. (2016). Cleavage by Caspase 8 and Mitochondrial Membrane Association Activate the BH3-Only Protein Bid during TRAIL-Induced Apoptosis. *J. Biol. Chem.* 291, 11843–11851. doi:10.1074/jbc.M115.711051

Jost, P. J., Grabow, S., Gray, D., McKenzie, M. D., Nachbur, U., Huang, D. C. S., et al. (2009). XIAP Discriminates between Type I and Type II FAS-Induced Apoptosis. *Nature* 460, 1035–1039. doi:10.1038/nature08229

Kalkavan, H., and Green, D. R. (2018). MOMP, Cell Suicide as a BCL-2 Family Business. *Cel Death Differ* 25, 46–55. doi:10.1038/cdd.2017.179

Kato, Y., Maeda, T., Suzuki, A., and Baba, Y. (2018). Cancer Metabolism: New Insights into Classic Characteristics. *Jpn. Dental Sci. Rev.* 54, 8–21. doi:10.1016/j.jdsr.2017.08.003

Kato, Y., Ozawa, S., Miyamoto, C., Maehata, Y., Suzuki, A., Maeda, T., et al. (2013). Acidic Extracellular Microenvironment and Cancer. *Cancer Cel Int.* 13, 89. doi:10.1186/1475-2867-13-89

Khajah, M. A., Almohri, I., Mathew, P. M., and Luqmani, Y. A. (2013). Extracellular Alkaline pH Leads to Increased Metastatic Potential of Estrogen Receptor Silenced Endocrine Resistant Breast Cancer Cells. *PLOS ONE* 8, e76327. doi:10.1371/journal.pone.0076327

Kumar, Y., Mazurek, S., Yang, S., Failing, K., Winslet, M., Fuller, B., et al. (2010). *In Vivo* factors Influencing Tumour M2-Pyruvate Kinase Level in Human Pancreatic Cancer Cell Lines. *Tumor Biol.* 31, 69–77. doi:10.1007/s13277-009-0010-3

Lagadic-Gossmann, D., Huc, L., and Lecureur, V. (2004). Alterations of Intracellular pH Homeostasis in Apoptosis: Origins and Roles. *Cel Death Differ* 11, 953–961. doi:10.1038/sj.cdd.4401466

Lee, Y. J., Song, J. J., Kim, J. H., Kim, H.-R. C., and Song, Y. K. (2004). Low Extracellular pH Augments TRAIL-Induced Apoptotic Death through the Mitochondria-Mediated Caspase Signal Transduction Pathway. *Exp. Cel. Res.* 293, 129–143. doi:10.1016/j.yexcr.2003.09.015

Legler, K., Hauser, C., Egberts, J.-H., Willms, A., Heneweer, C., Boretius, S., et al. (2018). The Novel TRAIL-Receptor Agonist APG350 Exerts superior Therapeutic Activity in Pancreatic Cancer Cells. *Cell Death Dis* 9, 5. doi:10.1038/s41419-018-0478-0

Lemke, J., Noack, A., Adam, D., Tchikov, V., Bertsch, U., Röder, C., et al. (2010). TRAIL Signaling Is Mediated by DR4 in Pancreatic Tumor Cells Despite the Expression of Functional DR5. *J. Mol. Med.* 88, 729–740. doi:10.1007/s00109-010-0619-0

Lemke, J., von Karstedt, S., Zinngrebe, J., and Walczak, H. (2014). Getting TRAIL Back on Track for Cancer Therapy. *Cel Death Differ* 21, 1350–1364. doi:10.1038/cdd.2014.81

Luo, X., Budihardjo, I., Zou, H., Slaughter, C., and Wang, X. (1998). Bid, a Bcl2 Interacting Protein, Mediates Cytochrome C Release from Mitochondria in Response to Activation of Cell Surface Death Receptors. *Cell* 94, 481–490. doi:10.1016/S0092-8674(00)81589-5

Matsuyama, S., Llopis, J., Deveraux, Q. L., Tsien, R. Y., and Reed, J. C. (2000). Changes in Intramitochondrial and Cytosolic pH: Early Events that Modulate

Caspase Activation during Apoptosis. *Nat. Cel Biol* 2, 318–325. doi:10.1038/35014006

Matsuyama, S., and Reed, J. C. (2000). Mitochondria-dependent Apoptosis and Cellular pH Regulation. *Cel Death Differ* 7, 1155–1165. doi:10.1038/sj.cdd.4400779

Meurette, O., Rébillard, A., Huc, L., Le Moigne, G., Merino, D., Micheau, O., et al. (2007). TRAIL Induces Receptor-Interacting Protein 1-Dependent and Caspase-dependent Necrosis-like Cell Death under Acidic Extracellular Conditions. *Cancer Res.* 67, 218–226. doi:10.1158/0008-5472.CAN-06-1610

Michl, J., Park, K. C., and Swietach, P. (2019). Evidence-based Guidelines for Controlling pH in Mammalian Live-Cell Culture Systems. *Commun. Biol.* 2, 1. doi:10.1038/s42003-019-0393-7

Nahacka, Z., Svadlenka, J., Peterka, M., Ksandrova, M., Benesova, S., Neuzil, J., et al. (2018). TRAIL Induces Apoptosis but Not Necroptosis in Colorectal and Pancreatic Cancer Cells Preferentially via the TRAIL-R2/dr5 Receptor. *Biochim. Biophys. Acta (Bba) - Mol. Cel Res.* 1865, 522–531. doi:10.1016/j.bbamcr.2017.12.006

Novak, I., Haanes, K. A., and Wang, J. (2013). Acid-base Transport in Pancreas-New Challenges. *Front. Physiol.* 4, 380. doi:10.3389/fphys.2013.00380

Özören, N., and El-Deiry, W. S. (2002). Defining Characteristics of Types I and II Apoptotic Cells in Response to TRAIL. *Neoplasia*, 4, 551–557. doi:10.1038/sj.neo.7900270

Pallagi, P., Hegyi, P., and Rakonczay, Z., Jr (2015). The Physiology and Pathophysiology of Pancreatic Ductal Secretion. *Pancreas* 44, 1211–1233. doi:10.1097/MPA.0000000000000421

Pedersen, S. F., Novak, I., Alves, F., Schwab, A., and Pardo, L. A. (2017). Alternating pH Landscapes Shape Epithelial Cancer Initiation and Progression: Focus on Pancreatic Cancer. *BioEssays* 39, 1600253. doi:10.1002/bies.201600253

Rawla, P., Sunkara, T., and Gaduputi, V. (2019). Epidemiology of Pancreatic Cancer: Global Trends, Etiology and Risk Factors. *World J. Oncol.* 10, 10–27. doi:10.14740/wjon1166

Riedl, S. J., and Salvesen, G. S. (2007). The Apoptosome: Signalling Platform of Cell Death. *Nat. Rev. Mol. Cel Biol* 8, 405–413. doi:10.1038/nrm2153

Schneider, C. A., Rasband, W. S., and Eliceiri, K. W. (2012). NIH Image to ImageJ: 25 Years of Image Analysis. *Nat. Methods* 9, 671–675. doi:10.1038/nmeth.2089

Schnipper, J., Dhennin-Duthille, I., Ahidouch, A., and Ouadid-Ahidouch, H. (2020). Ion Channel Signature in Healthy Pancreas and Pancreatic Ductal Adenocarcinoma. *Front. Pharmacol.* 11, 1614. doi:10.3389/fphar.2020.568993

Sergeeva, T. F., Shirmanova, M. V., Zlobovskaya, O. A., Gavrina, A. I., Dudenkova, V. V., Lukina, M. M., et al. (2017). Relationship between Intracellular pH, Metabolic Co-factors and Caspase-3 Activation in Cancer Cells during Apoptosis. *Biochim. Biophys. Acta (Bba) - Mol. Cel Res.* 1864, 604–611. doi:10.1016/j.bbamcr.2016.12.022

Sutoo, S., Maeda, T., Suzuki, A., and Kato, Y. (2020). Adaptation to Chronic Acidic Extracellular pH Elicits a Sustained Increase in Lung Cancer Cell Invasion and Metastasis. *Clin. Exp. Metastasis* 37, 133–144. doi:10.1007/s10585-019-09990-1

Swietach, P. (2019). What Is pH Regulation, and Why Do Cancer Cells Need it? *Cancer Metastasis Rev.* 38, 5–15. doi:10.1007/s10555-018-09778-x

Tannock, I. F., and Rotin, D. (1989). Acid pH in Tumors and its Potential for Therapeutic Exploitation. *Cancer Res.* 49, 4373–4384.

Trauzold, A., Schmiedel, S., Röder, C., Tams, C., Christgen, M., Oestern, S., et al. (2003). Multiple and Synergistic Deregulations of Apoptosis-Controlling Genes in Pancreatic Carcinoma Cells. *Br. J. Cancer* 89, 1714–1721. doi:10.1038/sj.bjc.6601330

Trauzold, A., Siegmund, D., Schniewind, B., Sipos, B., Egberts, J., Zorenkov, D., et al. (2006). TRAIL Promotes Metastasis of Human Pancreatic Ductal Adenocarcinoma. *Oncogene* 25, 7434–7439. doi:10.1038/sj.onc.1209719

Trauzold, A., Wermann, H., Arlt, A., Schütze, S., Schäfer, H., Oestern, S., et al. (2001). CD95 and TRAIL Receptor-Mediated Activation of Protein Kinase C and NF-Kb Contributes to Apoptosis Resistance in Ductal Pancreatic Adenocarcinoma Cells. *Oncogene* 20, 4258–4269. doi:10.1038/sj.onc.1204559

Valiahdi, S. M., Egger, A. E., Miklos, W., Jungwirth, U., Meelich, K., Nock, P., et al. (2013). Influence of Extracellular pH on the Cytotoxicity, Cellular Accumulation, and DNA Interaction of Novel pH-Sensitive 2-Aminoalcoholatoplatinum(II) Complexes. *J. Biol. Inorg. Chem.* 18, 249–260. doi:10.1007/s00775-012-0970-4

van de Kooij, B., Verbrugge, I., de Vries, E., Gijsen, M., Montserrat, V., Maas, C., et al. (2013). Ubiquitination by the Membrane-Associated RING-CH-8 (MARCH-8) Ligase Controls Steady-State Cell Surface Expression of Tumor Necrosis Factor-Related Apoptosis Inducing Ligand (TRAIL) Receptor 1*. *J. Biol. Chem.* 288, 6617–6628. doi:10.1074/jbc.M112.448209

Vander Heiden, M. G., Cantley, L. C., and Thompson, C. B. (2009). Understanding the Warburg Effect: The Metabolic Requirements of Cell Proliferation. *Science* 324, 1029–1033. doi:10.1126/science.1160809

Vaupel, P., Schmidberger, H., and Mayer, A. (2019). The Warburg Effect: Essential Part of Metabolic Reprogramming and central Contributor to Cancer Progression. *Int. J. Radiat. Biol.* 95, 912–919. doi:10.1080/09553002.2019.1589653

von Karstedt, S., Conti, A., Nobis, M., Montinaro, A., Hartwig, T., Lemke, J., et al. (2015). Cancer Cell-Autonomous TRAIL-R Signaling Promotes KRAS-Driven Cancer Progression, Invasion, and Metastasis. *Cancer Cell* 27, 561–573. doi:10.1016/j.ccell.2015.02.014

von Karstedt, S., Montinaro, A., and Walczak, H. (2017). Exploring the TRAILs Less Travelled: TRAIL in Cancer Biology and Therapy. *Nat. Rev. Cancer* 17, 352–366. doi:10.1038/nrc.2017.28

Yang, S., Wang, X., Contino, G., Liesa, M., Sahin, E., Ying, H., et al. (2011). Pancreatic Cancers Require Autophagy for Tumor Growth. *Genes Dev.* 25, 717–729. doi:10.1101/gad.2016111

Yao, J., Czaplinska, D., Ialchina, R., Schnipper, J., Liu, B., Sandelin, A., et al. (2020). Cancer Cell Acid Adaptation Gene Expression Response Is Correlated to Tumor-specific Tissue Expression Profiles and Patient Survival. *Cancers* 12, 2183. doi:10.3390/cancers12082183

Conflict of Interest: The authors declare that the research was conducted in the absence of any commercial or financial relationships that could be construed as a potential conflict of interest.

Publisher's Note: All claims expressed in this article are solely those of the authors and do not necessarily represent those of their affiliated organizations, or those of the publisher, the editors and the reviewers. Any product that may be evaluated in this article, or claim that may be made by its manufacturer, is not guaranteed or endorsed by the publisher.

frontiers in Cell and Developmental Biology

ORIGINAL RESEARCH
published: 24 February 2022
doi: 10.3389/fcell.2022.728771

CTLA-4 Facilitates DNA Damage–Induced Apoptosis by Interacting With PP2A

*Qiongyu Yan[1], Bin Zhang[2], Xi Ling[1], Bin Zhu[1], Shenghui Mei[1], Hua Yang[1], Dongjie Zhang[1], Jiping Huo[1] and Zhigang Zhao[1]**

[1]Department of Pharmacy, Beijing Tiantan Hospital, Capital Medical University, Beijing, China, [2]Department of Neurosurgery, Beijing Tiantan Hospital, Capital Medical University, Beijing, China

Cytotoxic T-lymphocyte–associated protein 4 (CTLA-4) plays a pivotal role in regulating immune responses. It accumulates in intracellular compartments, translocates to the cell surface, and is rapidly internalized. However, the cytoplasmic function of CTLA-4 remains largely unknown. Here, we describe the role of CTLA-4 as an immunomodulator in the DNA damage response to genotoxic stress. Using isogenic models of murine T cells with either sufficient or deficient CTLA-4 expression and performing a variety of assays, including cell apoptosis, cell cycle, comet, western blotting, co-immunoprecipitation, and immunofluorescence staining analyses, we show that CTLA-4 activates ataxia–telangiectasia mutated (ATM) by binding to the ATM inhibitor protein phosphatase 2A into the cytoplasm of T cells following transient treatment with zeocin, exacerbating the DNA damage response and inducing apoptosis. These findings provide new insights into how T cells maintain their immune function under high-stress conditions, which is clinically important for patients with tumors undergoing immunotherapy combined with chemoradiotherapy.

Keywords: CTLA-4, PP2A, ATM, DNA damage response, apoptosis

OPEN ACCESS

Edited by:
Triona Ni Chonghaile, Royal College of Surgeons in Ireland, Ireland

Reviewed by:
Ella L. Kim, Johannes Gutenberg University Mainz, Germany
Raheleh Roudi, University of Minnesota, United States
Quan Cheng, Central South University, China

****Correspondence:***
Zhigang Zhao
1022zzg@sina.com

Specialty section:
This article was submitted to Cell Death and Survival, a section of the journal Frontiers in Cell and Developmental Biology

Received: *22 June 2021*
Accepted: *06 January 2022*
Published: *24 February 2022*

Citation:
Yan Q, Zhang B, Ling X, Zhu B, Mei S, Yang H, Zhang D, Huo J and Zhao Z (2022) CTLA-4 Facilitates DNA Damage–Induced Apoptosis by Interacting With PP2A. Front. Cell Dev. Biol. 10:728771. doi: 10.3389/fcell.2022.728771

INTRODUCTION

T lymphocytes (T cells) execute various functions in defense against pathogens and tumors and interact with other cells involved in immune responses. T cells have a life span of several decades and the highest proliferative potential, and T-cell DNA is damaged by diverse endogenous and environmental stress factors (Opzoomer et al., 2019). Therefore, these cells have developed a complex DNA damage response (DDR) to promote the maintenance of genome integrity (Bouwman and Jonkers, 2012). Appropriate communication between cell cycle regulation, DDR, and apoptosis is important to ensure the effectiveness of DDR (Vermeulen et al., 2003; Finn et al., 2012). Double strand breaks (DSBs) are the most harmful DNA lesions in cells. These "dirty" DSBs that remain "uncleaned" may cause gene mutations, genomic instability, and carcinogenesis (Ciccia and Elledge, 2010; Hanahan and Weinberg, 2011). Apoptosis is a major type of cell death in which unwanted cells are removed. Therefore, the identification and development of mechanisms that induce T-cell apoptosis or increase susceptibility to genomic stress are useful for maintaining the health of organisms.

Conventional cancer therapies, including radiotherapy and/or chemotherapy, not only lead to the direct killing of cancer cells but also induce immunogenic cell death. Immune cells undergo apoptosis or lose their function during cancer therapy—problems that urgently require a solution.

Immunotherapy, also known as immune checkpoint blockade, is currently one of the most exciting and promising modalities of investigation and development in the field of cancer therapy, and T cells play central roles in cancer immunotherapy (Shklovskaya and Rizos, 2021). Cytotoxic T-lymphocyte–associated protein 4 (CTLA-4) is an immunoregulatory molecule found on T cells and a negative regulator of T-cell activation (Teft et al., 2006). CTLA-4 plays a critical role in maintaining the balance of immune homeostasis, functioning as an immune checkpoint (Schlosser et al., 2016). Since 2000, immune checkpoint inhibitors such as ipilimumab and tremelimumab, CTLA-4 inhibitors that are used in a new and effective treatment strategy for immunotherapy in cancer, have been in clinical development (Chang et al., 2019). The incorporation of chemotherapy, radiotherapy, or chemoradiotherapy with immunotherapy may enhance antitumor immune responses (Chicas-Sett et al., 2018; Wang et al., 2019; Paz-Ares et al., 2021). However, no relevant studies examining the effect of conventional cancer therapies on the immunosuppressive role of CTLA-4 have been published. In one study, CTLA-4–deficient mice were born healthy but exhibited a large number of activated T cells within 5–6 days of birth and died when 18–28 days old as a result of fatal hyperactivation of the immune system and tissue destruction (Sobhani et al., 2021). Based on these results, CTLA-4 has been shown to downregulate T-cell responses and modulate peripheral self-tolerance. Because of this negative regulation, CTLA-4 has been proposed to be related to several autoimmune diseases, although the mechanisms are not fully understood (Ghaderi, 2011). CTLA-4 regulates T-cell activation through multifaceted pathways. Because CTLA-4 and CD28 show significant homology, considerable information is available on CTLA-4 competition with CD28 (Liu et al., 2021). However, very little information is available regarding the inherent plasticity of CTLA-4 signaling. A striking characteristic of CTLA-4 is the conservation of its cytoplasmic domain, implying that this segment is essential for its functions (Qureshi et al., 2012). Some studies have shown that CTLA-4 negatively regulates T-cell activation through the delivery of an inhibitory signal by its cytoplasmic tail (Greenwald et al., 2002; Teft et al., 2009; Haanen and Robert, 2015). Recent studies have shown that CTLA-4 is mainly located in the cytoplasm of resting T cells, while the CTLA-4 level in the cell membrane is higher during T-cell activation, with its membrane level changing in a very dynamic (unstable) manner (Van Coillie et al., 2020). Other reports have documented various CTLA-4 gene expression levels in different cell lines, including T lymphoid, B lymphoid, myeloid, and erythroid (K562)–derived cells; granulocytes; stem cells; and placental fibroblasts (Wang et al., 2002; Pistillo et al., 2003; Contardi et al., 2005). CTLA-4 expression is mainly detected in the cytoplasm of all these cells, except granulocytes. However, the precise function of CTLA-4 in the cytoplasm remains unclear.

Protein phosphatase 2A (PP2A) is a Ser/Thr protein phosphatase that is highly conserved from yeast to humans (Shi, 2009). PP2A consists of three subunits, including a common scaffolding subunit A, two subtypes of catalytic subunit C (α and β), and a regulatory subunit B. PP2A-B was shown to mediate the specificity and localization of PP2A. PP2A-A and PP2A-C comprise the essential enzyme core (Janssens and Goris, 2001). PP2A is a well-known phosphatase that participates in the administration of the DNA damage response (Ramos et al., 2019; Lei et al., 2020). PP2A controls the DNA damage response by regulating the level of ataxia–telangiectasia mutated (ATM) autophosphorylation/activation, which was formerly proven to facilitate DNA damage repair, regulate the cell cycle, and induce apoptosis (Goodarzi et al., 2004). The cytoplasmic CTLA-4 population is associated with PP2A and has been shown to regulate the Raf/MEK/ERK path in T cells (Chuang et al., 2000; Teft et al., 2009). However, the relationship between DDR signaling and the PP2A-CTLA-4 interaction in the cytoplasm has not yet been clarified.

In the present study, we reveal for the first time that CTLA-4 activates ATM by anchoring the ATM inhibitor PP2A in the cytoplasm of T cells following transient treatment with zeocin and, consequently, exaggerating the DNA damage response and inducing apoptosis.

MATERIALS AND METHODS

Mice

B7-1/B7-2$^{-/-}$ and B7-1/B7-2/CTLA-4$^{-/-}$ C57BL/6 mice were purchased from Suzhou Cyagen Co. (Suzhou, Jiangsu, China). About 6- to 8-week-old female mice were used in this study. Experiments on the mice were performed in accordance with approved protocols.

Cell and Transfection

B7-1/B7-2$^{-/-}$ and B7-1/B7-2/CTLA-4$^{-/-}$ T cells were isolated from the lymph nodes of the indicated mice using CD4 MicroBeads (Miltenyi Biotec, #130117043). CD4^{+} T cells were cultured in a sterile RPMI-1640 medium (Gibco, #A1049101) supplemented with 10% fetal bovine serum (Gibco, #16170078), 1% penicillin/streptomycin (Gibco, #15070063), 10 mM HEPES buffer (Gibco, #15630106), 2 mM L-glutamine, and 50 mM 2-mercaptoethanol (Gibco, #21985023).

HeLa cells were purchased from ATCC and cultured in DMEM (Gibco, #11965084) supplemented with 10% fetal bovine serum. The constructs were transiently transfected into the HeLa cells using Lipofectamine™ 2000 (Invitrogen, #11668019) according to the manufacturer's instructions. About 24 hours after transfection, the cells were treated with 500 μg/ml zeocin (XYbio, #X10014) for 1 h in an incubator, and experiments were subsequently conducted.

The cells were maintained at 37°C in a humidified atmosphere containing 5% CO_2.

Plasmid Construction

A plasmid encoding human Myc-CTLA-4 was purchased from OriGene (#NM005214). GFP-CTLA-4 constructs were prepared by excising full-length CTLA-4 from Myc-CTLA-4, and subcloning it into the EcoR I and Kpn I sites of the pEGFP-N1 vector. GFP-CTLA-4-TAIL constructs were prepared by excising the transmembrane plus cytoplasmic tail of CTLA-4

from Myc-CTLA-4 and subcloning this fragment into the EcoR I and Kpn I sites of the pEGFP-N1 vector.

Mutagenesis of Myc-CTLA-4 and GFP-CTLA-4 was performed using a QuikChange Site-Directed Mutagenesis Kit (Agilent, #210518). The sequences of the forward and reverse primers were as follows:

A602T, F: 5′-gggggcattttcacaaagacccctgttgtaagagg-3′,
R: 5′-cctcttacaacaggggtctttgtgaaaatgccccc-3′, and
A653T, F: 5′-cgcgtattgatgggaataaaaaaaggctgaaattgcttttcac-3′,
R: 5′-gtgaaaagcaatttcagccttttttttattcccatcaatacgcg-3′.

Immunofluorescence Staining

Immunofluorescence staining of HeLa cells was performed as described previously (Yan et al., 2017). Briefly, the cells were cultured on coverslips, washed with PBS, fixed with 4% paraformaldehyde for 10 min at room temperature, permeabilized with 0.2% Triton X-100 for 2 min, and blocked with 1% BSA for 1 h. The cells were then incubated with anti-Myc (Abcam, #ab32072, 1:200) and anti-PP2A-A antibodies (Santa Cruz Biotechnology, #sc-13600, 1:50) at 4°C overnight. Alexa Fluor 594-conjugated goat anti-rabbit IgG (Molecular Probes, #A31632, 1:500) and Alexa Fluor 488-conjugated goat anti-mouse IgG secondary antibodies (Molecular Probes, #A31619, 1:500) were used. The nuclei were detected using DAPI staining. The images were acquired with a laser scanning confocal microscope (Zeiss, LSM 710).

The T cells were washed with PBS and plated on coverslips coated with poly-L-lysine (Sigma, P8130). The next steps were similar to those described in the HeLa cell experiment mentioned above. The primary antibodies used for this experiment were anti-P-ATM (GeneTex, GTX132146, #sc-47739, 1:100), anti-53BP1 (Cell Signaling Technology, #4937, 1:200), and anti-γH2AX (Cell Signaling Technology, #9718, 1:200). The percentage of cells with γH2AX and 53BP1 nuclear foci was quantified using ImageJ software, and the data were plotted using GraphPad Prism software.

Immunoblotting

Western blotting was performed as previously described (Yan et al., 2017). Briefly, the cells were lysed in a cell lysis buffer for western blotting and immunoprecipitation (IP) (Beyotime, #P0013) containing protease inhibitors (Roche, #04693116001) and phosphatase inhibitors (Coolaber, #SL1087, 1:100), followed by centrifugation at 14,000 *g* for 30 min at 4°C. The supernatant was collected; the protein concentration was estimated; and equal amounts of protein from each sample were separated on SDS-PAGE and electrotransferred to polyvinylidene fluoride membranes. The membranes were blocked with 5% nonfat milk in TBS-T buffer for 1 h at room temperature and incubated with primary antibodies overnight at 4°C. The following primary antibodies were used: DNA Damage Antibody Sampler Kit (Cell Signaling Technology, #9947, 1:1,000), anti-phospho-Histone H2AX (Cell Signaling Technology, #2577, 1:1,000), anti-p53 (Cell Signaling Technology, #2524, 1:1,000), anti-phospho-p95/NBS1 (Cell Signaling Technology, #3001, 1:1,000), anti-MRE11 (Cell Signaling Technology, #4895, 1:1,000), anti-RAD50 (Santa Cruz Biotechnology, #sc-74460, 1:200), anti-NBS1 (Cell Signaling Technology, #3002, 1:1,000), anti-CTLA-4 (Santa Cruz Biotechnology, #sc-376016, 1:50), anti-GFP (Abmart, #7G9, 1:2000), and anti-actin (Sigma, #A5441, 1:1,000). On the second day, the membranes were washed and incubated with the appropriate HRP-conjugated secondary antibodies (Jackson Research, 1:5,000) for 1 h at room temperature. Protein bands were detected using chemiluminescence (ECL) reagent (Millipore, CPS350) and evaluated using densitometry. The experiment was repeated three times independently.

2.6 Co-immunoprecipitation

Co-immunoprecipitation (co-IP) was performed as previously described (Yan et al., 2017). The cells were washed once with cold PBS, lysed in lysis buffer for IP (Beyotime, #P0013) containing a protease inhibitor cocktail (Roche) at 4°C for 1 h, and then centrifuged at 12,000 *g* for 15 min at 4°C. After centrifugation, a small fraction of the supernatant was frozen for subsequent analysis (cell extract) as the input. The remaining fraction was incubated at 4°C with 1 μg of the desired antibody on a rotator overnight. Then, the mixtures were incubated with Protein A/G agarose beads (Abcam, #ab193262) with rotation at 4°C for 6 h. After the incubation, the beads were washed three times with wash buffer, boiled in loading buffer at 95°C, and then subjected to western blotting. The following specific secondary antibodies were used to avoid overlap of the bands for the target proteins with those of the immunoglobulin light chain and heavy chain: IPKine HRP Goat AntiMouse IgG HCS (Abbkine, #A25112, 1:5,000), IPKine HRP Goat AntiRabbit IgG HCS (Abbkine, #A25222, 1:5,000), IPKine HRP AffiniPure Goat AntiMouse IgG Light Chain (Abbkine, #A25012, 1:5,000), and IPKine HRP AffiniPure Mouse AntiRabbit IgG Light Chain (Abbkine, #A25022, 1:5,000).

Comet Assay

A neutral comet assay was performed as previously described (Yan et al., 2017). DNA damage was quantified with a neutral comet assay (CometAssay Kit, Trevigen, #4250–050) according to the manufacturer's instructions. Briefly, after zeocin treatment for 1 h, the B7-1/B7-2$^{-/-}$ and B7-1/B7-2/CTLA-4$^{-/-}$ cells were harvested after the indicated periods, placed in molten agarose, and then spread on the surface of comet slides. After a series of incubations, lysis, and washes at 4°C, the slides were immersed in the lysis solution for electrophoresis, stained with SYBR Green, and then examined with a Zeiss ImagerA2 microscope. The comet assay was quantitated by measuring the percentage of cells with a tail (comet +) from 500 cells using Adobe Photoshop CS6.

Isolation of Cytoplasmic and Nuclear Cell Fractions

Nuclear extracts were prepared using an NE-PER Nuclear Cytoplasmic Extraction Reagent Kit (Thermo Scientific™, #78835) according to the manufacturer's instructions. Briefly, after stimulation with zeocin, the cells were collected, washed twice with cold PBS, and harvested by centrifugation at 800 rpm

for 3 min. The cell pellets were resuspended in cytoplasmic extraction reagent I plus protease inhibitor cocktail by vortexing and allowed to swell on ice for 10 min. Then, cytoplasmic extraction reagent II was added, incubated for 1 min on ice, and the mixture was centrifuged for 5 min at 16,000 *g* at 4°C. The supernatant fraction was obtained as the cytoplasmic extract, transferred to a clean tube, and stored at −80°C. For further nuclear protein extraction, the sediment was suspended in a nuclear extraction reagent by vortexing, incubated on ice for 10 min, and then centrifuged for 10 min at 16,000 *g* at 4°C. The supernatant was obtained as the nuclear extract.

Cell Apoptosis Assay

Cell apoptosis was analyzed using an Annexin V-FITC/propidium iodide (PI) apoptosis assay kit (Beyotime, #C1062M) according to the manufacturer's instructions. Briefly, the B7-1/B7-2$^{-/-}$ and B7-1/B7-2/CTLA-4$^{-/-}$ T cells were harvested and washed twice with cold PBS. After treatment, the cells were suspended in Annexin V binding buffer containing Annexin V-FITC/PI. After incubation on ice in the dark for 30 min, the cell apoptosis rate was measured by flow cytometry.

Cell Cycle Analysis

The cell cycle assay was performed using the Cell Cycle and Apoptosis Analysis Kit (Beyotime, #C1052) according to the manufacturer's instructions. Briefly, the HeLa cells were collected and fixed with cold 70% ethanol overnight at 4°C. After centrifugation (1,200 rpm, 5 min, 4°C), the cells were washed with cold PBS. Subsequently, PI was used to stain the cells in the presence of 20 μg/ml RNase A in the dark at room temperature for 30 min. The cell cycle was measured by flow cytometry.

RESULTS

CTLA-4 Increases the Risk of T Cells Undergoing DNA Damage–Induced Apoptosis

We assessed the CTLA-4 activity in response to the genotoxic stress to explore the function of cytoplasmic CTLA-4 in the DDR. Zeocin, a member of the bleomycin family, binds to and intercalates into DNA, leading to the formation of DSBs in a manner similar to that of ionizing radiation (Peres de Oliveira et al., 2020). A previous study verified that zeocin treatment induced a significant decrease in the number of T cells in the peripheral blood (Hu et al., 2018). CTLA-4–deficient mice die at 18–28 days due to the generation of self-reactive T cells (Chambers et al., 2001). Therefore, we referred to a report in which B7-1/B7-2/CTLA-4$^{-/-}$ mice were generated, and they were found to have a normal life span and produce CTLA-4–deficient T cells (Greenwald et al., 2002). We investigated the role of CTLA-4 in the genotoxic stress response induced by zeocin treatment by comparing freshly isolated CD4^{+} T cells from B7-1/B7-2$^{-/-}$ and B7-1/B7-2/CTLA-4$^{-/-}$ mice. We evaluated the effects of the zeocin dose on cell apoptosis. B7-1/B7-2$^{-/-}$ and B7-1/B7-2/CTLA-4$^{-/-}$ cells were pretreated with increasing concentrations of zeocin (0, 100, 200, 500, and 800 μg/ml) for 1 h and then cultured in fresh media without zeocin for 24 h. In the absence of zeocin (ctl) and in the presence of low zeocin doses (100 and 200 μg/ml), the B7-1/B7-2$^{-/-}$ and B7-1/B7-2/CTLA-4$^{-/-}$ cells exhibited similar levels of apoptosis. Treatment with 500 μg/ml zeocin resulted in an obvious increase in the B7-1/B7-2$^{-/-}$ cell apoptosis rate compared with the B7-1/B7-2/CTLA-4$^{-/-}$ cell apoptosis rate. These cells showed approximately equal apoptosis rates after treatment with 800 μg/ml zeocin (**Figure 1A**). Therefore, we chose to administer a 500 μg/ml zeocin pulse treatment to detect the apoptosis rates at different times (0, 4, 8, 12, and 24 h). The results showed gradual increases in the apoptosis rates at 0 and 4 h after a 1-h transient treatment with 500 μg/ml zeocin, with the B7-1/B7-2$^{-/-}$ cells exhibiting a rate similar to that of the B7-1/B7-2/CTLA-4$^{-/-}$ cells. After zeocin treatment for 8, 12, and 24 h, the B7-1/B7-2$^{-/-}$ cells exhibited a significantly higher apoptosis rate (approximately twofold greater) than the B7-1/B7-2/CTLA-4$^{-/-}$ cells (**Figures 1B,C**). Western blotting analyses were performed to examine the levels of apoptosis markers (cleaved caspase-3 and cleaved PARP) and confirm the apoptosis rates, and the results showed marked increases in the levels of these proteins in the B7-1/B7-2$^{-/-}$ cells after zeocin treatment for 12 and 24 h (**Figure 1D**), indicating that the B7-1/B7-2$^{-/-}$ cells are hypersensitive to DSBs induced by zeocin. In other words, CTLA-4 induced massive cell apoptosis after DNA damage induction.

Zeocin Treatment Causes Overwhelming DNA Damage in CTLA-4–Expressing Cells

DNA-damaging agents are potent inducers of cell apoptosis (Roos and Kaina, 2013). We tested whether CTLA-4 induced more DNA damage after drug treatment to investigate the role of CTLA-4 in apoptosis triggered by DNA damage. γH2AX, which refers to histone H2AX phosphorylated at Ser139, is a key protein that is involved in the cellular response to DNA damage and is a sensitive biomarker of DSBs (Rothkamm et al., 2015). Specifically, γH2AX forms nuclear foci that enable visualization and quantification of a DSB site. During apoptosis, the nuclei shrink and are fragmented, and the chromatin is increasingly condensed. Our results showed that the B7-1/B7-2$^{-/-}$ and B7-1/B7-2/CTLA-4$^{-/-}$ cells exhibited a typical apoptotic appearance after zeocin treatment for 24 h. We examined the level of γH2AX in apoptotic cells using immunocytochemical staining and western blotting analyses. A significantly greater amount of γH2AX was present in the B7-1/B7-2$^{-/-}$ cells than in the B7-1/B7-2/CTLA-4−/− cells 24 h after transient zeocin treatment. Thus, H2AX is phosphorylated when cells undergo apoptosis and the B7-1/B7-2$^{-/-}$ cells undergo excessive DNA damage during apoptosis (**Figures 2A–C**). Collectively, our results indicate that CTLA-4 leads to an increased DNA damage–induced apoptosis rate after drug treatment.

We confirmed the role of CTLA-4 in DNA damage by performing a DNA damage analysis at the other treatment time points to determine CTLA-4 function in the first 24 h of treatment. After the cessation of zeocin treatment and culture in a fresh medium, we chose two time points: a massive number of

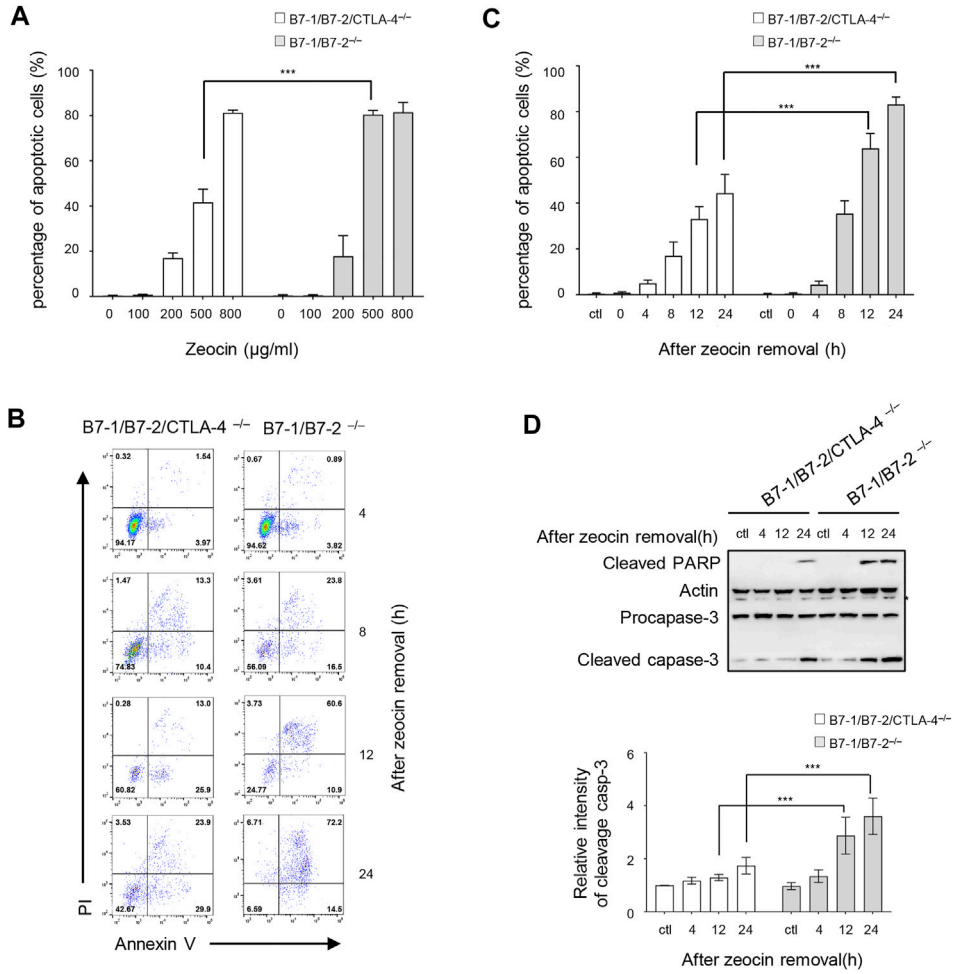

FIGURE 1 | CTLA-4 increases the risk of T cells undergoing DNA damage–induced apoptosis. **(A)** Percentage of apoptotic cells (Annexin V-positive stained cells). $CD4^+$ T cells from B7-1/B7-$2^{-/-}$ and B7-1/B7-2/CTLA-$4^{-/-}$ mice were treated with 100, 200, 500, or 800 μg/ml zeocin for 1 h and then cultured without zeocin for 24 h. The cells were collected, and apoptosis was detected. These results are representative of three experiments. All values represent the averages ±SEM of three independent experiments. ***$p < 0.001$. Ctl indicates untreated control cells. **(B)** Annexin V-PI dual-staining assay and flow cytometry analysis. $CD4^+$ T cells from B7-1/B7-$2^{-/-}$ and B7-1/B7-2/CTLA-$4^{-/-}$ mice were treated with 500 μg/ml zeocin for 1 h, cultured without treatment for the indicated times and collected to detect apoptosis. **(C)** Percentage of apoptotic cells (Annexin V-positive stained cells) of the cells shown in **(B)**. These results are representative of three experiments. All values are presented as the averages ±SEM of three independent experiments. ***$p < 0.001$. **(D)** The levels of cleaved PARP and caspase-3 in $CD4^+$ T cells from B7-1/B7-$2^{-/-}$ and B7-1/B7-2/CTLA-$4^{-/-}$ mice were detected using western blotting. The asterisk indicates a nonspecific band. The bar chart shows the fluorescence intensity of the cleaved caspase-3 band in the immunoblot.

cells incubated with zeocin for 4 h showed imminent apoptosis, and 12 h after treatment, the apoptosis rate of the B7-1/B7-$2^{-/-}$ cells was higher than that of the B7-1/B7-2/CTLA-$4^{-/-}$ cells. A comet assay was performed to detect DNA damage in individual cells. As expected, zeocin treatment contributed to DNA damage, resulting in the fragmentation of DNA that produced comet tails in the assay. In the comet assay, the percentage of cells with tails (>10% with a tail DNA signal) was the determinant of DNA damage. Untreated cells did not show DNA damage; however, following transient zeocin treatment, the B7-1/B7-$2^{-/-}$ cells displayed obvious DNA tails, and a greater number of the cells exhibited tails, indicating a large number of severe DNA breaks (**Figures 2D,E**). The γH2AX level in the cell sample with which the comet assay was performed was determined using immunoblotting (**Figures 2F,G**). Similar results were obtained, where upon zeocin pulse treatment, the B7-1/B7-$2^{-/-}$ cells showed higher levels of γH2AX than the B7-1/B7-2/CTLA-$4^{-/-}$ cells.

The 53BP1 protein rapidly accumulates at the site of DNA damage and recruits DDR proteins to DSBs. A 53BP1 foci assay was performed to detect DSBs, as previously described (Wang et al., 2016; von Morgen et al., 2018). We examined the formation of γH2AX or 53BP1 foci and counted the number of positive cells. The extent of γH2AX and 53BP1 accumulation caused by different zeocin pulse regimens was uniformly increased in the presence of CTLA-4 (**Figures 3A,B**). In addition, the immunofluorescence results were consistent with the findings of the western blotting experiments and comet assays, suggesting

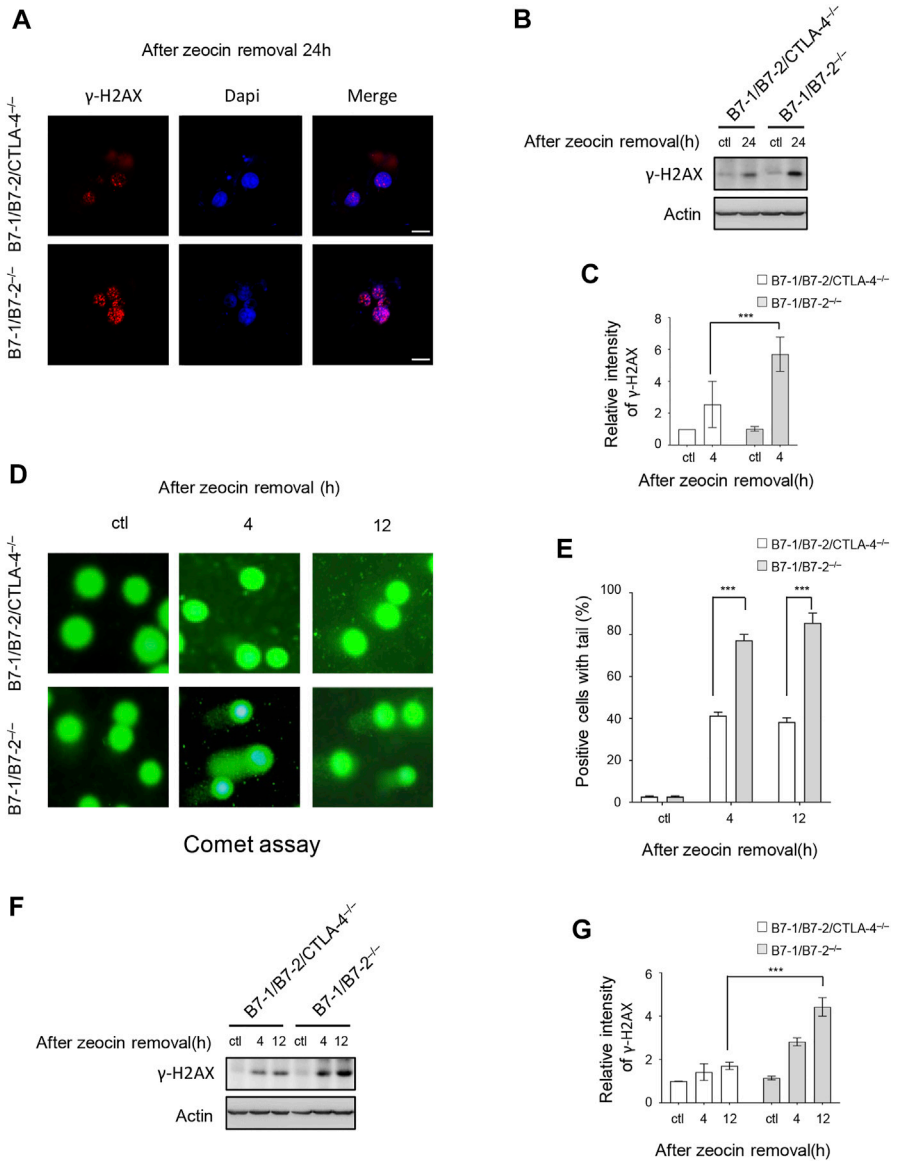

FIGURE 2 | Zeocin treatment causes overwhelming DNA damage in CTLA-4–expressing cells. CD4$^+$ T cells from B7-1/B7-2$^{-/-}$ and B7-1/B7-2/CTLA-4$^{-/-}$ mice were treated with 500 μg/ml zeocin for 1 h and then released and harvested at the indicated times. **(A)** Representative bright field and immunofluorescence images of γH2AX in treated T cells. Scale bar, 10 μm. **(B)** Cells prepared for the assay shown in panel A were analyzed for γH2AX levels using western blotting. **(C)** Quantification of the γH2AX immunoblot intensity. Each experiment was independently performed three times (n = 3). **(D)** DNA damage was assessed using the comet assay. Representative images of cellular DNA damage are presented. **(E)** Histogram showing the percentage of T cells with tail DNA greater than 10%. Experiments were performed three times independently (n = 3), and more than 100 cells per sample were counted in each experiment. Data are presented as the mean ±SEM; ***$p < 0.001$. **(F)** DNA damage was determined by measuring changes in the γH2AX levels in the cells shown in panel C using western blotting. **(G)** Quantification of the γH2AX band intensity in the corresponding groups. Each experiment was independently performed three times (n = 3).

that the B7-1/B7-2$^{-/-}$ cells incurred a greater number of severe DSBs than the B7-1/B7-2/CTLA-4$^{-/-}$ cells.

CTLA-4 Affects ATM Signaling and Arrests Cells in G2/M Phase Upon DNA Damage

We investigated whether CTLA-4 plays a role in the DDR signaling pathway to understand the mechanisms underlying the increased DNA damage in the B7-1/B7-2$^{-/-}$ cells. ATM and ATR (ATM- and Rad3-related) proteins are key regulators and sensors of the DDR that induce apoptosis (Blackford and Jackson, 2017). The ATR signaling is activated by stalled replication forks and single-strand (ss) DNA formation during DNA replication (Awasthi et al., 2016). Our time course analysis of both the B7-1/B7-2/CTLA-4$^{-/-}$ and B7-1/B7-2$^{-/-}$ cells indicated that ATR activation was not obviously affected by changes in CTLA-4 expression (**Figures 4A,B**). ATM is activated by autophosphorylation at Ser1981 in response to the cellular DSBs; therefore, phosphorylation at Ser1981 is a marker of

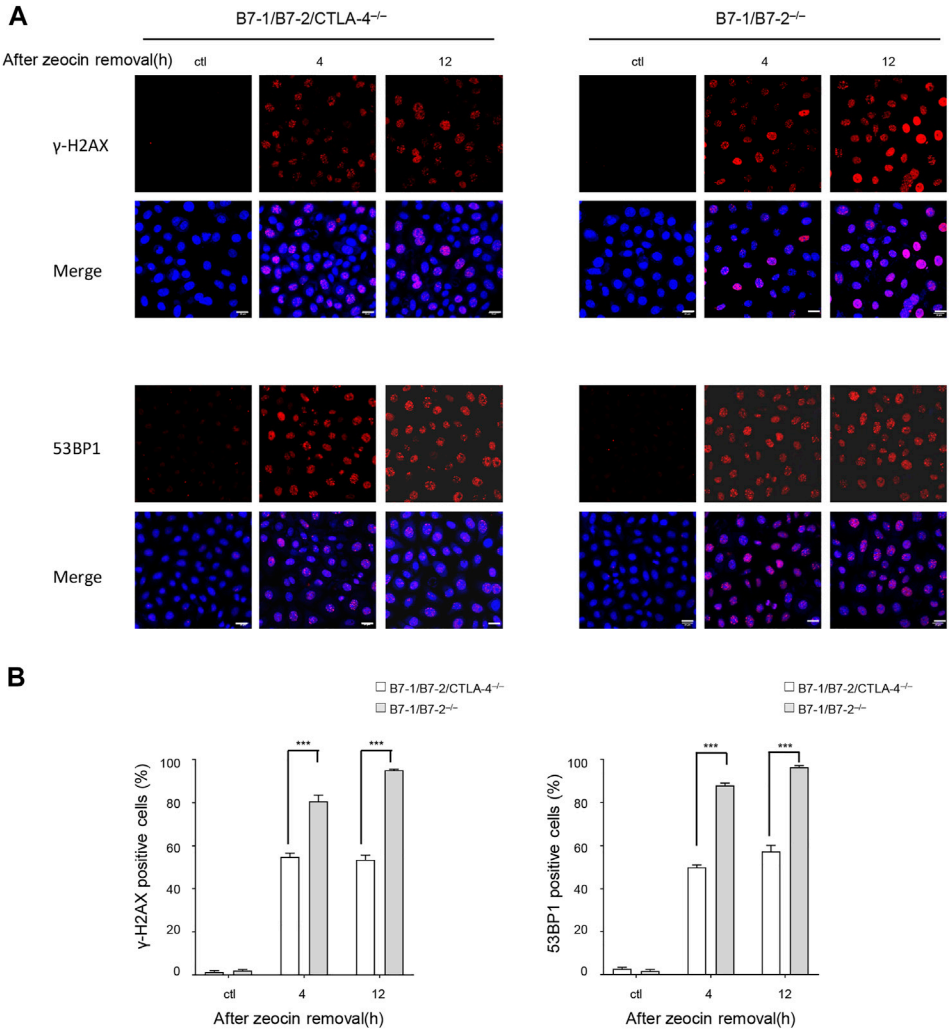

FIGURE 3 | Zeocin treatment induced more γH2AX foci and 53BP1 foci in CTLA-4–expressing cells. γH2AX and 53BP1 protein accumulation at DNA damage sites forms cytologically discernible foci. **(A)** DNA damage was measured by determining the number of γH2AX and 53BP1 foci using immunofluorescence detection. Representative images are presented. The B7-1/B7-2$^{-/-}$ and B7-1/B7-2/CTLA-4$^{-/-}$ T cells were treated without or with 500 μg/ml zeocin for 1 h followed by culture in a normal medium for the indicated times and then stained for γH2AX (red), 53BP1 (red), and nuclei (DAPI, blue). Scale bar, 20 μm. **(B)** Quantitation of the data shown in **(A)**. The histograms represent the percentage of cells with more than 10 γH2AX and 53BP1 nuclear foci. Each experiment was independently performed three times (n = 3), and more than 100 cells were counted in each experiment. The data are presented as the mean ±SEM; ***p < 0.001.

ATM activation. The DSBs are sensed by the MRE11, RAD50, and NBS1 (MRN) complex, which recruits ATM and plays a pivotal role in the activation of ATM signaling. ATM subsequently phosphorylates numerous targets, including the MRN complex and other downstream substrates, such as CHK2 (Bekker-Jensen et al., 2006; Zhang et al., 2012; Tripathi et al., 2018). We investigated whether CTLA-4 triggers the DDR pathway by activating ATM in cells after zeocin treatment. We analyzed ATM signaling during cellular responses to DNA damage using WB and found that the levels of ATM phosphorylation at Ser1981, CHK2 at Thr68, and NBS1 at Ser343 mediated by CTLA-4 were significantly higher in the B7-1/B7-2$^{-/-}$ cells than in the B7-1/B7-2/CTLA-4$^{-/-}$ cells. In addition, the activation of p53 has been previously shown to be critical for determining the cell fate after DNA is damaged (Zager and Johnson, 2019). The levels of p53 and p53 phosphorylated at Ser15 were negligibly detected and were accompanied by an increase in the expression of the target protein p21 in the B7-1/B7-2$^{-/-}$ and B7-1/B7-2/CTLA-4$^{-/-}$ cells treated with zeocin; p21 expression was more pronounced in the B7-1/B7-2$^{-/-}$ cells (**Figure 4A**). We then examined ATM activation in these cells after zeocin treatment for 8 h using immunofluorescence staining with antibody probes specific for phosphorylated ATM. Consistent with the immunoblot data, zeocin-induced phosphorylation of ATM was more significant in the nucleus of the B7-1/B7-2$^{-/-}$ cells than that of the B7-1/B7-2/CTLA-4$^{-/-}$ cells (**Figure 4C**). We concluded from these results that CTLA-4 leads to increased phosphorylation of ATM kinase in zeocin-treated cells and thus induces DDR.

The CD4^{+} T lymphocytes are difficult to maintain and remodel to some extent; therefore, we designed a feasible

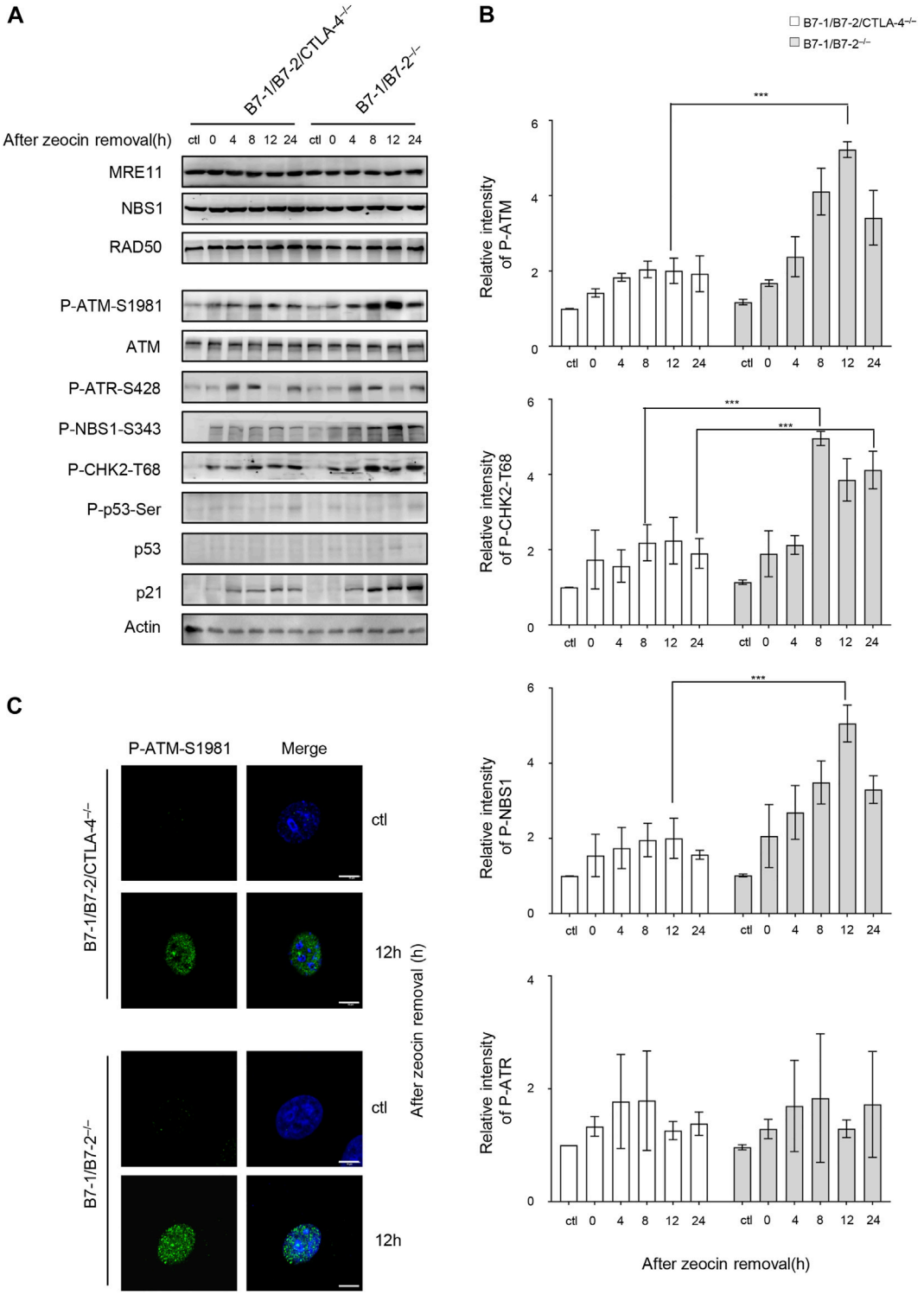

FIGURE 4 | CTLA-4 causes greater zeocin-induced activation of ATM and ATM-dependent signaling pathways. The $CD4^+$ T cells from B7-1/B7-$2^{-/-}$ and B7-1/B7-2/CTLA-$4^{-/-}$ mice were treated with 500 μg/ml zeocin for 1 h and then harvested at the indicated times. **(A)** Representative western blotting analyses are shown. The cells were lysed and analyzed at the indicated time intervals. The bar chart represents the intensity of the immunoblot bands in the corresponding group. **(B)** Quantification of P-ATM and P-CHK2-T68 immunoblots in the corresponding groups. Each experiment was independently performed three times (n = 3). **(C)** P-ATM-S1981 was detected using immunofluorescence staining. The cells were subjected to immunofluorescence staining using specific antibodies against P-ATM-S1981 (green) and nuclei (DAPI, blue). Scale bar, 10 μm.

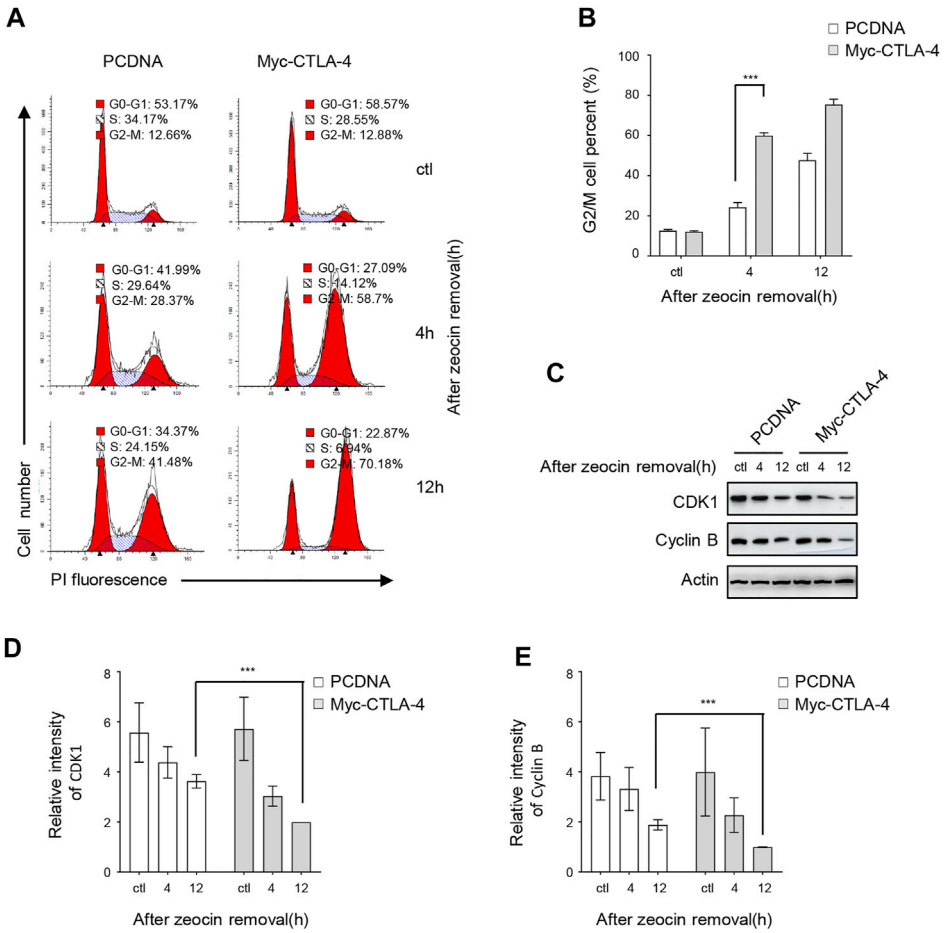

FIGURE 5 | CTLA-4 promotes zeocin-induced cell cycle arrest in the G2/M phase. HeLa cells were transfected with pcDNA and Myc-CTLA-4. After 24 h, the cells were exposed to 500 μg/ml zeocin for 1 h and harvested at the indicated times. **(A)** The cell cycle distribution was analyzed using flow cytometry. **(B)** The percentages of cells in the G2/M cycle phase are depicted. **(C)** Levels of the cell cycle regulatory proteins CDK1 and cyclin B were detected using western blotting. **(D,E)** Quantification of immunoblots of CDK1 and cyclin B levels in the corresponding groups.

model system in which CTLA-4 was expressed at various levels. Furthermore, we characterized CTLA-4 involvement in the DDR using a model of transiently transfected HeLa cells expressing Myc-CTLA-4 to construct a CTLA-4 overexpression system. The cellular responses to DNA damage usually include the induction of cell cycle arrest (Kramer et al., 2004; Smith et al., 2010). The nuclear DNA content of transiently transfected HeLa cells exposed to zeocin was detected using flow cytometry analysis to determine the regulatory effect of CTLA-4 on the cell cycle. In the untreated control group, CTLA-4 overexpression did not affect the cell cycle (**Figures 5A,B**). However, the cell cycle analysis showed that zeocin treatment increased the number of pcDNA-transfected cells and CTLA-4–transfected cells in the G2/M phase (**Figures 5A,B**), consistent with previous findings (Tounekti et al., 1993). Moreover, the number of CTLA-4 transfected in the G2/M phase was significantly increased after zeocin treatment. For confirmation, the expression of the G2/M cell cycle–regulated proteins [cyclin-dependent protein kinase 1 (CDK1) and cyclin B] was determined using WB. In cells overexpressing CTLA-4, the levels of CDK1 and cyclin B were elevated compared with those in cells expressing pcDNA (**Figures 5C–E**). Consistent with the flow cytometry results, CTLA-4 caused G2/M arrest of cells treated with zeocin.

CTLA-4 Interacts With PP2A, Promotes the Translocation of PP2A Into the Cytoplasm, and Induces ATM Activation After Zeocin Treatment

CTLA-4 mainly resides in intracellular vesicles and is rapidly transported to the cell surface only upon T-cell activation (Chikuma, 2017). Some reports have discovered that the CTLA-4 cytoplasmic domain interacts with PP2A, which involves CTLA-4 residues surrounding Y201 (Baroja et al., 2002). We tested the interaction of PP2A and CTLA-4 in the HeLa cells transfected with the wild-type CTLA-4 (WT) and mutant CTLA-4 (MT) which was mutated at tyrosine residues 201 and 218, after zeocin treatment. A co-IP assay with a Myc antibody against CTLA-4 revealed that the CTLA-4 interaction with endogenous PP2A increased after zeocin treatment

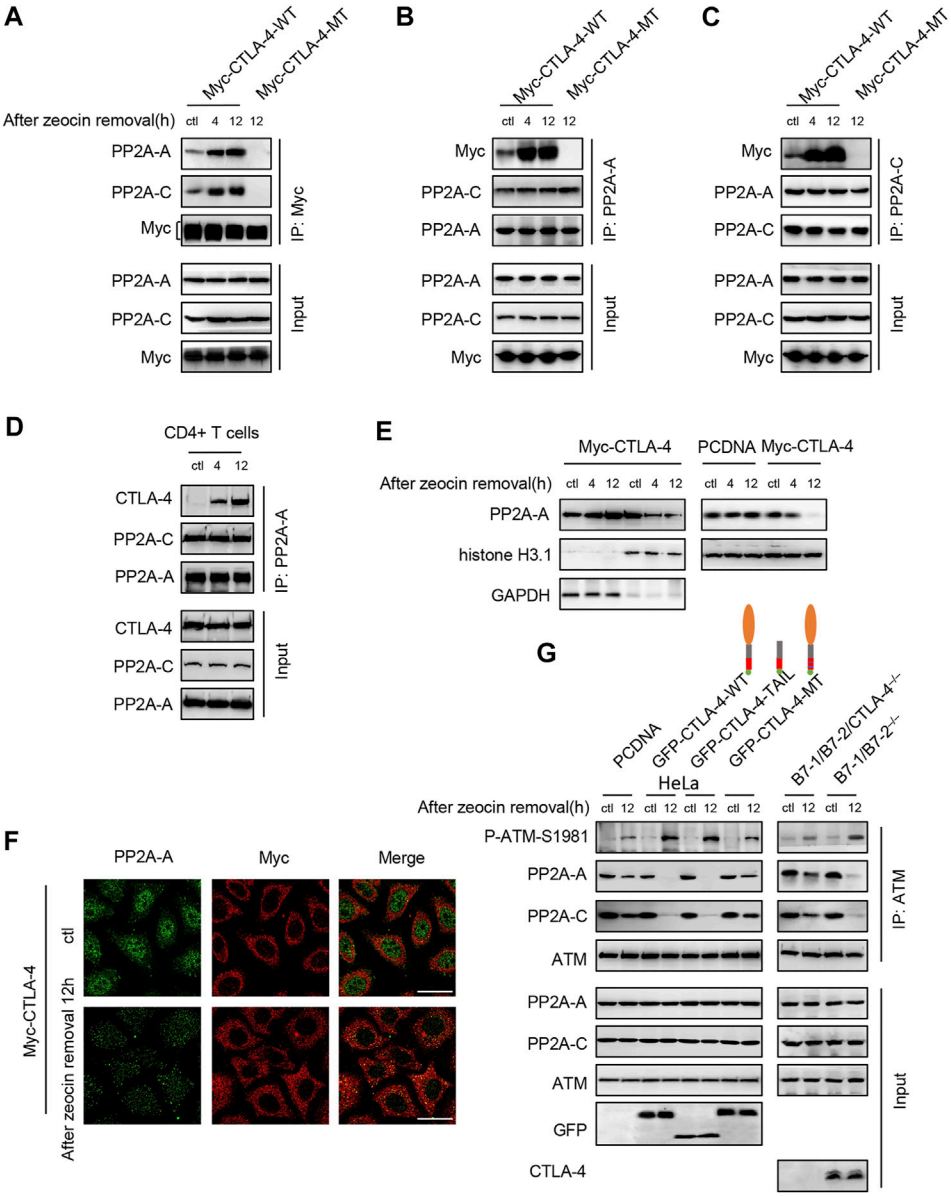

FIGURE 6 | CTLA-4 interacts with PP2A, promotes the translocation of PP2A-A into the cytoplasm, and induces autophosphorylation of ATM at Ser1981 after zeocin treatment. **(A–C)** Co-IP analysis of the interaction of CTLA-4 with PP2A. HeLa cells were transfected with Myc-CTLA-4-WT and Myc-CTLA-4-MT proteins with the Y201F and Y218F mutations. About 24 h after transfection, the cells were treated with 500 μg/ml zeocin for 1 h and harvested at the indicated times. **(D)** For endogenous co-immunoprecipitation experiments, $CD4^+$ T cells from B7-1/B7-$2^{-/-}$ mice were lysed. **(E)** Nuclear and cytoplasmic levels of PP2A-A in HeLa cells were detected using western blotting. HeLa cells were transfected with Myc-CTLA-4 (left panel), and pcDNA and Myc-CTLA-4 (right panel) for 24 h. At the indicated times after cessation of treatment, the cells were lysed and separated into nuclear and cytosolic fractions. GAPDH, a marker of the cytosolic fraction; histone H3.1, a marker of the nuclear fraction. **(F)** Double immunofluorescence staining was performed to detect the PP2A-A and CTLA-4 proteins and their colocalization in HeLa cells. HeLa cells were transfected with Myc-CTLA-4 for 24 h. The cells were treated with 500 μg/ml zeocin for 1 h, harvested at the indicated time points, and then subjected to immunofluorescence staining using specific antibodies against PP2A-A (green), CTLA-4 (red), and Scale bar, 20 μm. **(G)** ATM was immunoprecipitated and immunoblotted to detect the levels of P-ATM-S1981, total ATM, and the PP2A-A and PP2A-C subunits. Right panel: HeLa cells were transfected with pcDNA, GFP-CTLA-4-WT, a GFP-CTLA-4-TAIL (tail only) mutant, and GFP-CTLA-4-MT sequences containing Y201F and Y218F mutations. About 24 h after transfection, the cells were treated with 500 μg/ml zeocin for 1 h and harvested at the indicated time points. The CTLA-4 extracellular domain is shown as orange ovals, the transmembrane domain is indicated by gray bars, the CTLA-4 cytoplasmic tail is shown as red bars, the double-mutant Y201F/Y218 is shown with blue lines, and GFP is indicated by green circles. Left panel: $CD4^+$ T cells from B7-1/B7-$2^{-/-}$ and B7-1/B7-2/CTLA-$4^{-/-}$ mice were treated with 500 μg/ml zeocin for 1 h and then released and harvested at the indicated time points.

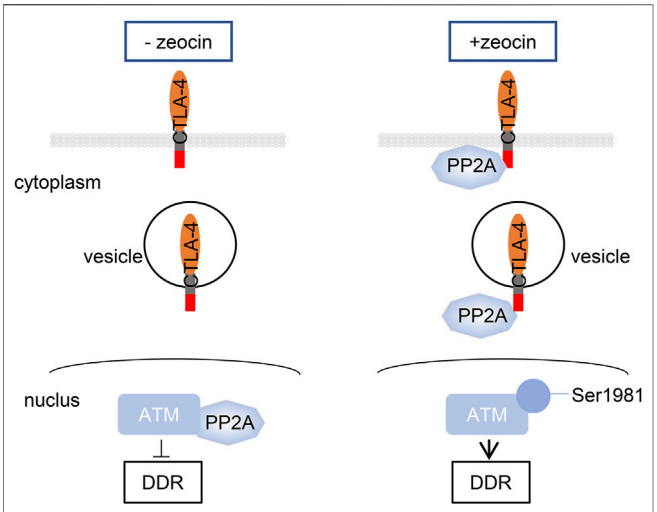

FIGURE 7 | CTLA-4 activates ATM by anchoring the ATM inhibitor PP2A in the cytoplasm following transient treatment with zeocin in T cells, exacerbating the DNA damage response and inducing apoptosis.

(**Figure 6A**). Anti-PP2A-A and anti-PP2A-C antibodies also co-precipitated CTLA-4, and the amount of co-precipitated CTLA-4 was higher after the HeLa cells were treated with zeocin (**Figures 6B,C**). These findings were confirmed in primary murine T cells (**Figure 6D**). We found that mutating the conserved tyrosine residues present in the CTLA-4 tail abrogated the PP2A-CTLA-4 interaction (**Figures 6A–C**, lane 4). Cell lysates subjected to WB with anti-PP2A and anti-Myc showed equivalent sample loading.

PP2A interacts with ATM and inhibits ATM autophosphorylation and activity in the cell nucleus (Goodarzi et al., 2004; Freeman and Monteiro, 2010). We examined whether CTLA-4 affected the subcellular expression and localization of PP2A during DNA damage–induced stress to determine the mechanism by which CTLA-4 modulates the ATM signaling pathway. Interestingly, in zeocin-treated cells, the interaction with CTLA-4 promoted PP2A translocation from the nucleus to the cytoplasm (**Figures 6E,F**). We then investigated whether PP2A translocation to the cytoplasm affected ATM activation. Our results suggested that CTLA-4 contributed to the PP2A translocation to the cytoplasm, away from ATM, and induced ATM activation in cells treated with zeocin (**Figure 6G**, lane 4). CTLA-4 resides in the endocytic vesicles, with the tail located in the cytoplasm (Lo et al., 2015). We next wanted to explore whether the CTLA-4 tail alone was sufficient for PP2A binding. We found that the CTLA-4 cytoplasmic tail was sufficient and necessary for the co-IP of PP2A and activation of ATM after the treatment with zeocin (**Figure 6G**). These findings were confirmed with $CD4^+$ T cells from B7-1/B7-$2^{-/-}$ and B7-1/B7-2/CTLA-$4^{-/-}$ mice (**Figure 6G**, left panel). Our results indicated that the cytoplasmic tail of CTLA-4 attaches PP2A to the cytoplasmic vesicles.

In this study, we found that CTLA-4 activates ATM by sequestering the ATM inhibitor PP2A in the cytoplasm following transient treatment with zeocin in T cells, exaggerating the DNA damage response and inducing apoptosis (**Figure 7**).

DISCUSSION

CTLA-4 is a well-recognized immune checkpoint that can be therapeutically targeted. The most important aspect of the current understanding of CTLA-4 function is its role as an external receptor, although CTLA-4 is predominantly located intracellularly. Three compartments containing intracellular CTLA-4 have been identified: the trans-Golgi apparatus (TGN), endosomes, and lysosomes (Valk et al., 2006). The cytoplasmic tail of CTLA-4 binds to the PI3K SH2 domains SHP-2 and PP2A, leading to posttranslational modifications of downstream targets and activation of the corresponding intracellular signaling pathways (Chuang et al., 2000; Chikuma et al., 2003; Rudd et al., 2009; Iiyama et al., 2021). Recent studies have focused on the regulation of CTLA-4 subcellular localization and the capacity of CTLA-4 to reduce T-cell activation. CTLA-4 resides on tumor cells at various densities and triggers apoptosis associated with the sequential activation of caspase-8 and caspase-3 (Contardi et al., 2005). CTLA-4 arrests cell cycle progression and then inhibits T-cell proliferation by suppressing IL-2 production (Yakoub and Schulke, 2019). CTLA-4 may also induce Fas cell surface death receptor–independent apoptosis of activated T cells (Sun et al., 2008). Previously, CTLA-4 was suggested to exert these regulatory functions in a ligand interaction-dependent manner (Contardi et al., 2005). In our study, we found that CTLA-4 interacts with PP2A to activate DNA damage–induced apoptosis.

In our system, a large number of γH2AX foci were detected in cells treated with 500 μg/ml zeocin for 24 h by using confocal microscopy (**Figure 2A**). These data support the results reported by Mukherjee et al. (2006), who indicated that H2AX is phosphorylated during DNA fragmentation and is related to apoptosis. In addition, the increase in the γH2AX foci depends on ATM kinase phosphorylation and activation (Banath et al., 2004). Therefore, we examined the activation of the ATM signaling pathway. In the cells treated with zeocin, the phosphorylation of ATM, CHK2, and NBS1 showed a clear increasing trend (**Figures 4A,B**). This finding is consistent with those of previous studies showing that ATM plays a pivotal role in sensing DNA damage in cells pretreated with DSB-inducing agents and undergoes autophosphorylation at residue S1981, resulting in an increase in the active ATM kinase levels and activation of downstream signal transduction. The MRN complex is the initial sensor of DNA DSB damage. The levels of the MRN complex did not increase with zeocin treatment, consistent with the results reported by Zhou et al. (2017).

Generally, in the presence of a low amount of DNA damage, p53 initiates DNA damage repair, and it is continuously activated by high levels of DNA damage, which promotes apoptosis to remove irreparably damaged cells (Zhang et al., 2011; Roos et al., 2016). Consistent with the broad and sometimes contradictory functions of p53 reported in recent years, the mechanisms by which p53 is activated and stabilized and the downstream events of this activation, which exhibit cell type–specific patterns, remain unclear. Our data (**Figure 4A**) are consistent with previous

findings indicating that the total protein and phosphorylation levels of p53 were negligible in resting $CD4^+$ T cells after the treatment with zeocin, as indicated by WB (Hu et al., 2018). However, the expression of the p53 downstream target gene p21 was significantly increased in the B7-1/B7-$2^{-/-}$ cells after zeocin treatment, which may have been due to other ATM activators inducing the expression of p21 (Ju and Muller, 2003; Ocker and Schneider-Stock, 2007). This finding is consistent with the observation that ATM functions through p53-independent signaling pathways to activate p53 downstream targets during cell growth and survival (Uhlemeyer et al., 2020).

Because DNA damage–mediated cell cycle checkpoint progression is essential for DDR and ATM function, which are primarily activated by DSB signaling that triggers cell cycle checkpoint activation, we examined the effect of CTLA-4 on cell cycle progression. The CDK1/cyclin B complex plays an important role in regulating the G2/M phase and facilitates the G2/M cell cycle transition (McGrath et al., 2005). The level of the CDK1/cyclin B complex has been shown to be reduced during cell cycle arrest in the G2/M phase (Gavet and Pines, 2010). In the present study, the cell cycle distribution was analyzed using flow cytometry and quantification of the DNA content (**Figure 5A**), and CTLA-4 was attributed to a G2/M phase delay in the cell cycle; this finding was supported by WB showing a decrease in cyclin B and CDK1 levels in CTLA-4–overexpressing cells after zeocin treatment (**Figures 5C–E**). The results of these two experiments are summarized as follows: following genomic stress induced by zeocin treatment, CTLA-4–expressing cells showed a profound delay in the G2/M phase transition. The cells were arrested in the G2/M phase upon activation of the ATM/CHK2/Cdc25 pathway through a mechanism independent of p53 (Tsou et al., 2006; Chang et al., 2016). This outcome may be at least partially explained by ATM activation and CTLA-4–induced arrest of cells in the G2/M phase following DNA damage.

CTLA-4 interaction with PP2A has been reported to be critical for the regulatory activity of T cells mediated by the PI3K-PKB-AKT pathway (Baroja et al., 2002; Resjo et al., 2002). In our study, CTLA-4 interacted with PP2A under resting conditions in normal cells (**Figures 6A–D**, line 1), consistent with the study by Baroja et al. (2002). According to the study by Goodarzi et al. (2004), the binding of PP2A to ATM in the cell nucleus tends to suppress ATM activation. Under normal circumstances without DNA damage, ATM constitutively interacts with PP2A. In response to DNA damage, which releases the inhibition by PP2A, ATM activation is increased (Volonte et al., 2009). This supposition appears to be consistent with our results (**Figure 6G**). Interestingly, in our system, a majority of PP2A colocalized with CTLA-4 in the cytoplasm, not near ATM (**Figure 6F**), after critical DNA-damaging stress induction. This colocalization excessively activated ATM autophosphorylation from a basal state, exaggerated the response to DNA damage, and induced cellular apoptosis. Furthermore, the tail of CTLA-4 was sufficient for PP2A binding and activation of ATM. This result is consistent with previous studies by Chuang et al. (2000). Our data suggested that CTLA-4 triggers a signaling network that culminates in an increase in ATM function in response to DNA damage. These observations present a new and promising approach to understanding cancer and developing new molecular therapeutics. Further *in vivo* evaluation is needed to validate the function of CTLA-4.

PP2A is associated with the cytoplasmic domains of CD28 (Chuang et al., 2000). However, this association invoked a DNA damage response in cells treated with zeocin (data not shown). By analyzing the structure of the cytoplasmic domains with coiled-coil proteins or by altering the phosphorylation state of tyrosine residues, a research group (Chuang et al., 2000) observed the difference between the mechanisms of CTLA-4 and PP2A interaction or the difference in affinity of CTLA-4 for PP2A and CD28, ultimately showing that CD28 interacts with PP2A. Thus, a different binding mechanism may account for the inability of CD28 to interact with PP2A in response to DNA damage.

Our model is supported by the findings of Lingel et al. (2017), to some extent. Other groups identified some downstream effectors of CTLA-4, including Ku70, BRCA1, SSRP1, and WRNIP1, as well as the associated signaling pathways in T cells, showing that these molecules play fundamental roles in the DDR (Kumari et al., 2009; Saha and Davis, 2016; Yoshimura et al., 2017; Yue et al., 2020). Therefore, these effectors should be studied to determine the numerous molecular mechanisms of the CTLA-4–mediated DDR. Furthermore, CTLA-4 is involved in regulating cell cycle progression and cell proliferation (Greenwald et al., 2002). However, further studies are required to investigate the mechanism by which CTLA-4 senses DNA damage.

What is the clinical significance of CTLA-4–mediated apoptosis induced by DNA damage in T cells? Previous studies have shown that chemotherapy or radiotherapy elicits antitumor effects through the immune system, which might lead to increased immunotherapy activity and better outcomes. Immunotherapy combined with chemoradiotherapy may result in an enhanced curative effect on cancer (Goyal et al., 2015; Chicas-Sett et al., 2018; Paz-Ares et al., 2021). Our study suggested that T cells may maintain their immune capacity under high-stress conditions by inhibiting CTLA-4–mediated apoptosis, which helps us to understand that CTLA-4 inhibitors such as ipilimumab function not only as terminators of CTLA-4 immune checkpoint signaling but also as coordinators for maintaining the immune capacity of T cells, which is clinically important for patients with tumors who are receiving immunotherapy combined with conventional cancer therapies.

Of course, our study has some limitations. Most CTLA-4 molecules reside in the cytoplasmic vesicles, and only a fraction transiently resides on the T-cell surface. Consistent with our conclusion, PP2A is adsorbed onto the vesicle surface by CTLA-4. Colocalization of the recycling

endosome marker Rab11, TGN marker STX6, and the PP2A protein in T cells with DNA damage should be examined using immunofluorescence analyses to test this hypothesis. Moreover, the extracellular segment of CTLA-4 binds to B7 ligands with high affinity. We did not determine whether this binding alters the interaction of the CTLA-4 cytoplasmic tail with PP2A in cells with DNA damage in our study. Eventually, the findings of this study must be validated *in vivo*.

In the present study, we determined that CTLA-4 plays an essential role in apoptosis induced by DNA damage. This finding will help to partially explain the reasons why immunotherapy-based strategies combined with chemotherapy and/or radiotherapy exhibit greater therapeutic efficacy.

DATA AVAILABILITY STATEMENT

The original contributions presented in the study are included in the article/Supplementary Material, further inquiries can be directed to the corresponding author.

ETHICS STATEMENT

Ethical review and approval was not required for the animal study because mice (6- to 8-weeks-old) were used for T-cell isolation.

AUTHOR CONTRIBUTIONS

QY conceived and designed the experiments. QY, DZ, XL, and JH performed WB. QY, BZa, SM, HY, and BZu analyzed the data. QY and ZZ wrote and revised the manuscript. All authors read and approved the final manuscript.

ACKNOWLEDGMENTS

We thank all the members of ZZ's laboratory for participating in insightful scientific discussions. We thank the statistical services at the Beijing Neurosurgical Institute. We appreciate Lin Guo for his assistance with data analysis. We thank Baiyun Liu and his colleagues for sharing laboratory facilities. This work was supported by the Beijing Postdoctoral Research Foundation.

REFERENCES

Awasthi, P., Foiani, M., and Kumar, A. (2016). ATM and ATR Signaling at a Glance. *J. Cel Sci* 129 (6), 1285. doi:10.1242/jcs.188631

Banáth, J. P., Macphail, S. H., and Olive, P. L. (2004). Radiation Sensitivity, H2AX Phosphorylation, and Kinetics of Repair of DNA Strand Breaks in Irradiated Cervical Cancer Cell Lines. *Cancer Res.* 64 (19), 7144–7149. doi:10.1158/0008-5472.CAN-04-1433

Baroja, M. L., Vijayakrishnan, L., Bettelli, E., Darlington, P. J., Chau, T. A., Ling, V., et al. (2002). Inhibition of CTLA-4 Function by the Regulatory Subunit of Serine/threonine Phosphatase 2A. *J. Immunol.* 168 (10), 5070–5078. doi:10.4049/jimmunol.168.10.5070

Bekker-Jensen, S., Lukas, C., Kitagawa, R., Melander, F., Kastan, M. B., Bartek, J., et al. (2006). Spatial Organization of the Mammalian Genome Surveillance Machinery in Response to DNA Strand Breaks. *J. Cel Biol* 173 (2), 195–206. doi:10.1083/jcb.200510130

Blackford, A. N., and Jackson, S. P. (2017). ATM, ATR, and DNA-PK: The Trinity at the Heart of the DNA Damage Response. *Mol. Cel* 66 (6), 801–817. doi:10.1016/j.molcel.2017.05.015

Bouwman, P., and Jonkers, J. (2012). The Effects of Deregulated DNA Damage Signalling on Cancer Chemotherapy Response and Resistance. *Nat. Rev. Cancer* 12 (9), 587–598. doi:10.1038/nrc3342

Chambers, C. A., Kuhns, M. S., Egen, J. G., and Allison, J. P. (2001). CTLA-4-mediated Inhibition in Regulation of T Cell Responses: Mechanisms and Manipulation in Tumor Immunotherapy. *Annu. Rev. Immunol.* 19, 565–594. doi:10.1146/annurev.immunol.19.1.565

Chang, M.-C., Chen, Y.-J., Liou, E. J.-W., Tseng, W.-Y., Chan, C.-P., Lin, H.-J., et al. (2016). 7-Ketocholesterol Induces ATM/ATR, Chk1/Chk2, PI3K/Akt Signalings, Cytotoxicity and IL-8 Production in Endothelial Cells. *Oncotarget* 7 (46), 74473–74483. doi:10.18632/oncotarget.12578

Chang, X., Lu, X., Guo, J., and Teng, G.-J. (2019). Interventional Therapy Combined with Immune Checkpoint Inhibitors: Emerging Opportunities for Cancer Treatment in the Era of Immunotherapy. *Cancer Treat. Rev.* 74, 49–60. doi:10.1016/j.ctrv.2018.08.006

Chicas-Sett, R., Morales-Orue, I., Rodriguez-Abreu, D., and Lara-Jimenez, P. (2018). Combining Radiotherapy and Ipilimumab Induces Clinically Relevant Radiation-Induced Abscopal Effects in Metastatic Melanoma Patients: A Systematic Review. *Clin. Translational Radiat. Oncol.* 9, 5–11. doi:10.1016/j.ctro.2017.12.004

Chikuma, S. (2017). CTLA-4, an Essential Immune-Checkpoint for T-Cell Activation. *Curr. Top. Microbiol. Immunol.* 410, 99–126. doi:10.1007/82_2017_61

Chikuma, S., Imboden, J. B., and Bluestone, J. A. (2003). Negative Regulation of T Cell Receptor-Lipid Raft Interaction by Cytotoxic T Lymphocyte-Associated Antigen 4. *J. Exp. Med.* 197 (1), 129–135. doi:10.1084/jem.20021646

Chuang, E., Fisher, T. S., Morgan, R. W., Robbins, M. D., Duerr, J. M., Vander Heiden, M. G., et al. (2000). The CD28 and CTLA-4 Receptors Associate with the Serine/threonine Phosphatase PP2A. *Immunity* 13 (3), 313–322. doi:10.1016/s1074-7613(00)00031-5

Ciccia, A., and Elledge, S. J. (2010). The DNA Damage Response: Making it Safe to Play with Knives. *Mol. Cel* 40 (2), 179–204. doi:10.1016/j.molcel.2010.09.019

Contardi, E., Palmisano, G. L., Tazzari, P. L., Martelli, A. M., Falà, F., Fabbi, M., et al. (2005). CTLA-4 Is Constitutively Expressed on Tumor Cells and Can Trigger Apoptosis upon Ligand Interaction. *Int. J. Cancer* 117 (4), 538–550. doi:10.1002/ijc.21155

Finn, K., Lowndes, N. F., and Grenon, M. (2012). Eukaryotic DNA Damage Checkpoint Activation in Response to Double-Strand Breaks. *Cell. Mol. Life Sci.* 69 (9), 1447–1473. doi:10.1007/s00018-011-0875-3

Freeman, A. K., and Monteiro, A. N. (2010). Phosphatases in the Cellular Response to DNA Damage. *Cell Commun. Signaling* 8, 27. doi:10.1186/1478-811X-8-27

Gavet, O., and Pines, J. (2010). Progressive Activation of CyclinB1-Cdk1 Coordinates Entry to Mitosis. *Dev. Cel* 18 (4), 533–543. doi:10.1016/j.devcel.2010.02.013

Ghaderi, A. (2011). CTLA4 Gene Variants in Autoimmunity and Cancer: a Comparative Review. *Iran J. Immunol.* 8 (3), 127–149.

Goodarzi, A. A., Jonnalagadda, J. C., Douglas, P., Young, D., Ye, R., Moorhead, G. B. G., et al. (2004). Autophosphorylation of Ataxia-Telangiectasia Mutated Is Regulated by Protein Phosphatase 2A. *EMBO J.* 23 (22), 4451–4461. doi:10.1038/sj.emboj.7600455

Goyal, S., Silk, A. W., Tian, S., Mehnert, J., Danish, S., Ranjan, S., et al. (2015). Clinical Management of Multiple Melanoma Brain Metastases: A Systematic Review. *JAMA Oncol.* 1 (5), 668–676. doi:10.1001/jamaoncol.2015.1206

Greenwald, R. J., Oosterwegel, M. A., van der Woude, D., Kubal, A., Mandelbrot, D. A., Boussiotis, V. A., et al. (2002). CTLA-4 Regulates Cell Cycle Progression during a Primary Immune Response. *Eur. J. Immunol.* 32 (2), 366–373. doi:10.1002/1521-4141(200202)32:2<366:aid-immu366>3.0.co;2-5

Haanen, J. B. A. G., and Robert, C. (2015). Immune Checkpoint Inhibitors. *Prog. Tumor Res.* 42, 55–66. doi:10.1159/000437178

Hanahan, D., and Weinberg, R. A. (2011). Hallmarks of Cancer: the Next Generation. *Cell* 144 (5), 646–674. doi:10.1016/j.cell.2011.02.013

Hu, Q., Xie, Y., Ge, Y., Nie, X., Tao, J., and Zhao, Y. (2018). Resting T Cells Are Hypersensitive to DNA Damage Due to Defective DNA Repair Pathway. *Cell Death Dis* 9 (6), 662. doi:10.1038/s41419-018-0649-z

Iiyama, M., Numoto, N., Ogawa, S., Kuroda, M., Morii, H., Abe, R., et al. (2021). Molecular Interactions of the CTLA-4 Cytoplasmic Region with the Phosphoinositide 3-kinase SH2 Domains. *Mol. Immunol.* 131, 51–59. doi:10.1016/j.molimm.2020.12.002

Janssens, V., and Goris, J. (2001). Protein Phosphatase 2A: a Highly Regulated Family of Serine/threonine Phosphatases Implicated in Cell Growth and Signalling. *Biochem. J.* 353 (Pt 3), 417–439. doi:10.1042/0264-6021:3530417

Ju, R., and Muller, M. T. (2003). Histone Deacetylase Inhibitors Activate p21(WAF1) Expression via ATM. *Cancer Res.* 63 (11), 2891–2897.

Krämer, A., Lukas, J., and Bartek, J. (2004). Checking Out the Centrosome. *Cell Cycle* 3 (11), 1390–1393. doi:10.4161/cc.3.11.1252

Kumari, A., Mazina, O. M., Shinde, U., Mazin, A. V., and Lu, H. (2009). A Role for SSRP1 in Recombination-Mediated DNA Damage Response. *J. Cel. Biochem.* 108 (2), 508–518. doi:10.1002/jcb.22280

Lei, X., Ma, N., Du, L., Liang, Y., Zhang, P., Han, Y., et al. (2020). PP2A and Tumor Radiotherapy. *Hereditas* 157 (1), 36. doi:10.1186/s41065-020-00149-7

Lingel, H., Wissing, J., Arra, A., Schanze, D., Lienenklaus, S., Klawonn, F., et al. (2017). CTLA-4-mediated Posttranslational Modifications Direct Cytotoxic T-Lymphocyte Differentiation. *Cell Death Differ* 24 (10), 1739–1749. doi:10.1038/cdd.2017.102

Liu, W., Yang, Z., Chen, Y., Yang, H., Wan, X., Zhou, X., et al. (2021). The Association between CTLA-4, CD80/86, and CD28 Gene Polymorphisms and Rheumatoid Arthritis: An Original Study and Meta-Analysis. *Front. Med.* 8, 598076. doi:10.3389/fmed.2021.598076

Lo, B., Zhang, K., Lu, W., Zheng, L., Zhang, Q., Kanellopoulou, C., et al. (2015). Patients with LRBA Deficiency Show CTLA4 Loss and Immune Dysregulation Responsive to Abatacept Therapy. *Science* 349 (6246), 436–440. doi:10.1126/science.aaa1663

McGrath, C. F., Pattabiraman, N., Kellogg, G. E., Lemcke, T., Kunick, C., Sausville, E. A., et al. (2005). Homology Model of the CDK1/cyclin B Complex. *J. Biomol. Struct. Dyn.* 22 (5), 493–502. doi:10.1080/07391102.2005.10531227

Mukherjee, B., Kessinger, C., Kobayashi, J., Chen, B. P. C., Chen, D. J., Chatterjee, A., et al. (2006). DNA-PK Phosphorylates Histone H2AX during Apoptotic DNA Fragmentation in Mammalian Cells. *DNA Repair* 5 (5), 575–590. doi:10.1016/j.dnarep.2006.01.011

Ocker, M., and Schneider-Stock, R. (2007). Histone Deacetylase Inhibitors: Signalling towards P21cip1/waf1. *Int. J. Biochem. Cel Biol.* 39 (7-8), 1367–1374. doi:10.1016/j.biocel.2007.03.001

Opzoomer, J. W., Sosnowska, D., Anstee, J. E., Spicer, J. F., and Arnold, J. N. (2019). Cytotoxic Chemotherapy as an Immune Stimulus: A Molecular Perspective on Turning up the Immunological Heat on Cancer. *Front. Immunol.* 10, 1654. doi:10.3389/fimmu.2019.01654

Paz-Ares, L., Ciuleanu, T.-E., Cobo, M., Schenker, M., Zurawski, B., Menezes, J., et al. (2021). First-line Nivolumab Plus Ipilimumab Combined with Two Cycles of Chemotherapy in Patients with Non-small-cell Lung Cancer (CheckMate 9LA): an International, Randomised, Open-Label, Phase 3 Trial. *Lancet Oncol.* 22 (2), 198–211. doi:10.1016/S1470-2045(20)30641-0

Peres de Oliveira, A., Basei, F. L., Slepicka, P. F., de Castro Ferezin, C., Melo-Hanchuk, T. D., de Souza, E. E., et al. (2020). NEK10 Interactome and Depletion Reveal New Roles in Mitochondria. *Proteome Sci.* 18, 4. doi:10.1186/s12953-020-00160-w

Pistillo, M. P., Tazzari, P. L., Palmisano, G. L., Pierri, I., Bolognesi, A., Ferlito, F., et al. (2003). CTLA-4 Is Not Restricted to the Lymphoid Cell Lineage and Can Function as a Target Molecule for Apoptosis Induction of Leukemic Cells. *Blood* 101 (1), 202–209. doi:10.1182/blood-2002-06-1668

Qureshi, O. S., Kaur, S., Hou, T. Z., Jeffery, L. E., Poulter, N. S., Briggs, Z., et al. (2012). Constitutive Clathrin-Mediated Endocytosis of CTLA-4 Persists during T Cell Activation. *J. Biol. Chem.* 287 (12), 9429–9440. doi:10.1074/jbc.M111.304329

Ramos, F., Villoria, M. T., Alonso-Rodríguez, E., and Clemente-Blanco, A. (2019). Role of Protein Phosphatases PP1, PP2A, PP4 and Cdc14 in the DNA Damage Response. *Cst* 3 (3), 70–85. doi:10.15698/cst2019.03.178

Resjö, S., Göransson, O., Härndahl, L., Zolnierowicz, S., Manganiello, V., and Degerman, E. (2002). Protein Phosphatase 2A Is the Main Phosphatase Involved in the Regulation of Protein Kinase B in Rat Adipocytes. *Cell Signal.* 14 (3), 231–238. doi:10.1016/s0898-6568(01)00238-8

Roos, W. P., and Kaina, B. (2013). DNA Damage-Induced Cell Death: from Specific DNA Lesions to the DNA Damage Response and Apoptosis. *Cancer Lett.* 332 (2), 237–248. doi:10.1016/j.canlet.2012.01.007

Roos, W. P., Thomas, A. D., and Kaina, B. (2016). DNA Damage and the Balance between Survival and Death in Cancer Biology. *Nat. Rev. Cancer* 16 (1), 20–33. doi:10.1038/nrc.2015.2

Rothkamm, K., Barnard, S., Moquet, J., Ellender, M., Rana, Z., and Burdak-Rothkamm, S. (2015). DNA Damage Foci: Meaning and Significance. *Environ. Mol. Mutagen.* 56 (6), 491–504. doi:10.1002/em.21944

Rudd, C. E., Taylor, A., and Schneider, H. (2009). CD28 and CTLA-4 Coreceptor Expression and Signal Transduction. *Immunol. Rev.* 229 (1), 12–26. doi:10.1111/j.1600-065X.2009.00770.x

Saha, J., and Davis, A. J. (2016). Unsolved Mystery: the Role of BRCA1 in DNA End-Joining. *J. Radiat. Res.* 57 (Suppl. 1), i18–i24. doi:10.1093/jrr/rrw032

Schlößer, H. A., Drebber, U., Kloth, M., Thelen, M., Rothschild, S. I., Haase, S., et al. (2016). Immune Checkpoints Programmed Death 1 Ligand 1 and Cytotoxic T Lymphocyte Associated Molecule 4 in Gastric Adenocarcinoma. *Oncoimmunology* 5 (5), e1100789. doi:10.1080/2162402X.2015.1100789

Shi, Y. (2009). Serine/threonine Phosphatases: Mechanism through Structure. *Cell* 139 (3), 468–484. doi:10.1016/j.cell.2009.10.006

Shklovskaya, E., and Rizos, H. (2021). MHC Class I Deficiency in Solid Tumors and Therapeutic Strategies to Overcome it. *Ijms* 22 (13), 6741. doi:10.3390/ijms22136741

Smith, J., Mun Tho, L., Xu, N., and A. Gillespie, D. (2010). The ATM-Chk2 and ATR-Chk1 Pathways in DNA Damage Signaling and Cancer. *Adv. Cancer Res.* 108, 73–112. doi:10.1016/B978-0-12-380888-2.00003-0

Sobhani, N., Tardiel-Cyril, D. R., Davtyan, A., Generali, D., Roudi, R., and Li, Y. (2021). CTLA-4 in Regulatory T Cells for Cancer Immunotherapy. *Cancers* 13 (6), 1440. doi:10.3390/cancers13061440

Sun, T., Zhou, Y., Yang, M., Hu, Z., Tan, W., Han, X., et al. (2008). Functional Genetic Variations in Cytotoxic T-Lymphocyte Antigen 4 and Susceptibility to Multiple Types of Cancer. *Cancer Res.* 68 (17), 7025–7034. doi:10.1158/0008-5472.CAN-08-0806

Teft, W. A., Chau, T. A., and Madrenas, J. (2009). Structure-Function Analysis of the CTLA-4 Interaction with PP2A. *BMC Immunol.* 10, 23. doi:10.1186/1471-2172-10-23

Teft, W. A., Kirchhof, M. G., and Madrenas, J. (2006). A Molecular Perspective of CTLA-4 Function. *Annu. Rev. Immunol.* 24, 65–97. doi:10.1146/annurev.immunol.24.021605.090535

Tounekti, O., Pron, G., Belehradek, J., Jr., and Mir, L. M. (1993). Bleomycin, an Apoptosis-Mimetic Drug that Induces Two Types of Cell Death Depending on the Number of Molecules Internalized. *Cancer Res.* 53 (22), 5462–5469.

Tripathi, V., Agarwal, H., Priya, S., Batra, H., Modi, P., Pandey, M., et al. (2018). MRN Complex-dependent Recruitment of Ubiquitylated BLM Helicase to DSBs Negatively Regulates DNA Repair Pathways. *Nat. Commun.* 9 (1), 1016. doi:10.1038/s41467-018-03393-8

Tsou, T.-C., Tsai, F.-Y., Yeh, S.-C., and Chang, L. W. (2006). ATM/ATR-related Checkpoint Signals Mediate Arsenite-Induced G2/M Arrest in Primary Aortic Endothelial Cells. *Arch. Toxicol.* 80 (12), 804–810. doi:10.1007/s00204-006-0110-4

Uhlemeyer, C., Müller, N., Griess, K., Wessel, C., Schlegel, C., Kuboth, J., et al. (2020). ATM and P53 Differentially Regulate Pancreatic Beta Cell Survival in Ins1E Cells. *PLoS One* 15 (8), e0237669. doi:10.1371/journal.pone.0237669

Valk, E., Leung, R., Kang, H., Kaneko, K., Rudd, C. E., and Schneider, H. (2006). T Cell Receptor-Interacting Molecule Acts as a Chaperone to Modulate Surface Expression of the CTLA-4 Coreceptor. *Immunity* 25 (5), 807–821. doi:10.1016/j.immuni.2006.08.024

Van Coillie, S., Wiernicki, B., and Xu, J. (2020). Molecular and Cellular Functions of CTLA-4. *Adv. Exp. Med. Biol.* 1248, 7–32. doi:10.1007/978-981-15-3266-5_2

Vermeulen, K., Berneman, Z. N., and Van Bockstaele, D. R. (2003). Cell Cycle and Apoptosis. *Cell Prolif* 36 (3), 165–175. doi:10.1046/j.1365-2184.2003.00267.x

Volonte, D., Kahkonen, B., Shapiro, S., Di, Y., and Galbiati, F. (2009). Caveolin-1 Expression Is Required for the Development of Pulmonary Emphysema through Activation of the ATM-P53-P21 Pathway. *J. Biol. Chem.* 284 (9), 5462–5466. doi:10.1074/jbc.C800225200

von Morgen, P., Lidak, T., Horejsi, Z., and Macurek, L. (2018). Nuclear Localisation of 53BP1 Is Regulated by Phosphorylation of the Nuclear Localisation Signal. *Biol. Cel* 110 (6), 137–146. doi:10.1111/boc.201700067

Wang, J., Yin, L., Zhang, J., Zhang, Y., Zhang, X., Ding, D., et al. (2016). The Profiles of Gamma-H2AX along with ATM/DNA-PKcs Activation in the Lymphocytes and Granulocytes of Rat and Human Blood Exposed to Gamma Rays. *Radiat. Environ. Biophys.* 55 (3), 359–370. doi:10.1007/s00411-016-0653-6

Wang, X.-B., Giscombe, R., Yan, Z., Heiden, T., Xu, D., and Lefvert, A. K. (2002). Expression of CTLA-4 by Human Monocytes. *Scand. J. Immunol.* 55 (1), 53–60. doi:10.1046/j.0300-9475.2001.01019.x

Wang, Y., Liu, Z.-G., Yuan, H., Deng, W., Li, J., Huang, Y., et al. (2019). The Reciprocity between Radiotherapy and Cancer Immunotherapy. *Clin. Cancer Res.* 25 (6), 1709–1717. doi:10.1158/1078-0432.CCR-18-2581

Yakoub, A. M., and Schülke, S. (2019). A Model for Apoptotic-Cell-Mediated Adaptive Immune Evasion via CD80-CTLA-4 Signaling. *Front. Pharmacol.* 10, 562. doi:10.3389/fphar.2019.00562

Yan, Q., Zhu, H., Lan, L., Yi, J., and Yang, J. (2017). Cleavage of Ku80 by Caspase-2 Promotes Non-homologous End Joining-Mediated DNA Repair. *DNA Repair* 60, 18–28. doi:10.1016/j.dnarep.2017.10.001

Yoshimura, A., Seki, M., and Enomoto, T. (2017). The Role of WRNIP1 in Genome Maintenance. *Cell Cycle* 16 (6), 515–521. doi:10.1080/15384101.2017.1282585

Yue, X., Bai, C., Xie, D., Ma, T., and Zhou, P.-K. (2020). DNA-PKcs: A Multi-Faceted Player in DNA Damage Response. *Front. Genet.* 11, 607428. doi:10.3389/fgene.2020.607428

Zager, R. A., and Johnson, A. C. M. (2019). Acute Kidney Injury Induces Dramatic P21 Upregulation via a Novel, Glucocorticoid-Activated, Pathway. *Am. J. Physiology-Renal Physiol.* 316 (4), F674–F681. doi:10.1152/ajprenal.00571.2018

Zhang, T., Penicud, K., Bruhn, C., Loizou, J. I., Kanu, N., Wang, Z.-Q., et al. (2012). Competition between NBS1 and ATMIN Controls ATM Signaling Pathway Choice. *Cel Rep.* 2 (6), 1498–1504. doi:10.1016/j.celrep.2012.11.002

Zhang, X.-P., Liu, F., and Wang, W. (2011). Two-phase Dynamics of P53 in the DNA Damage Response. *Proc. Natl. Acad. Sci.* 108 (22), 8990–8995. doi:10.1073/pnas.1100600108

Zhou, H., Kawamura, K., Yanagihara, H., Kobayashi, J., and Zhang-Akiyama, Q.-M. (2017). NBS1 Is Regulated by Two Kind of Mechanisms: ATM-dependent Complex Formation with MRE11 and RAD50, and Cell Cycle-dependent Degradation of Protein. *J. Radiat. Res.* 58 (4), 487–494. doi:10.1093/jrr/rrx014

Conflict of Interest: The authors declare that the research was conducted in the absence of any commercial or financial relationships that could be construed as a potential conflict of interest.

Publisher's Note: All claims expressed in this article are solely those of the authors and do not necessarily represent those of their affiliated organizations, or those of the publisher, the editors, and the reviewers. Any product that may be evaluated in this article, or claim that may be made by its manufacturer, is not guaranteed or endorsed by the publisher.

Advantages of publishing in Frontiers

OPEN ACCESS
Articles are free to read for greatest visibility and readership

FAST PUBLICATION
Around 90 days from submission to decision

HIGH QUALITY PEER-REVIEW
Rigorous, collaborative, and constructive peer-review

TRANSPARENT PEER-REVIEW
Editors and reviewers acknowledged by name on published articles

Frontiers
Avenue du Tribunal-Fédéral 34
1005 Lausanne | Switzerland

Visit us: www.frontiersin.org
Contact us: frontiersin.org/about/contact

REPRODUCIBILITY OF RESEARCH
Support open data and methods to enhance research reproducibility

DIGITAL PUBLISHING
Articles designed for optimal readership across devices

FOLLOW US
@frontiersin

IMPACT METRICS
Advanced article metrics track visibility across digital media

EXTENSIVE PROMOTION
Marketing and promotion of impactful research

LOOP RESEARCH NETWORK
Our network increases your article's readership